

*University of Split  
Faculty of Electrical Engineering,  
Mechanical Engineering and  
Naval Architecture*



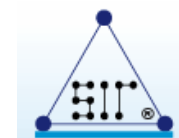
*Slovak Academy of Science  
Institute of Materials and  
Machine Mechanics*



*Sveučilište u Splitu*  
*Sveučilišni*  
*odjel za stručne studije*

Croatian Society for  
Materials and Tribology

**Dublin Institute  
of Technology**

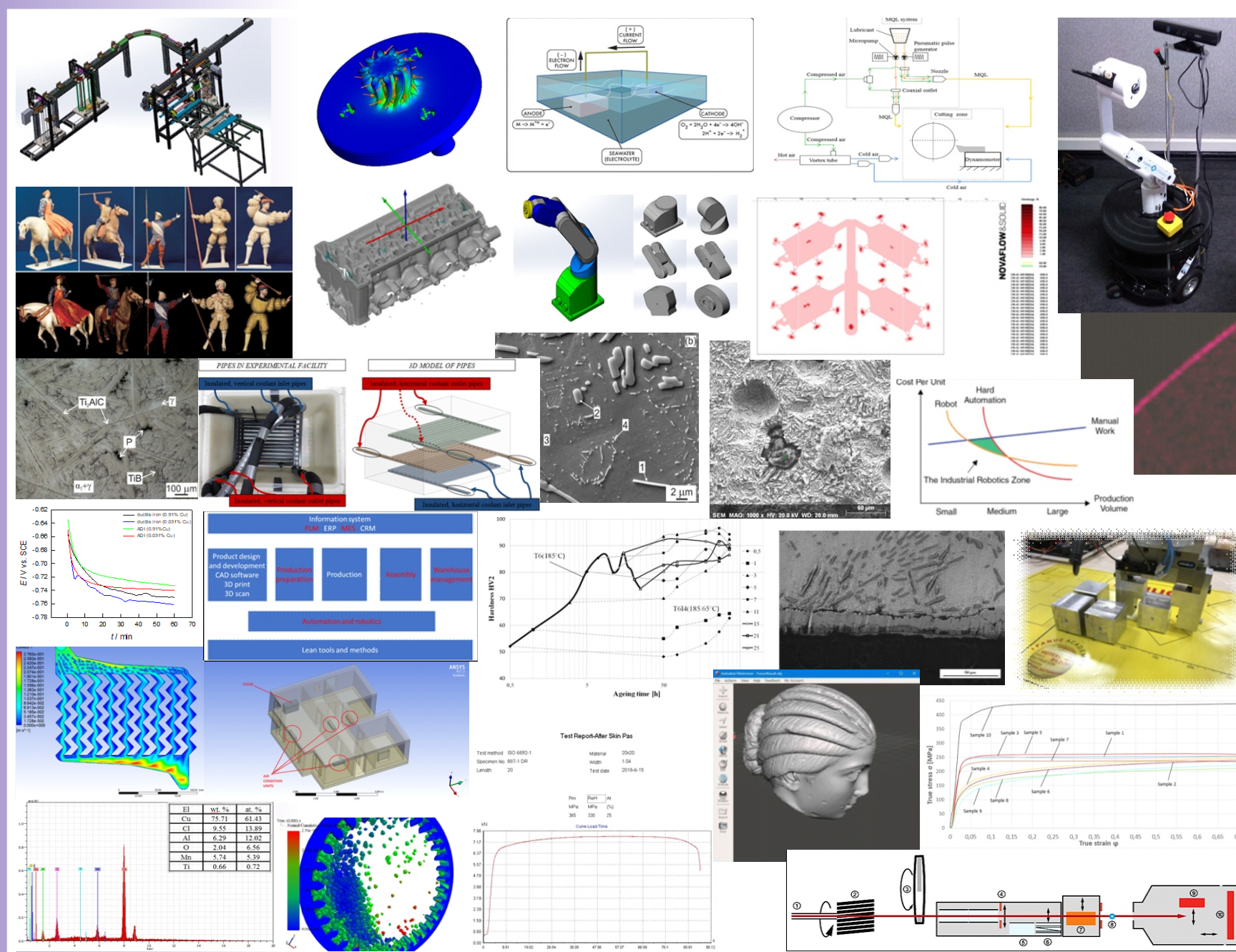


**Rogante Engineering  
Office**

**ISSN 1847-7917**

# *Mechanical Technologies and Structural Materials 2018*

***University of Split - Faculty of Electrical Engineering,  
Mechanical Engineering and Naval Architecture  
The Split - Dalmatia County  
EVN Croatia Plin d.o.o.***



***<http://www.strojarska-tehnologija.hr>***

*September, 27<sup>th</sup> - 28<sup>th</sup>, 2018.*  
*FESB, Ruđera Boškovića 32, Split*

# **CONFERENCE PROCEEDINGS**

ZBORNIK RADOVA

## **MECHANICAL TECHNOLOGIES AND STRUCTURAL MATERIALS**

STROJARSKE TEHNOLOGIJE I KONSTRUKCIJSKI  
MATERIJALI

**Split**

**Croatia / Hrvatska**

27. - 28. September / rujan 2018.

### **ORGANIZED BY / ORGANIZATOR:**

CROATIAN SOCIETY FOR MECHANICAL TECHNOLOGIES, Croatia

HRVATSKO DRUŠTVO ZA STROJARSKE TEHNOLOGIJE, Hrvatska

### **CO-ORGANIZERS / SURGANIZATORI:**

UNIVERSITY OF SPLIT  
FACULTY OF ELECTRICAL ENGINEERING, MECHANICAL ENGINEERING  
AND NAVAL ARCHITECTURE

CROATIAN SOCIETY FOR MATERIALS AND TRIBOLOGY

DUBLIN INSTITUTE OF TECHNOLOGY

SLOVAK ACADEMY OF SCIENCE INSTITUTE OF MATERIALS AND MACHINE  
MECHANICS

ROGANTE ENGINEERING OFFICE

UNIVERSITY OF SPLIT  
UNIVERSITY DEPARTMENT OF PROFESSIONAL STUDIES

**SPONSORS / SPONZORI:**

UNIVERSITY OF SPLIT

SPLIT – DALMATIA COUNTY

EVN CROATIA PLIN d.o.o.

**PUBLISHER / IZDAVAČ:**

CROATIAN SOCIETY FOR MECHANICAL TECHNOLOGIES, Croatia

HRVATSKO DRUŠTVO ZA STROJARSKE TEHNOLOGIJE, Hrvatska

c/o FESB, Ruđera Boškovića 32, 21000 SPLIT

tel.: +385 21 305 910; fax.: +385 21 463 877

e-mail: [info@strojarska-tehnologija.hr](mailto:info@strojarska-tehnologija.hr)

<http://www.strojarska-tehnologija.hr>

**EDITORS / UREDNICI:**

PhD Sonja Jozić, Associate Professor

PhD Nikola Gjeldum, Assistant Professor

ISSN 1847-7917

ISSUE / NAKLADA: 70

**ORGANIZING COMMITTEE:**  
**ORGANIZACIJSKI ODBOR**

- Sonja JOZIĆ (Croatia) - Chairman
- Branimir LELA (Croatia) – Vice Chairman
  
- Ante ALUJEVIĆ (Croatia)
- Ante BAROVIĆ (Croatia)
- Nikša ČATIPOVIĆ (Croatia)
- Zvonimir DADIĆ (Croatia)
- Ivana DUMANIĆ (Croatia)
- Igor GABRIĆ (Croatia)
- Nikola GJELDUM (Croatia)
- Dario ILJKIĆ (Croatia)
- Jure KROLO (Croatia)
- Neven KUZMANIĆ (Croatia)
- Petar LJUMOVIĆ (Croatia)
- Zvonimir MRDULJAŠ (Croatia)
- Stipe PERIŠIĆ (Croatia)
- Slaven ŠITIĆ (Croatia)

**PROGRAMME AND REVIEW COMMITTEE:**  
**PROGRAMSKI I RECENZIJSKI ODBOR**

- Dražen ŽIVKOVIĆ (Croatia) – President
- Dražen BAJIĆ (Croatia) – Vice President
  
- Boris ANZULOVIĆ (Croatia)
- Frane BARBIR (Croatia)
- Franjo CAJNER (Croatia)
- Goran CUKOR (Croatia)
- Vinko IVUŠIĆ (Croatia)
- Zlatko JANKOSKI (Croatia)
- Jaroslav JERZ (Slovakia)
- Sonja JOZIĆ (Croatia)
- David KENNEDY (Ireland)
- Branimir LELA (Croatia)
- Zoran PANDILOV (Macedonia)
- Mladen PERINIĆ (Croatia)
- Massimo ROGANTE (Italy)
- Zdravko SCHAUPERL (Croatia)
- František SIMANČIK (Bratislava)
- Božo SMOLJAN (Croatia)
- Goran ŠIMUNOVIĆ (Croatia)
- Katica ŠIMUNOVIĆ (Croatia)
- Matej VESENJAK (Slovenia)
- Ivica VEŽA (Croatia)



# CONTENT

1. <i>Andrej BAŠIĆ, Marko MLADINEO, Ivan PEKO, Amanda ALJINović</i> 3D SCANNING, CAD OPTIMIZATION AND 3D PRINT APPLICATION IN CULTURAL HERITAGE: AN EXAMPLE ON STATUE FROM THE ANCIENT SALONA	1
2. <i>Denis CHIKURTEV, Milena GRUEVA, Nikolay STOIMENOV</i> METHOD FOR TESTING THE GRINDING MEDIA IN MILLS	7
3. <i>Ivana DUMANIĆ, Sonja JOZIĆ, Dražen BAJIĆ, Mihovil SUČIĆ</i> EXPERIMENTAL INVESTIGATION AND MULTI-OBJECTIVE OPTIMIZATION OF CONTROLLABLE PARAMETERS IN TURNING PROCESS USING TAGUCHI METHOD AND GREY RELATIONAL ANALYSIS	13
4. <i>Andrea GATTO, Paolo MENGUCCI, Massimo ROGANTE, Fabio GRILLI</i> STUDY OF QUALITY AND COMPOSITION OF ZINC ANODES FOR CATHODIC SHIP PROTECTION	23
5. <i>Antonio GEČI, Željko PENG, Gojmir RADICA, Sandro NIŽETIĆ</i> COMPUTATIONAL FLUID DYNAMICS ANALYSIS AND IMPROVEMENT OF MANIFOLD DESIGN FOR PLATE TYPE HEAT EXCHANGERS	33
6. <i>Livio GIULIANI, Massimo ROGANTE, Peter WADHAMS, Barbara ZAVAN</i> RESEARCH ON ELECTROMAGNETIC FIELD (EMF) AND RELATED BIOLOGICAL HAZARDS: STATE-OF-THE-ART	45
7. <i>Stanislav GYOSHEV, Stefan KARASTANEV, Bogomil POPOV</i> ICT FOR 3D MODELING AND 3D TACTILE VISUALIZATION OF SITES OF CULTURAL AND HISTORICAL HERITAGE	53
8. <i>Ivo FABJANAC, Željko PENG, Gojmir RADICA, Sandro NIŽETIĆ</i> COMPUTATIONAL FLUID DYNAMICS ANALYSIS AND OPTIMIZATION OF RESIDENTIAL BUILDING AIR CONDITIONING	57
9. <i>Dario ILJKIĆ, Luciano GRŽINIĆ, Goran VRATOVIĆ</i> AKTIVACIJA AUSTENITNOG NEHRĐAJUĆEG ČELIKA ZA POSTUPAK BESTRUJNOGA NANOŠENJA NI-P PREVLAKA	71
10. <i>Sonja JOZIĆ, Dražen BAJIĆ, Ivana DUMANIĆ, Marko KODŽOMAN</i> OPTIMIZATION OF HIGH PRESSURE DIE CASTING PROCESS USING TAGUCHI METHOD AND COMPUTER AIDED CASTING SIMULATION TECHNIQUE	77

<b>11. Mišo JURČEVIĆ, Željko PENG, Branko KLARIN, Sandro NIŽETIĆ</b> NUMERICAL ANALYSIS AND EXPERIMENTAL VALIDATION OF TRANSIENT HEAT TRANSFER DURING SOLIDIFICATION/ MELTING INSIDE AN INSULATED TANK	83
<b>12. Mate JURJEVIĆ, Žarko KOBOEVIĆ, Nikša KOBOEVIĆ, Nino STORELLI</b> ADVANTAGES OF THE INTERMEDIATE SHAFT MADE OF COMPOSITE MATERIAL COMPARED TO STEEL	95
<b>13. Kateryna KAMYSHNYKOVA, Juraj LAPIN</b> PROCESSING AND PROPERTIES OF IN-SITU TIAL-BASED MATRIX COMPOSITE REINFORCED WITH CARBIDE PHASE PARTICLES	101
<b>14. Stefan KARASTANEV</b> RENOVATING OF USED INDUSTRIAL ROBOTS FOR NEW PURPOSES	107
<b>15. Jure KROLO, Branimir LELA Domagoj KOJUNDŽIĆ, Jelena ŠERIĆ</b> COMPRESSIVE FLOW STRESS AND HARDNESS DETERMINATION FOR COMPOSITES BASED ON ALUMINUM WASTE	111
<b>16. Duško LUKAČ</b> COMPUTER SIMULATIONS OF ROBOT INTEGRATED PRODUCTION PROCESSES WITH KUKA SIM PRO	119
<b>17. Mauro MARETIĆ, Luciano GRŽINIĆ, Goran VRATOVIĆ</b> PVD TECHNOLOGY	125
<b>18. Ratko MIMICA</b> HARDNESS VERSUS TIME DEPENDENCY DURING ARTIFICIAL AND INTERRUPTED AGEING OF ALMGSI0.5 ALUMINIUM ALLOY	133
<b>19. Anja MUJKANOVIĆ, Duško PAVLETIĆ, Graciela ŠTERPIN VALIĆ, Maja FOREMPOHER ŠKUVER</b> INVERSE MEASUREMENT METHOD FOR INTAKE AND EXHAUST MANIFOLD OF CYLINDER HEAD	141
<b>20. Peter PANEV</b> DEVELOPMENT OF AUTOMATIC PACKING LINE FOR SINGLE PACKS	149
<b>21. Miglena PANEVA</b> RESEARCH OF MECHANICAL CHARACTERISTICS IN TENSILE TESTS OF LOW CARBON STEEL SAMPLES DURING TRANSFORMATION FROM HOT ROLLED TO COLD ROLLED SHEET METAL	153

<b>22. Massimo ROGANTE, Vasily T. LEBEDEV, Aurel RADULESCU</b> SANS CHARACTERIZATION OF MONO-ETHYLENE-GLYCOL BASED INDUSTRIAL POLYURETHANES SAMPLES	159
<b>23. Goran SALOPEK, Marko DUNĐER, Mladen PERINIĆ, David IŠTOKOVIĆ, Zoran JURKOVIĆ, Maja MARKOVIĆ</b> ADVANTAGES OF ADDITIVE MANUFACTURING IN PRODUCTION OF GEARS FOR PLANETARY REDUCERS	167
<b>24. Nikolay STOIMENOV, Nikola SABOTINKOV, Bogomil POPOV</b> INVESTIGATION OF MATERIALS BEHAVIOR IN AUTOGENOUS GRINDING MILL	173
<b>25. Željko STOJKIĆ, Igor BOŠNJAK</b> CONCEPT OF LEARNING FACTORY AT FSRE	177
<b>26. Michaela ŠTAMBORSKÁ, Juraj LAPIN, Alena KLIMOVÁ, Tatiana PELACHOVÁ, Oto BAJANA</b> USING THE 3-POINT BENDING METHOD TO STUDY FRACTURE BEHAVIOUR OF CAST IN-SITU TIAL MATRIX COMPOSITE	183
<b>27. Amra TALIC-ČIKMIŠ, Fuad HADŽIKADUNIĆ, Malik ČABARAVDIĆ, Kenan VARDA</b> OFFLINE NUMERICAL SIMULATION OF 2AJ-RV ROBOT KINEMATIC MECHANISM CAD MODEL USING LABVIEW AND SOLIDWORKS	189
<b>28. Ladislav VRSALOVIĆ, Radosna JERČIĆ, Senka GUDIĆ, Ivana IVANIĆ, Stjepan KOŽUH, Borut KOSEC, Milan BIZJAK, Mirko GOJIĆ</b> THE INFLUENCE OF PH AND ELECTROLYTE TEMPERATURE ON CORROSION BEHAVIOUR OF CuAlMnTi ALLOY RIBBONS IN NaCl SOLUTION	193
<b>29. Ladislav VRSALOVIĆ, Nikša ČATIPOVIĆ, Dražen ŽIVKOVIĆ, Zvonimir DADIĆ, Stjepan KOŽUH, Mirko GOJIĆ, Josip BATINOVIĆ</b> THE INFLUENCE OF COPPER CONTENT ON CORROSION BEHAVIOR OF DUCTILE IRON AND AUSTEMPERED DUCTILE IRON	199

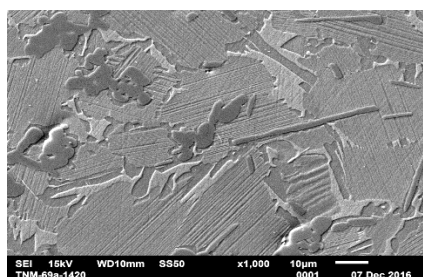
# Design, processing and properties of cast TiAl + Ti<sub>3</sub>Al matrix in-situ composites reinforced with MAX phase particles

Juraj Lapin, Alena Klimová

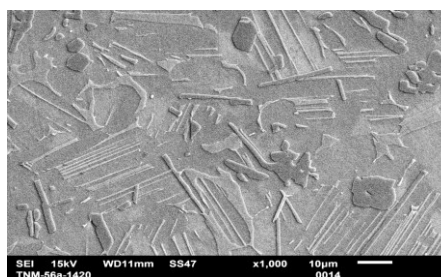
E-mail: [juraj.lapin@savba.sk](mailto:juraj.lapin@savba.sk)

Titanium aluminides are attractive materials for high-temperature structural applications providing a unique set of physical and mechanical properties for the automotive engines, stationary gas turbines and aircraft engines. However, inherent poor ductility at room temperature and insufficient strength at high temperatures (above 800 °C) limit their wide-scale applications. Intermetallic matrix composites may improve the deficiency of these lightweight alloys at high temperatures because of good combination of the properties of intermetallic matrix and reinforcement. Among various ceramic reinforcements, ternary MAX phases with the general formula of  $M_{n+1}AX_n$  ( $n = 1, 2, 3$ ) such as Ti<sub>2</sub>AlC and Ti<sub>2</sub>AlN shows a significant role in toughening and reinforcing of  $\gamma$ (TiAl) +  $\alpha_2$ (Ti<sub>3</sub>Al) matrix composites. These ternary MAX phases belong to a new type of machinable ceramics, which are formed in-situ during solidification and solid phase transformation processes.

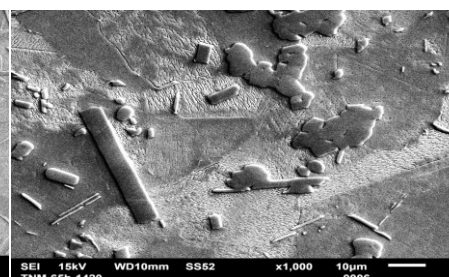
Cast in-situ  $\gamma$  +  $\alpha_2$  matrix composites reinforced with MAX phase particles were prepared by vacuum induction melting and solidification in graphite crucibles. Microstructure characterisation of the as-solidified samples was carried out by optical microscopy (OM), scanning electron microscopy (SEM), X-ray diffraction analysis (XRD), energy dispersive spectroscopy (EDS) and quantitative image analysis. Chemical composition of primary MAX phase particles can be influenced by alloying of master Ti–Al–Mo–B alloy with niobium, carbon and nitrogen. The analysis of chemical composition showed that niobium substitutes partially for titanium in primary (Ti,Nb)<sub>2</sub>AlC particles. Alloying by nitrogen hinders niobium atoms to substitute for titanium in Ti<sub>2</sub>AlN particles. The effect of solute atom redistribution on nanohardness and elastic modulus of MAX phase particles and matrix is reported.



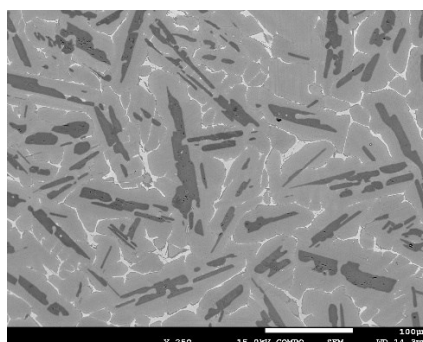
Ti-38Al-8Nb-0.8Mo-3.6C



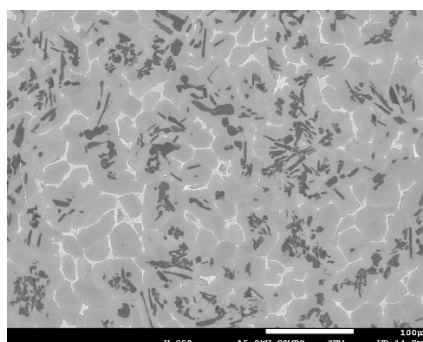
Ti-42Al-8Nb-0.8Mo-3.6C



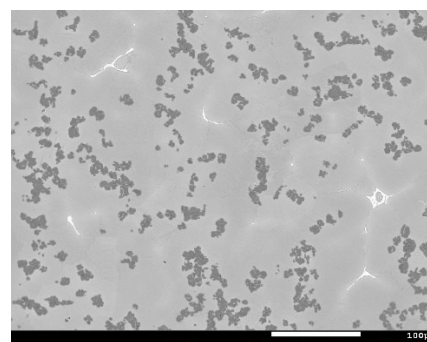
Ti-45Al-8Nb-0.8Mo-3.6C



Ti-38Al-4Nb-1Mo-5C-0.1N



Ti-38Al-4Nb-1Mo-2.5C-2N



Ti-38Al-4Nb-1Mo-0.3C-5N

## Division of Properties of Materials and Structures

Institute of Materials and Machine Mechanics, Slovak Academy of Sciences

Dúbravská cesta 9, 845 13 Bratislava, Slovak Republic

Head of the Division: Ing. Juraj Lapin, DrSc.



# 3D Scanning, CAD Optimization and 3D Print Application in Cultural Heritage: An Example on Statue from the Ancient Salona

Andrej BAŠIĆ<sup>1)</sup>, Marko MLADINEO<sup>1)</sup>,  
Ivan PEKO<sup>1)</sup> and Amanda ALJINOVIC<sup>1)</sup>

1) University of Split, Faculty of Electrical Engineering, Mechanical Engineering and Naval Architecture, Department for Production Engineering  
Sveučilište u Splitu, Fakultet elektrotehnike, strojarstva i brodogradnje, R. Boskovicova 32, 21 000 Split, Croatia

[andrej@fesb.hr](mailto:andrej@fesb.hr)

[marko.mladineo@fesb.hr](mailto:marko.mladineo@fesb.hr)

[ipeko@fesb.hr](mailto:ipeko@fesb.hr)

[Amanda.Aljinovic@fesb.hr](mailto:Amanda.Aljinovic@fesb.hr)

## Keywords

3D Scanning  
Fused Deposition Modeling  
Reversible Engineering  
Model Optimization  
Cultural Heritage

## Ključne riječi

3D Skeniranje  
Taložno očvršćivanje materijala  
Reverzibilni inženjering  
Optimizacija modela  
Kulturna baština

*Professional paper*

**Abstract:** Modern technologies applied in industry and manufacturing can also be very useful in the preservation and popularization of cultural heritage. Some of the monuments or sculptures can be time-consuming for the academic sculptor to produce a true copy. Today, the process of reversible engineering can be applied, which is a significantly faster process and also more cost effective. In this paper, the application of reversible engineering is presented on the example of important historical heritage from the ancient Salona dated to the 2nd century.

*Stručni rad*

**Sažetak:** Suvremene tehnologije primijenjene u industriji i proizvodnji također mogu biti vrlo korisne u očuvanju i popularizaciji kulturne baštine. Neki od spomenika ili skulptura mogu od akademskog kipara zahtijevati dosta vremena da se stvori istinska replika. Danas možemo primijeniti proces reverzibilnog inženjeringa koji je ujedno znatno brži i isplativiji postupak. U ovom radu primjena reverzibilnog inženjeringa predstavljena je na primjeru važne povijesne baštine iz drevne Salone iz 2. stoljeća.

## 1. Introduction

The technology of 3D print was developed by the Massachusetts Institute of Technology (MIT) in USA where terms 3D printer and 3D printing were coined [1]. 3D printing can be defined as a manufacturing of 3D products from various materials using from digital files [2]. Today, various techniques of 3D printing can be used, such as: Stereolithography – SLA; Selective Laser Sintering – SLS; Fused Deposition Modeling – FDM; Laminated Object Manufacturing – LOM; Polyjet; Electron Beam Modeling – EBM, and Solid Ground Curing – SGC [3, 4, 5]. Very widely used and very cost effective is FDM, which uses wire shape plastomers which are heated and extruded through nozzle (controlled by a computer which dimensions read as coordinates) layer by layer thus forming the 3D shape [5, 6]. FDM printers use two different materials, one for modeling and one as support. FDM has several advantages, such as less energy consumption, it does not use the laser beam, no special demands for cooling and ventilation, small maintenance costs, several prototypes

can be manufactured at once. On the other hand, the limitation is the limited number of materials that can be used for production; the lines between layers are visible, etc. [7, 8, and 9].

Materials that are usually used in FDM are polylactide (PLA), acrylonitrile butadiene styrene (ABS), Polyetylenetefestalat – polyester (PETG), Nylon, and others [10, 11, 12, and 13].

Although any designed model can be printed, in cultural heritage application, usually 3D printing preceded 3D scanning and CAD optimization. A 3D scanner is a device used for scanning an object or environment by collecting data about its dimensions and outer appearance (such as texture or color) [14, 15]. Thus collected data is used for building 3D objects. 3D laser scanners have high precision and using the tools for reverse engineering 3D model can be obtained relatively fast.

Building the prototype has several steps: computed product construction (design) or 3D scanning of the real object; transferring CAD model to STL file; preparation

for printing; printing of model; and final processing of printed model.

After designing or scanning of the object, the STL file of a model can be edited in several program packages such as Zprint™ or Autodesk® Meshmixer™ [16, 17]. Using these methodologies the manufacturing lasts from two to three days, which is drastically shorter than the classical approach.

Thus, reverse engineering has found its application also in cultural heritage preservation and popularization, especially taking into consideration that it is an undestructive method.

## 2. Materials and methods

The sculpture (head) known as the "Girl from Salona" or Plautila (Figure 1) is dated to 2nd century AD, and the scanning was ordered by the museum "Dom kulture Zvonimir" in Solin, Croatia [18]. The head was scanned in situ using DAVID SLS-3 3D Scanner [19] (Figure 2, 3 and 4).



Figure 1. "Girl from Salona" or Plautila

The model was exported to STL file, but it needed optimization before printing as 3D model had more than million dots (3 million triangles). The number of dots resulted in a file larger than 700 MB which was not suitable for 3D printing. Thus CAD optimization was used to reduce unnecessary detail that will not be visible

on the replica and to turn the models into simpler models for 3D print. Also, models need to be optimized to remove the irregularities made by 3D scanner and removal of generic irregularities of the model (scans cannot lap perfectly which produces irregularities on model), and all of that to improve the process of 3D printing.

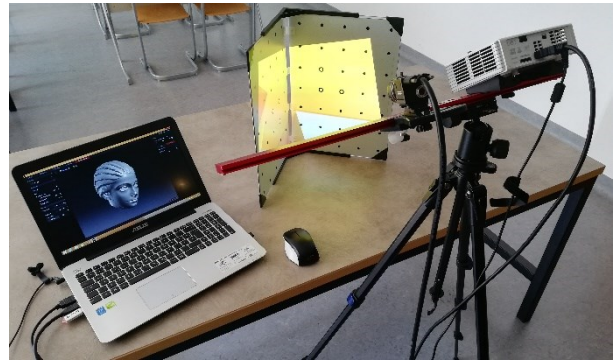


Figure 2. DAVID SLS-3 3D Scanner

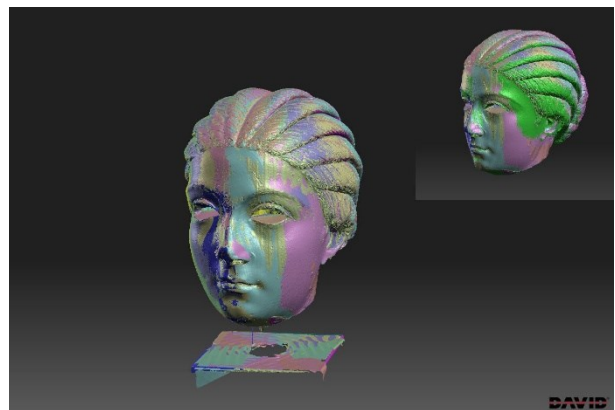


Figure 3. Scanned model of the sculpture

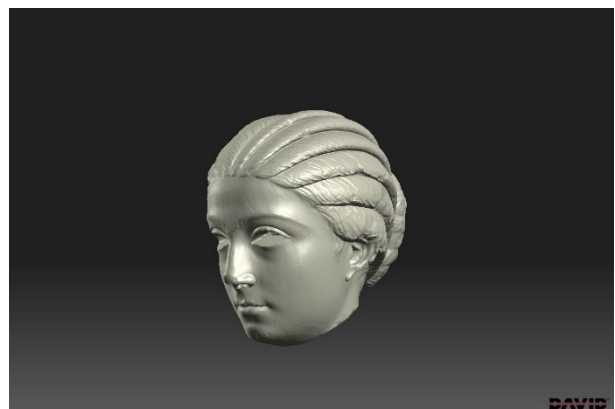


Figure 4. Scanned model of the sculpture after fusion the texture and silhouettes

The model was post-processed using software Autodesk® Meshmixer™ using various options [17]. First, the

number of dots was optimized that object contained using tool Reduce. The reduction of the number of dots by 90 % reduced the total number of dots to 150,000. In the other step, the tool Smoother was used to remove the irregularities from specific surface parts using different parameters from this tool. Additionally, other tools were used when needed, such as Draw (to fulfill the empty places on the object), Flatten (to remove bulges from object) and Drag (to create bulges on the object). Also, option Analysis was used to analyze object characteristics (holes, dimensions, thickness, stability) as well as Overhangs (which detects parts of an object that would need support during printing).

The model was printed on 3D printer CubePro Duo [20] (Figure 5) and afterward manually treated for final finish to remove irregularities caused by the printing process.



Figure 5. 3D printer CubePro Duo

### 3. Results

The 3D model of the scanned head before optimization is shown in figure 6. The optimization of the number of dots that object contained using tool Reduce revealed that the model had sufficient quality for 3D print (Figure 7). The difference in model quality before and after the application of tool Reduce on Autodesk® Meshmixer™ (Figure 8 and 9). The result of the 3D print final product is shown in Figure 10.

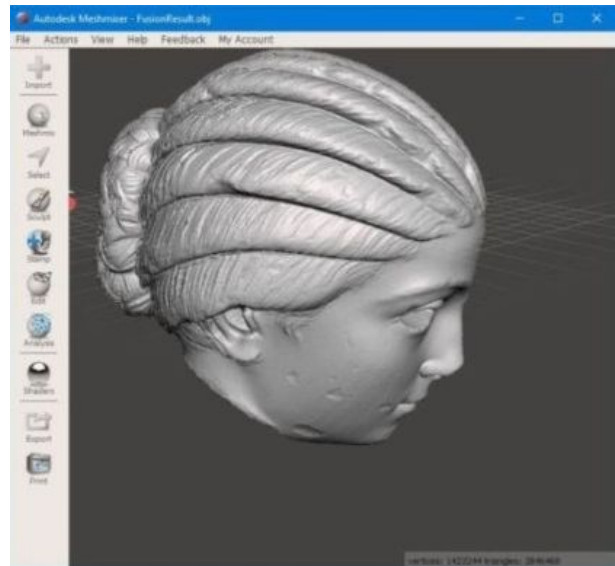


Figure 6. Model of the scanned head before optimization

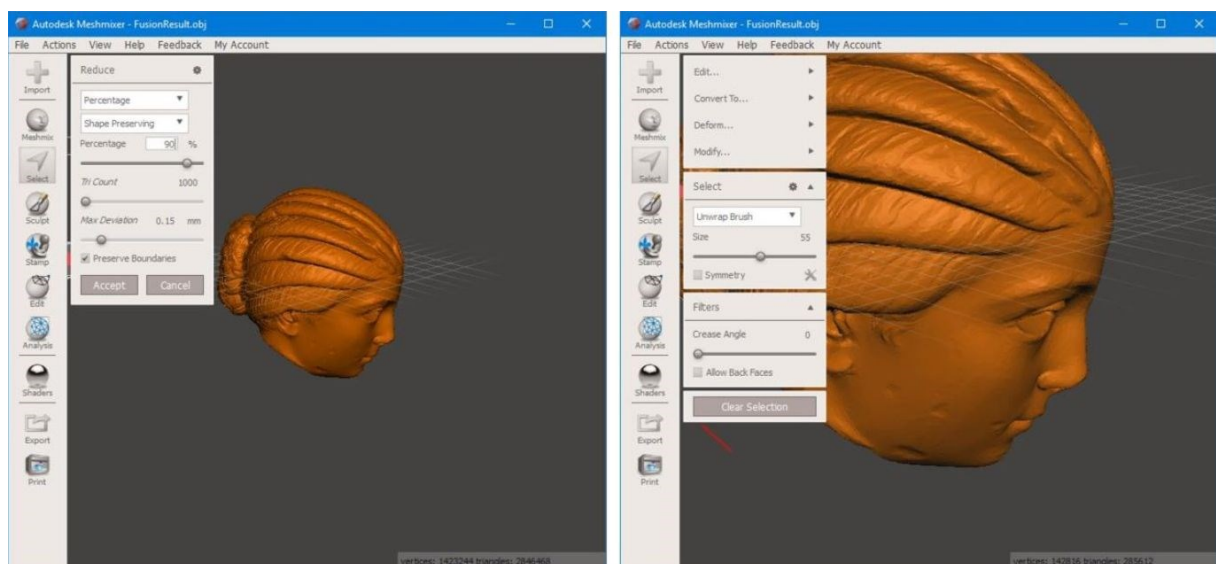


Figure 7. Optimization of the number of dots



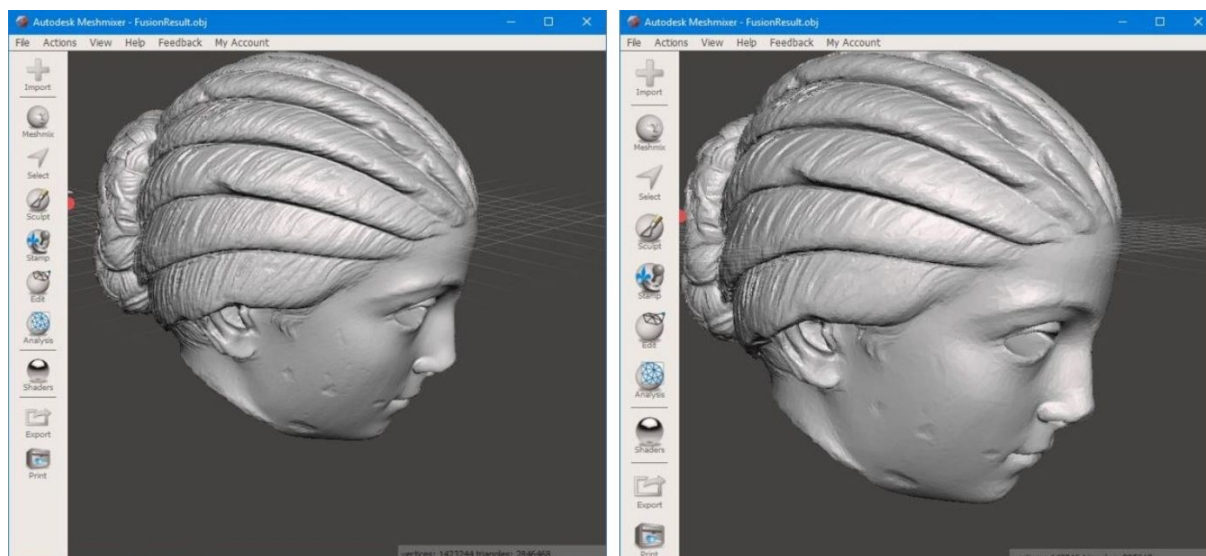


Figure 8. 3D model with 1.5 mil. dots (left), and 3D model with 150 000 dots (right)

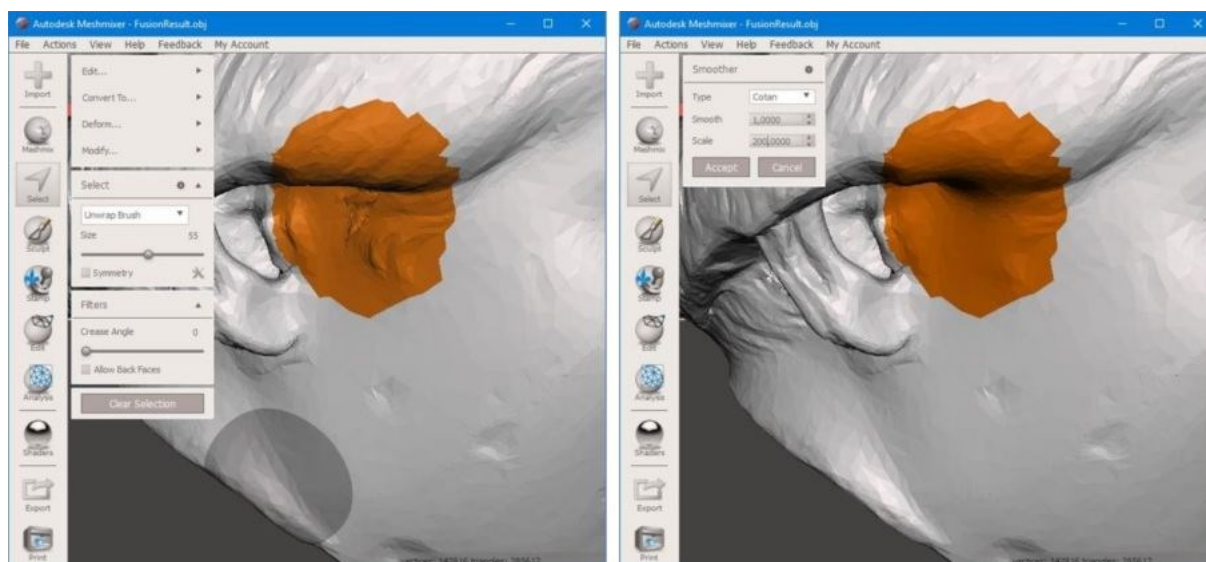


Figure 9. Smoothing the surface of the model that contains significant irregularities

After manually treatment the 3D printed model and removing the irregularities the model of the head was used to produce the molds which were done by the "Dom kulture Zvonimir" in Solin (Figures 11 and 12).

#### 4. Discussion and conclusion

Use of 3D scanner, optimization of the model with Autodesk<sup>®</sup> Meshmixer<sup>™</sup> and 3D printing revealed that this approach presents a complete solution for optimization of 3D models. The advantage of the freeware Autodesk<sup>®</sup> Meshmixer<sup>™</sup> is its compatibility with most of the 3D printers which enable the printing

from that software. The approach of 3D scanning, optimization and 3D printing in for cultural heritage purposes showed that the principles used in manufacturing can be transferred to other fields, in this case, preservation and presentation of cultural heritage. The project resulted in the successful production of souvenirs and the two of the souvenirs made by additive technology are presented in Figures 13 and 14. These souvenirs help museum to earn funds which are absolutely needed for the preservation of the cultural heritage. Since the whole process of the souvenir development was low-cost, it represents a sustainable solution for the commercial activities of the museums.





**Figure 10.** 3D printed model that need to be manually treated for final finish to remove irregularities



**Figure 11.** Molds made out of 3D model (courtesy of museum "Dom kulture Zvonimir" in Solin)



**Figure 12.** Souvenirs made out of plaster (courtesy of museum "Dom kulture Zvonimir" in Solin)



**Figure 13.** Magnet of head the "Girl from Salona" (courtesy of museum "Dom kulture Zvonimir" in Solin)



**Figure 14.** Statue of the head the "Girl from Salona" (courtesy of museum "Dom kulture Zvonimir" in Solin)

## REFERENCES

- [1] Sachs, E., Cima, M., Brancazio, D., Curodeau, A., & Shalon, T., (1990), *Three Dimensional Printing. Rapid Fabrication of Molds for Casting*. Advances in Integrated Product Design.
- [2] Gebhardt, A., (2012), *Understanding additive manufacturing: rapid prototyping-rapid tooling-rapid manufacturing*. Carl Hanser Verlag GmbH Co KG.
- [3] Grimm, T., (2004), *User's guide to rapid prototyping*. Society of Manufacturing Engineers.
- [4] Jacobs, P. F., (1992), *Rapid prototyping & manufacturing: fundamentals of stereolithography*. Society of Manufacturing Engineers.

- [5] Wong, K. V., & Hernandez, A., (2012), *A review of additive manufacturing*. ISRN Mechanical Engineering, 2012.
- [6] Zein, I., Hutmacher, D. W., Tan, K. C., & Teoh, S. H., (2002), *Fused deposition modeling of novel scaffold architectures for tissue engineering applications*. Biomaterials, 23(4), 1169-1185.
- [7] Mohamed, O. A., Masood, S. H., & Bhowmik, J. L., (2015), *Optimization of fused deposition modeling process parameters: a review of current research and future prospects*. Advances in Manufacturing, 3(1), 42-53.
- [8] Peko, I., Krolo, J., Bagavac, P., Đurić, S., Kostić, N., & Bašić, A., (2017), *Modeling and Optimization of Tensile Strength of ABS Parts Manufactured by the Fused Deposition Modeling Process*. In International conference "Mechanical Technologies and Structural Materials".
- [9] Grimm, T., (2003), *Fused deposition modeling: a technology evaluation*. Time-compression technologies, 11(2), 1-6.
- [10] Novakova-Marcincinova, L., & Kuric, I., (2012), *Basic and advanced materials for fused deposition modeling rapid prototyping technology*. Manuf. and Ind. Eng, 11(1), 24-27.
- [11] Singh, R., & Singh, S., (2014), *Development of nylon based FDM filament for rapid tooling application*. Journal of The Institution of Engineers (India): Series C, 95(2), 103-108.
- [12] El-Farahaty, K. A., Sadik, A. M., & Hezma, A. M., (2007), *Study of Optical and Structure Properties of Polyester (PET) and Copolyester (PETG) Fibers by Interferometry*. International Journal of Polymeric Materials, 56(7), 715-728.
- [13] Novakova-Marcincinova, L., & Novak-Marcincin, J., (2013), *Verification of mechanical properties of abs materials used in FDM rapid prototyping technology*. Proceedings in manufacturing systems, 8(2), 87-92.
- [14] [https://www8.hp.com/us/en/campaign/3Dscanner/overview.html?jumpid=va\\_t1345uf8k6](https://www8.hp.com/us/en/campaign/3Dscanner/overview.html?jumpid=va_t1345uf8k6) [accessed 26.8.2018]
- [15] Boehler, W., & Marbs, A., (2002), *3D scanning instruments*. Proceedings of the CIPA WG, 6, 9-18.
- [16] <https://www.3dsystems.com/software/3d-sprint> [accessed 26.8.2018]
- [17] <http://www.meshmixer.com/> [accessed 26.8.2018]
- [18] Buzov, M., (2009), *Plautilla, sudbina jedne princeze*. Archaeologia Adriatica, 2(2), 473-488.
- [19] [https://www8.hp.com/us/en/campaign/3Dscanner/overview.html?jumpid=va\\_t1345uf8k6](https://www8.hp.com/us/en/campaign/3Dscanner/overview.html?jumpid=va_t1345uf8k6) [accessed 26.8.2018]
- [20] <https://www.3dsystems.com/shop/support/cubepro/videos> [accessed 26.8.2018]

# Method for testing the grinding media in mills

**Denis CHIKURTEV<sup>1)</sup>, Milena GRUEVA<sup>1)</sup> and Nikolay STOIMENOV<sup>1)</sup>**

1) Institute of Information and Communication Technologies – Bulgarian Academy of Sciences,  
bl. 2, ac. G. Bonchev str, 1113 Sofia,  
**Bulgaria**

[dchikurtev@gmail.com](mailto:dchikurtev@gmail.com)

[nikistoimenov@gmail.com](mailto:nikistoimenov@gmail.com)

## Keywords

*Ball Mills*

*Lifters*

*Mobile Robot*

*Robotic Arm Manipulator*

*3D Scanning and Modeling*

## Early information

**Abstract:** This article describes a method for studying the wear of lifters in mills. In order to perform this study, it is necessary to make a 3D model of lifters using a 3D scanner. After that, it is necessary to compare it with the original 3D model with the new one. Due to the unfavourable and dangerous environment in the mills, it is advisable to avoid accessing people in them. Because of these prerequisites, the purpose of this study is to achieve remote capture of lifters through a robot and 3D scanner. The requirements for the robot's parameters and characteristics, as well as the necessary properties of the 3D scanner, are described. Methods are explored for remotely controlling the robot and the 3D scanner as well as for transmitting the captured data of the 3D models to a remote device.

## 1. Introduction

In modern production conditions, ball mills are a broad class of machines designed for grinding, grinding and / or mixing materials, using metal or other spherical bodies, the so-called working grinding media. Constructively, the ball mill is a relatively simple device with a simple construction, but unlike the construction, it has the complexity of the work process.

The ball mill is a cylindrical vessel mounted on a foundation that allows rotary movement of the drum by propulsion from an electric motor with a corresponding transmission. Grinding and crushing of materials occurs most often in ball mills. The most common ball mills are semi-autogenous or autogenous.

Most often, these mills are used for ore extraction, crushing and grinding processes. Crushing and milling is done with the help of grinding bodies and lifts (cladding slabs), which are also subjected to aggressive working environment besides the grinding bodies themselves. This process is extremely energy-intensive (around 20% of the world's energy is used for this process). For this reason, it is highly explored. Of great importance is the proper functioning of the mill, grinding bodies, lifts, speeds and other factors to achieve good work and high productivity [1-3].

The purpose of this article is to investigate a method for creating a 3D model of grinding media in ball mills. In this way, we can study the wear and tear of the grinding environment and the lifts. The algorithm for scanning and comparison of the made model with the original was created for realization of the study. Such a method will improve the measurement of wear lifters will shorten the process of measuring wear and will contribute to

improving the construction of the mills by showing vulnerabilities.

The research method involves the use of a mobile robot equipped with a robotic manipulator and a laser scanner or 3D sensor. The robot will be placed in the mill, and then the mill is scanned. Upon receipt of a 3D model from a robot, this model is compared to a cad model of the mill in its original form. The article describes some peculiarities in track mobile platforms. The parameters and capabilities of 3D sensors are set out, communication and management criteria are presented. Finally, an algorithm for implementing the procedure is presented.

## 2. Service mobile robot and robotic arm manipulator

### 2.1. Mobile robot

Serving robots are used in various areas of industry and people's everyday lives. In this case, we will present the application to track mobile platform for work in mills. Regarding the robotic manipulator mounted on the mobile platform, it must have sufficient degrees of freedom to scan the whole mill.

Given the nature and peculiarities of the environment in which the robot moves, we use a tracked mobile platform. Tracked mobile robot can be viewed as a special case of a wheeled robot with differential drive. In fact, the only difference is better manoeuvrability of the track robot on uneven terrain and greater cornering friction due to multiple contact points of the chains with the surface. This type of control is easy to implement and allows good positioning [4].



Driving straight, forward:  $v_L = v_R$ ,  $v_L > 0$

Driving in a right curve:  $v_L > v_R$ , e.g.  $v_L = 2 \cdot v_R$

Turning on the spot, counter-clockwise:  $v_L = -v_R$ ,  $v_L > 0$

The mobile platform of the robot is controlled by wireless joystick. The receiver of the joystick is connected to the robot's computer and the data does not go through web-sockets. The robot's computer receives the data through the USB port.

## 2.2. Robotic arm manipulator

At the end, effector of the robotic manipulator is placed the 3D scanner. A robotic arm manipulator will perform pre-calculated trajectories to scan the entire surface of the mill. An operator that sets the desired position by means of buttons performs manipulator control. An important condition is that the movement of the handle is smooth, with no sudden displacements and constant speed. In addition, the manipulator must be able to preserve its position in the scanning process. This guarantees qualitative scanning. We are using the robotic manipulator Mover4 shown in fig. 1.

The MOVER 4 robot of Commonplace Robotics GmbH [5] has four degrees of freedom and has a planar kinematic structure. Figure 1 is the robot scheme and in Table 1 are the kinematics parameter values. Three of the degrees of mobility provide the positioning, and the fourth orientates the end effector (EE) relative to the Z-axis of the coordinate system associated with the base of the robot. The coordinates of any point in the kinematic chain, and in particular the EE, can be derived from geometric considerations. In this case, a specialized language is used to describe the OKC [6].

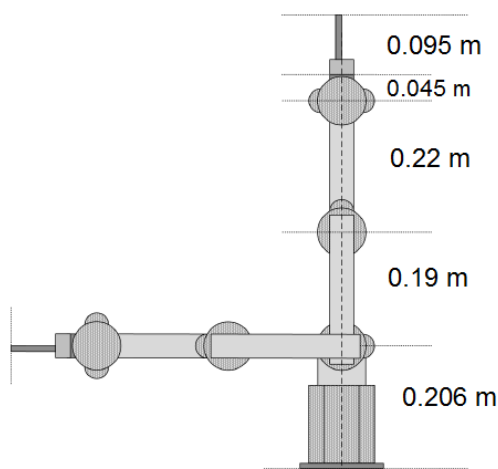


Figure 1. Robot Mover4

Description of the MOVER 4

RDq1(-150,150), RAD(90), TS(S1);

RDq2(-50,65), TA(L2);

RDq3(-110,140), TA(L3);

RDq4(-140,135), TA(L4);

The generated equations for the (X,Y,Z)-coordinates of the EE are [8]:

$$X = \cos(q_1) \cdot (\cos(q_2) \cdot L_2 + \cos(q_2 + q_3) \cdot L_3 + \cos(q_2 + q_3 + q_4) \cdot L_4)$$

$$Y = \sin(q_1) \cdot (\cos(q_2) \cdot L_2 + \cos(q_2 + q_3) \cdot L_3 + \cos(q_2 + q_3 + q_4) \cdot L_4)$$

$$Z = S_1 + \sin(q_2) \cdot L_2 + \sin(q_2 + q_3) \cdot L_3 + \sin(q_2 + q_3 + q_4) \cdot L_4$$

Table 1. Kinematic parameters

Joint number	Constraints	Length	Twist angle	Offset
<b>n</b>	<b><math>\theta_n</math> [DEG]</b>	<b><math>L_n</math> [m]</b>	<b><math>\alpha_n</math> [DEG]</b>	<b><math>S_n</math> [m]</b>
1	-150,150	0	90	0.206
2	-50,65	0.19	0	0
3	-110,140	0.22	0	0
4	-140,135	0.095	0	0

## 3. Scanning method and algorithm

### 3.1. Scanning method

Scanning will be performed by using the application Skanect. It is specialized software for scanning and creating 3D models of objects, people or premises. Given the ability to scan rooms makes it convenient to capture the mills, since the dimensions are roughly the same. In addition, the app maintains a number of 3D sensors, allowing choosing the most appropriate case or preference.

The supported 3D sensors are:

- Structure sensor [8]
- Microsoft Kinect (Windows & Xbox) [9]
- Asus Xtion & PrimeSense Carmine [10]

To get the best possible details of the 3D model, you need to use a computer with a powerful video controller. The application developers give this requirement. As higher, is the frame rate during scanning as better and detailed is the 3D model. The process of scanning requires scanning of the entire surface (area) of the room. When we are done, the app processes the collected scan data and generates a 3D model. In addition, there are built-in options and tools to process the 3D model.

### 3.2. Scanning algorithm

Proper robotic movement is essential to the quality of the 3D model. Due to the complexity of the scanning process, an algorithm for optimal performance of the task is applied. The robot moves forward and backward in the mill, and the manipulator responds to position and move the 3D sensor.

If necessary, the operator can take a turn on the mobile platform. Scanning will be done in layers, with one layer being equal to that of the mill, and its width depends on the parameters of the 3D sensor. After one layer has been captured (the robot moves from one end of the mill to the



other), the manipulator rotates the 3D sensor to a next layer scan position, and the robot returns to the starting position. This procedure is repeated until a complete scan of the entire mill (fig. 3).

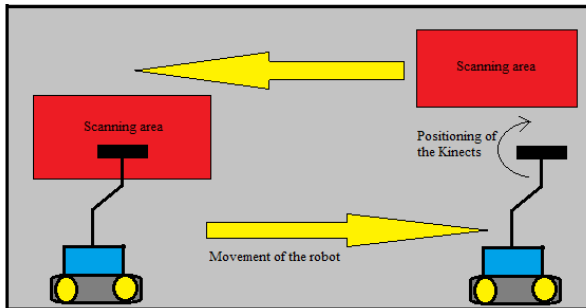


Figure 2. Scanning procedure in the mill

Data from the Skanect application is transmitted to the operator's computer. He monitors the process of building the 3D model of the environment. Its role is to move the robot from one end of the mill to the other. The positioning of the 3D sensor for the next layer is performed semi-automatically. When changing the position, the operator sends a command with buttons for a previous position, next position or starting position. In order to automate the entire process, the mobile platform should be moved automatically as well as the robotic manipulator. The robot can move independently forward and backward, in a final position automatically positions the robotic manipulator.

#### 4. Communication and user interface

The communication between the service robot and the operator is a important issue. It determines how fast he will adapt to the system and starts using its full potential. That is why we created user interface for controlling the robot. With this interface the control, setup and communication with the robot could be done via any decent device with a web browser – smartphone, tablet, laptop or a personal computer. This type of interface allowed us to reduce costs for hardware to their minimum, because this interface was hosted on the already existent computer in the robot.

For the interface we used the Python based web framework – Django. We implemented two sided video and audio communication in real time via the WebRTC library, which is already supported in most of the modern web browsers. The interface also provides access to all parameters of our robot assistant system and saves any modification of them, which makes personalization and tuning of the robot a very pleasant and user-friendly task. There is also a virtual joystick for controlling the position of the robot and live video stream from its camera. In addition, the status of the platform is shown on the interface. We made special buttons for voice synthetizing

of important to our person information, like the weather or the current time [11].

In manual mode, the user sees four windows (fig. 2). Camera of the robot, user's device camera, virtual joystick and robot info. In this mode, the user controls every movement of the robot by itself (Fig. 1).

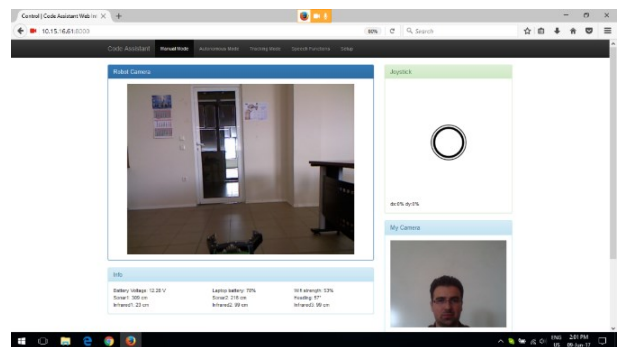


Figure 3. Web based user interface

Virtual joystick: It works like a single analog stick on a physical joypad. It is integrated into the web user interface and allows easy remote control of the system via any web browser. Therefore, here we can change the analogue virtual stick with analogue virtual pushbuttons. Pressing any of the buttons will result in rotation or movement in the desired direction.

Data from the Skanect application is transmitted to the operator's computer. He monitors the process of building the 3D model of the environment. Its role is to move the robot from one end of the mill to the other and to move the position of the manipulator with the buttons.

#### 5. Experiment and results

For initial experiments, we did scanning of a part of a room. The sensor used is Kinect, a wheel mobile robot is used for a mobile platform (fig. 4), which is controlled by the differential control function [12]. So replacing the wheelbase with a track mobile platform does not have to change the platform control parameters.

The received 3D models of the captured room have good contours and details. The edges and the individual elements can be easily distinguished.

Figure 5 shows the image without having undergone additional processing. Here the colour is all but the edges and contours can still be seen. After processing, the edges can be tightened or reduced according to the purpose of the research.

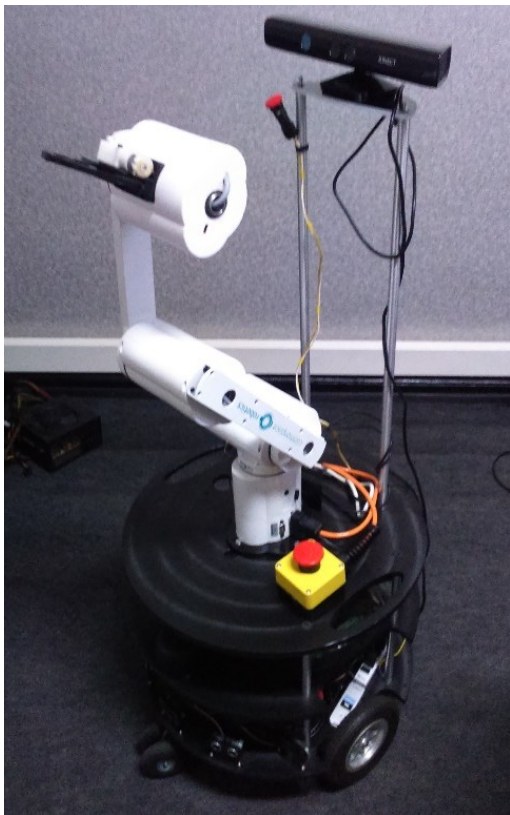


**Figure 4.** Service mobile robot and Mover 4

Figure 6 shows the result after processing the model. In this case, a colour pattern with smooth edges is reproduced. Colours are very close to the real ones and give clarity to the model.

The scanning process itself proceeds quite quickly if the smooth operation of the robot and the robotic manipulator is observed.

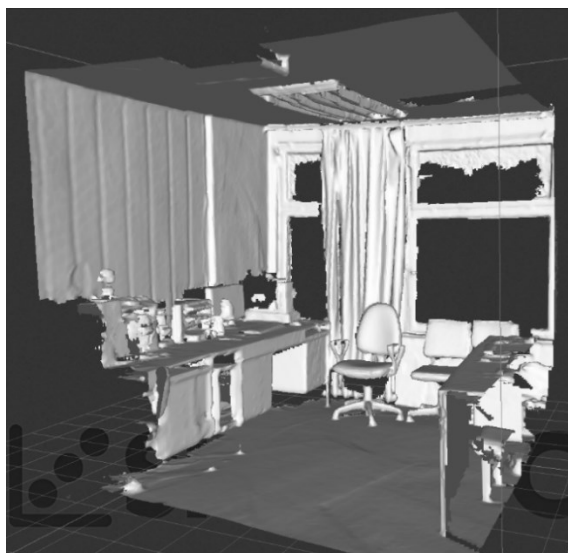


**Figure 5.** 3D uncoloured model of the scanned area



**Figure 6.** 3D colour model of the scanned area

## 6. Conclusion

The applied method successfully deals with scanning rooms and creating 3D models. The models obtained are satisfactory and can be used for comparative analysis. Thus determining the wear of the mills of the mills.

To improve the 3D models obtained can be used on 3D sensors that have a higher resolution. Another important parameter is the configuration of the computer used.

For the future, it is planned to study the autonomous scanning of the mills by developing the autonomous movement of the platform and the autonomous movement of the robotic manipulator.

## Acknowledgements

The paper is supported by Bulgarian NFS Grant "Young Scientists – 2017" No DM 17/8 - 2017.

## REFERENCES

- [1] K. Craig, "Grinding mill modeling and control: Past, present and future," (2012). *Proceedings of the 31st Chinese Control Conference*, Hefei, pp. 16-21.
- [2] R. Bischoff, U. Huggenberger and E. Prassler, (2011) "*KUKA youBot - a mobile manipulator for research and education*," 2011 IEEE International Conference on Robotics and Automation, Shanghai, pp. 1-4.
- [3] J. Wang, J. Zhang and Q. Xu, (2014). "Research on 3D laser scanning technology based on point cloud data acquisition," *2014 International Conference on Audio, Language and Image Processing*, Shanghai, pp. 631-634.

- [4] D. Chikurtev (2016). *Correction of Odometry Errors in Service Mobile Robots*, International Conference on Tribology BULTRIB'16, 27-29 October, Sofia, Bulgaria, p. 352-358, ISSN: 1313-9878.
- [5] *User Guide Mover4 Version 2015/03* (SW V902-08-008, HWE 2MV23 HWM V05 DOC V14). Commonplace Robotics GmbH. Germany
- [6] Yankov K. (2002). *Application-Oriented Language for Describing Open Kinematic Chains*, Proc. 16-th Int.Conf. "Systems for Automation of Engineering and Research" SAER'2002, St.Konstantin resort, Varna, Bulgaria, 20-22 sept. pp. 95-99.
- [7] Kaloyan Yankov, (2017). *Inverse Kinematics for Educational Robot MOVER 4*, Journal of the Faculty of Technics and Technologies, Trakia University, Vol. 5, November 2017, pp. 212-224, DOI: 10.15547/artte.2017.03.009
- [8] M. Kalantari & M. Nechifor (2016). *Accuracy and utility of the Structure Sensor for collecting 3D indoor information*, Geo-spatial Information Science, 19:3, 202-209, DOI: 10.1080/10095020.2016.1235817
- [9] Peter Henry, Michael Krainin, Evan Herbst, Xiaofeng Ren, and Dieter Fox, RGB-D mapping: *Using Kinect-style depth cameras for dense 3D modeling of indoor environments*, The International Journal of Robotics Research, Vol 31, Issue 5, pp. 647 – 663, doi.org/10.1177/0278364911434148
- [10] H. Haggag, M. Hossny, D. Filippidis, D. Creighton, S. Nahavandi and V. Puri, (2013). *"Measuring depth accuracy in RGBD cameras,"* 2013, 7th International Conference on Signal Processing and Communication Systems (ICSPCS), Carrara, VIC, 2013, pp. 1-7. doi: 10.1109/ICSPCS.2013.6723971
- [11] D. Chikurtev, K. Yovchev, E. Chikurtev, (2016). *Design and functionality of Web User interface for control of service mobile robot through the Internet*, PROBLEMS OF ENGINEERING CYBERNETICS AND ROBOTICS, Vol 67, Sofia, 2016, p. 51-60, ISSN 0204-9848.
- [12] D. Chikurtev, M. Grueva, D. Karastoyanov (2016). – *Intelligent Service Mobile Robots – Localization, Navigation And Observation Using IR Thermal Camera*, ADP 2016, June, Sozopol, Bulgaria; p. 200-207, ISSN 1310-39461





# Experimental investigation and multi-objective optimization of controllable parameters in turning process using Taguchi Method and Grey Relational Analysis

**Ivana DUMANIĆ, Sonja JOZIĆ, Dražen BAJIĆ and Mihovil SUČIĆ**

Faculty of Electrical Engineering,  
Mechanical Engineering and Naval  
Architecture, University of Split  
Ruđera Boškovića 32, 2100 Split,  
**Republic of Croatia**  
Fakultet elektrotehnike, strojarstva i  
brodogradnje, Sveučilište u Splitu  
Ruđera Boškovića 32, 21000 Split,  
**Republika Hrvatska**

[iduman00@fesb.hr](mailto:iduman00@fesb.hr)

[sonja.jozic@fesb.hr](mailto:sonja.jozic@fesb.hr)

[dbajic@fesb.hr](mailto:dbajic@fesb.hr)

[msucic00@fesb.hr](mailto:msucic00@fesb.hr)

## Keywords

*Turning*

*MQL*

*Compressed cold air cooling*

*Grey relational analysis*

*Multi-objective optimization*

## Ključne riječi

*Tokarenje*

*MQL*

*Hlađenje hladnim komprimiranim zrakom*

*Siva relacijska analiza*

*Višekriterijsko optimiranje*

*Original scientific paper*

**Abstract:** In the present research work investigation of different cutting conditions such as dry machining, minimum quantity lubrication (MQL) and MQL with compressed cold air on average surface roughness, cutting force and material removal rate is presented. Experiments were designed based on three input parameters (cutting speed, feed rate and depth of cut) and three different cutting environments when turning of EN AW-2011 alloy. The Taguchi-based grey relational analysis during longitudinal turning was used to identify the optimal process parameters by which will be achieved minimum surface roughness, minimum cutting force and maximum material removal rate. The results showed that dry machining, high cutting speed, low feed rate and intermediate depth of cut gives the best machining performances.

*Originalni znanstveni rad*

**Sažetak:** U ovom radu istraživao je utjecaj različitih uvjeta obrade, suha obrada, obrada uz korištenje minimalne količine sredstva za podmazivanje (MQL) te obrada uz korištenje minimalne količine sredstva za podmazivanje i hladnog komprimiranog zraka na hrapavost površine, sile rezanja te proizvodnost. Plan eksperimenata se temelji na tri razine ulaznih parametara (brzine rezanja, posmaka, dubine rezanja) te tri različita uvjeta obrade za tokarenje legure EN AW-2011. Taguchi metoda i siva relacijska analiza pri uzdužnom tokarenju je korištena za pronalaženje optimalnih parametara obrade za postizanje minimalne hrapavosti i sile rezanja uz maksimalnu proizvodnost. Rezultati su pokazali da sa suhom obradom, velikim brzinama rezanja, malim posmakom i srednjom dubinom rezanja moguće je postići najbolje vrijednosti promatranih svojstava obrade.

## 1. Introduction

Designers constantly strive to design products and processes that can run faster, last longer and operate more precisely. The modern development of high-speed machines has resulted in higher loading and increased speeds of moving parts which requires that bearings, seals, shafts, machine guides, gears, etc. must be dimensionally and geometrically accurate or the surface texture of the produced parts must be precise [1]. Therefore, the objective of machining operations is to produce parts with specified quality as productively as possible [2].

Surface roughness is the major indicator of surface quality on the machined parts. Surface roughness is mainly the result of process parameters such as tool geometry, cutting conditions, tool properties, etc. In this study, the roughness average ( $R_a$ ) is the surface

parameter used to evaluate surface roughness. This parameter is the mean of the absolute value of the heights of roughness irregularities from the centreline.

Cutting forces are one of the important physical variables that provide relevant process information in machining (machinability, tool conditions, power consumption, etc.). Cutting parameters, chip, cutting fluid, cutting tool are one of the important parameters that affect the cutting forces.

Material removal rate ( $MRR$ ) indicates the quantity of material removed from the workpiece per time unit. The greater the values of the cutting parameters, the greater the value of the material removal rate,  $MRR$  [ $\text{mm}^3/\text{s}$ ] and thus the lesser cycle time.

A great importance in mentioned terms has the heat which is generated in the cutting zone. Therefore, the cooling process becomes an integral part of any machining operation. As a result of the economic (high

cost of cutting fluids) and ecological (negative effects on humans and the environment) pressures, the industry seeks for newer methods to minimize the consumption of harmful lubricants [3]. Several technologies have been developed in recent years in order to increase the overall effectiveness of the process like cryogenic cooling, solid coolants / lubricants, flood cooling, minimum quantity lubrication (MQL) / near dry machining (NDM), high pressure coolants (HPC), internal tool cooling and use of compressed air / gases [4]. The concept of dry machining, which has been suggested by many contemporary researches, has many advantages, such as non-pollution of the atmosphere or water, no danger to health, reduction of cleaning cost. The loss of its positive effects, namely lubrication, cooling and chip flushing, are imposed by the elimination of coolant [5]. Also, at dry machining, the mechanical and thermal loads of the cutting tool are increased [6], [7]. Minimum quantity lubricant or MQL is a cooling technique wherein a very small amount of lubricant agent is implemented during the machining process. MQL leads to a significant reduction in the cutting temperatures along with favourable work-chip and work-tool interactions. This leads to a reduction in the surface roughness as well as cutting forces. Itoigawa et al. [8] concluded that the lubricant in the MQL process gave good lubrication. Dhar et al. [9] have investigated the MQL technique for turning and their results of the study indicated that MQL machining is better than a conventional flood coolant system. Priarone et al. [10] performed milling experiments with different types of lubricating conditions, dry, wet, MQL. It was shown that MQL gave the best results in term of surface roughness even when compared to wet machining [10], [11]. Sharma et al. [12] concluded that MQL leads to decreasing of the cutting temperature which results in improving tool life as well as the surface roughness. Maruda et al. [13], [14] conclude that the use of the MQL method reduces the machined surface roughness parameters and cutting force value when turning the carbon steel compared with compressed air cooling and dry cutting. MQL research literature, so far, indicates that the MQL technique has proved its efficiency, for example: allowing a reduction in lubricant use (50% – 90%) [15], energy consumption, better performance, and environment protection [16].

Extension of the MQL system is minimum quantity cooling lubrication (MQCL) where very less quantity of lubricant/coolant is combined with compressed cold air. In such systems, oil is used to reduce friction and compressed cold air enhances the cooling action [17]. The application of MQCL and MQL definitely improves machinability, extends the cutting tool life and influences many other factors of the machining process – it reduces the cutting forces, improves heat dissipation, reduces the machined surface roughness and influences the process of chip formation [18].

Pervaiz et al. [17], explored the machinability of Ti6Al4V using a vegetable oil-based MQL system mixed with sub-zero temperature air. It was observed that vegetable oil-based MQCL cooling strategy has promising potential to replace conventional flood cooling methods. Yuan et al. [19] reported that MQL with compressed cold air significantly reduces cutting force, tool wear and surface roughness. Singh and Sharma [20] concluded that using a Rahque-Hilsch vortex tube in addition to the MQL cooling process led to an improvement reducing surface roughness values and cutting forces when compared to MQL process.

Also, it is important for the researchers to model and quantify the relationship between surface roughness, cutting forces, material removal rate and the parameters affecting their value. The appropriate data can be analysed by statistical methods, resulting in valid and objective conclusions. Hence, design of experiments methods such as factorial design, response surface methodology and Taguchi methods are now widely used for planning the experiment [21]. Using Taguchi optimization methodology, Fratila and Caizar [22] minimized cutting power and the surface roughness during milling. Conventional flood lubrication, minimal quantity lubrication and dry milling were used in their investigation. Nouiouaer et al. [16] used Taguchi method which was based on signal-to-noise ratio in order to optimize the cutting parameters in turning to obtain the smallest value of surface roughness. Experiments have been performed under dry cutting, conventional wet cooling and MQL. Yan and Li [23] used a multi-objective optimization of milling parameters in order to reduce the surface roughness, minimize the cutting energy consumed during machining and maximize the MRR. They concluded that the highest value of the depth of cut, feed rate and cutting speed maximized the amount of material removal per second. The Taguchi method and grey relational analysis (GRA) have been used to optimize multi-objective criteria [24], [25], [26]. Lin [27] has used the Taguchi method together with GRA to deal with optimization of the turning operations with the multiple performance characteristics (tool life, cutting force, surface roughness). Malagi et al. [28] investigated the factors influencing cutting forces in turning and reported that cutting force increase as the feed rate and depth of cut increases. Asilturk and Neseli [29] modeled surface roughness during turning under the absence of cutting fluid. Response Surface Method (RSM) was applied to evaluate the impact of cutting parameters on surface quality. Actually, a number of researchers have focused on various predictive modeling and optimization techniques to determine optimal or near optimal machining parameters [30], [31], [32], [33], [34], [35]. The results of the works concluded that the feed rate was the parameter that has the highest influence on the obtained value of surface roughness [35], [36], [37], [38].

The objective of this study is to investigate the effects of cutting environments (dry machining, MQL, MQL + compressed cold air), cutting speed, feed rate and depth of cut on surface roughness, cutting force component in the Z direction and on material removal rate in the oldest and most common cutting process, conventional turning. Cutting force components in X and Y direction has not been used into consideration because of the negligible small values of the  $F_x$  and  $F_y$  in comparison to the  $F_z$ . In this study, the use of the Taguchi method to designed the tests and grey relational analysis to found an optimum cutting condition from the machining response such as cutting force, surface roughness and material removal rate is reported. Confirmation test has been established after optimizing machining parameters.

## 2. Experimental work

The turning experiments were carried out on the universal lathe machine PRVOMAJSKA RAŠA with a spindle motor of 11 kW and the spindle speeds in the range of 11.2 rpm to 2240 rpm. Turning inserts, the

VCGT 160404-AS produced by ISCAR were mounted on the tool holder SVJCR 2020K-16. The workpiece material used for experiments was EN AW-2011, aluminium alloy with dimensions of 300 mm length and 75 mm in diameter. The chemical composition of material in mass fraction was Al (91.4%), Cu (6%), Fe (0.7%), Pb (0.6%), Bi (0.6%), Si (0.4%) and Zn (0.3%). The surface roughness was measured using the MitutoyoSurfext SJ 301 profilometer. Every measurement was repeated at three different locations and the average value was considered. The cutting force ( $F_z$ ) was examined using dynamometer Kistler 9257A set between the cutting tool and tool support as well as using multi-channel charge amplifier Kistler 5007A that amplifies the electrical charges delivered from dynamometer into a corresponding voltage and then forwards the voltage signals to the A/D interface board. The NextView 4 program was used for analysing the cutting forces. All the measuring instruments were calibrated before the measurements were carried out. Measurements and analysis equipment are shown in Figure 1.

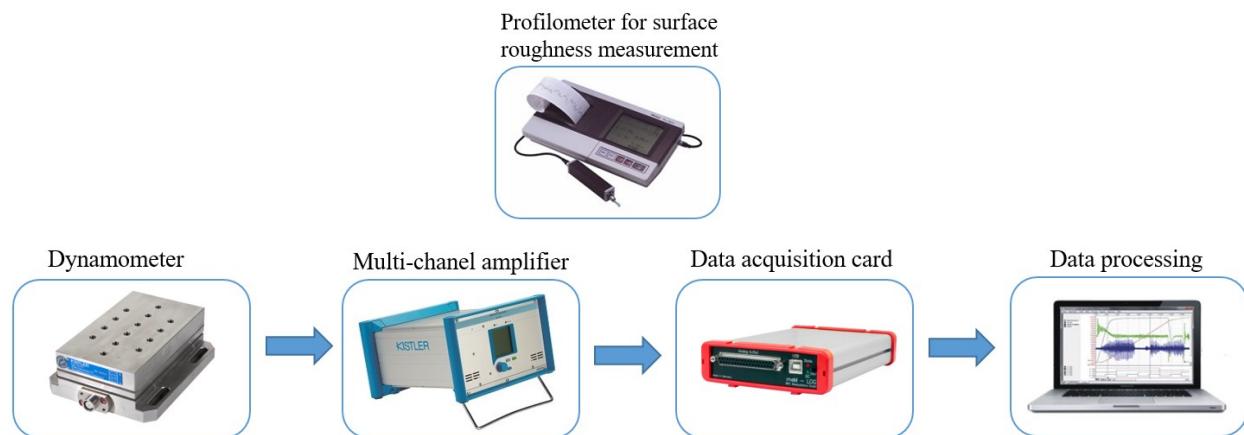


**Figure 1.** Measurement and analysis equipment

**Slika 1.** Oprema za mjerenje i analizu

### 2.1. Controllable parameters

Cutting speed  $v_c$ , feed rate  $f$ , depth of cut  $a_p$  and environment conditions were considered as controllable variables.

**Table 1.** Cutting parameters and their levels  
**Tablica 1.** Ulazni parametri i njihove razine

Machining parameters	Level 1	Level 2	Level 3
Cutting speed, $v_c$ [m/min]	200	300	400
Feed rate, $f$ [mm/rev]	0.05	0.15	0.25
Depth of cut, $a_p$ [mm]	1	1.75	2.5
Cutting conditions, $cc$	Dry	MQL	MQL+cca

The values of cutting parameters were selected from the manufacturer's handbook recommended for the tested

material together with the machine tool capabilities. All of these factors have three levels as shown in Table 1. Dry cutting, MQL and MQL with compressed cold air (cca) were used in the experiments.

### 2.2. The minimum quantity lubrication and vortex tube system

For the purpose of this investigation the minimum quantity lubrication system Vectolub. In this system, every micropump, which working frequency is set by a pneumatic pulse generator, delivers the lubricant through the coaxial line into a bifluid projection nozzle. Compressed cold air is provided by an external compressor and fed into the MQL. The air and the lubricant are parallel conducted in a coaxial line. In the nozzle, the lubricant is broken down and transported into

microdroplets by the air. Thus, homogeneous lubricant film at the friction point is formed.

In this study, Cold Air Guns which use vortex tube was used to improve the performance of the MQL process as shown in Figure 2. To begin with, a vortex tube is a mechanical device that split the input compressed air into two lower pressure streams, one colder and the other

warmer than the incoming stream. After passing through the chamber, the compressed inlet air accelerates at a high rate of speed. High-pressure air stream enters into the vortex tube tangentially. The hot gas stream leaves the tube through the control valve, while cold gas stream exits through at the cold end, near the entrance nozzle.

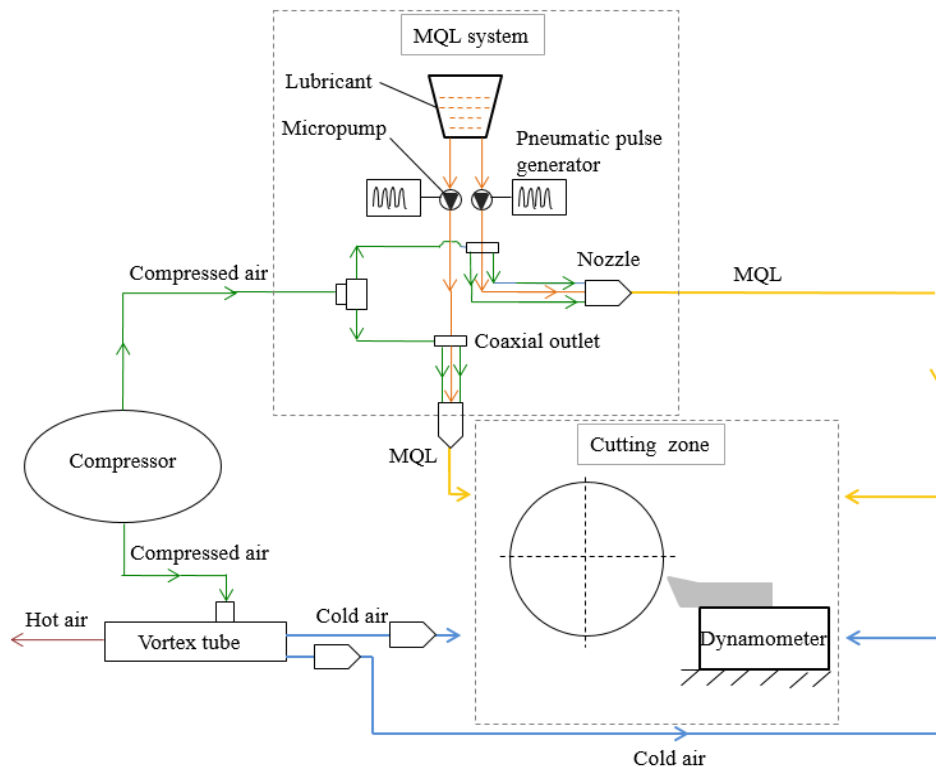


**Figure 2.** Shematic view of the experimental set up

**Slika 2.** Shematski prikaz eksperimenta

### 2.3. Taguchi design

Taguchi experimental design system uses the orthogonal arrays to obtain information about process parameter space with a small number of experiments. Testing only a limited collection of factors combinations is allowed by the fact that at this design every factor appears on the same number of levels and every factor on any level is in all combinations with other factors. Taguchi L9 orthogonal array has been used to study the effect of four machining process parameters at three levels ( $v_c$ ,  $f$ ,  $a_p$ , cutting condition) on three cutting parameters ( $F_c$ ,  $R_a$ ,  $MRR$ ). The plan of experiments is given in Table 2.

Grey relational analysis, GRA, is adopted in the study to find optimal controllable variables for multi-objective function. Desirable for the turning process are the small values of surface roughness  $R_a$  and cutting force  $F_c$  and the large value of the material removal rate. Also, the optimal combination of the process parameters was found.

Furthermore, a statistical analysis of variance is performed to find the influence of the controllable process factors on the multi-objective function.

## 3. Results and discussion

The different machining aspects of EN AW-2011 studied using dry, MQL, MQL + cca machining environments are presented below.

### 3.1. Surface roughness and material removal rate

The three machining parameters, namely, the cutting speed, feed rate and depth of cut are found to influence the surface roughness but as mentioned in the introduction the feed rate is the parameter that has the highest influence on the surface roughness. Figure 3 represents the value of surface roughness with the increasing of feed rate at varied machining environments. From Figure 3 it can be observed that the surface

roughness sharply increases with the increase in the feed rate for all machining environments. This is because at large feed rates the distance between peaks and valleys of the feed marks generated by the tool grooves is much more important. Also, it can be seen that at low level of feed rate, the surface roughness has the lowest value during MQL + cca cutting environment. At the high level of feed rate, the surface roughness has the lowest value during MQL cutting environment.

**Table 2.** Design of experiments based on L9 orthogonal array

**Tablica 2.** Plan eksperimenata, L9 ortogonalno polje

Machining trials	Cutting speed [m/min]	Feed rate [mm/rev]	Depth of cut [mm]	Cutting condition
1	200	0.05	1	Dry
2	200	0.15	1.75	MQL
3	200	0.25	2.5	MQL+cca
4	300	0.05	1.75	MQL+cca
5	300	0.15	2.5	Dry
6	300	0.25	1	MQL
7	400	0.05	2.5	MQL
8	400	0.15	1	MQL+cca
9	400	0.25	1.75	Dry

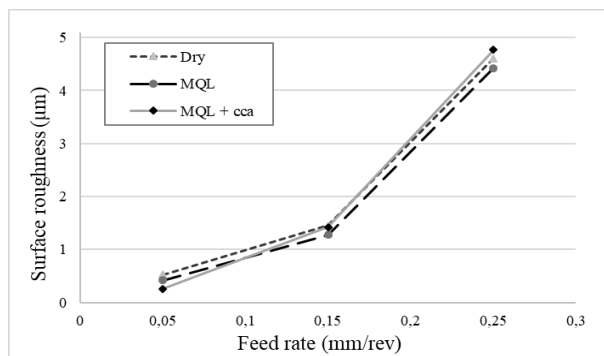


**Figure 3.** Influence of feed rate to surface roughness  
**Slika 3.** Utjecaj posmaka na hrapavost površine

Experimental runs with the result are given in Table 3. In this study, material removal rate in the turning process is calculated using the equation:

$$MRR = v_c a_p f \quad (1)$$

As mentioned earlier, when the values of the cutting parameters are greater, more material is removed from the workpiece per cutting pass, thus cutting environment does not have an influence on it, Table 3

**Table 3.** Surface roughness and material removal rate obtained from experiments

**Tablica 3.** Eksperimentalni rezultati hrapavosti površine i proizvodnosti

	Cutting speed [m/min]	Feed rate [mm/rev]	Depth of cut [mm]	Cutting condition	Ra [μm]	MRR [mm³/s]
1	200	0.05	1	Dry	0.53	166.67
2	200	0.15	1.75	MQL	1.28	875
3	200	0.25	2.5	MQL+cca	4.77	2083.33
4	300	0.05	1.75	MQL+cca	0.26	437.50
5	300	0.15	2.5	Dry	1.45	1875
6	300	0.25	1	MQL	4.42	1250
7	400	0.05	2.5	MQL	0.42	833.33
8	400	0.15	1	MQL+cca	1.42	1000
9	400	0.25	1.75	Dry	4.61	2916.67

### 3.2. Cutting forces

Table 4 shows experimental results of cutting force  $F_z$ . The cutting force has minimal value during the 1st trial. The cutting force increases with the increase of depth of cut and feed rate due to an increase of cutting action area. Also, an increase of those two parameters cause thus material removal becomes difficult due to increasing shear force. Above mentioned characteristics results in a higher cutting force.

**Table 4.** Effect of machining parameters on cutting force

**Tablica 4.** Utjecaj ulaznih parametara na iznos sile rezanja

Machining trials	1	2	3	4	5	6	7	8	9
Cutting force [N]	46	160	337	69	267	164	107	100	270

### 3.3. Grey relation analysis

A grey system is used for the optimization of multiple performance characteristics. The multiple response optimization problem is simplified into an optimization of a single response grey relational grade (GRG).

The first step of the grey relation analysis, GRA is the grey relation generation performed in order to make experimental data comparable. During this step, cutting force, surface roughness and  $MRR$  are normalized between zero and one.

Depending on characteristics of a data sequence, various methodologies of carrying out grey generation are available. In this study, a linear data pre-processing method for the cutting force and surface roughness is the lower-the-better and is expressed as:

$$x_{ij} = \frac{\max y_{ij} - y_{ij}}{\max y_{ij} - \min y_{ij}} \quad (2)$$



where  $x_{ij}$  is the value after the grey relation generation,  $\min y_{ij}$  is the smallest value of original data  $y_{ij}$  for the  $j$ th response of experiment  $i$ , and  $\max y_{ij}$  is the largest value of  $y_{ij}$  for the  $j$ th response.

The normalized value of the original sequence for material removal rate which is larger-the-better performance characteristic can be expressed as:

$$x_{ij} = \frac{y_{ij} - \min y_{ij}}{\max y_{ij} - \min y_{ij}} \quad (3)$$

Table 5 shows the normalized values of surface roughness  $Ra$ , cutting force  $F_z$  and material removal rate  $MRR$ .

**Table 5.** Normalized experimental results

**Tablica 5.** Normalizirane vrijednosti eksperimentalnih rezultata

	$Ra$ [μm]	$F_z$ [N]	$MRR$ [mm <sup>3</sup> /s]
1	0.9401	1	0
2	0.7738	0.6087	0.2576
3	0	0	0.6970
4	1	0.9196	0.0984
5	0.7361	0.2394	0.6212
6	0.0776	0.5939	0.3939
7	0.9645	0.7889	0.2424
8	0.7428	0.8161	0.3030
9	0.0355	0.2292	1

The second step of the GRA is a determination of the referent sequence  $x_{0j}$  for  $j$ th response. The performance of experiment  $i$  is considered as the referent for the response  $j$  if the normalized value  $x_{ij}$  is equal to 1 or nearer to 1 than the value for any other experiment.

In the next step, the grey relation coefficient is used for determining relation degree between  $x_{ij}$  and  $x_{0j}$ . The larger the grey relation coefficient, the closer  $x_{ij}$  and  $x_{0j}$ . The grey relation coefficient  $\xi_{ij}$  can be calculated as:

$$\xi_{ij} = \frac{\Delta_{\min} + \zeta \Delta_{\max}}{\Delta_{ij} + \zeta \Delta_{\max}} \quad (4)$$

where  $\zeta$  is the index of distinguishability called distinguishing coefficient  $\zeta \in (0,1]$ . In this work, the value of coefficient  $\zeta$  is assumed as 0.5.

$$\Delta_{ij} = |x_{0j} - x_{ij}|, \quad (5)$$

$$\Delta_{\min} = \min \{ \Delta_{ij}, i=1,2,\dots,m; j=1,2,\dots,n \}, \quad (6)$$

$$\Delta_{\max} = \max \{ \Delta_{ij}, i=1,2,\dots,m; j=1,2,\dots,n \}. \quad (7)$$

The last step is a determination of the grey relation grade which enables multiple optimizations and is calculated using equation:

$$y_i = \frac{1}{n} \sum_{j=1}^n \xi_{ij} \quad (8)$$

where  $n$  is a number of process response.

**Table 6.** Grey relational coefficients and grey relational grade  
**Tablica 6.** Sivi relacijski koeficijent i siva relacijska ocjena

	$Ra$ [μm]	$F_z$ [N]	$MRR$ [mm <sup>3</sup> /s]	Grade	Grey order
1	0.0600	0	1	0.7421	1
2	0.2262	0.3913	0.7424	0.5507	6
3	1	1	0.3030	0.4298	9
4	0	0.0804	0.9015	0.7394	2
5	0.2639	0.7606	0.3788	0.5401	7
6	0.9224	0.4061	0.6061	0.4518	8
7	0.0355	0.2111	0.7576	0.6782	3
8	0.2572	0.1839	0.6970	0.6030	4
9	0.9645	0.7708	0	0.5783	5

The larger value of grey relation grade, the closer the corresponding controllable parameter combination to optimal. Therefore, the experiment with the highest grey relation grade would be the best choice. Table 6 shows the grey relation coefficients and grade for each experiment.

The highest grey relational grade is the order to 1. The nearest optimum controllable parameters combination is in experiment 1 (A1B1C1D1). Table 7 shows the means of the grey relation grades for each level of controllable parameters. The optimal levels, levels with the highest grey relation grade, of the process parameters are dry machining, high cutting speed (400 m/min), low feed rate (0.05 mm/rev) and intermediate depth of cut (1.75 mm). These optimal levels are shown in bold in Table 7.

**Table 7.** Means for grey relational grades

**Tablica 7.** Srednje vrijednosti sivih relacijskih ocjena

Parameter	Level 1	Level 2	Level 3	Rank (max-min)
$v_c$ [m/min]	0.5742	0.5771	<b>0.6198</b>	4 (0.0456)
$f$ [mm/rev]	<b>0.7199</b>	0.5646	0.4866	1 (0.2333)
$a_p$ [mm]	0.5990	<b>0.6228</b>	0.5493	2 (0.0735)
$cc$	<b>0.6202</b>	0.5602	0.5907	3 (0.06)

### 3.4. Analysis of variance for grey relation grade

The percentage contribution by the sum of squares each of the process parameters to the total sum of squared deviations was used to evaluate the importance of the controllable parameter on the performance characteristic. The sum of squared deviations  $SS$  for a considered factor can be defined as:

$$SS = \frac{k}{m} \sum_{i=1}^k y_i^2 - \frac{y^2}{m} \quad (9)$$

where  $k$  is a number of levels,  $m$  is the total number of experiments,  $y_i$  is the total sum of the grey relation grade at  $i$ th level and  $y$  is the total sum of the grey relation grade. The total sum of the squared deviations  $SS_T$  can be defined as:

$$SS_T = \sum_{i=1}^m \sum_{j=1}^n y_{ij}^2 - \frac{y^2}{m} \quad (10)$$

where  $y_{ij}$  are individual observations.

Finally, the percentage contribution  $P$  can be calculated as:

$$P = \frac{SS}{SS_T} \quad (11)$$

It can be observed from Table 8 that the feed rate influenced the grey relation grade the most.

**Table 8.** Percentage contribution of input parameters on response variables

**Tablica 8.** Utjecaj ulaznih parametara na izlazne promatrane veličine u postotcima

	SS	Percentage contribution
$v_c$	0.0039	4%
$f$	0.0846	83%
$a_p$	0.0085	8%
$cc$	0.0054	5%
$SS_T$	0.1024	

For multiple performance characteristics, the cutting environment does not have an impact on the experiments. The cutting environment might have an effect on some performance characteristics individually.

### 3.5. Confirmation test

Once the optimal level of controllable parameters is selected, the final step is to predict and verify improvement of the performance characteristic using the optimal level of controllable parameters. Based on the previous discussion, the most significant parameters with optimal level are cutting speed at level 3, feed rate at level 1 and depth of cut at level 2. The estimated grey relation grade  $\hat{y}$  can be calculated as:

$$\hat{y} = y_t + \sum_{i=1}^p (y_i - y_t) \quad (12)$$

where  $y_t$  is the total mean of the grey relation grade,  $p$  is the number of the controllable parameter that significantly affects the multiple performance characteristic and  $y_i$  is the mean of the grey relation grade at the optimal level. Table 9 shows the estimated grey relational grade for optimal controllable parameters calculated using Eq. (12). Also, Table 9 presents the results of the confirmation experiment. In this study, a confirmation experiment was conducted by utilizing the levels of the optimal parameters combination of the turning process, A3B1C2D1. As shown in Table 9, surface roughness was improved from 0.53  $\mu\text{m}$  to 0.39  $\mu\text{m}$ , cutting force was slightly increased from 46 N to 49 N and material removal rate increased from 166.67  $\text{mm}^3/\text{s}$  to 583.33  $\text{mm}^3/\text{s}$ . Also, a good agreement between the actual and predicted grey relational grade was obtained and multiple characteristics in turning operations are improved.

**Table 9.** Results of the confirmation experiment

**Tablica 9.** Rezultati eksperimenta potvrde

	Initial controllable parameters	Optimal controllable parameters	
		Predicition	Experiment
Setting level	A1B1C1D1	A3B1C2D1	A3B1C2D1
$Ra$ [ $\mu\text{m}$ ]	0.53		0.39
$F_z$ [N]	46		49
$MRR$ [ $\text{mm}^3/\text{s}$ ]	166.67		583.33
GRG	0.7421	0.7818	0.7673
Improvement in GRG			0.0252

## 4. Conclusion

In this paper, use of the Taguchi method and grey relational analysis to optimize the turning operations with the multiple performance characteristics has been reported. Optimum values of cutting parameters and optimum machining condition were found out to minimize two response variables: the surface roughness and cutting force and to maximize the material removal rate. The optimum cutting conditions established are with a high cutting speed, low feed rate, intermediate depth of cut and dry cutting environment, and with this combination it is possible to decrease the surface roughness, cutting force and maximize the removal material rate. Feed rate plays the most important role in affecting surface roughness, cutting force and  $MRR$ .

## REFERENCES

- [1] Kant, G., & Sangwan, K. S. (2015). *Predictive modelling and optimization of machining parameters to minimize surface roughness using artificial neural network coupled with genetic algorithm*. Procedia CIRP, 31, 453-458.
- [2] Bajić, D., Celent, L., & Jozić, S. (2012). *Modeling of the influence of cutting parameters on the surface roughness, tool wear and the cutting force in face milling in off-line process control*. Strojniski vestnik-Journal of Mechanical Engineering, 58(11), 673.
- [3] Singh, G., & Sharma, V. S. (2017). *Analyzing machining parameters for commercially pure titanium (Grade 2), cooled using minimum quantity lubrication assisted by a Ranque-Hilsch vortex tube*. The International Journal of Advanced Manufacturing Technology, 88(9-12), 2921-2928.
- [4] Sharma, V. S., Dogra, M., & Suri, N. M. (2009). *Cooling techniques for improved productivity in turning*. International Journal of Machine Tools and Manufacture, 49(6), 435-453.
- [5] Jozić, S., Bajić, D., & Celent, L. (2015). *Application of compressed cold air cooling: achieving multiple*

- performance characteristics in end milling process.* Journal of cleaner production, 100, 325-332.
- [6] Jianxin, D., Tongkun, C., & Lili, L. (2005). *Self-lubricating behaviors of Al<sub>2</sub>O<sub>3</sub>/TiB<sub>2</sub> ceramic tools in dry high-speed machining of hardened steel.* Journal of the European Ceramic Society, 25(7), 1073-1079.
- [7] Schulz, H., Dörr, J., Rass, I. J., Schulze, M., Leyendecker, T., & Erkens, G. (2001). *Performance of oxide PVD-coatings in dry cutting operations.* Surface and Coatings Technology, 146, 480-485.
- [8] Itoigawa, F., Childs, T. H. C., Nakamura, T., & Belluco, W. (2006). *Effects and mechanisms in minimal quantity lubrication machining of an aluminum alloy.* Wear, 260(3), 339-344.
- [9] Dhar, N. R., Islam, M. W., Islam, S., & Mithu, M. A. H. (2006). *The influence of minimum quantity of lubrication (MQL) on cutting temperature, chip and dimensional accuracy in turning AISI-1040 steel.* Journal of Materials Processing Technology, 171(1), 93-99.
- [10] Priarone, P. C., Rizzuti, S., Rotella, G., & Settineri, L. (2012). *Tool wear and surface quality in milling of a gamma-TiAl intermetallic.* The International Journal of Advanced Manufacturing Technology, 61(1-4), 25-33.
- [11] Sarıkaya, M., & Güllü, A. (2014). *Taguchi design and response surface methodology based analysis of machining parameters in CNC turning under MQL.* Journal of Cleaner Production, 65, 604-616.
- [12] Sharma, V. S., Singh, G., & Sørby, K. (2015). *A review on minimum quantity lubrication for machining processes.* Materials and manufacturing processes, 30(8), 935-953.
- [13] Maruda, R. W., Legutko, S., Krolczyk, G. M., & Raos, P. (2015). *Influence of cooling conditions on the machining process under MQCL and MQL conditions.* Tehnički vjesnik, 22(4), 965-970.
- [14] Maruda, W. R., Legutko, S., & Krolczyk, G. M. (2014). *Influence of Minimum Quantity Cooling Lubrication (MQCL) on chip formation zone factors and shearing force in turning AISI 1045 steel.* In Applied Mechanics and Materials (Vol. 657, pp. 43-47). Trans Tech Publications.
- [15] Dixit, U. S., Sarma, D. K., & Davim, J. P. (2012). *Environmentally friendly machining.* Springer Science & Business Media.
- [16] Nouioua, M., Yallese, M. A., Khettabi, R., Chabbi, A., Mabrouki, T., & Girardin, F. (2017, March). *Optimization of Machining Process During Turning of X210Cr12 Steel Under MQL Cooling as a Key Factor in Clean Production.* In International Conference Design and Modeling of Mechanical Systems (pp. 855-863). Springer, Cham.
- [17] Pervaiz, S., Rashid, A., Deiab, I., & Nicolescu, C. M. (2016). *An experimental investigation on effect of minimum quantity cooling lubrication (MQCL) in machining titanium alloy (Ti6Al4V).* The International Journal of Advanced Manufacturing Technology, 87(5-8), 1371-1386.
- [18] Maruda, W. R., Legutko, S., & Krolczyk, G. M. (2014). *Effect of minimum quantity cooling lubrication (MQCL) on chip morphology and surface roughness in turning low carbon steels.* In Applied Mechanics and Materials (Vol. 657, pp. 38-42). Trans Tech Publications.
- [19] Yuan, S. M., Yan, L. T., Liu, W. D., & Liu, Q. (2011). *Effects of compressed cold air temperature on cryogenic machining of Ti-6Al-4V alloy.* Journal of Materials Processing Technology, 211(3), 356-362.
- [20] Singh, G., & Sharma, V. S. (2017). *Analyzing machining parameters for commercially pure titanium (Grade 2), cooled using minimum quantity lubrication assisted by a Ranque-Hilsch vortex tube.* The International Journal of Advanced Manufacturing Technology, 88(9-12), 2921-2928.
- [21] Aggarwal, A., Singh, H., Kumar, P., & Singh, M. (2008). *Optimizing power consumption for CNC turned parts using response surface methodology and Taguchi's technique—a comparative analysis.* Journal of materials processing technology, 200(1-3), 373-384.
- [22] Fratila, D., & Caizar, C. (2011). *Application of Taguchi method to selection of optimal lubrication and cutting conditions in face milling of AlMg3.* Journal of Cleaner Production, 19(6-7), 640-645.
- [23] Yan, J., & Li, L. (2013). *Multi-objective optimization of milling parameters—the trade-offs between energy, production rate and cutting quality.* Journal of Cleaner Production, 52, 462-471.
- [24] Siddiquee, A. N., Khan, Z. A., & Mallick, Z. (2010). *Grey relational analysis coupled with principal component analysis for optimisation design of the process parameters in in-feed centreless cylindrical grinding.* The International Journal of Advanced Manufacturing Technology, 46(9-12), 983-992.
- [25] Balasubramanian, S., & Ganapathy, S. (2011). *Grey relational analysis to determine optimum process parameters for wire electro discharge machining (WEDM).* International journal of engineering Science and Technology, 3(1), 95-101.
- [26] Sadasiva Rao, T., Rajesh, V., & Venu Gopal, A. (2012, March). *Taguchi based grey relational analysis to optimize face milling process with multiple performance characteristics.* In International Conference on Trends in Industrial and Mechanical Engineering (ICTIME'2012) (Vol. 24, p. 25).

- [27] Lin, C. L. (2004). *Use of the Taguchi method and grey relational analysis to optimize turning operations with multiple performance characteristics*. Materials and manufacturing processes, 19(2), 209-220.
- [28] Malagi, R. R., & Rajesh, B. C. (2012). *Factors influencing cutting forces in turning and development of software to estimate cutting forces in turning*. Int J Eng Innov Technol, 2, 14-30.
- [29] Asiltürk, I., & Neşeli, S. (2012). *Multi response optimisation of CNC turning parameters via Taguchi method-based response surface analysis*. Measurement, 45(4), 785-794.
- [30] Sangwan, K. S., & Kant, G. (2017). *Optimization of machining parameters for improving energy efficiency using integrated response surface methodology and genetic algorithm approach*. Procedia CIRP, 61, 517-522.
- [31] Garg, A., Lam, J. S. L., & Gao, L. (2016). *Power consumption and tool life models for the production process*. Journal of Cleaner Production, 131, 754-764.
- [32] Kant, G., & Sangwan, K. S. (2015). *Predictive modelling and optimization of machining parameters to minimize surface roughness using artificial neural network coupled with genetic algorithm*. Procedia CIRP, 31, 453-458.
- [33] Sangwan, K. S., Saxena, S., & Kant, G. (2015). *Optimization of machining parameters to minimize surface roughness using integrated ANN-GA approach*. Procedia CIRP, 29, 305-310.
- [34] Kant, G., & Sangwan, K. S. (2015). *Predictive modelling for energy consumption in machining using artificial neural network*. Procedia Cirp, 37, 205-210.
- [35] Camposeco-Negrete, C. (2015). *Optimization of cutting parameters using Response Surface Method for minimizing energy consumption and maximizing cutting quality in turning of AISI 6061 T6 aluminum*. Journal of cleaner production, 91, 109-117.
- [36] Hanafi, I., Khamlichi, A., Cabrera, F. M., Almansa, E., & Jabbouri, A. (2012). *Optimization of cutting conditions for sustainable machining of PEEK-CF30 using TiN tools*. Journal of Cleaner Production, 33, 1-9.
- [37] Debnath, S., Reddy, M. M., & Yi, Q. S. (2016). *Influence of cutting fluid conditions and cutting parameters on surface roughness and tool wear in turning process using Taguchi method*. Measurement, 78, 111-119.
- [38] Cetin, M. H., Ozcelik, B., Kuram, E., & Demirbas, E. (2011). *Evaluation of vegetable based cutting fluids with extreme pressure and cutting parameters in turning of AISI 304L by Taguchi method*. Journal of Cleaner Production, 19(17-18), 2049-2056.
- [39] Prabal R., Ratan G., Ashok P., (2002), *Influence of Heat Treatment Parameters on Structure and Mechanical Properties of an HSLA-100 Steel*, Steel Research 73 No. 8, p 347-355 Germany





# Study of quality and composition of zinc anodes for cathodic ship protection

**Andrea GATTO<sup>1)</sup>, Paolo MENGUCCI<sup>2)</sup>,  
Massimo ROGANTE<sup>3)</sup> and Fabio  
GRILLI<sup>4)</sup>**

1) Dipartimento DIEF, Università di Modena e  
Reggio Emilia, Via Vivarelli 10, I-41125  
Modena, **Italy**

2) Dipartimento SIMAU, Università  
Politecnica delle Marche, I-60131 Ancona,  
**Italy**

3) Rogante Engineering Office, Contrada San  
Michele n. 61, I-62012 Civitanova Marche,  
**Italy**

4) Officina Meccanica Navale Grilli s.a.s., Via  
Pier Capponi, I-62012 Civitanova Marche,  
**Italy**

agatto@unimore.it  
p.mengucci@univpm.it  
main@roganteengineering.it  
info@grillisas.com

## Keywords

*Zinc anodes  
Cathodic protection  
Scanning electron microscopy  
X-rays diffraction  
PIXE*

## Original scientific paper

**Abstract:** Quality and composition of the sacrificial zinc anodes are main issues in order to guarantee an efficient cathodic ship protection avoiding possible malfunctioning and failures. In the present study, sacrificial zinc anodes samples of different provenance and origins have been investigated, used for the galvanic protection of ships, and the composition has been identified able to guarantee satisfactory efficiency. This study concerns also the methodological approach to select and use one or more analysis techniques suitable for this purpose. Both traditional and advanced characterization techniques have been taken into account, actually, particularly useful for adequately interpreting chemical properties and other features of the considered materials.

## 1. Introduction

The present study arises from the aim of determining the possible causes related to the possible malfunction of sacrificial zinc anodes used for the galvanic protection of ships, and to identify the composition able to guarantee a satisfactory efficiency.

Zinc anodes are usually produced by small enterprises using both ingots and worn out anodes. Therefore it is possible to obtain anodes containing tracks of mineral as Ca due to their use in sea diving. This kind of contamination has low effect on the anodes efficiency. Contrary that the cross-contamination during the melting process can cause a dramatic effect on the anode characteristic. This paper points out the need for a severe chemical control also for the small enterprise operating as subcontractors for shipbuilding.

The study concerns first of all the selection and use of one or more analysis techniques useful for this purpose. Both traditional techniques and advanced

characterization techniques have been taken into consideration, particularly useful for adequately interpreting chemical properties, in order to investigate the possible defects. The activities carried out are the following:

- examination of the topic in question and the relative state-of-the-art
- identification and selection of sacrificial anodes useful for this research
- identification of the possible methodological approach, with reference to the constituent materials of the anodes
- identification and selection of one or more characterization techniques and of the most appropriate analysis instrumentation in terms of performance and reliability
- performing of the analyzes (also comparative) of the selected samples, and data treatments.

**Symbols/Oznake** $E$  - X-ray energy, keV

-

 $\eta$ 

- electrical efficiency, %

-

**Greek letters/Grčka slova** $\epsilon$ 

- anode electrochemical capacity, Ah/kg

-

 $\gamma$ - specific weight, g/cm<sup>3</sup>

-

**2. Galvanic corrosion and protection**

Galvanic corrosion is a particular electro-chemical reaction which is activated when metal parts having different electrical potential, being immersed in a conducting liquid - called electrolyte -, come in mutual contact, either directly or through the action of an element further, which serves as a link. The electrical current consequently originated is able to attack the metal part characterized by the lower potential, which acts as an anode: the constitutive metal is generally the less noble one, which is then corroded. Marine water, as an excellent electrolyte, is a habitat very prone to triggering this corrosive phenomenon, involving the metal parts of the naval vessels that are immersed (that is, for example, keel plates, propeller shafts, propellers and taken at sea) and, consequently, also those that are in contact with these elements (that is, for example, pipes, valves and welded structures). Furthermore, the likelihood of triggering galvanic corrosion is directly proportional to the salinity level of the sea water.

The main cause of corrosion is oxygen, which is combined with metal because there is an exchange of electrical charges, i.e. a circulation of electric current. The painting is generally insulating, not letting electrical charges pass: therefore, corrosion, until there are metal parts in contact with the environment, does not occur. Each metal is different from the other and this diversity is related to the so-called "degree of nobility", measurable as the potential that the metal assumes if immersed in an electrolyte. Sea water is an excellent electrolyte to trigger corrosion processes. By coupling two metals of different nobility (eg, zinc and steel), it is noted that:

- electrical current passes through the connection
- the less noble metal between the two (the zinc) is consumed, while the noblest metal (the steel) tends slightly to cover itself with a very delicate protective patina.

The steel hulls can indifferently be protected by zinc, aluminum or magnesium anodes: the only difference with the aluminum hulls is that the former must be protected even with active protection. Flat anodes are generally installed fairly uniformly on the hull by thickening them slightly near the bow wheel and in the helicoidal area, i.e. in the parts where the greatest oxygen supply occurs due to the effect of the boat's motion.

When sacrificial anodes are used, they are physically connected (e.g., by bolts or welding) to the components and structures of the boat. As shown in Figure 1, an electrochemical cell is formed between the anode and the cathode (the structure to which the anode is connected) through the surrounding electrolyte (in our case, sea water).

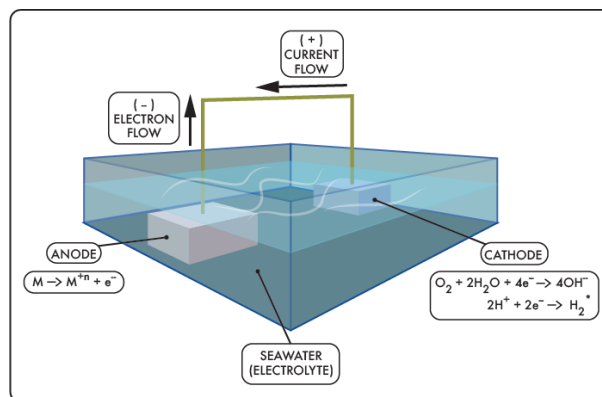


**Figure 1.** Electrochemical cell (illustration by Lorenzo Rogante)

The anode is preferentially corroded or "sacrificed", producing an electron flow to the cathode which results in a reduction or elimination of corrosion at the cathode. The numbers and dimensions of the anodes are determined by the wet surface area of the hull, the planned replacement cycle of the anodes and the corrosion history of the vessel.

With regard to problems related to installation and maintenance, a common error consists in painting under the anode, or even the anode even if partially, so that the flow of electrons is interrupted and the circuit stops working. The metal to be protected, if the cathodic protection works well, does not corrode. If you continue to see new traces of oxidation on a protected metal, it means that something is not working properly: at this point, check the number of anodes to be installed and their size: the main recommendation is to install many anodes how many have been foreseen in the original project, but above all of the same dimension and of the same material. The installation of a larger number of anodes must be decided only if after a haulage they have lost more than 50%, exceptionally 75% of their original weight. If these wear levels are exceeded, this means that

the number of anodes is insufficient, so that the number or surface must be increased to keep the hull properly protected. The new anodes are to be installed favoring the area near the bow wheel and the aft area around the propeller. Once mounted, the anodes should start showing signs of corrosion soon.

Procedures for calculating the number and type of anodes exist, which are reported in open scientific and technical literature (e.g., [1] and [2]). There are numerous producers of zinc sacrificial anodes in the international market, and among the various data available concerning such productions, those of Table 1 can be reported.

**Table 1.** Example of placing small table in a column-formatted text

<i>data</i>	<i>value</i>
$\gamma$	7.14
$\varepsilon$	780
$\eta$	95
metal consumed to produce 1 A / year Kg	11.20

Table 2 shows, instead, the standard chemical composition of zinc anodes produced according to the universally recognized specifications US Mil-A-18001K [3] (annex 1) and ASTM B418-II [4]. Other data according to the US Mil-A-18001K specification are:

- Ag/AgCl potential = -1.05 V
- capacity = 780 Ah / Kg.

The norm [4], in particular, concerns machined and forged galvanized zinc anodes used for cathodic protection of nobler metals and alloys in sea water, brackish water, other saline electrolytes or other corrosive environments. The anodes must undergo chemical and spectrochemical analyses, as well as they must comply with the required chemical compositions of aluminum, cadmium, iron, lead, copper and zinc.

Another rule that similarly regards cathodic protection for naval vessels is reported in [5].

**Table 2.** Standard chemical composition of zinc anodes produced according to the universally recognized specifications US Mil-A-18001K and ASTM B418-II.

	US Mil-A-18001K	ASTM B418-II
<i>element</i>	<i>% in weight</i>	<i>% in weight</i>
Al	0.10-0.50	0.005 max
Si	0.125 max	
Cd	0.025-0.07	0.03 max
Fe	0.005 max	0.0014 max
Pb	0.006 max	0.003 max
Cu	0.005 max	0.002 max
Zn	bal.	bal.

This alloy is produced from high quality pure zinc (99.995% purity) and therefore linked to the above specifications: minor variations can have an important consequence on the effectiveness of alloys and their durability. Some manufacturers test each melt using an internal spectrometer to verify the correct chemical composition, ensuring that high quality anodes are produced.

### 3. Materials and methods

The sacrificial anodes that have been selected for this research are listed in Table 3.

The samples were sectioned by means of a cutting off machine, in order to obtain for each a fragment of the approximate size of  $1 \times 1 \times 1 \text{ cm}^3$ , one side of which is the original outer surface.

The fragments obtained, afterwards, were subjected to a surface finishing preparative treatment by means of a manual metallographic cleaning machine ("REMET" model L1), with a work disk and abrasive paper up to 320 mesh, a 200 mm diameter disk and a fixed speed of 300 rpm.

**Table 3.** Analyzed samples of sacrificial anodes.

<i>sample</i>	<i>ref.</i>	<i>description</i>
A	Figure 2	recycled sample, i.e. made by rebuilding scrap of used sacrificial zinc that had worked properly; this sample has been tested as installed at the hull of a ship for about a year, and worked correctly
B	Figure 3	sample made by melting ingots of zinc (see in Table 4 the composition of such ingots); the sample has been tested as installed at the hull of a ship for about a year, and did not work at all
C	Figure 4	recycled sample, i.e. made by rebuilding scrap of used sacrificial zinc that had worked properly; this sample is new (still unused)
D	Figure 5	sample from the market, well known for its excellent quality and guaranteed to work properly
E	Figure 6	sample made by melting ingots of zinc (see in Table 3 the composition of such ingots); this sample is new (still unused)

**Table 4.** Composition of zinc ingots - from which the B and E samples were produced - as per analysis certification provided by the supplier.

Cu	Pb	Sn	Fe	Al	Ni	Mn	Sb	Cd	Si	Zn
0.0008	0.0027	0.0001	0.0001	0.0001	-	-	-	0.0001	-	bal.



**Figure 2.** Sample A (ref. Table 3).



**Figure 5.** Sample D (ref. Table 3).



**Figure 3.** Sample B (ref. Table 3).



**Figure 6.** Sample E (ref. Table 3).



**Figure 4.** Sample C (ref. Table 3).

Concerning the possible methodological approach, with reference to the constituent materials, it was decided to perform analytical and comparative tests between the samples, in particular the elementary composition, in order to interpret chemical properties and other features of the considered anods and to investigate the possible presence of responsible or co-responsible elements related to the not proper work of sample B.

The following characterization techniques have been chosen as suitable for the purpose of the present study:

- scanning electron microscopy (SEM) + Energy Dispersive X-ray microanalysis (EDX)
- proton induced X-ray emission spectrometry (PIXE).

The SEM technique [6-8] allows the observation of samples of material with magnifying power and resolution 1000 times higher than that of traditional optical microscopy, thanks to the fact that the wavelength of the electrons is much lower than that of photons. This technique exploits the generation of a high energy



electron beam in the vacuum, focused by an appropriate system of lenses and deflections in order to investigate specific selected areas of the sample in question. The beam interacts with the same sample, producing different signals that are then acquired by appropriate detectors and then processed to form a gray level image. In detail, the sample - kept in a vacuum to avoid interference - is subjected to a line-by-line scan with the electron beam over a specific area, and as a response it re-emits several signals, e.g. backscatter and secondary electrons, and X-rays. The penetration of the electron beam changes depending on the atomic number of the element: it is of higher grade in lighter and lower materials in heavier materials. Consequently, also the quantity of backscattering electrons re-emitted from the sample, and detected by a specific detector, is proportional to the hardness of the material itself.

Some SEM instruments are equipped with detectors for microanalysis (EDS or EDX - Energy Dispersive X-ray microanalysis): this instrumental analytical method exploits the characteristic emission of X-rays generated by an electron accelerated electron beam incident on the sample. The non-destructive EDX method allows to analyze stable solid samples at low pressure and under the action of electronic and electrically conductive bombardment (possibly with a uniform layer of carbon on its surface), providing the analysis of the constituent elements. The complete instrumentation is commonly composed of SEM-EDX scanning electron microscope and EDX detector (lithium doped silicon monocrystal) maintained at 77K with liquid nitrogen. In this way, it is possible to associate both techniques and to correlate the morphological and compositional characterization, analyzing the distribution of the chemical phases, tracing concentration profiles and performing quantitative chemical analyzes. The SEM technique, ultimately, allows obtaining the following data related to the investigated surface of the sample under examination: morphology, physical chemical composition, contamination, electrical defects, assessment of potentials.

This technique has been chosen to perform micrographs of the surface of the samples studied, and the elemental microanalysis EDX for the verification of the local chemical composition. The used instrumentation is that of the "Enzo Ferrari" Engineering Department of the University of Modena and Reggio Emilia, Italy. Figure 7 shows the analyzed fragments positioned in the sample holder of the SEM instrumentation. The PIXE spectrometric technique is applied as a non-destructive analysis of the constituent elements of objects and samples.

The bombardment of the beam from high energy ions, protons of energy at MeV level, creates the ionizations of the internal structure. The electrons of the external structure descend and fill the vacant sites of the internal structure.

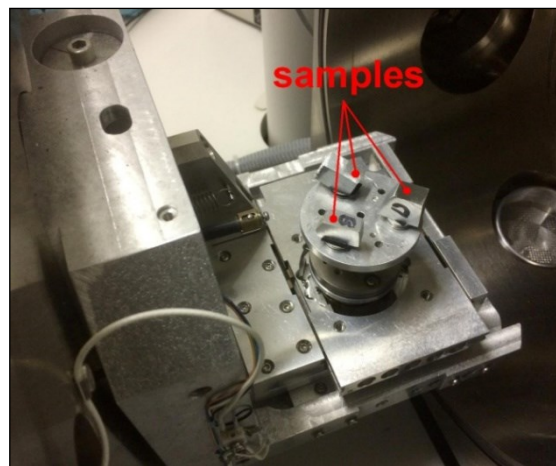


**Figure 7.** The analyzed fragments of zinc anodes (samples A, B and D) positioned in the sample holder of the SEM instrumentation.

When an empty site is filled, an X-photon of energy characteristic is emitted for the target atom [9]. An energy dispersion detector is then applied to measure the characteristic X-rays emitted, the X-ray spectrum is analyzed off-line and the characteristic radiographic intensities are converted into elemental concentrations [10,11].

The used instrumentation is the 5MV Van De Graaff accelerator of the Wigner Institute of Particle and Nuclear Physics, Hungarian Academy of Sciences. The elemental composition of the base material can be determined in the superior layer of the analyzed object, having a 10  $\mu\text{m}$  thickness. This instrumentation employs a proton beam correctly collimated by 2.5 MeV of energy, and for the measurements the window-target distance is selectable; at a distance of 10 mm, e.g., it corresponds a beam diameter of about 1.5 mm. The characteristic X-rays are collected by an Amptek X-123 spectrometer. An SDD detector of  $25\text{ mm}^2 \times 500\text{ }\mu\text{m}$  of active volume can be positioned at a certain angle (e.g.,  $135^\circ$ ) with respect to the beam direction. The proton beam of 2.5 MeV, e.g., can be used with currents around 2 nA and variable measurement times in the range of 600÷1800 seconds. The sensitivities are in the range 50÷1000 ppm, and they vary depending on the elements and they also depend on the composition of the matrix. Since the proton beam size on the target can be small (that is, in the range 0.8÷3 mm), small spots and selected particulars on the samples can also be analyzed. This technique of spectrometry contributes to the verification of the content of the constituent elements of the considered samples. The investigation is carried out at surface level, providing complementary information to those acquired through the SEM. Figure 8 shows a sample during the investigation.





**Figure 8.** A sample of zinc anode during the PIXE analysis.

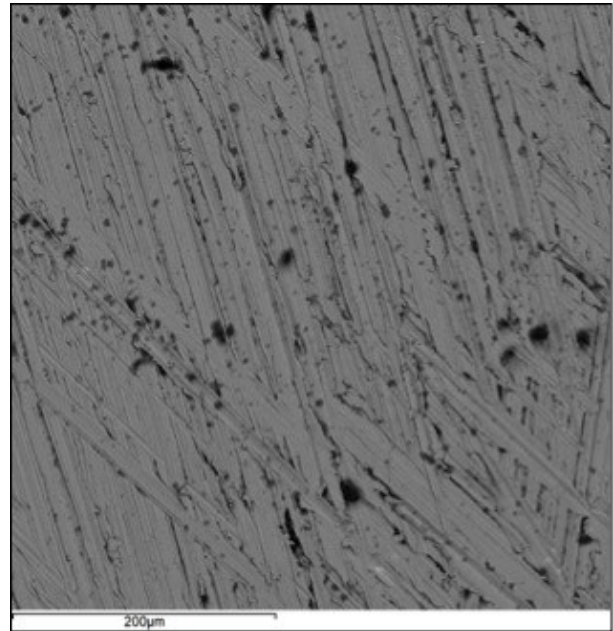
## 4. Results and discussion

### 4.1. Characterization by SEM + EDX

The observations made on different areas for each of the three sample (A, B and D) respectively representing the three different types of anodes have always reported consistent results.

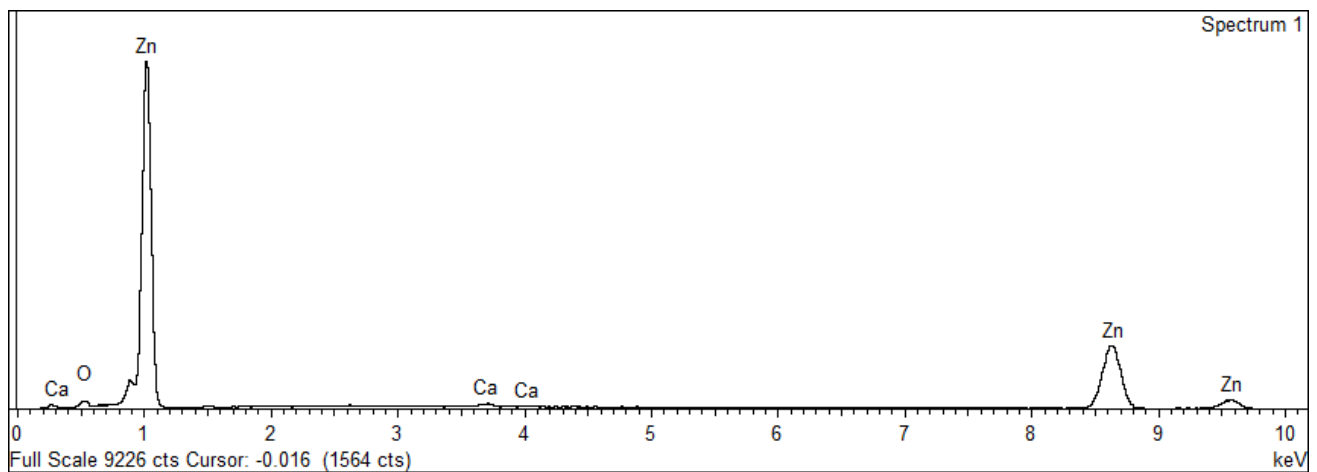
The results are shown below.

Figure 9 shows the surface micrograph of sample A.



**Figure 9.** SEM micrograph of the surface of sample A.

Figure 10 shows the typical spectrum related to the examined surfaces of sample A



**Figure 10.** EDX spectrum related to the examined areas of sample A.

Table 4 shows the typical chemical composition of sample A from EDX microanalysis.

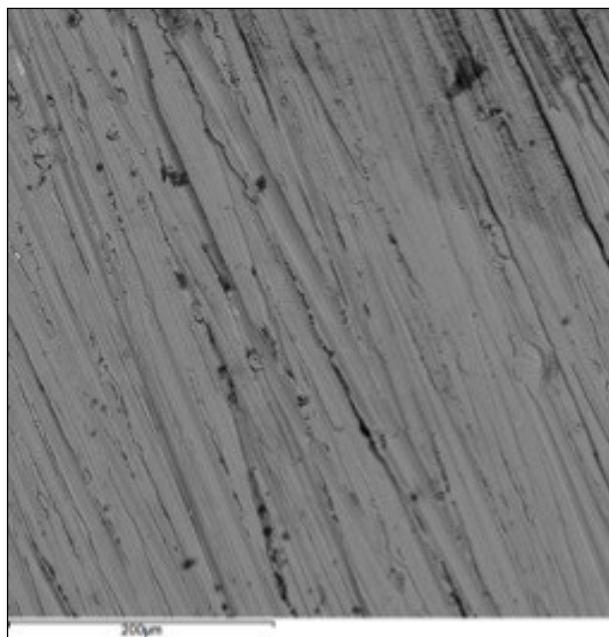
From the EDX microanalysis carried out on sample A, a small percentage of calcium is detected, probably coming from deposits on the old anodes which were then re-melted.

Figure 11 shows the surface micrograph of sample B.

From a visual examination of the fragment belonging to the sample B, moreover, there is the appearance of craters

that indicate the presence of impurity in the material (perhaps floating slag), as shown in Figure 12.

Figure 13 shows the typical spectrum related to the examined surfaces of sample B.



**Figure 11.** SEM micrograph of the surface of sample B.



**Figure 12.** Fragment belonging to sample B.

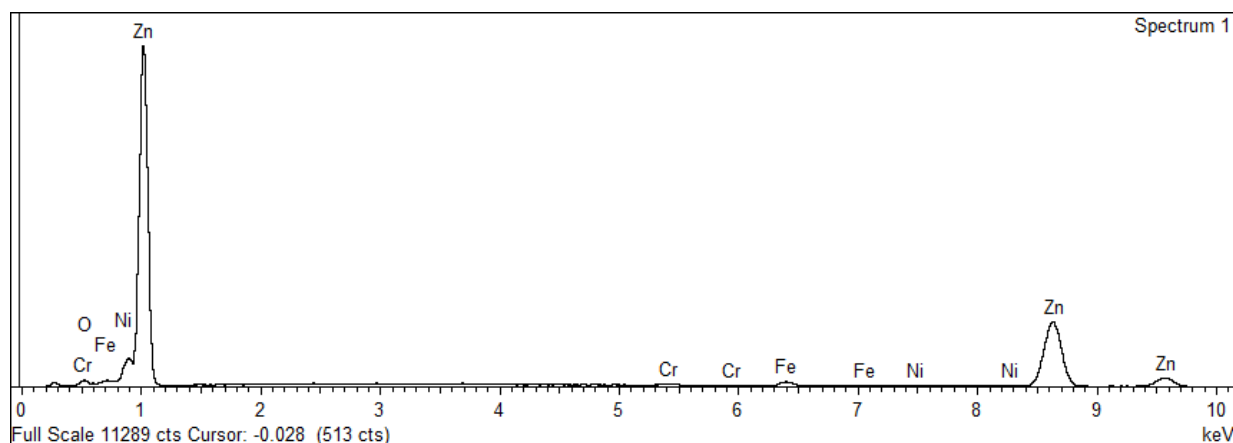


**Figure 13.** EDX spectrum related to the examined areas of sample B.

Table 5 shows the typical chemical composition of sample B from EDX microanalysis.

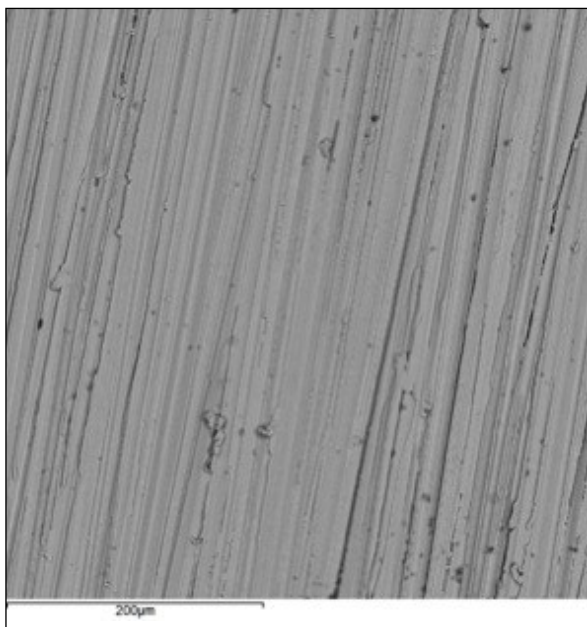
From the EDX microanalysis carried out on sample B, an unexpected percentage of iron, nickel and chromium is detected, so it is assumed that there has been a contamination with other material (most probably, stainless steel) during the production of the anodes.

Figure 14 shows the surface micrograph of sample D.

Figure 15 shows the typical spectrum related to the examined surfaces of sample D.

**Table 5.** Typical chemical composition of sample B from EDX microanalysis.

<i>Element</i>	<i>weight (%)</i>
O	$2.38 \pm 0.17$
Cr	$0.50 \pm 0.07$
Fe	$1.94 \pm 0.09$
Ni	$0.56 \pm 0.08$
Zn	$94.62 \pm 0.22$



**Figure 14.** SEM micrograph of the surface of sample D.

Table 6 shows the typical chemical composition of sample D from EDX microanalysis.

**Table 6.** Typical chemical composition of sample D from EDX microanalysis.

<i>Element</i>	<i>weigh (%)</i>
Zn	100.00 ± 0.00

From the EDX microanalysis carried out on sample D, it has been found that the constitutive material of the same sample is almost pure zinc.

#### 4.2. Characterization by PIXE

The PIXE analysis has been carried out on all the 5 fragments related to the samples described in Table 1.

The diameter of the proton beam directed on the sample was about 1 mm. Each sample has been analyzed in the central area of a clean surface (no additional cleaning was applied).

Figure 16 shows, e.g., the spectrum relative to the examined area of sample B.

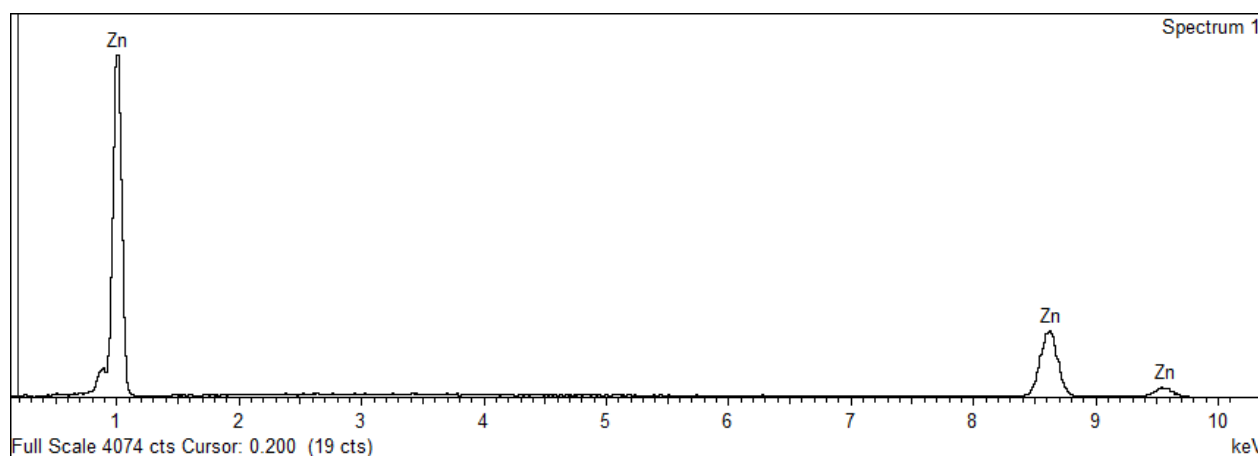


**Figure 15.** EDX spectrum related to the examined areas of sample D.

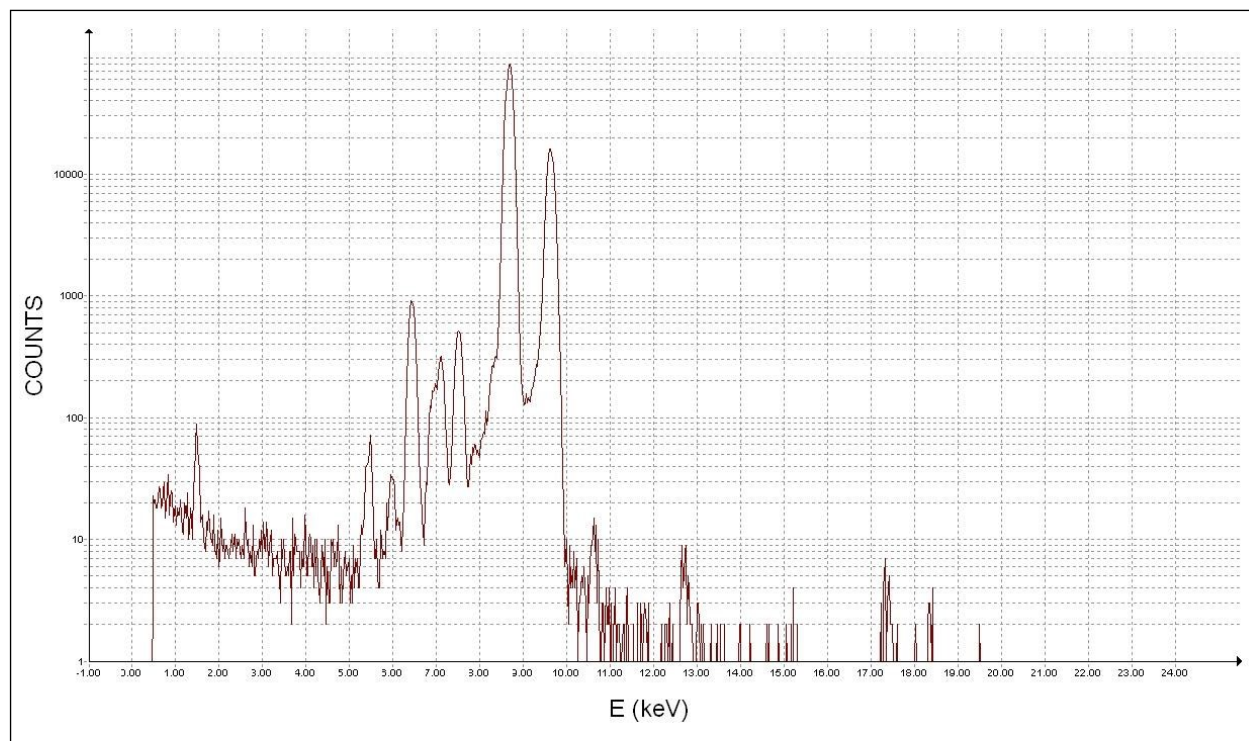


**Figure 16.** PIXE spectrum related to the examined area of sample B.

Tables 7 and 8 show the results obtained by the PIXE analysis, respectively in ppm and in mass %.

**Table 7.** Elemental composition (ppm) of the different samples, obtained by PIXE analysis.

sample	Cr	Fe	Ni	Zn	Pb
A	235.2	354	272.6	998534	602.7
B	4687	18026	4280	971883	1124
C	226.1	483.2	283.2	998417	587.3
D	0	721.5	296.5	992231	257.7
E	1273	3459	1368	993894	0
A	169.8	383.5	169.8	998556	718.1

**Table 8.** Elemental composition (% m/m) of the different samples, obtained by PIXE analysis.

sample	Cr	Fe	Ni	Zn	Pb
A	0.02	0.04	0.03	99.85	0.06
B	0.47	1.80	0.43	97.19	0.11
C	0.02	0.05	0.03	99.84	0.06
D	0.00	0.07	0.03	99.22	0.03
E	0.13	0.35	0.14	99.39	0.00
A	0.02	0.04	0.02	99.86	0.07

From the PIXE analyzes carried out on samples B and E, similarly to the EDX micro-analyzes, an unforeseen percentage of iron, nickel and chromium is detected, so it is assumed there has been contamination with other material during the production of the anodes.

## 5. Conclusions

In the anode A, which worked correctly and was made from the melting of used zinc scrap that had worked correctly also, a small percentage of Ca (not detectable by the PIXE analysis) was detected by EDX microanalysis. Such presence of Ca can be related probably to deposits of organisms on the old anodes that were then refunded: Ca has proved to not affect the functionality of the anode, which then evidenced to work properly. From both EDX and PIXE analyzes of the anodes B and E (in particular, the anode B), instead, the unforeseen presence of Fe, Ni and Cr was detected (considering the various results, in the respective intervals of percentage values of about  $1.80 \div 2.03$ ,  $0.43 \div 0.64$  and  $0.47 \div 0.57$ ). The presence of Fe, in particular, is tolerated by the universally recognized specifications US Mil-A-18001K [3] (annex 1) and ASTM B418-II [4] respectively up to 0.005% and 0.0014% by weight, for which it is assumed that there has been a contamination with other material (most probably, stainless steel) during the production of the anodes by melting the ingots. This paper points out the need for a severe process control also for the small enterprise operating as subcontractors for shipbuilding.

**REFERENCES**

- [1] Meillier A., (2003), *A review of galvanic anode cathodic protection design procedure*, The Journal of Corrosion Science and Engineering 4, p. 29 U.S.A.
- [2] Netherlands National Water Board, (2008), *Sacrificial anodes, merchant shipping and fisheries*, Netherlands National Water Board - Water Unit in cooperation with Deltares and TNO p. 47 Netherland
- [3] *Military Specification Anodes Sacrificial Zinc Alloy*, MIL-A-18001K w/INT. AMENDMENT 3, 24 October 2007, U.S.A.
- [4] *Standard Specification for Cast and Wrought Galvanic Zinc Anodes*, ASTM B418 Norm, ASTM International, U.S.A.
- [5] *E2 - Cathodic protection, ABYC standard*, (2013), The American Boat & Yacht Council, Annapolis, MD, U.S.A.
- [6] Smith K.C.A., Oatley C.W., (1955), *The scanning electron microscope and its fields of application*, British Journal of Applied Physics 6/11, p. 391-399 Great Britain
- [7] Goldstein G.I., Newbury D.E., Echlin P., Joy D.C., Fiori C., Lifshin E., (1981), *Scanning electron microscopy and x-ray microanalysis*, Plenum Press, New York, U.S.A.
- [8] Rinaldi R., (1985), *Microanalisi-X: recenti sviluppi e aspetti pratici*, Rendiconti della Società Italiana di Mineralogia e Petrologia 40, p. 241-254 Italy
- [9] Johansson T.B., Akselsson R., Johansson S.A.E., (1970), *X-ray analysis: elemental trace analysis at the  $10^{-12}$  g level*, Nuclear Instruments and Methods 84, p. 141-143 The Netherlands
- [10] Maenhaut W., Malmqvist K.G., (2002), *Particle-induced X-ray emission analysis*, Handbook of X-ray Spectrometry, 2nd ed., p. 719-810 U.S.A.
- [11] Mandò P.A., Przybyłowicz W.J., (2009), *Particle-Induced X-ray Emission (PIXE)*, Encyclopedia of Analytical Chemistry, John Wiley & Sons, U.S.A.



# Computational fluid dynamics analysis and improvement of manifold design for plate type heat exchangers

**Antonio GEČI<sup>1)</sup>, Željko PENG<sup>1)</sup>,  
Gojmir RADICA<sup>1)</sup> and Sandro  
NIZETIĆ<sup>1)</sup>**

1) University of Split, Faculty of Electrical  
Engineering, Mechanical Engineering and  
Naval Architecture  
Sveučilište u Splitu, Fakultet  
elektrotehnike, strojarstva i brodogradnje  
R. Boškovića 32, 21000 Split, Croatia

[ageci00@fesb.hr](mailto:ageci00@fesb.hr)

[zpenga@fesb.hr](mailto:zpenga@fesb.hr)

[goradica@fesb.hr](mailto:goradica@fesb.hr)

[snizetic@fesb.hr](mailto:snizetic@fesb.hr)

## Keywords

*Computational Fluid Dynamics*

*Plate Type Heat Exchangers*

*Manifold design*

*Pressure drop and velocity profile*

*Optimization*

## Ključne riječi

*Numeričko modeliranje strujanja*

*Pločasti izmjenjivači topline*

*Konfiguracija sabirnice*

*Pad tlaka i profil brzine*

*Optimizacija*

## Original scientific article

**Abstract:** Plate type heat exchangers are commonly used in marine industry due to their favorable characteristics vs. shell and tube heat exchangers, such as smaller volume for similar heat exchange rates.

The manifold design is optimized in this work via computational fluid dynamics (CFD) analysis to result in uniform flow distribution along the entire flow field. Different manifold configurations are compared in terms of pressure drop and velocity profiles along the flow field cross-section for two different manifold inlets – longitudinal and transverse, in respect to the flow channels. Several designs are compared for one single-cell in terms of heat exchange capacity for a fixed external geometry frame. Performance is compared for the optimal manifold geometry for different mass flow rates of the cooling fluid.

The objective of the study is to design compact heat exchanger with simple flow field geometry for the prescribed outlet temperature of the hot fluid.

## Izvorni znanstveni rad

**Sažetak:** Pločasti izmjenjivači topline obično se koriste u pomorskoj industriji zbog svojih povoljnih svojstava u odnosu na cijevne izmjenjivače topline, kao što je manji volumen za slične vrijednosti izmjenjene topline. Dizajn sabirnice optimiran je u ovom radu primjenom numeričkog modeliranja strujanja kako bi se postigla jednolika raspodjela protoka duž čitavog polja strujanja. Usporedene su različite konfiguracije sabirnice usporedbom pada tlaka i profila brzine duž presjeka u poprečnom smjeru s obzirom na polje strujanja. Različite izvedbe uspoređuju se za jedinični članak, pri čemu je fiksiran obuhvatni geometrijski okvir (odnosno vanjske dimenzije izmjenjivača). Izvršene su usporedbe dvije različite izvedbe ustrojnih kanala – u uzdužnom i poprečnom smjeru s obzirom na polje strujanja fluida. Izvršena je usporedba performansi optimirane sabirnice pri različitim masenim protocima rashladnog fluida.

Konačan cilj istraživanja je projektiranje kompaktnog izmjenjivača topline za propisanu željenu izlaznu temperaturu toplijeg fluida.

## 1. Introduction

Heat exchangers are devices used to transfer heat between two or more fluids, where the temperature of one fluid is decreased while the temperature of remaining fluid is increased. The principle of heat exchanger operation is based on the thermodynamic process of heat transfer. Plate type (PT) heat exchangers are made of thin sheets or plates with different types of channels. They are used for heat exchange with various combinations, most commonly for different fluid-fluid or gas-fluid setups. By increasing the number of the plates, the heat transfer is enhanced. PT heat exchangers are characterized by relatively low mass flow rates and intense heat transfer rates. The main disadvantage is that they cannot withstand high pressures and temperatures, mostly due to the limitations of the sealing materials which are commercially supplied.

PT heat exchangers have a wide application in: central heating plants (boilers, radiators), hot water installations, refrigeration systems (evaporators, condensers), chemical and food industries such as heaters, condensers, crystallizers, dryers, as well as in thermoelectric plants as steam boilers, steam heaters, air heaters, etc., and they are one of the most frequently acquired equipment component in the process industries. In marine industry PT heat exchangers are used as a cooling system component, fresh water distiller, diesel fuel pre-heating, central cooling, cooling of lubrication oil, etc.

In recent years, the importance of the heat exchanger has drastically increased from the point of view of conservation, conversion and energy saving, as well as the successful implementation of new energy sources. The objective of this paper is to develop a new PT heat exchanger design and ensure uniform flow distribution along the entire flow field by employing computational

**Symbols/Oznake**

$C_p$  - specific heat capacity, kJ/(kgK)  
- specifični toplinski kapacitet

$E$  - total fluid energy, J  
- ukupna energija fluida

$\vec{f}$  - mass force, m/s<sup>2</sup>  
- masena sila

$g$  - gravity, m/s<sup>2</sup>  
- gravitacija

$p$  - fluid pressure, Pa  
- tlak fluida

$\vec{u}$  - velocity vector, m/s  
- vector brzine

$T$  - temperature, K  
- temperatura

$t$  - time, s  
- vrijeme

**Greek letters/Grčka slova**

$\lambda_{eff}$  - fluid effective thermal conductivity, W/(mK)  
- efektivna toplinska vodljivost fluida

$\mu$  - dynamic viscosity, Pas  
- dinamička viskoznost

$\rho$  - density, kg/m<sup>3</sup>  
- gustoća

fluid dynamics analysis (CFD). Uniform flow distribution is achieved by designing several manifold configurations and introducing specially designed obstacles to ensure uniform velocity distribution along the symmetry line perpendicular to the general flow, i.e. perpendicular to the flow channels. After the optimization process is completed, the optimal PT heat exchanger geometry is used to design PT heat exchanger stack and the results are compared to the original design.

## 2. Governing equations

Computational Fluid Dynamics (CFD) is a technique based on numerical methods which aims at analyzing fluids movement, heat transfer, mass transfer, and chemical reaction, etc [3]. The present study seeks to examine the fluid flow and heat transfer within a PT heat exchanger, commonly used in various industry processes and sectors. Governing equations solved by Fluent<sup>TM</sup> used for this simulation are explained. Flow equations and energy equations are described in detail in the following sub-chapters.

### 2.1. Flow Calculation

The flow is governed by the continuity equation, the energy equation and Navier-Stokes momentum equations. Transport of mass, energy and momentum occur through convective flow and diffusion of molecules and turbulent eddies. All equations are set up over a control volume where  $i; j; k = 1; 2; 3$  correspond to the three dimensions [1].

#### 2.1.1. Continuity Equation

The continuity equation describes the conservation of mass and it is described in equation [1].

$$\frac{\partial \rho}{\partial t} + \nabla \cdot (\rho \vec{u}) = 0 \quad (1)$$

#### 2.1.2. Momentum Equations (Navier-Stokes Equations)

The momentum balance, also known as the Navier-Stokes equations, follows Newton's second law: The change in momentum in all directions equals the sum of forces acting in those directions. There are two different kinds of forces acting on a finite volume element, surface forces and body forces. Surface forces include pressure and viscous forces and body forces include gravity, centrifugal and electro-magnetic forces [1].

$$\frac{\partial}{\partial t}(\rho \vec{u}) + \nabla \cdot (\rho \vec{u} \vec{u}) = \mu \nabla^2 \vec{u} - \nabla p + \rho \vec{g} + \vec{f} \quad (2)$$

#### 2.1.3. Energy Equation

Energy is present in many forms in flow i.e. as kinetic energy due to the mass and velocity of the fluid, as thermal energy, and as chemically bounded energy. Thus, the total energy can be defined as the sum of all these energies [1].

$$\frac{\partial}{\partial t}[\rho E] + \nabla \cdot [(\rho E + p)\vec{u}] = \nabla \cdot (\lambda_{eff} \nabla T) + \rho \vec{g} \cdot \vec{u} \quad (3)$$

## 3. Geometry

For the desired efficient heat exchanger operation, it is necessary to ensure uniform flow distribution along the entire flow field. Hence, the design of the manifolds and the flow channels are very important. CFD analysis is performed in this work for laminar flow to reduce the number of elements of the mesh and enhance the calculation speed due to the requirement for running relatively large number of different design configurations. The simulations and optimization are carried out in commercial software ANSYS Fluent<sup>TM</sup>

17.2. Geometry is based on design of heat exchangers typically found in marine industry. Since there are quite different manifold configurations found in the commercial marine application PT heat exchangers, the objective of this work was to design a manifold from scratch and to try and achieve uniform flow distribution between fixed geometry parallel flow channels. Heat exchanger geometry is designed in the ANSYS workbench design module, and two of the design configurations are shown in Figure 1 and Figure 2.

The designs shown in Figure 1 and Figure 2 represent the geometry of the CFD model for longitudinal and transverse inlets. Dimensions of the channels are fixed for each studied case. The dimensions of the geometry of heat exchanger for transverse and longitudinal inlets are outlined in Table 1 and Table 2.

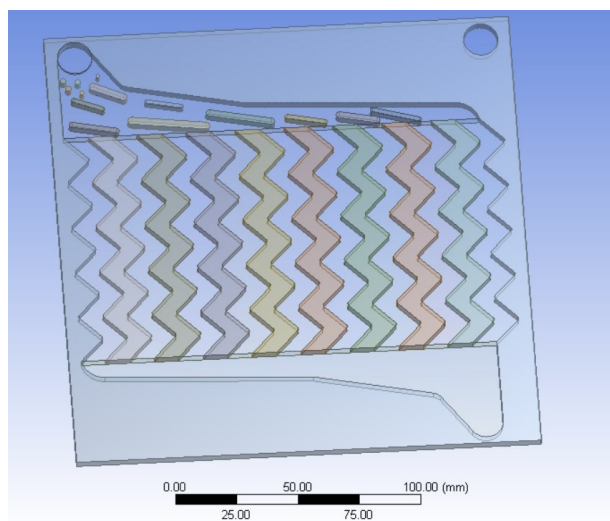


**Figure 1.** Manifold configurations for transverse mass flow inlet

**Slika 1.** Izgled sabirnica za poprečno ustrujavanje fluida

**Table 1.** Heat exchanger dimension for transverse inlet

**Tablica 1.** Dimenzije izmjenjivača topline za poprečno ustrujavanje fluida

No.	Description	Unit	Value
1	Overall dimensions	mm	95x95x30
2	Channel dimensions	mm	100x10x4
3	Number of channels		9
4	Mass flow inlet	mm	Ø14

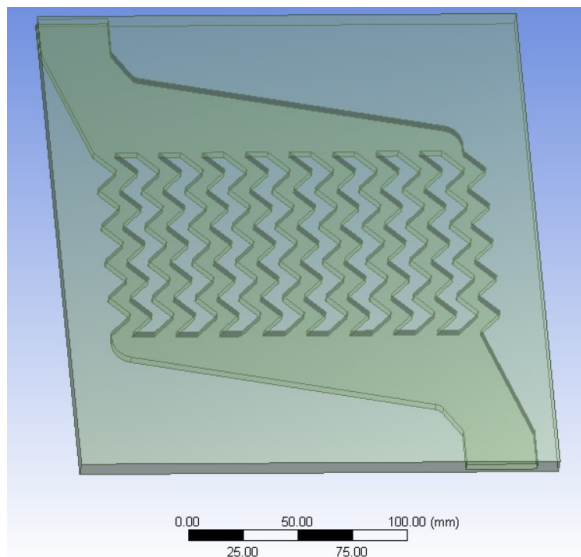


**Figure 2.** Manifold configurations for longitudinal mass flow inlet

**Slika 2.** Izgled sabirnica za uzdužno ustrujavanje fluida

**Table 2.** Heat exchanger dimension for longitudinal inlet

**Tablica 2.** Dimenzije izmjenjivača topline za uzdužno ustrujavanje fluida

No.	Description	Unit	Value
1	Overall dimensions	mm	250x224x30
2	Channel dimensions	mm	100x10x4
3	Number of channels		9
4	Mass flow inlet	mm	18,6x32,6x4

#### 4. Mesh and boundary conditions

One of the most important parts of simulation process is selecting a suitable meshing process to calculate fundamental equations governing the heat-exchanger operation. Selecting a proper meshing can contribute to a suitable convergence in solving the equations while an improper meshing can lead to instability and divergence, i.e. faulty results. Meshing is the discretization of the domain into small volumes where the equations are solved by the help of iterative numerical methods.

For transverse inlet, mesh contains mixed cells (tetrahedral, hexahedral, pyramid and wedge elements). The preferred mesh type is hexahedral, due to heat transfer involved in the calculations and relatively thin plates (i.e. it is required to have at least 4 cells across each gap) and for this reason the geometry is divided into several primitive parts to achieve the desired mesh configuration. Finer mesh, i.e. smaller element size, is generated in regions where the fluid flows, such as manifold and channels. Tetrahedral mesh was used due



to highly complex geometry involved. Figure 3 shows orthogonal quality of mesh for transverse and longitudinal inlet.

For longitudinal inlet, mesh contains hexahedral quadrilateral cells. This results in higher mesh quality and the reason is that for the longitudinal inlet case, the fluid inlet is of a rectangular cross-section, while the transverse case has circular inlet cross-section, therefore it is more complex to generate a structured mesh for such

configuration. At the transverse inlet the obstacles are reducing the orthogonal quality of the mesh due to their irregular curved shape.

The size of mesh elements was set to 1 mm, and the desired size of the elements was achieved using functions Edge Sizing and Body Sizing. The average orthogonal quality was 0.8829 and 0.8923 with standard deviation of 0.13. This is considered a high-quality mesh for this type of geometry. The generated mesh is shown in Figure 3.

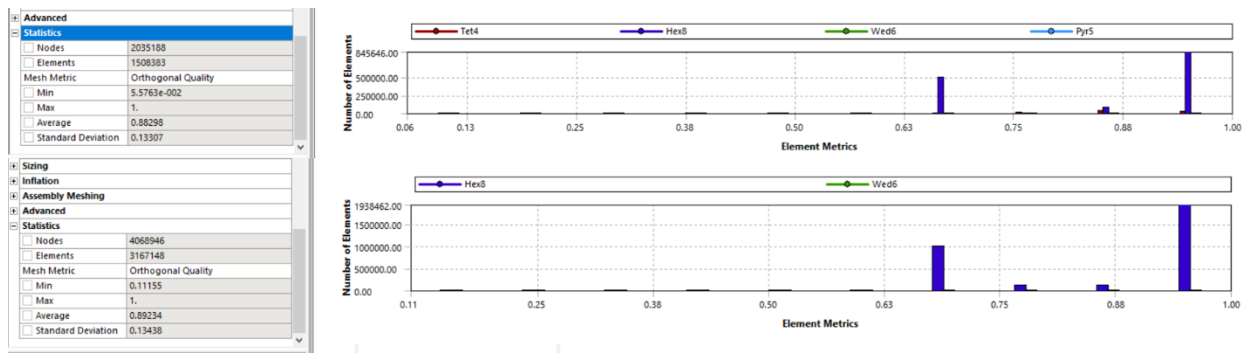


**Figure 3.** Orthogonal quality of mesh for transverse and longitudinal inlet

**Slika 3.** Kvaliteta mreže konačnih volumena za poprečno i uzdužno usstrujavanje fluida

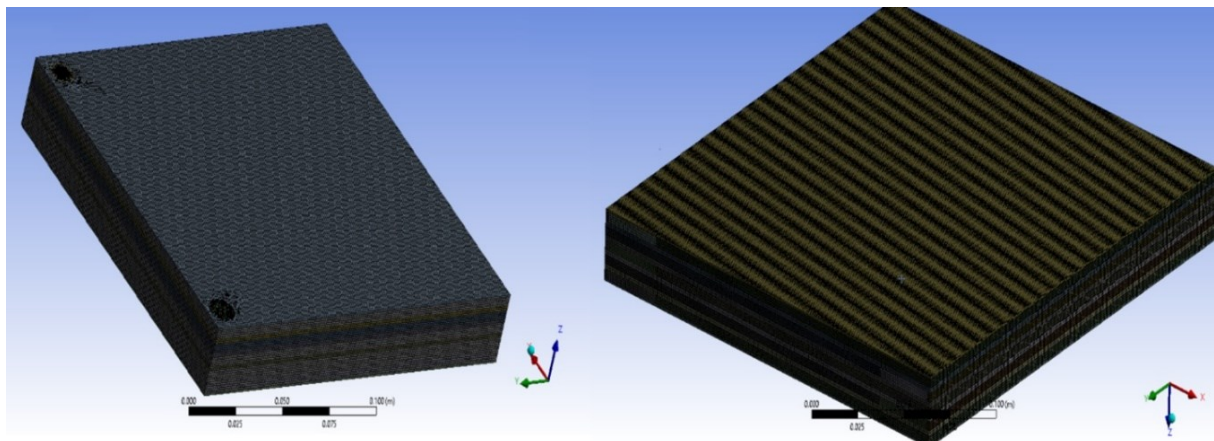


**Figure 4.** Mesh of heat exchanger for transverse and longitudinal inlet

**Slika 4.** Mreže konačnih volumena izmjenjivača topline za poprečno i uzdužno usstrujavanje fluida

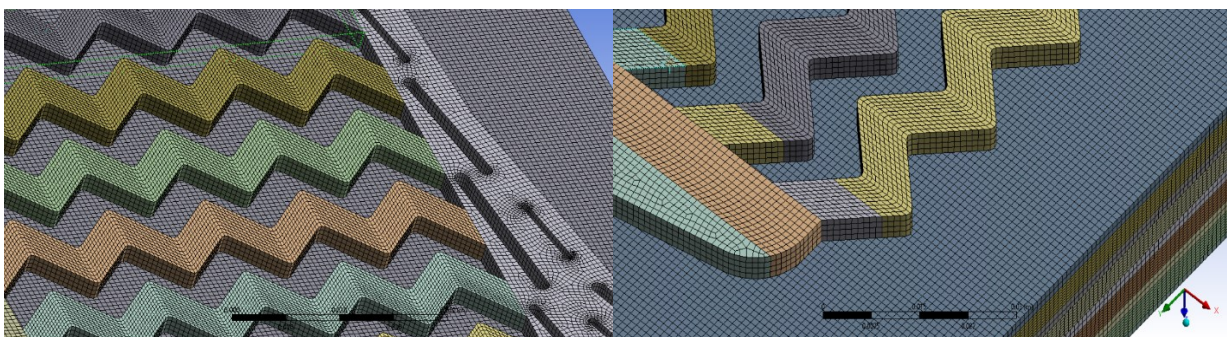


**Figure 5** Mesh of manifolds and channels

**Slika 5.** Mreže konačnih volumena sabirница i kanala

Grid independency study has been carried out for manifold and channels in this work to ensure that numerical results are independent of mesh size. Starting value of elements was  $1\text{ mm}$ , and then the sizing was decreased to  $0.5\text{ mm}$  via Edge Sizing function. With edge size of  $1\text{ mm}$  the number of elements was 119748, with  $0.5\text{ mm}$  the number of elements was 462400, and with Inflation function incorporated the number of elements was 1020256. Difference in results with different edge sizing was minimal, while the velocity profile through channels are approximately equal. With Inflation method, the overall velocity is a little bit higher, but with equal regularity of growth, this is due to higher number of elements across each channel where the data is extracted, while the area-weighted average velocity across the channels was quite similar to the mesh with incorporated edge sizing. Therefore, the grid independent mesh is the one with edge sizing of  $1\text{ mm}$ , ensuring faster calculation time, i.e. convergence. Grid independency study velocity profiles for different mesh configurations are shown in Figure 6.

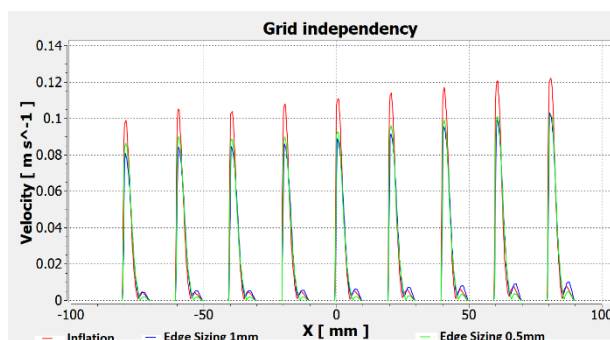


Figure 6. Grid independency

Slika 6. Ovisnost rezultata o broju konačnih volumena

#### 4.1. Inlet boundary conditions

For inlet boundary conditions it is defined that hot fluid is liquid water, while the coolant is sea water. Mass flow and temperature are defined as inlet boundary conditions. Parameters at the inlet of hot fluid are: mass flow inlet  $0.005\text{ kg/s}$  for transverse inlet and  $0.01\text{ kg/s}$  for longitudinal inlet. Temperature at the inlet of hot fluid (for both cases) is set at  $353\text{ K}$ . For cold fluid the inlet temperature is set at  $293\text{ K}$ . Materials of solid parts are set to represent titanium with its corresponding density, heat capacity and thermal conductivity.

### 5. Improvement process

The aim of improvement was to achieve uniform flow distribution along the entire flow field. Optimization was carried out for two different manifold inlets, transverse and longitudinal.

#### 5.1. Improvement of manifold with transverse inlet

Improvement of transverse manifold inlet was more difficult to achieve, therefore, the improvement is carried out in higher number of steps when compared to the longitudinal inlet. The first step was to create manifold with transverse inlet and observe the velocity distributions through the channels.

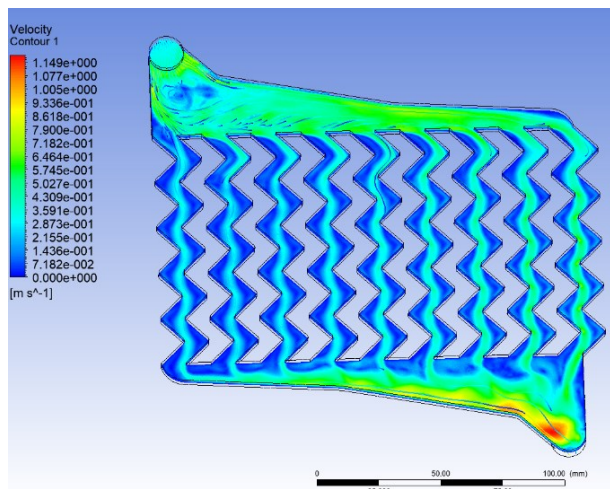


Figure 7. Initial manifold design for improvement with velocity contours and velocity streamlines

Slika 7. Početni dizajn sabirnice za poboljšanje, konture brzine i strujnice

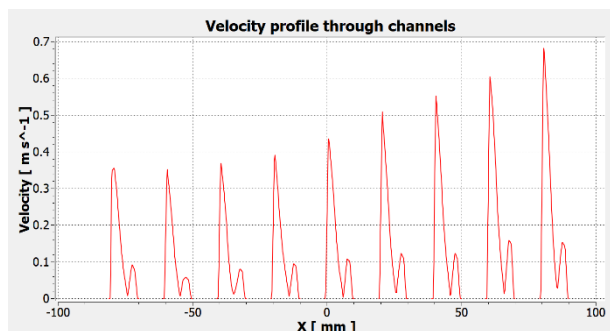


Figure 8. Velocity profile through channels

Slika 8. Profil brzine kroz kanale

As it can be seen from Figure 7 and 8, the velocity profiles show that velocity is increasing in the positive X-direction (perpendicular to the channels). To achieve uniform flow distribution, the velocity magnitude must be increased through the first channels, and decrease through the channels at end. This is adjusted by introducing rectangular obstacles inside the manifold, Figure 9.

By adding rectangular obstacles, the flow distribution is rearranged, resulting in quite different velocity distribution through the channels. As it is shown in Figures 9 and 10, the velocity profiles are quite uniform throughout the first three channels, and then they start to decrease. To achieve more uniform flow distribution, a



different configuration of the obstacles is introduced, Figure 11.

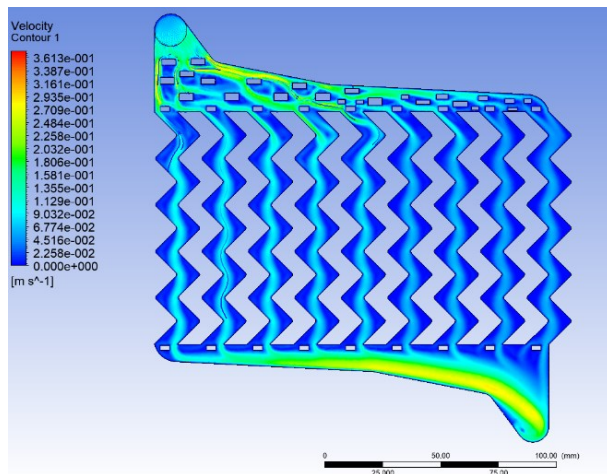


**Figure 9.** Modification of manifold, version 2  
**Slika 9.** Modifikacija sabirnica, pokušaj 2

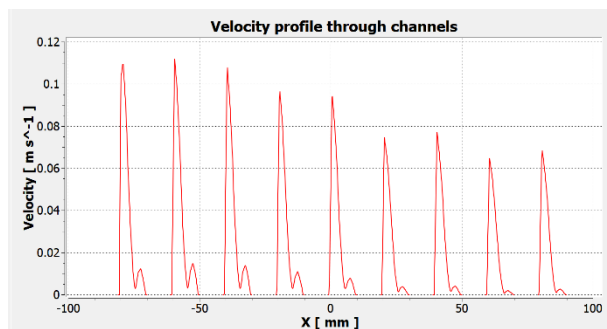


**Figure 10.** Velocity profile through channels  
**Slika 10.** Profil brzine kroz kanale

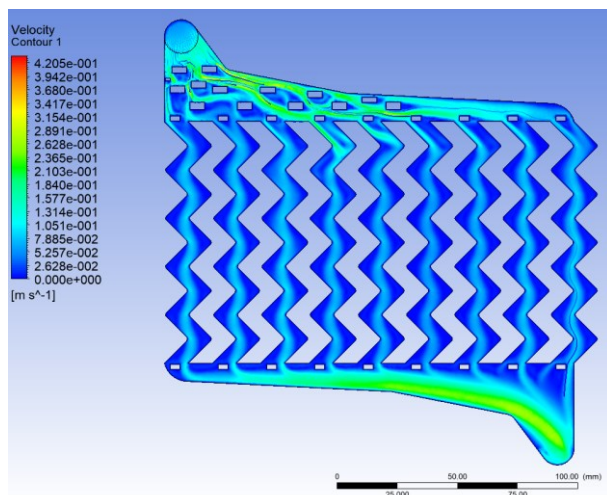


**Figure 11** Modification of manifold, version 3  
**Slika 11.** Modifikacija sabirnica, pokušaj 3

By rearranging the obstacles and decreasing their number in close proximity to the channels with formerly

decreased velocity, more uniform velocity distribution is achieved.

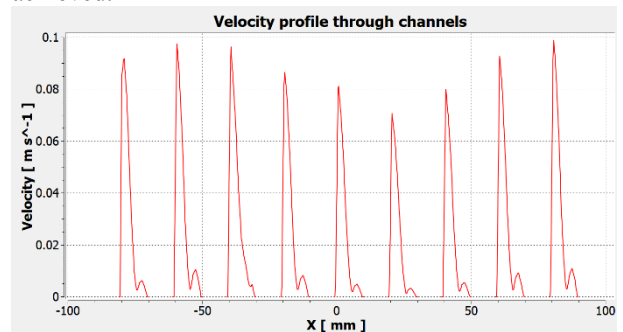


**Figure 12.** Velocity profile through channels  
**Slika 12.** Profil brzine kroz kanale

Figures 11 and 12 show that velocity profiles are good through the first three and last two channels, however it is still required to optimize the obstacle design for the middle ones. Further optimization with rectangular obstacles was not feasible for this case, therefore cylindrical obstacles are introduced, as seen in Figure 13.

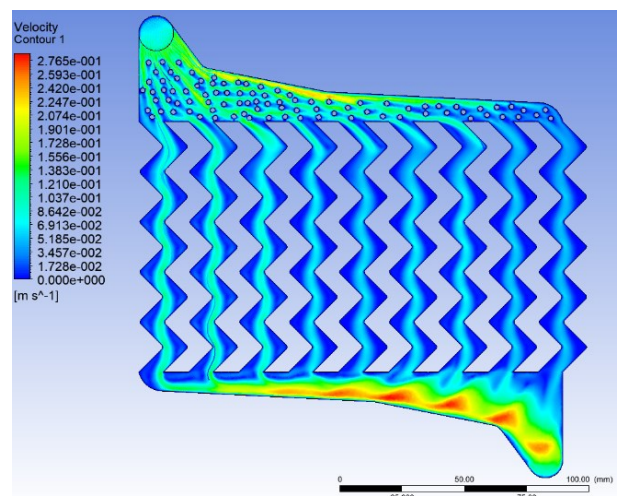


**Figure 13** Modification of manifold, version 4  
**Slika 13.** Modifikacija sabirnica, pokušaj 4

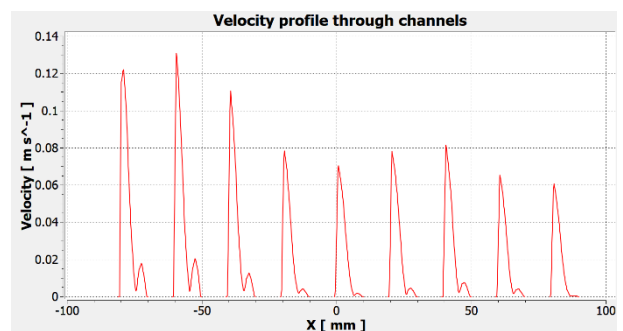


**Figure 14.** Velocity profile through channels  
**Slika 14.** Profil brzine kroz kanale

With purely circular obstacles, shown in Figure 13, redirection of fluid didn't show good results, as seen in

Figure 14, therefore hybrid type of obstacles is introduced – cylindrical and elliptical, Figure 15.

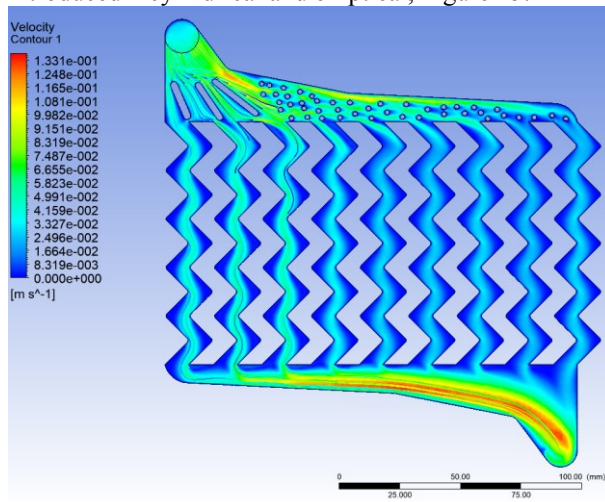


**Figure 15.** Modification of manifold, version 5  
**Slika 15.** Modifikacija sabirnica, pokušaj 5

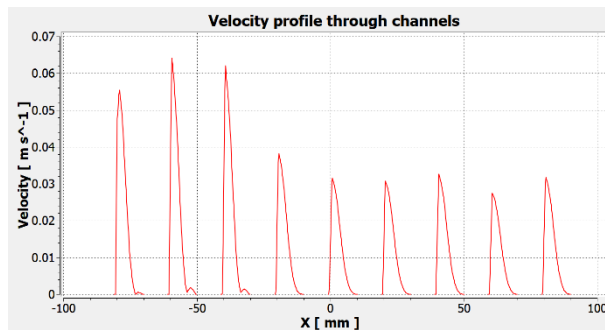


**Figure 16** Velocity profile through the channels  
**Slika 16.** Profil brzine kroz kanale

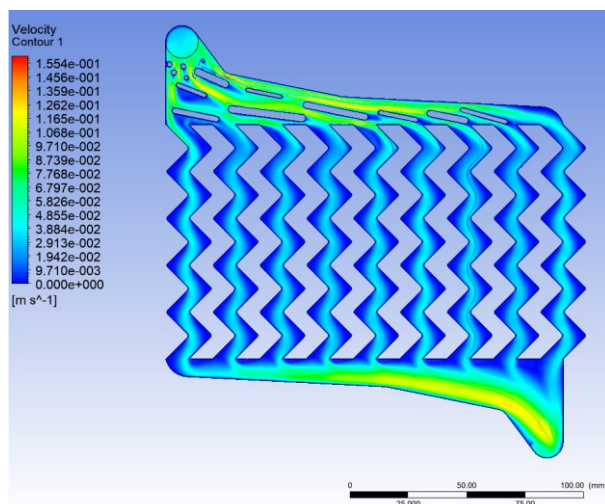


**Figure 17** Final manifold design  
**Slika 17** Konačni izgled sabirnica

Circular and elliptical obstacles show good velocity distribution for 5 channels. Additional optimization of the first three channels is required to achieve uniform

velocity profiles and uniform flow distribution. Finally, the optimal configuration is shown in Figure 17.

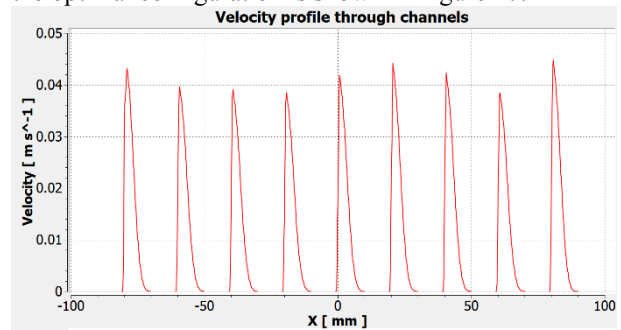


**Figure 18.** Velocity profile through the channels  
**Slika 18.** Profil brzine kroz kanale

With proper position of obstacles, uniform velocity profiles, i.e. uniform flow distribution is achieved. Optimized manifold is shown in Figure 17 and its corresponding velocity profile through the channels is shown in Figure 18. Finally, this manifold design is used for heat exchanger calculations with transverse inlet.

## 5.2. Improvement of manifold with longitudinal inlet

Improvement of longitudinal manifold inlet was easier to achieve, and optimization is carried out in lower number of steps when compared to the transverse inlet case. The manifold design improvement process was similar to the one seen previously. In the initial step a primitive manifold shape was created with longitudinal inlet and outlet, Figure 19, and the velocity profiles through the channels are observed, Figure 20.

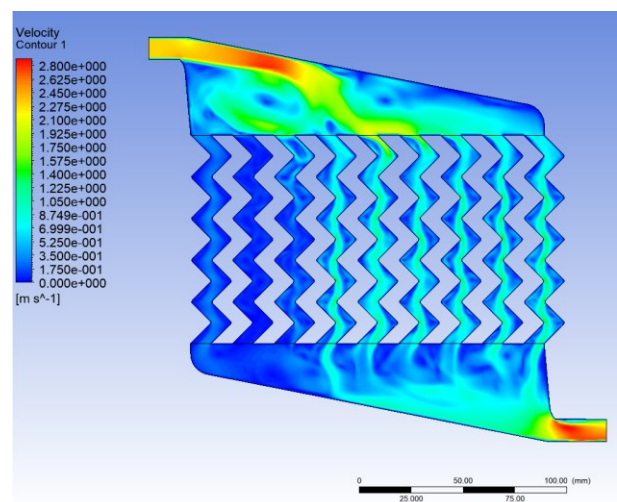


**Figure 19.** Initial manifold for improvement and velocity contours

**Slika 19.** Početni dizajn sabirnica za poboljšanje i konture brzine

As it can be seen from Figures 19 and 20, velocity profiles show that the flow distribution is highly non-uniform and mass flow rate through the initial channels

is quite low, therefore the design of the manifold is modified, Figure 21.

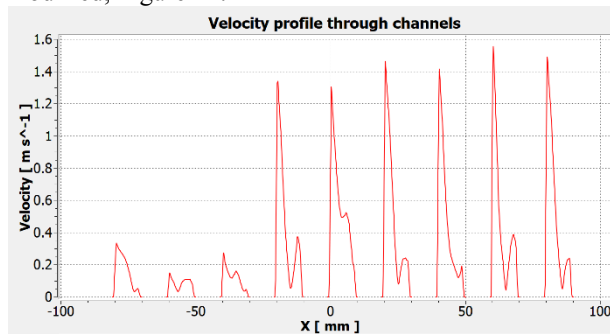


**Figure 20** Velocity profile through channels

**Slika 20.** Profil brzine kroz kanale

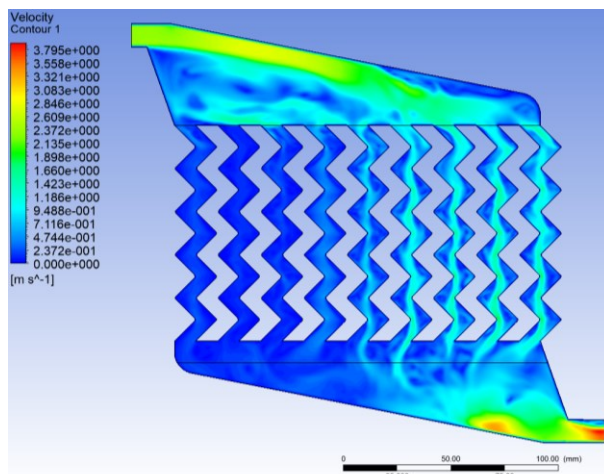


**Figure 21.** Modification of manifold, version 2

**Slika 21.** Modifikacija sabirnica, pokušaj 2

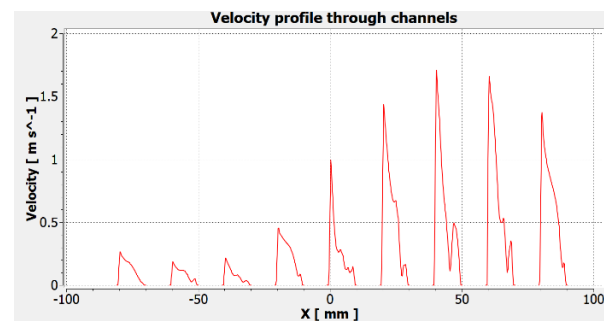


**Figure 22.** Velocity profile through channels

**Slika 22.** Profil brzine kroz kanale

It is evident from Figure 22 that modification of the manifold outer boundaries does not have high impact on the overall flow distribution, therefore the inlet position is altered, the new design is shown in Figure 24. The new, optimal, design results in quite uniform flow distribution along the entire flow field, as illustrated in Figure 23.

The manifold configuration shown in Figure 24 is also used to create a PT heat exchanger stack and it is compared to the design shown previously in Figure 17.

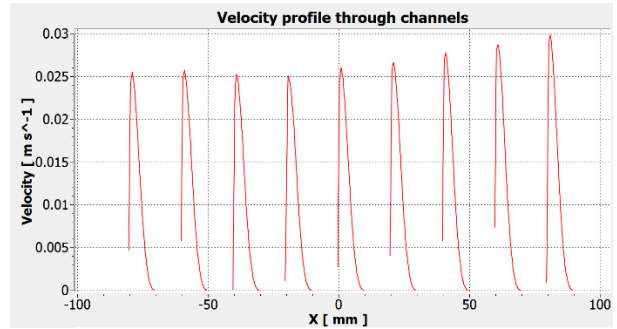


**Figure 23.** Velocity profile through channels

**Slika 23.** Profil brzine kroz kanale

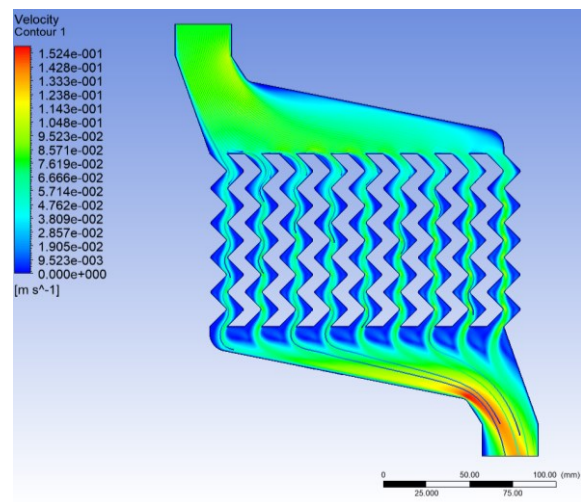


**Figure 24** Final manifold design

**Slika 24.** Konačni izgled sabirnica

## 6. Results

Velocity profiles for both heat exchangers are shown in Figures 24 and 25. Figure 24 represents velocity profile for hot and cold fluid through channels for heat exchanger with longitudinal inlet, and Figure 25 for heat exchanger with transverse inlet.

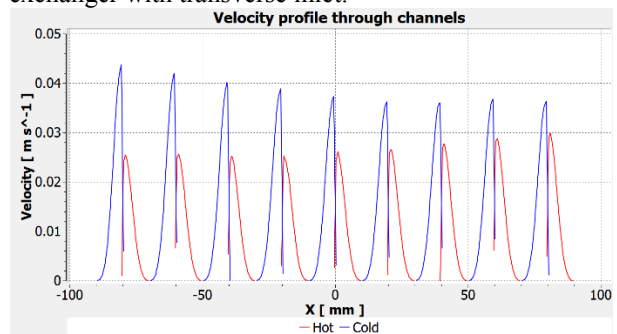


**Figure 25.** Velocity profile of heat exchanger with longitudinal inlet through the channels

**Slika 25.** Profil brzine izmjenjivača topline s uzdužnim ustrujavanjem kroz kanale

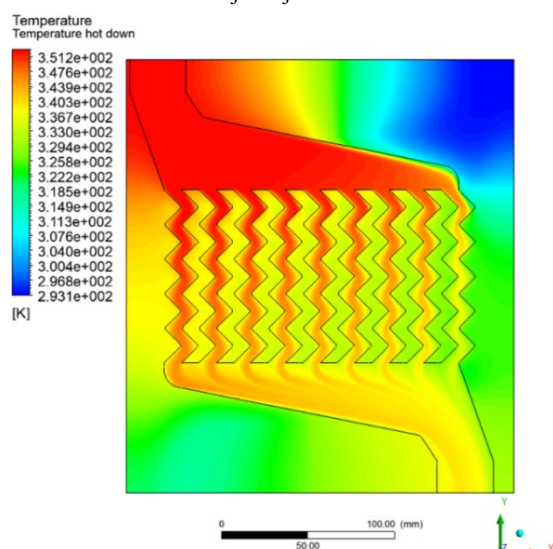
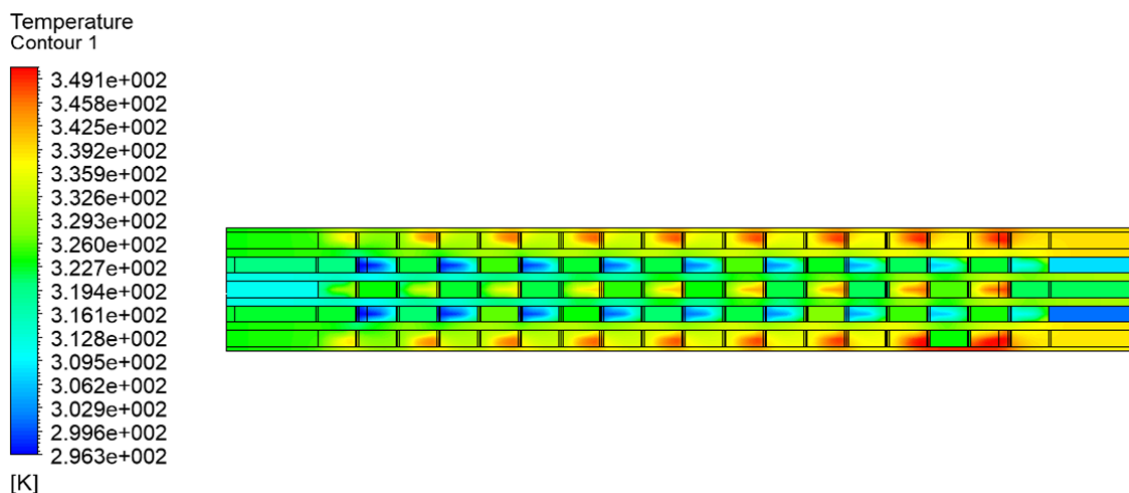
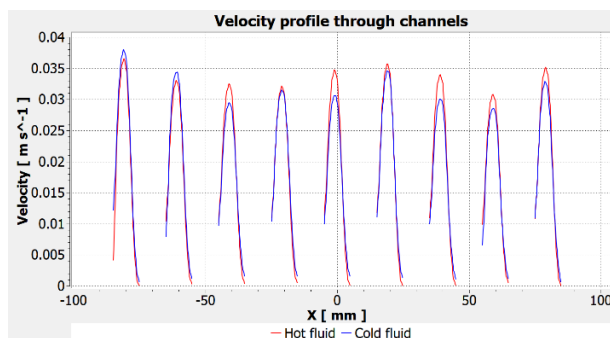
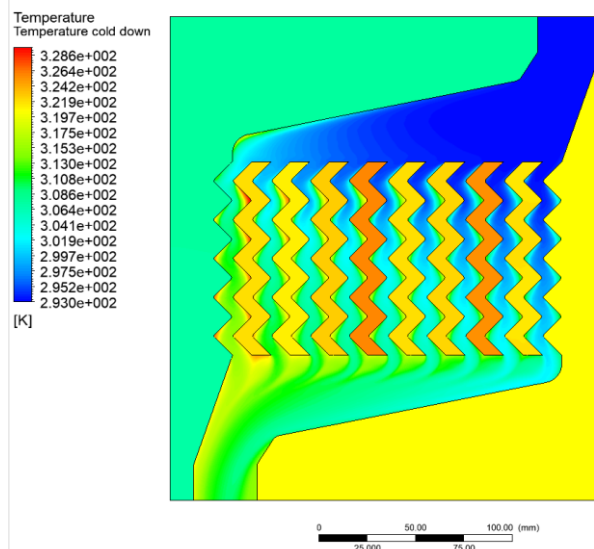
The desired outlet temperature of the hot fluid (entering the stack at 353 K, i.e. 80 °C) was set to 333 K, i.e. 60 °C. The resulting temperature distribution is shown in Figures 27, 28 and 29.

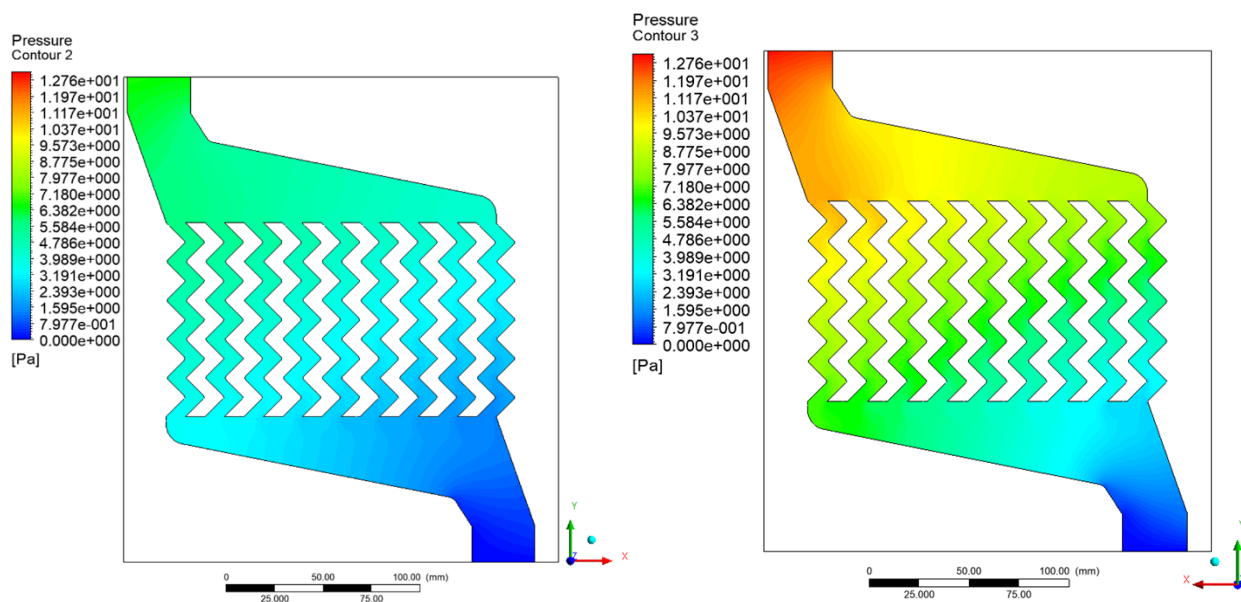


**Table 3.** Values of heat transfer, inlet and outlet temperatures of cold and hot fluid for the longitudinal inlet**Tablica 3.** Vrijednosti izmjenjenog toplinskog toka, ulazne i izlazne temperature toplog i hladnog fluida za

No.	Description	Unit	Value
1	Mass flow	kg/s	0.01
2	Inlet temperature of hot fluid	K	353
3	Inlet temperature of cold fluid	K	293
4	Outlet temperature of hot fluid	K	333
5	Outlet temperature of cold fluid	K	314
6	Heat transfer	J/s	836.4

uzdužno ustrujavanje fluida

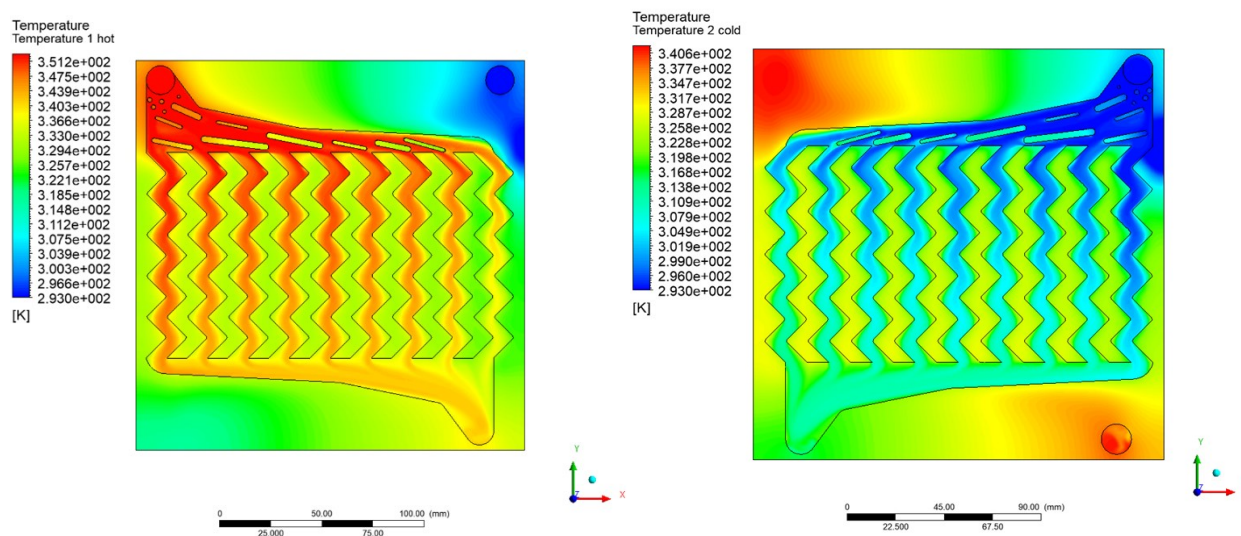
**Figure 27.** Temperature distribution upper hot plate of heat exchanger, longitudinal inlet**Slika 27.** Raspodjela temperature gornje tople ploče izmjenjivača topline, uzdužno ustrujavanje**Figure 29.** Temperature distribution of heat exchanger with longitudinal inlet**Slika 29.** Raspodjela temperature izmjenjivača topline s uzdužnim ustrujavanjem**Figure 26.** Velocity profile of heat exchanger with transverse inlet through the channels**Slika 26.** Profil brzine izmjenjivača topline s uzdužnim i poprečnim ustrujavanjem kroz kanale**Figure 28.** Heat exchanger cold plate temperature distribution**Slika 28.** Raspodjela temperature hladne ploče izmjenjivača topline, uzdužno ustrujavanje



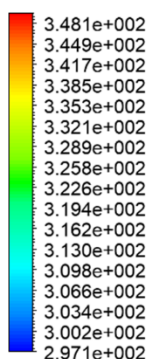
**Figure 30.** Pressure distribution of heat exchanger with longitudinal inlet  
**Slika 30.** Raspodjela tlaka izmjenjivača topline s uzdužnim ustrujavanjem

Pressure drop for heat exchanger with longitudinal inlet is small, maximum value is 12.7 Pa which can be seen in Figure 30. Heat transfer is 836.4 J/s. Because of small pressure drop, good heat transfer and unique velocity

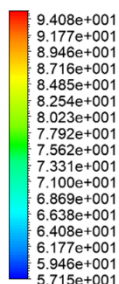
profiles and uniform flow distribution, it would be practically to make this heat exchanger with more than 5 plates.



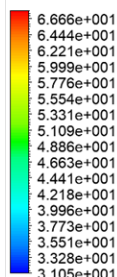


Temperature  
Contour 1

[K]

**Figure 31.** Temperature distribution of heat exchanger with transverse inlet**Slika 31.** Raspodjela temperature izmjenjivača topline s poprečnim ustrujavanjemPressure  
Contour 2

[Pa]

Pressure  
Contour 3

[Pa]

**Figure 32.** Pressure distribution of heat exchanger with transverse inlet**Slika 32.** Raspodjela tlaka izmjenjivača topline s poprečnim ustrujavanjem**Table 4.** Values of heat flux, inlet and outlet temperatures of cold and hot fluid for transverse inlet**Tablica 4.** Vrijednosti izmjenjenog toplinskog toka, ulazne i izlazne temperature toplog i hladnog fluida za poprečno ustrujavanje fluida

No.	Description	Unit	Value
1	Mass flow	kg/s	0.005
2	Inlet temperature of hot fluid	K	353
3	Inlet temperature of cold fluid	K	293
4	Outlet temperature of hot fluid	K	321
5	Outlet temperature of cold fluid	K	315
6	Heat transfer	J/s	669.1

The desired outlet temperature of the hot fluid (entering the stack at 353 K, i.e. 80 °C) was set to 321 K, i.e. 48°C. The resulting temperature distribution is shown in Figure 31.

For the heat exchanger with transverse inlet there is a bigger increase in pressure than for the heat exchanger with longitudinal inlet, that can be seen from Figure 32. The pressure increases from values of 30 Pa to 91 Pa, which represents small increase of pressure. This type of heat exchanger shows good heat transfer characteristics, which is 669.1 J/s.

The goal was to achieve any desired outlet temperature of fluids. This could be done by changing the mass flow. This process shows Figure 33, where the goal was to cool down hot fluid to 325 K. That was achieved with increasing mass flow of cold fluid from 0.01kg/s to 0.1 kg/s.

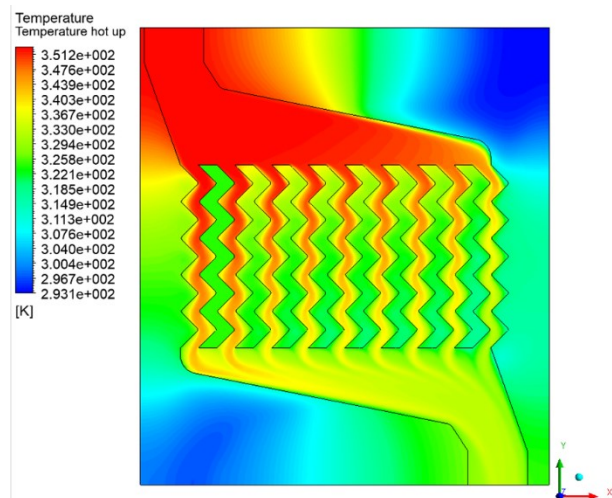


**Figure 33.** Temperature distribution of hot fluid, outlet temperature 325 K

**Slika 33** Raspodjela temperature toplog fluida, izlazna temperatura 325 K

## 7. Conclusion and future work

CFD analysis in this paper shows how improve the heat exchangers in terms of achieving uniform flow distribution and equal velocity profile along the entire flow field, minimize pressure drop and achieve wanted outlet temperatures of hot and cold fluid. Adding additional plates with hot and cold fluid would be good for higher fluid mass flow rates.

Future goals are to made heat exchangers with more plates of hot and cold fluid, especially for transverse inlet which shows better results. Analyse difference of counter flow vs direct flow in terms of heat transfer and change of outlet temperatures.

## REFERENCES

- [1] B. Andersson, R. Andersson, L. Hakansson, M. Mortensen, R. Sudiyo, and B. V. Wachem, (2010). *"Computational Fluid Dynamics for Chemical Engineers"*, sixth ed.
- [2] Usman Ur Rehman, *"Heat Transfer Optimization of Shell and Tube Heat Exchanger"*, Chalmers University of Technology, Goteborg, Sweden, Master's Thesis
- [3] Khashayar Sharifi, Morteza Sabeti, Mehdi Rafiei, Amir H. Mohammadi, Laleh Shirazi, *"Computational fluid dynamics (CFD) technique to study the effects of helical wire inserts on heat transfer and pressure drop in a double pipe"*, Applied Thermal Engineering
- [4] Siddhant Singh Yogesh, Arun Saco Selvaraj, Dinesh Kumar Ravi, Thundil Karuppa Raj Rajagopal, *"Heat transfer and pressure drop characteristics of inclined elliptical fin tube heat exchanger of varying ellipticity ratio using CFD code"*, International Journal of Heat and Mass Transfer
- [5] W. Youssef, Y.T. Ge, S.A. Tassou, *"CFD modelling development and experimental validation of a phase change material (PCM) heat exchanger with spiral wired tubes"*, Energy Conversion and Management
- [6] Nižetić S., Radica G., *Rashladna tehnika*, online script, FESB, Split
- [7] Nižetić S., *Termodinamika II*, online script, FESB, Split
- [8] <https://dieselship.com/marine-technical-articles/marine-engineering-knowledge-general/plate-type-heat-exchanger/>, online source, access date 05.04.2018.
- [9] <https://www.tranter.com/products/plate-heat-exchangers/configurations>, online source, access date 05.04.2018.

# Research on electromagnetic field (EMF) and related biological hazards: state-of-the-art

**Livio GIULIANI<sup>1, 5, 6)</sup>, Massimo ROGANTE<sup>2)</sup>,  
Peter WADHAMS<sup>3)</sup> and Barbara ZAVAN<sup>4)</sup>**

- 1) University of Abruzzo, Centro Riabilitazione Specialistica, Corso di Laurea in Fisiatria, I-66100 Chieti Scalo, **Italy**
- 2) Rogante Engineering Office, Contrada San Michele n. 61, I-62012 Civitanova Marche, **Italy**
- 3) University of Cambridge, Centre for Mathematical Sciences, Wilberforce Road, CB3 0WB Cambridge, **United Kingdom**
- 4) University of Padua, Dept. of Biomedical Sciences, Via Ugo Bassi n. 58/B, I-35131 Padua, **Italy**
- 5) International Commission for Electromagnetic Safety (ICEMS), VEGA1-Ente Zona Industriale di Porto Marghera, I-30175 Venice, **Italy**
- 6) European Cancer and Environmental Research Institute (ECERI), Square de Meeus 38-40, 1000 Bruxelles, **Belgium**

[giuliani.livio@gmail.com](mailto:giuliani.livio@gmail.com)  
[main@roganteengineering.it](mailto:main@roganteengineering.it)  
[pw11@cam.ac.uk](mailto:pw11@cam.ac.uk)  
[barbara.zavan@unipd.it](mailto:barbara.zavan@unipd.it)

## Keywords

EMF exposure  
 electro smog  
 biological hazard  
 mobile phones  
 WLAN  
 GPRS  
 UMTS

## 1. Introduction

EMF, which generally combines EF and MF, was discovered during the 19th century, despite existing since life first emerged (due to its creation via natural phenomena); photons (quanta) are the particles carrying the electromagnetic waves [1].

The most significant parameters describing the EMF are frequency and wavelength, and they are inversely proportional: an increase of frequency corresponds to a shortening of wavelength, which carries more energy in comparison with lower frequency waves. Other parameters are phase, amplitude and wave forms.

Two main categories of EMF exist, depending on the energy levels of the electromagnetic quanta (ionizing or non-ionizing radiation). The ionizing radiation (e.g., X-rays,  $\gamma$ -rays and high ultraviolet) possesses adequate

## Review article

**Abstract:** The demands of multiple performances by modern equipment such as mobile and cordless phones, mobile phone base stations, data cards for laptops and notebook computers, general packet radio service (GPRS), universal mobile telecommunications system (UMTS), and wireless local area networks (WLAN), is increasingly stringent. The combination of the involved low and high frequency electric fields (EF), magnetic fields (MF) and electromagnetic fields (EMF) of different signal patterns, thus, is fostering more and more questions regarding whether they have a hostile effect on humans and other organisms.

This paper, after an introduction about the topic, is briefly reporting a state-of-the-art on the related research, especially concerning the EMF and the possible subsequent biological hazards to living organisms.

energy per quantum in order to ionize molecules: this radiation is able to cause chemical reactions and to break the bonds between molecules, damaging living cells and genes, and producing tumours. The non-ionizing radiation does not possess enough energy per quantum to break molecular bonds in empty space or in air. Non-ionizing radiation forms are the following, where the radio frequency (RF) ranges are, according to the International Telecommunication Union (ITU) designation:

Micrometre waves

- ultraviolet A (UVA) ( $\nu = 750 \div 950$  THz;  $\lambda = 315 \div 400$  nm)
- visual light (VL) ( $\nu = 430 \div 750$  THz;  $\lambda = 0,4 \div 0,7$   $\mu\text{m}$ )
- near infrared (NR) ( $\nu = 300 \div 430$  THz;  $\lambda = 700$  nm  $\div$  1  $\mu\text{m}$ )
- infrared (IR) ( $\nu = 0,3 \div 300$  THz;  $\lambda = 1$   $\mu\text{m} \div 1$  mm)

**Symbols/Oznake**

$P$	- power flow density, W/m <sup>2</sup>		
	- ...		
$B_{ac}$	- alternate magnetic field, T		
	- ...		
		$\lambda$	<b>Greek letters/Grčka slova</b>
			- wavelength, m
			- ...
		$\nu$	- frequency, Hz
			- ...

## Radiofrequency waves

- extremely high frequency (EHF) ( $\nu = 30 \div 300$  GHz;  $\lambda = 1 \text{ mm} \div 1 \text{ cm}$ )
- super high frequency (SHF) ( $\nu = 3 \div 30$  GHz;  $\lambda = 1 \text{ cm} \div 1 \text{ dm}$ )
- ultra high frequency (UHF) ( $\nu = 0.3 \div 3$  GHz;  $\lambda = 1 \text{ dm} \div 1 \text{ m}$ )
- very high frequency (VHF) ( $\nu = 30 \div 300$  MHz;  $\lambda = 1 \div 10 \text{ m}$ )
- high frequency (HF) ( $\nu = 3 \div 30$  MHz;  $\lambda = 10 \div 100 \text{ m}$ )
- middle frequency (MF) ( $\nu = 0.3 \div 3$  MHz;  $\lambda = 100 \text{ m} \div 1 \text{ Km}$ )
- low frequency (LF) ( $\nu = 30 \div 300$  kHz;  $\lambda = 1 \div 10 \text{ Km}$ )
- very low frequencies (VLF) ( $\nu = 3 \div 30$  kHz;  $\lambda = 10 \div 100 \text{ Km}$ )
- ultra low frequency (ULF) ( $\nu = 0.3 \div 3$  kHz;  $\lambda = 1 \times 10^6 \div 1 \times 10^7 \text{ m}$ )
- super low frequency (SLF) ( $\nu = 30 \div 300$  Hz;  $\lambda = 1 \times 10^7 \div 1 \times 10^8 \text{ m}$ )
- extremely low frequency (ELF) ( $\nu = 3 \div 30$  Hz;  $\lambda = 1 \times 10^7 \div 1 \times 10^8 \text{ m}$ )

According to radioprotectionists, ELFs includes SEFs and fall below the cut-off of 3 Hz, between 1 and 300 Hz [2].

Man-made sources of non-ionizing radiation include mobile and cordless phones, mobile phone base stations, radio and TV, GSM, UMTS, LTE, 5G, GPRS, data cards for laptops and notebook computers, WLAN as well as several other electrical devices widely employed in daily life (e.g., microwave ovens, or the smart metering for electricity, gas and water consumption).

In addition to the geomagnetic field (varying from 25 to 60  $\mu\text{T}$  [3]), the averaged natural radiofrequency field is usually estimated as having a power density of  $10^{-7} \text{ W/m}^2$  on the earth's surface [4].

Radiofrequency industrial devices are usually classified as LF-, MF- or HF- devices, as their emission falls in the band LF/VLF/UHF/SHF/ELF, in the band MF or in the band HF/VHF/UHF/SHF/EHF, respectively. LF and MF, in recent literature, are called Intermediate Frequencies (IF), as well. Hereafter MF will be included in HF.

## 2. Comparing standard ceiling values and natural background

To compare the global natural RF-background with today's artificial bath of RFs, let's keep in mind the upper quoted average of natural RFs and consider the ceiling values for people exposures to RFs introduced in several countries (almost everywhere, apart from Africa). Let us consider lowest and highest levels in the standards for human global exposure.

For RFs, both LF and HF, the lowest standard for human global exposure is from Switzerland [5] - 1  $\mu\text{T}$  for the magnetic field in SLF band and 0,05-0,1  $\text{W/m}^2$  in HF band - the highest one is common to G7 countries, except Italy [6-9]. China has an intermediate ceiling value standard, derived from the IEEE standard, provided a further safety factor equal to 4.

Finally, we can compare the lowest and highest ceiling value of standards for human global exposures – that are supposed to be saturated in many areas by the telecommunication industry - with the natural background. We find that, in terms of power density, the ratio between the lowest ceiling value and the natural background is  $0.1/0.1 \text{ W/m}^2 / (10^{-7} \text{ W/m}^2) = 10^6$  that increases up to  $10^8$  if we consider the highest ceiling value, proposed by IEEE, CENELEC, ICNIRP and recommended by EU.

The lowest standard for exposure to the head is from USA, i.e. 1.6  $\text{W/kg}$  averaged on 1 gram of tissue [10], while the standard of the EU [7] - that has been suggested from a private organization, the International Commission on Non-Ionizing Radiation Protection (ICNIRP) [11], censured by the Parliament Assembly of Council of Europe (PACE) (see [12], Paragraph 8.1.2) - is the highest one: 2.0  $\text{W/kg}$  average upon 10 g of continuous tissue with a period of 6'. China adopted the latter standard for partial exposures to the head in 2008.

The USA standard for partial exposures to the head is derived from the radioprotectionists practice in the frame of ionizing radiation. An increasing factor, equal to 20, is applied to the ceiling value for global exposure, in order to get the ceiling value for partial exposure (better for partial exposures to arms, not to the head). The EU standard factor = 25 has no justification - and the Recommendation 1999/519/EEC was not approved by Italy - but the convenience is for the German industry of telephones (finally frustrated by the market).

Indeed, humans today are mainly exposed to electromagnetic fields produced by the said manmade sources. In particular, the levels of power emitted by some of these sources are reported in Table 1.

**Table 1.** Levels of exposure to EMF produced by some man-made sources (order of magnitude)

<i>Device</i>	<i>P(W)</i>
mobile phones	1
cordless phones	0.1
GSM mobile phone base stations	100
UMTS, LTE	10
data cards for laptops and notebook computers	0.1
WLAN	1
microwave ovens	1000
Radio antennas FM	1000
CW-MW Radio Systems	1,000,000
Radio /TV Towers	1,000,000
High voltage power lines	1,000,000

Obviously, the upper table has only a finding aim, because not power but power density is meaningful in the interaction between RFs and living organisms.

Better, we should distinguish between thermal and non thermal effects, since power density is relevant only for thermal effects [13], while non thermal effects arise only in windows of frequency and intensity, as discovered by Bowin and Ross Adey more than 40 years ago [14-16], and confirmed by Carl Blackman and collaborators at US EPA [17-18].

Furthermore the thermal mechanism beyond thermal effects of NIR is quite different whether the band of the incident radiation is in LF (and lower) or in HF (and higher RF bands).

In the case of LFs, the main recognized mechanism is the electric Joule effect, experienced in ohmic or almost ohmic conductors [19]. In the case of HF, the main mechanism is the mechanical Joule effect, since the electromagnetic wave induces a rotation of the water electric dipole, as fast as the frequency of the incident wave - and water is more than 90% of living matter - realizing real Joule in nanoscopic scale [20].

The mechanisms of non thermal interaction of electromagnetic field with living matter are less known. Between them we shall consider:

- the parametric or cyclotron ion resonance related to the so called Blackman-Liboff-Zhadin (BLZ) effect [21-24]
- the electromagnetic acceleration of electron transfer in cell biochemical reaction [25]
- DNA radioemission and radio reception [26-28]. Furthermore, it has been supposed that a cell membrane works as a radio receiver/transmitter, as well [29].

### 3. Standard constraints

IEEE standard C95 (1992), ICNIRP Guidelines (1998) and CENELEC standard 50166 (1994) [5, 6, 10, 19], are all limited in considering only thermal effects of radiations. Indeed, the recalled censure of PACE (ref. [12], Paragraph 8.1.2) could be extended to IEEE and to CENELEC as well as to EU Council Recommendation 1999/519/EEC. In 2009, ICNIRP reaffirmed its 1998 guidelines, since according to their opinion, the published scientific literature had not provided any evidence of any negative effect below the established limits and no immediate revision of its guidance for the limitation of exposure to high frequency electromagnetic fields was necessary.

Despite this statement, in 2011 WHO IARC included RFs, generated by handy phones, in class 2b as a possible carcinogenic agent, for heavy ipsilateral users. The new draft of ICNIRP, now undergoing public inquest, is again limited only considering thermal effects. The International EMF Scientist Appeal [30] and other scientists bodies, even the ones quoted by PACE (ref. [12], Annexed Doc. 12608, Paragraphs 43 and 44), as well as individual eminent scientists [31-34] claim the ICNIRP guidelines and other international standards are insufficient to protect public health, since they do not consider long-term exposures and low-intensity (i.e. non thermal) effects.

### 4. State-of-the-art

Several scientific publications have shown that EMFs influence living organisms at levels well below many national and international guidelines. The effect is increased by gravity, genetic damage, structural and reproductive system problems, learning and memory deficits, neurological disorders and negative impacts on the general well-being of human beings, since there are more and more evidences of animals. A massive literature exists, concerning electromagnetic field (EMF) and related biological hazards, which provides a high level of scientific certainty in particular for the following eight different pathophysiological effects caused by non-thermal microwave frequency EMF exposures [13]:

- cellular DNA damage: single strand and double strand breaks in cellular DNA and oxidized bases in cellular DNA, leading to cancer causation and chromosomal and other mutational changes
- lowered fertility
- neurological/neuropsychiatric effects
- apoptosis/cell death (a process in production of neurodegenerative diseases that is also important in producing infertility responses)
- oxidative stress/free radical damage (key mechanisms involved in almost all chronic diseases, and direct cause of cellular DNA damage)
- endocrine, i.e. hormonal effects



- increased intracellular calcium ( $\text{Ca}_2^+$ ), with consequent production of several pathophysiological responses, as well as increased calcium signalling
- Cancer causation (brain cancer, salivary cancer, acoustic neuromas and two other types of cancer), reported to go up with cell phone use, and increased cancer rates, reported for people living near cell phone towers.

A recent monograph, which illustrates the non-thermal mechanisms and effects due to the electromagnetic interaction with living organisms, with particular reference to potential non-thermal toxic effects, includes articles on the following subjects: influence of mobile phone radiation on cognitive function; impact of DECT cordless phone radiation on heart rate variability and on the autonomic nervous system; impact of radiofrequency radiation on the blood-brain barrier; microwave/radiofrequency radiation and cancer causation; epidemiological studies of EMF impact on human reproduction [14]. One of these papers realistically shows that protection against non ionizing radiation, based on parameters adopted by international standards organizations, seems not to be adequate, nor able to protect people and workers [30].

A recent report of the National Toxicology Program (NTP) related to the NTP's cell phone radiation studies has evidenced that exposure to cell phone radiation caused a rare cancer in the hearts of male rats, brain cancer in male and female rats and cancer of the adrenal glands in male rats [35]. Exposure levels ranged from 1.5 to 6 watts per kilogram, and the low power level was equal to the highest level permitted for local tissue exposures to cell phone emissions today. The animals were exposed for 10-minute on, 10-minute off cycles that totalled more than 9 hours each day. The studies adopted 2G and 3G frequencies and modulations that are still used in voice calls and texting. 50 tissues in each animal were analysed by pathologists in order to look for signs of cancer or other changes. Other studies of 4G technologies gave very similar results.

Another recent review, conducted by a multidisciplinary, expert steering group including physicists who study electromagnetic fields, has found that electromagnetic fields emitted by power lines, Wi-Fi, broadcast and cell towers pose a credible threat to wildlife, and that the fifth generation cellular technology (5G) could cause greater harm. Moreover, an analysis of 97 peer-reviewed studies by the EKLIPSE project (see ref. [36]) concluded that electromagnetic radiation (EMR) is a potential risk to insect and bird orientation and to plant health, and that EMR exposure may affect plant metabolism due to production of reactive oxygen species often resulting in reduced plant growth [37, 38]. A recent study has shown that cell phone towers are the most dominant contributor to environmental RF radiation exposure in most outdoor areas. RF-EMF measurements were taken in places in Australia, Ethiopia, Nepal, South Africa, Switzerland and

the U.S.A. by means of portable measurement devices, which considered exposure from cell phone towers, TV and FM radio broadcast antennas, cell phone handsets and Wi-Fi [39].

A paper has been recently published reporting the estimation of the interaction between an E-shaped patch antenna (3.5 GHz) and human models, by means of finite-difference time-domain (FDTD) method. Different human models have been considered in diverse exposure conditions (antenna at different distances from the human model, in changed positions, and orientations), and whole-body, 10 and 1 g local specific absorption rate and magnetic field value ( $B_{\text{max}}$ ) were evaluated. In some worst-case scenarios involving male and female children's exposure, the maximum radiofrequency energy absorption (hot spots) resulted located in more sensitive organs such as eye, genitals and breast [40]. A collection of abstracts of newly-published scientific papers on wireless radiation and EMF, updated about once a month since August 2016, is available in the web page

<https://drive.google.com/file/d/1Sxzv69YschkFz5OGa9jC5CtyVTIEnLQN/view>.

A sharp rise in unspecific, often stress-associated health problems is occurring since various years, which progressively present physicians with the task of complex differential diagnosis. On the other hand, scarce care has been accorded so far is increasing electro smog exposure, happening in addition to chronic stress in personal and working life, which links with a general situation of chronic stress that can lead to exhaustion. A guideline, thus, has been developed by the Austrian Medical Association for differential diagnosis and potential treatment of unspecific stress-related health problems associated with electro smog, [41]. The main aim of such guideline - which includes a flow chart for diagnosing EMF-related health problems, as well as a patient questionnaire to simplify a systematic history of health problems and EMF exposure - has been to provide members of the medical profession with a compilation of the state of the scientific and political debate from a medical perspective and with specific recommendations for action. In particular, in supplement to basic diagnostic tests (i.e., laboratory tests and those related to the cardiovascular system), additional diagnostic tests have been indicated related to specific individual parameters depending on symptoms. Basic (low-frequency alternating magnetic and electric fields, high-frequency electromagnetic radiation) and additional (individual frequency-selective of common frequencies in the high frequency range) measurements of MEF exposure have been indicated, moreover, and benchmarks have been indicated to be applied to regular exposure of more than four hours per day, in relation to the following parameters:

- high-frequency electromagnetic radiation (as power flow density)

- low-frequency alternating magnetic fields
- low-frequency alternating electric fields.

New EMF guideline have been published, then (see ref. [42]) with the following aims:

- to give an overview of the current knowledge regarding EMF-related health risks
- to deliver preliminary recommendations for the diagnosis, treatment and accessibility measures of EHS to progress and restore individual health outcomes, as well as for the development of strategies for prevention.

Such guidelines indicate also precautionary EMF guidance values for ELF, very low frequencies (VLF) magnetic and electric fields, for areas where people spend extended periods of time (>4 hours per day) and also for sleeping areas. Precautionary guidance values for selected RF sources are also indicated. These values are based on data published in scientific literature.

## 5. Conclusions

Fast growing communication technologies, despite offering real solutions to globalization developing requirements, can be considered a significant source of overall pollution, producing hazards both to the environment and the human life. EMF is a specifically critical phenomenon, which should be seriously taken into account if one wants to ensure good health and well-being of people. Based on the related scientific literature, the following normal limits to the regular exposure of about four hours or more per day:

- high-frequency electromagnetic radiation (as power flow density):  $\leq 1 \mu\text{W}/\text{m}^2$
  - low-frequency alternating magnetic fields:  $\leq 20 \text{ nT}$
  - low-frequency alternating electric fields:  $\leq 0.3 \text{ V/m}$ .
- These limits are indicative, and each case should be considered separately, taking into account duration and period of exposure (night or day), simultaneity of exposures to different EMF sources, additional exposure to noise, chemicals and individual regulation capacity status [41].

More realistic exposure limits should be adopted, in the HF band, according to the already quoted PACE Resolution 2011/1815, whose paragraph 8.2.1 states:

*"set preventive thresholds for levels of long-term exposure to microwaves in all indoor areas, in accordance with the precautionary principle, not exceeding 0.6 volts per meter, and in the medium term to reduce it to 0.2 volts per meter"*. In our context, the term microwaves includes UHF/SHF/EHF bands.

The threshold of 0.6 V/m for microwaves is the same recommended in the Salzburg Resolution signed by scientists convened at the International Conference on Cell Tower Siting, Salzburg, June 7-8, 2000 [43].

All Countries should adopt, as soon as possible, the standard actually limiting people exposures in Switzerland, in front of single plants, provided in the

Federal Ordinance, already quoted in [5].

Regarding the possible prevention from biological hazards on humans, the two cases of HF and LF exposition can be considered primarily. In the HF case and even in the case of higher frequencies, it is possible to create a shield in particular in homes and in general where there is prolonged exposure to these frequencies. Suitable conductive materials should be adopted (e.g., based on Al, Cu or Fe) as constitutive of special fabrics to apply to windows. An example could be a woven curtain with a metallic lattice, the dimension of each square of the lattice  $10\div 100$  times lower than the length of the incident radiation. In the LF cases and even in the case of lower frequencies, it is not possible to shield if not using materials like layers made of carbon steel alloys, to be applied to the internal walls of the houses. It is evident that while in the first case the solutions could be quite cheap, even if it is still not so used at the moment, in the second case there is a fairly high cost and the solutions could be rather invasive. The ideal, however, is to analyse case by case, planning the most appropriate interventions and adopting the most suitable precautions (for example, in the positioning of the equipment and in the style of use) for the possible best prevention.

## Acknowledgements

The authors would like to acknowledge the contribution of the COST Action CA16122.

## REFERENCES

- [1] Kocaman A., Altun G., Kaplan A.A., Deniz Ö. G., Yurt K. K., Kaplan S., (2018), *Genotoxic and carcinogenic effects of non-ionizing electromagnetic fields*, Environmental Research 163, p. 71-79 The Netherlands
- [2] Touytou Y., Selmaoui B., (2012), The effects of extremely low-frequency magnetic fields on melatonin and cortisol, two marker rhythms of the circadian system, Dialogues in Clinical Neuroscience 14 No. 4, p. 381-399 France
- [3] Gould J. L., (1984), *Magnetic-field sensitivity in animals*, Annual Review of Physiology 46, p. 585-598 U.S.A.
- [4] Russo A. A., D'Elia R., *Radiazioni non ionizzanti - Aspetti normativi*, SIRM Congress, Oct. 1st 1997, Naples, Italy
- [5] CH Federal Ordinance ORNI 29.12.1999, Switzerland
- [6] IEEE Standard C95-1, (1992), U.S.A.
- [7] EU Council, *Recommendation of 12 July 1999 on the limitation of exposure of the general public to electromagnetic fields (0 Hz to 300 GHz)*, EU report 1999/519/EEC

- [8] Republic of Italy, DM 1998/381 of September 11<sup>th</sup> 1998
- [9] Republic of Italy, DPCM July 8<sup>th</sup> 2003, Gazzetta Ufficiale 2003/200
- [10] <https://www.fcc.gov/general/cell-phones-and-specific-absorption-rate>
- [11] International Commission on Non-Ionizing Radiation Protection, (1998), *Guidelines for limiting exposure to time-varying electric, magnetic, and electromagnetic fields (up to 300 GHz)*, Health Physics 74 No. 4, p. 494-522 Germany
- [12] Council of Europe, PACE Resolution 2011/1815
- [13] Giuliani L., (2010), *An Introduction*, in Giuliani L., Soffritti M., Eds., *Non-Thermal Effects and Mechanisms between EMFs and Living Matter*, an ICEMS Monograph, Institute Bernardino Ramazzini, European Journal of Oncology Library 5, p. IX-XI, Mattioli1885, Fidenza, Italy
- [14] Bawin, S. M., Kaczmarek, L. K., Ross Adey, W., (1975), *Effects of Modulated VHF Fields on the Central Nervous System*, Annals of the New York Academy of Sciences 247, p. 74-91. U.S.A.
- [15] Bawin, S. M., Adey, W. R., (1976), *Sensitivity of Calcium Binding in Cerebral Tissues to Weak Environmental Electric Fields Oscillating at Low Frequency*, Proceedings of the National Academy of Sciences 73, p. 1999–2003 U.S.A.
- [16] Sheppard A. R., Bawin S. M., Adey W. R., (1979), *Models of long-range order in cerebral macromolecules: Effects of sub-ELF and of modulated VHF and UHF fields*, Radio Science 14 No. 6S, p. 141-145 U.S.A.
- [17] Blackman C. F., Elder J. A., Well G. M., Benane G. S., Eichinger D. C., House D. E., (1979), *Induction of calcium-ion efflux from brain tissue by radio-frequency radiation: Effects of modulation frequency and field strength*, Radio Science 14 No. 6S, p. 93-98 U.S.A.
- [18] Blackman C. F., Benane S. G., House D. E., Joines W. T., (1985), *Effects of ELF (1-120 Hz) and modulated (50 Hz) RF fields on the efflux of calcium ions from brain tissue in vitro*, Bioelectromagnetics 6 No. 1, p. 1-11 U.S.A.
- [19] CENELEC, (1994), Standard 50166-1, EU
- [20] CENELEC, (1994), Standard 50155-2, EU
- [21] Liboff A. R., (1985), *Geomagnetic cyclotron resonance in living cells*, Journal of Biological Physics 13 No. 4, p. 99-102
- [22] Blanchard J. P., Blackman C. F., (1994), *Clarification and Application of an Ion Parametric Resonance Model for Magnetic Field Interactions with Biological Systems*, Bioelectromagnetics 15 No. 5, p. 493 Erratum in 15 No. 3, p. 217-238 U.S.A. U.S.A.
- [23] Zhadin M. N., Novikov V. V., Barnes F. S., Pergola N. F. (1994), *Combined Action of Static and Alternating Magnetic Fields on Ionic Current in Aqueous Glutamic Acid Solution*, Bioelectromagnetics 19 No. 1, p. 41-45 Russia-U.S.A.
- [24] Giuliani L., D'Emilia E. S., Grimaldi S., Lisi A., Bobkova N., Zhadin M. N., (2009), *Investigating the Icr Effect in a Zhadin's Cell*, International Journal of Biomedical Science 5 No. 2, p. 181-186 Italy-Russia
- [25] Blank M., Soo L., (2001), *Electromagnetic acceleration of electron transfer reactions*, Journal of Cellular Biochemistry 81 No. 2, p. 278-283 U.S.A.
- [26] Montagnier L., Aissa J., Ferris S., Montagnier J.L., Lavallée C., (2009), *Electromagnetic signals are produced by aqueous nanostructures derived from bacterial DNA sequences*, Interdisciplinary Sciences Computational Life Sciences 1 No. 2, p. 81-90 Switzerland
- [27] Montagnier L., Aissa J., Lavallée C., Mbamy M., Varon J., Chenal H., (2009), *Electromagnetic detection of HIV DNA in the blood of AIDS patients treated by antiretroviral therapy*, Interdisciplinary Sciences Computational Life Sciences 1 No. 4, p. 245-253 Switzerland
- [28] Blank M., Goodman R., (2011), *DNA is a fractal antenna in electromagnetic fields*, International Journal of Radiation Biology 87 No. 4, p. 409-415 United Kingdom
- [29] Liboff A. R., (2017), *Local and holistic electromagnetic therapies*, Electromagnetic Biology and Medicine 26 No. 4, p. 315-325 United Kingdom
- [30] <https://www.emfscientist.org>
- [31] Pall M. L., (2018), *5G: Great risk for EU, U.S. and International Health! Compelling Evidence for Eight Distinct Types of Great Harm Caused by Electromagnetic Field (EMF) Exposures and the Mechanism that Causes Them*, EU-EMF2018-6-11US3 report, Washington State University, p. 90, [https://www.salzburg.gv.at/gesundheit/\\_Document/s/Pall-EU-EMF2018-6-11US3.pdf](https://www.salzburg.gv.at/gesundheit/_Document/s/Pall-EU-EMF2018-6-11US3.pdf)
- [32] Han Y. Y., Ghandi O. P., De Salles A., Herberman R. B., Davis D. L., (2010), *Comparative assessment of models of electromagnetic absorption of the head for children and adults indicates the need for policy changes*. In Giuliani L., Soffritti S., Eds., *Non-Thermal Effects and Mechanisms between EMFs and Living Matter*, an ICEMS Monograph, Institute "Bernardino Ramazzini", European Journal of Oncology Library 5, p. 301-318 Italy
- [33] Blackman C.F., (2009), *Cell phone radiation: Evidence from ELF and RF studies supporting more*

- inclusive risk identification and assessment*, Pathophysiology 16 No. 2-3, p. 205-216 U.S.A.
- [34] Blank M., (2015), *Cell biology and EMF Safety Standard*, Electromagnetic Biology and Medicine 34 No. 4, p. 387-389 United Kingdom
- [35] Moskowitz J. M., (2018), *Evaluation of Carcinogenicity of Cell Phone Radiation: NTP Draft Technical Reports (TR 595, TR 596) vs. Expert Panel Vote*, National Toxicology Program (NTP) Cell Phone Radiation 2-Year Study, [https://drive.google.com/file/d/1DXh7\\_KHKMaFJELrvNvb6gipSVgqu-7Ot/view](https://drive.google.com/file/d/1DXh7_KHKMaFJELrvNvb6gipSVgqu-7Ot/view)
- [36] EKLIPSE Project (Establishing a European Knowledge and Learning Mechanism to Improve the Policy-Science-Society Interface on Biodiversity and Ecosystem Services), <http://www.eclipse-mechanism.eu>
- [37] Malkemper E. P., Tschulin T., VanBergen A. J., Vian A., Balian E., Goudeseune L., (2018), *The impacts of artificial Electromagnetic Radiation on wildlife (flora and fauna). Current knowledge overview: a background document to the web conference*, report of the EKLIPSE project, p. 28, <http://bit.ly/Eclipseoverview>
- [38] Goudeseune L., Balian E., Ventocilla J., (2018), *The impacts of artificial Electromagnetic Radiation on wildlife (flora and fauna). Report of the web conference*, report of the EKLIPSE project, p. 32, <http://bit.ly/EKLIPSEconfreport>
- [39] Sagar S., Adema S. M., Struchena B., Loughrand S. P., Brunjesi M. E., Aranguai L., Dalviec M. A., Croft R. J., Jerrette M., Moskowitz J. M., Kuog T., Rösli M., (2018), *Comparison of radiofrequency electromagnetic field exposure levels in different everyday microenvironments in an international context*, Environment International 114, p. 297-306 The Netherlands
- [40] Siervo B., Morelli M. S., Landini L., Hartwig V., (2018), *Numerical Evaluation of Human Exposure to WiMax Patch Antenna in Tablet or Laptop*, Bioelectromagnetics 39 No. 5, p. 414-422 U.S.A.
- [41] Austrian Medical Association's EMF Working Group, (2012), *Guideline of the Austrian Medical Association (ÖAK) for the diagnosis and treatment of EMF-related health problems and illnesses (EMF syndrome)*, Wien, p. 17, <https://www.vagbrytaren.org/Guideline%20%20AG-EMF.pdf>
- [42] Belyaev I., Dean A., Eger H., Hubmann G., Jandrisovits R., Kern M., Kundi M., Moshhammer H., Lercher P., Müller K., Oberfeld G., Ohnsorge P., Pelzmann P., Scheingraber C., Thill R., (2016), *EUROPAEM EMF Guideline 2016 for the prevention, diagnosis and treatment of EMF-related health problems and illnesses*, Reviews on Environmental Health 31 No. 3, p. 363-397 Germany
- [43] Oberfeld G., Ed., (2000), *Proceedings, International Conference on Cell Tower Siting "Linking Science & Public Health"*, Salzburg, Austria, June 7-8, 2000, Public Health Department, Environmental Health & University of Vienna, Institute of Environmental Health, [www.land-sbg.gv.at/celltower](http://www.land-sbg.gv.at/celltower)





# ICT for 3D modeling and 3D tactile visualization of sites of cultural and historical heritage

Stanislav GYOSHEV<sup>1)</sup>, Stefan KARASTANEV<sup>1)</sup> and Bogomil POPOV<sup>1)</sup>

1) Institute of Information and Communication Technologies  
Sofia, Bulgaria  
[stanislavgyoshev@mail.bg](mailto:stanislavgyoshev@mail.bg)  
[dimikara@abv.bg](mailto:dimikara@abv.bg)  
[bogomildpopov@gmail.com](mailto:bogomildpopov@gmail.com)

## Keywords

3D modeling  
3D scanning  
3D visualization  
Braille  
Tactile plates

*Professional article*

**Abstract:** New technologies, such as 3D printing and 3D visualization, have become more and more popular, because these technologies could be used by blind people to "see" works they had no idea. Weak or blind people cannot enjoy all the richness of the cultural and historical heritage. Now with new technologies, everyone can enjoy this art. 3D printing is an affordable, practical and efficient method of obtaining copies of models that are usually or not always available in common. The addition of Braille annotations provides additional opportunities for visually impaired people to "see" and "understand" the work. In particular, 3D models can be used for various purposes: reconstruction of 3D models of events or artifacts that have been destroyed with the help of preserved fragments, pictures or other sources; making copies of original artifacts and works that are very fragile to be displayed in public places; reconstruction and then object analysis, part of architectural maps and geographic maps that help us to get to know the past.

## 1. Introduction

Weak or blind people cannot enjoy all the richness of the cultural and historical heritage. Now with new technologies, everyone can enjoy this art. 3D printing is an affordable, practical and efficient method of obtaining copies of models that are usually or not always available in common. The addition of Braille annotations provides additional opportunities for visually impaired people to "see" and "understand" the work, [1].

State of research.

In particular, 3D models can be used for various purposes:

- Reconstruction of 3D models of events or artifacts that have been destroyed using their fragments, pictures or other sources - Fig. 1.
- Makes copies of original artifacts and works that are very fragile to be displayed in public places.
- Reconstruction and then object analysis, part of architectural maps and geographic maps that help us to get to know the past.
- Study and comparison of objects from different sources.
- Collecting artifacts from different geographic areas from near epochs in time.

## 2. Methods for preparation

Modeling of tactile images (3D) from tapestries (2D) for the needs of visually impaired people proceeds in the following sequence - Fig. 2, [1], [2]:

- From a high-resolution image (Figure 2a), using the mathematical methods, the contours of individual characters and figures are selected by choosing which exact shapes are used to make a tactile image.

- Once we have the contours of all the individual pieces, they are separated by alternately changing their appearance (a convex figure behind it and then again convex), making use of the Adobe Photoshop software that allows each segment of to separate the picture into a separate layer. For a tactile image, between 20 and 30 layers are needed.



**Figure 1.** 3D models and 3D printed figures from the Battle of Pavia-1525 (tapestries) of individual characters, from left to right: The Lady in Red, followed by the French Army; Fernando Francesco d'Avalos; Gjerd von Frondsberg; Jean di Deesbach; the lady's groom in red

- Braille alphabet symbols have been added to each individual segment of the picture. The choice of each character is made individually based on location, significance and proximity to another object, the first letter of the name of the figure.
- Each tactical image is made on 3 levels: base level background and minor characters, level 1, inner and outer

contours of senior characters, and level 2 Braille symbols to mark each individual character.

- Each individual tactile image is processed with the Cinema 4D software, where depths are set at each level, then printed on a 3D printer - Fig. 2b.

- In the same way, the picture of Figure 3 is also shown, and part of the work on selecting the required contours in Figure 3a



**Figure 2.** Tapestry and its 3D tactile version: a - a picture of the true tapestry, b - 3D tactile version of the gable with protruding contours and Braille symbols.

The modelling of the tapestries for 3D printing was developed in several phases, [3]:

1. A high-resolution version of the tapestries was pre-processed using segmentation techniques to extract the interesting parts. So, an algorithm for the extraction of contours based on color characteristics was applied (the contours of segments were detected as significant changes in color levels). The DOG (Difference of Gaussian) operator was used to extract areas of isochromaticity with closed contours. The level of detail extraction was defined by the amplitude of the two Gaussian curves, and was chosen as a function of the segment's dimensional characteristics.
2. The individual segments were then selected and integrated on the basis of their relevance to the scene, both with reference to inner and outer contours. (Fig. 3a, b).
3. Photoshop was used to acquire image contours and each segment was isolated as a different level. The picture was thus decomposed into 2÷3 levels (Fig. 3a).
4. Each segment was then matched with symbols from the Braille alphabet. The choice of the symbol was made on the basis of location, proximity and meaning. On the

same basis, it was decided to reproduce the segment in full or empty mode. The symbols were optimally positioned within each segment, (Fig. 3b).

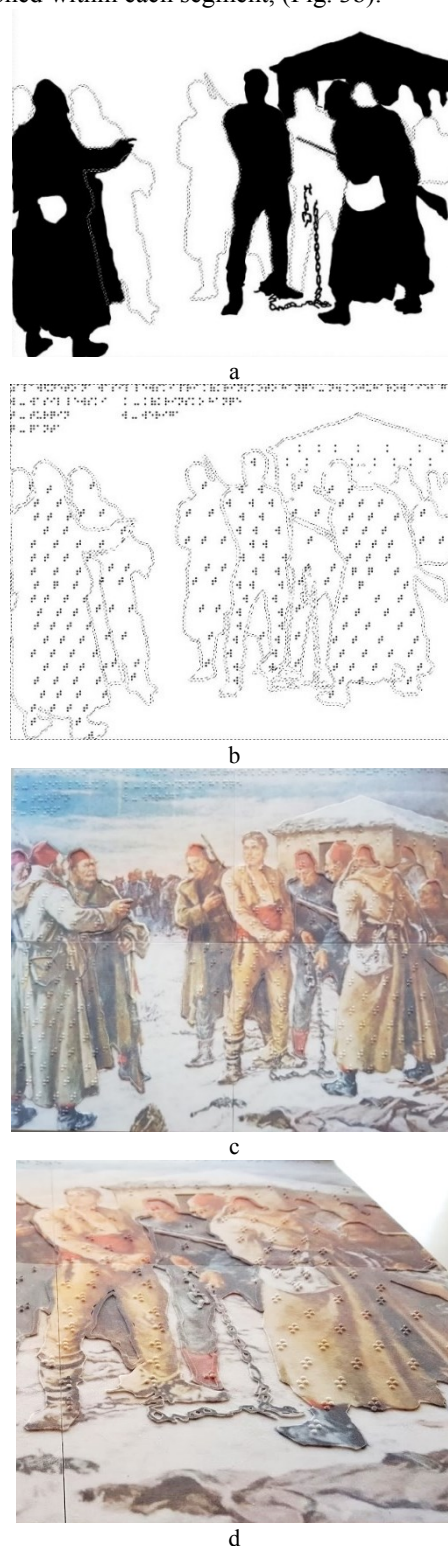


**Figure 3.a-** Selection of thick and contoured shapes for making the tactile tile, b – Braille symbols on the objects, c- ready tactile tile, d – fragment from the ready tactile tile



5. Each tactile tile of the picture was then reproduced at three depths:

Base level: for bottom and inner contours in full segments;

Level 1: for all the outer contours, for the inner contour points of full segments (in white), and for Braille identifiers of empty segments (in black);

Level 2: for Braille letters that identify full segments.

6. The picture was processed with BODYPAINT 3D software and protruded respecting the different depths.

7. Finally, the 3D model of the tactile tile was processed with ProJet 460Plus full color 3D software 3D Edit Pro and then produced on the colored surface of the tile. (Fig. 3c, d).

Implementation with color 3D printer

The ProJet 460Plus full-color 3D printer (Fig. 4) is one of the most affordable color 3D printers in its class in relation to the ease-of-use it provides. It incorporates 3 CMY color channels and operates with VisiJet® PXL Core i.e. calcium sulfate hemihydrate, a material which consists of a milky colored, chalky mineral powder containing special additives that make it immune to moisture; the printer actively controls the powder and produces no liquid waste.

Technical specifications include: 300 x 450 dpi resolution, 0.15 mm minimum size, 0.1 mm layer thickness,) and 203 x 254 x 203 mm (xyz) net product volume. Input data file formats supported are: STL, VRML, PL Y, 3DS, FBX, ZPR. The software associated with the printer allows prototypes or functional parts, devices and assembly to be designed, created, communicated, planned, directed, and produced in a fast way.

Vertical printing speed is 23 mm/h, so printing out a 20 cm tall character from one of the tapestries takes nine hours while a 40 x 75 cm tactile tapestry takes approximately two hours (20 min for each block of 20 x 25 cm). Obviously with the same running time as many characters as can be aligned on the printing table can be printed.



**Figure 4** Color 3D printer ProJet 460 plus

### 3. Conclusion

In recent years, thousands of industrial robots have emerged on the market, [4], which after renovation can be used in other areas. For example, from the automotive industry comes robots with fully functioning mechanics and motors. Such robots, renovated with new hardware and software, can be used to work with casting and stamping machines.

This approach can be used when a renovated robot works with a machine for stamping plastic models (fig. 5) from objects of cultural and historical heritage in museums and galleries for people with special needs (3D tactile graphical tiles - fig. 6).

Also, it is possible to use renovated robots operated in high-temperature technological lines for production of materials and alloys, [5], or for production of special matrix compositions, [6].

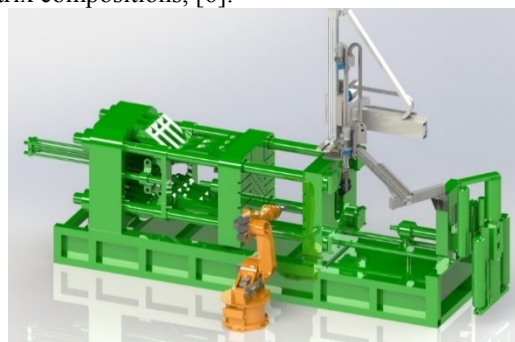


**Figure 5** Renovated robot with a machine for stamping



**Figure 6** 3D tactile graphical tile for visual impaired people

### Acknowledgements

The paper is partly supported by Bulgarian National Science Fund Grant No DFNP 17-98/29.08.2017 and by the Bulgarian SME SPESIMA LTD.

**REFERENCES**

- [1] Cantoni V., Karastoyanov D., Mosconi M., Setti A., (2015). *CVML and SMART LAB at the Exhibition* (Pavia, The Battle, The Future - 1525-2015 Nothing was the same again).
- [2] Gyoshev S., Stoimenov N., (2016). *3D Tactical presentation of the battle at Pavia*, Science magazine, vol. 6/2016, vol. XXVI, Issue of the Union of Scientists in Bulgaria. 47-50.
- [3] Karastoyanov D., Stoimenov N., Gyoshev S., (2018). Tactile graphical tiles for visual impaired people., Bulgarian Patent Application, No 112716
- [4] Karastoyanov D., (2010). *Control of robots and of other mechatronic systems.*, Acad. Publishing House „Marin Drinov”, Sofia, 2010, ISBN 978-954-322-415-9 (in Bulgarian)
- [5] Karastoyanov D., Ivanova D., Stoimenov N., (2015). *Technology for production of high-temperature materials and alloys including nano elements.*, *Recent Advances in Systems*, 19th International Conference on Systems (part of CSCC`15), Zakynthos Island, Greece, July 16-20, pp. 177-181, ISSN: 1790-5117, ISBN: 978-1-61804-321-4.
- [6] Ruzic J., Stoimenov N., (2016). *Advanced copper matrix composites.*, “Prof. Marin Drinov” Publishing house of Bulgarian Academy of Sciences, ISBN 978-954-322-859-1

# Computational Fluid Dynamics analysis and optimization of residential building air conditioning

Ivo FABJANAC<sup>1)</sup>, Željko PENG<sup>1)</sup>,  
Gojmir RADICA<sup>1)</sup> and Sandro  
NIŽETIĆ<sup>1)</sup>

1) University of Split, Faculty of Electrical  
Engineering, Mechanical Engineering and  
Naval Architecture  
Sveučilište u Splitu, Fakultet  
elektrotehnike, strojarstva i brodogradnje  
R. Boškovića 32, 21000 Split, Croatia

[ifabjana@fesb.hr](mailto:ifabjana@fesb.hr)

[zpenga@fesb.hr](mailto:zpenga@fesb.hr)

[goradica@fesb.hr](mailto:goradica@fesb.hr)

[snizetic@fesb.hr](mailto:snizetic@fesb.hr)

## Keywords

*Computational Fluid Dynamics*

*Heat and Mass Transfer*

*Air Conditioning*

*Thermal Comfort*

*Optimization*

## Ključne riječi

*Numeričko modeliranje strujanja*

*Prijenos topline i tvari*

*Klimatizacija*

*Uvjeti komfora*

*Optimizacija*

## Early information

**Abstract:** Energy efficiency is of paramount importance in engineering practice today, especially in air conditioning of commercial buildings. To decrease the impact on the environment which is a result of increasing power consumption, as well as the operational costs of the system, it is important to design an efficient system.

This paper deals with numerical analysis of apartment cooling using computational fluid dynamics analysis (CFD). Besides fluid dynamics, the model also incorporates heat transfer and mass transfer modeling (i.e. conduction, convection and relative humidity modeling). Previously conducted analysis using conventional calculation approach, according to the VDI 2078 norm, is carried out and the input from the analytical approach is used for the CFD model. The CFD model is developed to resolve the thermal comfort parameters to the higher extent when compared to the conventional analytical approach and to give insight in the spatially resolved air flow, heat transfer and relative humidity distributions in the numerical domains.

The first objective of the research is to determine the optimal positioning of a single air conditioning unit in the apartment to result in the desired temperature and relative humidity distributions inside the unit, according to the thermal comfort requirements. The second objective is to determine if it is possible to decrease the total power consumption by installing two or more air conditioning units of lower cumulative nominal power. The CFD analysis results are compared to the results of the previously conducted analytical approach.

## Prethodno priopćenje

**Sažetak:** Energetska učinkovitost je od neophodnog značaja u inženjerskoj praksi danas, posebice prilikom klimatizacije komercijalnih zgrada. Kako bi se umanjio utjecaj na okoliš, što je rezultat povećane potrošnje energije, kao i cijene rada sustava, važno je dizajnirati što učinkovitiji sustav.

U ovom radu prezentirana je numerička analiza hlađenja apartmanske jedinice primjenom numeričkog modeliranja strujanja fluida (CFD – computational fluid dynamics). Osim strujanja fluida, model također inkorporira prijenos topline i tvari (odn. modeliranje kondukcije, konvekcije i relativne vlažnosti). Tijekom prethodnog istraživanja korišten je konvencionalni analitički proračun prema normi VDI 2078, pri čemu su ulazni parametri iz analitičkog proračuna inkorporirani kao granični uvjeti prilikom numeričke analize. Numerički model razvijen je kako bi se omogućio detaljan uvid u prostornu raspodjelu parametara toplinskog komfora (prostorna raspodjela strujanja zraka, prijenosa topline i relativne vlažnosti), što nije moguće postići korištenjem konvencionalnog analitičkog proračuna.

Primarni cilj provedenog istraživanja je odrediti optimalan položaj klimatizacijske (u ovom slučaju rashladne) jedinice u apartmanskoj jedinici kako bi se postigla željena prostorna raspodjela temperature i relativne vlažnosti pri čemu će biti zadovoljeni uvjeti komfora. Sekundarni cilj je ustanoviti je li moguće umanjiti ukupnu potrošnju električne energije ugradnjom dviju ili više klimatizacijskih jedinica manje nominalne potrošnje električne energije. Rezultati analize numeričkog modeliranja strujanja su uspoređeni s rezultatima prethodno provedenog istraživanja analitičkim pristupom.



**Symbols**

$C_p$	- specific heat capacity, kJ/(kgK) - specifični toplinski kapacitet	$t$	- time, s - vrijeme
$\vec{f}$	- mass force, N - masena sila	$T$	- temperature, K - temperatura
$g$	- gravity, m/s <sup>2</sup> - ubrzanje Zemljine sile teže	$U$	- average velocity, m/s - prosječna brzina
$p$	- fluid pressure, Pa - tlak fluida	$k$	- turbulent kinetic energy, J/kg - turbulentna kinetička energija
$\vec{u}$	- velocity vector, m/s - vektor brzine	$C_{\epsilon 1}, C_{\epsilon 2}$	- closure coefficients for k- $\epsilon$ model - koeficijent zatvaranja za k- $\epsilon$ model

**Greek letters**

$\mu$	- dynamic viscosity, Pa s - dinamička viskoznost	$\nu_T$	- turbulent viscosity, m <sup>2</sup> /s - turbulentna kinematska viskoznost
$\rho$	- density, kgm <sup>-3</sup> - gustoća	$\tau$	- temperature, °C - temperatura

**Subscripts**

int	- internal (heat load) - unutarnje toplinsko opterećenje	pass	- heat generated from objects passing through room - toplina koju odaju predmeti pri prolasku kroz prostoriju
ext	- external (heat load) - vanjsko toplinsko opterećenje	other	- other heat sources - ostali izvori topline
res	- heat generated by residents - toplina koju odaju osobe	ext,wall	- heat generated from surroundings by conduction and convection through outer wall - toplina dovedena iz okolice provođenjem i konvekcijom kroz vanjski zid
lux	- heat generated by lighting fixtures - toplina koju odaju rasvjetna tijela	win,conv	- heat generated from surroundings by conduction and convection through glass surfaces - toplina dovedena iz okolice provođenjem i konvekcijom kroz ostakljenje plohe

**Symbols**

	- heat generated by machines, devices and equipment		- heat generated from surroundings by radiation through the glass surfaces
MDE	- toplina koju odaju strojevi, uređaji i oprema	win,rad	- toplina dovedena iz okolice zračenjem kroz ostakljenje plohe
int,wall	- heat generated from neighboring rooms or ground by convection and conduction through inner wall, ceiling or floor		- heat generated by natural ventilation
	- toplina dovedena iz susjednih prostorija ili podzemlja provođenjem i konvekcijom kroz unutarnji zid, strop ili pod	vent	- toplina dovedena uslijed prirodne ventilacije
j	- unit vector in the y axis direction		- optimal (project temperature)
	- jedinični vektor u smjeru y osi	opt	- optimalna projektna temperatura
	-		
DA	- dry air		- surrounding (project temperature)
	- suhi zrak	sur	- okolna projektna temperatura
		i	- unit vector in the x axis direction
			- jedinični vektor u smjeru x osi

**1. Introduction**

Air conditioning is a process of preparing air for the purpose of creating an appropriate degree of comfort for the lives of people as well as other living beings. In a broader sense, the term may refer to any form of cooling, heating, ventilation or disinfection that alters the condition of the air.

Air conditioning as a technology branch involves technical procedures for achieving the desired air parameters and maintaining them in space using commercially available thermodynamic systems throughout the year. The desired parameters to be controlled in the optimal boundary values are related to the conditions of thermal comfort. These are temperature, relative humidity, flow rate, air purity, noise, etc.

Today, energy consumption, i.e. energy savings, are one of the most important topics related to the air conditioning systems. As the energy costs increase, it is very important to be energy efficient.

Calculations for the required air conditioning parameters (including cooling, heating and ventilation) of living spaces (commercial buildings) as well as industrial facilities are carried out conventionally using simplified calculation models. However, those calculations are very comprehensive and cover a variety of heat sources and the ways the heat is generated inside the facility of interest. One of the obstacles for determining the appropriate air conditioning system for the specified facility is the requirement for experienced professional to

determine the optimum configuration. The second more important obstacle is the absence of the specific geometrical parameters, i.e. layout, of the observed facility. If there are many obstructions or space dividers, it all influences the air stream and conditions for cooling. Any kind of mistakes after equipment installment could be very costly (especially for big projects). Such mistakes could be faulty positioning of the crucial elements, insufficient nominal power required to achieve desired conditions or exaggeration of nominal power which results in much higher operating costs (very common practice today with inexperienced engineers). Hence, it would be useful to carry out numerical analysis, i.e. computational fluid dynamics (CFD) to gain insight in spatially resolved thermal comfort parameters, thereby ensuring energy savings and minimizing the operational and equipment costs.

Surprisingly, there is quite little available literature dealing with CFD analysis of complex air conditioning systems, so it is new research area. Most of the works in the literature deal with overly simplified models where the emphasis is mostly related to the air flow distribution, neglecting the influence of various heat sources and relative humidity distribution.

This paper deals with air conditioning of a living space, i.e. residential apartment. The objective was to carry out CFD analysis of air conditioning (cooling) for the chosen apartment and to determine the optimal installment position of air conditioning unit as well as the optimal direction of inlet air stream and to determine if the

desired thermal comfort requirements could even be achieved after all. The CFD analysis uses realistic modeling assumptions, air is modeled as ideal gas species mixture with including modeling of the relative humidity. After the CFD analysis is carried out, the obtained results are compared with conventional calculation data and discussed in detail.

Properties that were taken in concern were surrounding temperature (extracted from conventional calculation) for the most unfavorable period of the year, e.g. surface temperature of outer walls, thermal comfort parameters, realistic properties of materials (for windows, load bearing and nonbearing walls, fluid-ideal gas and stove as a heat source), convection through the windows, velocity magnitude and direction of air conditioning inlet air stream and inlet air properties.

## 2. Results from conventional analytical calculation

In Croatia, the calculation of heat loads, is commonly carried out according to German norm VDI 2078, as seen

in a previous study [2]. The results of the calculations are shown in Figure 1. The reason that methodology according to ASHRAE (the second most common approach), is not used, is simply because German construction methods show higher similarity to the Croatian construction methods. Calculations are carried out for the summer month that is the most unfavorable.

### 2.1. General equations used for conventional calculation

Total heat load (of both internal and external factors):

$$\dot{Q}_{tot} = \dot{Q}_{int} + \dot{Q}_{ext} \quad (1)$$

Internal heat load:

$$\dot{Q}_{int} = \dot{Q}_{res} + \dot{Q}_{lux} + \dot{Q}_{MDE} + \dot{Q}_{int,wall} + \dot{Q}_{pass} + \dot{Q}_{other} \quad (2)$$

External heat load:

$$\dot{Q}_{ext} = \dot{Q}_{ext,wall} + \dot{Q}_{win,conv} + \dot{Q}_{MDE} + \dot{Q}_{win,rad} + \dot{Q}_{vent} \quad (3)$$

		Time of day [h]																	
		2	4	6	8	9	10	11	12	13	14	15	16	17	18	19	20	22	24
Internal heat load [W]	Q <sub>res</sub>	460	460	460	460	460	460	460	460	460	460	460	460	460	460	460	460	460	460
	Q <sub>lux</sub>	378	378	378	378	378	378	378	378	378	378	378	378	378	378	378	378	378	378
	Q <sub>MDE-PC</sub>	0	0	0	0	0	80	80	80	80	80	80	80	80	80	80	80	80	80
	Q <sub>MDE-TOASTER</sub>	0	0	0	0	250	250	250	250	250	250	250	250	250	250	250	0	0	0
	Q <sub>MDE-VAC CL</sub>	0	0	0	0	0	0	0	0	0	50	50	50	50	50	0	0	0	0
	Q <sub>MDE-TV</sub>	175	0	175	175	175	175	175	175	175	175	175	175	175	175	175	175	175	175
	Q <sub>MDE-IRON</sub>	500	0	0	0	0	0	0	0	0	0	0	0	0	0	0	0	500	500
	Q <sub>MDE-REFRIG</sub>	500	500	500	500	500	500	500	500	500	500	500	500	500	500	500	500	500	500
	Q <sub>MDE-RADIO</sub>	40	40	40	40	40	40	40	40	40	40	40	40	40	40	40	40	40	40
	Q <sub>MDE-STOVE</sub>	0	0	0	3000	3000	3000	3000	3000	3000	3000	3000	3000	3000	3000	3000	3000	0	0
External heat load [W]	Q <sub>int,wall</sub>	226,04	226,04	226,04	226,04	226,04	226,04	226,04	226,04	226,04	226,04	226,04	226,04	226,04	226,04	226,04	226,04	226,04	226,04
	Q <sub>other</sub>	30	30	30	30	30	30	30	30	30	30	30	30	30	30	30	30	30	30
	Q <sub>pass</sub>	0	0	0	0	0	0	0	0	0	0	0	0	0	0	0	0	0	0
	Q <sub>ext,wall</sub>	34,398	31,7772	28,8288	27,1908	27,5184	28,5012	30,4668	32,4324	34,398	36,036	37,3464	38,3292	38,6568	39,312	39,6396	39,6396	38,9844	37,0188
	Q <sub>ext,wall</sub>	71,91492	66,03097	59,49325	53,6093	50,99422	49,68667	49,68667	50,99422	53,6093	58,18571	62,76211	67,99229	72,56869	77,1451	79,76018	81,06773	81,06773	77,9887
	Q <sub>ext,wall</sub>	45,36168	41,70348	37,67946	33,35544	31,82634	30,72888	29,63142	29,2656	29,2656	29,99724	31,0947	32,55798	35,11872	38,4111	41,70348	44,99586	48,65406	48,28824
	Q <sub>wind,conv</sub>	264,8	264,8	264,8	264,8	264,8	264,8	264,8	264,8	264,8	264,8	264,8	264,8	264,8	264,8	264,8	264,8	264,8	264,8
	Q <sub>wind,rad</sub>	135,432	126,4032	146,4758	195,2188	271,4922	367,2162	453,6864	501,4224	500,9454	461,3742	383,8338	306,7641	267,4902	238,0248	208,9044	189,6048	162,5184	153,4896
	Q <sub>vent</sub>	-	-	-	-	-	-	-	-	-	-	-	-	-	-	-	-	-	-
	Q <sub>tot</sub> [W]	2860,947	2164,755	2346,317	5383,214	5785,671	5879,973	5967,311	6017,955	6022,058	6039,433	5968,877	5899,484	5867,674	5846,733	5773,848	5509,148	2985,065	2970,436

Figure 1. Tabular display of results gained from conventional calculation [2]

## 3. Initial and desired conditions

Summer project temperature for Split, Croatia is 34°C [4]. That temperature was taken as initial condition of external and internal air temperature for conventional calculation as well as for CFD analysis.

Initial relative humidity was set according to literature [6, 7], to 60%. Absolute humidity was extracted from Mollier's h-x chart [8] for the mentioned relative humidity and initial temperature, and consequently the initial absolute humidity was set to 0,0175 kg<sub>H2O</sub>/kg<sub>D.A.</sub>

Desired internal air temperature, or optimal air temperature for living space (for summer project temperature) is calculated using equation

$$\tau_{opt} = \frac{1}{2}(\tau_{sur} + 20)^\circ\text{C} = 27^\circ\text{C} \quad (4)$$

Regarding the desired relative air humidity, the objective of the CFD analysis was to also check whether condensation will occur (which would be undesired effect) and to establish and maintain the desired range for relative humidity between 30% and 70% [1].

#### 4. Methodology and numerical modeling

The simulations are carried out using commercial software package ANSYS Fluent™ 17.2. with its corresponding modules.

In conventional calculation there is a higher number of considered heat sources when compared to the CFD analysis. The influence of those remaining heat sources (that were omitted from the CFD analysis) was not considered in this paper due to the necessary simplifications of the geometry and boundary conditions to avoid the unreasonably high computational complexity.

##### 4.1. Governing equations

CFD is a technique based on numerical methods which aims at analyzing fluid flow, heat transfer, mass transfer, species transport and chemical reactions, as well as other topics. The present study sought to examine the fluid flow, heat transfer and species transport within the apartment. The flow is governed by the continuity equation, the energy equation and Navier-Stokes momentum equations. Transport of mass, energy and momentum occur through convective flow and diffusion of molecules and turbulent eddies. All equations are set up over a control volume where  $i, j, k = 1, 2, 3$  correspond to the three dimensions [9].

The continuity equation (flow equation) describes the conservation of mass and it is described in equation:

$$\frac{\partial \rho}{\partial t} + \nabla \cdot (\rho \vec{u}) = 0 \quad (5)$$

The momentum balance (momentum equation – flow equation), also known as the Navier-Stokes equation, follows Newton's second law: The change in momentum in all directions equals the sum of forces acting in those directions. There are two different kinds of forces acting on a finite volume element, surface forces and body forces. Surface forces include pressure and viscous forces and body forces include gravity, centrifugal and electromagnetic forces [9].

Momentum equation reads:

$$\frac{\partial}{\partial t} (\rho \vec{u}) + \nabla \cdot (\rho \vec{u} \vec{u}) = \mu \nabla \cdot \vec{u} - \nabla p + \rho \vec{g} + \vec{f} \quad (6)$$

Energy is present in many forms in flow i.e. as kinetic energy due to the mass and velocity of the fluid, as thermal energy, and as chemically bounded energy. Thus, the total energy can be defined as the sum of all of these components [9], as indicated in equation:

$$\frac{\partial}{\partial t} [\rho E] + \nabla \cdot [(\rho E + p) \vec{u}] = \nabla \cdot (\lambda_{eff} \nabla T) + \rho \vec{g} \cdot \vec{u} \quad (7)$$

Turbulence arises due to the instability in the flow. This happens when the viscous dampening of the velocity

fluctuations is slower than the convective transport, i.e. the fluid element can rotate before it comes in contact with wall that stops the rotation. For high Reynolds numbers the velocity fluctuations cannot be dampened by viscous forces and the flow becomes turbulent. Turbulence model in this paper is standard  $k$ - $\varepsilon$  model with two equations [10], consisting of turbulent kinetic energy,  $k$ :

$$\frac{\partial k}{\partial t} + \langle U_j \rangle \cdot \frac{\partial k}{\partial x_j} = \nu_T \cdot \left[ \left( \frac{\partial \langle U_i \rangle}{\partial x_j} + \frac{\partial \langle U_j \rangle}{\partial x_i} \right) \frac{\partial \langle U_i \rangle}{\partial x_j} \right] - \varepsilon + \frac{\partial}{\partial x_j} \left[ \left( \nu + \frac{\nu_T}{\sigma_k} \right) \frac{\partial k}{\partial x_j} \right] \quad (8)$$

and turbulent dissipation,  $\varepsilon$ :

$$\frac{\partial \varepsilon}{\partial t} + \langle U_j \rangle \cdot \frac{\partial \varepsilon}{\partial x_j} = C_{\varepsilon 1} \nu_T \frac{\varepsilon}{k} \cdot \left[ \left( \frac{\partial \langle U_i \rangle}{\partial x_j} + \frac{\partial \langle U_j \rangle}{\partial x_i} \right) \frac{\partial \langle U_i \rangle}{\partial x_j} \right] + C_{\varepsilon 2} \frac{\varepsilon^2}{k} + \frac{\partial}{\partial x_j} \left[ \left( \nu + \frac{\nu_T}{\sigma_\varepsilon} \right) \frac{\partial \varepsilon}{\partial x_j} \right] \quad (9)$$

##### 4.2. Geometry

The layout of the apartment with indicated possible positions of air condition units (solid black hatch) is shown in Figure 2. First step in numerical analysis was to generate 3D geometry model of the apartment, consisting of bearing and nonbearing walls, windows, doors, ceiling, floor surfaces, cooking stove and air conditioning units, as seen in Figure 3. The geometry was generated using ANSYS *DesignModeler*™.

##### 4.3. Domain boundary conditions

The domain type for all internal geometry domains (representing air ideal gas) are defined as fluid bodies. Windows, walls (including ceiling and floor) and doors in particular cases (if they are closed for that case) are defined as solid bodies (with corresponding defined materials and their properties, Table 1).

##### 4.4. Inlet boundary conditions

The velocity inlet boundary condition is defined at the air conditioning outflow surface. The velocity inlet is specified with the following parameters: velocity magnitude, which was fixed to 0,3 m/s (due to the thermal comfort constraint), direction of the outflow (two considered cases for each unit, 0° and 45° in respect to the horizontal plane), stream outflow temperature (which was set at different values to determine the required temperature for meeting the thermal comfort constraints), and species mass fractions (defined in respect to the operating temperature – extracted from Mollier's h-x chart [8]).





#### 4.5. Wall boundary conditions

Wall boundary conditions are defined for bearing walls, windows and stove.

Non-slip boundary conditions are applied to the walls and they are defined as stationary walls.

The temperature was set as fixed temperature for the outside of exterior bearing walls and for the stove.

Depending on the bearing wall orientation (i.e. north, east, west, south), temperature was set slightly different. For the south bearing walls (characterized by highest solar radiation exposure), the temperature was set at 307 K (34°C). For the east, west and north bearing wall, the temperature was set at 305 K (32°C). Temperature for the stove was set at 333 K (60°C).

Properties of the materials for the stove, bearing and nonbearing walls are defined and assigned correspondingly as shown in Table 1.

Convection conditions were defined for the windows. Value of heat transfer coefficient was fixed to 1,2 W/m<sup>2</sup>K for all windows. Free stream temperature was set slightly different, depending on the window orientation (same values as set for the walls).

Properties of materials for windows were defined and assigned correspondingly, Table 1.

#### 4.6. Materials

Properties and values of defined materials are specified and listed in Table 1. Those properties are taken from literature [14-19].

**Table 1.** Properties and values of defined materials

MATERIAL	DENSITY Y (kg/m <sup>3</sup> )	SPECIFIC HEAT - Cp (J/kgK)	THERMAL CONDUCTIVITY (W/mK)	VISCOSITY (kg/ms)	MOLECULAR WEIGHT (kg/kmol)
Wood (doors)	610	1300	0,14	/	/
Glass (windows)	2500	840	1	/	/
Wall (non- bearing)	1500	900	1	/	/
Wall (bearing)	1775	900	0,3	/	/
Aluminium (stove)	2719	871	202,4	/	/
Air	ideal gas	1006,43	0,0242	polynomial $\mu(T) = (1e-06) + (7e-08)T + (5e-11)T^2 + (2e-14)T^3 - (4e-18)T^4$	28,966
MIXTURE					
Carbon- dioxide	1,7878	piecewise- polynomial	0,0145	0,0000137	44,00995
Nitrogen	1,138	piecewise- polynomial	0,0242	0,00001663	28,0134
Oxygen	1,2999	piecewise- polynomial	0,0246	0,00001919	31,9988
Water- vapour	0,5542	piecewise- polynomial	0,0261	0,0000134	18,01534

#### 4.7. Mesh

Grid dependency study was not carried out because of the size of the apartment, initial mesh settings and the hardware requirements that would be required for more refined mesh. However, the mesh size and element

quality surpass the sizing and quality of similar works from other authors.

Considering the size of the apartment model, mesh was defined accordingly. The size of the mesh elements was set to 0,05 m (5 cm). The objective was to generate pure hexahedral, fully structured mesh with uniform element

sizing. The initial size of the mesh elements produced results in accordance with similar works found in the literature and further refinement was not necessary (hence, grid dependency study wasn't required).

Methods that were employed to ensure mesh uniformity and the best possible quality are: *Edge Sizing*, *Face Sizing* and *Body Sizing*. *CutCell* method was finally

employed for assembly meshing and generation of pure hexahedral structured uniformly sized mesh. Mesh metrics and element quality are displayed in Figure 4. It can be seen that average orthogonal quality is 0,99905, which is considered to be quite ideal since maximum (perfect case) mesh quality is 1. The final mesh is shown in Figure 5.

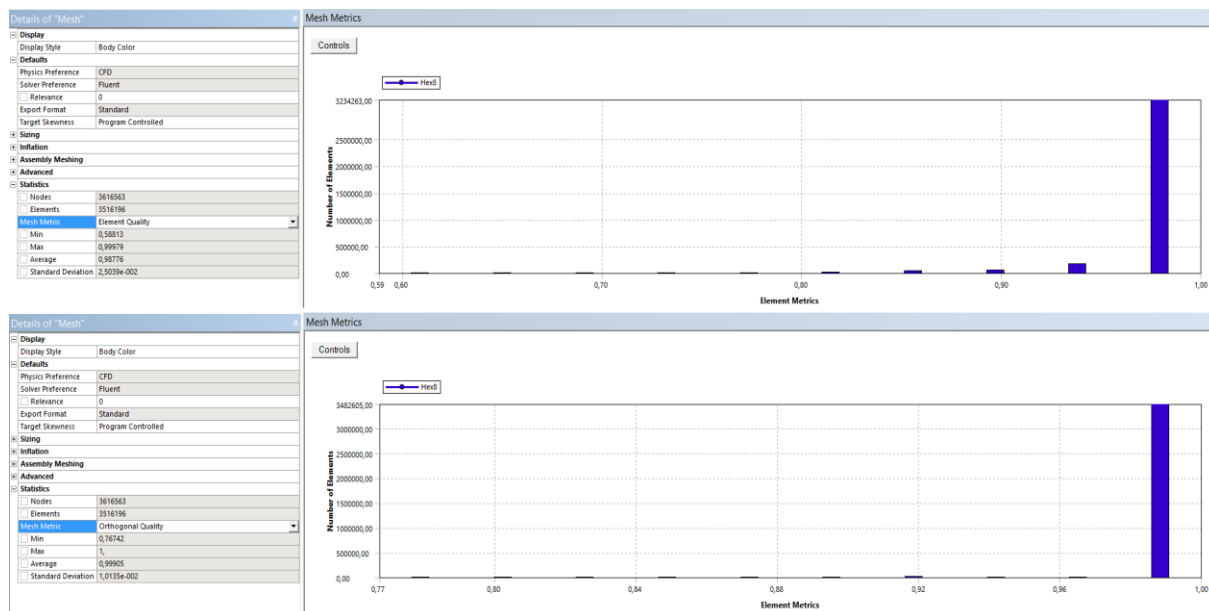


**Figure 4.** Mesh metrics and element quality

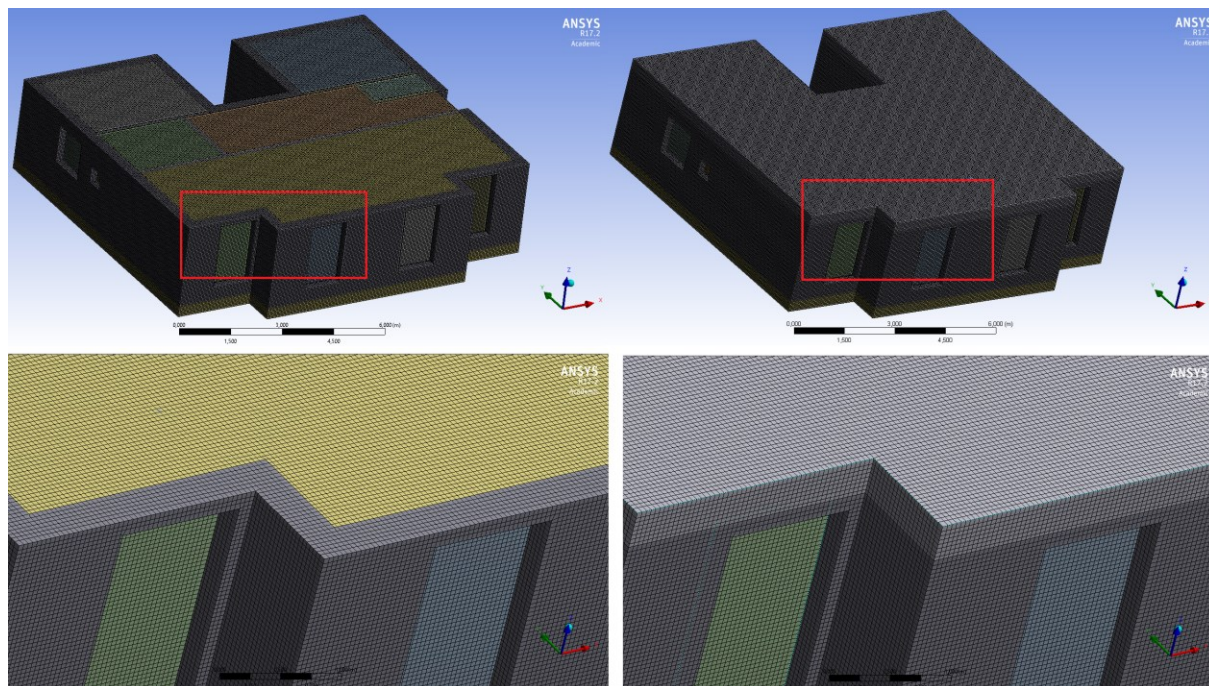


**Figure 5.** The final result of the generated mesh

## 5. Results and discussion

The results from CFD analysis for all variations that were simulated are shown below. First, for all cases with one air conditioning unit placed in the living room (with varying positions), Table 2. Secondly, cases with two air conditioning units, one placed in the living room and one in the hallway (with varying positions in hallway). The results are compared and discussed.

### 5.1. Cases with one air conditioning unit

All the cases with one air conditioning unit that were simulated are listed in Table 2. Temperature of the air outflow was set at 22 °C for these cases.

**Table 2.** Cases with one air conditioning unit

CASE	POSITION	AIR OUTFLOW DIRECTION
1	South wall	0°
2	South wall	45°
3	East wall	0°
4	East wall	45°

Since the air is modeled as a species mixture, first step was to observe if there are any regions where the condensation may occur. Figure 6 shows the contours with highest relative humidity at the air condition outlet due to the lowest temperature, however this is due to the applied boundary condition of fixed temperature of the air inflow and of low probability due to high air circulation in the mentioned zone.

Figure 7 shows comparison of the results for the temperature distributions in all cases. It can be seen that minimum (31,85 °C) and maximum (34,059 °C) temperature for all cases is identical. The difference is in distribution of local temperature which varies depending on the position of the air condition unit and the direction of the air outflow.

The air conditioning unit positioned on the south wall and with 45° angle of the air outflow direction results in most uniform distribution of local temperatures, with the lower (more desired) temperature covering larger surface.

However, the minimal temperature is still higher than the desired temperature from equation (4).

Considering the relative humidity, the desired range and distributions are achieved, and the conditions of thermal comfort are met, Figure 8.

The velocity streamlines, shown in Figure 9, indicate that the local air velocity distributions are below the target value of 0,3 m/s, and that there is a convective current in all of the apartment rooms to ensure the required air mixing, therefore this requirement is also met.

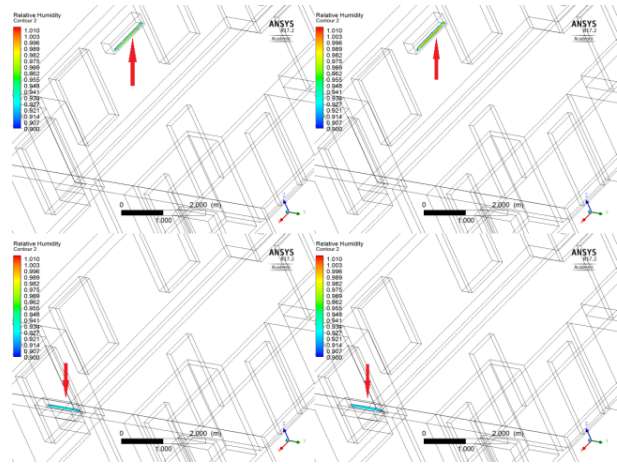


**Figure 6.** Possible condensation on the air outflow inlet

The temperature was set to 20 °C, 18°C and 16°C, and neither case achieved the desired project temperature. Minimal and maximum temperature are identical as in case with 22°C, however, distribution of local temperature is more favorable, Figure 10.

Relative humidity meets the desired conditions of thermal comfort, Figure 11.

As in the cases with higher temperature, condensation may occur only on the air outflow inlet, but with there is very low probability, Figure 12, due to relatively high air flow in these regions.

### 5.2. Cases with two air condition units

In cases with two units, the first one is on the south wall in the living room. The second one is placed in the hallway, and there are two cases – north and south wall of the hallway. Direction of the air outflow is 45° for all cases and initial temperature 22°C.

As can be seen on Figure 13, the desired temperature could not be achieved. The case with the air condition unit on the south wall in hallway (Case 1) is more favorable because of the local temperature distributions. Comparing these cases with those with one unit, minimal and maximum temperature are somewhat lower, minimum being 31,419°C and maximum 33,776°C.

Considering the relative humidity, desired range and distribution was achieved, and the conditions of thermal comfort are met, Figure 14.

Condensation may occur only on the air outflow inlet, but with there is very low probability.

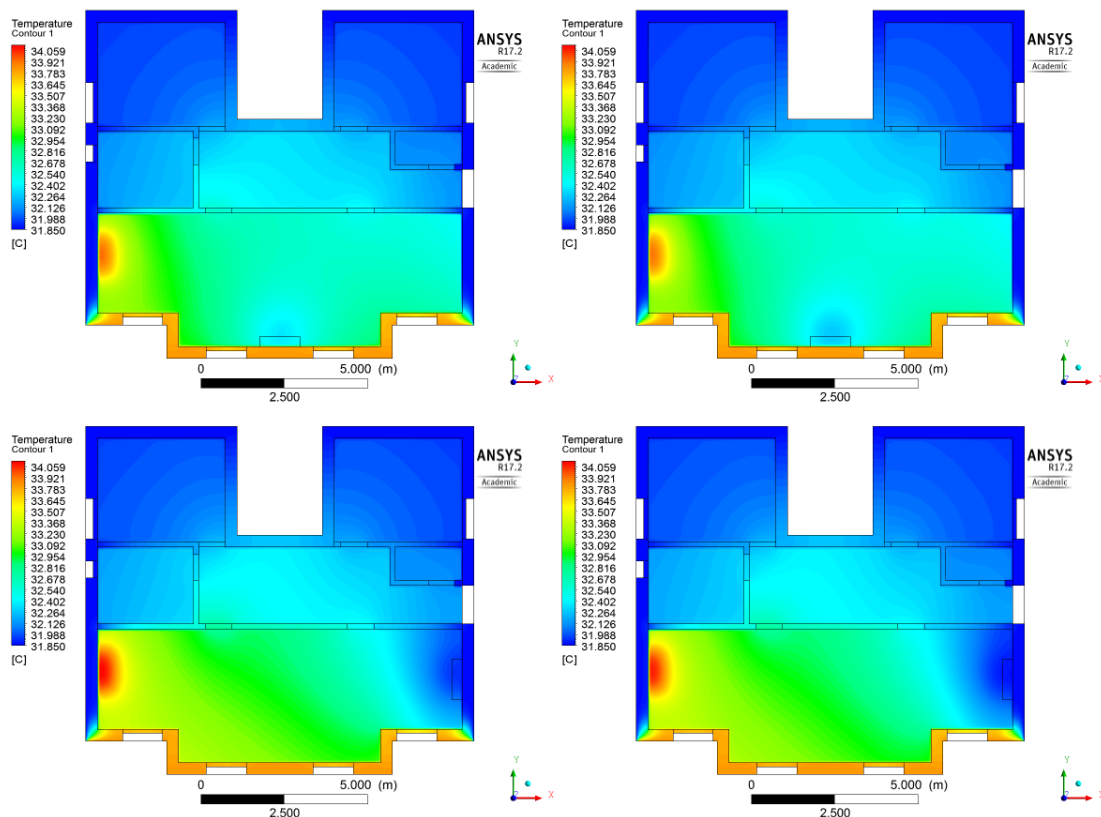


**Figure 7.** Results of the temperature distribution for cases with one air condition unit

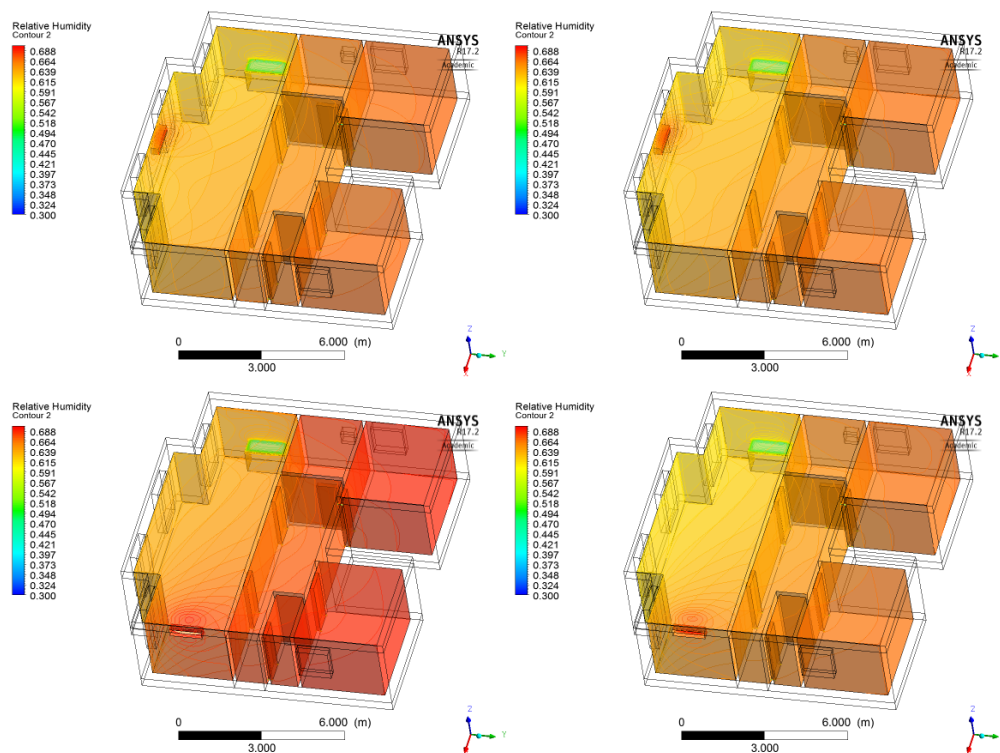


**Figure 8.** Results of the relative humidity distribution through the apartment for cases with one air condition unit



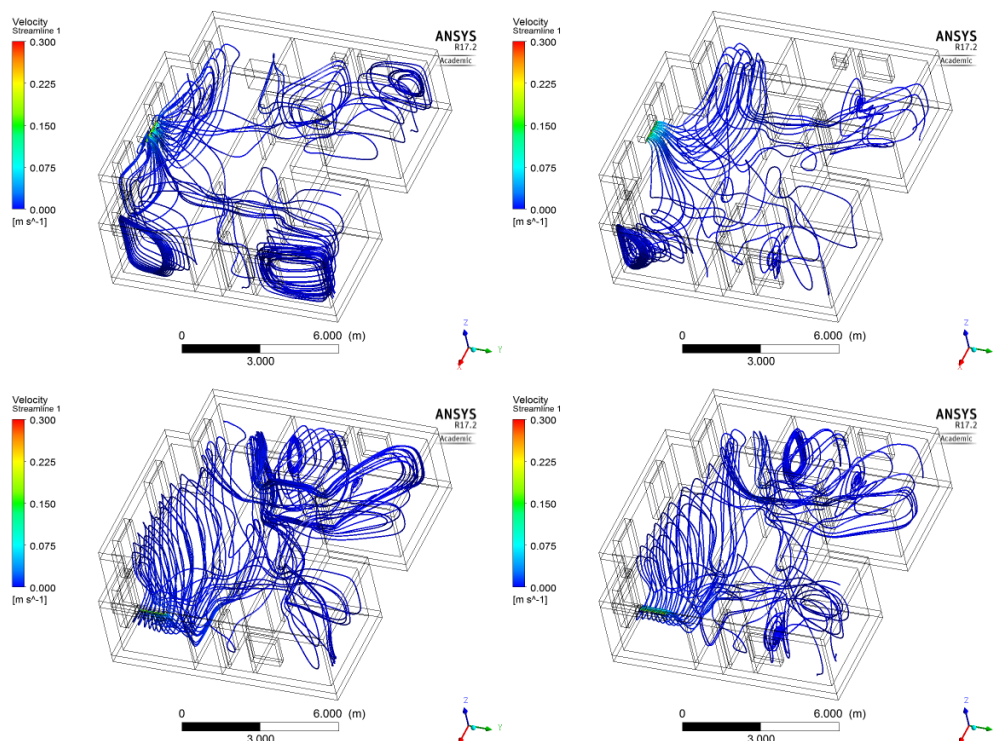


**Figure 9.** Streamlines of velocity distribution through the apartment

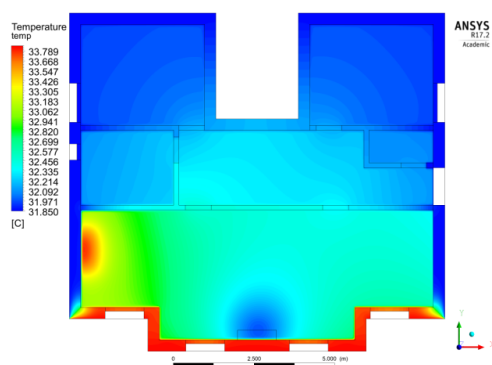


**Figure 10.** Results of the temperature distribution for case 2 (16°C)

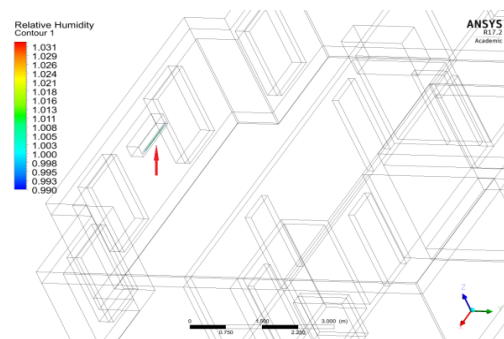


**Figure 12.** Possible condensation on the air outflow inlet for case 2 (16°C)

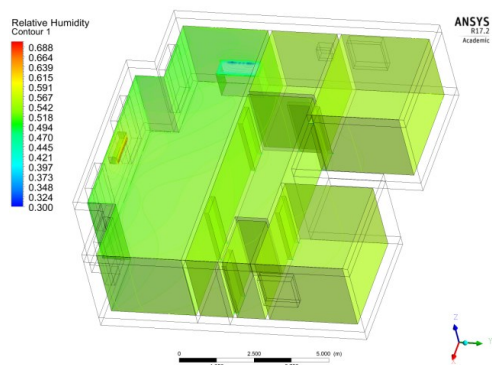


**Figure 11.** Results of the relative humidity distribution through the apartment for case 2 (16°C)

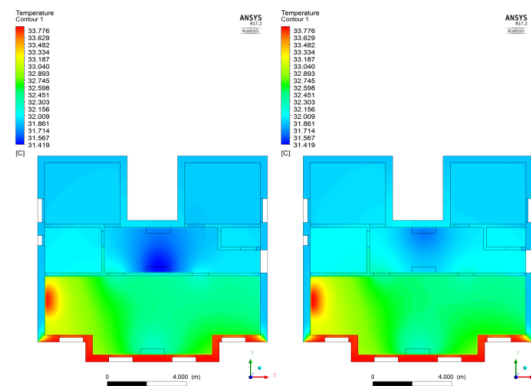


**Figure 13.** Results of the temperature distribution for cases with two air condition units



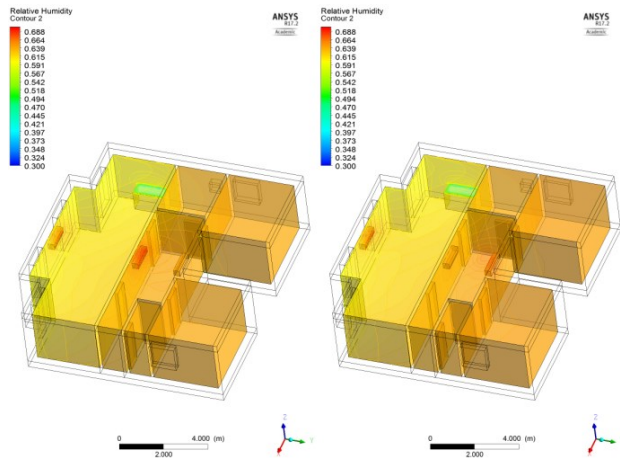


**Figure 14.** Results of the relative humidity distribution through the apartment for cases with two air condition units

### 5.3. Case 1 (two units) – temperature optimization

Conclusion for the cases with two units is that the case 1 is favorable but temperature of 22°C is not enough to reach the project temperature.

Decreasing the temperature to 20 °C, 18°C and 16°C, did not result in achieving the desired project temperature. However, according to some literature [1], [4], local temperature distribution is good enough to achieve thermal comfort, Figure 15.

Relative humidity meets the desired conditions of thermal comfort, Figure 16.

Condensation may occur only on the air outflow inlet of the air condition in the hallway, but with there is very low probability, Figure 17.

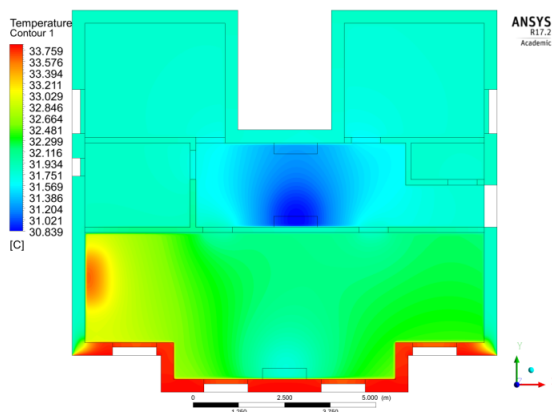


**Figure 15.** Results of the temperature distribution for case 1 (16°C)

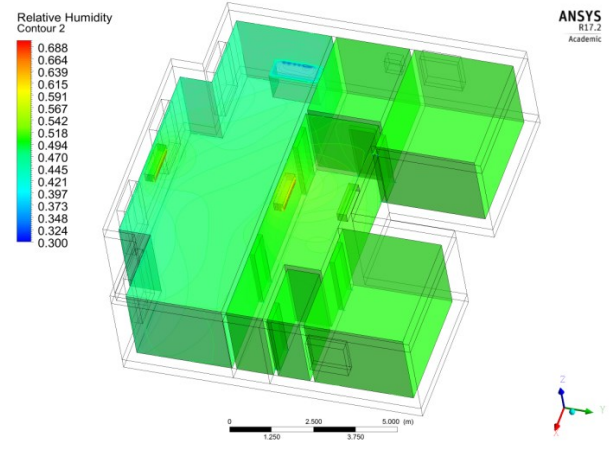


**Figure 16.** Results of the relative humidity distribution through the apartment for case 1 (16°C)

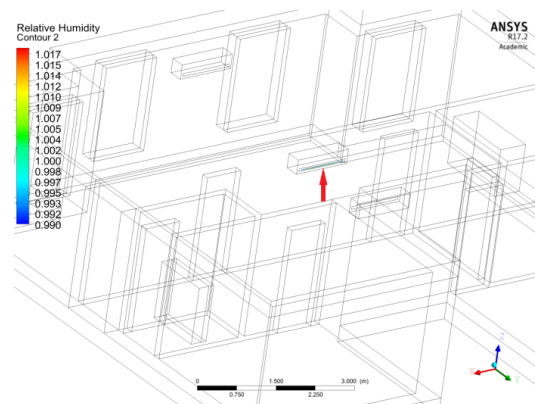


**Figure 17.** Possible condensation on the air outflow inlet of hallway unit (Case 1)

## 6. Conclusions and future work

CFD analysis of air conditioning is very useful. It takes in concern all obstacles in living spaces, distribution of temperature, humidity and stream velocity can be checked. However, to be accurate as possible it requires very precise modeling which is a long term process starting from scratch and requires extensive material parameter input.

Due to all simplifications, the developed model has resulted in inaccurate cooling predictions. It is unrealistic that two air condition units failed to achieve project temperature, or even come close to it.

Reason is that air condition units are simulated very simply, meaning that there is only air outflow. Warm air remains in the room and cooled air is being blown in, while the temperatures of the outside walls are fixed, which is not realistic. Such a way simply cannot achieve desired conditions in any normal circumstances and gives evidence of the paramount

importance of applying the appropriate boundary conditions.

The next step, to develop more realistic model, is to model and simulate realistic air conditioning unit (split type) by introducing sink and source terms for heat transfer inside the air conditioning unit, as well as to account for the momentum source which will represent the air conditioning fan. By using this approach, the exact effective power of the air conditioning unit will be defined and consequently the heat exchange rates will be much faster and require less power. Additionally, the future calculations will also account for the solar radiation and for the natural convection on the outside walls which will result in a more realistic model. This work did not use this approach due to very little available data in the literature regarding the modeling of residential building cooling. Therefore, the boundary conditions were simply extracted from the conventional approach which is for CFD analysis quite unrealistic and therefore of limited applicability.

As far as the heat loads are concerned, the objective is to include more of them (as seen in conventional analytical calculation).

Once such realistic model is developed, the data will be compared with experimental measurements.

## REFERENCES

- [1] Nižetić S., Radica G., *Rashladna tehnika*, online script, FESB, Split
- [2] Fabjanac I., (2017), *Grijanje i klimatizacija – projektni zadatci*, FESB, Split
- [3] Nižetić S., *Racionalno korištenje energije*, online script, FESB, Split
- [4] Nižetić S., *Grijanje i klimatizacija*, online script, FESB, Split
- [5] ANSYS, Inc., *ANSYS Fluent 17.2 Manual*, [https://www.sharcnet.ca/Software/Ansys/17.2/en-us/help/ai\\_sinfo/ai\\_sinfo.html](https://www.sharcnet.ca/Software/Ansys/17.2/en-us/help/ai_sinfo/ai_sinfo.html)
- [6] *Vrijeme i klima hrvatskog Jadrana*, online source, <http://jadrano.gfz.hr/vlaznost.html>, access date 01.05.2018.
- [7] *World Weather & Climate Information*, online source, <https://weather-and-climate.com/average-monthly-Humidity-perc.split.Croatia>, access date 01.05.2018
- [8] Mollier h-x diagram, <http://www.aldacs.com/images/hxDiag500LiCl.jpg>, online source, access date 05.05.2018
- [9] Andersson B., Andersson R., Hakansson L., Mortensen M., Sudiyo R., Wachem B.V., *Computational Fluid Dynamics for Chemical Engineers*, (2012), Cambridge, United Kingdom
- [10] Rehman U.U., *Heat Transfer Optimization of Shell-and-Tube Heat Exchanger through CFD Studies*, Master's Thesis in Innovative and Sustainable Chemical Engineering, (2011), Chalmers University of Technology, Goteborg, Sweden
- [11] [https://en.wikipedia.org/wiki/Thermal\\_comfort](https://en.wikipedia.org/wiki/Thermal_comfort), online source, access date 01.05.2018.
- [12] [https://en.wikipedia.org/wiki/Relative\\_humidity](https://en.wikipedia.org/wiki/Relative_humidity), online source, access date 01.05.2018.
- [13] <http://www.afs.enea.it/project/neptunius/docs/fluent/html/th/node58.htm>, online source, access date 01.06.2018.
- [14] <http://www.bipv.ch/index.php/en/technology-top-en/thermal-aspects/heat-transfer-coefficient>, online source, access date 01.05.2018.
- [15] Pruteanu M., Vasilache M., (2013), *Thermal conductivity determination for autoclaved aerated concrete elements used in enclosure masonry walls*, Faculty of Civil Engineering and Building Services, Tuiasi, Romania.
- [16] Balaji N.C., Monto M., Venkatarama Reddy B.V., *Thermal performance of the building walls*, Indian Institute of Science, Bangalore, India, <http://www.ibpsa.org/proceedings/BSA2013/16.pdf>
- [17] <http://www.greenspec.co.uk/building-design/thermal-mass/>, online source, access date 01.05.2018.
- [18] Pitroda J., Bhut A.K., Bhimani A.H., Chhayani N.S., Bhatu R.U., Chauhan D.N., *A Critical Review on Non-Load Bearing Wall Based on Different Materials*, (2016), International Journal of Constructive Research in Civil Engineering, [https://www.researchgate.net/publication/309727475\\_A\\_Critical\\_Review\\_on\\_Non-Load\\_Bearing\\_Wall\\_Based\\_on\\_Different\\_Materials](https://www.researchgate.net/publication/309727475_A_Critical_Review_on_Non-Load_Bearing_Wall_Based_on_Different_Materials)
- [19] *The Constructor-Civil Engineering Home for Civil Engineers*, <https://theconstructor.org/building/common-walls-materials-properties-and-applications/7246/>, online source, access date 01.05.2018.



# Aktivacija austenitnog nehrđajućeg čelika za postupak bestrujnoga nanošenja Ni-P prevlake

**Dario ILJKIĆ<sup>1</sup>, Luciano GRŽINIĆ<sup>2</sup> and Goran VRATOVIĆ<sup>3</sup>**

- 1) Sveučilište u Rijeci, Tehnički fakultet, Zavod za materijale  
University of Rijeka, Faculty of Engineering,  
Department of Materials Science and Engineering  
Vukovarska 58, 51000 Rijeka, **Croatia**
- 2) ULJANIK Strojogradnja Diesel d.d.  
ULJANIK Mechanical Engineering Diesel  
JSC  
Flaciusova 1, 52100 Pula, **Croatia**
- 3) Plazma tehnika d.o.o.  
Plazma tehnika d.o.o.  
Zona male privrede 12, 52216 Galižana, **Croatia**

darioi@riteh.hr  
luciano.grzinic@uljanik.hr  
gvratovic@gmail.com

## Ključne riječi

*Bestrujno nanošenje*  
*Nehrđajući čelik*  
*Mikro-tvrdoća*  
*Adhezivnost*

## Keywords

*Electroless deposition*  
*Stainless steel*  
*Micro-hardness*  
*Adhesivity*

## Izvorni znanstveni rad

**Sažetak:** U ovom radu prikazana je nova metoda nanošenja Ni-P prevlake na austenitni čelik postupkom bestrujnoga nikljanja. Budući da je bestrujnim nikljanjem vrlo teško formirati Ni-P prevlaku na površini austenitnog čelika, potrebno je izvršiti aktivaciju površine postupkom „nickel strike“. Pošto operacija „nickel strike“ komplicira postupak nanošenja Ni-P prevlake, u ovom je istraživanju izbjegnuta ta operacija. Studija je usmjerena na utjecaj novih procesa aktivacije na adhezivnost, mikrotvrdoću i mikrostrukturnu analizu bestrujno dobivene Ni-P prevlake. Adhezivnost i mikrotvrdoća su procijenjeni pomoću Vickersove metode. Mikrostruktura uzoraka analizirana je optičkim i pretražnim elektronskim mikroskopom. Na osnovi eksperimentalnih rezultata može se zaključiti da se novom metodom aktivacije Ni-P prevlake na austenitnom nehrđajućem čeliku dobiva zadovoljavajuća adhezivnost i mikro tvrdoća.

## Activation of austenitic stainless steel for deposition of electroless Ni-P layer

### Original scientific paper

**Abstract:** In this work a new method for Ni-P depositing on austenitic stainless steel by electroless processing is presented. Since, it is very difficult to form Ni-P deposit by electroless process on austenitic stainless steel as substrate, the activation with a weak acid etch, i.e., nickel strike should be applied. Since nickel strike pre-coating treatment makes Ni-P coating process, in this research, nickel strike operation was avoided. Study has been focused on influence of new activation process on adhesivity, microhardness and microstructure analysis of electroless Ni-P coatings. Adhesivity and microhardness was estimated by Vickers method. Microstructure of the electroless treated specimens were analyzed by optical and scanning electron microscopy. Based on experimental results, it can be concluded that new method of activation of surface, electroless nickel - phosphorous coatings on austenitic stainless steel gives satisfactory adhesiveness and microhardness.

## 1. Uvod

Bestrujno dobivena Ni-P prevlaka ima veću tvrdoću i bolju otpornost na koroziju od nehrđajućeg čelika AISI 316 [1]. Ali, vrlo je teško bestrujnim nikljanjem formirati Ni-P prevlaku na austenitnom nehrđajućem čeliku. Iz tog razloga treba primijeniti aktivaciju površine postupkom „nickel strike“ [2]. Operacija „nickel strike“ čini proces nanošenja Ni-P prevlake na austenitni nehrđajući čelik složenijima, u usporedbi s ostalim sličnim nanošenjima Ni-P prevlake na drugim vrstama čelika, aluminijskim legurama i tako dalje. Toplinsku obradu treba primijeniti nakon procesa nanošenja Ni-P prevlake, uglavnom za povećanje tvrdoće i adhezije Ni-P prevlake sa supstratom [2].

Pojava kristalne strukture u Ni-P prevlaci ovisi o sadržaju fosfora [3, 4-8]. Držanjem Ni-P prevlake na visokim

temperaturama, amorfna struktura kristalizira i gubi amorfni karakter. Istodobno, dobiva se veća tvrdoća sloja zbog difuzije fosfora [9]. Tvrdoća se povećava i s povećanjem udjela kristalne strukture [2, 4, 5, 10] i zbog pojave Ni<sub>3</sub>P faze [10].

Maksimalna tvrdoća se može dobiti ako je sadržaj fosfora oko 4% masenog udjela [3, 4-8].

Mikro tvrdoća Ni-P prevlake ovisi o toplinskoj obradi, sadržaju fosfora i sadržaju drugih elemenata legure u oblogama [3, 4, 11-14]. Nikal s amorfnom strukturom ima nižu tvrdoću od nikla s kristalnom strukturom [5-7, 13, 15-27]. Veličina zrna Ni-P prevlake ima značajan utjecaj na tvrdoću [19]. Toplinsko obrađivanje Ni-P slojeva nanesenih bestrujnim postupkom može imati značajan utjecaj na njihovu tvrdoću i adheziju [8]. U ovom radu istraživanje je usmjereno na utjecaj novih

procesa aktivacije na adhezivnost, mikrotvrdoću i mikrostrukturnu analizu Ni-P prevlake. Adhezivnost koja se odnosi na optimizaciju bestrujnog nanošenja Ni-P prevlake procijenjena je Vickersovom metodom.

## 2. Optimizacija aktiviranja bestrujnog postupka nanošenja Ni-P prevlake na austenitni nehrđajući čelik

Proces aktivacije elektrolita obavljen je uranjavanjem posebne aluminijske elektrode u elektrolit zajedno s tretiranim cilindričnim uzorkom od 8 mm promjera i duljine 50 mm. Kemijski sastav austenitnog čelika AISI 316 prikazan je u tablici 1.

Upotrijebljena je Nikora kupelj na osnovi vodene otopine natrijevog hipofosfita. Površine podloge su isprane i aktivirane u aktivacijskom agensu UNICLEAN 675. Nakon ispiranja primijenjen je glavni proces bestrujnoga nanošenja (slika 1) [28].

Nakon bestrujnog niklanja, uzorci su toplinski obrađeni na temperaturi od 500 °C tijekom 60 minuta u atmosferi peći [17, 28].

Sadržaj željeza, kroma, nikla i fosfora uzorka koji nije toplinski obrađen vrednovan je SEM i EDS mapiranjem. Na slici 2-5 prikazana je mapa sadržaja željeza, kroma, nikla i fosfora. Očito je da su nikal (slika 2) i fosfor (slika 3) smješteni u prevlaci i supstratu. Željezo (slika 4) i krom (slika 5) nalaze se samo u supstratu. Fosfor je ravnomjerno raspoređen u Ni-P prevlaci.

SEM i EDS mapiranje sadržaja željeza, kroma, nikla i fosfora na toplinski obrađenom uzorku prikazano je na slici 6-9. Očito je da je raspodjela kemijskih elemenata u premazu i supstratu slična raspodjeli kemijskih elemenata u uzorku koji nije toplinski obrađen. Na Ni-P prevlaci i u supstratu nalaze se nikal (slika 6) i fosfor (slika 7), a željezo (slika 8) i krom (slika 9) nalaze se samo u supstratu. Utvrđeno je da toplinski obrađeni i toplinski neobrađeni uzorci imaju oko 9% fosfora. Ni-P prevlaka može se prepoznati po svjetlijoj boji, nasuprot tamnom supstratu. Debljina toplinski neobrađene Ni-P prevlake je 8 µm, dok je debljina toplinski obrađene Ni-P prevlake 7,5 µm [28].

Vickersova mikro tvrdoća svakog uzorka procijenjena je pomoću Vickersovog tvrdomjera Struers Duramin. izmjerena mikro tvrdoća toplinski neobrađene Ni-P prevlake na supstratu od austenitnog nehrđajućeg čelika AISI 316 iznosila je  $429 \pm 17 \text{ HV}_{0,01}$ , dok je tvrdoća toplinski obrađene Ni-P prevlake na supstratu od austenitnog nehrđajućeg čelika iznosila  $853 \pm 26 \text{ HV}_{0,01}$ . Adhezivnost je procijenjena pomoću Vickersove metode. Na slici 10 može se vidjeti da se delaminacija Ni-P prevlake ne pojavljuje na uzorku obrađenom posebnom aktivacijom. Primjena toplinske obrade bez posebne aktivacije površine prije nanošenja Ni-P prevlake dovoljna za dobivanje zadovoljavajuće adhezije između Ni-P prevlake i supstrata.

**Tablica 1.** Kemijski sastav čeličnog supstrata

**Table 1.** Chemical composition of steel substrate

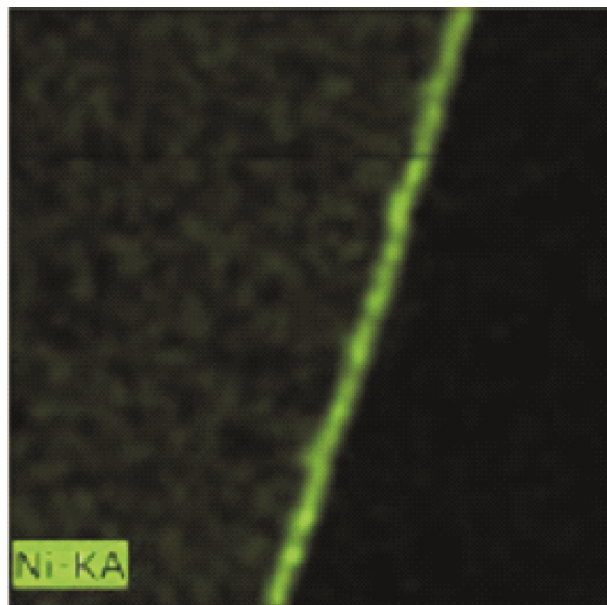
Kemijski sastav, maseni udio (w/%)							
C	Si	Mn	P	S	Cr	Mo	Ni
0,07	0,71	1,36	0,031	0,021	17,1	2,42	11,6



**Slika 1.** Dijagram toka postupka bestrujnog niklanja na supstratu od austenitnog čeliku AISI 316

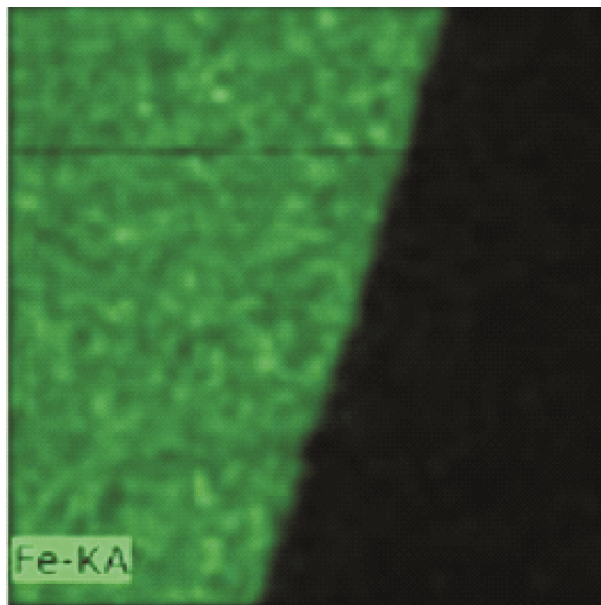
**Figure 1.** Flow-chart diagram of the electroless process of nickel plating on an austenitic-steel AISI 316 substrate





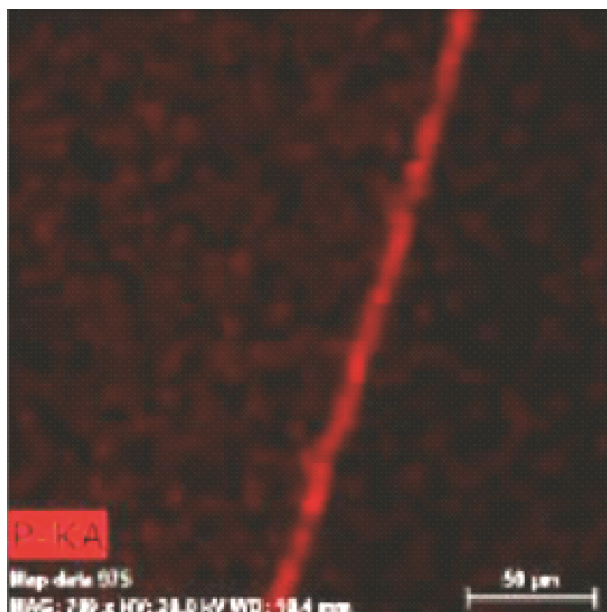
**Slika 2.** SEM i EDS mapiranje nikla toplinski neobrađenog uzoraka

**Figure 2.** SEM and EDS mapping of the nickel of the non-heat-treated samples



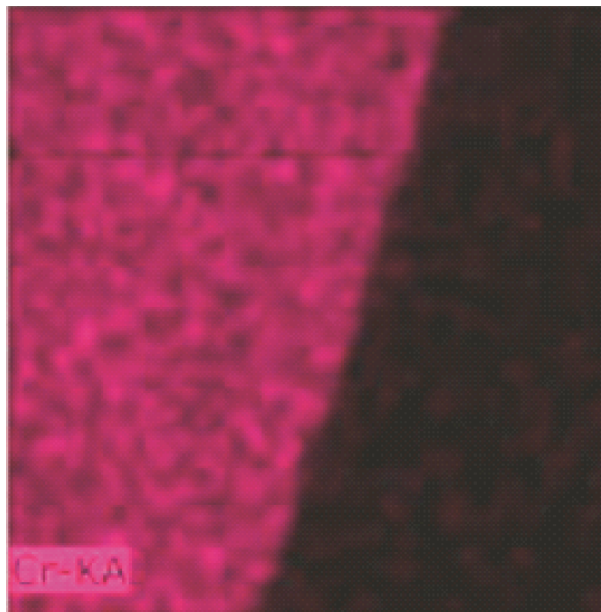
**Slika 4.** SEM i EDS mapiranje željeza toplinski neobrađenog uzoraka

**Figure 4.** SEM and EDS mapping of the iron of the non-heat-treated samples



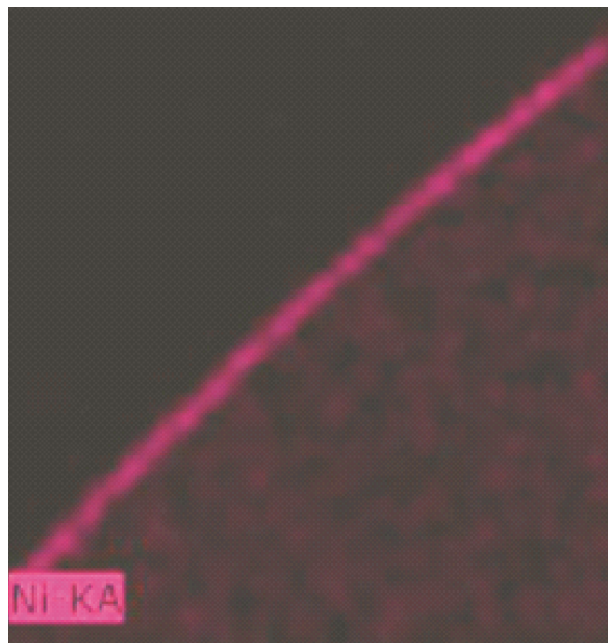
**Slika 3.** SEM i EDS mapiranje fosfora toplinski neobrađenog uzoraka

**Figure 3.** SEM and EDS mapping of the phosphorus of the non-heat-treated samples



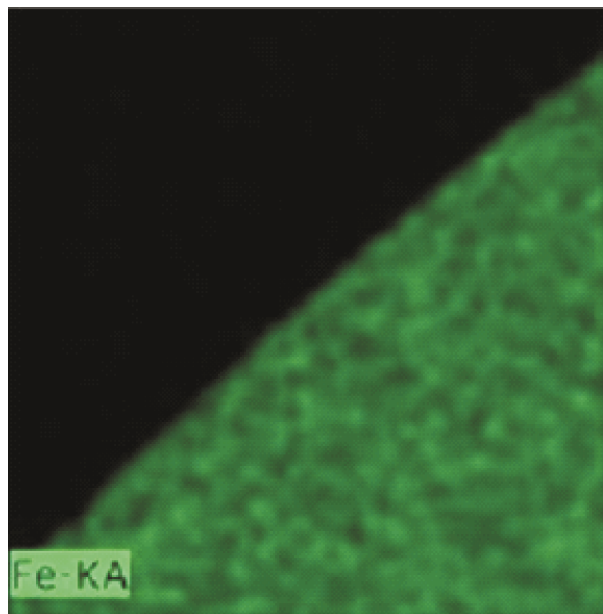
**Slika 5.** SEM i EDS mapiranje kroma toplinski neobrađenog uzoraka

**Figure 5.** SEM and EDS mapping of the chromium of the non-heat-treated samples



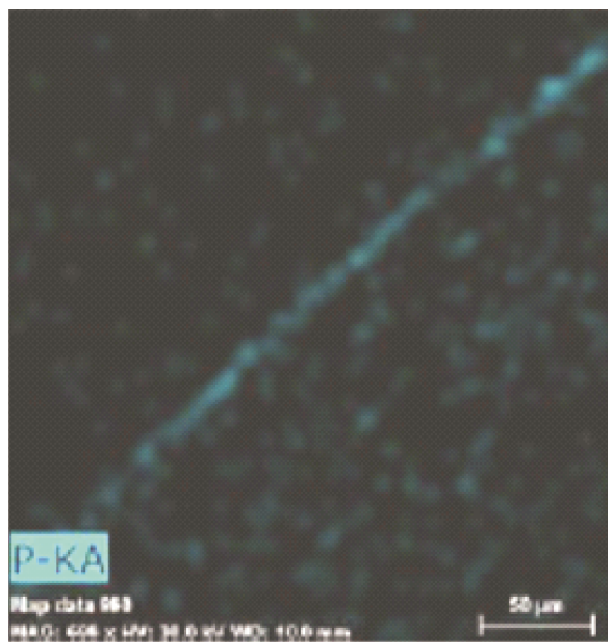
**Slika 6.** SEM i EDS mapiranje nikla toplinski obrađenog uzoraka

**Figure 6.** SEM and EDS mapping of the nickel of the heat-treated samples



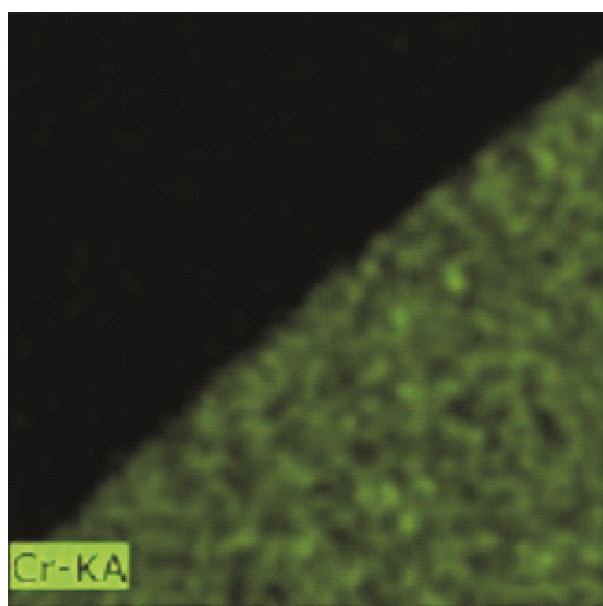
**Slika 8.** SEM i EDS mapiranje željeza toplinski obrađenog uzoraka

**Figure 8.** SEM and EDS mapping of the iron of the heat-treated samples



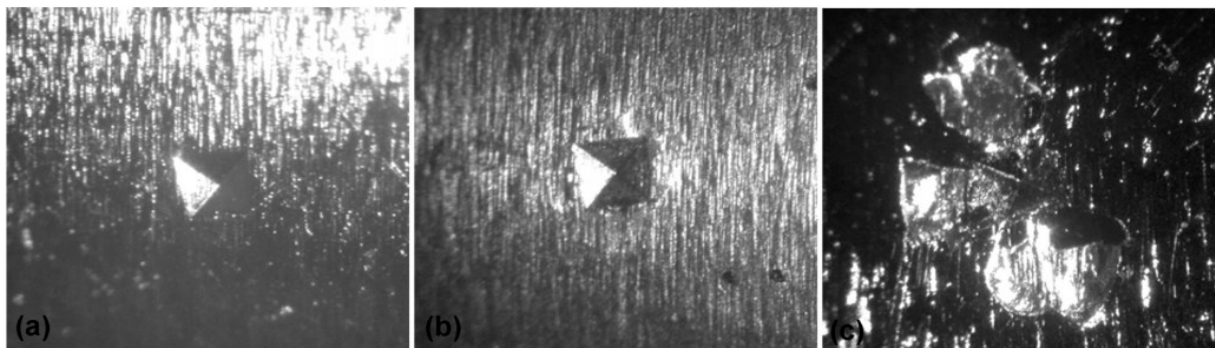
**Slika 7.** SEM i EDS mapiranje fosfora toplinski obrađenog uzoraka

**Figure 7.** SEM and EDS mapping of the phosphorus of the heat-treated samples



**Slika 9.** SEM i EDS mapiranje kroma toplinski obrađenog uzoraka

**Figure 9.** SEM and EDS mapping of the chromium of the heat-treated samples



**Slika 10.** Rezultati procjene adhezivnosti Ni-P prevlake, povećanje 35:1, a) posebna aktivacija + bestrujno nanošenje Ni-P prevlake, b) posebna aktivacija + bestrujno nanošenje Ni-P prevlake + toplinska obrada na 500 °C, c) bez posebne aktivacije + bestrujno nanošenje Ni-P prevlake + toplinska obrada na 500 °C

**Figure 10.** Indentation results for adhesivity of Ni-P electroless coatings, mag. 35:1, a) chemical pre-coating treatment of the surface + electroless coating, b) pre-coating treatment of the surface + electroless coating + aging at 500 °C, c) electroless coating + aging at 500 °C

### 3. Zaključak

Analizirana je primjena posebne elektrode u aktivaciji austenitnog čelika AISI 316 kao supstrata bestrujno niklane nanese Ni-P prevlake. Ni-P prevlake nanešene postupkom bestrujnog niklanja bile su kemijski jednolike formirane. Vickersovim ispitivanjima mikro čvrstoće utvrđeno je da primjenom toplinske obrade može postići veća tvrdoća Ni-P prevlake. Debljina Ni-P prevlake ne ovisi o toplinskoj obradi. Na temelju Vickersovih rezultata analize adhezivnosti Ni-P prevlake može se zaključiti da se primjenom pravilnog postupka aktivacije, prilikom bestrujnog nanošenja Ni-P prevlake može postići zadovoljavajuća adhezivnost.

### Potpore

Ovaj rad je sufinancirala Hrvatska zaklada za znanost projektom 5371.

Ovaj rad je sufinanciralo Sveučilište u Rijeci, broj potpore 13.09.1.1.02.

### LITERATURA

- [1] WU Y. H., LIU T. M., LUO S. X., (2009), *Corrosion characteristics of electroless Ni-P coating in sulfur-bearing solution*, Materials and Corrosion 60 No. 12, p 987-990
- [2] Baudrand D. W., (1994), *Electroless Nickel Plating*, ASM Handbook, ASM International, Materials Park, OH, p 290
- [3] Hari Krishnan K., John S., Srinivasan K. N., Praveen J., Ganesan M., Kavimani P. M., (2006), *An overall aspect of electroless Ni-P depositions –A review article*, Metallurgical and Materials Transactions A 37 No. 6, p 1917-1926
- [4] Taheri R., (2002), *Evaluation of Electroless Nickel-Phosphorus (EN) Coatings*, Ph. D. thesis, University of Saskatchewan
- [5] Balaraju J. N., Sankara Narayanan T. S. N., Seshadri S. K., (2006), *Structure and Phase Transformation Behaviour of Electroless Ni-P Composite Coatings*, Materials Research Bulletin 41 No. 4, p 847-860
- [6] Zuleta A. A., Galvis O. A., Castaño J. G., Echeverría F., Bolivar F. J., Hierro M. P., Pérez-Trujillo F. J., (2009), *Preparation and characterization of electroless Ni-P-Fe<sub>3</sub>O<sub>4</sub> composite coatings and evaluation of its high temperature oxidation behavior*, Surface & Coatings Technology 203 No. 23, p 3569-3578
- [7] Sahoo P. Das S. K., (2011), *Tribology of electroless nickel coatings – A review*, Materials and Design 32 No. 4, p 1760-1775
- [8] Maretić M., Smoljan B., Iljkić D., (2017), *Heat treatment of electroless Ni-P layers on an austenitic stainless-steel substrate*, Materials and technology 51 No. 3, p 413-417
- [9] *The Engineering Properties of Electroless Nickel Coatings*, (1980), Report, ELNIC Inc., Nashville, TN, C3-C27
- [10] Ma C., Wu F., Ning Y., Xia F., Liu Y., (2014), *Effect of heat treatment on structures and corrosion characteristics of electroless Ni-P-SiC nanocomposite coatings*, Ceramics International 40 No. 7A, p 9279-9284
- [11] Shao Z. C., Cai Z. Q., Hu R., Wei S. Q., (2014), *The study of electroless nickel plating directly on magnesium alloy*, Surface and Coatings Technology 249, p 42-47
- [12] Wang Y., Kang M., Jin S. W., Fu X. Q., Wang X. S., (2014), *Electrochemical behaviour in process of*

- electrodeposition Ni-P alloy coating*, Surface Engineering 30 No. 8, p 557-561
- [13] Soror T. Y., (2013), *Structure and Wear Resistance Properties of Electroless Ni-P Alloy and Ni-P-SiC Composite Coatings*, European Chemical Bulletin 2 No. 8, p 562-567
- [14] Sudagar J., Lian J., Sha W., (2013), *Electroless nickel, alloy, composite and nano coatings – A critical review*, Journal of Alloys and Compounds 571, p 183-204
- [15] Ploof L., (2008), *Electroless Nickel Composite Coatings*, Advanced Materials & Processes 166 No. 5, p 36-38
- [16] Hartung R., Schmidt J., Both S., (2008), *Tribologische Nickel-Dispersionsschichten Mit Hexagonalem Bornitrid*, Galvanotechnik 12, p 2931-2939
- [17] Alirezai S., Monirvaghefi S. M., Salehi M., Saatchi A., (2004), *Effect of Alumina Content on Surface Morphology and Hardness of Ni-P-Al<sub>2</sub>O<sub>3</sub> (α) Electroless Composite Coatings*, Surface and Coating Technology 184 No. 2-3, p 170-175
- [18] Apachitei I., Tichelaar F. D., Duszczek J., Katgerman L., (2001), *Solid-State Reaction in Low-Phosphorus Autocatalytic NiP-SiC Coatings*, Surface and Coating Technology 148 No. 2-3, p 284-295
- [19] Balaraju J. N., Rajam K. S., (2007), *Electroless Deposition and Characterization of High Phosphorus Ni-P-Si<sub>3</sub>N<sub>4</sub> Composite Coatings*, International Journal of Electrochemical Science 2 No. 10, p 747-761
- [20] Ma H., Tian F., Li D., Guo Q., (2009), *Study on the Nano-Composite Electroless Coating of Ni-P/Ag*, Journal of Alloys and Compounds 474 No. 1-2, p 254-267
- [21] Novaković J., Vassiliou P., Samara Kl., Argyropoulos Th., (2006), *Electroless NiP-TiO<sub>2</sub> Composite Coatings: Their Production and Properties*, Surface & Coatings Technology 201 No. 3-4, p 895-901
- [22] Cheng Y. H., Zou Y., Cheng L., Liu W., (2009), *Effect of the microstructure on the properties of Ni-P deposits on heat transfer surface*, Surface & Coatings Technology 203 No. 12, p 1559-1564
- [23] Karthikeyan S., Ramamoorthy B., (2014), *Effect of reducing agent and nano Al<sub>2</sub>O<sub>3</sub> particles on the properties of electroless Ni-P coating*, Applied Surface Science 307, p 654-660
- [24] Islam M., Shehbaz T., (2011), *Effect of synthesis conditions and post-deposition treatments on composition and structural morphology of medium-phosphorus electroless Ni-P films*, Surface & Coatings Technology 205 No. 19, p 4397-4400
- [25] Shen Y. F., Xue W. Y., Liu Z. Y., Zuo L., (2010), *Nanoscratching deformation and fracture toughness of electroless Ni-P coatings*, Surface & Coatings Technology 205 No. 2, p 632-640
- [26] Liu Y., Beckett D., Hawthorne D., (2011), *Effect of heat treatment, top coatings and conversion coatings on the corrosion properties of black electroless Ni-P films*, Applied Surface Science 257 No. 9, p 4486-4494
- [27] Sahoo P., (2009), *Wear behaviour of electroless Ni-P coatings and optimization of process parameters using Taguchi method*, Materials and Design 30 No. 4, p 1341-1349
- [28] Iljkić D., Smoljan B., Maretić M., Smokvina Hanza S., Štic L., Vratović G., (2018), *An activation of electroless process of ni-p depositing on austenitic stainless steel*, Proceedings of METAL 2018, 23-25 May 2018, Brno, Czech Republic



# Optimization of High Pressure Die Casting Process using Taguchi method and Computer Aided Casting Simulation Technique

**Sonja JOZIĆ<sup>1)</sup>, Dražen BAJIĆ<sup>1)</sup>, Ivana DUMANIĆ<sup>1)</sup> and Marko KODŽOMAN<sup>1)</sup>**

1) Faculty of Electrical Engineering,  
Mechanical Engineering and Naval  
Architecture, University of Split  
Ruđera Boškovića 32, 21000 Split,  
Republic of Croatia

[sonja.jozic@fesb.hr](mailto:sonja.jozic@fesb.hr)  
[drazen.bajic@fesb.hr](mailto:drazen.bajic@fesb.hr)  
[iduman00@fesb.hr](mailto:iduman00@fesb.hr)

## Keywords

*High-pressure die casting  
Taguchi method  
Castings parameters  
NOVAFlow&Solid*

*Original scientific paper*

**Abstract:** This paper presents approach to design an optimal mould using advantage of the simulation tools. The considered casting process is high pressure die casting process which is used to manufacture complex shaped products in light alloys. Combination of the design of experiments and computer assisted casting simulation techniques allow the die filling process to be evaluated and help faster optimization of the cavity mould geometry and process parameters. Simulation of casting process was performed, according to the Taguchi based L9 orthogonal array. Output process variables were filling time and shrinkage obtained in the end of simulation process. Gray relational analysis and analysis of variance were performed. Analysis of variance results indicate that the cavity mould geometry has the most significant influence on the filling time and shrinkage of the casting. Number of iterations using casting simulation software NOVAFlow&Solid was performed for mould filling and solidification analysis.

## 1. Introduction

High pressure die casting (HPDC) is a manufacturing process in which the molten metal is forced at high pressure and relatively high speed into a steel mould or die to form products. High-pressure die castings are characterized by excellent surface finish and accuracy, at least when the die is undamaged, [1].

Although the tooling is expensive, the productivity is high and part price is thereby modest. As such the process is highly popular, so that over 50 % of all Al alloy castings are produced by HPDC, [2]. It has a much faster production rate in comparison to other casting methods. In this process, the metal is injected into the die at high speed from 30 m/s to 100 m/s, (for aluminum alloy speed is about 40 m/s to 60 m/s) and under high pressure through complex gate and runner systems, [3].

HPDC process has a large number of parameters that may affect the quality of the casting and optimization of the process is essential. Researchers have attempted to model the complex die casting process and studied the influence of various parameters on the quality of cast product. There are issues related to the control of die temperature, solidification of the components and quality of the castings. The mechanical properties of a die-cast product are related, among other things, to the die temperature, the metal velocity at the gate and applied casting pressure.

Zheng et al [4] used artificial neural network to generalize the correlation between surface defects and die-casting parameters, such as mold temperature,

pouring temperature, and injection velocity. They optimized the process with trained neural network and achieved acceptable surface quality. Mahesh and Shrikant [5] used Taguchi method to identify optimized parameters in order to minimize the cycle time.

Defining the geometry of the injection system is mainly based on experience of engineers, past solutions, knowledge gained over the years, and trial-and-fail-method. Recently, simulation tools have been used to save time, reduce the costs of the casting system design and enable to meet the desired quality of the product. Simulation can make optimal casting system: it allows production of high quality castings with fewer experiments. Furthermore, economical use of materials and environmental saving can be achieved when the number of test castings decrease. Krimpenis et al [6] used neural networks and genetic algorithm to perform numerical simulation of casting process and find optimum process parameters for pressure die casting process. Hassan et al. [7] simulated casting process of the impeller using MAGMASOFT Software. The effect of the location and size of feeders and gates on parameters such as filling pattern, pressure and velocity, cooling rate, solidification and related defects were studied.

The casting filling process is perhaps the most critical one. Velocities parameters and the casting geometry can lead to turbulence and/or solidification issues.

This paper deals with multi-objective optimization problem of the casting process parameters, and geometry as well as the layout of the castings in the mould cavity.



The Taguchi design approach is utilized for experimental planning and gray relational analysis was used to find the optimal casting process parameters. The analysis of variance was carried out to obtain significant parameters influencing multi-performance characteristics of the process.

All experiments were performed in virtual environment in a special program designed for casting simulation and developed by the company NOVACAST, Sweden. This software, based on the control volume mesh technology allows the surface of the 3D model to control the shape of the mesh elements on the border of the casting. This methodology enables very fast and reliable precise generation of the results.

## 2. Methodology

In this paper importance is given for the parameter design stage. The basic steps to investigate the role of process parameters and mould geometry in level of shrinkage defects and total casting time, are summarized as follows:

- selection of the most significant die casting parameters having influence on the shrinkage and total casting time,
- selection of the appropriate design of experiments,
- performing simulation of the die casting process under the experimental conditions dictated by the chosen design of experiments,
- collection and analysis the data and
- making decisions regarding optimum setting of control parameters.

Solid modeling of electronic part cover of the machine, shown in Figure 1., was conducted by means of CATIA V5.

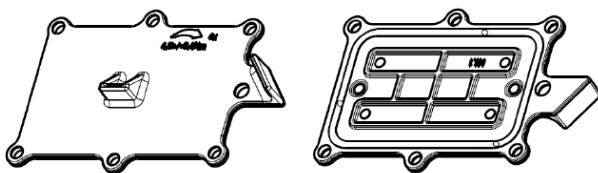


Figure 1. Cover of the electronic part

The other necessary parts of casting cavity such as bisquit, runners, gates and overflows were also modeled. Figure 2 shows the 3D model of casting – designed as configuration typ 2. Otherwise, there are three configurations to be observed.

## 3. Design of experiments for casting analysis

The literature review indicates that the Taguchi method is suitable in experimental design for designing and developing robust products or processes irrespective of

variation in process parameter (within set limits) and or variation in casting geometry.

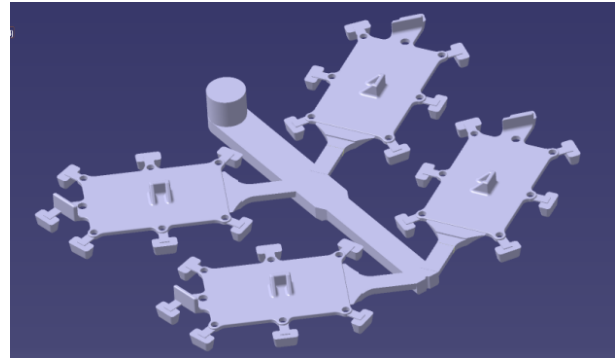


Figure 2. 3D model used for simulation - Configuration typ 2

The present research is associated with high pressure die casting process casting which involves various parameters at different levels and influence on the shrinkage and total casting time. Those parameters are velocity, pressure and mould geometry. Different mould geometry are determined with number of cavites (four and six) and runner geometry. Runner geometry are defined in three configurations differing in disposition of casting towards the runner and number of casting, presented in Figure 3.

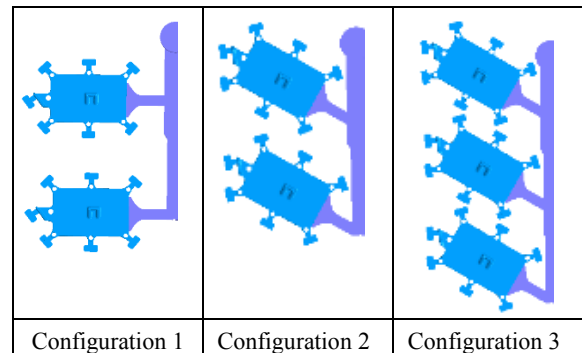


Figure 3. Three different configurations

The experimental design for three controllable variables with three levels, presented in Table 1, is organized by the Taguchi's L9 orthogonal array. The L9 orthogonal array has three columns and nine rows.

Table 1. The experimental factors and their levels

Levels of variables	Mould geometry A	Plunger velocity, $v_t$ [m/s] B	Pressure, $p$ [MPa] C
1	1	20	40
2	2	40	60
3	3	60	80

The casting model has to be imported into the simulation program NOVA Flow&Solid as the *stp* file.

Experimental runs with results are given in Table 2. Two process variables are read from the report obtained at the end of the simulation, i.e. after each experiment.

In high pressure die casting process, castings and moulds geometry design, as well as casting parameters, gating and cooling systems, die layout and the heat flow paths can be optimized by using simulation programs. Data resulting from them are very valuable information for investigate the problem and make a diagnosis as well as in die design and process parameter optimization as they simulate casting solidification and predict hot spots.

Benefits of those software are shared by customers and die casters, so the number of rejected products can be significantly reduced, leading to shortened delivery times, improved quality and indirect cost-reduction (less material waste and no need for empirical tests or trials).

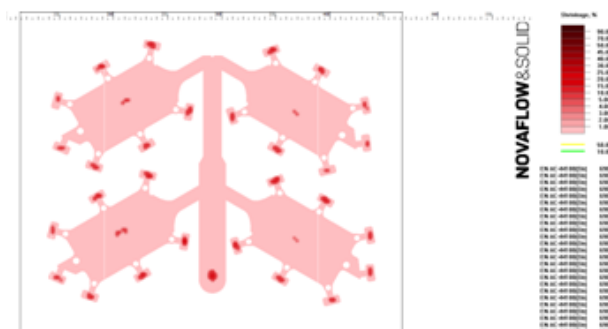


**Figure 4.** Shrinkage prediction obtained from Autoreport generated after each simulation

In the computer simulation it is possible to identify shape and location of porosities and to predict air entrapment by tracking its flow, as shows in figure4.

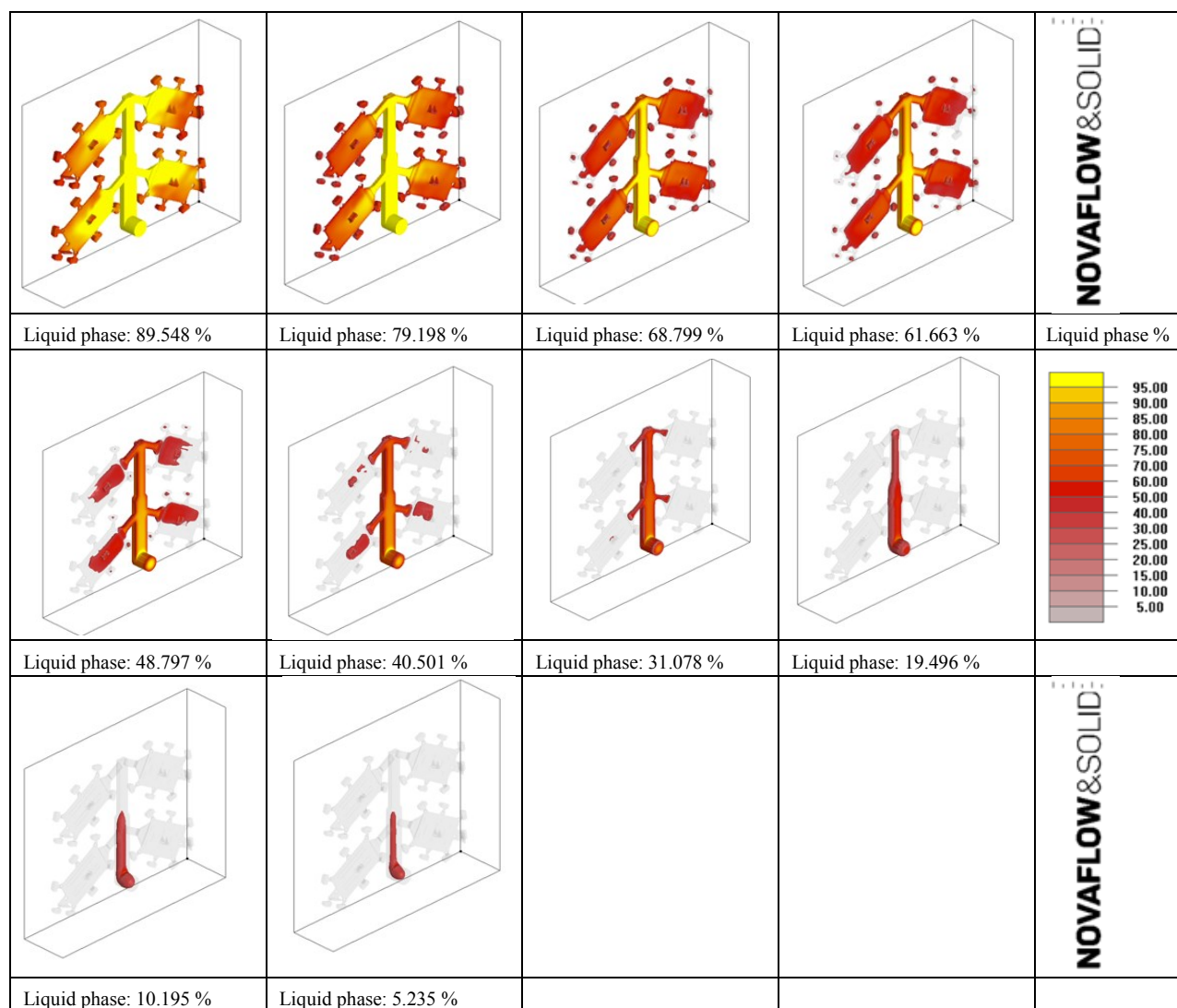


**Figure 5.** Mould-filling process of the simulation.

Figure 5 shows the liquid phase and confirms that construction and all casting parameters are properly designed.

In this study, further processing procedure should find optimal controllable variables for multi objective function using the GRA method. Two quality objectives of the process were chosen, including the total casting time and shrinkage of the material. Typically, the small values of total casting time and shrinkage of the material are desirable for the casting operations.

**Table 2.** Experimental layout using L9 orthogonal array and results

Runs	A	B	C	Total casting time [s]	Shrinkage [%]
1.	1	2	3	246,408	0,52
2.	3	2	2	331,951	0,562
3.	3	1	3	386,769	0,346
4.	1	1	1	296,763	0,857
5.	3	3	1	355,235	0,872
6.	2	3	3	240,115	0,493
7.	2	2	1	256,27	0,81
8.	2	1	2	262,022	0,483
9.	1	3	2	248,567	0,75

### 3.1. Grey relational analysis

A grey system presents a system in which a part of information is known and the other part is unknown, [8]. Because of the uncertainty that always exists, grey systems will give a variety of available solutions. Grey relational analysis, based on this theory, can be further effectively adapted for solving the complicated interrelationships among the designated performance characteristics. Through this analysis, the grey relational grade (GRG) is favourably defined as an indicator of multiple performance characteristics for evaluation. In grey relational analysis, the complex multiple response optimization problem can be simplified into an optimization of a single response grey relational grade. The procedure for determining the grey relational grade is discussed below.

Data pre-processing is performed in order to transfer original sequence to a comparable sequence. Numerical data are normalized between zero and one. Depending on characteristics of data sequence, various methodologies of data pre-processing are available. In this study, the normalized value of original sequence for total casting time and shrinkage, which are smaller-the-better performance characteristic, can be expressed as:

$$x_{ij} = \frac{\max(y_{ij}) - y_{ij}}{\max(y_{ij}) - \min(y_{ij})} \quad (1)$$

where  $y_{ij}$  are original data.

The normalized values of total casting time and shrinkage are shown in Table 3.

For a response  $j$  of experiment  $i$ , if the value  $x_{ij}$  which has been processed by data pre-processing procedure is equal to 1 or nearer to 1 than the value for any other experiment, then the performance of experiment  $i$  is considered as the best for the response  $j$ . The reference sequence  $X_0$  is defined as  $(x_{01}, x_{02}, \dots, x_{0j}, \dots, x_{0n}) = (1, 1, \dots, 1, \dots, 1)$ , where  $x_{0j}$  is the reference value for  $j$ th response and it aims to find the experiment whose comparability sequence is the closest to the reference sequence. Table 4 shows deviation sequences.

Next, the grey relational coefficient is used for determining how close  $x_{ij}$  is to  $x_{0j}$ . The larger the grey relational coefficient, the closer  $x_{ij}$  and  $x_{0j}$ .

**Table 3.** Normalized experimental results

Runs	Total casting time	Shrinkage
1.	0,957	0,669
2.	0,374	0,589
3.	0	1
4.	0,614	0,028
5.	0,215	0
6.	1	0,72
7.	0,89	0,118
8.	0,85	0,739
9.	0,942	0,232

**Table 4.** Deviation sequences

Runs	Total casting time	Shrinkage
1.	0,043	0,331
2.	0,626	0,411
3.	1	0
4.	0,386	0,972
5.	0,785	1
6.	0	0,28
7.	0,11	0,882
8.	0,15	0,261
9.	0,058	0,768

The grey relational coefficient can be determined as:

$$\gamma(x_{0j}, x_{ij}) = \frac{(\Delta_{\min} + \xi \Delta_{\max})}{(\Delta_{ij} + \xi \Delta_{\max})} \quad (2)$$

for  $i = 1, 2, \dots, m$  and  $j = 1, 2, \dots, n$

where

$\gamma(x_{0j}, x_{ij})$  is the grey relational coefficient between  $x_{ij}$  and  $x_{0j}$ ,

$$\Delta_{ij} = |x_{0j} - x_{ij}|, \quad (3)$$

$$\Delta_{\min} = \min\{\Delta_{ij}, i = 1, 2, \dots, m; j = 1, 2, \dots, n\} \quad (4)$$

$$\Delta_{\max} = \max\{\Delta_{ij}, i = 1, 2, \dots, m; j = 1, 2, \dots, n\} \quad (5)$$

$\xi$  is distinguishing coefficient,  $\xi \in (0,1]$ . In the present study the value of  $\xi$  is assumed as 0.5. Distinguishing coefficient ( $\xi$ ) is the index for distinguishability. The smaller  $\xi$ , the higher its distinguishability.

The measurement formula for quantification in grey relational space is called the grey relational grade. A grey relational grade is a weighted sum of the grey relational coefficients and it is calculated using equation:

$$\Gamma(X_0, X_i) = \sum_{j=1}^n w_j \gamma(x_{0j}, x_{ij})$$

for  $i = 1, 2, \dots, m$  (6)

where  $\sum_{j=1}^n w_{jj} = 1$

$\Gamma(X_0, X_i)$  is the grey relational grade between comparability sequence  $X_i$  and reference sequence  $X_0$ .

The weight of response  $j$  is  $w_j$  and usually depends on decision makers' judgment.

The grey relational grade indicates the degree of similarity between the comparability sequence and the reference sequence. If an experiment gets the highest grey relational grade with the reference sequence, it means that comparability sequence is most similar to the reference sequence and that experiment would be the best choice.

Table 5 shows the grey relational coefficients and grade for each experiment. The highest grey relational grade is the order of 1.

The experiment number 6, highlighted in grey, is the nearest optimum controllable parameters combination: geometry, plunger velocity and pressure.

The means of the grey relational grade for each level of controllable parameters were calculated from Table 5 and summarized in Table 6.

The larger the grey relational grade, the better the multiple performance characteristics. Therefore, the optimal values of the controllable parameters are as follows: mould geometry – configuration 2 (level 2), plunger velocity of 6 m/s (level 2), and pressure of 80 MPa- (level 3).

Figure. 6 shows the input parameters in relation to the grey relational grade.

**Table 5.** Grey relational coefficients and grey relational grade.

	Filling time	Shrinkage	Grade	Grade order
1.	0,9208	0,6016	0,7612	2
2.	0,444	0,5488	0,4964	7
3.	0,3333	1	0,6666	4
4.	0,5643	0,3396	0,4519	8
5.	0,3891	0,3333	0,3612	9
6.	1	0,641	0,8205	1
7.	0,8196	0,3617	0,5906	6
8.	0,7692	0,657	0,7131	3
9.	0,896	0,3943	0,6451	5

**Table 6.** Response table for grey relational grade.

Parameter	Level 1	Level 2	Level 3	Rang (max-min)
A	0,6194	0,708	0,508	0,2
B	0,601	0,616	0,608	0,0016
C	0,4679	0,6182	0,7494	0,2815
Total mean value of the grey relational grade = 0,624				

### 3.2. Analysis of variance for grey relational grade

The analysis of variance (ANOVA) is a method which is used in this study to find out which controllable parameter significantly affects the performance characteristic. This is accomplished by separating the total variability of the grey relational grades, which is measured by the sum of the squared deviations from the total mean of the grey relational grade into contributions by each controllable parameter and the error.

The percentage contribution by each of the process parameters in the total sum of the squared deviations was used to evaluate the importance of the controllable parameter change on the performance characteristic.

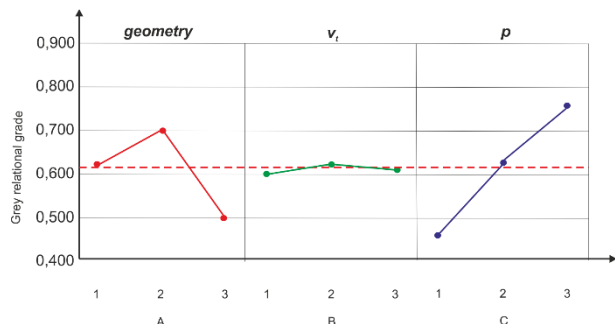


**Figure. 6.** Grey relational grade graph.

The results of ANOVA for the grey relational grade values are shown in Table 7. The results indicate that the percentage contribution of the geometry, plunger velocity, and pressure are 33,04 %, 0,05 % and 65,28 %, respectively. Geometry and pressure significantly influenced the grey relational grade, and pressure is the most significant parameter for multiple performance characteristics.

**Table 7.** Results of the analysis of variance.

	df	Seq SS	Adj MS	F-ratio	Contrib.
G	2	0,060257	0,030128822	20,2558	33,04%
$v_p$	2	8,393E-05	4,19658E-05	0,02821	0,05%
$p$	2	0,119058	0,059529451	40,0220	65,28%
E	2	0,002974	0,001487416		
T	8	0,18237			

G- geometry, E – error, T – Total, df - Degree of freedom, SS - Sum of square, MS – Mean square

## 4. Conclusions

In this paper, the controllable parameters influencing the multiple performance characteristics of HPDC process were studied on the basis of Taguchi's experimental design method. The optimum parameters were determined for the better multiple performance characteristics (total casting time and shrinkage) by using the grey relational analysis. This research proposed the orthogonal array combined with the grey relational analysis.

The conclusions were summarized as follows:

1. It can be concluded from the grey relational grade and the response table for the grey relational grade that the larger the grey relational grade, the better the multiple performance characteristics. So, the optimal levels of HPDC parameters for the desired performance characteristics is the combination labeled as A2B2C3.
2. Based on the ANOVA of the GRG results, it is observed that pressure has a significant influence on multiple responses.
3. Using die casting simulation programs for shrinkage porosity prediction can lead to significant costs reduction thanks to major improvements in material and energy consumption, labour resources, and scraps reduction.

## REFERENCES

- [1]. Mohammad Sadeghi and Jafar Mahmoudi, (2012). *Experimental and Theoretical Studies on the Effect of Die Temperature on the Quality of the Products in High-Pressure Die-Casting Process*. Advances in Materials Science and Engineering, Volume 2012, Article ID 434605, 9 pages.
- [2]. Campbell J. (2011). 2011 "Complete Casting Handbook" University of Birmingham, UK Elsevier.
- [3]. Matthew S. Dargusch, Gilles Dour, N. Schauer, C. M. Dinnis, George M. Savage. (2006). *The influence of pressure during solidification of high pressure die cast aluminium telecommunications components* Journal of Materials Processing Technology 180(1-3), DOI: 10.1016/j.jmatprotec.2006.05.001.
- [4]. Jiang Zheng, Quodong Wang, Peng Zhao, Congbo Wu. (2009). *Optimization of high-pressure die casting process parameters using artificial neural network*, International Journal of Advanced Manufacturing Technology, 44; pp. 667-674.
- [5]. Mahesh N Adke, Shrikant V Karanjkar. (2014). *Optimization of die-casting process parameters to identify optimized level for cycle time using Taguchi method*, International journal of innovation in engineering and technology, Vol 4, Issue 4, pp. 365-375
- [6]. Krimpenis A., Bernardos P.G., Vosniakos G.C. Koukouvitaki. (2006). *Simulation based selection of optimum pressuredie-casting process parameters using neural nets and genetic algorithms*, International Journal of Advanced Manufacturing Technology 27; pp. 509-517.
- [7]. Hassan Iqbal, Anwar K., Sheikh, AbdulHadi Al-Yousef and M., Younas. (2012). *Mould Design Optimization for Sand Casting of Complex Geometries Using Advance Simulation Tools*, Material Manufacturing Process, 27(7), pp. 775-785.
- [8]. Venkata Rao, R. (2011). *Advanced Modelling and Optimization of Manufacturing Processes*, International Research and Development. Springer-Verlag London Limited.



# Numerical analysis and experimental validation of transient heat transfer during solidification/melting inside an insulated tank

Mišo JURČEVIĆ<sup>(1)</sup>, Željko PENG<sup>(1)</sup>,  
Branko KLARIN<sup>(1)</sup> and Sandro  
NIŽETIĆ<sup>(1)</sup>

1) University of Split, Faculty of Electrical  
Engineering, Mechanical Engineering and  
Naval Architecture  
Sveučilište u Splitu, Fakultet  
elektrotehnike, strojarstva i brodogradnje  
R. Boškovića 32, 21000 Split, Croatia

[misjurce@fesb.hr](mailto:misjurce@fesb.hr)

[zpenga@fesb.hr](mailto:zpenga@fesb.hr)

[bklarin@fesb.hr](mailto:bklarin@fesb.hr)

[snizetic@fesb.hr](mailto:snizetic@fesb.hr)

## Keywords

Computational Fluid Dynamics  
Floating platforms  
Transient heat transfer  
Solidification/melting  
Experimental validation

## Ključne riječi

Numeričko modeliranje strujanja  
Plutajuće platforme  
Nestacionaran prijenos topline  
Zamrzavanje/odmrzavanje  
Eksperimentalna validacija

## Original scientific article

**Abstract:** Floating platforms using ice as a support structure are a promising candidate for replacing the conventional floating platforms due to their favorable characteristics, i.e. lower initial investment and manufacturing costs, reasonable operational costs, sufficient load capacity and strength. The new experimental setup was recently developed to enable conducting experiments during transient solidification/melting of water inside an insulated tank with purpose to give a more detailed insight of the temperature distribution inside the tank and the influence of the coolant inlet temperature on the formation of ice. This work expands the experimental research by developing a three-dimensional computational fluid dynamics (CFD) model for transient heat transfer during the solidification/melting of ice around the cooling pipes inside the experimental setup. Since the solidification/melting model cannot be used for compressible flows the analysis considers the latent heat of fusion and constant water properties. The analysis is carried out to determine the influence of the coolant inlet temperature on spatially resolved formation of ice in the experimental tank. The CFD model also accounts for the change in the coolant temperature during the passage through the tank and the heat transfer through the insulation plates. Additional CFD analysis was performed without solidification/melting model but with realistic water/ice properties (i.e. density and viscosity are temperature dependent). This analysis represents reference point for future improvements of the CFD and experimental model. Furthermore, the CFD results are compared with the experimentally obtained data and the results are used to determine the future steps for improving the concept and consequently up-scaling for commercial applications.

## Izvorni znanstveni rad

**Sažetak:** Plutajuće platforme s ledenom nosivom strukturom su obećavajući kandidat za zamjenu konvencionalnih plutajućih platformi zbog njihovih povoljnih karakteristika, tj. nižih početnih ulaganja i troškova proizvodnje, razumnih operativnih troškova te zadovoljavajuće nosivosti i čvrstoće. Nedavno je razvijen novi eksperimentalni postav kako bi se omogućilo provođenje eksperimenata pri nestacionarnim uvjetima zamrzavanja/odmrzavanja vode unutar izoliranog spremnika s ciljem detaljnijeg uvida u raspodjelu temperature unutar spremnika i utjecaja ulazne temperature rashladnog sredstva na stvaranje leda. Ovaj rad nadograđuje eksperimentalno istraživanje razvijanjem trodimenzionalnog numeričkog modela strujanja (CFD) za nestacionarni prijenos topline tijekom zamrzavanja/odmrzavanja leda oko rashladnih cijevi unutar eksperimentalnog postava. Analiza uzima u obzir latentnu toplinu fuzije i konstantna svojstva vode budući da se model zamrzavanja/odmrzavanja ne može koristiti za kompresibilne tokove. Analiza se provodi kako bi se utvrdio utjecaj ulazne temperature rashladnog sredstva na prostorno profiliranje leda u eksperimentalnom spremniku. CFD model uzima u obzir promjenu temperature rashladnog sredstva tijekom prolaska kroz spremnik i prijenos topline kroz izolacijske ploče. Provedena je dodatna CFD analiza bez modela zamrzavanja/odmrzavanja, ali s realnim svojstvima vode (tj. gustoća i viskoznost ovise o temperaturi). Ova analiza predstavlja referentnu točku za buduća poboljšanja CFD i eksperimentalnog modela. Nadalje, rezultati CFD analize su uspoređeni s eksperimentalno dobivenim podacima, a izlazni podaci će se koristiti prilikom utvrđivanja sljedećih koraka za poboljšavanje i posljedično komercijaliziranje koncepta.

<u>Symbols/Oznake</u>			
$C$	- constant - konstanta	<u>Greek letters/Grčka slova</u>	
$C_p$	- specific heat capacity, $\text{kJ kg}^{-1}\text{K}^{-1}$ - specifični toplinski kapacitet	$\rho$	- density, $\text{kg m}^{-3}$ - gustoća
$h$	- sensible enthalpy of PCM, $\text{kJ kg}^{-1}$ - osjetna entalpija	$\beta$	- liquid fraction - tekuća faza
$H$	- total enthalpy of PCM, $\text{kJ kg}^{-1}$ - ukupna entalpija PCM-a	<u>Subscripts/Indeksi</u>	
$K$	- thermal conductivity, $\text{W m}^{-1}\text{K}^{-1}$ - toplinska vodljivost	<i>liqu</i>	- at liquid state - u tekućoj fazi
$L$	- latent heat of PCM, $\text{kJ kg}^{-1}$ - latentna toplina PCM-a	<i>mush</i>	- Mushy zone - mješavina tekuće i krute faze
$S$	- momentum source term, $\text{N m}^{-3}$ - pojam izvora momenta	<i>pcm</i>	- phase change material - material sa promjenjivim fazama
$T$	- temperature, K - temperature	<i>ref</i>	- reference - referentni
$t$	- time, s - vrijeme	<i>solid</i>	- at solid state - u krutoj fazi
$\vec{u}$	- velocity vector, $\text{m s}^{-1}$ - vektor brzine		

## 1. Introduction

The vast majority of worlds' largest cities are located on the coast, and they are massively overpopulated and spatially deficient. The aspiration of every civilization is to spread and prosper, so it is only a matter of time when large water surfaces transform from obstacles to opportunities and finally into advantages. Having in mind humanity's insatiable hunger for energy, sea surfaces are likely to become home for energy hotspots. Already today, there is a strong tendency to position the wind turbines at the open sea [1], in order to achieve the highest efficiency and to use potentially fertile land as little as possible. Also, the dislocation of heavy industry on the sea is anticipated so that way possible risk for the population is minimized. Nuclear power plants are good candidates for dislocation on the sea because of unlimited access to cooling water, the seismic damping effect of large water surfaces and the option of sinking power plant in case of emergency. Examples of this are already emerging, such as Akademik Lomonosov, Russian floating nuclear power station. It is not hard to see that

colonization of the sea is a process that has already begun. Floating platforms are the promising solution for sea conquest. This paper is part of the larger project which is focused on the development of the revolutionary floating platform with supporting structure based on ice. The idea of sea colonization by means of ice platforms was developed by Alexander Bolonkin in his work [2] where he proposes a cheap floating platform created from a natural ice taken from Antarctica or Arctic. Unlike Bolonkin's idea, but for purposes of this paper and the project itself, ice is created in an insulated tank. The tank's heat insulation is made of polystyrene panels. Within the tank there are three levels of coolant pipes with 90% propylene glycol coolant. The coolant pipes are used to cool water (and air) inside the tank. In principal, experimental setup works as a heat exchanger where the heat is transferred through the thermodynamic process from water to propylene glycol. Water can be classified as a phase changing material. Phase change materials (PCM) have been attracting increasing attention in recent years since they have compact design, high energy density and capability of storing large amount of energy

in a narrow temperature range [3]. Khodadadi and Hosseinzadeh did the numerical analysis on the solidification of water with Cu nanoparticles [4]. Shuying Wu and others in their work on thermal energy storage behavior of  $\text{Al}_2\text{O}_3\text{-H}_2\text{O}$  nanofluids [5] claim that by adding only 0.2 wt%  $\text{Al}_2\text{O}_3$  nanoparticles, the total freezing time of water can be reduced by 20.5%. Since the total freezing time is not of vital importance for the creation of a relatively inexpensive ice platform (rather, it is more important to keep it frozen) water used for the experiment was acquired from the municipal water supply system without any supplements. The experiment is investigated with the developed three-dimensional computational fluid dynamics (CFD) models for transient heat transfer. Temperature inside the tank and the solidification/melting of ice around the cooling pipes are monitored both experimentally and via CFD analysis. Both numerically and experimentally obtained results will be used for future development and possible improvements on the floating platform.

## 2. Experimental setup and procedure

The test facility that was used consists of the air-cooled refrigeration unit, heat exchanger, accumulation tank, circulation pump and the water-filled tank with polystyrene insulation as represented schematically in Figure 1.

The tank was filled partially to ensure that the temperature of the air in the close proximity to the free-surface is of sufficiently low temperature to improve the solidification process. The mass flow rate of the propylene glycol coolant was sufficiently high to ensure uniform temperature distribution along the entire tank, i.e. maximal temperature gradient of the coolant is ca. 2 K (in pipes that are submerged underwater). Two levels of pipes are submerged underwater and the third one is in the air (max temperature gradient of the coolant located in pipes that are surrounded by the air is ca. 0.1 K) to ensure lower propylene glycol temperature since coolant from all pipes is mixed inside the accumulation tank, Figure 1.

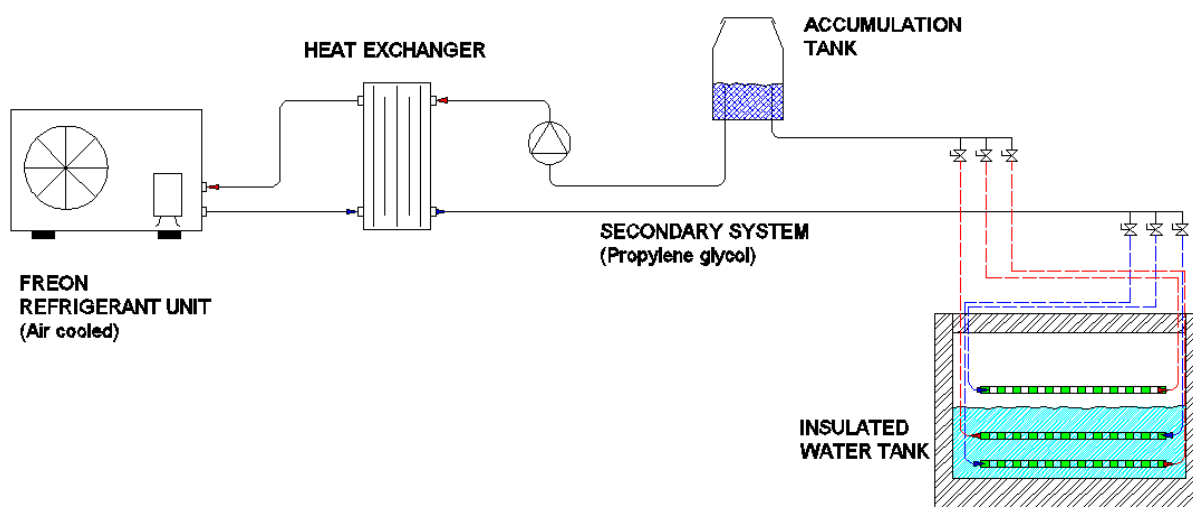


**Figure 1.** Schematic of the experimental test facility

The experimental research was conducted to determine the water, ice and air distributions throughout the tank when freezing process reaches steady-state. Furthermore, the temperatures have been monitored and recorded in real-time in several points throughout the tank (Figure 2) and one point of interest in the polystyrene insulation surrounding the tank. Temperature sensors (T-type) with waterproof cap probe (4 mm diameter) and operating temperature range from  $-60^{\circ}\text{C}$  to  $+200^{\circ}\text{C}$  with  $0.5^{\circ}\text{C}$  accuracy were used to measure the temperatures. The temperature signals were sampled using data logger (Pico TC08) connected to a PC with the sampling interval of 10 minutes. During the experiment the coolant temperature at the inlet side was maintained at  $268.15\text{ K}$ . The experiment was proceeded until it reached steady-state conditions.

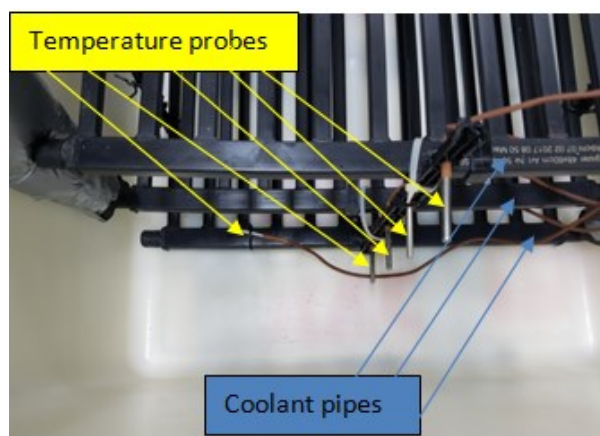


**Figure 2.** Temperature sensors and coolant pipes

### 3. Mathematical background and CFD

In this article CFD analysis deals with phase change material (PCM), which is water.

The following assumptions were taken in account for solidification/melting process solver:

- The flow is incompressible, transient, and laminar.
- The thermo-physical properties of the water and the propylene glycol are independent of the temperature (due to model limitations).

The CFD analysis is based on solving the equations listed below.

#### Continuity equation:

$$\frac{\partial \rho}{\partial t} + \nabla \cdot (\rho \vec{u}) = 0 \quad (1)$$

#### Momentum equation:

$$\frac{\partial}{\partial t} (\rho \vec{u}) + \nabla \cdot (\rho \vec{u} \vec{u}) = \mu \nabla \cdot \vec{u} - \nabla p + \rho \vec{g} + S \quad (2)$$

where  $S$  is the momentum source term due to the reduced porosity in the mushy zone and can be expressed as [6]:

$$S = \frac{(1-\beta)^2}{(\beta^3 + \epsilon)} C_{mush} \vec{u} \quad (3)$$

where  $\epsilon$  is a small number (0.001) to prevent division by zero,  $C_{mush}$  is the mushy zone morphology constant. This constant measures the amplitude of the damping and describes how steeply the velocity is reduced to zero when the material solidifies. This constant should be in the range of  $10^4$ - $10^7$  [6].

#### Energy equation:

$$\frac{\partial}{\partial t} [\rho H] + \nabla \cdot [\rho \vec{u} H] = \nabla \cdot (K \nabla T) + S \quad (4)$$

The melting-solidification processing is evaluated by defining the liquid fraction ( $\beta$ ) quantity. This considers the fraction of liquid at each cell in the PCM domain. The liquid fraction is determined based upon the enthalpy ( $H$ ) balance at each cell [6]. As explained in Eq. (5)-(8).

$$h = h_{ref} + \int_{T_{pcm,ref}}^{T_{pcm}} C_{p,pcm} dT \quad (5)$$

where  $h$  is the sensible enthalpy,  $h_{ref}$  is the reference enthalpy at the reference temperature  $T_{ref}$  and  $C_p$  is the specific heat [6].

$$H = h + \Delta H \quad (6)$$

where  $\Delta H$  is the latent heat of fusion [6].

$$\beta = \Delta H / L \quad (7)$$

where  $\beta$  the liquid fraction. The liquid fraction can be expressed in terms of temperatures as [6]:

$$\beta = \begin{cases} 0 & T_{pcm} < T_{pcm,solid} \\ 1 & T_{pcm} = T_{pcm,solid} \\ \frac{T_{pcm} - T_{pcm,solid}}{T_{pcm,liq} - T_{pcm,solid}} & T_{pcm,solid} < T_{pcm} < T_{pcm,liq} \\ 1 & T_{pcm} > T_{pcm,liq} \end{cases} \quad (8)$$

where  $T_{solid}$  is the temperature of the PCM when the last liquid content is solidified and  $T_{liq}$  is the temperature of the PCM when the last solid content is liquefied [6].

### 4. CFD model

The three-dimensional computational fluid dynamics (CFD) model for transient heat transfer was developed using ANSYS Fluent. The geometry of a 3D model was designed with ANSYS DesignModeler™ (Figure 3) and after that the discretization was performed using ANSYS Meshing™. Since the solidification/melting model cannot be used for compressible flows all material properties in the simulation were temperature independent.

For that reason, another simulation was performed where solidification/melting was excluded from consideration, while the properties were defined to be functionally correlated to the temperature.

#### 4.1. Geometry

Geometry of the model was based on the experimental setup with minor differences regarding some dimensional specifics of the considered tank that can be neglected. Basic dimensions of model's geometry are given in Table 1.

**Table 1.** The insulated tank's dimensions in mm

Length (mm)	Depth (mm)	Height (mm)	Insulation thickness/ top and sideways	Insulation thickness/ bottom
800	550	550	150	300

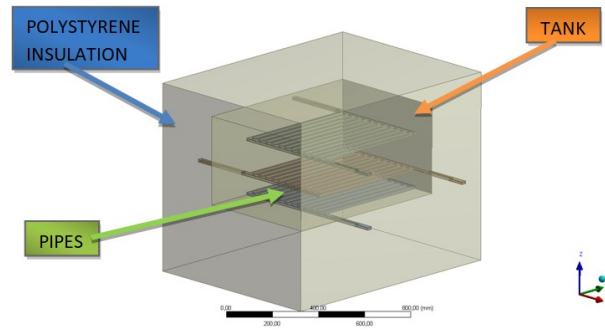


**Figure 3.** Geometry of the 3D model

The geometry of the pipes was simplified regarding the coolant inlet and outlet pipelines in order to simplify the generation of structured hexahedral mesh. In the experimental assembly, the inlet and the outlet pipelines with the coolant fluid are vertical unlike in the developed 3D model where the mentioned pipelines are horizontal, Figure 4. This was altered because those pipelines are heavily insulated, therefore the coolant temperature was not significantly affected by the surrounding water in the specified regions.



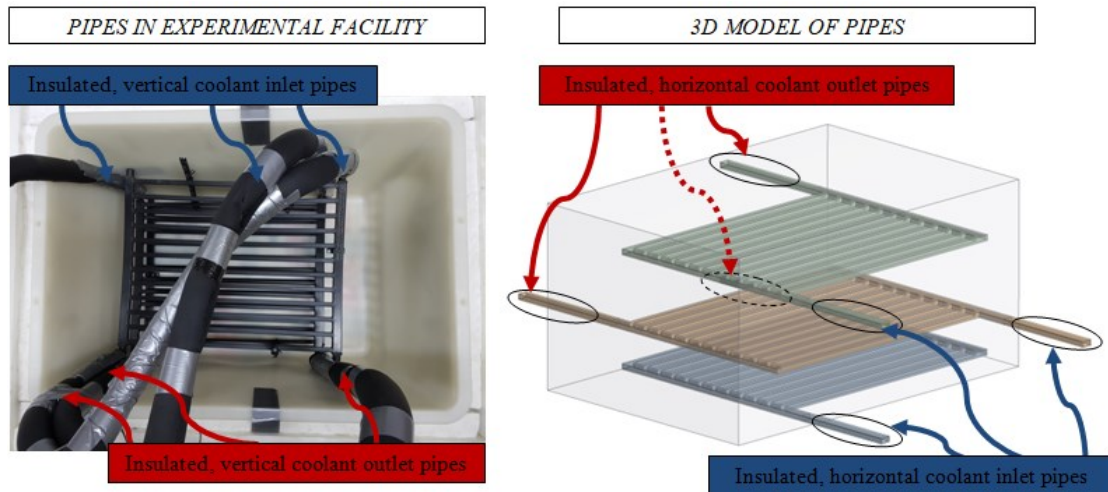


**Figure 4.** Comparison of the experimental (right) and the 3D model (left) coolant inlet and outlet pipelines

#### 4.2. Meshing

The parallel processing was used in order to enable fine-tuning and to reduce the time for mesh generation. The grid dependency study was conducted for steady state simulation on four meshes with different number of elements:

1. 779566
2. 1083722
3. 2763268
4. 14071842

The solution proved to be grid independent, Figure 5.

Having that in mind, it can be concluded that the simulation can run with a relatively low number of elements without major impact on results, which is highly relevant for this study due to the required transient analysis.

Selected mesh has ca. 2.9 million finite volumes. The element sizes that were selected for the mesh grid, Figure 6, Figure 7, are:

1. Pipes and coolant in pipes domains: 2 mm
2. Water and air domains: 10 mm
3. Insulation domain: 10 mm

Hex Dominant Method was used both for water and insulation domains to generate all quad mesh type.

Selected mesh has ca. 2.9 million finite volumes.

The element sizes that were selected for the mesh grid, Figure 6, Figure 7, are:

1. Pipes and coolant in pipes domains: 2 mm
2. Water and air domains: 10 mm
3. Insulation domain: 10 mm

Hex Dominant Method was used both for water and insulation domains to generate all quad mesh type.

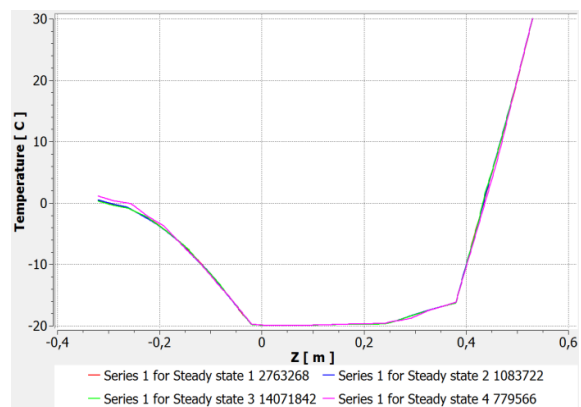


**Figure 5.** Grid dependency test – temperature plot along the Z-axis

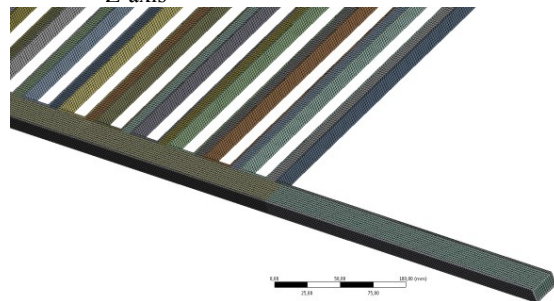


**Figure 6.** Pipe mesh

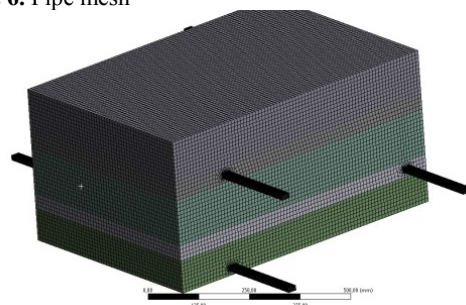


**Figure 7.** Water and air domain mesh



#### 4.3. Domains and material properties

The analysis contains both solid and fluid domains. Solid domains are high density polyethylene (HDPE) pipes and expanded polystyrene (EPS) insulation while fluid

domains are water, air and propylene glycol coolant. The list of materials properties is given in Table 2.

**Table 2.** Properties of materials

MATERIAL	WATER	AIR	PROPYLENE GLYCOL [7]	HDPE	EPS
Density, $\text{kg m}^{-3}$	998.2	1.225	1071.4	960	20
Specific Heat ( $C_p$ ), $\text{J kg}^{-1}\text{K}^{-1}$	4182	1006.43	2448	2250	1300
Thermal Conductivity, $\text{W m}^{-1}\text{K}^{-1}$	0.6	0.0242	0.209	0.47	0.038
Viscosity, $\text{kg m}^{-1}\text{s}^{-1}$	0.001003	0.000017894	0.17978	/	/
Pure Solvent Melting Heat, $\text{J kg}^{-1}$	335000	/	/	/	/
Solidus Temperature, K	273.15	/	/	/	/
Liquidus Temperature, K	273.15	/	/	/	/

#### 4.4. Inlet boundary conditions

The velocity inlet boundary conditions are defined for propylene glycol domain on the inlet side of pipes. This boundary condition is specified with velocity magnitude and temperature (since this is energy calculation). The velocity magnitude was set to  $0.6 \text{ m s}^{-1}$ . The flow regime inside the pipes is laminar. Temperature on pipe's velocity inlets was set to 268.15 K.

The outlet boundary condition is set to pressure outlet with zero gauge pressure.

#### 4.5. Wall boundary conditions

Thermal boundary conditions are required for heat transfer calculations. Stationary no-slip wall boundaries were fixed on the outer side of the insulation where temperatures were set at 297 K.

### 5. Results and discussion

The results of the experiments and the CFD analysis are compared over period of 480 minutes for temperatures in six points obtained through six measurement channels in domains:

- AIR: *Channel 1*
- WATER: *Channel 2, Channel 4, Channel 5, Channel 6*
- INSULATION: *Channel 7*

A comparison of the experimentally and numerically obtained results of temperature in air domain are outlined in Figure 8.

The difference between these two is due to the insulation imperfections on the experimental assembly, air properties were modeled as a non-temperature dependent (i.e. constant density) resulting in the absence of the convective flow, therefore the temperature at the air-water interface was higher in the CFD analysis when compared to the experimentally obtained results. Temperatures measured inside the water domain are displayed in Figure 9.

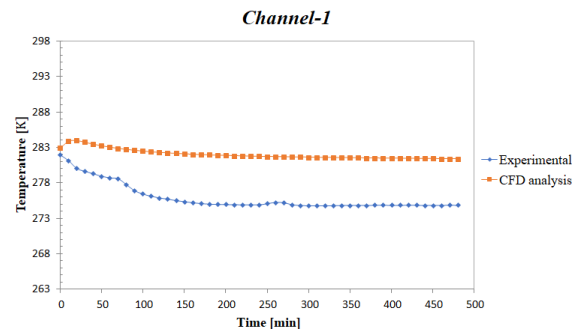


**Figure 8.** Comparison of the numerical and experimental results for the temperature in air domain

Even though all channels from Figure 9 are in the same domain they show large differences, especially for *Channel-5*.

As shown in Figure 9, the CFD analysis results more or less follow the trend set by experimental results in channels 2, 4 and 6 but still, there are differences in temperatures that can't be neglected. A reason for the discrepancy is the fact that realistic water properties were not taken into account (i.e. density and viscosity are not temperature dependent). This leads to slower heat transfer since there is no convective flow inside the water, that is, water doesn't mix. The results from channel-5 show a remarkable similarity between CFD and experimental results and the reason for this is the position of the point in the tank for which results on the *Channel-5* were recorded. This point is closer to the pipes (i.e. cooling source) so the lack of convective flow isn't that important, unlike points 2, 4 and 6 that are farther away from cooling source.

Temperature contours for all domains are shown in Figure 10 vs. flow time. Flow time marks the period of time from the beginning of simulation to the desired moment in time. In the Figure 10 it can be seen that, as a result of lower specific heat capacity, the air around the first level of pipes cools faster than the water around other two levels of pipes.

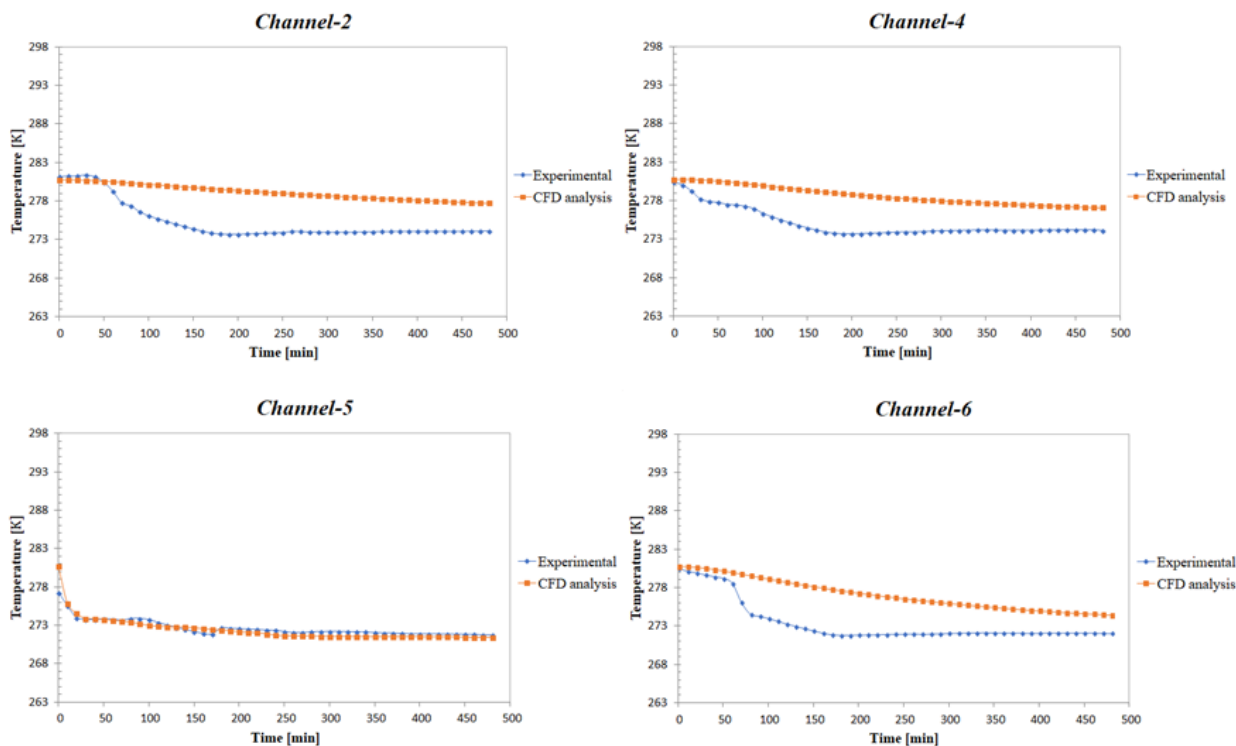


Figure 9. Comparison of the numerical and experimental results for the temperatures in water domain

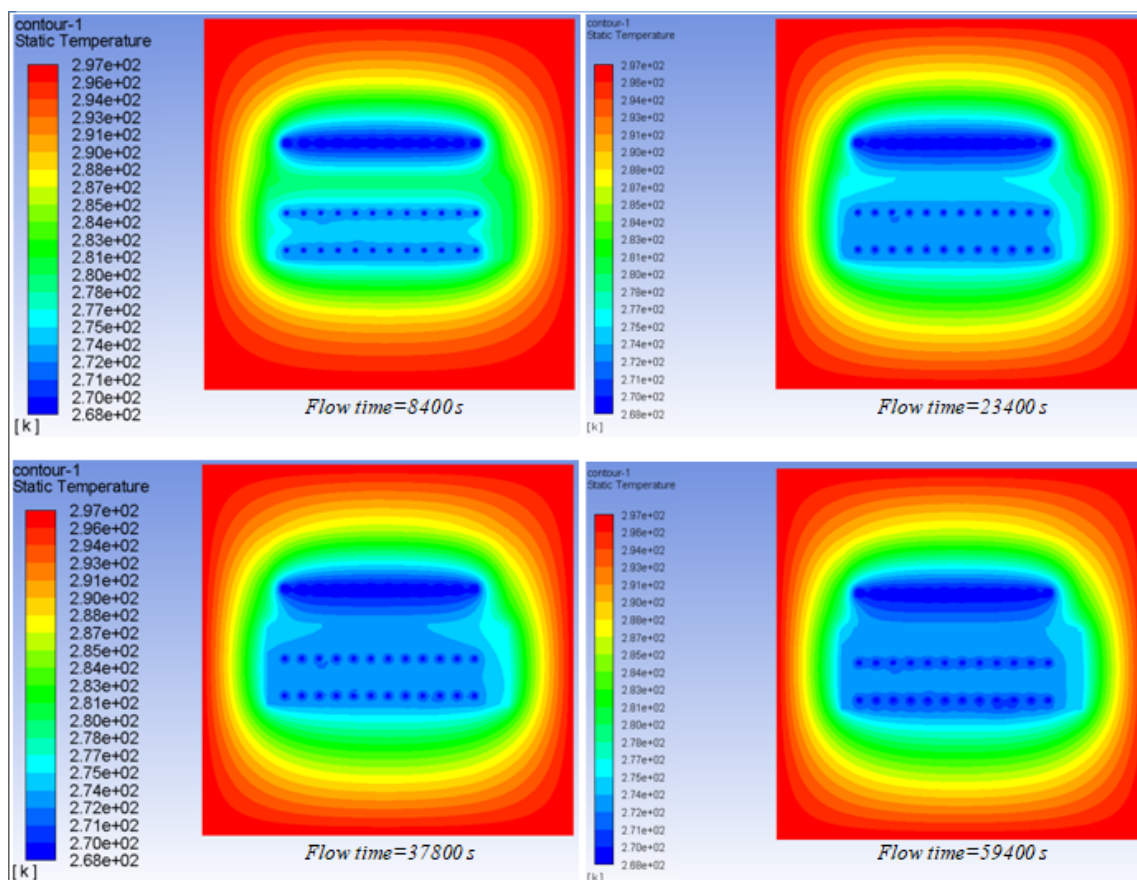
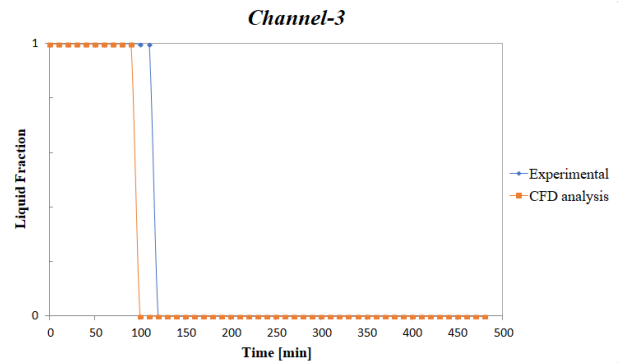


Figure 10. Results of the temperature distribution in all domains with different flow times of the simulation

Mastering the physics of ice formation in the CFD analysis is a complex process in which liquid fraction represents a monitoring tool. Furthermore, liquid fraction quantity is compared at one point in the water domain, Figure 11. The liquid fraction is a quantity computed at each iteration and it is based on an enthalpy balance. It is associated with each cell in the water domain to indicate the fraction of the cell volume that is in liquid form.

The mushy zone is a region in which the liquid fraction lies between 0 and 1. The mushy zone is modeled as a "pseudo" porous medium in which the porosity decreases from 1 to 0 as the material solidifies. When the material has fully solidified in a cell, the porosity becomes zero and hence the velocities also drop to zero [8]. Values of liquid fraction both for the CFD analysis and the experiment are 1 or 0. Reason for this is that during the experiment, there was no way to monitor liquid fraction values between 1 and 0, the cell in the domain is in either liquid or solid form.

*Channel-3* and *Channel-5* share the same location in water and that is the reason why CFD and experimental results in Figure 11 are in higher agreement.



**Figure 11.** Comparison of the numerical and experimental results for the liquid fraction on one location in the water

Figure 12 shows the history of ice formation along the ZX plane. Two red squares represent air domain (up) and liquid water domain (down). With time, the ice front emerges around pipes in water. It is fair to conclude that this process is slow especially if compared with the formation of ice in the experiment.

The experiment demonstrated that this process is much faster and the reason for this is the lack of convective flow in water, which slows down the cooling of the tank.

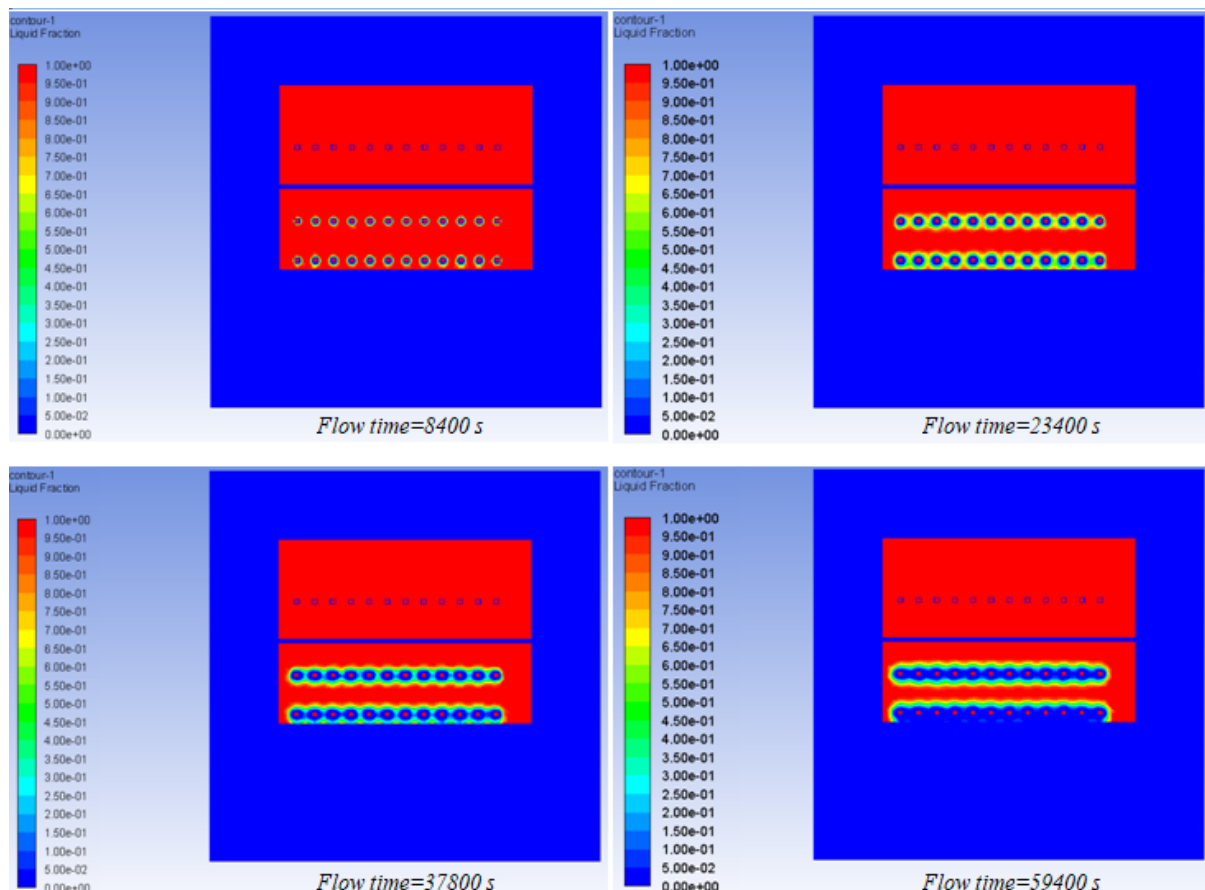


**Figure 12.** Results of the liquid fraction distribution in all domains with different flow times of the simulation

In case that considered simulation did have more realistic air and water/ice properties, the margin between the experiment and the CFD analysis would be much closer. The temperature in the insulation was also monitored and as it can be seen from Figure 13 the CFD analysis results follow the trend of the experimental results. The difference that exists is a result of the warmer water and air in the CFD simulation due to absence of the convective flow, as mentioned earlier in the text. It can be concluded that the insulation properties were quite similar in the simulation and the experiment.

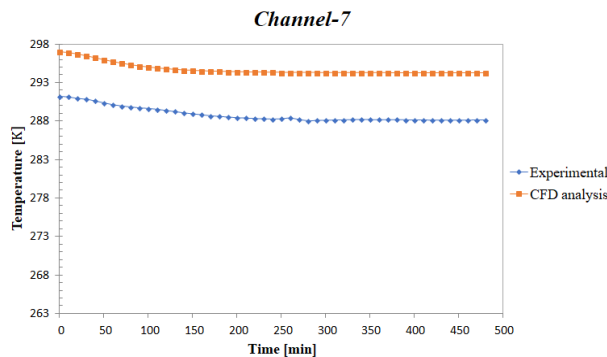


Figure 13. Comparison of the numerical and experimental results for the temperature in insulation domain

## 6. Simplified model with realistic water properties

ANSYS Fluent™ solidification/melting model is primarily predetermined for the calculation of liquid-solid in pure metals as well as in binary alloys. Since it can be used to solve fluid flow problems involving solidification/melting taking place at one particular temperature or over a range of temperatures, this model was used for developing a three-dimensional computational fluid dynamics model for transient heat transfer during the solidification/melting of water/ice and this proved to be unsatisfactorily precise. A possible reason for this might be found in the software limitations. According to ANSYS Fluent™ Manual, the following limitations apply to the solidification/melting model [9]:

1. The solidification/melting model can be used only with the pressure-based solver; it is not available with the density-based solvers.
2. The solidification/melting model cannot be used for compressible flows.
3. Of the general multiphase models (VOF, mixture, and Eulerian), only the VOF model can be used with the solidification/melting model.
4. With the exception of species diffusivities, you cannot specify separate material properties for the solid and liquid materials through the user interface. However, if needed, separate solid and liquid properties can be specified with user-defined functions using the DEFINE\_PROPERTY macro.

5. When using the solidification/melting model in conjunction with modeling species transport with reactions, there is no mechanism to restrict the reactions to only the liquid region; that is, the reactions are solved everywhere.

As it is stated in limitations, the solidification/melting model cannot be used for compressible flows. Compressible flow by definition has significant changes in fluid density. It is unclear what is a significant change for the solidification/melting model. For this reason, additional CFD analysis was performed with excluded solidification/melting model but with realistic water/ice properties (i.e. density and viscosity are temperature dependent) and the coolant temperature was set to 275.15 K.

The geometry of this CFD model is a simplified version of the previously used geometry. Now, there are two pipes with the coolant inside and water (transparent in Figure 15) surrounding them while insulation (yellow in Figure 15) is located beneath the water domain. The symmetry boundary conditions were used on the sides of water and insulation domains, vertically on the coolant flow. The materials used were the same as in the previous analysis.

The water-air heat exchange is modeled using convection boundary conditions where the free stream temperature of the air domain is set to 287.36 K and the heat transfer coefficient is set to  $0.6 \text{ W m}^{-2}\text{K}^{-1}$ .

This kind of analysis asks for exceptional mesh and in this case, average orthogonal quality is 0.99609, what is considered to be very high since maximum mesh quality is 1, Figure 14.

The following polynomial expression describes temperature dependent water density in this CFD analysis:

$$\rho(T) = 0.0000394315T^3 - 0.0401238282T^2 + 13.1522969633T - 402.6381590471 \quad (9)$$

Absolute (dynamic) viscosity of water is described by this expression:

$$\mu(T) = -0.0000000092T^3 + 0.0000086359T^2 - 0.0027131695T + 0.2862620884 \quad (10)$$

In the Figure 15 can be seen that density maximum is at the bottom of the water domain, while at the same location (Figure 16) is the lowest temperature (ca.  $4.5^\circ\text{C}$ ) of this domain. This means that water anomaly was detected.

Figure 17 and Figure 18 show that realistic water properties generate different velocities throughout the water, which leads to increased heat transfer. As a result, water mixes and the convective flow emerges, resulting in more uniform temperature distribution throughout the tank when compared to the previously conducted study with solidification/melting model activated.

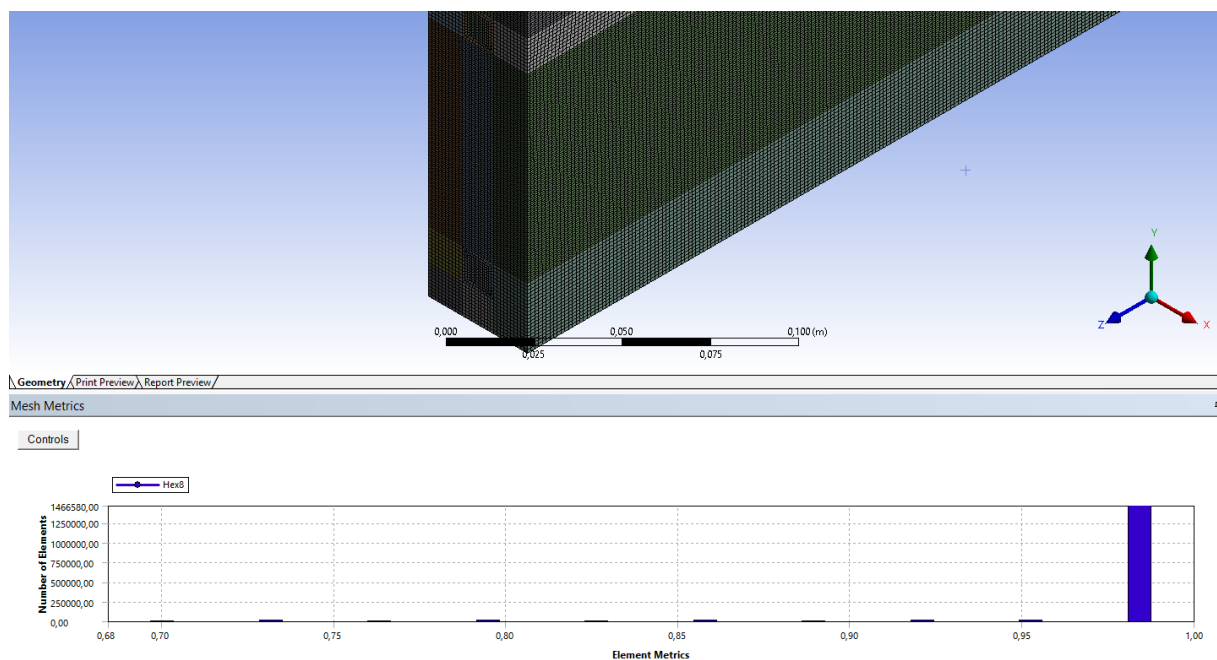


Figure 14. Mesh metrics and mesh

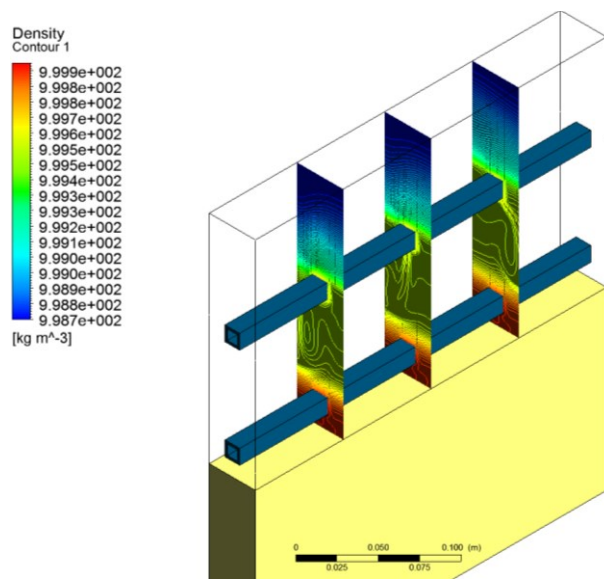


Figure 15. Water density contours

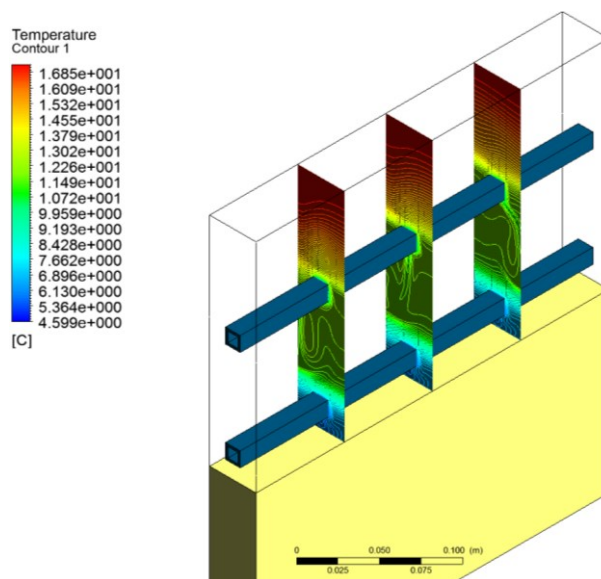


Figure 16. Water temperature contours



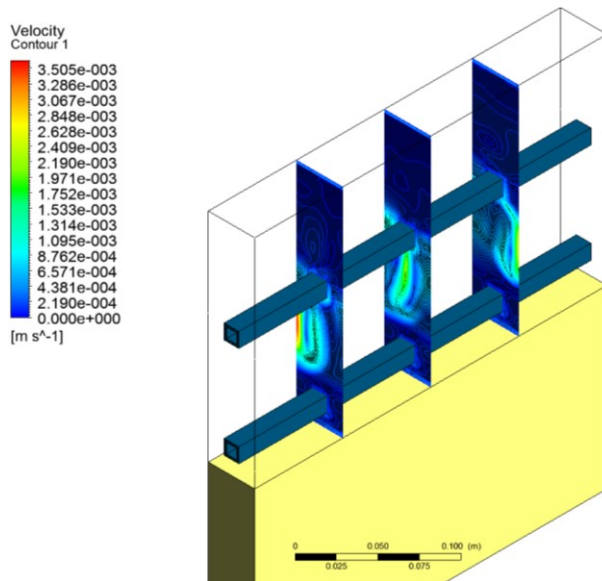


Figure 17. Water velocity contours

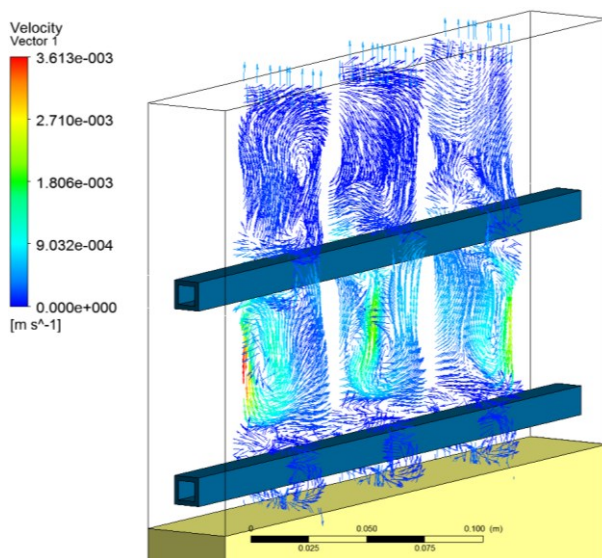


Figure 18. Vectors of velocity in water

## 7. Conclusions

Conducted experimental and numerical study showed that concept of the floating platform with a structure based on the ice has a promising future. In order to commercialize this concept, plenty of work has yet to be done since CFD's solidification/melting model proved to be of unsatisfactory precision due to the software limitations. However, this might be resolved if solidification/melting model will be adapted in a way that the compressible flows with significant density changes can be used, or by developing modifications of the current model via user-defined-functions. In the geometrically simplified CFD model, presented in the second part of this paper it can be seen that the convective currents have high impact on the overall temperature

distributions inside the tank and they cannot be neglected in the future studies.

## REFERENCES

- [1] Klarin B. *Energy Islands – Hybrid Off-shore Plant*, FESB, Split
- [2] Bolonkin A. (2018). *Floating Cities, Islands and States* Article Floating City
- [3] Arıcı M, Tütüncü E., Kan M, Karabay H, *Melting of nanoparticle-enhanced paraffin wax in a rectangular enclosure with partially active walls*, Kocaeli University, Department of Mechanical Engineering, Umuttepe Campus, 41380 Kocaeli, Turkey
- [4] Khodadadi J.M., Hosseini-zadeh S.F., (2007) *Nanoparticle-enhanced phase change materials (NEPCM) with great potential for improved thermal energy storage*, Int. Commun. Heat Mass Transfer 34 534–543.
- [5] Wu S., Zhu D., Li X., Li H., Lei J., (2009) *Thermal energy storage behavior of  $Al_2O_3$ - $H_2O$  nanofluids*, Thermochim. Acta 483 73–77.
- [6] Youssef W., Ge Y.T., Tassou S.A., *CFD modelling development and experimental validation of a phase change material (PCM) heat exchanger with spiral-wired tubes*, RCUK National Centre for Sustainable Energy Use in Food Chains (CSEF), Institute of Energy Future, Brunel University London, Uxbridge, Middlesex UB8 3PH, UK
- [7] *Engineering and Operating Guide for DOWFROST and DOWFROST HD Inhibited Propylene Glycol-based Heat Transfer Fluids*, [http://msdssearch.dow.com/PublishedLiteratureDOWCOM/dh\\_010e/0901b8038010e417.pdf?filepath=heattrans/pdfs/noreg/180-01286.pdf&fromPage=GetDoc](http://msdssearch.dow.com/PublishedLiteratureDOWCOM/dh_010e/0901b8038010e417.pdf?filepath=heattrans/pdfs/noreg/180-01286.pdf&fromPage=GetDoc), online source, access date 05.05.2018.
- [8] ANSYS, Inc., *ANSYS Fluent 17.2 Manual*, [https://www.sharcnet.ca/Software/Ansys/17.2/en-us/help/flu\\_th/flu\\_th\\_sec\\_melt\\_theory.html](https://www.sharcnet.ca/Software/Ansys/17.2/en-us/help/flu_th/flu_th_sec_melt_theory.html), online source, access date 07.04.2018.
- [9] ANSYS, Inc., *ANSYS Fluent 17.2 Manual*, [https://www.sharcnet.ca/Software/Ansys/16.2.3/en-us/help/flu\\_th/flu\\_th\\_sec\\_melt\\_limits.html](https://www.sharcnet.ca/Software/Ansys/16.2.3/en-us/help/flu_th/flu_th_sec_melt_limits.html), online source, access date 10.04.2018.



# Prednosti međuosovine izrađene od kompozitnog materijala u odnosu na čelične

Mate Jurjević<sup>(1)</sup>, Žarko Koboević<sup>(1)</sup>,  
Nikša Koboević<sup>(1)</sup> and Nino Storelli<sup>(2)</sup>

1) University of Dubrovnik, Maritime  
Department, Sveučilište u Dubrovniku,  
Pomorski odjel, Čira Carića 4, 20000  
Dubrovnik, Hrvatska

2) Explore Dubrovnik, Koločepska 8, 20000  
Dubrovnik, Hrvatska

mjurjevic@unidu.hr  
zarko.koboevic@unidu.hr  
niksa@unidu.hr  
nininoni098@gmail.com

## Keywords

composite materials,  
infusion method,  
torque curve momentum

## Ključne riječi

kompozitni materijali,  
metoda infuzije,  
moment uvijanja materijala

## Advantages of the intermediate shaft made of composite material compared to steel

Professional paper

**Abstract:** The paper describes the advantages of using composite materials for making components of the propulsion system in relation to other materials. The technology of composite component making is described by applying a vacuum infusion method. This process provides the most advanced components made of composite materials and thus ensures that the finished product does not contain small air bubbles that are trapped in the binder material between the reinforcement. Also, regression analysis of the oscillation moments of steel and composite intermediate shaft is shown in relation to the angular acceleration. The intermediate shaft made of composite materials has better characteristics than the steel intermediate shaft.

Stručni rad

**Sažetak:** U radu je opisana prednost primjene kompozitnih materijala za izradu komponenti porivnog sustava u odnosu na druge materijale. Opisana je tehnologija izrade komponenti od kompozita primjenom metode vakuumske infuzije. Tim se postupkom dobivaju najsavršenije komponente izrađene od kompozitnih materijala, te se tako osigurava da u gotovom proizvodu ne bude sitnih mjehurića zraka koji su zarobljeni u vezivnom materijalu između ojačanja. Također su prikazane regresijske analize momenata uvijanja čelične i kompozitne međuosovine u odnosu na kutno ubrzanje. Međuosovina izrađena od kompozitnog materijala ima bolje karakteristike od međuosovine izrađene od čelika.

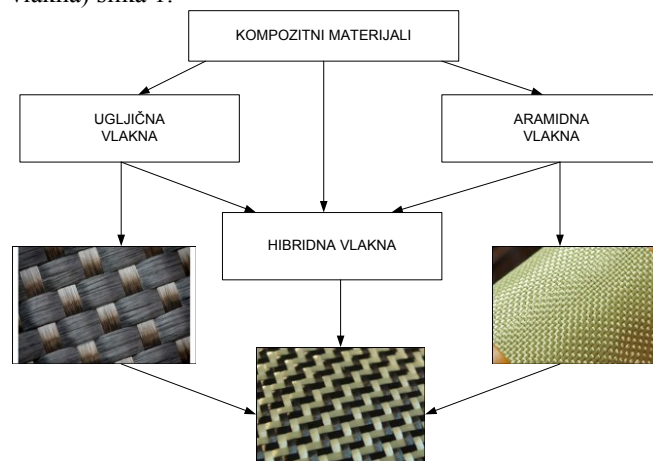
## 1. Uvod

Kompozitni materijal je sastavljen od nekoliko komponenti. Svojstva kakva ima kompozitni materijal ne posjeduje niti jedna komponenta sama za sebe. S njim se postiže: povećanje krutosti, čvrstoće i dimenzijske stabilnosti, povećanje udarne žilavosti, povećanje toplinske postojanosti, smanjenje apsorpcije vode, smanjenje toplinske ekspanzije, poboljšanje otpornosti na trošenje, veću korozijsku postojanost, smanjenje mase, poboljšanu konstrukcijsku fleksibilnost. Kompoziti se stvaraju u cilju poboljšanja kombinacija mehaničkih karakteristika kao što su krutost i žilavost, te čvrstoće u uvjetima djelovanja okoline odnosno pri povišenim temperaturama [1][2]. Da bi se dobio optimalan omjer matrice i ojačanja koristi se tehnika vakuumske infuzije. U radu je napravljena analiza momenta uvijanja u odnosu na kutno ubrzanje za međuosovinu od kompozita i čelika.

## 2. Kompozitni materijali za izradu komponenti brodskih sustava

Ugradnjom komponenti na porivnom sustavu od kompozitnih materijala, visokokvalitetne legure čelika, pa čak i keramički dijelovi dovode do poboljšanja

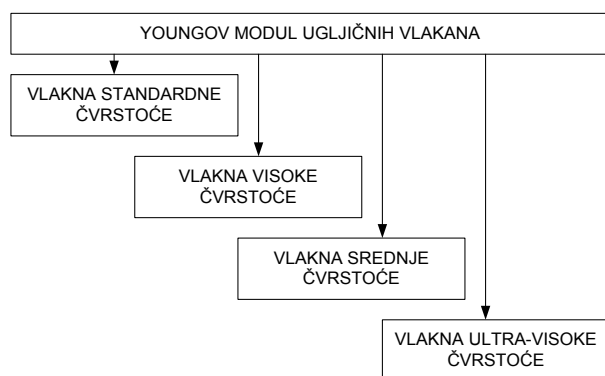
kvalitete sustava, pa tako i brodskih sustava. Ono što bi poboljšalo učinkovitost i konkurentnost uređaja su komponente brodskih sustava izrađene od kompozitnih materijala i njihovih međusobnih kombinacija (hibridna vlakna) slika 1.



Slika 1. Kompozitni materijali koji se koriste u brodogradnji [1][3][4][5][6]

Figure 1. Composite materials used in shipbuilding [1][3][4][5][6]

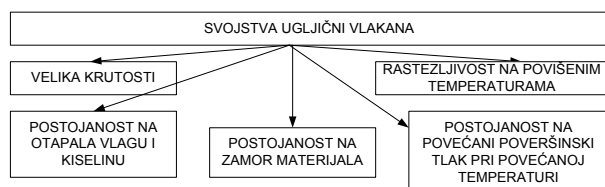
Najčešće se koriste ugljična vlakna, a postupkom grafitizacije dobivaju se najčešće od poliakrilonitrila (PAN) koji daje najbolja svojstva vlaknima [3][4]. Proizvode se još od katrana i celuloze, a podešavanjem parametara tijekom procesa grafitizacije dobivaju se vlakna visoke rastezne čvrstoće ili vlakna visokog modula rastezljivosti. Kada se oblikuje tretira se nanošenjem apreture kako bi se poboljšalo prijanjanje uz matricu. Promjer vlakana je 4  $\mu\text{m}$  do 10  $\mu\text{m}$ . Na osnovu vrijednosti modula vlakana (Youngov modul) slika 2 dijele se na vlakna standardne, srednje, visoke i ultra visoke čvrstoće.



**Slika 2.** Podjela ugljikovih vlakana na osnovu vrijednosti modula vlakana (Youngov modul)[1][3][4]

**Figure 2.** Distribution of carbon fibres based on fibre modulus values (Youngov module) [1] [3] [4]

Kompozitna struktura napravljena od ugljičnih vlakana i epoksidne smole koristi se u svim područjima tehnike i proizvodnje, a u zadnje vrijeme ima sve veću primjenu u brodogradnji i industriji vezanoj za nju.



**Slika 3.** Svojstva ugljičnih vlakna.

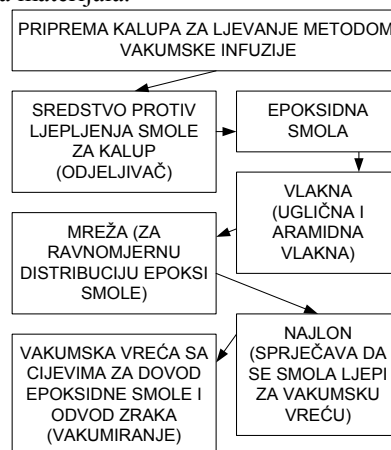
**Figure 3.** Properties of carbon fibre

Aramidna vlakna najčešće se koriste u kombinaciji s epoksidnim i poliesterskim smolama. Ta vlakna su umjetni organski polimeri (aromatski poliamid), proizvedeni predenjem kontinuiranog vlakna iz kapljevite smjese. Karakterizira ih visoka rastezna čvrstoća i niska gustoća, tako da imaju jako dobar omjer čvrstoće i mase što im daje prednost nad metalom. Najčešća aramidna vlakna su „Kevlar“. Na temperaturi od -200°C do +200°C zadržavaju dobra mehanička svojstva. Najviše ih oštećuje jaka kiselina, za razliku od otapala i drugih kemikalija gdje su postojana. Aramidna vlakna imaju dobru udarnu žilavost i različitim mješavinama nadomještaju čelik i aluminij. Koriste se

tamo gdje se traži izuzetna toplinska i mehanička svojstva. Hibridna vlakna su sastavljena od dvaju ili više vrsti vlakana. Spajanjem vlakana postižu se optimalna svojstva. Hibridizacija se izvodi najčešće izravno pri proizvodnji kompozitnog proizvoda. Najčešće se u brodogradnji i zrakoplovstvu primjenjuju hibridna vlakna. Upotrebom hibrida proizvodu se poboljšava udarna žilavost, sprječava galvanska korozija [1][2][3][4]. Na takav način mogu se postići neuobičajene kombinacije svojstava, kao što su krutost, čvrstoća, tvrdoća, težina, ponašanje pri visokim temperaturama, kemijska postojanost (antikoroziivnost), ili vodljivost (električna i toplinska) [1][2][3][4].

### 3. Izrada komponenti od kompozitnog materijala primjenom metode vakuumske infuzije

Za izradu komponenti porivnog sustava po karakteristikama najbolje bi odgovarala ugljična vlakna ili kombinacija ugljičnih vlakna i aramidnih vlakana. Za ovakovu kombinaciju ugljičnih i aramidnih vlakana najbolje odgovara kao vezivo epoksidna smola. Sam proces izrade komponente trebao bi se izraditi metodom vakuumske infuzije. Jedino tom metodom dobije se optimalan omjer matrice i ojačanja, a višak smole se odstranjuje tako da komponenta postaje lakša. Prije korištenja metode vakuumske infuzije potrebno je napraviti kalup koji podržava tu metodu. Postupak nanošenja materijala zahtijeva niz radnji koje se ne mogu preskakati jer u suprotnom dolazi do greške u postupku nanošenja materijala.



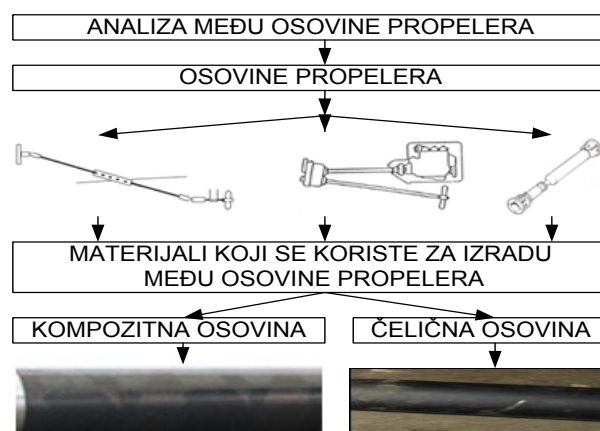
**Slika 4.** Izrada komponente metodom vakuumske infuzije[1][8]

**Figure 4.** Component preparation by vacuum infusion method [1] [8]

Slijed pripreme za metodu nanošenja materijala na kalup vakuuskom infuzijskom je prikazan na slici 4. Kalupe prije nanošenja materijala za izradu komponenti treba premazati sredstvom koje će spriječiti da se epoksidna smola zalijepi za kalup. To sredstvo nazivamo odijeljivač („Poly Vinyl Alcohol”) i sa njim se nekoliko puta namaže kalup. Nakon što se nanese odijeljivač potrebno je nanijeti „gel coat“ s kompresorom i posebno dizajniranim zračnim kistom na bazi epoksidne smole. Kada se „gel coat“ osuši stavljaju se vlakna od materijala koji smo odabrali npr. ugljična ili aramidna vlakna. Stavlja se nekoliko slojeva ovisno o debljini koju želimo postići. Na vlakna se stavlja posebna mreža koja pomaže ravnomjernoj distribuciji epoksidne smole, a na nju se stavlja najlon tzv. „peel ply“. Peel ply je zapravo poseban najlon koji sprječava da se epoksidna smola lijepi na vakuusku vreću kojom se cijeli kalup pokriva. Nakon prekrivanja kalupa vakuuskom vrećom krajevi se pažljivo lijepe posebnom ljepljivom trakom. Ta traka se lijepi tako da sve bude savršeno nepropusno. Na jednu stranu vakuumske vreće se probije mala rupica u koju se uvuče cijev kojom će se smola dovesti unutar kalupa. Isto se napravi na suprotnoj strani vakuumske vreće samo cijev koja se koristi za odvodnju viška smole. Također tom istom cijevi se vakuumira cijeli kalup. Obje cijevi se posebnom trakom lijepe za vakuusku vreću i osiguravaju nepropusnost zraka unutar vakuumiranog dijela. Sam proces vakuumske infuzije počinje kada se uključi vakuumska pumpa kojom se izvuče sav zrak koji se nalazi između kalupa i vakuumske vreće. Nakon toga se cijev koja je uvedena kroz tu vreću u kalup uroni u posudu u koju je prethodno zamiješana epoksidna smola. Epoksidna smola tom cijevi putuje unutar kalupa. Pošto je cijeli kalup pod vakuumom epoksidna smola se ravnomjerno raspoređuje cijelom njegovom površinom i prodire u ojačanje koje smo stavili, te ga potpuno natopi. Zbog toga što je sve pod vakuumom smola će prodrijeti u svaki dio ojačanja i pritom istisnuti sve mjehuriće zraka. Ti mjehurići zraka bi mogli stvarati probleme, jer bi komponenta imala slabe točke zbog nesavršenosti u procesu proizvodnje. Kada je vidljivo da je sve natopljeno smolom, cijev gdje ulazi smola se izvuče posebnom stezaljkom. Kroz tu izvučenu cijev zrak ne ulazi unutar kalupa. Vakuumska pumpa i dalje pravi vakuum unutar kalupa, te se kroz cijev koja ide na vakuusku pumpu izvuče sav višak smole. Kalup se ostavlja pod vakuumom 24 sata da se sve dobro stvrdne i tada se može "oguliti" s njega vakuumska vreća i komponenta se može odvojiti od kalupa[1][8]. Na ovaj način dobiva se komponenta, koja je ako se izradi od ugljičnih vlakana, nekoliko puta čvršća od komponente izrađene od metala, a višestruko je lakša.

#### 4. Analiza momenata uvijanja u odnosu na kutno ubrzanje čelične i kompozitne međuosovine

Kompozitni materijali su idealni za izradu međuosovina jer su osovine izrađene od visokokvalitetnih ugljičnih vlakana nekoliko puta otpornije na uvijanje nego osovine izrađene od čelika. Kao primjer imamo dvije propellerske međuosovine potpuno istih dimenzija, jedna napravljena od ugljičnih vlakana, a druga standardna čelična slika 5.



Slika 5. Prikaz međuosovine istih dimenzija od kompozita i čelika.

Figure 5. Display of composite and steel intermediate shafts of the same dimensions.

Osovinu napravljenu od kompozitnog materijala je nekoliko puta laganija od standardne čelične osovine. Osovine na kojima se provodio test su sljedećih dimenzija i prikazane su u tablici 1.

Tablica 1. Dimenzije analiziranih međuosovina [1]

Table 1. Dimensions of analyzed intermediate shafts [1]

ČELIČNA MEĐUOSOVINA	
MASA	6,8 kg
DUŽINA	1100 mm
PROMJER	100 mm
DEBLJINA STJENKI	2,1mm
MEĐUOSOVINA OD KOMPOZITA	
MASA	2,9kg
DUŽINA	1100 mm
PROMJER	100 mm
DEBLJINA STJENKI	2,79mm

Testom uvijanja dobivene su sljedeće vrijednosti prikazane u tablici 2. Iz tablice je vidljivo da je čelična



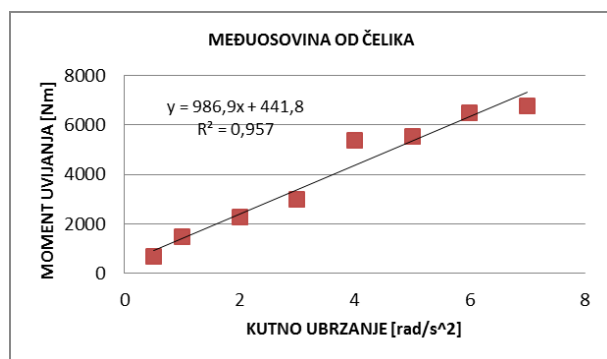
međuosovina puknula pri kutnom ubrzanju od  $7 \text{ rad/s}^2$  i momentu uvijanja od 6766,44 Nm, a međuosovina od kompozitnog materijala pri kutnom ubrzanju  $14 \text{ rad/s}^2$  i momentu uvijanja 6793,56 Nm.

**Tablica 2.** Mjerne vrijednosti uvijanja međuosovine od kompozita i čelika

**Table 2.** Measured values of tensile strength of composite and steel intermediate shaft

Kutno ubrzanje (rad/s <sup>2</sup> )	4.1.1.1. Moment uvijanja (Nm)	
	Čelična	Kompozitna
0,5	691,56	474,6
1	1491,6	678
2	2291,64	1030,56
3	2983,2	1491,6
4	5396,88	1993,32
5	5559,6	2454,36
6	6481,68	2996,76
7	6766,44	3593,4
		4054,44
9		4678,2
10		5356,2
11		5627,4
12		6224,04
13		6644,4
14		6793,56

Korištenjem podataka iz tablice 2 regresijskom analizom definirana je ovisnost između momenta uvijanja [Nm] i kutnog ubrzanja  $\text{rad/s}^2$  međuosovine od kompozitnog materijala i čelika.

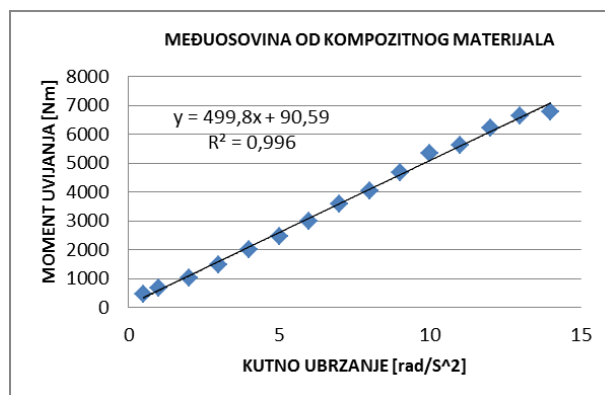


**Slika 6.** Regresijska analiza momenta uvijanja i kutnog ubrzanja međuosovine od čelika

**Figure 6.** Regression analysis of bending torque and angle acceleration of steel intermediate shaft

Iz slike 6. je vidljivo da linearna krivulja najbolje odgovara dobivenim podacima. Krivulja je opisana sa jednažbom  $Y = 986,9x + 441,89$ , koeficijentom determinacije  $R^2 = 0,957$  i koeficijentom korelacije

$r = \sqrt{R^2} = 0,978$  koeficijent  $r$  nam pokazuje da je ovo jaka korelacijska veza.



**Slika 7.** Regresijska analiza momenta uvijanja i kutnog ubrzanja međuosovine od kompozitnog materijala

**Figure 7.** Regression analysis of torsion torque and angle acceleration of composite intermediate shaft

Iz slike 7. je vidljivo da linearna krivulja najbolje odgovara dobivenim podacima. Krivulja je opisana sa jednažbom  $Y = 499,8x + 90,59$ , koeficijentom determinacije  $R^2 = 0,996$  i koeficijentom korelacije  $r = \sqrt{R^2} = 0,998$  koeficijent  $r$  nam pokazuje da je ovo jaka korelacijska veza.

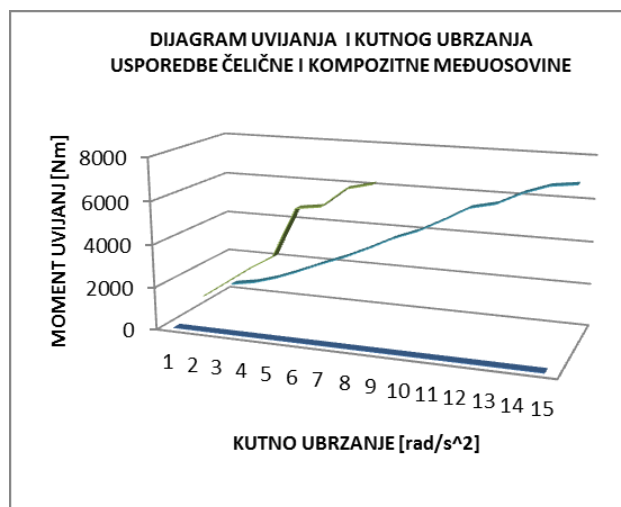
**Tablica 3.** Jednažbe regresije, koeficijenti determinacije  $R^2$  i koeficijenti regresije  $R$  za sva analizirana kutna ubrzanja za međuosovinu od čelika i kompozita.

**Table 3.** Regression equations, coefficients of the determination  $R^2$  and regression coefficients  $R$  for all analysed acceleration angles of the steel and the composite intermediate shafts.

$Y = f(x)$	JEDNAŽBA REGRESIJE	$R^2$	$R$
$Y = f(x)$	$Y = 986,9x + 441,89$	0,957	0,978
$Y = f(x)$	$Y = 499,8x + 90,59$	0,996	0,998

Iz rezultata regresije za moment uvijanja i kutno ubrzanje međuosovinu koristeći podatke sa slike 6 i 7 prikazane u tablici 3, gdje vidimo da dobivene podatke najbolje aproksimira linearna krivulja.

Iz dobivenih rezultata ispitivanja vidljivo je da osovinu napravljenu od kompozita može izdržati dvostruko veće kutno ubrzanje. Veće kutno ubrzanje postignuto je zbog toga što je osovinu od kompozita znatno laganija od čelične osovine i ima manju inerciju od čelične osovine



**Slika 8.** Usporedba momenta uvijanja čelične i kompozitne međuosovine u odnosu na kutno ubrzanje

**Figure 8.** Comparison of the torsional moment of the steel and composite intermediate shaft in relation to angular acceleration

## 5. Zaključak

Iz ovog rada i analize je vidljivo da osovina izrađena od ugljičnih vlakana ima veliku prednost pred standardnom

čeličnom osovinom. Nakon dobivenih rezultata dolazimo do zaključka da bi se ugradnjom dijelova od kompozita postigla veća pouzdanost sustava, i kompletan sustav bi mogao podnijeti veća opterećenja. Većom primjenom visoko kvalitetnih kompozitnih materijala otvara se mogućnost sve češće primjene u brodogradnji, koje zbog svojih karakteristika istiskuju druge materijale koji su se dosad stalno koristili i bili nezamjenjivi.

## LITERATURA

- [1] N. Storelli, (2015). *Analiza i čimbenici koji utječu na rad Voith-Schneider propelera*, „Diplomski rad“, Sveučilište u Dubrovniku, Dubrovnik
- [2] Mr. sc. Stjepan Golubić, (2018). *Tehnički materijali*, Visoka tehnička škola u Bjelovaru, Bjelovar
- [3] <https://chargedevs.com/newswire/swedish-researchers-carbon-fiber-can-serve-as-both-body-panel-and-battery/>
- [4] <http://www.centralcarbonfiber.com/>
- [5] [www.kompozit-kemija.hr](http://www.kompozit-kemija.hr)
- [6] W. Kunej, (2006). *Poliesterski kompoziti*, 2. Prošireno izdanje, Zagreb
- [7] <http://www.solarcomposites.com/composites/compositehybrid.html>
- [8] <http://www.tropicalboating.com/2012/04/creating-the-extremely-light-boat>



# Processing and properties of in-situ TiAl-based matrix composite reinforced with carbide phase particles

**Kateryna KAMYSHNYKOVA<sup>1,2)</sup> and Juraj LAPIN<sup>1)</sup>**

1) Institute of Materials and Machine Mechanics, Slovak Academy of Sciences, Dúbravská cesta 9, 845 13 Bratislava, **Slovak Republic**

2) Faculty of Materials Science and Technology Slovak University of technology in Bratislava, Paulinska 16, 917 24 Trnava, **Slovak Republic**

kateryna.kamysnykova@savba.sk

## Keywords

*Titanium aluminides; TiAl; Composites; Casting; Microstructure; Mechanical properties*

## Original scientific work

**Abstract:** The induction melting in graphite crucibles and centrifugal casting into graphite moulds of Ti-46.4Al-5.1Nb-1C-0.2B (at.%) alloy was carried out to prepare in-situ TiAl-based matrix composite reinforced with carbide particles. Hot isostatic pressing (HIP) was applied to remove porosity present in the centrifugally cast (CC) samples. Non-destructive 3D X-ray Computed Tomography (CT) was used to evaluate size and distribution of casting defects and porosity in the as-cast and HIP-ed samples. The microstructure analysis was performed by light microscopy (LM), scanning electron microscopy in backscattered mode (BSEM), energy dispersive spectroscopy (EDS) and X-ray diffraction analysis. The microstructure of the as-cast in-situ composite is equiaxed and consists of lamellar  $\alpha_2(\text{Ti}_3\text{Al}) + \gamma(\text{TiAl})$  matrix reinforced with homogeneously distributed plate-like  $\text{Ti}_2\text{AlC}$  particles. The applied HIP leads to a chemical homogenisation of the as-cast samples connected with a grain coarsening. Vickers hardness of the as-cast samples is higher than that of the samples after the HIP, what can be attributed to a smaller grain size of the centrifugally cast samples. High-temperature creep behaviour of the in-situ composite is also evaluated and discussed.

## 1. Introduction

Titanium aluminides with lamellar  $\alpha_2(\text{Ti}_3\text{Al}) + \gamma(\text{TiAl})$  microstructure have gained large interests as light high-temperatures materials for the aerospace and automotive industries due to their low density, high specific strength and corrosion resistance [1,2]. These alloys allow reducing weight of aircraft engines and improve dynamic characteristics of turbochargers of combustion engines [2]. However, their inherent poor ductility at room temperature and insufficient strength at high temperatures (above 800 °C) limit their practical industrial applications. Intermetallic matrix composites may improve the deficiency of these alloys at high temperatures because of good combination of the properties of intermetallic matrix and reinforcement. Strengthening of TiAl matrix can be achieved by various reinforcements such as  $\text{Al}_2\text{O}_3$ ,  $\text{Y}_2\text{O}_3$ ,  $\text{TiB}_2$ ,  $\text{Ti}_5\text{Si}_3$ . Among various ceramic reinforcements, ternary phases such as  $\text{Ti}_2\text{AlC}$  show a significant role in toughening and reinforcing of TiAl-based matrix composites [3,4]. The  $\text{Ti}_2\text{AlC}$  phase (H-phase) belongs to the group of so-called MAX phases, which can be characterised by exciting combination of both ceramic and metallic properties such as high thermal shock resistance, good machinability, high thermal and electrical conductivities, high melting temperature, high elastic stiffness, and high oxidation and corrosion resistance. [5,6].

In general, several methods have been reported for the processing of in-situ TiAl-based matrix composites reinforced by  $\text{Ti}_2\text{AlC}$  particles. The studied processing techniques include powder metallurgy, mechanical

alloying, reactive hot pressing, spark plasma sintering, vacuum arc remelting and combustion synthesis [6-8]. Among various processing techniques applied for in-situ TiAl-based matrix composites, induction melting combined with precise casting represents widely applied technology allowing processing near net shape industrial components which might facilitate potential applications of these new materials. Moreover, centrifugal precise casting leads to a better surface quality, no misruns in thin sections and less cracks compared to those of gravity cast components [2,9,10].

The aim of this article is to study processing and properties of in-situ  $\alpha_2 + \gamma$  matrix composite reinforced with carbide particles. The in-situ composite is prepared by induction melting of Ti-46.4Al-5.1Nb-1C-0.2B (at.%) alloy followed by solidification in graphite crucibles or centrifugal casting into graphite mould. In this in-situ composite, niobium improves oxidation resistance and strength properties of the matrix at both room and high temperatures [11]. Boron refines grain microstructure and carbon improves creep resistance through the formation of reinforcing primary and secondary carbide particles [12-15].

## 2. Experimental procedure

Samples with a chemical composition Ti-46.4Al-5.1Nb-1C-0.2B (at.%) were machined to cylindrical pieces with a diameter of 38 mm and length of 26 mm and placed into graphite crucibles with a diameter of 49 mm (outside diameter) and length of 75 mm. Each graphite crucible

**Symbols**

$\alpha_2$	- Ti <sub>3</sub> Al intermetallic phase	$P$	- Porosity
$\gamma$	- TiAl intermetallic phase	$SEM$	- Scanning electron microscopy
$\alpha$ or $\beta$	- Ti-based solid solution with hexagonal or cubic crystal structure, respectively	$BSEM$	- Scanning electron microscopy in backscattered mode
$CT$	- Computed Tomography	$XRD$	- X-ray diffraction
$HIP$	- Hot isostatic pressing	$LM$	- Light microscopy
$CC$	- Centrifugally cast sample	$EDS$	- Energy-dispersive spectroscopy
$AS$	- As-solidified sample		

was put into a protective alumina crucible equipped with a pouring cup which was connected to a cylindrical graphite mould. The sample was melted in an induction furnace under protective argon atmosphere and held at a temperature of 1680 °C for 60 s. The melt was either solidified in the melting graphite crucible by switching off the induction power [16] or centrifugally cast into the graphite mould at a rotation speed of 250 rpm in the apparatus shown in Fig. 1 [17]. The as-solidified samples with a diameter of 45 mm and length of about 30 mm were removed from the graphite crucibles and cut longitudinally using wire spark machining. The centrifugally cast (CC) conical samples with a minimum diameter of 11 mm, maximum diameter of 14 mm and length of 150 mm were subjected to a non-destructive inspection. The non-destructive testing was carried by 3D X-ray computed tomography (CT).

Hot isostatic pressing (HIP) was applied to remove casting porosity of the CC samples. The samples were put into alumina crucible, heated to a temperature of 1360 °C and held at this temperature under a pressure of 200 MPa for 4 h in argon. The cooling of the HIP-ed samples to room temperature was carried out in the HIP apparatus at an average rate of 8 °C/min.

Instrumented hardness measurements were performed by universal hardness testing machine. Martens hardness test was carried at an applied load of 50 N, holding time at the point of load application of 2 s and speed of load application was of 15 N/s on the samples after centrifugal casting, HIP and heat treatments.

Metallographic preparation of the samples consisted of standard grinding using abrasive papers, polishing on diamond pastes with various grain size up to 1 µm and etching in a solution of 100 ml H<sub>2</sub>O, 6 ml HNO<sub>3</sub> and 3 ml HF. Microstructure evaluation was performed by light microscopy (LM) and scanning electron microscopy in backscattered mode (BSEM). Chemical composition of the samples was analysed by energy dispersive spectroscopy (EDS). X-ray diffraction (XRD) analysis was performed by a diffractometer equipped with X-ray tube with rotating Cu anode operating at 12 kW. Average content of carbon in the in-situ composite was measured by LECO CS844 elemental analyser. Grain and carbide particle size were measured by computerised image

analysis using digitalised micrographs and measured data were treated statistically.



**Figure 1.** Titancast 700 apparatus for induction melting and centrifugal casting.

### 3. Results and discussion

#### 3.1. Induction melting and solidification in crucibles

Fig. 2 shows the macrostructure of the as-solidified (AS) in-situ composite. The macrostructure consists of coarse equiaxed and fine equiaxed grains formed at the top and in the rest of the sample, respectively. The surface layer of the sample in contact with the graphite crucible contains fine equiaxed grains. Fig. 3 shows microstructure of the as-solidified sample. The equiaxed grains with fully lamellar microstructure contain long plate-like particles distributed preferentially along the lamellar grain boundaries. Table 1 summarises the results of statistical analysis of the measured grain size and length of the Ti<sub>2</sub>AlC particles of the as-solidified sample. Fig. 4 shows the typical XRD pattern of the AS in-situ composite indicating the presence of four phases:  $\gamma$ (TiAl),  $\alpha_2$ (Ti<sub>3</sub>Al), Ti<sub>2</sub>AlC and TiB. Based on the chemical composition of the in-situ composite and the coexisting regions measured by EDS and XRD analysis, four different phases can be identified: lamellar  $\alpha_2 + \gamma$  regions, single  $\gamma$  phase formed in the interdendritic region, plate-like Ti<sub>2</sub>AlC and ribbon like TiB particles. Since data about phase equilibria of the studied alloy is not available, a ternary Ti-Al-C phase diagram calculated by Witusiewicz et al. [18] is used to explain mechanisms



of the in-situ composite formation during the induction melting connected with further centrifugal casting.

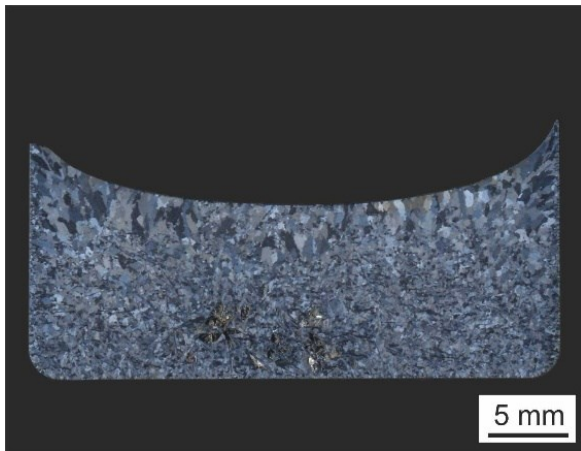


**Figure 2.** The macrostructure of as-solidified in-situ composite.

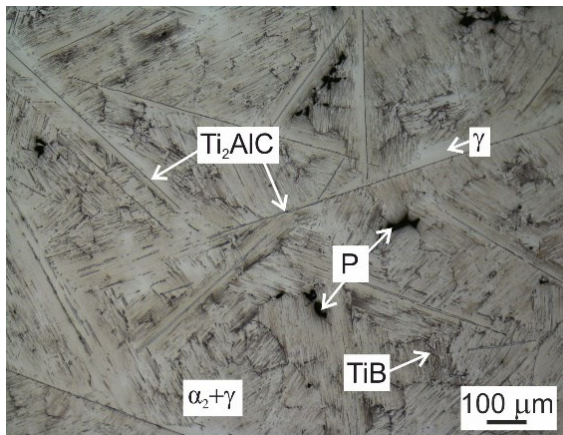


**Figure 3.** The microstructure of as-solidified in-situ composite, LM. P – porosity.

According to the Ti-Al-C phase diagram, the melt temperature of 1680 °C used in the present study corresponds to two phase L(liquid) +  $TiC_{1-x}$  region. However, it is worth to mention, that 5 at.% Nb in the studied alloy can shift the calculated liquidus temperature for the ternary Ti-Al-C systems to higher values and  $\beta$  phase field to higher Al concentration. The amount of solid  $TiC_{1-x}$  particles depends on the carbon content and decreases with decreasing carbon content [6,18]. During the cooling the  $TiC_{1-x}$  particles transform to plate-like  $Ti_2AlC$  and a new phase equilibrium is achieved according to a transformation pathway  $L + TiC_{1-x} \rightarrow L + Ti_2AlC$ . The solidification of the in-situ composite continues by the formation of a secondary phase which nucleates preferentially on the plate-like  $Ti_2AlC$  particles present in the melt. As reported by Lapin and Kamyshnykova [17], the solidification path of studied alloy is finalised by a peritectic reaction of the type  $L + Ti_2AlC + \beta \rightarrow \alpha + Ti_2AlC + TiB$ . The lamellar

microstructure of the matrix is formed by the decomposition of the  $\alpha$  phase according to sequences  $\alpha + Ti_2AlC + TiB \rightarrow \alpha + \gamma + Ti_2AlC + TiB \rightarrow \alpha_2 + \gamma + TiB$  during cooling of the in-situ composite in the crucible.

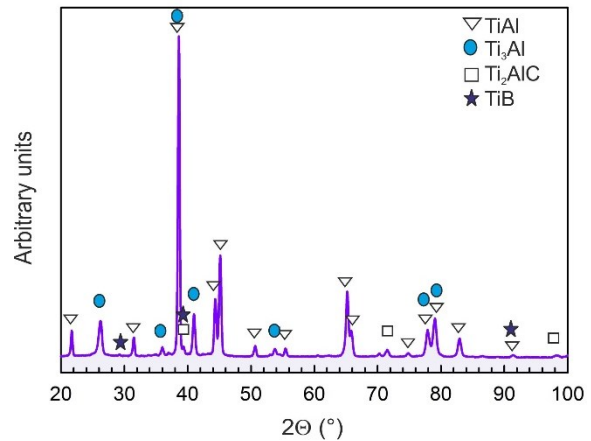


**Figure 4.** The typical XRD pattern of as-solidified in-situ composite.

### 3.2. Centrifugal casting into graphite moulds

Fig. 5 shows the example of the CC in-situ composite. A high surface quality of the samples is achieved after the centrifugal casting into the cold graphite mould but the surface quality continuously decreases with increasing number of casting trials.



**Figure 5.** Centrifugally cast in-situ composite.

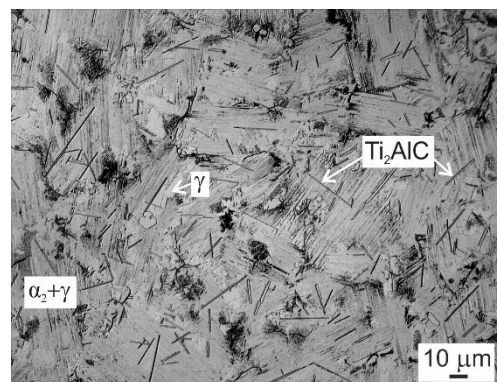


**Figure 6.** Microstructure of centrifugally cast in-situ composite, LM.

The microstructure of the CC in-situ composite is similar that of the as-solidified samples (Fig. 3) and consists of fully lamellar equiaxed  $\alpha_2 + \gamma$  grains with numerous plate-like  $\text{Ti}_2\text{AlC}$  particles, as shown in Fig. 6. It is clear from Table 1 that the grain size and length of carbide particles measured in the CC in-situ composite are significantly lower than those of the AS samples. The microstructure refinement observed in the CC in-situ composite can be related to a faster cooling rate in the cold graphite mould compared to in the graphite crucible during solidification [16,17]. The formation of plate-like  $\text{Ti}_2\text{AlC}$  particles and microstructure refinement (grain size of about  $43 \mu\text{m}$ ) has been also reported for Ti-46Al-8Nb-1.4C (at.%) alloy prepared by non-consumable arc remelting [19].

**Table 1.** Statistical measurements of grain size and length of  $\text{Ti}_2\text{AlC}$  particles in as-solidified and centrifugally cast in-situ composite

Designation of sample	Grain size, $\mu\text{m}$	Carbides length, $\mu\text{m}$
AS	$302.9 \pm 3.0$	$326.7 \pm 8.5$
CC	$53.2 \pm 1.2$	$8.73 \pm 0.12$

### 3.3. Hot isostatic pressing

It is very well-known that TiAl-based have low castability and large solidification shrinkage porosity [20,21]. Fig. 7a shows the typical 3D X-ray CT reconstructed image of a half part of the centrifugally cast sample. Large shrinkage porosity was identified in the feeding head area as well as numerous relatively small pores along the longitudinal axis.

Large casting porosity has been reported also by Jeon et al. [22] in a central region of as-cast Ti-45Al-2Mn-2Nb+0.8 vol.%  $\text{TiB}_2$  alloy. The closure of casting porosity in TiAl-based alloys can be achieved by HIP [21,22]. Fig. 7b shows the typical 3D X-ray CT reconstructed image of a half part of the samples before and after applying HIP at  $1360^\circ\text{C}$  for 4 h, where is no evidence of the porosity. It indicates that the HIP removes all closed porosity in the as-cast sample. However, HIP leads to the formation of coarse-grained structure [17]. The driving force for the growth of coarse grains is the plastic deformation and strain energy stored in the deformed regions of the sample due to the collapse of the porosity during HIP [22].

The amount of plastic deformation is a maximum at the surface of shrinkage porosity and decreases with the distance from the porosity. The nucleation and growth of the recrystallised  $\alpha$  grains occurs predominantly at the central region of the samples where the porosity is filled with the deformed material. When the sample is cooled from the HIP temperature, the coarse  $\alpha$  grains decompose by the nucleation and growth of  $\gamma$  lath to lamellar  $\alpha + \gamma$  type of microstructure.

Fig. 8 shows fully lamellar microstructure of the as-cast sample before and after HIP. Both microstructures consist of well-aligned  $\alpha_2$  and  $\gamma$  laths, plate-like  $\text{Ti}_2\text{AlC}$  particles, ribbon-like  $\text{TiB}$  particles and single  $\gamma$  phase, as shown in Figs. 8a and 8b. Fig. 8b clearly indicates that the HIP leads to a chemical homogenisation of the in-situ composite and full removal of dendritic microsegregation inhomogeneity observed in the CC samples (Fig. 8a).

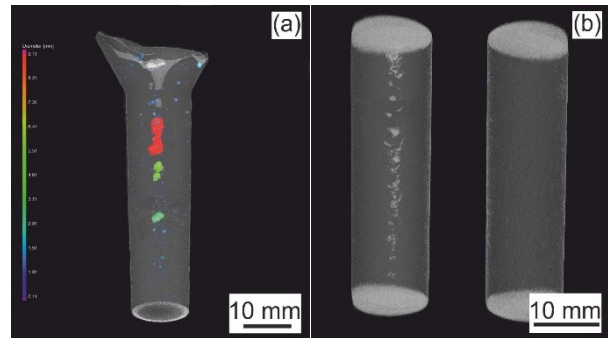


**Figure 7.** 3D X-ray CT reconstruction of centrifugally cast samples before and after the HIP.

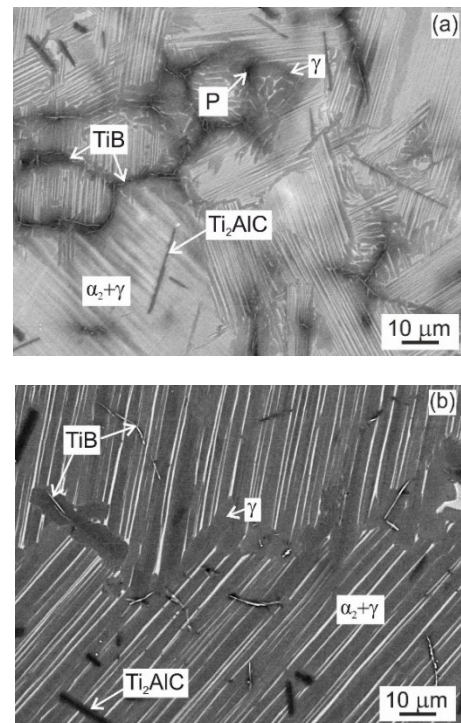
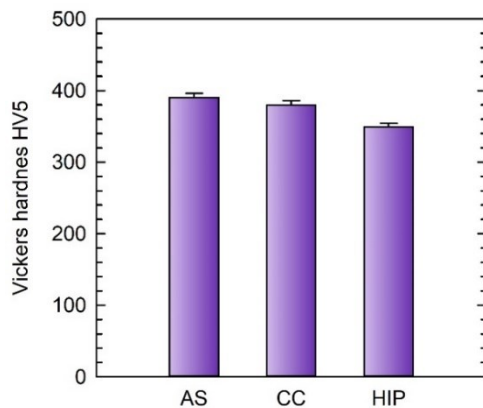


**Figure 8.** Microstructure of centrifugally cast samples: (a) before and (b) after the HIP, BSEM. P – porosity.

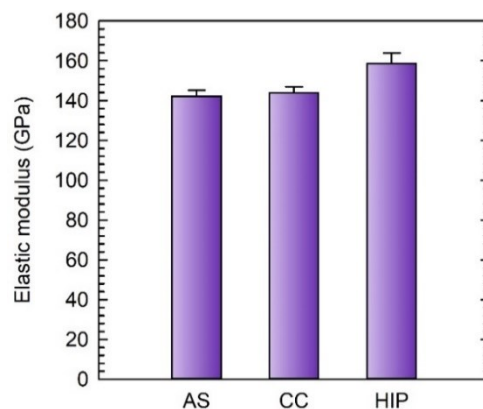
### 3.4. Mechanical properties

Fig. 9 shows that the measured Vickers hardness  $\text{HV}_5$  depends on the applied processing techniques. The induction melting followed by the solidification in the graphite crucible leads to higher hardness values compared to those measured after the centrifugal casting

or HIP. The difference in the hardness of the AS and CC in-situ composites, which are prepared at different solidification conditions, can be attributed to a preservation of higher volume fraction of the soft  $\gamma$  phase in the microstructure of the CC sample, as indicated in Figs. 3 and 6. The softening of the in-situ composite after HIP can be related to the microstructure homogenisation and formation of regular lamellae with a significantly reduced volume fraction of hard  $\alpha_2$  phase. Fig. 10 shows that the solidification in graphite crucible or casting into cold graphite mould have no influence on the measured elastic modulus. However, the elastic modulus increases after HIP. This increase can be explained by removal of fine dendritic porosity observed in the AS and CC in-situ composites, as seen in Figs. 3 and 8.



**Figure 9.** Vickers hardness HV5 of the AS, CC and HIP-ed in-situ composite.



**Figure 10.** Indentation elastic modulus of the AS, CC and HIP-ed in-situ composite.

After reaching a minimum value at a strain ranging from 0.5 to 0.9%, the creep rate increases with increasing strain. No steady-state stage is observed at the applied creep conditions. The in-situ composite shows improved creep resistance compared to that of Ti-45Al-2W-0.6Si-0.7B, Ti-46Al-8Ta and Ti-46Al-2W-0.5Si (at.%) alloys with nearly lamellar, convoluted and pseudoduplex microstructure, respectively [17]. The improvement in the creep strength of the studied in-situ composite can be attributed to the stabilisation of fully lamellar  $\alpha_2 + \gamma$

microstructure and its reinforcement with the plate-like  $\text{Ti}_2\text{AlC}$  particles as well as with fine secondary carbide precipitates forming in carbon containing TiAl-based alloys during heat treatments and creep exposure.

Fig. 11 shows the measured creep deformation curves at an applied stress of 200 MPa and temperatures ranging from 850 to 950 °C.

The creep curves exhibit primary creep stage which is directly followed by the tertiary creep.

Fig. 12 shows variation of instantaneous creep rate with the strain. During the primary creep stage the creep rate decreases with increasing strain.

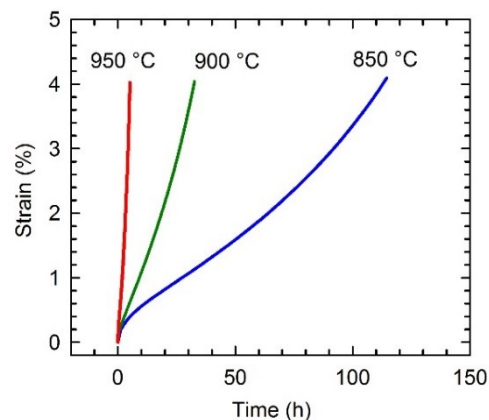


**Figure 11.** Creep deformation curves at an applied load of 200 MPa for the HIP-ed in-situ composite. The test temperatures are indicated in the figure.

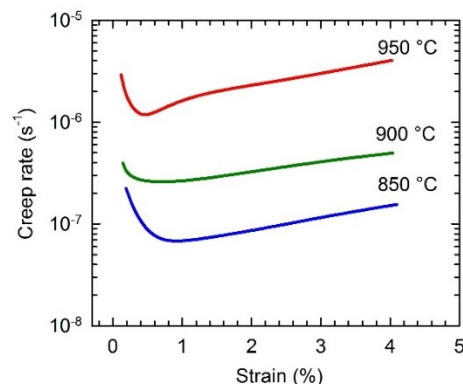


**Figure 12.** Dependence of instantaneous creep rate on strain at an applied load of 200 MPa for the HIP-ed in-situ composite.

#### 4. Conclusions

The induction melting of intermetallic alloy with the chemical composition Ti-47Al-5Nb-1C-0.2B (at.%) followed by solidification in the graphite crucibles leads to the formation of coarse equiaxed lamellar  $\alpha_2 + \gamma$  grains, long plate-like  $\text{Ti}_2\text{AlC}$  and ribbon-like TiB particles. The reinforcing  $\text{Ti}_2\text{AlC}$  particles are formed in the melt and serve as nucleation sites for the  $\beta$  dendrites during solidification. The centrifugal casting of the in-situ



composite into cold graphite mould leads to a significant refinement of the grain size and length of primary carbide particles. The HIP of the CC samples in the  $\alpha$  phase field results in a removal of the casting porosity and leads to the chemical homogenisation and grain coarsening. The Vickers hardness depends on the applied processing techniques. The highest hardness values are measured for the AS sample and lowest for the HIP-ed sample. The elastic modulus of the CC samples increases after HIP. The creep curves exhibit primary creep stage which is directly followed by the tertiary creep. During the primary creep stage the creep rate decreases with increasing strain. After reaching a minimum value at a strain ranging from 0.5 to 0.9%, the creep rate increases with increasing strain.

### Acknowledgment

This work was financially supported by the Slovak Research and Development Agency under the contract APVV-15-0660 and the Slovak Grant Agency for Science under the contract VEGA 2/0125/16.

### REFERENCES

- [1] Bewlay B.P., Nag, S., Suzuki, A., Weimer, M.J., (2016), *TiAl alloys in commercial aircraft engines*, Mater. A. T. High. Temp. 33, p 549–559.
- [2] Shouren, W., Peiquan, G., Liying, Y., (2008), *Centrifugal precision cast TiAl turbocharger wheel using ceramic mold*, J. Mater. Process. Technol. 204, p 492–497.
- [3] Lapin J., Ondruš L., Bajana O., (2003), *Effect of  $Al_2O_3$  particles on mechanical properties of directionally solidified intermetallic Ti-46Al-2W-0.5Si alloy*, Mater. Sci. Eng. A, 360, p 85–95.
- [4] Niu H.Z., Xiao S.L., Kong F.T., Zhang C.J., Chen, Y.Y., (2011), *Microstructure characterization and mechanical properties of TiB<sub>2</sub>/TiAl in situ composite by induction skull melting process*, Mater. Sci. Eng. A, 532, p 522–527.
- [5] Song X.J., Cui H.Z., Hou N., Wei N., Han Y., Tian J., Song Q., (2016), *Lamellar structure and effect of Ti<sub>2</sub>AlC on properties of prepared in-situ TiAl matrix composites*, Ceram. Int. 42, p 13586–13592.
- [6] Lapin J., Klimová A., Gabalcová Z., Pelachová T., Bajana O., Štamborská M., (2017), *Microstructure and mechanical properties of cast in-situ TiAl matrix composites reinforced with (Ti,Nb)<sub>2</sub>AlC particles*, Mater. Des. 133, p 404–415.
- [7] Chen R., Fang H., Chen X., Su Y., Ding H., Guo J., Fu H., (2017), *Formation of TiC/Ti<sub>2</sub>AlC and  $\alpha_2$ + $\gamma$  in in-situ TiAl composites with different solidification paths*, Intermetallics 81, p 9–15.
- [8] Lapin J., Štamborská M., Pelachová T., Bajana O., (2018), *Fracture behaviour of cast in-situ TiAl matrix composite reinforced with carbide particles*, Mater. Sci. Eng., A 721, p 1–7.
- [9] Liu K., Ma Y.C., Gao M., Rao G.B., Li Y.Y., Wei K., Wu X., Loretto M.H., (2005), *Single step centrifugal casting TiAl automotive valves*, Intermetallics 13, p 925–928.
- [10] Cegan T., Szurman I., (2017), *Thermal stability and precipitation strengthening of fully lamellar Ti-45Al-5Nb-0. 2B-0. 75C alloy*, Kovove Mater. 55, p 421–430.
- [11] Lin J.P., Zhao L.L., Li G.Y., Zhang L.Q., Song X.P., Ye F., Chen G.L., (2011), *Effect of Nb on oxidation behavior of high Nb containing TiAl alloys*, Intermetallics 19, p 131–136.
- [12] Hecht U., Witusiewicz V., Drevermann A., Zollinger J., (2008), *Grain refinement by low boron additions in niobium-rich TiAl-based alloys*, Intermetallics 16, p 969–978.
- [13] Hecht U., Witusiewicz V.T., (2017), *Grain refinement and texture mitigation in low boron containing TiAl-alloys*, JOM 69, p 2588–2595.
- [14] Li M., Xiao S., Xiao L., Xu L., Tian J., Chen Y., (2017), *Effects of carbon and boron addition on microstructure and mechanical properties of TiAl alloys*, J. Alloy. Comp. 728, p 206–221.
- [15] Schwaighofer E., Rashkova B., Clemens H., Stark A., Mayer S., (2014), *Effect of carbon addition on solidification behavior, phase evolution and creep properties of an intermetallic  $\beta$ -stabilized  $\gamma$ -TiAl based alloy*, Intermetallics 46, p 173–184.
- [16] Kamyshnykova K., Lapin J., (2018), *Vacuum induction melting and solidification of TiAl-based alloy in graphite crucibles*, Vacuum 154, 218–226.
- [17] Lapin J., Kamyshnykova K., (2018), *Processing, microstructure and mechanical properties of in-situ Ti<sub>3</sub>Al+TiAl matrix composite reinforced with Ti<sub>2</sub>AlC particles prepared by centrifugal casting*, Intermetallics 98, p 34–44.
- [18] Witusiewicz V.T., Hallstedt B., Bondar A.A., Hecht U., Sleptsov S.V., Velikanova T.Y., (2015), *Thermodynamic description of the Al-C-Ti system*, J. Alloy. Comp. 623, p 480–496.
- [19] Wu Z., Hu R., Zhang T., Zhang F., Kou H., Li J., (2017), *Understanding the role of carbon atoms on microstructure and phase transformation of high Nb containing TiAl alloys*, Mater. Char. 124, p 1–7.
- [20] Harding R.A., Wickins M., Wang H., Djambazov G., Pericleous K.A., (2011), *Development of a turbulence-free casting technique for titanium aluminides*, Intermetallics 19, p 805–813.
- [21] Simpkins R.J., Rourke M.P., Bieler T.R., McQuay P.A., (2007), *The effects of HIP pore closure and age hardening on primary creep and tensile property variations in a TiAl XDTC alloy with 0.1 wt.% carbon*, Mater. Sci. Eng., A 463, p 208–215.
- [22] Jeon J.-H., Godfrey A.B., Blenkinsop P.A., Voice W., Hahn Y.-D., (1999), *Recrystallization in cast 45-2-2 XDTC titanium aluminide during hot isostatic pressing*, Mater. Sci. Eng., A 271, p 128–133.

# Renovating of used industrial robots for new purposes

**Stefan KARASTANEV**

Institute of Information and Communication  
Technologies – Bulgarian Academy of  
Sciences  
Bl. 2, ac. G. Bonchev str., 113 Sofia,  
**Bulgaria**

[dimikara@abv.bg](mailto:dimikara@abv.bg)

## Keywords

Robotics  
Mechatronics  
Renovating  
Adaptation

*Professional paper*

**Abstract:** The paper commented on the advantages and economic benefits when used industrial robots have been renovated. The industrial robot is described as a mechatronic system. The necessary procedures for the renovation of an universal robot and its redirection for the robotization of another type of production are presented. Changes and novelties in robot mechanics, electronics and software have been discussed. Examples are given with the inclusion of new functions - adaptive seam tracking for robotized arc welding, and working with casting and stamping machines. The problems and the requirements for the robot and for the additional equipment - power supplies, fixing modules, sensors, manipulators of the details, welding torches, etc. are analyzed.

## 1. Introduction

The word "mechatronics" was created in 1969 by an engineer at "Jaskava" - Japan. In 1971, a commercial registration was made, which the company gave up in 1982 after the widespread use of the term. Initially, and so far with a more superficial and conservative interpretation, the term was perceived as a mechanical and electronic device. Among the many interpretations, the definition of mechatronics is: The integration of mechanical engineering with electronics and intelligent computer software in the design and manufacture of products and technologies.

In Figure 1. a simplified circuit composition of the scientific field "mechatronics" is presented:

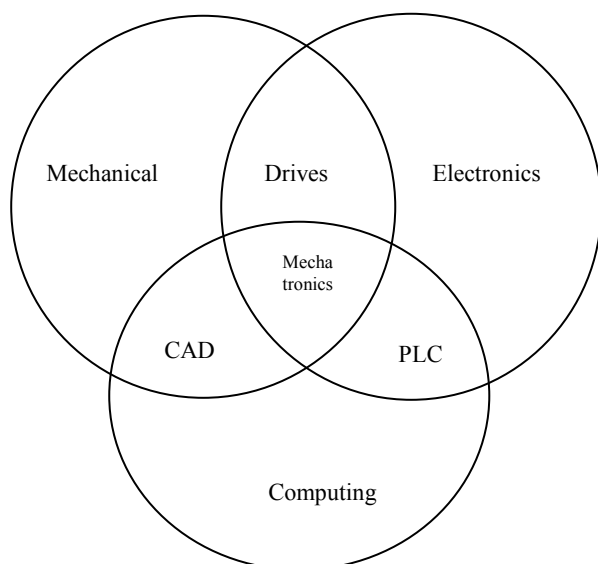


**Figure 1.** A circuit composition of the scientific field "mechatronics"

A modern industrial robot is a complex system consisting of a mechanical structure, motion transmitting elements,

power supplies and drives, working organs, computer electronics, program control, sensors and communication tools [2]. In this sense, industrial robots are typical mechatronic systems with a full set of components.

One of the main areas of application of industrial robots are welding, assembly and servicing of machines (manipulation with details).

The graphs in Figure 2 show the world's annual production of industrial robots (IR), rising and standing in recession

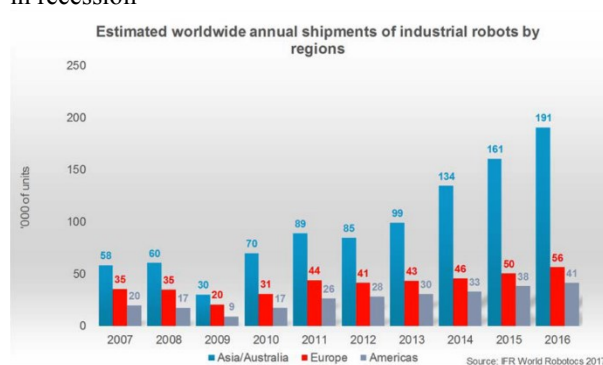


**Figure 2.** World's annual production of IR

Reengineering of universal industrial robots has a tremendous potential, as more than 80,000 robots appear on the secondary market annually and can be upgraded to other specific areas and industries such as:

- chemical and cement industry;
- metallurgy;
- machine building;
- food industry;
- warehouse and logistics;
- galvanic and chemical treatments;
- welding and many other operations;
- plasma welding and others.



Figure 3 shows that over 50% of IR have been deployed in the automotive industry.

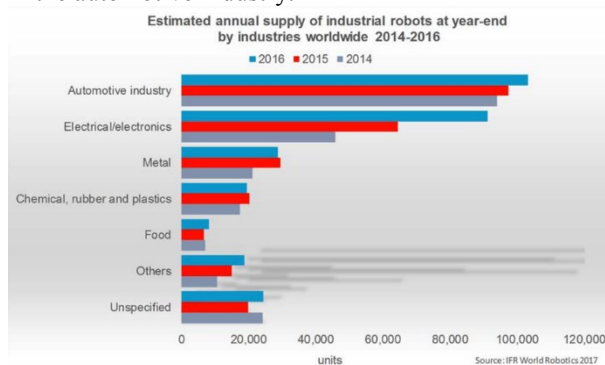


**Figure 3.** Industrial sectors in which the IR are implemented

Reengineering as an activity is economically and technically advantageous for the following reasons:

- the maintenance of fitting main mechanical components and the upgrading of robot hardware and software is an optimal and highly effective approach to reengineering high-tech mechatronics such as industrial robots;
- in most cases, IR that are out of use or discarded retain their mechanical fitness. Problems mainly create control systems and application software. Therefore, a large part of the IR offered on the secondary market are without control systems and / or servo drives (invertors);
- repairing old controllers and servo drives is a temporary solution, if at all possible, as manufacturers keep their know-how and do not provide information about hardware and software. The only option is to look for alternative modern controllers and servo drives for reengineering and upgrading of the IR, which not only make them fit for regular use but also to bring them closer to or equalize technologically with new ones on the market.

## 2. Robots for arc welding

Industrial robots and mechanized equipment have become indispensable for high-performance industrial welding [3], as manual welding results in low productivity due to unfavorable working environment, [4]. Dynamic market behavior and strong competition forces manufacturing companies to look for optimal production processes. As shown in Figure 4 [5], for small and medium production volumes, robotic production gives the best price per unit of output compared to manual and rigid automation. In addition to competing unit costs, robotic welding systems bring other benefits such as improved productivity, safety, welding quality, flexibility, little work space and reduced labor costs.

Welding is an integral part of modern industrial production and robotic welding is considered to be a major symbol of modern welding technology [6]. In the earliest robotic welding applications (the first generation of robotic welding systems), the welding was considered

as a two-pass welding, in which the first pass was devoted to the study of seam geometry and was followed by actual tracking and welding of the seam in the second pass. With the development of technology came the second generation of robotic welding, that track the seam in real time, while performing the phases of studying and tracking the seams. The latest technology in robotic welding is third-generation, in which the system not only works in real-time but also studies the rapidly changing seam geometry while working in unstructured environments [7].

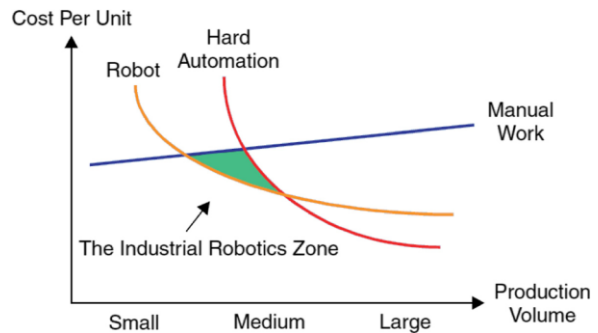


**Figure 4.** Area of robotized welding

## 3. Problems in robotic welding

In robotic welding, the following problems often occur:

- The cohesiveness required for welding a detail after a detail in the absence of proper control can lead to quality fluctuations due to poor fixation or variations in the metal forming process.
- In the case of low or average production or repair, the time and effort required to program the welding robot of a new part may be quite high [8].
- Robotic welding requires appropriate design of the parts, coordinated forms of the field of welding (seam) and tolerance in sizes not exceeding 0.5 to 1 mm. Seam deviation requires the use of sensor technology to fill it, [9].
- The automation of welding through robotic systems is at a high starting price, so accurate calculation of the initial price and accurate calculation of ROI are essential [10].
- The possible shortage of qualified welders with the necessary knowledge and training is a limitation.
- Unlike adaptive human behaviours, robots can not independently take autonomous corrective decisions and must be complemented by the use of sensors and a robust system of control and decision-making.
- Robotic welding can not be easily carried out in some areas such as pressure vessels, internal tanks and ship bodies due to workspace constraints [11].
- Most intelligent sensor systems available on the market are not tightly integrated with the robot controllers, which limits the performance of the robotic system, and most industrial robots offer about 20-Hz feedback as a

programming interface. Therefore, the robot can not respond to the sensor information quickly, resulting in delay and sometimes unstable production.

Welding robotic complexes of KUKA are one of the most widespread - Figure 5. They are suitable for MIG / MAG arc welding, they are equipped with their own welding power source, they have developed trajectory control. When fitted with a suitable sensor, they can perform adaptive welding.

The shown KUKA VK30 welding Robot has the following data:

- Year of manufacture: 1996
- Range: 1950 mm
- 3 positioning table for the details - 600 mm diameter
- Equipped with MIG / MAG power source (production year 2012, water cooling, remote control)



**Figure 5.** Welding robot KUKA VK30

#### 4. IR requirements for reengineering

Some basic approaches to future IR reengineering are identified:

- New generation discarded IR are usually equipped with servomotors. In most cases they are fully up and running for many years. It is only necessary to check their suitability.
- Selection of a suitable digital servo control system for the motors is required. It must have an open platform, a wide range of parameters and procedures for adjustment and adaptation. Since the IRs are equipped with different types of servomotors, it is necessary to adapt the chosen type of servo drive to different types of servomotors. A typical example is the IR of the German company KUKA. Since their servomotors are manufactured by Siemens but designed only for KUKA, the manufacturer does not provide information about their technical parameters. In this case it is necessary to study servomotors and adapt the servo to it.
- For IR control, it is necessary to choose a modern industrial controller providing high computing power, a rich set of digital interfaces and real-time operation. We also need a flexible software platform with a rich set of technological features to develop the robot's control software.

- It is necessary to look for an opportunity for IR reengineering based on inspection of the mechanical construction, development of new hardware and software and directing them to other industries with specific requirements.

Reverse engineering of universal robots has been found to be a huge resource, with more than 80,000 robots emerging on the secondary market annually, which after modernization can be turned into a number of other specific areas and industries.

#### 5. Research on the mechanics, electronics and software of the IR

In accordance with the objectives and the tasks, the kinematic and dynamic characteristics of the selected IR representative, subject to reengineering, are determined. The activities here determine the metric and kinematic parameters of the mechanical design of the selected robot. For this purpose the type and gear ratios of the gearboxes, the used compounds, oils and grease were investigated. On the basis of FEM (Finite Element Method), the dynamics of the robot - representative - was also studied. The electrical characteristics of the engines, the feedback sensors and the servo drives were studied. The mathematical apparatus, which solves the normal and the inverse problem of kinematics in the robot's anthropomorphic structure, is analyzed. For this purpose, the methods of virtual simulation and the developed metric and mathematical models for a similar type of research are used. The developed and implemented software for the control of the KUKA series of robots produced under the name KSS (Kuka System Software), [12] was examined and analyzed. For the KUKA KR 30 surveyed robot, the software is provided by two main components: KSS - to implement the basic features and operational capabilities of the robot, and Windows XP embedded 2.x with Service Pack 2, providing a user-friendly interface for communication with the system user.

#### 6. Building of upgraded IR

After testing and renovating the mechanical structure and drives, the hardware (the controller) and the software (program functions) of the robot are replaced in order to perform a sequence of actions in the new field of application. The Servo Drive Type is DB4 - Producer: Elektroinvent Ltd, Bulgaria. The in/out controller is also from the local SME.

In addition, a special program was developed - a simulator, for testing and validation, as well as for facilitating the creation of technological programs and program series. As a basic platform for application software, the Qt environment, with the appropriate QtCreator, QtDesigner, and QtLinguist development tools, has been used because of its open source code,

multiplatforming, and support for multiple processor architectures. The Qt environment supports the following operating systems: Windows, Android, and MacOS. On the other hand, the Qt platform provides a number of embedded modules to meet the basic application needs. The main programming languages are C and C++. The same applies to the simulator. As a consequence of the task of reengineering is synthesized an IR control system characterized by a high degree of complexity. The study of such a complex system has necessitated the development of methodologies for the detailed examination of individual nodes, the ultimate goal being to verify the reliable operation of the whole system. Such methodologies have been developed during the study of the elements, such as sensor system, servo drives, power supplies, interface for connection with external devices for interaction with the surrounding machines and equipment, for the realization of the necessary production or other process. The detailed methodologies are directed to simple yet secure testing of the specified modules or blocks. Verification was performed on the basis of:

- the developed methodologies for the research of the mechanical design, hardware and software of the investigated type representative of the IR;
- the research carried out on the renewed mechanical design and the developed hardware and software for managing the functioning laboratory model of the re-engineered robot KUKA KR-30.

## 7. Conclusion

The upgraded IR can be used as a welding robot and as a robot for working with casting and machines. If suitable sensors for seam tracking are added, it can perform adaptive welding. To service the casting and stamping machines, Figure 6, the following functions are needed:

- extracting the finished piece from the machine,
- exit from the machine's working area,
- inspection of the part (s),
- cooling of the workpiece,
- punching excess material,
- alignment of the finished product.



Figure 6. KUKA robot with die-casting machine

## Acknowledgements

This research was supported by the Bulgarian SME SPESIMA LTD.

## REFERENCES

- [1] Karastoyanov D., (2010). *Control of robots and of other mechatronic systems*, Acad. Publishing House „Marin Drinov“, Sofia, , ISBN 978-954-322-415-9 (in Bulgarian)
- [2] Karastoyanov D., Nachev G., (1984). *Adaptive Control of Industrial Robot for Arc Welding*, 9th IFAC World Congress, Budapest, Hungary, July 2-6, vol. VI, 50-55
- [3] P. Kah, M Shrestha, E Hiltunen and J Martikainen39., (2015). Robotic arc welding sensors and programming in industrial applications International Journal of Mechanical and Materials Engineering 10:13 DOI 10.1186/s40712-015-0042-Y
- [4] Laiping, C. Shanben and L. Tao, (2005). "The modeling of welding pool surface reflectance of aluminum alloy pulse GTAW," Materials Science and Engineering: A, vol. 394, no. 1-2, p. A 320-326,
- [5] Pires, JN, Loureiro, A, Godinho T, Ferreira P, Fernando B, Morgado J. (2003). "Welding robots," IEEE Robotics & Automation Magazine, 45-55.
- [6] Cui, H, Dong, J, Hou, G, Xiao, Z, Chen, Y, & Zhao, Z. (2013). "Analysis on arcwelding robot visual control tracking system", in 2013 International Conference on Quality, Reliability, Risk, Maintenance, and Safety Engineering (QR2MSE).
- [7] Pires, JN, Loureiro, A, & Bölmsjö, G. (2006). *Welding robots: technology*. London: System Issue and Application. Springer-Verlag. p. 74.
- [8] Dinham, M, & Fang, G. (2013). *Autonomous weld seam identification and localisation using eye-in-hand stereo vision for robotic arc welding*. Robotics and Computer-Integrated Manufacturing, 29(5), 288-301.
- [9] Robot Welding, "Key issues for robotic welding," [Online]. Available: <http://www.robotwelding.co.uk/key-issues.html>. [Accessed 4 September 2013].
- [10] Rochelle, B. (2010). "Think before you integrate (robotic welding)," thefabricator.com
- [11] Robotics Bible, "Arc welding robot," Available: [http://www.roboticsbible.com/arc-welding\\_robot.html](http://www.roboticsbible.com/arc-welding_robot.html). [Accessed 12 May 2013].
- [12] Kuka, (2010). "System Software 5.5 "Operating and Programming Instructions for System Integrators", " Kuka,

# Compressive flow stress and hardness determination for composites based on aluminum waste

Jure KROLO<sup>1)</sup>, Branimir LELA<sup>1)</sup>  
Domagoj KOJUNDŽIĆ<sup>1)</sup> and Jelena  
SERIĆ<sup>1)</sup>

1) University of Split, Faculty of Electrical  
Engineering, Mechanical Engineering and  
Naval Architecture, Department for  
Production Engineering  
Sveučilište u Splitu, Fakultet  
elektrotehnike, strojarstva i brodogradnje,  
R. Boskovicica 32, 21 000 Split, Croatia

[jkrolo@fesb.hr](mailto:jkrolo@fesb.hr)  
[blela@fesb.hr](mailto:blela@fesb.hr)  
[dkojundz@fesb.hr](mailto:dkojundz@fesb.hr)  
[jelena.seric.02@fesb.hr](mailto:jelena.seric.02@fesb.hr)

## Keywords

*Solid state recycling*  
*Aluminum waste composites*  
*Severe plastic deformation*  
*Hardness*  
*Compressive flow stress curves*

## Ključne riječi

*Recikliranje u čvrstom stanju*  
*Kompoziti od aluminijskog otpada*  
*Velika plastična deformacija*  
*Tvrdoća*  
*Krivulje tečenja*

*Original scientific paper*

**Abstract:** Main aim of this paper is to present a novel method for aluminum chips recycling without remelting and to present production of composites based on aluminum waste. With presented method environmental pollution is significantly smaller compared to conventional aluminum recycling. Aluminum chips were mixed with aluminum oxide ( $Al_2O_3$ ) powder, compacted into billets and direct hot extruded into round bars. Obtained bars were finally processed with severe plastic deformation (SPD) in order to produce high quality recycled composites. SPD was performed utilizing equal channel angular pressing (ECAP) process. Influence of aluminum oxide addition in the recycled samples on compressive flow stress curves and hardness was determined. Compressive flow stress curves and hardness were determined for samples obtained by direct hot extrusion and for samples obtained by combination of direct hot extrusion and ECAP process. Results are compared with commercially produced EN AW 6082 in T6 and O temper conditions.

*Izvorni znanstveni rad*

**Sažetak:** Glavni cilj ovoga znanstvenog rada je predstaviti inovativnu metodu recikliranja bez pretaljivanja strojnom obradom nastalih aluminijskih odvojenih čestica i predstaviti proizvodnju kompozitnog materijala zasnovanog na njima. Ova metoda omogućuje značajno smanjenje zagađenja okoliša u usporedbi s konvencionalnom metodom recikliranja aluminija. Aluminijske odvojene čestice pomiješane su s prahom aluminijevog oksida ( $Al_2O_3$ ), sabijene u brikete a zatim su direktnim istiskivanjem u toplom stanju formirani okrugli profili. Tako dobiveni profili naposljetku su podvrgnuti velikoj plastičnoj deformaciji (engl. "severe plastic deformation" - SPD) kako bi se proizveo kvalitetan, recikliranjem nastali kompozit. SPD je proveden uz pomoć kutnog kanalnog istiskivanja (engl. "equal channel angular pressing" - ECAP). Ispitan je utjecaj količine dodanog aluminijevog oksida na krivulje tečenja i tvrdoću dobivenih uzoraka. Krivulje tečenja i tvrdoća određene su za uzorke koji su istisnuti u toplom stanju te za uzorke koji su istisnuti u toplom stanju, a zatim obrađeni ECAP procesom. Rezultati su uspoređeni s komercijalno proizvedenom aluminijskom legurom EN AW 6082 u T6 i O stanju.

## 1. Introduction

Aluminum recycling is extremely important for aluminum industry. Aluminum production from bauxite ore uses 157 GJ/t in European Union industry, while aluminum recycling energy consumption is only 8.85 GJ/t [1]. Despite 95 % lower energy consumption, constant improvements in aluminum recycling technologies and strategies are necessary. According to the International Aluminum Institute (IAI), material consumption on global level is constantly increasing. Projections from 2015. to 2050. predict that aluminum demand will be doubled [2-3].

According to the Intergovernmental Panel on Climate Change (IPCC) global aim is to reduce  $CO_2$  emission into the atmosphere 50 % to 80 % compared to  $CO_2$  emissions

levels in 1990s [4]. In order to increase scrap reuse potential and to reduce greenhouse emission in the atmosphere, solid state recycling process (SSR) was developed lately. SSR is recycling of the aluminum scrap without remelting. Energy consumption for SSR is only 10 % compared to conventional recycling process that uses remelting [2, 4]. Aluminum is highly reactive material and it has tendency to form aluminum oxide on its surface. This is even more pronounced for lightweight aluminum scrap due to its high surface to mass ratio. During remelting process this oxide is floating on the melt surface mixed with dross [5]. Therefore, aluminum lightweight scrap (chips, foils, sheet skeletons) is problematic when conventional recycling technology is used because up to 20 % of aluminum can be lost due to the mixing with dross and burning.



When SSR is employed material losses are much smaller because remelting phase is completely avoided. According to previous research papers concerned with SSR process it is possible for material yield to be over 90 % when this type of recycling is employed [4, 6]. In order to produce solid state recycled samples with appropriate quality, combination of the high temperature, normal stress, shear stress and plastic deformation should be achieved. Therefore, the most used process for SSR is direct hot extrusion, but lately severe plastic deformation (SPD) processes opened new possibilities [7]. Severe plastic deformation is usually used to produce materials with fine grain structure. It is possible to achieve submicron or nano-size material grains. A finer grain size increases the strength and the fracture toughness of the material and provides the potential for superplastic deformation at moderate temperatures and high strain rates [8]. SPD processes used for SSR were: ECAP [9-10], cyclic extrusion compression (CEC) [11], high pressure torsion (HPT) [12].

There were a few attempts were researches tried to mix machined chips with reinforcement or hardening phase and produce composites based on aluminum waste. Main purpose of the reinforcement phase is to improve mechanical properties of the solid state recycled material. Gronostajski et al. 1996 presented solid state recycling of composites based on aluminum waste. Their process included cold pressing and hot extrusion of aluminum and aluminum alloys (AlMg2, AlCu4) granular chips mixed with tungsten, graphite powder and aluminum bronze. Tungsten powder addition increased strength properties, but the porosity and the lack of diffusion bonds in some parts of recycled samples decreased these properties. Graphite addition resulted in discontinuities in the structure, which decreased strength and plastic properties of the material. Finally, by adding comminuted aluminum bronze chips, composite with good tribological properties were produced [6]. Fogagnolo et al. 2003 recycled chips machined from aluminum matrix based composite reinforced with  $\text{Al}_2\text{O}_3$ . Composite chips were compacted and hot extruded. Recycled composite had higher ultimate tensile strength (UTS) compared with the former as cast composite. Authors explained that recycled composites had increased UTS because they had refined microstructure and higher content of oxides caused by the machining and the hot extrusion process [13]. Samuel 2003 investigated solid state recycling by hot extrusion to produce composite material from granulated Al-2014 scrap alloy and  $\text{Al}_2\text{O}_3$  Saffil fiber addition. Sintering process was carried out between cold compaction and hot extrusion. Hot extrusion process resulted in more uniform and homogeneous distribution of Saffil ceramic fibers inside the metal matrix while porosities were reduced. Recycled samples showed improved strength compared to conventional Al-2014. The best combination of strength and stiffness was obtained using

small granulated chips with 10 vol% Saffil ceramic fiber addition due to very good internal cohesion associated with smaller fiber content [14]. Tekkaya et al. 2009 considered solid state recycled EN AW 6060 aluminum chips with SiC particles addition. These hardening particles caused destruction in many spots of the extruded profiles and the surface roughness was increased. The tensile test revealed reduction in flow stress, which reduced the strength [15]. Ahmad et al. 2017 produced aluminum AA 6061 based metal matrix composites using hot press process. Mixture of recycled aluminum and 2 wt.% aluminum oxide ( $\text{Al}_2\text{O}_3$ ) powder was heated and forged on elevated temperature. Recycled composites produced as described showed higher hardness value compared to samples recycled by hot press forging without  $\text{Al}_2\text{O}_3$  powder addition [16].

In this study aluminum machining chips were first mixed with aluminum oxide powder ( $\text{Al}_2\text{O}_3$ ) and compacted into billets. All of the compacted billets had mass of 150 g including 2 g, 5 g and 8 g aluminum oxide powder addition. Aluminum chips without any aluminum oxide powder addition were also compacted. These billets were than directly hot extruded into round profiles. Obtained bars were finally processed with severe plastic deformation (SPD) in order to produce recycled composites. SPD was performed by utilizing equal channel angular pressing (ECAP) process. Compressive flow stress curves of the recycled samples were determined for samples obtained by direct hot extrusion and for samples obtained by combination of direct hot extrusion and ECAP process. Additionally, compressive flow stress curves were determined for commercially produced EN AW 6082 aluminum alloy in annealed condition and in extruded T6 temper condition. Hardness measurements for all composite samples were also obtained.

## 2. Experimental procedure

In this paper mixture of EN AW 6082 aluminum alloy chips and aluminum oxide ( $\text{Al}_2\text{O}_3$ ) powder was solid state recycled in order to create composites based on aluminum waste. Chips were obtained by dry turning process without any cooling and lubrication cutting fluid to prevent chips contamination. However, if chips are contaminated it is possible to clean them using chemical and thermal treatment [6, 7]. Chemical composition of selected aluminum alloy EN AW 6082 was according to EN-573-3 standard: 0.7-1.3 % Si, 0-0.5 % Fe, 0-0.1 % Cu, 0.4-0.1 % Mn, 0.6-1.2 % Mg, 0-0.25 % Cr, 0-0.2 % Zn, 0-0.1 % Ti, other 0-0.1 %. Aluminum chips and aluminum oxide powder were mixed and afterwards compacted into billets with 38 mm in diameter. Before compaction step aluminum chips were mixed with 2 g, 5 g and 8 g aluminum oxide powder and with suitable amount of chips to obtain billets with same mass of 150 g. Furthermore, chips without any aluminum oxide were also compacted. Chips average length, thickness and



width were 10 mm, 0.8 mm and 1.8 mm, respectively. Three compaction steps were necessary to obtain chips based billets. Compaction was performed on 1 MN hydraulic press. First two steps were performed with 200 kN compaction force. Final step was performed with 300 kN compaction force. Force measurement during compaction phase was achieved utilizing HBM load cell C6A 1MN. After compaction billets were preheated 20 minutes on 460 °C and then directly hot extruded (DE) into a round bars with 15 mm diameter. Diameter of the extrusion cylinder was 40 mm. Extrusion temperature and extrusion ratio were 450 °C and 7.11, respectively. These 15 mm bars were finally processed with severe plastic deformation (SPD) in order to produce high quality recycled composite. SPD was performed by utilizing equal channel angular pressing (ECAP) process. Tool geometry in ECAP process is mainly defined by two angles, inner die angle  $\phi$  and outer die angle  $\psi$ . ECAP tool used in this process has 90° inner die angle and 12° outer die angle. Outer die angle is defined by 3 mm radius. The diameter of the ECAP tool channel is 15.1 mm. Graphite grease was used for lubrication on room temperature. Figure 1 shows ECAP tool.



Figure 1. ECAP tool

After SSR route compressive flow stress curves were determined for samples obtained by direct hot extrusion and for samples obtained by combination of direct hot extrusion and ECAP process. Therefore, eight compressive flow stress curves were determined for aluminum chips based composites. Additionally, compressive flow stress curves were determined for commercially produced EN AW 6082 in annealed condition and in T6 temper condition.

Suggested sample height/diameter ratio for flow stress determination curves is from 1.5 to 2.0. [17]. In this work specimens were prepared on lathe machine with dimensions of 20 mm in height and 13 mm in diameter which resulted in height/diameter ratio of 1.54. Figure 2 shows experimental rig utilized for flow stress curves

determination. All samples for flow stress determination were lubricated with Teflon to minimize influence of friction coefficient on samples. Main aim to minimize friction coefficient is to achieve homogenous deformation and to avoid samples "barreling".



Figure 2. Experimental rig for flow stress curves determination

Eight solid state recycled samples with different process routes and  $\text{Al}_2\text{O}_3$  addition were produced. Also, two samples from commercially produced EN AW 6082 in annealed temper (O) and T6 temper were used for comparison purposes. Overview of SSR process routes, amount of  $\text{Al}_2\text{O}_3$  powder addition and flow stress values for selected true strain values:  $\phi = 0.1$ ,  $\phi = 0.2$ ,  $\phi = 0.3$  and  $\phi = 0.5$  are given in Table 1.

Table 1. Samples composition and flow stress values at selected true strain values

Sample	Process route	$\text{Al}_2\text{O}_3$ addition [g]	True strain $\phi$			
			0.1	0.2	0.3	0.5
			Flow stress [MPa]			
1	DE+ECAP	/	249	251	252	253
2	DE	/	178	200	214	231
3	DE+ECAP	2	254	249	247	248
4	DE	2	187	209	222	239
5	DE+ECAP	5	258	260	261	263
6	DE	5	179	201	214	229
7	DE+ECAP	8	236	237	237	238
8	DE	8	166	183	192	204
Commercially produced EN AW 6082 extruded bar			True strain $\phi$			
			0.1	0.2	0.3	0.5
			Flow stress [MPa]			
9	Annealed		153	177	192	211
10	T6 temper		426	438	438	436

For metallography analysis purpose optical microscope "OPTON Axioskop" and computer software "BIOVIS MP2000" were utilized. Samples were etched for 10 s at room temperature in a reagent which consisted of 0.5 mL of 40 % HF (Hydrofluoric Acid) dissolved in 100 mL of water.

### 3. Results and analysis

The compressive flow stress curves measurements were performed at room temperature. Figure 3 presents flow stress curves for composites based on aluminum waste

(sample 1 to 8) and flow stress curves of commercially produced EN AW 6082 extruded bars in O and T6 temper condition, sample 9 and 10, respectively.

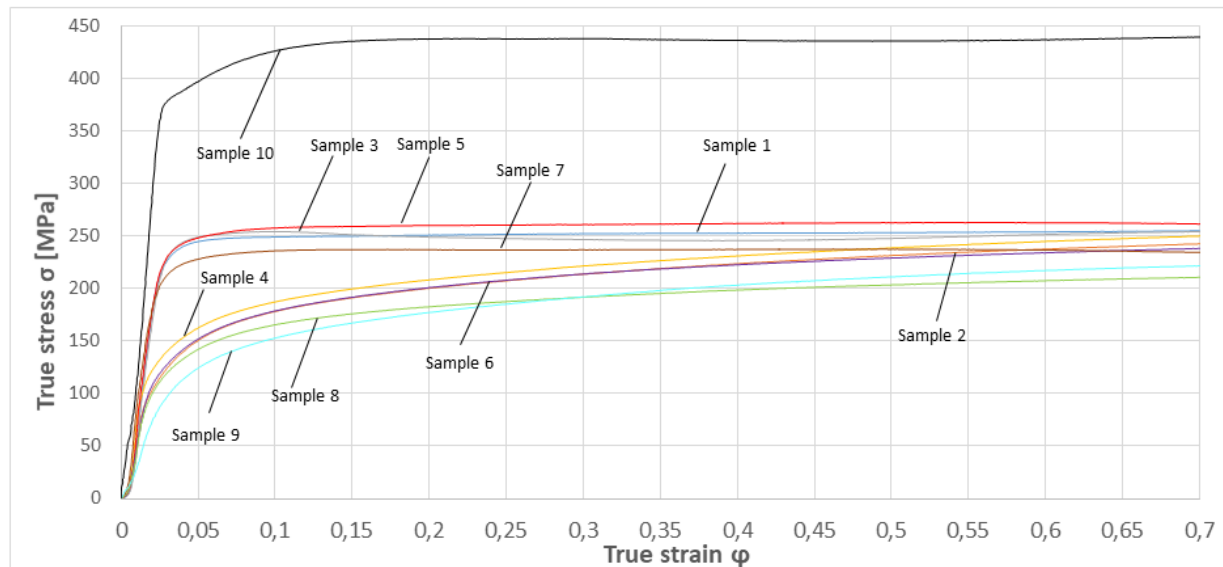


Figure 3. Compressive flow stress curves: true stress vs. true strain

According to the results presented in Figure 3 and Table 1, flow stress values are highest for commercially produced EN AW 6082 extruded bar in T6 temper condition. Flow stress values are lowest for commercially produced EN AW 6082 extruded bar in O temper condition until true strain value  $\phi = 0.3$ . After true strain  $\phi = 0.3$  lowest flow stress values are those from sample 8. Therefore, all SSR recycled composites based on aluminum waste have higher flow stress values than annealed commercial aluminum, except sample 8 after true strain  $\phi = 0.3$ . From SSR samples that were obtained only by DE, sample 4 (2 g  $\text{Al}_2\text{O}_3$  powder addition) has highest flow stress values. Sample 2 (without  $\text{Al}_2\text{O}_3$  powder addition) and sample 6 (5 g  $\text{Al}_2\text{O}_3$  powder addition) have similar values of flow stress. This clearly indicates that appropriate amount of  $\text{Al}_2\text{O}_3$  powder can increase compressive flow stress of SSR recycled samples obtained by DE.

Furthermore, all SSR composites based on aluminum waste obtained by combination of DE and ECAP process have significantly higher flow stress values than SSR samples obtained only by DE, Fig. 3. This occurs because of the finer grain structure caused by ECAP process. For samples obtained by combination of DE and ECAP, sample 7 (8 g  $\text{Al}_2\text{O}_3$  powder addition) has lowest flow stress values while sample 5 (5 g  $\text{Al}_2\text{O}_3$  powder addition) has highest flow stress values for whole true stress range, Fig. 3.

Sample 3 with 2 g  $\text{Al}_2\text{O}_3$  powder addition and sample 1 without  $\text{Al}_2\text{O}_3$  addition have similar flow stress values for whole true strain range (after true strain  $\phi = 0.15$ , sample

3 has slightly lower flow stress value). Flow stress curves analysis clearly indicated that for SSR samples obtained by DE or with combination of DE and ECAP small amount of  $\text{Al}_2\text{O}_3$  powder addition can improve compressive flow stress.

However, properties are deteriorated for SSR composite with 8 g  $\text{Al}_2\text{O}_3$  powder addition. Therefore, amount of  $\text{Al}_2\text{O}_3$  powder addition must be carefully chosen to obtain desirable samples properties. Hardness measurements for all eight SSR samples are presented in Figure 4.

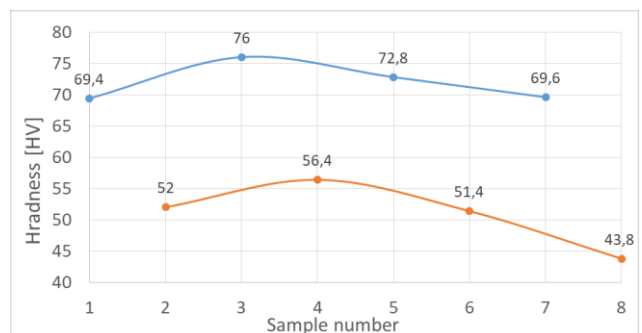


Figure 4. Hardness for 8 SSR composite samples

According to Figure 4, hardness of SSR composite samples 1, 3, 5 and 7 obtained by combination of DE and ECAP is much higher compared to samples 2, 4, 6 and 8 produced only by DE. For samples obtained by combination of DE and ECAP, sample 3 (2 g  $\text{Al}_2\text{O}_3$  powder addition) has highest hardness value of 76 HV.

Compared to sample 1 (without  $\text{Al}_2\text{O}_3$  powder addition) produced by DE+ECAP process, sample 3 has 9.5 % higher hardness. Additionally, samples 5 and 7 mixed and recycled with 5 g and 8 g of  $\text{Al}_2\text{O}_3$  powder addition have slightly higher hardness compared to sample 1 but lower compared to sample 3.

Considering samples obtained only with DE, sample 4 (2 g  $\text{Al}_2\text{O}_3$  powder addition) has highest hardness value (56.4 HV). This value is 8.5 % higher compared to

sample 2 recycled by DE without any  $\text{Al}_2\text{O}_3$  powder addition (52 HV). However, samples 6 and 7 with 5 g and 8 g  $\text{Al}_2\text{O}_3$  powder addition recycled with DE have lower hardness than sample 2.

Digital images of polished cross sections of composites based on aluminum waste are shown in Figure 5. Photos were taken with laboratory digital camera DigiMicro Profi and corresponding MicroCapture Pro computer software. All samples have 13 mm in diameter.

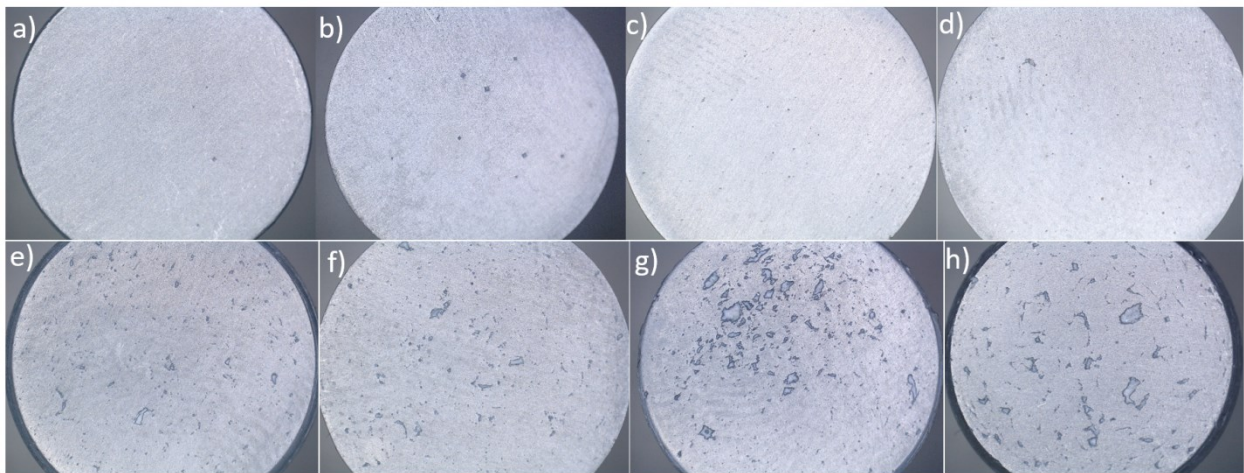


**Figure 5.** Composites based on aluminum waste: a) DE+ECAP without  $\text{Al}_2\text{O}_3$  b) DE without  $\text{Al}_2\text{O}_3$  c) DE+ECAP with 2 g  $\text{Al}_2\text{O}_3$  d) DE with 2 g  $\text{Al}_2\text{O}_3$  e) DE+ECAP with 5 g  $\text{Al}_2\text{O}_3$  f) DE with 5 g  $\text{Al}_2\text{O}_3$  g) DE+ECAP with 8 g  $\text{Al}_2\text{O}_3$  h) DE with 8 g  $\text{Al}_2\text{O}_3$

According to photos, samples 1 and 2 (no  $\text{Al}_2\text{O}_3$  powder addition) have homogeneous structure without any cracks and voids, Fig. 5 a) and b). Samples 3 and 4, with 2 g  $\text{Al}_2\text{O}_3$  powder addition, have desirable structure with small, homogeneously distributed  $\text{Al}_2\text{O}_3$  powder "clusters", Fig. 5 c) and d). Samples 5 and 6 (with 5 g  $\text{Al}_2\text{O}_3$  powder addition) also have visible  $\text{Al}_2\text{O}_3$  powder "clusters", Fig. 5 e) and f). However, this "clusters" are much larger compared to samples with 2 g  $\text{Al}_2\text{O}_3$  powder addition. Finally, for samples 7 and 8, with 8 g  $\text{Al}_2\text{O}_3$  powder addition,  $\text{Al}_2\text{O}_3$  powder "clusters" are significantly larger compared with ones from samples 3, 4, 5 and 6, Fig. 5 g) and h).

These  $\text{Al}_2\text{O}_3$  powder "clusters" clearly indicate that  $\text{Al}_2\text{O}_3$  powder is not homogeneously distributed inside recycled samples. This is probably because aluminum chips were not comminuted enough and mixing procedure was not sufficient to obtain homogeneous  $\text{Al}_2\text{O}_3$  powder distribution. When digital images of samples produced with and without ECAP are compared it can be stated that ECAP process reduced size of  $\text{Al}_2\text{O}_3$  powder "clusters", Fig. 5.

Furthermore, metallographic analysis was also performed. Figure 6 shows metallographic images for all 8 SSR recycled samples

According to the Figure 6 a) and b), SSR samples recycled without any  $\text{Al}_2\text{O}_3$  powder addition have fine

microstructure without any cracks or voids. Samples recycled with  $\text{Al}_2\text{O}_3$  powder addition have formed  $\text{Al}_2\text{O}_3$  powder clusters, Fig. 6 c-h. These clusters are much smaller for samples with 2 g  $\text{Al}_2\text{O}_3$  powder addition (Fig. 6 c and d) compared with samples obtained by 5 g and 8 g  $\text{Al}_2\text{O}_3$  powder addition (Fig. 6 e-h). However, for samples with 2 g and 5 g  $\text{Al}_2\text{O}_3$  powder addition, powder cluster size decreased after ECAP process, Fig. 6 c) and f) and Fig. 5 c) and f). For sample with 8 g  $\text{Al}_2\text{O}_3$  powder addition  $\text{Al}_2\text{O}_3$  clusters are the biggest and additional ECAP process only slightly decreased clusters size. Metallographic analysis clearly indicates that  $\text{Al}_2\text{O}_3$  powder is not homogeneously distributed inside recycled samples. However, despite inhomogeneous distribution of the  $\text{Al}_2\text{O}_3$  powder, SSR recycled composites have slightly increased compressive flow stress and hardness compared with samples obtained without any  $\text{Al}_2\text{O}_3$  powder addition.

Further improvement of mixing procedure and/or addition of chips comminution step should be sufficient to obtain more homogeneous  $\text{Al}_2\text{O}_3$  powder distribution. This should lead to the further improvement of material strength and hardness. Future research should be based on investigation of the heat treatment influence on mechanical properties of the composites based on aluminum waste.



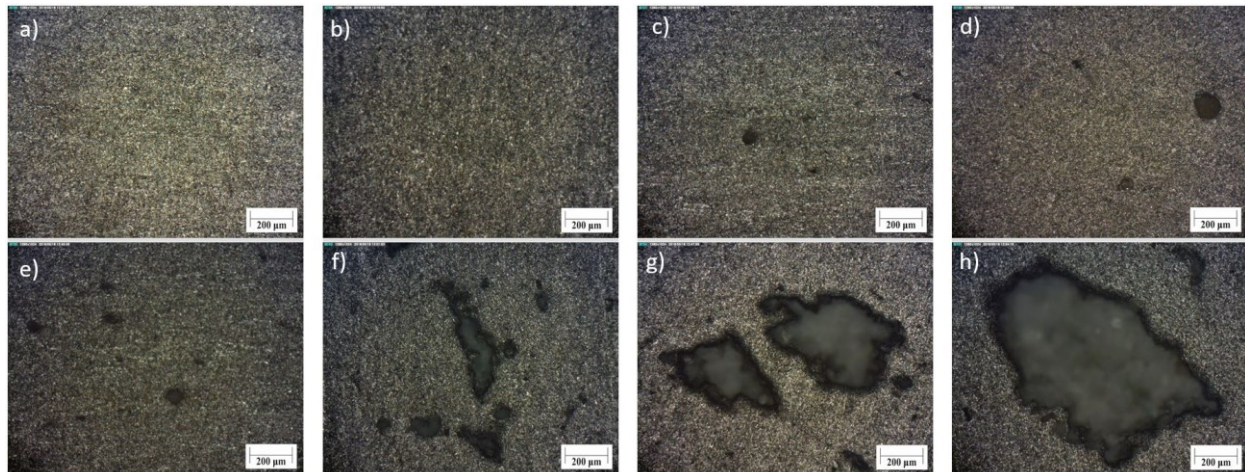


**Figure 6.** Composites based on aluminum waste: a) DE+ECAP without  $\text{Al}_2\text{O}_3$  b) DE without  $\text{Al}_2\text{O}_3$  c) DE+ECAP with 2 g  $\text{Al}_2\text{O}_3$  d) DE with 2 g  $\text{Al}_2\text{O}_3$  e) DE+ECAP with 5 g  $\text{Al}_2\text{O}_3$  f) DE with 5 g  $\text{Al}_2\text{O}_3$  g) DE+ECAP with 8 g  $\text{Al}_2\text{O}_3$  h) DE with 8 g  $\text{Al}_2\text{O}_3$

#### 4. Conclusion

According to this investigation, solid state recycling of EN AW 6082 alloy chips with  $\text{Al}_2\text{O}_3$  powder addition in order to produce composites based on aluminum waste can be successfully performed using the combination of DE and ECAP process. Further conclusion can be drawn:

- Improvement of mechanical properties of SSR composites produced only with DE can be achieved by additional SPD, i.e. ECAP process.
- Addition of  $\text{Al}_2\text{O}_3$  powder improves mechanical properties of recycled composite until certain limit when they start to deteriorate. More detailed research should try to find optimal amount of  $\text{Al}_2\text{O}_3$ .
- It can be stated that chips comminution and more homogeneously distributed  $\text{Al}_2\text{O}_3$  would lead to even better mechanical properties.

#### REFERENCES

- [1] Stacey, M., (2015), *Aluminium Recyclability and Recycling: Towards Sustainable Cities*, Published by Cwningen Press, International Aluminium Institute, Nottingham + Llundain, ISBN 978-0-9930162-1-9.
- [2] Allwood, J.M., Cullen J.M., Cooper, D.R., Milford, R.L., Patel, A.C.H., Carruth, M.A., McBrien M., (2010), *Conserving our metal energy: Avoiding melting steel and aluminum scrap to save energy and carbon*, WellMet2050 izvještaj, Sveučilište u Cambridgu, ISBN 978-0-903428-30-9, 2010.
- [3] Cullen, J.M., Allwood, J.M., (2013), *Mapping the Global Flow of Aluminum: From Liquid Aluminum to End-Use Goods*, Environmental Science & Technology, Vol. 47 (7), pp. 3057–3064.
- [4] Allwood, J.M., Cullen, J.M., Carruth, M.A., (2012), *Sustainable Materials with Both Eyes Open*, UIT Cambridge, ISBN 190686005X, 9781906860059.
- [5] Paraskevas, D., Kellens, K., Renaldi, Dewulf, W., Duflou, J.R., (2016), *4.10 Resource Efficiency in Manufacturing: Identifying Low Impact Paths*, 10th Global Conference on Sustainable Manufacturing, pp. 271-276.
- [6] Gronostajski, J., Matuszak, A., (1999), *The recycling of metals by plastic deformation: an example of recycling of aluminum and its alloy chips*. Journal of Materials Processing Technology, Vol. 92-93, pp. 35-41.
- [7] Shamsudin, S., Lajis, M.A., Zhong, Z.W., (2016), *Solid-state recycling of light metals: A review*, Advances in Mechanical Engineering, Vol. 8(8), pp. 1–23.
- [8] Vrelinden, B., (2003), *Severe plastic deformation of metals*, Metalurgija - Journal of Metallurgy, pp. 165-182.
- [9] Cui, J., Roven, H.J., (2010), *Recycling of automotive aluminum*, Transaction of Nonferrous Metals Society of China, pp. 2057-2063.
- [10] Luo, P., McDonald, D.T., Zhu, S.M., Palanisamy, S., Dargusch, M.S., Xia, K., (2012), *Analysis of microstructure and strengthening in pure titanium recycled from machining chips by equal channel angular pressing using electron backscatter diffraction*, Materials Science & Engineering A 538, pp. 252-258.
- [11] Cui, J., Guo, Wei, Roven, H.J., Wang, Q., Chen, Z., Peng, T., (2011), *Recycling of Aluminum Scrap by Severe Plastic Deformation*, Materials

- science forum, Trans Tech Publications, Vol. 667-669, pp. 1177-1182.
- [12] Mohamed, I.A.E.A., Eun, Y.Y., Hyoun, S.K., (2013) *Recycling of AlSi8Cu3 alloy chips via high pressure torsion*, Materials Science & Engineering: A, Vol. 560, pp. 121-128.
- [13] Fogagnolo, J.B., Ruiz-Navas E.M., Simon M.A., Martinez M.A., (2003), *Recycling of aluminum alloy and aluminum matrix composite chips by pressing and hot extrusion*, Journal of Materials Processing Technology, Vol. 143-144, pp.792-795.
- [14] Samuel, M., (2003), *Reinforcement of recycled aluminum-alloy scrap with Saffil ceramic fibers*. Journal of Materials Processing Technology, Vol. 142, pp. 295-306.
- [15] Tekkaya, A.E., Schikorra, M., Becker, D., Biermann, D., Hammer, N., Pantke, K., (2009), *Hot profile extrusion of AA-6060 aluminum chips*. Journal of Materials Processing Technology, Vol. 209, pp. 3343-3350.
- [16] Ahmad, A., Lajis, M.A., Yusuf, N.K. (2017), *On the Role of Processing Parameters in Producing Recycled Aluminum AA6061 Based Metal Matrix Composite (MMC-ALR) Prepared Using Hot Press Forging (HPF) Process*, Materials, Vol. 10 (9).
- [17] Duplančić, I. (2007), *Obrada deformiranjem*, Faculty of electrical engineering, mechanical engineering and naval architecture, Split.





# Computer Simulations of Robot integrated Production Processes with KUKA Sim Pro

**Duško LUKAČ**

IEEE German Section, Germany

dlukac@aol.com

## Keywords

*Industrial Robot*

*Simulation*

*Pick-and-Place, Cube*

*KUKA Sim Pro 3.0*

*Education*

## Early information

**Abstract:** This work presents the example of the simulation of the industrial robot system, as a part of the simulated production process for educational purposes. Already in an early project phase of the development of the production process, optimal layouts have to be provided, in order to simplify the practical implementation of the idea. In this early phase of the idea development, it should be recognized, whether the deliberate plan has the potential to become value-added process and with it rewardingly, or if it needs to be adapted, or even stopped. Simulation example is carried out by dint of the simulation software KUKA Sim Pro in version 3.0. Different functions for forming and connection of production components, as for example integration of the signals, physical properties, robot cinematics and accessories, are presented. The paper comprises the explanation of the simulation of the industrial robot KR6 R900 sixx (Agilus).

## 1. Introduction

According to the definition [1] "The simulation is the procedure to the replication of a system with his dynamic processes in an experimental model to reach the knowledge which is transferable on the reality." In the usual case, simulations are computer-aided processes; nevertheless, they can be processed also beyond a computer-aided system, for example, in the form of physical experiments. As a result of the progressive development of the computer technology, with the simulation has originated a method of the detailed description and post-sensation of systems, close to reality. In the industrial area, simulations are used for verifying, validating and optimizing manufacturing processes and, hence, can be applied in the planning phase, as well as in the realization and later operating phase. Comparing the simulation systems for robots of today with those of the 90s, it can be argued, that compared to the 90s, there are nowadays a lot of useful simulation systems which can be effortlessly used in the industrial practice and education. The rising offer of such simulation systems hangs immediately together up with the development of the IT technology and the computer engineering. As stated in [2], the middle and the end of the 90's have been marked by the use of the Java based systems. The main improvement of the robot simulation systems, has been caused by the development of the suitable simulation robot libraries, also of the libraries for older industrial robot models [3] which have been already mathematically well modelled in the 60's. There are many reasons nowadays why to use simulation systems in industrial practice. As stated by [3] by using of simulations wrong decisions can be avoided already in planning stadium and therefore they are sound decisive factor in the planning process. Furthermore they can save the costs because in

the regularly case, the simulation costs are much lower as investment costs or the target cost of the real process. Behind it, simulation leads to a more quick solution than analytic procedures, detailed representation of the existing system can lead to new cognitions and often the simulation technology is generally the only analytical possibility to scrutinize the project, because a real realization of the model would not be possible in practice. All those are factors, which support the idea of the necessity of simulation systems' usage in the industry but also in the educational practices at school and/or universities. However, the successful use of such systems requires profound knowledge, not only about the simulation software itself, but also about the margin disciplines and branches of learning, which concern the real simulation problem. Especially the 3D fabric simulation is complex and its implementation requires knowledge in different fields" [4, p. 634]. In the following section, it will be, with the help of a practical problem formulation explained, how industrial robot simulation software can be used in the practical case. At first sight, 3D simulation seems to be a complicated and special procedure which is suited only for bigger enterprises. Besides, the software can be used regardless of the company size and employee's number and thus achieve substantial success. The simulation software can be applied, as well as by the staff from the logistics and production, or from construction area. With the simulation software, it is possible to analyse changes in the operational procedures and it's the effects on the virtual world. With changes in the components and arrangements, the optimum investment construction can be presented, without having to carry out changes in the real circumstances. With the simulations of the production

planning, it is thereby possible to examine the processes, before the area is really realized. Depending on the precision of the simulation, the results are more valuable or not [5].

Costly and blind solutions, like calculation tables, are thereby cancelled and can be substituted with optically understandable representations. Altogether, with the simulation more quality and security can be reached.

## 2. System Components and Simulation Environment

The choice of the suitable simulation software is one of the important decisions in the simulation practice. To find right one for the use at university, requires the knowledge of the technical systems and also the knowledge about the industrial robot market. Different criteria influence this choice, as for instance. Functional demands, as e.g. functionality, IT-technical demands, as e.g. performance or IT-liability, demands to the architecture of the software, as e.g. Software Multitenancy, other criteria, as e.g. price, reputation, support, technical quality of simulation result etc.. Details about the criteria taken to choose the appropriate software are explained in [7]. Accordingly, especially hardware demands and the licensing conditions have to be taking into consideration [7, p. 1013]. Out of the different robot industrial simulation systems available on the market, as e.g. RoboGuide by FANUC or Robot Studio by ABB, the KUKA SIM Pro software has been used in the realization of the project described in this paper. The main reason for it, are the hardware demands, because simulation is applied to the existing industrial robot KUKA KR6 R900 sixx, which is also available in the library of the named simulation platform.

### 2.1. Simulation Software KUKA.Sim Pro

KUKA.Sim Pro is a special program for the creation of 3D-layouts of arrangements with KUKA industrial robots. Any layouts and draughts can be simulated and be examined with it. Therefore, the software system is appropriate for engineering or system integrators. The program library is extended compared with the older software versions and it disposes numerous smart components and geometries with own parametric behavior, as e.g. conveyor belts or light barriers. The software offers, also wide-ranging API and COM functionalities which allow the integration of the own plug-ins. An integration of the Python scripts is also possible. Optionally are available possibilities for imports of different CAD formats as Siemens NX, CATIA V5, STEP or Pro Engineer. By using of the virtual machine, the KUKA SIM Pro software can be directly coupled with the real time programming software of KUKA, so called Office Lite application, so that simulated program application can be transferred to the real industrial robot system and can be tested under the real environmental conditions [8,10].

### 2.2. Industrial Robot KR AGILUS R900 sixx

The KR AGILUS R900 sixx robot reaches maximum repeat accuracy and continuous precision thanks to his robust construction. It is known as one of the quickest robots of the world, what became successfully presented in numerous advertising campaigns of the KUKA Company [9]. At extreme speed the robot reduces the cycle times and on that way increases the manufacturing quality without getting out of the tact. The robot disposes with the highest precision characteristics on the smallest space thanks to his integrated energy supply and proven KR C4 compact control unit. Therefore this systems has been used in the following practical application, described in the next section. The main characteristics of the robot are summarized in the Table 1:

**Table 1.** Main Characteristics of KR AGILUS R900 sixx

CHARACTERISTIC	VALUE
Nominal load / Maximal load	3 kg / 6 Kg
Interfaces	USB, EtherNet, DVI-I
BUS connections	PROFINET, EtherNet/IP, PROFIBUS, DeviceNet, EtherCAT
Position repeat accuracy	+/- 0,03mm
Axis	6
Velocity with nominal load	300 °/s

## 3. Real Environment and Simulation

The real simulation environment is introduced in following block representation.

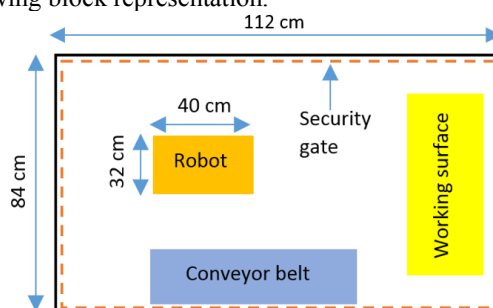


**Figure 1.** Block representation of the real environment

The purpose of the project is the creation of a program design in addition to the digital simulation of a really existing robot system in Sim KUKA Pro 2.2.2, using the available KUKA KR6 R900 sixx robot and conveyor belt connected with the robot control unit [11]. This is presented in the Figure 2.

Once the robot and conveyor belt program are started, if not already in the basic position, the robot moves first in its basic position. A conveyor belt, with integrated light barrier, transports an aluminium cube with the dimensions (HxWxD): 100 mm x 100 mm x 100 mm in the defined position. As soon as the conveyor belt is launched, the robot moves in the pre-position for removal of the cube and waits, till the workpiece interrupts the light barrier.



Figure 2. Robot system basic position



Figure 3. Conveyor belt with aluminium cube

Then, it removes the cube from the defined position and places it, in the working surface in the form of a palletizing task.



Figure 4. Palletizing the cubes

This continuously task is repeated till all 11 cubes are palletized.

### 3.1. Control program extract

The extract of the real control program written in KUKA Robot Language used for this task and combined with the PLC control unit is presented in the following:

*;1. First section*

*WAIT FOR (IN 7 , WORKPIECE CONVEYOR')*

*IF \$IN [7]==TRUE THEN*

*WAIT Time=1 sec*

*PTP BAND1 Vel=100% PDAT10 Tool[1]:flange Base[0]  
OUT 1 'Gripper open' State=FALSE OUT 4 'Gripper  
closed' State=TRUE PTP UBAND1 CONT Vel=100%  
PDAT9 Tool[2] Base[0] PTP UP11 CONT Vel=100%  
PDAT6 Tool[1]:flange Base[0] PTP P11 Vel=100%  
PDAT8 Tool[1]:flange Base[0] OUT 4 'Gripper closed'  
State=FALSE OUT 1 'Gripper open' State=TRUE PTP  
UP11 CONT Vel=100% PDAT6 Tool[1]:flange Base[0]  
PTP UBAND1 Vel=100% PDAT9 Tool[2] Base[0]*

*ELSE END IF*

The program waits on the workpiece at the removal position of the conveyor belt. This is realized with the *WAIT FOR (IN 7 ,WORKPIECE CONVEYOR')* command. After the input signal reaches the logical TRUE condition, the robot waits one second and moves to the gripping position „PTP BAND1“. On the workpiece storage position P11 the grip arm is opened again, the workpiece is stored and the waiting position over the decrease point of the conveyor belt is started up. Now, here the robot waits again for a new workpiece. In the both next other processes the procedure is the same, merely the storage position of the workpiece changes.

### 3.2. Simulation components

This task has been simulated. In the first step of the simulation, the components of the cube robot have been defined [12]. These are presented in the Figure 5.

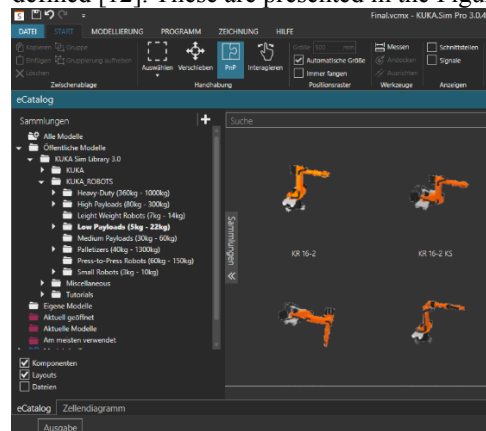


Figure 5. Simulation components draft

The simulation components are numerated and presented in the Table II.

**Table 2.** Simulation components

POSITION	DESCRIPTION
1	Robot KR6 R900sixx
2	Control Unit
3	Peripherie
4	Sensor (H-Sensors)
5	Security Gate
6	Conveyor belt
7	Creator

All listed components are real, excluding the "Creator", which is software based simulation function for creating the cubes. All components are selected and composed from the program library of KUKA Sim Pro 2.2 Library [cf. 10]

#### 4. Robot programming with the Simulation software

In this project the programming has been done with RSL and KUKA.Office-Lite. Taking into account the nominal amount of the publication pages, the following description is limited to the description of the RSL programming. The detailed steps of programming are described in [10,13]. In order to write the program, at first the robot must be activated. For this purpose, two options are possible, activation by choice of a "sheet" on the robot foot or activation by direct choice of a robot in the tab "Teachen".

##### 4.1. Main and subroutines

If the task is complex, it is recommended that subroutines containing similar characteristics are defined. The main sequence is already introduced by the simulation system. It is used for activation of the subroutines. For the realization of this task in total 13 subroutines have been written. The sequences mentioned are presented in the Figure 7:

The subroutines for gripping and release of the working piece, exist out of one instruction. The output necessary for gripping procedure and for release of the working piece, changes in this instruction the logical condition. This includes the definition of the gripping area, and becomes realized by changing the parameters of the robot. The subroutine BT1, contains the basic geometrical coordinates of the simulation space and is used for definition of the other subroutines in order to realize all gripping and release steps.

After following further adjustments necessary for creation of the simulation program, the final simulation has been realized. In-between, it is extend with visualization of the geometrical trajectories in order to show the differences between the movement types of the robot a for example point-to-point, cyclic or linear movement.

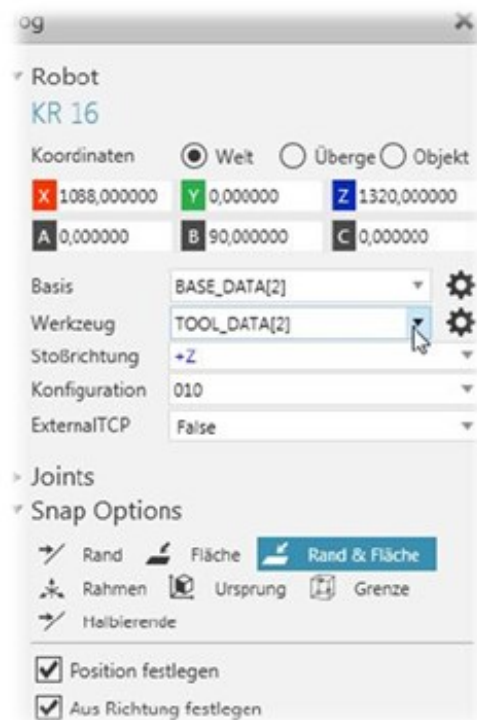


**Figure 6.** Activation of the robot

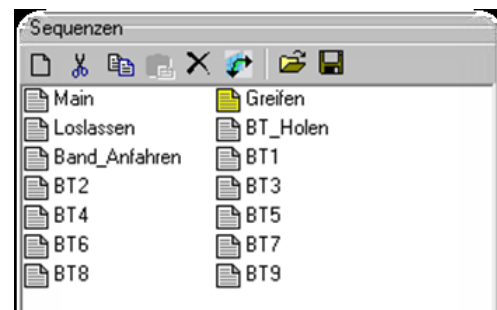


**Figure 7.** Main and subroutines

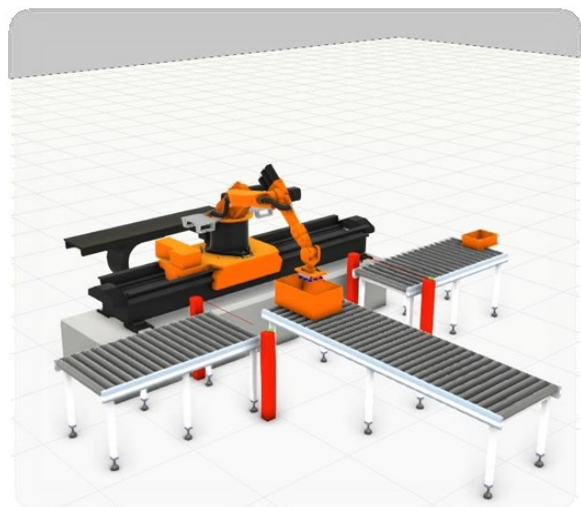


**Figure 8.** Signal simulation without tracing signals D



## 5. Conclusion

This work presents a practical example of realization of the industrial robot simulation based on the real KUKA robot system (KR6 R900 sixx (Agilus) and the Software KUKA Sim Pro V.3.0. It includes initial explanation how peripheral actuators can be implemented in the process by means of the simulation software and how the simulation software has been chosen. The main effort in the simulation task, is related to the configuration and programming of the geometric trajectories and calculations of them. It includes the transformation of the coordinates, by using of different coordination system transformation methods and including them into the program writing task. This part of the work is, by reason of the scale, not presented in this work.

## REFERENCES

- [1] VDI (2018) „*VDI-Richtlinie: VDI 3633 Anwendung der Simulationstechnik zur Materialflußplanung*“ [https://www.vdi.de/nc/richtlinie/alt\\_vdi\\_3633-anwendung\\_der\\_simulationstechnik\\_zur\\_materialflussplanung\\_/](https://www.vdi.de/nc/richtlinie/alt_vdi_3633-anwendung_der_simulationstechnik_zur_materialflussplanung_/), 03.07.2018, 11:46h
- [2] Wloka, DW (1991), *Robotersimulation, (Robot simulation)*, Springer-Verlag Berlin Heidelberg, ISBN: 978-3-540-53828-8
- [3] Degen, H.-J., Fraunholz, L., Klein, J (1992), *CBT-gestützte Demo-Version von RobotoCAM (CBT-supported demo version of RobotoCAM.)*, BIS Allgemeine Elektrotechnik 1992
- [4] Tewkesbury, G. and Sanders, D. (1999) "A new robot command library which includes simulation", *Industrial Robot: An International Journal*, Vol. 26 Iss: 1, pp.39 – 48
- [5] Niessner, Helmut (2013), „*Advantages of Simulations*“, Simulations, available at <http://simulations.at/wp/index.php/2013/01/vorteile-von-simulationen/>, 16.01.2017, 12:38h
- [6] Mozafari, Vajiha and Payvandy, Pedram (2016) "Study and comparison techniques in fabric simulation using mass spring model", *International Journal of Clothing Science and Technology*, Vol. 28 Iss: 5, pp.634 – 689
- [7] Lukac, Dusko (2016), "Using Robot Simulation Applications at the University – Experiences with the KUKA Sim", MIRPO IEEE Conference 2016, Opatija, Croatia, pp.1012-1016
- [8] KUKA AG (2017), „*KUKA SIM Pro*“, available at [http://www.kuka-robotics.com/germany/de/products/software/kuka\\_sim/kuka\\_sim\\_detail/PS\\_KUKA\\_Sim\\_Pro.htm](http://www.kuka-robotics.com/germany/de/products/software/kuka_sim/kuka_sim_detail/PS_KUKA_Sim_Pro.htm), 14.01.2017, 12:33h
- [9] KUKA AG (2017), Playing Tennis, <http://www.ingenieur.de/Fachbereiche/Robotik/Tischtennis-Duell-Timo-Boll-Kuka-Roboter-PR-Ente>
- [10] BBS Wolfsburg (2016), *Guide for Configuration of KUKA.SimPro and KUKA.OfficeLite*, Berufsbildende Schulen Wolfsburg, June 2016, pp.1.15
- [11] Lukac, Dusko, Lenz, R., Siebertz, J. and Unruh, A. (2017) "Design concept for the Realization of the Cube-Robots with Simulation Software KUKA SIM Pro 2.2.2", Project White Paper, December/January 2016/17, pp.1-29
- [12] Lukac, Dusko and Sperling, J. (2016), "Enhancement of the KR-Agilus robot with conveyor belt for positioning of the workpieces", Project White Paper, July - November 2016, pp.1-34
- [13] KUKA College (2012), "KUKA.SIM 2.2 Pro", KUKA Roboter AG, Version 08
- [14] .06.2012, pp.1-91



# PVD tehnologija

**Mauro MARETIĆ<sup>1</sup>, Luciano GRŽINIĆ<sup>2</sup>  
and Goran VRATOVIĆ<sup>3</sup>**

1) Politehnika Pula, Visoka tehničko-poslovna škola

Polytechnic of Pula, College of applied sciences

Riva 6, 52100 Pula, **Croatia**

2) ULJANIK Strojogradnja Diesel d.d.

ULJANIK Mechanical Engineering Diesel JSC

Flaciusova 1, 52100 Pula, **Croatia**

3) Plazma tehnika d.o.o.

Plazma tehnika d.o.o.

Zona male privrede 12, 52216 Galizana, **Croatia**

mauromaretic@gmail.com

luciano.grzanic@uljanik.hr

gvratovic@gmail.com

## Ključne riječi

*Tvrdoća*

*Prevlake*

*Nanošenje*

*Materijali*

## Keywords

*Hardness*

*Coating*

*Deposition*

*Materials*

## 1. Uvod

Nanošenjem tvrdih slojeva u parnoj fazi povećava se tvrdoća i otpornost na trošenje supstrata. Supstrati mogu između ostalih biti metalni materijali (čelici, Ti-legure, Al-legure) [1, 2]. U nanošenju tvrdih prevlaka dominiraju dva osnovna postupka:

- fizičko nanošenje prevlake u parnoj fazi (physical vapor deposition) [PVD]
- kemijsko nanošenje prevlake u parnoj fazi (chemical vapor deposition) [CVD].

Kod PVD postupka materijal koji se nanosi dovodi se u parnu fazu, te se naknadno taloži na površini supstrata

## Pregledni rad

**Sažetak:** Materijal, s obzirom na svoj kemijski sastav i strukturu ima određena svojstva (kemijska, fizikalna, mehanička, tehnološka). Svojstva materijala ovise o njihovom kemijskom sastavu, te o vezama između atoma i molekula. Svojstva materijala postižu se ovisno o postupku prerade. Često dobiveni materijal ne zadovoljava sva potrebna svojstva, pa se naknadnim različitim obradama pokušavaju postići željena svojstva. Poseban naglasak dan je na dobivanju mehaničkih svojstava. Kod strojnih dijelova posebna se pažnja mora posvetiti površinskoj tvrdoći. Tijekom povijesti posebno je mjesto zauzimalo površinsko otvrdnjavanje čelika postupcima toplinske obrade, zbog jedinstvene sposobnosti čelika da mu se utjecajem topline postignu željena svojstva. Nadalje, u primjeni su postupci toplinsko - kemijske obrade gdje u površinu materijala difundiraju elementi koji stvaraju tvrde slojeve. Elektrodepozicijskim postupcima se također mogu na površinu materijala nanositi tvrde prevlake i prevlake otporne na koroziju. U posljednjih tridesetak godina ubrzano se razvija postupak nanošenja tankih prevlaka u parnoj fazi debljine nekoliko mikrometara kojima se mogu poboljšati tražena svojstva. Na taj način dobivene tanke prevlake imaju jako dobra tražena svojstva i mogu se nanositi na mnogim metalnim materijalima, keramici, polimerima.

## PVD technology

### Review paper

**Abstract:** Every material, regarding its chemical composition and structure, has certain properties (chemical, physical, mechanical, technological). Properties of material are dependent of its chemical composition and bonds between atoms and molecules. Depending on processing method, different material properties are achieved. Often not all desired material properties are achieved, so different additional processing is applied to achieve them. Special emphasis is given to the achievement of desired mechanical properties. Special attention must be paid to the surface hardness of workpieces. Surface hardening of steel by heat treatment has historically had special importance because of the unique ability of steel to achieve desired properties by influence of heat. Different thermochemical treatments, where chemical elements that create hard layers diffuse into the surface of material, are used as well. Hard coatings and corrosion resistant coatings can be applied on materials surface by electrodeposition processes as well. In the last thirty years, process of application of thin, several micrometers thick layers in vapor phase, which improve desired properties, is developed rapidly. Thin coatings created by this method have very good desired properties and they can be applied on many metals, ceramics and polymers.

stvarajući tvrdi sloj. Kod CVD postupka materijal koji se nanosi dolazi na zagrijanu površinu supstrata kao kruti materijal iz parne faze, te kemijskim reakcijama stvara tvrdi sloj [1]. Ovim postupcima dobivaju se prevlake s veoma dobrim tribološkim svojstvima za izradu limova i izuzetno tvrde za izradu raznih alata [3]. Tvrde prevlake su uglavnom keramički spojevi oksidi, karbidi i nitridi [1]. Osim ovih postupaka postoji cijeli niz elektrokemijskih i kemijskih postupaka koji u mnogim aplikacijama imaju prednosti. U posljednje vrijeme posebnu pozornost privlači bestrujno (electroless) nanošenje NiP slojeva [4].

## 2. Nanošenje prevlake PVD postupkom

PVD i CVD postupkom se na površinu supstrata nanosi tanki sloj koji može poboljšati neka svojstva:

- tvrdoću
- otpornost na trošenje
- električna svojstva
- antikorozivna svojstva
- stvaranje lijepih boja za dekorativne potrebe.

Debljina sloja može se kretati u izrazito malim debljinama od nekoliko mikrometara. Prednost PVD metode nad CVD metodom je i velika brzina nanošenja sloja (u nekim slučajevima i 0,025mm/s). Ovom se metodom može nanijeti sloj na različitim supstratima (metali i njihove legure, te kompozitni materijali). Struktura i svojstva sloja ovise o bombardiranju rastućeg sloja na površini supstrata s česticama velike energije (ioni ili neutralne čestice) iz plazme [1]. PVD postupak se dijeli u dvije osnovne skupine, prema načinu prevođenja materijala prevlake:

- postupak raspršivanja
- postupak isparavanja.

### 2.1. Postupak raspršivanja

Ovim se postupkom energetskim projektilima gađa materijal kojeg nanosimo (odvajaju se atomi i molekule i nanose se na površinu supstrata). Materijal kojeg nanosimo i supstrat nalaze se u vakuumskoj komori. Nanosivi materijal je priključen na negativni pol izvora istosmjerne električne struje, a supstrat na pozitivni pol izvora istosmjerne električne struje. Materijal kojeg nanosimo se pogađa ionima iz plazme, te se raspršuje po supstratu. Radni tlak se kreće između 2,66 i 3 Pa. Proces započne kada se u komoru pusti inertni plin (najčešće argon) [1].

### 2.2. Postupak isparavanja

Kod postupka isparavanja para se stvara iz izvora materijala koji je zagrijavan različitim postupcima. Ti postupci mogu biti elektrootporni, elektromagnetskom indukcijom, električnim lukom, elektronskim snopom ili laserom. Osnovni princip rada je da izvor isparavanja, potrebni materijal dovede u stanje pare, te nanese tvrdi sloj na podlozi koja se nalazi nasuprot izvoru isparavanja [1].

Kod PVD postupka temperatura na kojoj se nanosi prevlaka iznosi do 500 °C [5-7].

U usporedbi s pojedinim tvrdim materijalima u širokoj primjeni

- alatni čelici:
  - kaljeni ugljični alatni čelici 57 – 65 HRC,
  - kaljeni brzorezni čelici 63 – 66 HRC,
  - kaljeni legirani alatni čelici za hladni rad 52 – 67 HRC,
- sinterirani tvrdi metali 1400 – 1750 HV [8],

vidljivo je da su tvrdoće prevlaka dobivenih PVD metodom znatno tvrđe (tablica 1) [9].

U tablici 1 vidi se da među različitim prevlakama postoji i razlika u tvrdoći. Sve te prevlake su tvrđe od navedenih materijala [8]. U tablici 1 i na slici 3 [10] vidi se da je debljina prevlaka izuzetno mala (do 6 µm).

Prema jednadžbi Halla i Petcha moguće je na osnovu veličine kristalnog zrna procijeniti tvrdoću dobivene prevlaka [1]:

$$H = H_0 + kd^{-1/2}, \quad (1)$$

gdje je  $H$  tvrdoća,  $H_0$  tvrdoća kristalne rešetke,  $d$  veličina zrna, a  $k$  konstanta ovisna o vrsti materijala.

Pošto su prevlake dobivene PVD metodom izuzetno tanke, i samo kristalno zrno je izuzetno malo. S tako malim kristalnim zrnom povećava se tvrdoća prevlake.

Adhezija je najznačajnije svojstvo prevlake, ali je najmanje istraženo i razjašnjeno [11, 12]. Za dobivanje kvalitetne adhezije potrebno je s površine supstrata eliminirati sve ostatke korozije. Da bi postigli zadovoljavajuću adheziju, supstrat mora imati sličnu strukturu zrna ili kristala, te sličnu istezljivost kao i materijal prevlake. Prije nanošenja prevlake potrebno je površinu supstrata očistiti i polirati. Kako ne bi utjecali na strukturu površine supstrata preporuča elektrolitičko čišćenje ili čišćenje dekapiranjem, te elektropoliranje. Mehaničkim čišćenjem se može izobličiti struktura zrna supstrata čime se otežava adhezija između supstrata i prevlake, stoga se ono ne preporuča. Za dobru adheziju je također potrebno da prevlaka bude koherentna, odnosno da materijal prevlake bude finoiznat i što čišći [12].

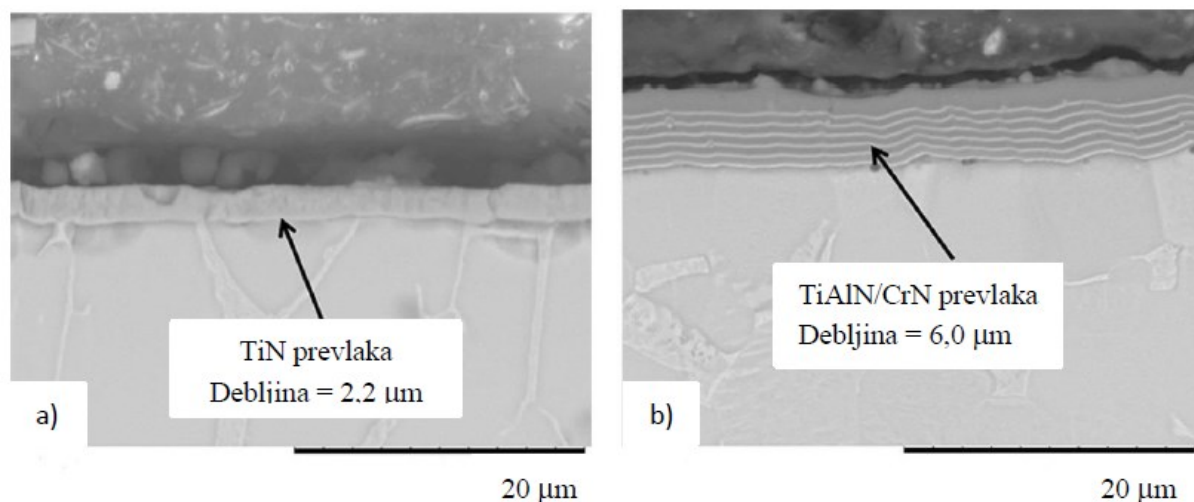
Poznata su četiri tipa adhezije (slika 4) [11].

Nadalje, za primjenu PVD tehnologije bitna su i tribološka svojstva. Prevlake dobivene pomoću PVD postupaka pokazala su veliku otpornost na trošenje [13-15].

**Tablica 1.** Svojstva prevlaka dobivenih PVD metodom [9]

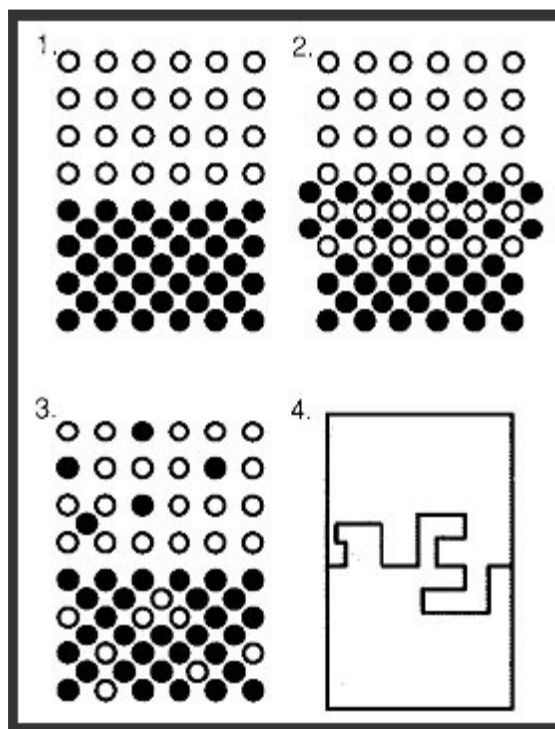
**Table 1.** Properties of PVD coating [9]

Materijal prevlake	TiN	TiCN	CrN	2TiAlN	TiAlN	TiAlN+WC/C
Mikrotvrdoća HV <sub>0,05</sub>	2300	3000	1750	3000	3500	2300
Koeficijent trenja prema čeliku (suho)	0,4	0,4	0,4	0,4	0,4	0,2
Debljina prevlake (µm)	1-4	1-4	1-4	1-5	1-3	2-6
Maksimalna radna temperatura (°C)	600	400	700	800	800	800-1000



**Slika 3.** Debljine prevlaka nanosenih PVD metodom a) TiN prevlaka, b) TiAlN/CrN prevlaka [10]

**Figure 3.** Thicknesses of PVD coating a) TiN coating, b) TiAlN/CrN coating [10]



**Slika 4.** Tipovi adhezije: 1. glatka adhezija, 2. sloj nastao miješanjem, 3. difuzijska granica, 4. mehaničko zaključavanje [11]

**Figure 4.** Types of adhesion: 1. smooth transition, 2. compound layer, 3. diffusion bond, 4. mechanical locking [11]

PVD prevlake se u strojarstvu koriste zbog:

- velike tvrdoće,
- otpornosti na trošenje,
- malog koeficijenta trenja,
- otpornosti na koroziju [1, 16, 17].

Zbog tih svojstva PVD tehnologija primjenjuje se u izradi alata, medicinske opreme, te za potrebe dekoracije [16-18].

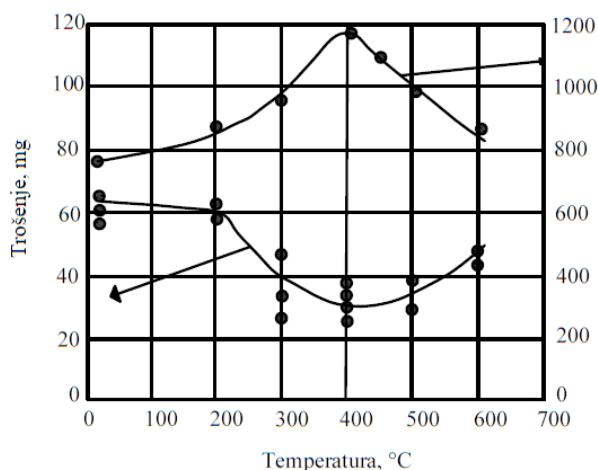
Osim u strojarstvu PVD tehnologija primjenjuje se u optoelektronici, mikroelektronici, memorijskoj tehnologiji, solarnoj tehnologiji [19, 20].

Do 2015 godine najveći porast PVD tehnologije zabilježen je u mikroelektronici, te je te godine 37,8% proizvodnje otpadalo na mikroelektroniku. 2013. godine izvršena je analiza i pretpostavilo se da će do 2024 godine sveukupni promet od 2 000 000 USD porasti na 5 000 000 USD [20].



### 3. Bestrujni (electroless) postupci nanošenja NiP slojeva

Osim ovih PVD i CVD postupaka postoji cijeli niz elektrokemijskih i kemijskih postupaka koji u mnogim aplikacijama imaju prednosti. U posljednje vrijeme posebnu pozornost privlači bestrujno (electroless) nanošenje NiP slojeva [4]. Mehanička svojstva zbog kojih se Ni-P prevlaka primjenjuje su visoka tvrdoća zbog koje Ni-P prevlaka također ima i veliku otpornost na abrazivno trošenje. Otpornost Ni-P prevlake na trošenje ovisi o sadržaju fosfora u prevlaci (slika 6) [21]. Trošenje također ovisi i o toplinskoj obradi jer se toplinskom obradom smanjuje trošenje prevlake (slika 7) [21]. Na slici 7 vidljivo je da se povećanjem temperature toplinske obrade povećavaju tvrdoća i otpornost prevlake na trošenje.



Slika 7. Utjecaj toplinske obrade na trošenje prevlake [21]

Figure 7. Effect of heat treatment on the wear of coating [21]

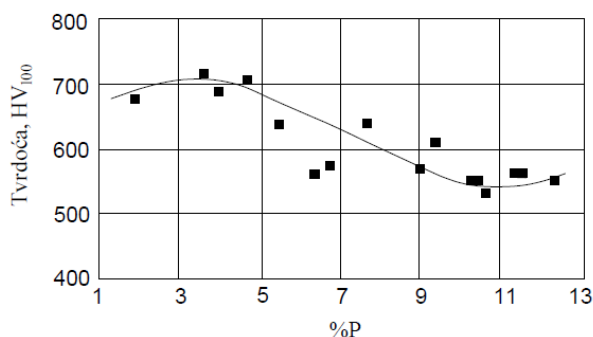
Pokazalo se da na trošenje Ni-P prevlake također utječu i sadržaj fosfora i toplinska obrada [22]. Toplinski neobrađena prevlaka manjeg sadržaja fosfora manje se troši od toplinski obrađene prevlake većeg sadržaja fosfora. Najveća otpornost na trošenje pojavljuje se pri toplinskoj obradi prevlake na temperaturi od 400 °C [23]. Tvrdoća bestrujno nanosene prevlake nikla ovisi o:

- sadržaju fosfora u prevlaci,
- toplinskoj obradi dobivene prevlake,
- sastavu legiranih elemenata u prevlaci.

U osnovi, sadržaj fosfora u kristalnoj rešetki nikla određuje hoće li mikrostruktura prevlake biti kristalnog ili amorfne oblika. Amorfni oblikom smanjuje se tvrdoća prevlake. Osnovna podjela prevlaka s obzirom na sadržaj fosfora i tvrdoću prikazana je u tablici 2 [24].

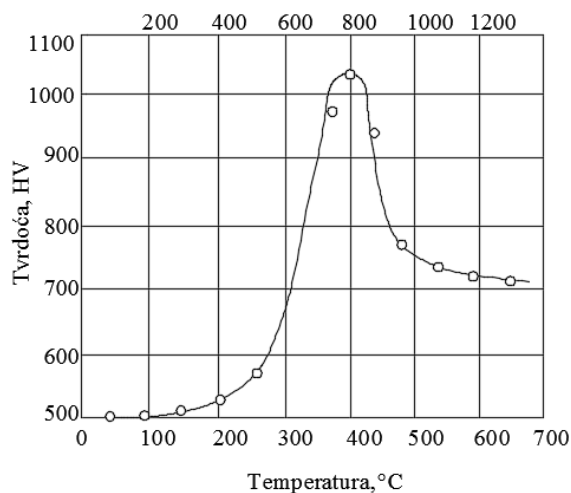
Ovisnost tvrdoće Ni-P prevlake o sadržaju fosfora prikazana je na slici 8 iz koje se može vidjeti da se najveća tvrdoća Ni-P prevlake dobiva kod sadržaja fosfora u prevlaci 3 – 4 %P, a najmanja kod sadržaja fosfora 10 – 11 %P [21]. U samoj prevlaci pri povišenim

temperaturama dolazi do strukturnih promjena koje ovise o sadržaju fosfora u prevlaci. Nakon toplinske obrade, prevlake sa manje od 4,5 %P i više od 11 %P (faze  $\beta$  i  $\gamma$ ) prelaze u  $\text{Ni}_3\text{P}$  fazu. Kod prevlaka koje sadrže između 4,5 %P i 11 %P,  $\beta$ -faza prelazi u  $\alpha$ -fazu. Toplinskom obradom prevlake, tvrdoća poraste na 950 do 1050 HV. Istraživanja su pokazala da se najveća tvrdoća prevlake može postići nakon zagrijavanja na temperaturi od 400 °C, u trajanju od jednog sata (slika 9) [21].



Slika 8. Ovisnost tvrdoće o sadržaju fosfora [21]

Figure 8. Dependence of hardness on phosphorus content [21]



Slika 9. Tvrdoća Ni-P prevlake s 10,5 % fosfora pri trajanju grijanja od jednog sata [21]

Figure 9. Hardness of Ni-P coatings with 10.5% phosphorus for a one-hour heating period [21]

Ispitivane su tvrdoće Ni-P prevlaka u odnosu na sadržaj fosfora te toplinskih obrada tih prevlaka. Rezultati ispitivanja prikazani su u tablici 3 [25]. Tvrdoća toplinski obrađene i toplinski neobrađene Ni-P prevlake ovisna o sadržaju fosfora. S porastom sadržaja fosfora smanjuje se tvrdoća Ni-P prevlake. Nadalje, ispitivane su i tvrdoće na Ni-P / Ni-B duplex prevlaci. Mjerena je tvrdoća s obzirom na debljine sloja i toplinsku obradu. Veća tvrdoća dobiva se kod dvoslojnih prevlaka, neovisno o tome jesu li toplinski obrađene. Najveća se tvrdoća može dobiti kod dvoslojnih toplinski obrađenih prevlaka [26].

Adhezija se može definirati kao privlačna sila koja djeluje između molekula različitih tijela koja se tijesno dodiruju. Adhezijske sile ovise o osnovnoj čvrstoći atomskih veza podloge (supstrata) i mikrostrukture prevlake. Zbog složenog odnosa između prevlake i podloge, još nisu poznati svi faktori koji djeluju na adheziju niti je poznat prihvatljiv način mjerenja adhezije.

Poznato je da se adhezija između prevlake i supstrata može povećavati eliminiranjem svih nečistoća sa supstrata prije nanošenja prevlake. Organska onečišćenja se uklanjaju na visokoj temperaturi (CVD postupak) [27]. Osim toga, s površine supstrata moraju biti eliminirani i svi ostaci korozije. Za postizanje zadovoljavajuće adhezije, materijal supstrata mora imati sličnu strukturu zrna ili kristala te sličnu istezljivost kao i materijal prevlake. Iz tog se razloga preporuča elektrolitičko čišćenje ili čišćenje dekapiranjem. Mehaničkim čišćenjem se može izobličiti struktura zrna supstrata čime se otežava adhezija između supstrata i prevlake, stoga se ono ne preporuča. Za dobru adheziju je također potrebno da prevlaka bude koherentna, odnosno da materijal prevlake bude sitnozrnat i što čišći [28].

Kod nanošenja prevlake, različiti supstrati s istom prevlakom stvaraju različite adhezijske sile. Kod supstrata s katalitičkim površinama za bestrujno nanošenje nikla, poput većine čelika i aluminija, adhezija je dobra. Ako se takvi materijali, primjerice aluminij, zagriju na temperaturu 190 – 210 °C u trajanju od 1,5 h, adhezija se povećava [29].

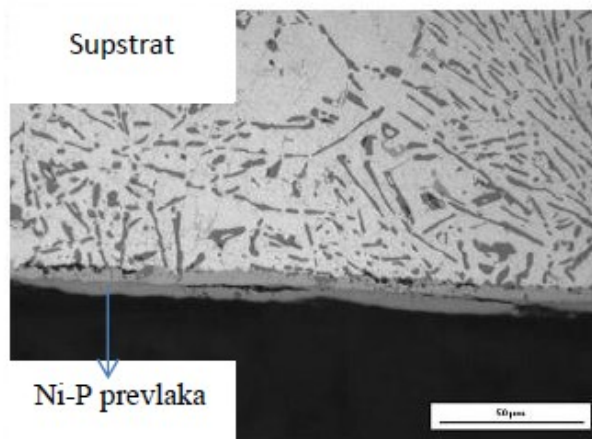
Kod nekatalitičkih površina, kao što su to površine nehrđajućih čelika, adhezija je znatno manja. Kod takvih vrsta prevlaka, adhezija se postiže stvaranjem međuprevlake između Ni-P prevlake i supstrata, koja će imati dobru adheziju sa niklom. Kod legura koje sadrže veće količine olova, kositra, kadmija i cinka, na površinu podloge nanosi se sloj bakra. Taj se postupak najčešće naziva „copper strike“. Adhezija se kod nekatalitičkih materijala povećava dugotrajnom toplinskom obradom jer na taj način fosfor iz područja u blizini supstrata difundira u sam supstrat [30].

Pokazalo se da se adhezija kod pojedinih aluminijskih legura može povećati nanošenjem sloja cinka [31; 32], dok se sa dva sloja cinka nanosena na isti način adhezijska sila dodatno povećava. Osim nanosenih slojeva cinka, adhezija ovisi i o toplinskoj obradi [32]. Istraživanja su pokazala da se adhezija Ni-P sloja na sinteriranom NdFeB materijalu može povećati i stvaranjem fosfatnog sloja [33].

Ispitivani su i utjecaji trajanja toplinske obrade na prevlaku, a dobiveni rezultati prikazani su na slikama 10 i 11 [34]. Iz slike 10 vidljivo je da nakon jednog sata grijanja između prevlake i supstrata postoje male pore, a iz slike 11 je vidljivo da nakon osam sati grijanja prevlaka i supstrat gotovo uopće nisu povezani.

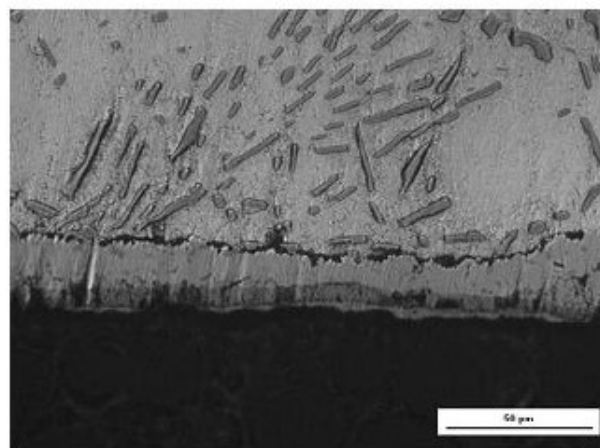
Već je napomenuto da austenitni čelik nije autokatalitički, stoga je prije nanošenja Ni-P prevlake na

takav čelik potrebno nanijeti tanki sloj nikla elektrodepozicijskim putem.



**Slika 10.** Presjek Ni-P prevlake; grijano na temperaturi od 550 °C u trajanju 1 h [34]

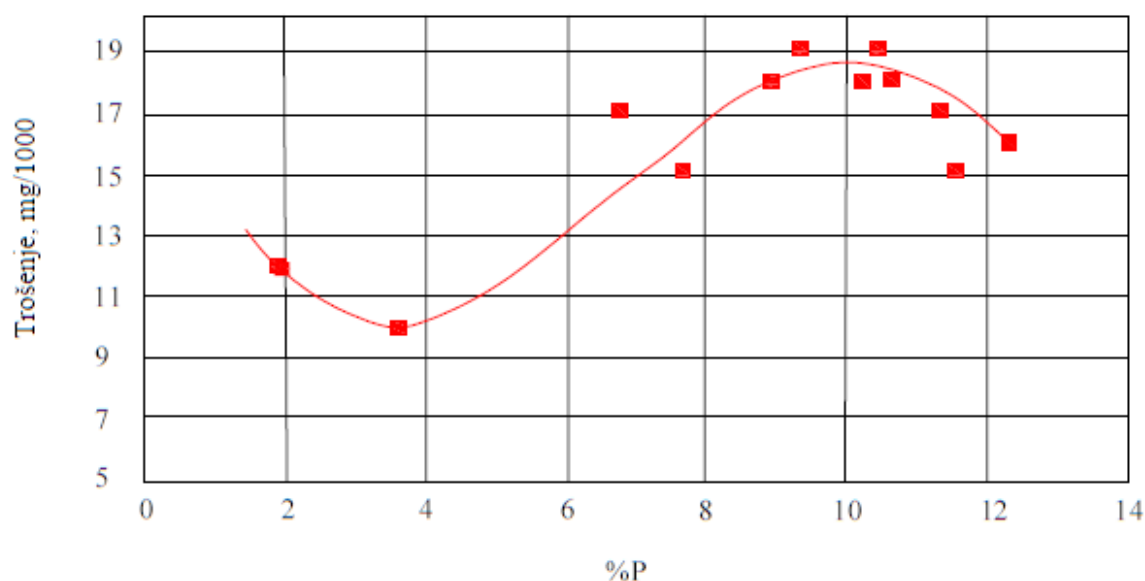
**Figure 10.** Cross section of Ni-P coatings; heated at 550 °C for 1 h [34]



**Slika 11.** Presjek Ni-P prevlake; grijano na temperaturi od 550 °C u trajanju 8 h [34]

**Figure 11.** Cross section of Ni-P coatings; heated at 550 °C for 8 h [34]

U postupku elektrodepozicijskog nanošenja nikla, austenitni čelik predstavlja katodu, a nikal anodu. Takav način nanošenja nikla zove se „nickel strike“. Sloj nikla nanosen na taj način dobro se povezuje s Ni-P prevlakom [29]. Kod nehrđajućeg čelika u zubarskoj tehnologiji prije bestrujnoga niklanja, elektronskim snopom u parnoj fazi (e-beam evaporation) nanosi se tanki sloj nikla debljine 50 nm te se zagrijava na temperaturu od 400 °C u trajanju od jednog sata [35]. Nadalje, dodatkom volframa u prevlaci (Ni-W-P) omogućuje se bolja adhezija Ni-P / Ni-W-P duplex prevlake na AZ91D magnezijevoj leguri [36]. Istraživanjem Ni-Cu-P prevlake nanosene bestrujnim postupkom na otvorene ćelije kod nehrđajućeg čelika, zaključeno je da bakar u prevlaci pomaže boljoj povezanosti sa supstratom [37].



**Slika 6.** Utjecaj sadržaja fosfora na otpornost na trošenje prevlake [21]

**Figure 6.** Influence of phosphorus content on coating wear resistance [21]

**Tablica 2.** Osnovna podjela prevlaka s obzirom na sadržaj fosfora i tvrdoću [24]

**Table 2.** The basic division of the coating with respect to the content of phosphorus and hardness [24]

Vrste prevlake	Sadržaj fosfora / %	Tvrdoća HRC	Struktura
Niski sadržaj	1 – 4	53 – 63	Kristalna
Srednji sadržaj	4 – 10	44 – 49	Kristalna
Visoki sadržaj	10,5 – 14	42 – 48	Amorfna

**Tablica 3.** Utjecaj sadržaja fosfora na tvrdoću toplinski neobrađene i obrađene prevlake [25]

**Table 3.** Influence of phosphorus content on hardness of untreated and treated coatings [25]

Sadržaj fosfora/%	Tvrdoća toplinski neobrađene prevlake HK100	Tvrdoća toplinski obrađene prevlake HK100
2 – 3	700	1000
6 – 9	550	920
10 – 12	510	880

#### 4. Zaključak

Zbog ubrzanog razvoja proizvoda i sve veće konkurencije na tržištu, rastu i zahtjevi prema materijalima koji se koriste. Da bi se zaštiti materijal od utjecaja okoline, posebnu pažnju treba posvetiti površini materijala. Što se tiče postizanja površinske tvrdoće, najbolji se rezultati dobivaju korištenjem postupaka u parnoj fazi (PVD). U vremenu koje slijedi, zbog povećanja zahtjeva prema materijalima koji se koriste, posebnu važnost treba usmjeriti na daljnji razvoj te tehnologije u cilju postizanja još boljih rezultata i ostvarivanja ekonomičnijeg tehnološkog procesa. Samom uspješnom realizacijom tih zahtjeva, postići će se i kvalitetna konkurencija na tržištu.

PVD postupci ne mogu zadovoljiti sve zahtjeve za površinskom modifikacijom strojnih dijelova. Pregled

moćnosti bestrujnih postupaka nanošenja pokazuje da se ovaj postupak nameće kao efikasan nadomjestak etabliranim postupcima modifikacija površina strojnih dijelova.

#### Potpora

Ovaj rad je sufinancirala Hrvatska zaklada za znanost projektom 5371.

Ovaj rad je sufinanciralo Sveučilište u Rijeci, broj potpore 13.09.1.1.02.

## LITERATURA

- [1] Rointan F. Bunshah, (2001), *Handbook of hard coatings*, University of California, Los Angeles, ISBN: 0-8155-1438-7, p 2, 8, 11, 12, 22, 62, 114
- [2] BALL SEAL, Ion implantation, PVD and CVD and their effects on Bal™ Seal performance, TR-24 (45-6-1) Rev. B / 05-07-02, p 2-9
- [3] Simon J. Montgomery, David M. Kennedy, Noel O'Dowd, *PVD and CVD Coatings for the Metal Forming Industry*, Dublin Institute of Technology, p 1-13
- [4] Maretić M., Smoljan B., Iljkić D., (2017), *Heat treatment of electroless Ni-P layers on an austenitic stainless-steel substrate*, *Materiali in tehnologije / Materials and technology* 51 No. 3, p. 413-417
- [5] Bouzakis K. D., Pappa M., Gerardis S., Skordaris G., Bouzakis E., (2012), *PVD Coatings' Strength Properties at Various Temperatures by Nanoindentations and FEM Calculations Determined*, *Tribology in Industry* 34 No. 1, p. 29-35
- [6] Polok-Rubinić M., Dobrzański L. A., Adamiak M., (2007), *Comparison of the adhesion and wear resistance of the PVD coatings*, *Journal of Achievements in Materials and Manufacturing Engineering* 20 No. 1-2, p. 279-282
- [7] Mercado-Solisa R. D., Mata-Maldonado J. G., Quinones-Salinasa M. A., Rodriguez-De-Andab E., Servín-Castañeda R., (2017), *Micro-Scale Abrasive Wear Testing of CrN Duplex PVD Coating on Pre-Nitrided Tool Steel*, *Materials Research* 20 No. 4, p 1092-1102
- [8] Bojan Kraut, (1982), *Strojarski priručnik*, Tehnička knjiga, Zagreb, p 373-377, 384
- [9] Mativenga P. T., Hon K. K. B., <http://slideplayer.com/slide/1716132/>
- [10] Cortez Alves De Oliveira V. M., Aguiar C., Vazquez A. M., Robin A. L. M., Barboza M. J. R., (2017), *Corrosion Behavior Analysis of Plasma-assisted PVD Coated Ti-6Al-4V alloy in 2 M NaOH Solution*, *Materials Research* 20 No. 2, p 436-444
- [11] Katalog tvrtke bohler, (2018), <http://www.bohler-uddeholm.in/media/BUIN%20Coating%20Catalog.pdf>
- [12] Paskvale S., (2018), *Properties of PVD hard coatings*, <https://pdfs.semanticscholar.org/8169/cf5d5971433fe02475d9e3913e5c6ada1eb3.pdf>
- [13] Sivarajan S., Padmanabhan R., (2017), *Tribological evaluation of wear resistant PVD Coatings*, *Journal of Manufacturing Engineering* 12 No. 2, p 99-102
- [14] Podob M., (1995), *Physical vapor deposition corrosion and wear resistant hardcoatings*, Finishing '95 conference and exposition, September 18-21, Cincinnati, Ohio
- [15] Nilsson M., Olsson M., *Tribological Testing of Some Potential PVD and CVD Coatings for Steel Wire Drawing Dies*, <https://www.diva-portal.org/smash/get/diva2:522147/FULLTEXT01.pdf>
- [16] Katalog tvrtke bohler, (2018), <http://hauckht.co.uk/PVD>
- [17] Potter C. E., (1968), *Elektrokemija Osnove I Primjena*, Školska Knjiga, Zagreb, p 238 Prijevod
- [18] Katalog tvrtke Industry & Applications, (2018), <http://pvdamerica.com/industry-application/>
- [19] Market summary, (2018), <https://www.pvd-coatings.co.uk/applications/market-summary/>
- [20] Physical Vapor Deposition (PVD) Market Analysis By Category (PVD Equipment, PVD Material, PVD Services) By Application (Microelectronics, Data Storage, Solar Products, Cutting Tools, Medical Equipment) And Segment Forecasts To 2024, (2018), <https://www.grandviewresearch.com/industry-analysis/physical-vapor-deposition-pvd-market>
- [21] Taheri R., (2002), *Evaluation of Electroless Nickel-Phosphorus (En) Coatings*, A Thesis Submitted to the College of Graduate Studies and Research in Partial Fulfillment of The Requirements for the Degree of Doctor of Philosophy in the Department of Mechanical Engineering University of Saskatchewan Saskatoon
- [22] Shahin G. E., (2009), *Comparison of Electroless Nickel & Functional Chromium*, ATOTECH USA, Rock Hill, South Carolina
- [23] Alirezai S., Monirvaghefi S. M., Salehi M., Saatchi A., (2007), *Wear behavior of Ni-P and Ni-P-Al<sub>2</sub>O<sub>3</sub> electroless coatings*, *Wear* 262 No. 7-8, p 980
- [24] Ploof L., (2008), *Electroless Nickel Composite Coatings*, *Advanced Materials & Processes*, p. 36-38
- [25] Agarwala R. C., Agarwala V., (2003), *Electroless Alloy/Composite Coatings: A Review*, *Sadhana* 28 No. 3&4, p 476, 483
- [26] Sankara Narayanan T. S. N., Krishnaveni K., Seshadri S. K., (2003), *Electroless Ni-P/Ni-B duplex coatings: preparation and evaluation of microhardness, Wear and corrosion resistance*, *Materials Chemistry and Physics* 82, p 779
- [27] Bunshah, R. F., (2001), *Handbook of Hard Coatings*, Noyes Publications, Park Ridge, New Jersey, p 114, 167. ISBN:0-8155-1438-7

- [28] Potter C. E., (1968), *Elektrokemija – osnove i primjena*, Školska knjiga, Zagreb, p 238, 292 Prijevod
- [29] Baudrand D. W., (1994), *Electroless Nickel Plating*, In ASM Handbook-Volume 5: Plating and Electroplating, Nonelectrolytic Deposition Processes, Material Park, Oh: ASM International, ISBN 0-87170-384-X.
- [30] The Engineering Properties of Electroless Nickel Coatings, (1980), RND: 1t
- [31] Murakami M., Hino M., Hiramatsu M., Osamura K., Kanadani T., (2006), *Effect of Zincate Treatment on Adhesion of Electroless Nickel-Phosphorus-Coating for Commercial Pure Aluminum*, Materials Transactions 47 No. 10, p 2523
- [32] Hino M., Murakami K., Hiramatsu M., Chen K., Saijo A., Kanadani T., (2005), *Effect of Zinicate Treatment on Adhesion of Electroless Ni-P Plated Film for Aluminium Alloy*, Materials Transactions 46 No. 10, p 2171
- [33] Wang Y., Deng Y., Ma Y., Gao F., (2011), *Improving Adhesion of Electroless Ni-P Coating on NdFeB Magnet*, Surface & Coatings Technology 206, p 1205
- [34] Novak M., Vojtěch D., Zelinková M., (2009), *Heat Treatment of Ni-P-Al<sub>2</sub>O<sub>3</sub> Electroless Coatings*, METAL 2009, Hardec Nad Moravici, Czech Republic
- [35] Redlich M., Katz A., Rapoport L., Wagner H. D., Feldman Y., Tenne R., (2008), *Improved Orthodontic Stainless Wires Coated with Inorganic Fullerene-Like Nanoparticles of WS<sub>2</sub> Impregnated in Electroless Nickel-Phosphorus Film*, Dental Materials 24, p 1641, 1642
- [36] Chen X., Li G., Lian J., (2008), *Deposition of Electroless Ni-P/Ni-W-P Duplex Coatings on AZ91D Magnesium Alloy*, Transactions of Nonferrous Metals Society of China 18, p 325, 326
- [37] Abdel Aal A., Shehata Aly M., (2009), *Electroless Ni-Cu-P Plating onto Open Cell Stainless Steel Foam*, Applied Surface Science 255, p 6653, 6654



# Hardness versus time dependency during artificial and interrupted ageing of AlMgSi0.5 aluminium alloy

**Ratko MIMICA**

Research and development department at  
Brodosplit  
Odjel istraživanja i razvoja u Brodosplitu  
Put Supavla 21, 21000 Split, Croatia

ratko.mimica@brodosplit.hr

## Keywords

*AlMgSi0.5 aluminium alloy*

*Heat treatments*

*Metastable precipitates*

*Interrupted ageing*

## Ključne riječi

*Aluminijeva legura AlMgSi0.5*

*Toplinsko očvršćavanje*

*Metastabilni precipitate*

*Prekinuto dozrijevanje*

*Original scientific paper*

**Abstract:** Al-Mg-Si aluminium alloys are characterized by excellent deformability, but mechanical properties are not significant in extruded state. Improvement of mechanical properties is achieved by heat treatment, a process which allows formation of metastable precipitates during subsequent ageing. In this work, hardness versus time dependency for artificially aged AlMgSi0.5 (EN AW-6060) aluminium alloy at 185°C is compared with results achieved by interrupted ageing performed at lower temperatures.

*Izvorni znanstveni rad*

**Sažetak:** AlMgSi aluminijeve legure karakterizira odlična deformabilnost, ali u ekstrudiranom stanju mehanička svojstva nisu značajna. Poboljšanja mehaničkih svojstava postižu se toplinskim očvršćivanjem koje je posljedica formiranja metastabilnih faza tokom procesa naknadnog dozrijevanja. U ovom radu uspoređena je ovisnost tvrdoće o vremenu umjetnog dozrijevanja na 185°C za AlMgSi0.5 (ENAW-6060) aluminijevu leguru s promjenom tvrdoće uslijed prekinutog dozrijevanja, izvođenog na nižim temperaturama..

## 1. Introduction

Aluminium is increasingly attractive due to its strength and stiffness to weight ratio. Al-Mg-Si alloys are age hardenable and widely used in both cast and wrought forms. Aluminium extrusions are used in a variety of structural applications ranging from building and automotive to aerospace industries. Al-Mg-Si series alloys claim over a 90% share of the total extruded volume owing to an attractive combination of mechanical properties, corrosion resistance, extrudability and an excellent response to surface finishing operations [1],[2]. Good corrosion resistance as well as the expertise of welding aluminium semi products explain the development of Al-Mg-Si series alloys in shipbuilding (AlSiMg(A), AlSi1MgMn) and coastal equipment(AlMgSi0,5) [3] as well. In extruded state mechanical properties are not significant so strengthening of Al-Mg-Si alloys is required based on a precipitation hardening process.

Magnesium and silicon are the main alloying elements and combine to form the stoichiometric compound, magnesium silicide ( $Mg_2Si$ ) when the weight ratio of magnesium to silicon is 1.73:1. The  $Mg_2Si$  makes Al-Mg-Si series alloys heat treatable [2]. Heat treatment provides a way to change microstructure by modifying

size, spacing, composition, type and precipitate morphology in heat treatable aluminium alloy.

Heat treatment usually comprises 3 main stages, namely:

- Solution heat treatment at a higher temperature within the single phase region, so as to dissolve the alloying elements;
- Quench, in order to form a supersaturated solid solution (SSSS) of these elements in Al, and
- Ageing, i.e. the controlled decomposition of the supersaturated solid solution to form a fine dispersion of precipitates. This can occur at any temperature below the solvus line, even at room temperature.

Temperatures and time kept on these temperatures are chosen in dependence of chemical composition of the alloy or desired structure to be formed. Upon ageing, a supersaturated solid solution will tend to transform towards the equilibrium structure  $\beta - Mg_2Si$ . However, before equilibrium is attained, a number of intermediate stages typically occur as can be seen in Table 1.

Precipitation hardening effect depends on the shape, size and morphology of the precipitates formed during ageing. Four main strengthening mechanisms are explained in Figure 1. It's important to note that these mechanisms are not mutually exclusive - many alloys are designed to take advantage of all four [5].

**Symbols/Oznake**

- HV2** - vickers hardness measurements at 2 kg load  
- čvrstoća po vickersu pri opterećenju od 2 kg
- T6** - temper designations (aged to peak hardness)  
- oznaka toplinske obrade (dozrijevano na vršnu tvrdoću)
- T6I4** - temper designations (interrupted ageing)  
- oznaka toplinske obrade (prekinuto dozrijevanje)

**Greek letters/Grčka slova**

- $\beta$**  - equilibrium precipitate,  
- ravnotežni precipitat

**Subscripts/Indeksi**

- primary precipitate incoherent with matrix  
- primarni precipitat ne koherentan sa matricom
- secondary precipitate coherent with matrix  
- sekundarni precipitat koherentan sa matricom

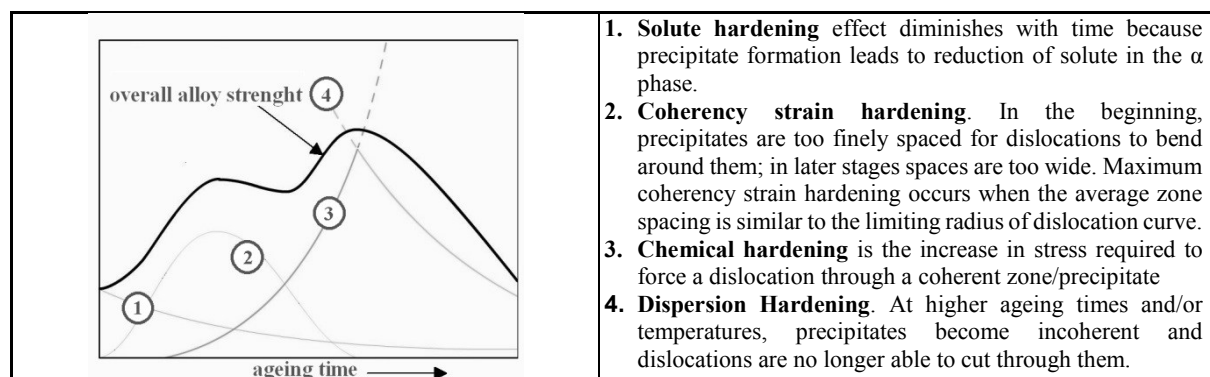


**Figure 1.** Four main hardening mechanisms and their contribution to overall strength [5]

**Table 1.** Overview of the complex precipitation sequence in Al-Mg-Si alloys [4]

Stage	Solute concentration (at. %)	Shape	Description, features
SSSS	0-5%*	Point defects	Supersaturated solid solution: substitutional Mg and Si atoms, large concentration of vacancies.
Atomic clusters	1-15%*	clusters	Early clustering of solute atoms, large degeneracy in formation enthalpy of structures, entropy effects very strong.
Clusters (1-5 nm)	10-25%	3d, 2d	Spherical and platelets
initial- $\beta''$	15-45%	needle	Monoclinic cell, single Si pillars
pre- $\beta''$	35-60%	needle	Monoclinic cell, double Si pillars, low density cylinder appears(LDC)
$\beta''$	50-90%	needle	Monoclinic cell, double Si pillars, LDC underwent 0.5b shift
B', $\beta'$ , U1, U2, U3	60-100%	rod/lath	Collection of hexagonal, trigonal and orthorhombic phases
$\beta$	95-100%	cube	Stable $Mg_2Si$ bulk phase with anti-fluorite structure, excess Si forms the diamond structure

\* No real distinction can be made between the precipitate and the matrix. The particles are too immature and contain too much Al to determine where the interface is

There are numerous temper designations that are standardized for heat treated aluminum alloys [6], in addition, newly developed multistage thermal treatments have shown significant improvement in mechanical properties [7]. One of those treatments known as T6I4 temper utilizes secondary precipitation after a short period of underageing at an elevated temperature to

achieve, or sometimes to surpass, the properties of the T6 temper, but with notably reduced times of artificial ageing at higher temperatures (Figure 2).

The scope of this work is to obtain and compare hardness vs. ageing time dependency curves for standard and interrupted ageing of AlMgSi0,5 alloy.

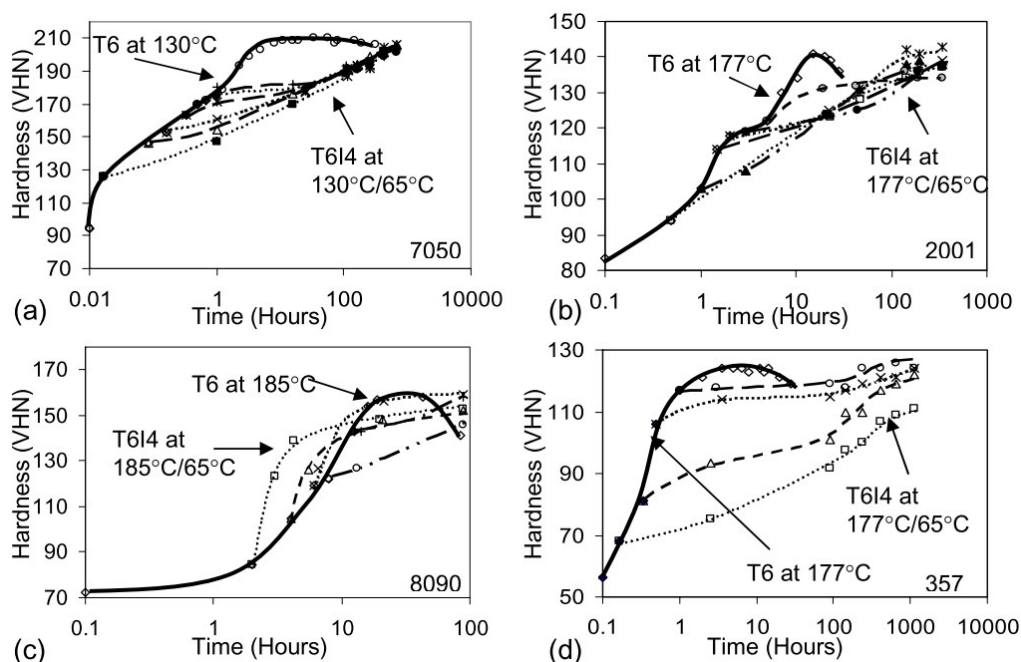


**Figure 2.** Secondary ageing curves (T6I4) compared with T6 curves for: a) 7050; b) 2001; c) 8090 and d) 357 aluminium alloys [7]

## 2. Experimental procedure

Experimental part of this work was conducted in welding laboratory of Department of Manufactural Engineering in Faculty of Electrical Engineering, Mechanical Engineering and Naval Architecture in Split. Material used is AlMgSi0,5 (EN-AW 6060) aluminum alloy with chemical composition shown in Table 2.

Base material is purchased in extruded form of a strip dimensions 40 x 5 x 6000 mm, temper designation was T6 which implies artificial ageing to peak hardness. Samples dimensions 5x8x40 mm were cut from base material, and afterwards grinded using 240, 360, 480 & 1000 grit sandpaper in order to minimize hardness measurements dispersion. The hardness test, because of its simplicity and correlation with tensile properties is a

common mechanical test used to estimate the mechanical strength of metallic materials [8], [2]. Vickers hardness measurements (2 kg load) were performed for each sample.

Values presented are average of five measurements. All measurements are conducted in compliance with ASTM E18-07 standard.

Heat treatment of samples included solid solution heat treatment (SSHT), quenching and artificial ageing. SSHT was carried out at 540°C for period of 1 hour. Quenching must be performed fast enough to avoid diffusion processes and loss of vacancies, easiest way to do that is quench in water at ambient temperature. Artificial ageing was performed at 185°C as a compromise between overall ageing time and required mechanical properties.

**Table 2.** Chemical composition AlMgSi0,5 alloy used in this investigation (%)

Mg	Si	Cu	Fe	Mn	Cr	Ti	Zn	Al
0,44	0,44	0,01	0,19	0,06	0,01	0,02	0,02	rest

### 3. Results and discussion

#### 3.1. Artificial ageing curve at 185°C – T6 temper

Base material hardness in as received (T6) condition is 80 HV2. Hardness versus ageing time curve for samples after SSHT and quenching is shown in Figure 3. Curve shape resembles typical two stage hardening curve which is common for heat treatable aluminium alloys.

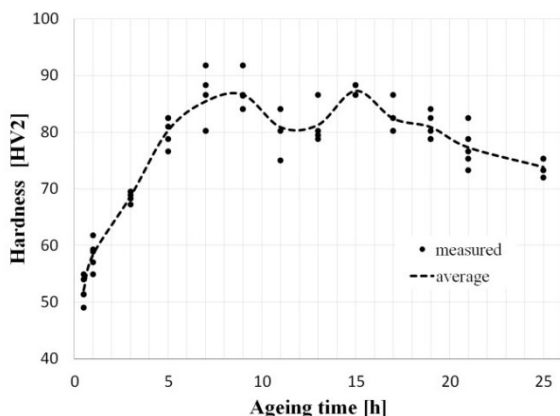


**Figure 3.** Hardness vs. ageing time at 185°C for AlMgSi0.5 aluminium alloy

Figure 3. also shows dispersion of the results which usually follows hardness measurements. Namely, besides magnesium and silicon, other alloying elements and impurities are also dissolved in aluminium matrix, so inhomogeneity of structure and thus the measurements is to be expected. But despite dispersion, average values outline changes in hardness related to artificial ageing time.

Comparing the measured average values with Figure 1. could provide insight in interaction of strengthening mechanisms active during artificial ageing (Figure 4.). Ideal fit between curves is not to be expected, firstly, because of abovementioned inhomogeneity, and secondly because first figure is related to increase in tensile strength which may not be in linear correlation with hardness. But nevertheless, understanding the resemblance between these two curves will be beneficial for further investigations of multistage thermal treatments.

Solution hardening in this alloy could not be dominant process mainly because AlMgSi0.5 have smallest amount of alloying elements compared to other alloys from that series. During artificial ageing, nucleation and growth of the precipitates further depletes the aluminium matrix from solute, reducing contribution to overall hardness from this mechanism.

Rapid increase in hardness during first hours of ageing may be explained with coherency strain hardening mechanism.

Maximum coherency strain hardening (recorded just before first hardness peak at 9-th hour of ageing) occurs

when the average zone spacing is similar to the limiting radius of dislocation curvature.

During later stages of ageing precipitation of partially incoherent phases such as  $\beta'$  occurs. New dislocations are formed on particle/matrix interface which reduces hardening effect by this mechanism, and with formation of incoherent (stable) phases coherency strain hardening effect ends.

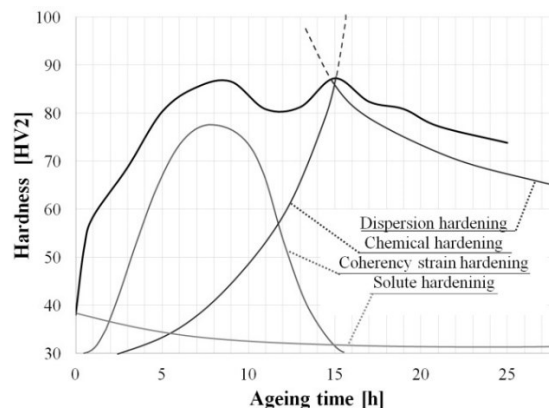


**Figure 4.** Schematic interpretation of results based on hardening mechanisms synergic effect.

Secondary peak in hardness (secondary hardening), observed after 13th hour of ageing and subsequent decrease after 15th hour could be result of two interactive mechanisms, chemical hardening and dispersion hardening. Hardening effect increases with radius of precipitate until moment at which less energy is required for dislocation to bow around precipitate instead of cutting through. In literature, this effect is known as Orowan bowing, and that radius of a particle is called critical radius. From that point onwards i.e., for particle radius larger than critical, dislocation must by-pass precipitate by one of a number of possible mechanisms (bowing, climb, cross-slip) making dispersion hardening the dominant mechanism.

It is interesting to notice that coherency strain hardening in this type of alloy is almost same by amount as combined effect of next two mechanisms (chemical and dispersion hardening), i.e., effect of secondary hardening is not pronounced like in Al-Cu or Al-Zn series of aluminium alloys [7]. In those types of alloys secondary hardening is interpreted with different sequence, shape and properties of metastable precipitates, although partially incoherent, still offer significant contribution to hardening. But, even in same series of alloys like AlMgSi0.8 or AlSi1MgMn effect of secondary hardening is noticeable [9]. Reasons for that kind of behavior could be related to the small amount of alloying elements contained in AlMgSi0.5 alloy. During first stages of ageing large number of small precipitates is formed impeding dislocation motions with strain fields induced in aluminium matrix. Those strain fields are not

solely dependent on particle radius, atom size or lattice mismatch of a formed precipitate in respect to matrix also make contribution to overall hardening effect. Particle radius plays much more important role in chemical and dispersion hardening mechanism, as mentioned above. So, smaller amount of alloying elements (building blocks of future precipitates) would definitely lead to smaller number of precipitates with critical radius size, and thus smaller hardening effect.

### 3.2. Secondary ageing - T6I4 temper

To achieve T6I4 temper, artificial ageing was interrupted at different stages, samples were quenched in water and aged at temperature of 65°C for period of 360 hours (15

days). Increase in hardness is due to secondary precipitation of solute atoms dissolved in aluminium matrix [7]. Since formation of late phases is not possible at these temperatures it is likely that nucleation of clusters and initial-  $\beta''$  occurs (Table 1). These phases are coherent with the matrix which suggests that increase in hardness is caused by coherency strain hardening. Strain hardening contribution to overall hardness, in addition to abovementioned criteria (size, dispersion and minimum dislocation radius) will also depend of available amount of solute atoms remaining in matrix. Newly formed precipitates coexist with those already formed in first stage of ageing at 185°C. Change in hardness for some of the samples interrupted in different stages of artificial ageing is shown in Figure 5.

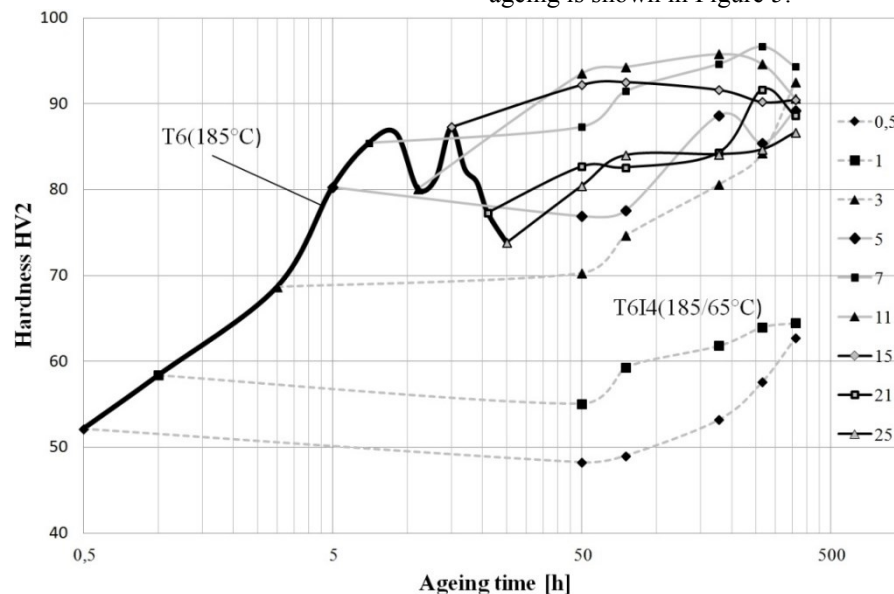


**Figure 5.** Secondary ageing curves (T6I4) compared with T6 curve for AlMgSi<sub>0,5</sub> aluminium alloy.

Hardness increase is visible in all samples, but final values and dynamic of reaching those values differ in regard to interruption time. For samples artificially aged half an hour and one hour before interruption hardness increased to 65HV<sub>2</sub>, while all other samples interrupted after achieved hardness between 85 HV and 95 HV<sub>2</sub>. Maximum hardness of 96HV<sub>2</sub> was measured in sample which was artificially aged at 185°C for seven hours, interrupted and then aged at 65°C for period of 260 hours.

**Fig 6a** shows overall hardness change of tested samples during secondary ageing, relative hardness increment for each sample is shown in **Fig 6b**.

From **Fig 6** three different areas could be distinguished up to 50 h of ageing, between 50 h and 240 h and after 240 h which may provide further insight in different hardness increment of tested samples:

- For samples interrupted in early stages of ageing (0,5 h and 1h) measurements shown slight decrease in hardness which then shows continuous rise up to 240th hour of ageing. After that period hardness of sample interrupted after 0,5 h continues to rise,

while it stagnates for sample interrupted after one hour.

- Samples interrupted before reaching first hardness peak in Figure 3 (after 3 h, 5 h and 7 h) shown no significant hardness change in first period of secondary ageing (up to 50 h). In second period increase in hardness was detected at a rate similar to early interrupted samples. In final period hardness continues to rise for 3 h aged sample to a maximum recorded increment of 24HV<sub>2</sub>. For samples previously aged 5 h and 7 h hardness decreases by small amount, which could suggest that those samples surpassed maximum hardening effect from coherency strains. Note: measured hardness difference of 4 vickers is relatively small value, which could indeed be result of precipitation mechanisms, but inhomogeneity of the structure could also show same amount of dispersion in results (Figure 3). So results should be taken with caution before making further conclusions.



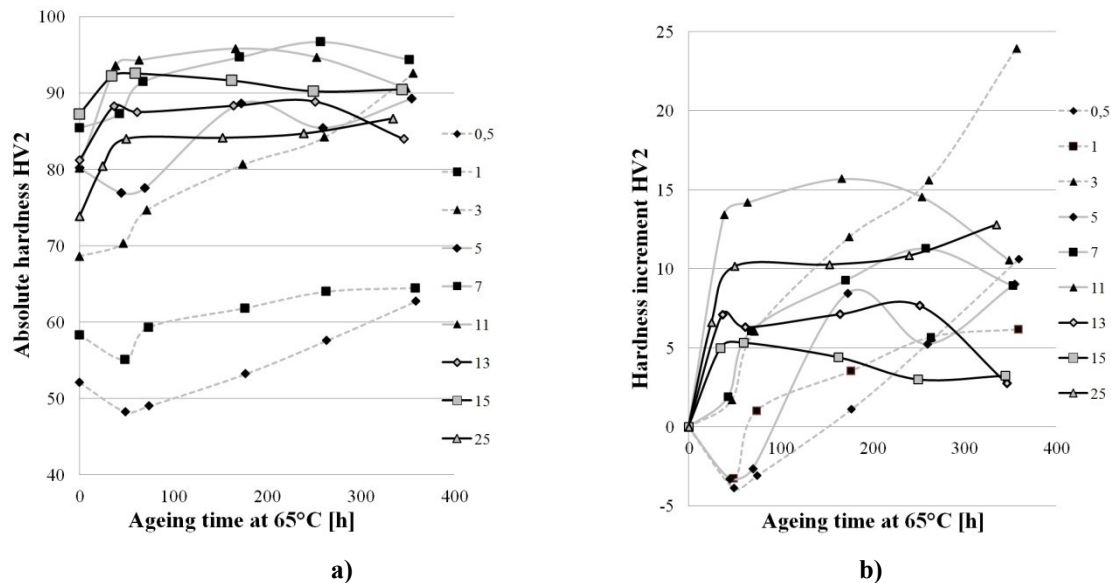


**Figure 6.** Hardness changes during secondary ageing at 65°C for samples interrupted at various stages: a) absolute hardness values; b) relative hardness increment.

- Samples aged longer before interruption show similar pattern of hardness increase. In first period of interrupted ageing hardness significantly increase, followed by stagnation in second period, and in third period loss of hardness was measured in almost all samples. Smallest change in hardness during secondary ageing (5HV2) was measured in sample previously aged to peak hardness.

Such behavior could be explained with abovementioned different types, sizes and dispersions of precipitates which coexist as a result of secondary precipitation at lower temperatures. That leads to different interaction of strengthening mechanisms compared to single stage thermal treatment (Figure 1).

Samples interrupted early in first ageing process (0.5h & 1 h) were comprised from early phases coherent with matrix which could not provide significant coherency hardening, mainly because their size and dispersion in regard to dislocation radius. Those early phases would eventually grow and coarsen if artificial ageing was continued, but interruption of the process takes away the energy needed for further growth. So immediately after interruption material should contain early phases with low amount of solute (Table 1) and aluminium matrix rich in solute atoms (those atoms would eventually precipitate in further stages of ageing). In secondary ageing process, in addition to already formed precipitates, nucleation of new precipitates begins from those atoms. Lower temperature (65°C instead of 185°C) suggests lower mobility of atoms, which favours formation of increased number of finely spaced nucleation sites leading to smaller effect of coherency strain hardening as a result of dislocation treading through

strain fields (minimum dislocation radius still too big). At later stages of secondary ageing growth and coarsening are expected to occur, albeit rather slowly, which will reduce number of precipitates and have positive effect on coherency strain hardening mechanism.

Longer ageing times at 185°C means more time and energy for formation of late phases combined with further depletion of matrix with solute atoms. That will result in smaller number of nucleation sites formed in consequent secondary ageing. With smaller number of sites formed, dislocation could more easily bend through strain fields increasing hardening effect. Samples held 3 h, 5 h and 7 h before interruption didn't show drastic increase in hardness during first period of secondary ageing, which could be due to minimum radius of dislocation still being too big, but with later coarsening hardness continues to rise. Samples kept even longer in first ageing process shown steep increase in hardness in first period of secondary ageing. Solute content in matrix of those samples is even lower resulting in even fewer nucleation sites. That means that maximum coherency strain hardening effect (average zone spacing similar to the limiting radius of dislocation curvature) is going to be reached a lot sooner than in samples with greater amount of solute at disposal. In further stages of ageing strain fields became too widely spaced, which has negative effect in overall resistance to dislocation motion, softening the material.

#### 4. Conclusion

Understanding the precipitation dynamic and hardening mechanisms is essential for optimization of heat treatments and mechanical properties of heat treatable

aluminium alloys. In this work, hardness versus time dependency for artificially aged AlMgSi0.5 (EN AW-6060) aluminium alloy at 185°C is compared with results achieved by interrupted ageing performed at lower temperatures. Hardness increase after interruption was recorded in all samples, but final values and dynamic of reaching those values differ in regard to interruption time. Maximum hardness of 96HV2 is reached by sample aged at 185°C for 7 hours, than interrupted and aged at 65°C for period of 240 h. Sample artificially aged for 3 hours before interruption shown maximum hardness increment of 24HV2, while minimum increment of 5HV2 was measured on peak aged sample (15 hours of ageing before interruption).

## REFERENCES

- [1] Birol, Y., 2013. *Precipitation during homogenization cooling in AlMgSi alloys*. Transactions of Nonferrous Metals Society of China (English Edition), 23(October 2012), pp.1875–1881.
- [2] Meng, C., 2010. *Effect of Preheating Condition on Strength of AA6060 Aluminium Alloy for Extrusion*. Ph. D thesis, Auckland University of Technology.
- [3] Christian Vargel, 2004. *Corrosion of Aluminium*, Elsevier Science 1st edition, pp. 346-350
- [4] Van Huis, M. a. et al., 2007. *Phase stability and structural features of matrix-embedded hardening precipitates in Al-Mg-Si alloys in the early stages of evolution*. Acta Materialia, 55, pp.2183–2199.
- [5] Precipitation hardening overview 2010. Available from: <http://aluminium.matter.org.uk/content/html/en/default.asp?catid=61&pageid=989848382> , [15 March 2015]
- [6] Benedyk, J.C., 2009. *International Temper Designation Systems for Wrought Aluminum Alloys*. Light Metal Age, 67, pp.3–6. Available at: <https://lightmetallage.com/PDFs/LMA-2009-10-026TempersPartI.pdf>.
- [7] Lumley, R.N., Polmear, I.J. & Morton, a. J., 2004. *Temper developments using secondary ageing*. Materials Forum, 28, pp.85–95.
- [8] Malin, V., 1995. *Study of Metallurgical Phenomena in the HAZ of 6061-T6 Aluminum Welded Joints*. Welding journal, pp.305–318.
- [9] Chen, J.H. et al., 2006. *Atomic pillar-based nanoprecipitates strengthen AlMgSi alloys*. Science (New York, N.Y.), 312(2006), pp.416–419.



# Inverse measurement method for intake and exhaust manifold of cylinder head

Anja MUJKANović<sup>(1)</sup>, Duško PAVLETIĆ<sup>(2)</sup>, Graciela ŠTERPIN VALIĆ<sup>(2)</sup> and Maja FOREMPOHER ŠKUVER<sup>(2)</sup>

1) AITAC d.o.o.

Žegoti 6/1, 51215 Kastav, **Croatia**

2) Sveučilište u Rijeci, Tehnički fakultet/

University of Rijeka, Faculty of

Engineering

Vukovarska 58, 51000 Rijeka, **Croatia**

dusko.pavletic@riteh.hr

## Keywords

3D digitalization

Cylinder head

Inverse measurement method

## Ključne riječi

3D digitalizacija

Glava motora

Inverzna metoda mjerenja

## Early information

**Abstract:** The paper is dealing with the measurement of engine head of the Riteh Racing team bolide developed at the Faculty of Engineering, University of Rijeka. For the further improvement of bolide engine performance it was needed a digitized model of the intake and exhaust manifold. The constraints was that the cylinder head can't be cut to assess right dimensions of inner parts, so the inverse measurement technique of castings made of polymeric material was used. Method includes making castings of intake and exhaust manifold and their digitization. Making the castings of platinum-based silicone rubber Mold Star 15 i.e. making their digitized models has proven to be an effective method of measuring the interior surfaces of the cylinder head. Deviations of digitized castings and digitized model of the cylinder head were obtained in the GOM Inspect software and measurements were made with ATOS Triple Scan III.

## Prethodno priopćenje

**Sažetak:** Predmet mjerenja ovoga rada je glava motora bolida Riteh Racing Teama Tehničkog fakulteta u Rijeci. S obzirom da je kupljena, tim ne posjeduje digitalizirani model što im onemogućuje daljnje unaprjeđenje bolida. U svrhu dobivanja digitaliziranog modela usisnog i ispušnog kanala, glava motora nije se smjela oštetiti te se primijenila inverzna tehnika mjerenja odljevaka izrađenih od polimernog materijala. Metoda se sastoji od izrade odljevaka usisnog i ispušnog kanala te digitalizacije tog odljevka. Kao materijal za izradu odljevaka korištena je silikonska guma na bazi platine Mold Star 15. Izrada odljevaka te izrada njihovih digitaliziranih modela pokazala se kao učinkovita metoda dobivanja unutarnjih površina usisnog i ispušnog kanala glave motora. Odstupanja digitaliziranih modela odljevaka te digitaliziranog modela glave motora dobivena je u GOM Inspect softveru, a mjerenja su se vršila ATOS III Triple Scan digitalizatorom što se pokazao kao dobar odabir za digitaliziranje odljevaka i glave motora u svrhu mjerenja njihovih odstupanja.

## 1. Introduction

Today market is characterized by a large variety of products and relatively strong demand for individual products. Numerically controlled machine tools, well established in production systems, caused changes in the field of measurement and quality control. The requirements in terms of accuracy and quality measurements are increased so to the control and measurement of the product should be given extra attention.

The paper is dealing with the measurement of engine head of the Riteh Racing team bolide developed at the Faculty of Engineering, University of Rijeka. Given that engine head is purchased, the team doesn't have a digitized model of the head itself nor main dimension of the internal surfaces (intake and exhaust manifold) what prevents them from further improvement of bolide.

In order to obtain a digitized model of the intake and exhaust manifold, the cylinder head was not allowed to be damage. Measurements in tight and complex areas and cavities such as ducts of the cylinder head are very

inconvenient and sometimes impossible without using one of the methods of destruction in order to reach parts for measurement. Given this, the measurement using coordinate measuring machines, laser 3D scanner, structured light scanner etc. were not possible [1].

In one example, when trying to get a digitized model of cylinder head [2], where complex internal geometry was inaccessible from the outside, the cylinder head was cut open to scan the insides and then cut pieces were laser scanned to capture inside holes for gasoline flow, spark plugs, etc. This was not an option in our case.

To recreate the details of the cylinder head's X-rays such as computed tomography can be used as one of the methods without destruction like when Rautenbach Aluminium-Technologie GmbH (Wernigerode, Germany) had to manufacture water jacket core of a cylinder head in aluminium being in production for several years. Unfortunately, there were no 3D-CAD data, only 2D drawings existed. They perform a reverse

engineering procedure, transforming the CT data into the customer's CAD-system [3].

In our example, in order to obtain the digitized model of intake and exhaust manifold, the inverse measurement technique of castings made of polymeric material was used.

Method includes making castings of intake and exhaust manifold and digitization of that casting. Also, the casting of the combustion chamber, which are completely visible for direct 3D-scanning, was also made, enabling comparison of accuracy of actual surface of exhaust and intake manifold and their casting.

By choosing materials from which the castings of intake and exhaust manifold of the cylinder head will be made, it must be taken into account that material shouldn't shrink when drying and that casting must be easily pull out from the mould without plastic deformation. Also, the castings must be sufficiently stable so they can stand, without support, on the rotary table during the scan. The accuracy and deviations of digitized models of castings of the cylinder head were obtained in the GOM Inspect software, and measurements were made with ATOS III Triple Scan digitizer [4].

Reverse engineering is a method that will, in this case, create a 3D virtual model of the existing exhaust manifold for use in 3D CAD, CAM, CAE and other software for comparison and improvement of the engine.

## 2. Selection of casting material

Platinum-based silicone rubber Mold Star 15 SLOW from SMOOTH-ON company is a two-component silicone rubber with high resistance to tearing, which was chosen as material for casting. Components are marked with A and B, Fig. 1.



**Figure 1.** Components A and B before mixing  
**Slika 1.** Komponente A i B prije miješanja

This type of silicon rubber is recommended for making castings for materials such as polyurethane, epoxies and polyester resin, wax, etc. It is chemically sensitive to latex and sulfur, and if it comes in contact with them solidification can be slowed and/or prevented. Mold Star

15 is silicone rubber mixed in a ratio 1A:1B per volume. It is characterized by low viscosity, and in the application is not necessary to use a vacuum degassing. The mixture is available for pouring for 50 minutes.

The duration of solidification is 4 hours at the temperature of 23°C. The temperature higher than recommended can drastically reduce pouring time as well as solidification time. During solidification material minimally shrinks: 0.00254 cm/cm, ie. 0.254% [5]. Also, it should be careful so that the mixture does not come into contact with latex (ie. gloves). It was not necessary to use a coating that would enable the extraction of casting from the mould because the walls of the exhaust and intake manifold were polished and cleaned with alcohol as well as external decanted surface (chamber), Fig. 2 and Fig. 3 [4].

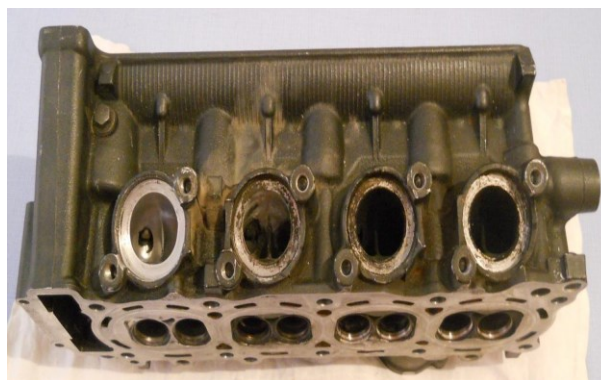


**Figure 2.** View of cleaned exhaust (left) and uncleaned exhaust manifolds (three on the right)

**Slika 2.** Pogled na očišćeni ispušni kanal (lijevo) i neočišćene ispušne kanale (tri s desne strane)



**Figure 3.** View of cleaned combustion chamber  
**Slika 3.** Očišćena komora izgaranja

To make a cast of the combustion chamber it is necessary to close the threaded hole (thread for the spark plug). Also, it is evident that it is necessary to set the boundaries in which silicone rubber will be poured and solidify, Fig. 4. Otherwise silicone rubber would be spilled over the entire cylinder head.





**Figure 4.** Boundaries for silicone rubber (three layers) and closed threaded hole

**Slika 4.** Granice kalupa za odljevak komore (tri sloja) i popunjeni otvor za svjećicu

Before mixing it is necessary to pour the same amount of the components A and B in separate containers. Ordinary plastic cup with ribs was used, where the ribs act as an indicator for the amount of poured material. After distribution in separate cups, A and B components were mixed together in a container as shown in Fig. 5 and Fig. 6. It should be ensured that the same amount of both components is poured into the cups. After pouring both components, it is important to mix them well and the final result is a mixture uniform in colour. For best results, it is necessary to pour a mixture with uniform jet and not from great distance in order to avoid backlogs of trapped air in the castings. Each casting was dried for 4 hours at a temperature of 23° C.



**Figure 5.** Pouring the components A and B into a common container

**Slika 5.** Izlijevanje komponenata A i B u zajednički spremnik

Moulded part of the chamber is finished when the drying process is over and it is shown in Fig. 7. The finished casting shows the reaction between mixture and the surface of the exhaust manifold valve, Fig.8.



**Figure 6.** Mixture of the components A and B  
**Slika 6.** Mješavina komponenata A i B

By 3D scanning i.e. comparing surface of the casting and the chamber it is able to see whether there has been significant deformation due to reactions.

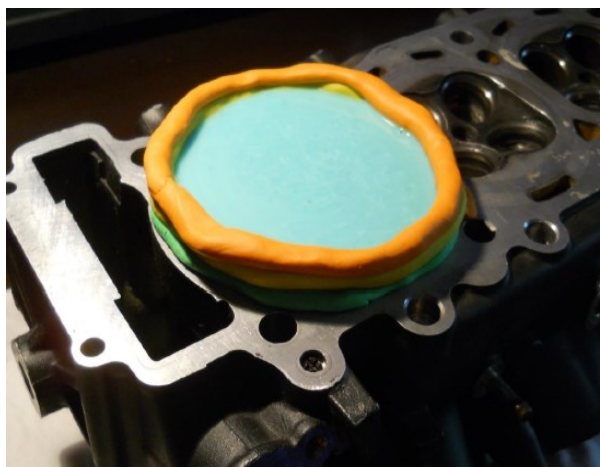


**Figure 7.** Poured mixture which is dried for 4 hours at 23° C  
**Slika 7.** Izlivena mješavina koja se suši 4 sata na 23°C

After four hours of drying, cast of the intake and exhaust valve is ready for extraction. After loosening the screws, the seal from the intake valve was removed, Fig. 9. The seal served as an extension for an additional part of the cast of intake valve which will help in removing. Castings of chamber, intake and exhaust manifold of the cylinder head have been successfully developed so the next step was to measure them, Fig. 10, Fig. 11 and Fig. 12.

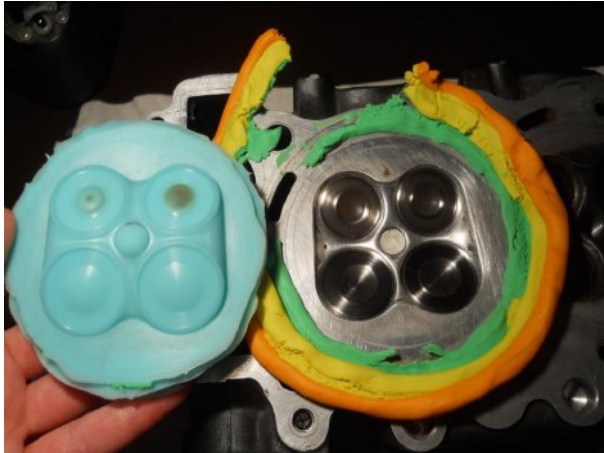


**Figure 8.** Finished cast of the combustion chamber  
**Slika 8.** Gotovi odljevnik komore izgaranja



**Figure 9.** Removing the seal  
**Slika 9.** Uklanjanje brtve

### 3. Measurement of casting

For measurement of castings calibration panel "GOM/CP 40/MV 100mm" was used. The Fig. 13 shows the calibration panel that was used for calibrating 3D scanner. During calibration, sensor position changes in relation to the panel through 19 different positions. After the last, nineteenth position, the software reports the results of the calibration. Since optical systems measure what they can see, it is not possible to scan the whole object from one position. In order to digitize the entire object, uncoded measurement points need to be pasted on the object in order to combine images from different positions of digitization, Fig. 14.

In each new position during digitization in the measuring volume, must be located (be visible) at least three known point from the active measurement series to connect scans.



**Figure 10.** Finished cast intake manifold, side view  
**Slika 10.** Gotovi odljevnik usisnog kanala, bočni pogled

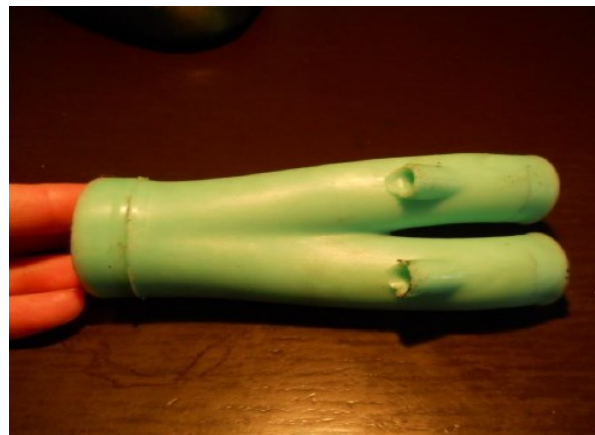


**Figure 11.** Finished cast intake manifold, valve guides view  
**Slika 11.** Gotovi odljevnik usisnog kanala, pogled na vodilice ventila



**Figure 12.** Different views of exhaust manifold cast  
**Slika 12.** Različiti pogledi na odljevnik ispušnog kanala

The cylinder head has a reflective and concave surface so it was necessary to treat it with the matting powder (titanium oxide powder). Special attention was given while cleaning the exhaust and intake manifold that was used for making castings, Fig. 15.



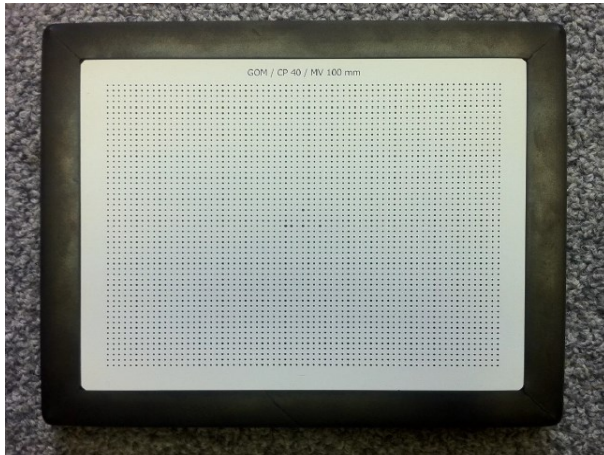


**Figure 13.** Calibration panel  
**Slika 13.** Ploča za umjeravanje

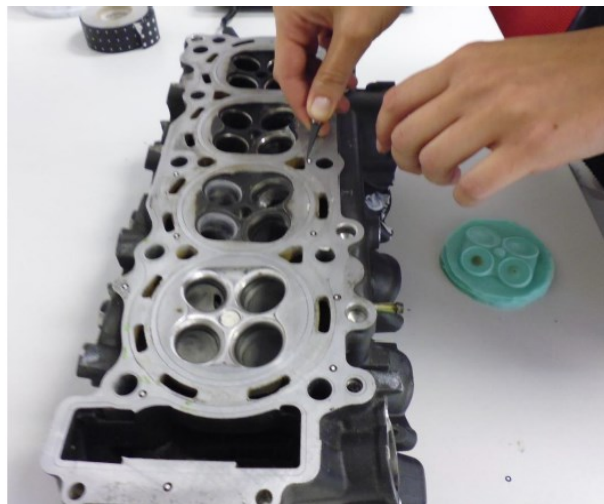


**Figure 14.** Sticking uncoded measurement points on the cylinder head  
**Slika 14.** Lijepljenje nekodiranih točaka na glavu motora

The casting chamber of the exhaust and intake channel was also necessary to treat with powder because the material is partially reflective and is not completely opaque. After treatment it is necessary to clean the powder from uncoded measurement points to make them visible.

After calibration and preparation of the measurement object, measurement can be started. It was necessary to adjust in the software to record twenty positions where the sensor is fixed, and the table is turned twenty times per  $18^\circ$ , so that in the active measurement series can be recorded twenty scans [6].

After recording one series (one side), the object is turned upside down and again scanned, after which the measurement series overlap. In this case, the turning table was rotated manually and the position of the scanner was changed, Fig. 16.

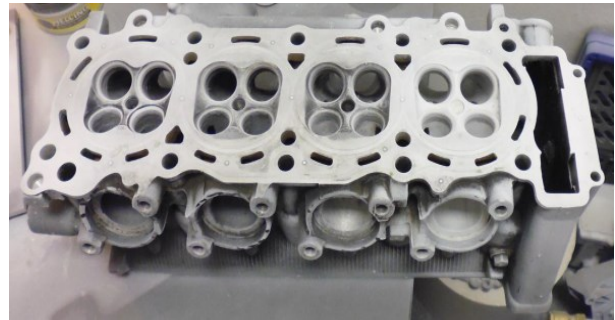


**Figure 15.** The cylinder head after treatment with titanium oxide powder

**Slika 15.** Glava motora nakon tretiranja prahom za matiranje



**Figure 16.** Measurement setup  
**Slika 16.** Mjerna postava

After the first scan, each point was given its own code which will retain in following measurement. The software will, according to the coded points, overlap matching measurement series. After making a series of scans, when the first measurement series is over new measurement series is created, Fig. 17 and Fig. 18. Joining of the measuring series was shown on Fig. 19 and Fig. 20.

In the first phase of digitization, data about the object is displayed in the form of cloud of points. After the measurement these points are converted into a polygon net (net of triangles, STL file) with process of polygonization, Fig. 21. The result is mesh structure which is suitable for further processing and if necessary, directly for 3D printing. The same process of measurements was performed on castings of chamber, intake and exhaust manifold. Digitized castings are shown in Fig. 22.

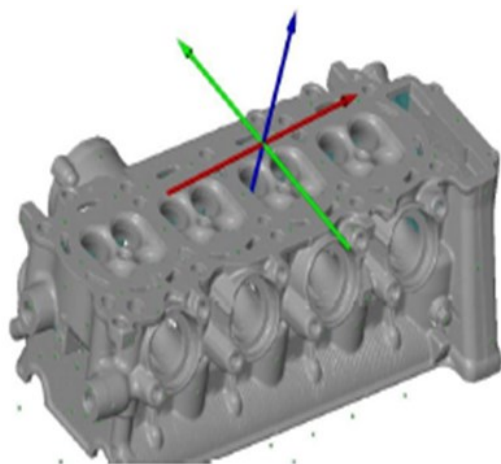


**Figure 17.** First measurement series  
**Slika 17.** Prva mjerna serija

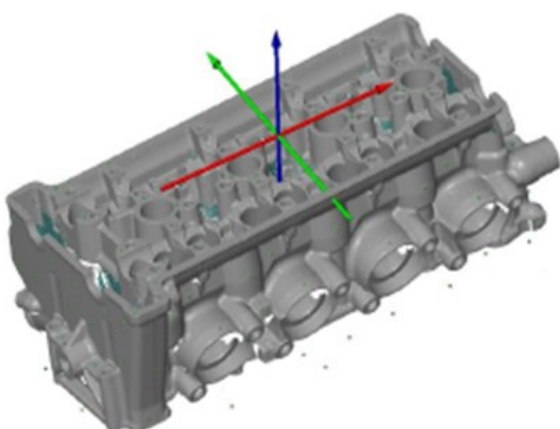


**Figure 18.** Second measurement series  
**Slika 18.** Druga mjerna serija

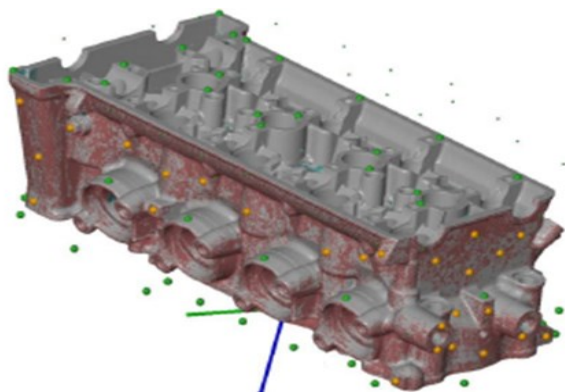


**Figure 19.** Joining of the measuring series (bottom view)  
**Slika 19.** Spajanje mjernih serija (pogled s donje strane)

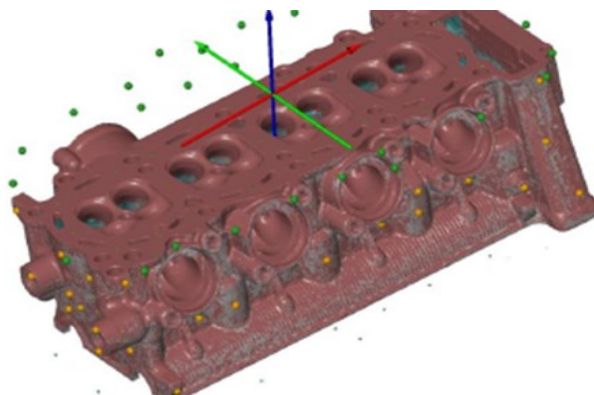


**Figure 20.** Joining of the measuring series (top view)  
**Slika 20.** Spajanje mjernih serija (pogled s gornje strane)

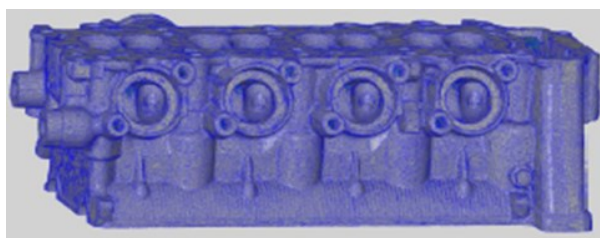


**Figure 21.** Mesh structure as a result of polygonization  
**Slika 21.** Poligonalna mreža trokuta kao rezultat digitalizacije

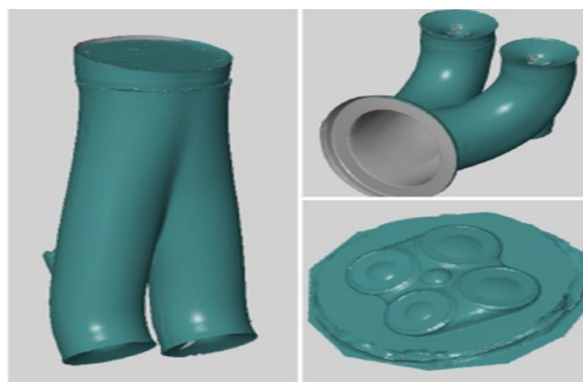


**Figure 22.** Digitized casting  
**Slika 22.** Digitalizirani odljevci

#### 4. Digitized and CAD models comparison

After completing overlap of CAD model and digitized model surfaces comparison can be performed, i.e. checking deviations between digitized castings and CAD model. Since the casting of the combustion chamber was made so that in case of no possibility of making valid digitization of intake and exhaust manifold, on it was made the first comparison. Next step was to compare the digitized models of exhaust and intake manifold. As already mentioned, after the measurement, data about the object are converted to a polygonal mesh with the process of polygonization. Each point of the polygon is taken into account and for each is calculated a direct perpendicular distance from the CAD model. Blue color



shows the surface of digitized model that lies beneath the surface of CAD model, red shows the surface that lies above the CAD model, while green shows the surface without deviation. On the Fig. 23, 24 and 25 are shown deviations between castings of chambers, intake and exhaust manifold and CAD model. They are less than a millimeter, which means that castings made of silicone rubber can represent the mould with acceptable accuracy in respect to the measurement objective.

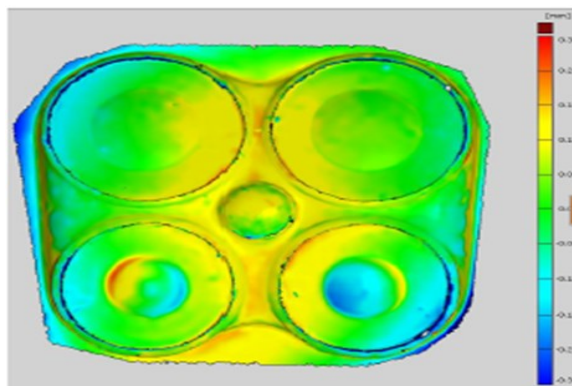


**Figure 23.** The deviation between casting of chamber and CAD model

**Slika 23.** Odstupanje modela odljevka komore od CAD modela

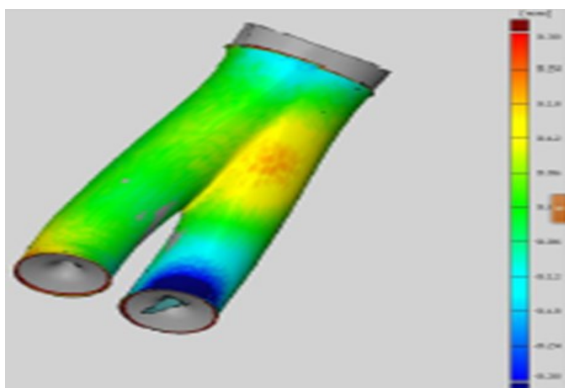


**Figure 24.** The deviation between casting of intake manifold and CAD model

**Slika 24.** Odstupanje modela odljevka usisa od CAD modela

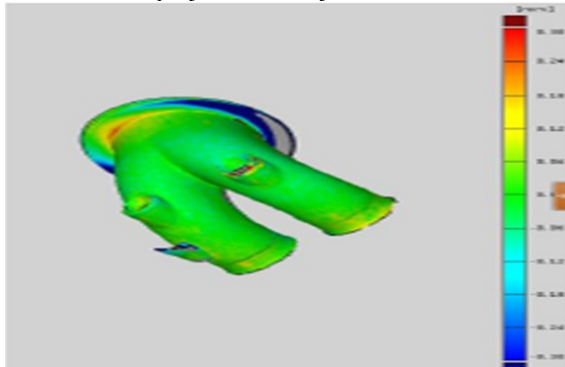


**Figure 25.** The deviation between casting of exhaust manifold and CAD model

**Slika 25.** Odstupanje modela odljevka ispuha od CAD modela

## 5. Conclusion

Castings of internal and external surfaces of the cylinder head made of silicone rubber were successfully developed. For the measurement was chosen ATOS III Triple Scan 3D digitizer. After measurements digitized models of castings and cylinder head were obtained. Then it was possible to make comparison of digitized castings with cylinder head CAD model. The comparison shows deviations less than one millimeter. Given that the digitized models of intake and exhaust manifold is going to be used for simulation of air flow, and then with an iterative process will be improved, tolerances were up to a few millimeters. In this case, making the castings of silicone rubber, ie. making their digitized models has proven to be an effective method of getting the interior surfaces of the intake and exhaust manifold of the cylinder head. Mold Star 15 has proved to be a good choice of material for making castings that minimally shrinks, do not stick to the cleaned surfaces of the cylinder head, can be easily removed and do not deform plastically when using pull-out force. ATOS Triple Scan III and related software have proven to be a good choice for digitizing castings and cylinder head in order to measure their deviation.

## Acknowledgements

Many thanks to company Topomatika for the support and implementation of measurement.

## REFERENCES

- [1] Biondić L., (2012), *Analiza upotrebljivosti 3D skeniranja kao tehnologije povratnog inženjerstva*, Fakultet strojarstva i brodogradnje, Sveučilište u Zagrebu
- [2] <https://www.laserdesign.com/3D+Scanning-Recreates-Complex-Fin-Geometry> (01.09.2018.).
- [3] [https://www.ndt.net/article/v04n07/bb67\\_8/bb67\\_8.html](https://www.ndt.net/article/v04n07/bb67_8/bb67_8.html) (01.09.2018.).
- [4] Mujkanović, A., (2013), *Mjerenje dimenzija glave motora 3D digitalizatorom*, Tehnički fakultet, Sveučilište u Rijeci
- [5] SMOOTH-ON, *Mold Star 15 SLOW*, user manual
- [6] <https://www.gom.com/metrology-systems/atos/atos-triple-scan.html> (05.12.2014.).





# Development of Automatic Packing Line for Single Packs

**Peter PANEV**

Institute of Information and Communication Technologies, at the Bulgarian Academy of Sciences.

Acad. G. Bonchev str., block 2, 1113 - Sofia, BULGARIA

[panevv@gmail.com](mailto:panevv@gmail.com)

## Keywords

*Automation of discrete production*

*Automatic lines*

*Productivity*

*Reliability*

*Manufacturing technologies*

*Professional article*

**Abstract:** In the presented paper the need for packaging and the functions of packaging are examined. Attention is paid to marketing requirements for packaging. The suitability for automation of the packing details is investigated. A methodology based on the structural analysis for the construction of the detail was used. The structure of the packing machine is described. Also some modules of the additional equipment are examined.

## 1. Introduction

The main challenge in the coming years is not only the significant increase the implementation of automation in the production, but also qualitative changes in the transition from small problems and tasks to complex problems and tasks, performing the whole mechatronic and automatic development of the products and their packaging.

The aim of the paper is to design an automatic packing line for single packs.

## 2. Requirement for packaging

The constantly increasing requirements for the appearance of the product, the quality, and the design of the packaging are the main factors determining the efficiency of the packaging automatic machines and lines. These machines are no longer able either to meet the high marketing requirements of packaging or to meet the needs of widely used raw materials, especially recycled materials.

The packaging of a certain product performs several functions: preserving the integrity of the product and of the transport processes, and presenting the complete product in a customer-friendly look. The integrity of the product is important factor. Therefore, the used technological processes and the individual packing operations must not change the product.

The packaged products must be delivered to the user without any breakage, damage, flooding, etc. The products can be transported by land, air and sea. To ensure that an appropriate packaging for a certain product is chosen, it is advisable to contact the appropriate transport company. It is necessary to consult on all the

details and current requirements, concerning the transport of a goods.

The aim of marketing is to have a very well-expressed impact on the appearance of the packaging. This also influences the applied new and principally new technological processes and packaging operations.

Packaging processes and operations in modern production is important to be analyzed. What is the role of packaging; how it affects in its consumption and influence on the sale of the entire product; what problems can be solved using the package; in what value it could help to increase its productivity and reliability in the various industries.

If the desired product for packaging is hazardous or not, it is necessary to take other properties of the packaging product in order to optimize the choice of packing method. These properties are: density, weight, hygroscopicity, types of packaging materials for the product, etc. Particular attention is paid to the used recycled materials for single packs.

## 3. Suitability for automation of packaging elements

The technology of the structure of the products is a complex concept. One of them is technology in terms of the ability to automate the assembly and assembling of units with minimal overall costs [1], [2], [3], [4].

The used methodology is based on the structural analysis of the structure of the product and its details. It is assumed that the implementation of the basic technological operations is justified. The evaluation parameters are arranged in seven steps [5], [6], [7], [8].

<u>Symbols/Oznake</u>		<u>Greek letters/Grčka slova</u>	
$B_{ii}$	- longitudinal analysis	$\delta$	- thickness, mm
	- specifična hidraulička energija		- turbulentna disipacija
$B_{\Sigma}$	- Sum of ball	$\tau$	- items, items/s
	- Gravitacija		- hidraulička korisnost turbine
$K_{cc}$	- Category of complexity		
	- hidraulički gubici		
$t_{wl}$	- limit working time, s		
	- bruto pad		
$t_{it}$	- idle time, s		
	- hod klipa servo-motora		
$\Sigma t_{ofc}$	- own off-cycle time losses, s		
	- turbulentna kinetička energija		
$\Sigma t_{et}$	- extra time, s		
	- konstanta dovodnog cjevovoda		
$t_{lr}$	- time losses due to repairs, s		
	- gubitak vremena zbog popravaka, s		

To evaluate the rate of readiness of the automated manufacturing details, a differential analysis is performed on a differential scheme to determine its  $B_{ii}$  numbers, the sum of the  $B_{\Sigma}$ , which determine the different categories of complexity  $K_{cc}$ .

Table 1 presents the data from the following: a longitudinal analysis to determine the  $B_{ii}$ ,  $B_{\Sigma}$ ,  $K_{cc}$  of the elements. The first two elements have a category of complexity  $K_{cc} = 4$ , and the last  $K_{cc} = 3$ . Due to the complexity of automatic orientation and manipulation, it is advisable to carry out a meticulous analysis of the structure of the elements, the individual parameters, etc. It is necessary to check the feasibility of the design solution.

**Table 1.** Code numbers, ball sum, and category of complexity.

No/	Name/ Naslov	$B_{ii}/$ $B_{ii}$	$B_{\Sigma} /$ $B_{\Sigma}$	$K_{cc}/$ $K_{cc}$
1	Micro corrugated cardboard	3797980	43	4
2	Complete package (kit)	1643661	27	4
3	Leg "Adils"	2512274	23	3

Fig. 1 shows the structure, shape and dimensions of the elements involved in the packing operations of the

assembly line. These items are as follows: assembly instruction, micro corrugated cardboard with thickness of  $\delta = 1,5$  mm, four metal screws, and metal disk (fig. 1a). Micro corrugated cardboard with thickness of  $\delta = 1,5$  mm (fig. 1b), and body of leg "Adils" (fig. 1c).

#### 4. Structure assembly of an automatic packing line

The system approach is used in the development and modular construction of several structural assembly variants. After the obtained results from the analysis, one of them is selected, in which the positive aspects of the other options were applied. The automatic packing line is a line of synchronous type.

*Determining the actual tact.* The actual tune of the automatic packing line is determined on the basis of the marketing studies, made on international markets, with a desired annual production program of around 7 million items per year. This is determined by the following equation:

$$\tau = t_{wl} + t_{it} + \Sigma t_{ofc} + \Sigma t_{et} + t_{lr} [\text{items/s}] \quad (1)$$

At  $t_{wl} = 3,94$ s limit of working hours,  $t_{it} = 1$ s idle time,  $\Sigma t_{ofc} = 0.02$ s own off-cycle time losses,  $\Sigma t_{et} = 0.02$ s extra time,  $t_{lr} = 0.02$ s time losses due to repairs.

$$\tau = 3,94 + 1 + 0,02 + 0,02 + 0,02 = 5 [\text{items/s}] \quad (2)$$

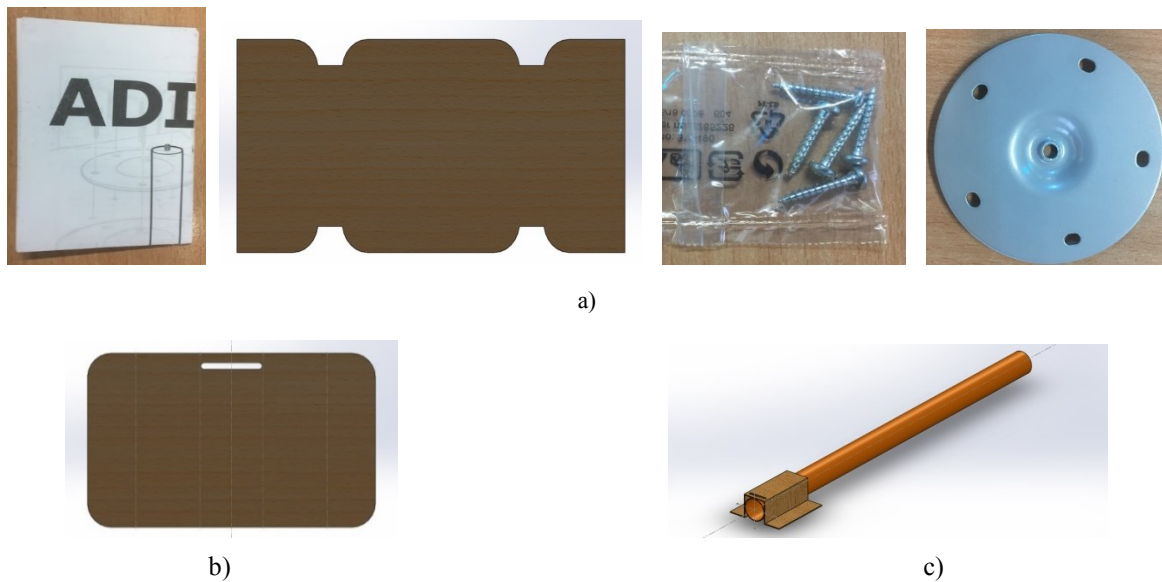


**Figure 1.** Elements for packaging: a) assembly instruction, micro corrugated cardboard, four metal screws, and metal disk; b) Micro corrugated cardboard; c) body of leg "Adils".

#### **Structure assembly of the automatic packaging line.**

An existing and working line (Fig. 2) for packaging of one detail using two types of cardboard is described as follows:

- Placing and folding of Micro corrugated cardboard 1 on conveyor belt.

Micro corrugated cardboards are loaded into a two-seat store. From the first position of the store, the manipulator picks up a micro corrugated cardboard and places it on the first assembly conveyor. The second position of micro corrugated cardboards is loaded with the help of operators. When emptying the work position of the store, during the transportation time of the conveyor automatically the empty store is replaced with a new one. A Manipulator takes micro corrugated cardboard 1 from the store and puts it on an assembly conveyor, whereupon the folding of the micro corrugated cardboards is first done.

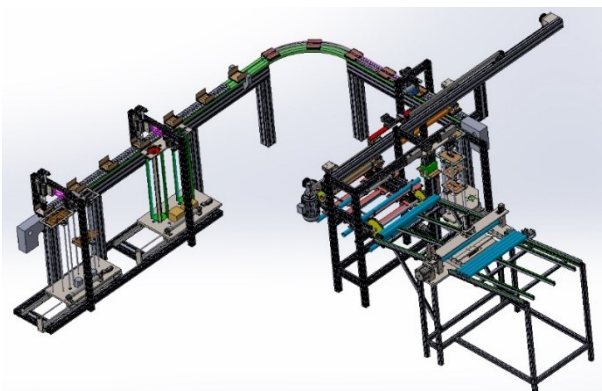


**Figure 2.** Assembly machine.

- Placing the metal disk "heel" detail in the formed box of cardboard 1.

Manipulator takes a detail "heel" from a two-seat store and puts it on the first assembly conveyor in the shaped box of cardboard 1. The manipulator takes from the full store position and the empty position is loaded by operator. The replacement of an empty and full position is made during the transport time of the first assembly conveyor.

- Placing a folded instruction with a pack of screws on a cardboard 1.

Due to the specifics of the folded instruction and the pack of screws, (not packed from our company) and to guarantee 100% insertion in each cardboard, installation will be carried out by an operator. Two additional positions are provided for subsequent automated insertion of a folded instruction and a pack of screws.

- Folding micro corrugated cardboard 1.

When the first assembly conveyor is moved by linear rails, the second fold of the cardboard 1 is carried out and the box closes from the top.

- Applying of heated glue for sticking of cardboard 2 with pipe to cardboard 1.
- Piling module for stopper "step" in painted leg named "Adils".

The module consists of: input store for painted legs, it is loaded by an operator; store for "step" stopper, loaded from the same operator; function module – piling stopper; outlet module store - from there the assembly conveyor 2 takes a leg with stopper.

- Second assembly conveyor

The second assembly conveyor takes a leg with a stopper on the outlet store of the piling module for stopper, and transports it to a cardboard 2 mounting position to the leg.

After that is transported to position from where the manipulator takes it and carries it to glue position with cardboard box 1 for sticking with the box 1.

- Folding cardboard 2 and mounting to leg with mounted stopper.

The monitor takes cardboard 2 from a two-seat store (from the full position), cardboard 2 folds it and puts it (mounted) to the foot with a mounted stopper on an second assembly conveyor. The empty position is manually loaded by operator. Changing the empty position is manually loaded by the operator. The replacement of the empty to full store takes place during the transport time of the second assembly conveyor.

- Manipulator carrying a leg with a mounted stopper and a mounted cardboard.

The pairing (with two transporting positions) manipulator simultaneously takes, carries and places the tube of cardboard 2 from the second assembly conveyor to the position for glue to the cardboard box 1. From the glue position to the cardboard box 1 and under the glue position, it takes the finished leg together with box 1 and transports it and places it on the input conveyor of the packaging machine.

- Input conveyor of the packaging machine.

The conveyor inserts the assembled leg with cardboard box into the packing machine for shrink film.

- Packaging machine.

Packaging the leg with the box in a heat shrink film.

- Thermal tunnel

In this position, the film shrinks and tightly encloses the leg with the box.

- Outgoing conveyor tunnel

The shrink filmed legs are transported to a packing position in a carton. A label is automatically fixed, before leaving the conveyor belt.

## 5. Future steps

The described assembly machine for packaging is used for packaging of details (legs) for IKEA furniture. Now in the technological process are included two human operators. Our plans for the future research and development are to increase the productivity of the packaging line by including of additional equipment – manipulators with flexible PLC based control system, [9], online wireless remote programing and monitoring, data bases for different details and packing types, etc.

## 6. Conclusion

A competitive structure of an automatic packing line for packing in a micro corrugated cardboards package of a complete package (set) and an "Adils" leg body with an actual tact  $\tau_d = 5s$  was developed. In the construction of the Automated Packaging Line the used bought components in the composite are about 86%.

## REFERENCES

- [1] *Automation of Discrete Production* (1990), Editor Ganovski V., Technics, Sofia, Bulgaria
- [2] Groove P., (2008), *Automation Production Systems and Computer-Integrated Manufacturing*, Third education, Pearson Prentice Hall International ISBN – 13 – 207073 – L.
- [3] Dimitrov L., (2009), *Principles of mechanical engineering design*, Heron press, Sofia, Bulgaria.
- [4] Boothroud G., Geoffrey, (1986), *Assembly Automation and Production Design*, Taylor & Francis Group, Published Bocaraton London, UK
- [5] *Innovations, European, national, and regional policy*, (2008), foundation „Fundamental research and communications“ ARC FUND, ISBN 978-954-9456-12-7, Bulgaria.
- [6] Ganovski V., Boyadzhiev I., Klochkov L., (1988), *Automation Lines*, TU-SOFIA, Bulgaria.
- [7] Boyadzhiev I., Klochkov L., Monov B., (1989), *Manual for laboratory exercises and design on automatic lines*, TU-Sofia, Bulgaria.
- [8] Volchkevich LI, (2005), *Automation of Production Processes*, Machine Building, Moscow, Russia
- [9] Kiriazov P., Veneva I., Karastanev S. (2011). *Controllability criteria in designing human assistive devices*, Series on Biomechanics, vol. 26, No 1-2, 2011, pp. 71-76



# Research of Mechanical Characteristics in Tensile Tests of Low Carbon Steel Samples during Transformation from Hot Rolled to Cold Rolled Sheet Metal

**Miglena PANEVA**

Institute of Information and Communication Technologies, at the Bulgarian Academy of Sciences.

Acad. G. Bonchev str., block 2, 1113 - Sofia, BULGARIA

[m.paneva7@gmail.com](mailto:m.paneva7@gmail.com)

## Keywords

*Hot rolling*

*Cold rolling*

*Thermal Annealing*

*Low carbon steel*

*Tensile strength*

*Spectral analysis*

*Professional article*

**Abstract:** In the presented paper is examined the difference between hot-rolled steel and cold-rolled steel, also the production technology and the applications of it. The stages of steel processing, influencing to the overall behavior and hardness of the metal are shown. The most important steps are the cold rolling and the heat treatment. An analysis of the mechanical characteristics is implemented by testing the tensile strength. Experimental results are obtained on a specialized proof machine for testing of metal samples. The results are represented by diagrams and tables.

## 1. Introduction

Carbon steels are steels with up to 2.14% carbon content (C). Soft steel (steel containing a small percentage of carbon, are strong and robust, but not slightly hardened), also known as carbon steel and low carbon steel. Low carbon steel has an approximate carbon content of about 0.05-0.25%, making it malleable and flexible. Those steels are one of the most important compounds in the global industry.

### *Composition and properties*

Iron-carbon alloys contains more than two elements, such as carbon (C), silicon (Si), manganese (Mn), phosphorus (P) and sulfur (S). The properties of the steel are largely determined by the content of these elements, and for carbon steels this content should be minimal (especially phosphorus and sulfur). Steels which have special mechanical and other properties by adding other chemical elements, such as chrome, nickel, tungsten, vanadium, molybdenum, cobalt, etc., or a combination of them, are so called alloy steels. About 90% of all steels produced in the world are carbon.

The carbon has great impact on the properties of the steel. The classification of the steels is based on their carbon content, indicating the content of alloying elements.

As the carbon content increases, the strength and the stiffness increase, reducing the relative protraction and impact strength.

The content of the other elements inevitably associated with the steels is approximately the following: Si <0.5%, P <0.05%, S <0.05%, Mn ~ 0.8%, but in some cases Mn

may exceed 1 % without steel being alloyed. Manganese and silicon increase the strength of steel, and if the Mn content is < 0.4%, there is a risk of pores in steel production, i.e. it acts as a deoxidizer. Silicon is also a deoxidizer (interacts with oxygen to produce, SiO<sub>2</sub>). The products of this deoxidation form non-metal inclusions in the metal and degrade its properties.

Phosphorus is an element that increases the hardness and reduces the plasticity of the metal, it is an unwanted impurity for the steel. Sulfur is also an unwanted element. Like phosphorus, it also falls into the steel during its extraction. The oxygen is a harmful impurity, it falls into the metal during its refining (when the impurities are burned) and occurs in the form of non-metal inclusions, which degrade the mechanical properties [1].

The aim of this article is to trace the mechanical properties of tensile testing of low-carbon steel samples during transformation from hot-rolled into cold-rolled sheet metal.

## 2. Difference between hot and cold rolled sheet metal and its application

### 2.1. Differences in rolling process

The rolling is a manufacturing process in which metal, plastic, paper, glass or other material changes its shape when passing between two shafts.

There are two types of rolling - flat and profiled. For flat rolled products, the final shape of the product is a sheet (thickness less than 3 mm) or plate (thickness over 3

mm). In the profile rolling, the end product is a rod, round, rectangular or more complex shapes.

#### **Symbols/Oznake**

C	- Carbon	S	- Sulfur
Si	- Silicon	Fe-C	- Iron carbon
Mn	- Manganese		
P	- Phosphorus		

The rolling is also classified, according to the temperature of the material. If the metal is above its recrystallization temperature (over 1000 °F), the process is called hot rolling, and if its temperature is below this range (temperatures more close to normal room temperature) - cold rolling. The cold rolling is often used to reduce the thickness of steel sheet and increase the yield strength and hardness of the metal [2]. During the cooling process, the hot-rolled steel (fig. 1) is re-configured, which gives to the finished product more free deviations from the original material. Compared to cold-rolled steel products (fig. 2), the hot rolled steel is softer, which allows to be forced into different shapes. Generally, the cost of cold rolled steel can be twice higher the price of hot-rolled steel, since cold rolling is a more complex process of metalworking than hot rolling.

## **2.2. Applications of hot rolled and cold rolled steel**

The hot-rolled steel is always used to create larger-sized products. It is used for various industrial applications, including steel pipes used in pressure vessels, shipbuilding, construction, gas containers, transportation and etc.



**Figure 1.** Hot rolled steel

Smaller products need to be more durable, always are made of cold-rolled steel. The material is made with hot-rolled steel process, and further thickness reduction is performed on a strip mill without the use of heat. Applications of cold-rolled steel including: automotive components, bathtubs, building and building

components, household appliances, electrical materials, furniture, etc. [3].



**Figure 2.** Cold rolled steel.

## **3. Metal processing technology**

### **3.1. Staining**

The staining is a process where oxides and rust are separated from the surface of metals and alloys by immersion in solutions of acids and bases. The staining may be the last operation before the galvanic coating is applied or the final operation in the processing of the copper and copper alloy products. In some cases, the staining is an intermediate operation that takes place before grinding, soldering, etc. The choice of the staining solutions depends on the type of metal to be treated and the purpose of the process.

The main acid used in the steel industry is hydrochloric acid, although sulfuric acid is more common. The speed is a mandatory for integration into automatic mills that operate at high speeds of production; speeds up to 800 ft / min ( $\approx 243$  meters / min) [4], [5], [6], [7].

In this study, the following sequence is used: The hot rolled roll first passes through washing in a bathtub with water. The next step is two bathtubs with hydrochloric acid, respectively 16% and 18%. The roll passes through four rinsing baths with water to wash off the acid, and the last bathtub is filled with hot water of 80 °C. The last stage is drying the roll. The manipulation is carried out on a continuous uninterrupted pickling line.

### 3.2. Cold rolling

In this study, the cold rolling of the metal is carried out under its recrystallization temperature (usually at room temperature), which increases the strength by hardening the stress up to 20%. It also improves the surface finish and has better tolerances.

The rolling takes place on a rolling mill with one roll (reverse) or multiple rolls (4 or 5), where the strip passes sequentially through each roll.

In this case, it is used a Rolling Mill with one roll, where the rolling tolerances are from 2.3 mm to 0.5 mm sheet thickness (fig. 3), band width - 550 mm. After the final thickness has been obtained, the tensile strength parameters are doubled and the crystal lattice atoms are displaced. The metal has grown from a plastic to a fragile and heat treatment is needed to rearrange the atoms in the crystal lattice and the metal to be plastic again.

In the study is used metal with an input thickness of 2 mm and a width of 550 mm, roll weight 6 tons. The output thickness after rolling is 1,13 mm, after 3 passes through the reversing rollers.

### 3.3. Heat treatment of the metal

The status chart (fig. 4) of iron carbon (Fe-C) for this study graphically presents the phase status of the iron-carbon alloys, depending on their chemical composition, the total load in the furnace and the temperature.



**Figure 3.** Rolling mill with one cell.

At temperatures of about 700 °C (this is the minimum temperature) the steel can be annealed. In modern ideas, this is the temperature of the austenitic eutectoid transformation into the steel [8].

The methodology of the diagram in Fig. 4 is described by the heat treatment process which takes place in 5 steps:

- 1) Compressed air cleaning;
- 2) Heating the metal to 350 °C for a period of 3 hours;
- 3) Subsequent heating of the metal from 300 °C to ~ 650 °C for a period of 6 hours;
- 4) Air cooling until the metal reaches 300 °C;
- 5) Water cooling from 300 °C to 80 °C.

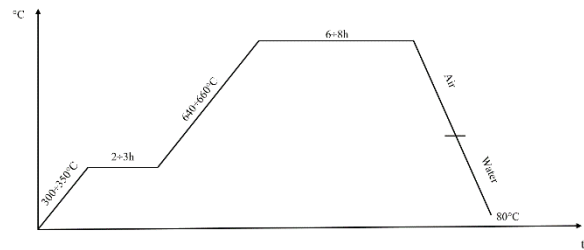


**Figure 4.** Iron carbon (Fe-C) status chart for the study.

A protective gas, which is a mixture of 96% nitrogen and 4% hydrogen, runs during the lighting cycle. The first step is an extremely important process and an invariable part of the cycle because the purpose of passing this protective gas is to expel the oxygen in the space between the coils. Otherwise oxidation of the metal will occur.

The coils are placed one on top of each other, separated by grids, and covered with special lids with heaters for the heating process and cooling towers respectively for the smoothing process (fig. 5). The whole heat treatment cycle takes place within 48 hours for one furnace with 30 tons of metal. During this period the atoms in the crystal lattice of the metal were arranged again and the mechanical indicators returned almost to their original state.



**Figure 5.** 3 heating towers and 3 cooling towers.

## 4. Experimental results

The obtained experimental results of the metal specimens during the different steps of the processing are made with WDW-300 Electromechanical Universal Testing Machine. The WDW series universal testing device (fig. 6) is designed for tension, compression, bend, shear, peel, tore, abrasion on metal, rubber, plastic, fiber, leather, braid, wire, cable, construction materials, wood to inspect their mechanics performances. It is a new type of material testing machine featuring the combination of the latest generation of green electronic technology and ingenious mechanical transmission design, demonstrating a low standby power consume, reduced operation noise, extended operating life and no pollution to the environment [9].

This equipment is with a refined structure that enables more steady loads and precise controls. It adopts the leading high-performance AEC-1200 Controller, which is usually equipped on high-end material testing



machines. The mechanical components collaborate with the pioneered modular Test Live computer testing software to ensure the stability, precision and reliability of the whole system. The maximum tensile load is 300kN, and load accuracy 0,5%. The equipment can test flat specimens from 0 to 20mm, and round specimens from 6 to 60mm. The jaw heads with a range of up to 20 mm work with hydraulics, and jaw heads larger than 20 mm are closed manually. The speed can be from 0,005 mm/min up to 500 mm/min. For the tested specimens is set speed of 20 mm/min [9].

The other used device is BRUKER Q2 ION OES Metals Analyzer [10], [11]. The spectrometer Q2 ION (fig. 7) elevates metal analysis for 30 seconds. It works with argon. It is a versatile multi-matrix system for comprehensive incoming material inspection and quality assurance of metal alloys. Its primary applications and metal matrices include copper, aluminum and iron at smaller foundries, inspection companies, metal recycling and metal fabricators.

The chemical composition of the explored steel is shown in Table 1. The mechanical properties during the different stages of metal processing is shown in Table 2.

**Table 1.** Chemical composition of the explored steel.

C	Mn	Si	P	S
%	%	%	%	%
0.06	0.19	0.01	0.008	0.007

The explored hot rolled steel is produced in Romania by ArcelorMittal Galati S.A.

#### 4.1. Mechanical properties during the different stages of metal processing

**Table 2.** Mechanical properties during the different stages of metal processing.

	Rm	Re	A
	Mpa	Mpa	%
Hot rolled steel	390	305	32
Cold rolled steel	695	695	2.5
After annealing	355	255	33
After skin pas	365	330	25

#### 4.2. Tensile strength diagrams

In Fig. 8 are shown mechanical properties. Fig. 8a shows the mechanical properties of the hot-rolled metal. The diagram clearly shows that the metal protraction plastic irreversible properties. The protraction is calculated using the formula, [12]:

$$\varepsilon_x = \frac{\Delta l}{l} \cdot 100\%.$$

(1) **Figure 7.** Spectrometer.

It is used for all graphics. The load increases rapidly, and after that a dynamic load test is made. The main objective of the experiment is to obtain the relationship between the normal stress and the axial deformation of the test body. This dependence is called working diagram of the material.

Fig. 8b shows a working diagram of the metal after cold rolling. It can be seen that the diagram has no yield line. For such materials, a deflection limit of 0,2 is defined as equal to the voltage at which the residual deflection is 0,2%. The metal already from plastic has become fragile and its durability increases double. The needed parameters are out of norms. To recover the metal to its normal state, it has to undergo thermal treatment. The regime, which is determined in accordance with its chemical composition and weight of the whole furnace is 300 °C/ 2h; 650 °C/6h.



**Figure 6.** Universal testing machine.



**Figure 7.** Spectrometer.

In Fig. 8c is shown a diagram of a mechanical steel test after heat treatment. The results show that the metal has restored its plasticity and the temperature applied to it is appropriate for achieving the goal.

After the heating, [13], [14], all the metal to be treated must pass through one final skin pass (fig. 8d), which is minimal with 3% deformation. It has almost no influence on the mechanical performance, but it favorably affects the appearance of the metal (making it smoother and strips the coil, if received after sticking the process). Only the yield strength increases slightly, [15].

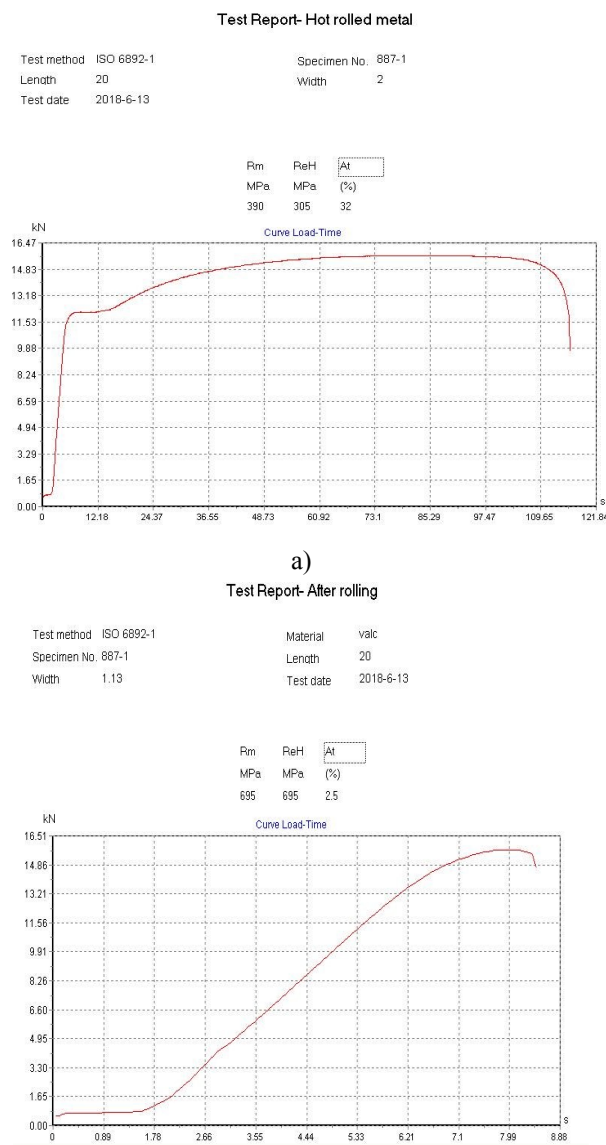
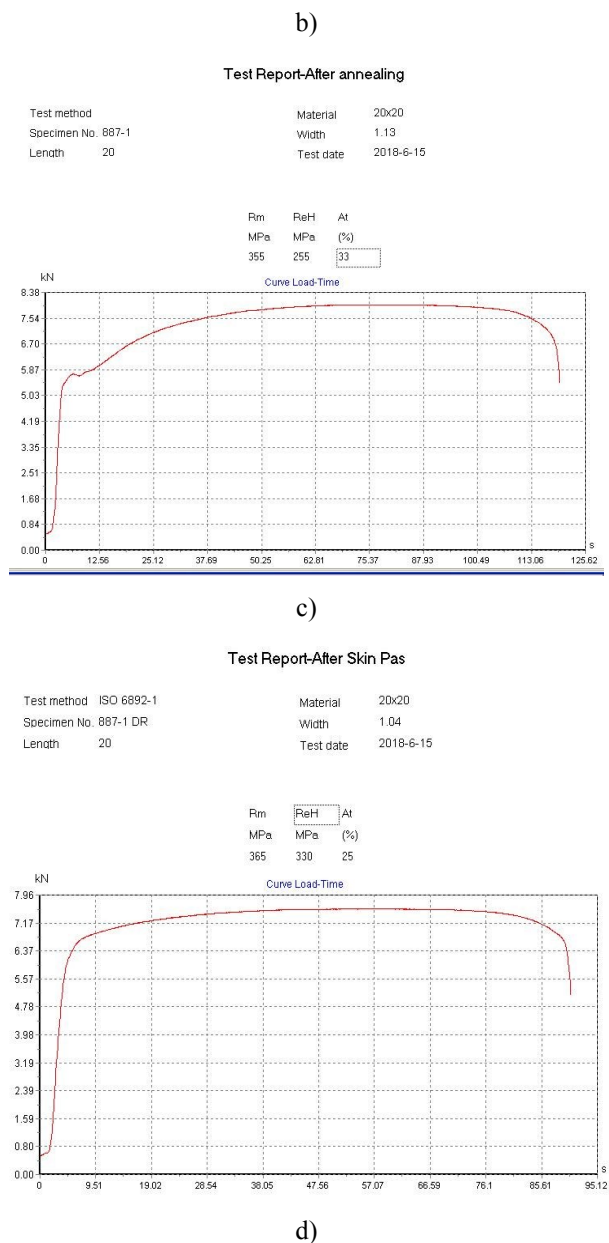


**Figure 8.** Mechanical properties.

## 5. Conclusion

From the obtained results, it was concluded, that before processing of low-carbon hot-rolled metal, it shows plastic properties and has low mechanical properties - the



metal is soft and easy to process. After his cold rolling, it loses these properties and becomes fragile, it has no deflection limit, and its mechanical indicators increases double, and the protraction drops to 2.5%. In this scenario, it is no longer suitable for use in the industry.



However, after its heat treatment, the steel returns its plasticity properties and becomes suitable for the production of tubes and other metal products. The last pass after heat treatment has a favorable appearance.

## REFERENCES

- [1] Wikipedia:  
[https://bg.wikipedia.org/wiki/%D0%92%D1%8A%D0%B3%D0%BB%D0%B5%D1%80%D0%BE%D0%B4%D0%BD%D0%B0\\_%D1%81%D1%82%D0%BE%D0%BC%D0%B0%D0%BD%D0%B0](https://bg.wikipedia.org/wiki/%D0%92%D1%8A%D0%B3%D0%BB%D0%B5%D1%80%D0%BE%D0%B4%D0%BD%D0%B0_%D1%81%D1%82%D0%BE%D0%BC%D0%B0%D0%BD%D0%B0)
- [2] Wikipedia:  
<https://bg.wikipedia.org/wiki/%D0%92%D0%B0%D0%BB%D1%86%D1%83%D0%B2%D0%B0%D0%BD%D0%B5>
- [3] <http://bg.buildingplate-exporter.com/info/differences-between-hot-rolled-coil-and-cold-r-22051379.html>
- [4] Liu, David Lipták, Béla G. (1997). *Environmental engineers' handbook*. CRC Press. p. 973. ISBN 978-0-8493.
- [5] CRCA Steel - Cold Rolled and Close Annealed". materialgrades.com. 4 November 2017. Archived from the original on 15 November 2017. Last visited 29 April 2018.
- [6] Hot Rolled vs Cold Rolled Steel. spaco.org. Archived from the original on 29 April 2018. Last visited 29 April 2018.
- [7] Eagleson, Mary (1994). *Concise encyclopedia chemistry*. Walter de Gruyter. p. 834. ISBN 978-3-11-011451-5.
- [8] Cold Rolled Steel". Archived from the original on 7 April 2014. Last visited 31 March 2018.
- [9] Manual for Working with an Electronic Computerized Tensile Strength Machine 2011
- [10] Manual for Spectrum Analyzer device.
- [11] Ivanov I. strength of materials, lectures 2006
- [12] Penchev T., Karastoyanov D., Gyoshev S., Altaparmakov I., (2016). *Monography - Innovative Impact Processes: Machines, Theory, Experiments, Modeling*, Academy publishing house, Sofi, ISBN 978-954-322-860-7
- [13] Karastoyanov D., Ivanova D., Stoimenov N., (2015). *Technology for production of high-temperature materials and alloys including nano elements.*, Recent Advances in Systems, 19th International Conference on Systems (part of CSCC'15), Zakynthos Island, Greece, July 16-20, pp. 177-181, ISSN: 1790-5117, ISBN: 978-1-61804-321-4.
- [14] Stoimenov N., Karastoyanov D., Vukov A., Neshkov T., Klochkov L., Gyoshev S., (2014). *Thermographic Study Of Rolls on Roller Batteries.*, XII International SAUM Conference on Systems, Automatic Control and Measurements., Nis, Serbia, November 12th-14th, pp 25-28, ISBN 978-86-6125-117-7
- [15] Gyoshev S., Penchev T., Karastoyanov D., (2014). *Study of parameters of controlled impact by impact deformation of elastic and elastic-plastic materials*. 5th European Conference of Mechanical Engineering (ECME' 14), November 22-24, Florence, Italy, p. 113-119, ISBN: 978-960-474-402-2

# SANS characterization of mono-ethylene-glycol based industrial polyurethanes samples

**Massimo ROGANTE<sup>1)</sup>, Vasily T. LEBEDEV<sup>2)</sup> and Aurel RADULESCU<sup>3)</sup>**

1) Rogante Engineering Office, Contrada San Michele n. 61, I-62012 Civitanova Marche, **Italy**

2) Petersburg Nuclear Physics Institute, Gatchina, St. Petersburg, **Russian Federation**

3) Forschungszentrum Jülich GmbH, Lichtenbergstr. 1, D-52748 Garching, **Germany**

main@roganteengineering.it

## Keywords

polyurethanes  
porosity  
SANS

*Original scientific paper*

**Abstract:** Distribution and dimensions of pores which are formed during the mixture's expansion of polyurethanes due to chemical reaction, and other defects, can influence notably material's performances. Mixture composition, injection speed and power, melt temperature and melt viscosity influence the appearance of these pores and the related parameters such as size distribution, interface area, concentration and volume fraction. The spatial distribution of these pores is not homogeneous, as it changes depending on the different zones of the mould in which the mixture is expanded. This paper concerns a characterization by small angle neutron scattering (SANS) of the bulk structure of commercial mono-ethylene-glycol based polyurethane samples of the safety footwear industry (manufactured with different reactant mixtures and obtained from diverse zones of the mould), especially with respect to micro- and nano-pores and their arrangement. Results are expected to be useful for different industrial sectors involving polyurethanes.

## 1. Introduction

Polyurethanes are polymers containing the urethane linkage in their backbone chain, and they are made by reacting di-isocyanates with di-alcohols. Polyurethane chains form easily from the hydrogen bond, hence these polymers can be very crystalline. Polyurethanes are largely adopted in different industrial sectors: in the safety footwear industry they are utilized for the production of microcellular shoe soles. Typical shoe-sole systems utilize a single surfactant. The combination of two different surfactant chemistries has improved dimensional stability, surface characteristics and, in general, physical properties of the final product. A complicated structural organization of polyurethanes, containing crystalline and amorphous domains, can really influence the material's functional properties: under particular conditions (e.g., mechanical and thermal loading, aggressive environment and aging), it leads to the material's degradation, even in fresh-prepared bulk samples and, in particular, if defects are present in the material. Distribution and dimensions of pores which are formed during the mixture's expansion due to chemical reaction, and other defects, can influence notably material's performances. Mixture composition, injection speed and power, melt temperature and melt viscosity influence the appearance of these pores and the related parameters such as size distribution, interface area, concentration and volume fraction. The interface

area, in particular, could play an important role in lending strength and durability to the considered materials. The spatial distribution of these pores is not homogeneous, as it changes depending on the different zones of the mould in which the mixture is expanded. A variation of one of the mentioned parameters influences the material's characteristics, thus knowledge of these parameters is important to understand and improve material's performances.

A high citation index exists on polymers (e.g., in *Macromolecules*, *Polymer Content*, *Physical Review*, etc.), and some publications have been produced, related neutron beam investigations of these materials (e.g., [1-5]) A SANS investigation was already performed of polyurethane samples changing in chemical composition and technology, obtained from a mixture of: 4-4' Methylene Diphenil Isocyanate, polyester resins, Mono Ethylene Glycol, Triethyldiamine and 1,4-Diazabicyclooctane and Tri Ethanol Amine as catalysts, Dabco DC-193 as surfactant and water as blowing agent. The adopted instrumentation covered a Q-range from  $0.004 \text{ \AA}^{-1}$  to  $0.5 \text{ \AA}^{-1}$ , allowing density composition and magnetization fluctuations in materials to be measured on a length scale of  $10 \text{ \AA}$  to  $1000 \text{ \AA}$ . Such study has shown the industrial applicability of SANS, and results are published in [6, 7].

**Symbols/Oznake**

$I(Q)$	- scattered intensity, ...
	- ...
$Q$	- scattering vector, $\text{\AA}^{-1}$
	- ...
$r$	- radius (size), nm
	- ...
$S(Q)$	- scattering cross section, $\text{cm}^{-1}$
	- ...

**Greek letters/Grčka slova**

$\theta$	- scattering angle, rad
	- ...
$\lambda$	- neutron beam wavelength, $\text{\AA}$
	- ...
$\rho$	- scattering length density, $\text{\AA}^{-2}$
	- ...

The main aim of the present work has been to check: the feasibility of SANS measurements of mono-ethylene-glycol based industrial polyurethanes samples by using a SANS instrument which combines the conventional pinhole and focusing lenses modes; the complementarity of this technique with the usually recommended X-ray (lab instrument) for seeing the defects in the material. The main scope has been to characterize the bulk structure of commercial polyurethane samples of the safety footwear industry (manufactured with different reactant mixtures and obtained from diverse zones of the mould), especially with respect to micro- and nano-pores and their arrangement (grouping). SANS allows detecting H inside the pores, while SAXS detects only N and C. The sizes of the mentioned pores can be different, due to the molecular orientation around these pores (internal surface effect). The information about these pores obtained by SANS progresses the knowledge already achieved by using fast-neutron radiography and -

tomography, which has allowed characterizing the structures of macro-scale pores inside the considered materials [8]. Neutron radiography, SANS and SAXS, in this case, are complementary. By SANS, due to a larger beam size (usually,  $1 \times 1 \text{ cm}^2$ ), an averaged view over a larger volume of sample is achieved, which makes the results more representative for the morphological properties of such disordered materials than the SAXS results, which are provided over rather punctual regions, due to the reduced beam size (hundreds of micrometre in size).

The present work is a part of a complete study of polyurethanes that the Rogante Engineering Office has designed by adopting advanced methodologies. It is focused in particular on the size distribution of nanosized pores, useful to understand the structural basis for the physico-chemical properties and consequently to advance quality and durability.

## 2. Materials and methods

Four polyurethanes samples have been selected for this study, which are listed in Table 1 and shown in Figure 1. These polyurethanes have been manufactured with varied known reactant mixture ratios with dissimilar branching levels and obtained from different zones of the production mould.

**Table 1.** List of the investigated polyurethanes samples.

sample	colour	density
1	black	B) expanded (low-density) systems
2	gray	A) compact (high-density) systems
3	semi-transparent	A) compact (high-density) systems
4	white	B) expanded (low-density) systems

The considered samples are made of the following two main polyester based polyurethanes systems: A) for compact parts such as shoe treads; B) for expanded parts such as intermediate shoe soles. The elemental formula

is  $\text{NH}+(\text{CO})+\text{O}+\text{C}_{15}\text{H}_{10}\text{N}_2\text{O}_2$  and the chemical composition is the following: polyol polyester;

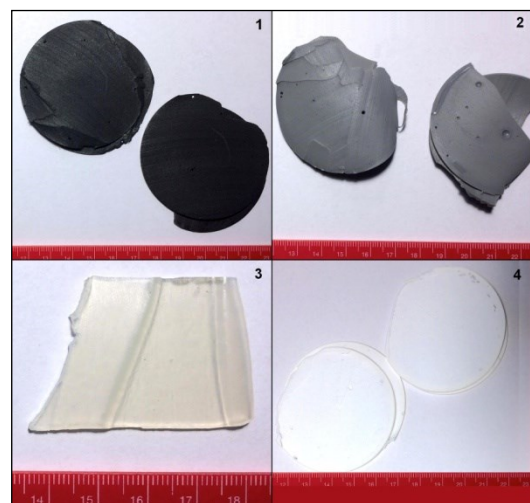


**Figure 1.** The investigated polyurethane samples, with reference to Table 1.

4,4-diphenylmethane diisocyanate; tertiary aliphatic amines, and chain extenders. Table 2 reports the main macroscopic (mechanical) characteristics.

**Table 2.** Main macroscopic characteristics of the investigated polyurethanes.

Characteristics	A	B
density (kg/m <sup>3</sup> )	1100	420-450
hardness (Shore A)	62-65	46-50
traction (MPa)	15.0	5.7
elongation (%)	600	390
bending at +20°C (kcycles)	30	30
A) compact (high-density) systems		
B) expanded (low-density) systems		

These samples have been already investigated by fast-neutron radiography and tomography: in particular, information on macro-scale bubble structures (bubbles down to 225µm) and defects with sizes of up to 1.5 mm inside the considered materials were achieved [8].

SANS deals with elastic and coherent scattering:  $I(Q)$  is measured as a function of the incoming neutron flux  $\Phi$ , the instrument specific constant  $A$ , the sample transmission  $T$  and the sample volume  $V$ .  $\Sigma$  is the total area of the interface per unit volume of the sample.  $d\Sigma/d\Omega$  is the so-called form-factor  $F(Q)$ , which contains information about the scattering particles of the sample. These particles are the nano-sized inhomogeneities in the studied material (e.g., pores and nano-cracks). The form factor, therefore, can be expressed with the characteristic size of the scattering particle. Scattering data are interpreted, then, by using specific models. SANS allows studying materials at the nano- and micro-levels in a non-destructive way: it provides statistical information averaged over a macroscopic volume, giving possibility to investigate the nanoscopic features, thus obtain

information on the processes in the whole volume of the sample. Parameters as diameter, concentration, volume fraction and area of interface can be monitored by measuring the scattering of the neutrons from the samples in angles smaller than 5 degrees. Knowledge of nano- and microstructural factors obtained by SANS (e.g., voids and inhomogeneities) can already induce on the material behaviour in the planning phase, playing a decisive role in the debugging of material selection and engineering design requirements. This method allows investigations on fine-pore porosity and pore size distribution. The structural features of nanoscale inhomogeneities are reflected by key parameters involved in the mathematical functions modelling the scattering intensity curves. The theoretical base of SANS technique can be found in various references [e.g., 9-11].

The SANS measurements have been carried out by using the KWS-2 instrumentation of the Heinz Maier-Leibnitz Centre, Garching, Germany. Such device is a classical pinhole SANS instrument where, combining the pinhole mode using different neutron wavelengths and detection distances with the focusing mode using MgF<sub>2</sub> lenses, a wide Q-range on one sample at once between  $1 \times 10^{-4}$  and  $0.5 \text{ \AA}^{-1}$  can be explored. Size levels and correlations between a few Angstroms and 1 micron can be investigated in a continuous way, and one single final scattering curve is obtained. A 3-mode spherical approximation has been used to describe the scattering from the bubbles imbedded into the polymer bulk. For the considered measurements, the pinhole was adopted using different neutron wavelengths (i.e., in the range  $5.000 \div 11.320 \text{ \AA}$ ), measurement times (i.e., in the range  $60 \div 1,000 \text{ s}$ ), detection distances and focusing with lenses. Figure 2 shows a scheme of the adopted instrument.

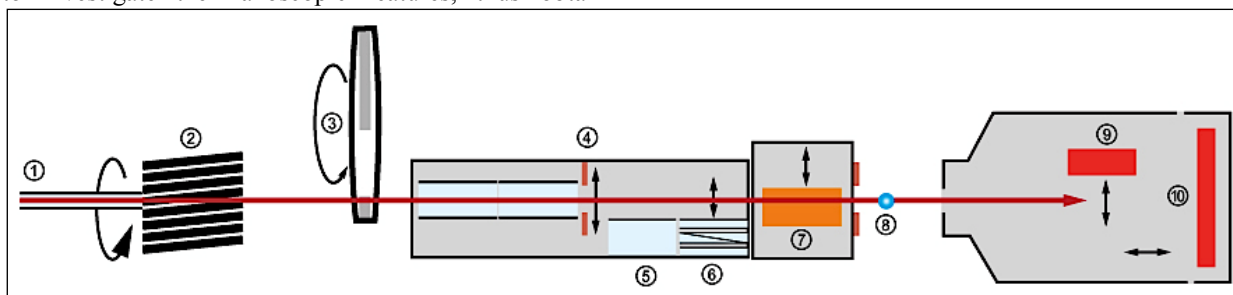


**Figure 2.** Scheme of the adopted KWS-2 SANS instrumentation: neutron guide (1); velocity selector (2); high-speed chopper (3); entrance aperture (4); neutron guide sections  $18 \times 1 \text{ m}$  (5); transmission polariser (6); MgF<sub>2</sub> focussing lenses (7); sample aperture (8); high resolution position-sensitive detector (9); <sup>3</sup>He tubes array detector (10).

### 3. Results and discussion

The samples of polymers (1-4) prepared by different technologies have been tested by SANS in wide range of momentum transfer,  $Q = 0.002 \div 5 \text{ nm}^{-1}$ , to search various levels of their molecular and supramolecular structure as well as micron sized domains of macromolecules at the

scales  $R \sim 10^0 \div 10^3 \text{ nm}$ . Samples 1, 2 and 4 have been investigated in two positions on the sample surface, while sample 3 only in one position. As a result of the experiments, the scattering cross sections of the samples  $\sigma(q) = d\Sigma/d\Omega$  per unit solid angle ( $\Omega$ ) and  $\text{cm}^3$  were evaluated. Figures 3 to 6 show respectively the obtained SANS curves for samples 1 to 4, while Figure 7 reports

the merging curves for all the considered samples.

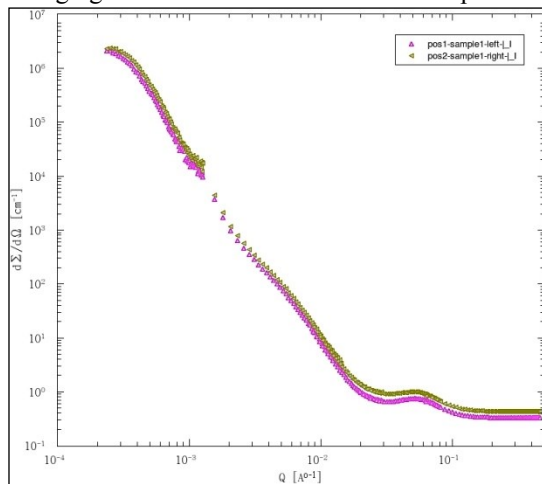


**Figure 3.** The two SANS curves for the sample 1.

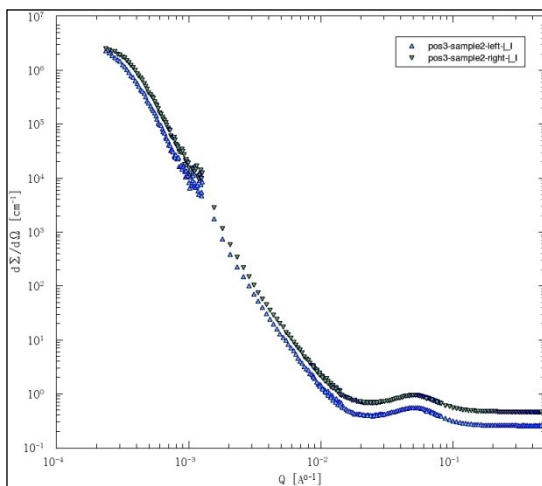


**Figure 4.** The two SANS curves for the sample 2.

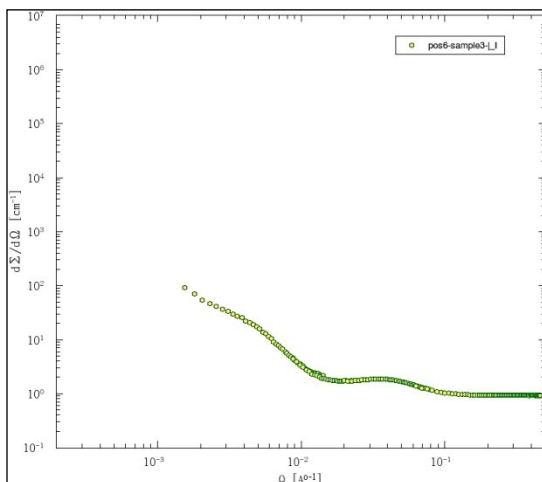


**Figure 5.** The SANS curve for the sample 3.

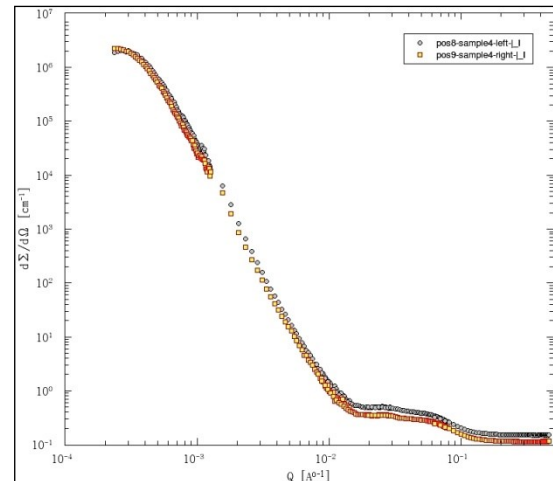


**Figure 6.** The two SANS curves for the sample 4.

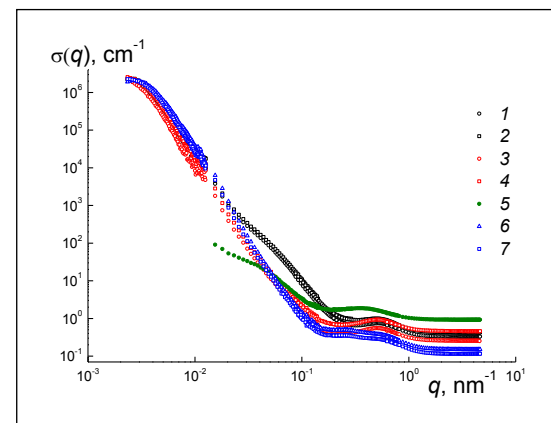


**Figure 7.** Scattering cross sections  $\sigma(q)$  of the samples vs. momentum transfer  $Q$ . The data for the samples 1, 2 and 4 are presented for two different point (left, right) in the films planes, i.e. (1,2), (3,4), (6,7). Only a single measurement (5) has been carried out for the sample 3.

The samples 1;2;4 demonstrate a quite similar scattering data in different point of the films tested. It confirms a satisfactory uniformity of their properties in the volumes of films that certifies the required technological conditions realized. All the samples show common features in the profiles of scattering curves. At low values of  $Q < 0.1 \text{ nm}^{-1}$  the cross sections (samples 1;2;4) reveal a great increase by seven orders in magnitude. This indicates the substantial inhomogeneity of polymers at nano(micro)scales. Obviously, the hump on the scattering curves at  $Q^* \sim 0.5 \text{ nm}^{-1}$  reflects a spacing  $\sim 2\pi/Q^* \sim 10 \text{ nm}$  between tiny regions with short range order in the package of chain segments. Another less pronounced hump at  $Q^{**} \sim 0.05 \text{ nm}^{-1}$  should be attributed to some density fluctuation at the scales comparable or larger macromolecular diameter  $\sim 2\pi/Q^{**}$ .



$\sim 100$  nm, since interpenetrating chains may form globular or fractal type structures. At last a saturation of the cross sections at the lower edge of  $Q$ -diapason means integration of the aforesaid structures into micron-sized domains.

To get a more quantitative structural information, the incoherent scattering contribution  $\sigma_{inc}$  has been removed from the scattering data. This contribution, approximately, is proportional to the concentration of hydrogen in the samples since protons induce very strong incoherent scattering. It is revealed a constant level of  $\sigma(Q) \approx \sigma_{inc} \sim 0.1$  cm<sup>-1</sup> at  $Q > 2$  nm<sup>-1</sup>. Assuming smooth borders of small polymer regions visible in the interval

of  $Q$ -values comparable to  $Q^* \sim 0.5$  nm<sup>-1</sup> (hump), the cross section were modified,  $Q^4\sigma(Q)$ . In this Porod's presentation, all the data obey a linear function:

$$Q^4\sigma(Q) = A + BQ^4 \quad (1)$$

Here, the parameter  $A = (\Delta K)^2 2\pi S_i$  is proportional to the squared contrast factor of the scattering objects, and  $S_i$  is their surface total area. The other parameter represents the incoherent background,  $B = \sigma_{inc}$ . Both parameters are given in Table 3.

**Table 3.** Parameters of function (1).

Sample No	A, nm <sup>-4</sup> cm <sup>-1</sup>	B, cm <sup>-1</sup>	A/B, nm <sup>-4</sup>	Averaged A/B, nm <sup>-4</sup>
1, left	0.0879±0.0004	0.3276±0.0001	0.2683 ± 0.0012	0.1503±0.0002
1, right	0.0630±0.0001	0.4316±0.0001	0.1460±0.0002	
2, left	0.0338±0.0001	0.2582±0.0001	0.1309±0.0004	0.1365±0.0004
2, right	0.0913±0.0006	0.4587±0.0001	0.1990±0.0013	
3	0.1150±0.0010	0.9238±0.0002	0.1245±0.0011	0.1245±0.0011
4, left	0.0270±0.0001	0.1523±0.0001	0.1773±0.0007	0.2019±0.0006
4, right	0.0431±0.0002	0.1135±0.0001	0.3797±0.0018	

Figure 8 illustrates the fitting procedure for the sample 1 (left).

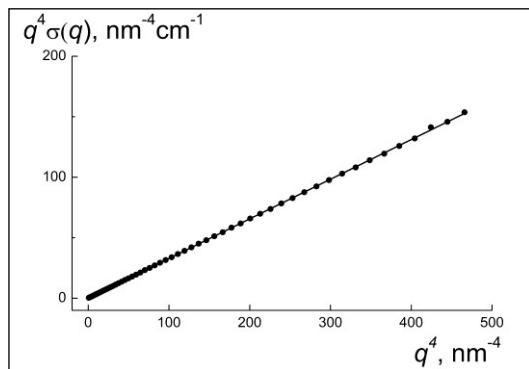


**Figure 8.** Data in Porod's presentation for the sample 1 (left). The line shows the fit by function (1).

It is of principal importance that all the samples demonstrate Porod's scattering law,  $\sigma(Q) - \sigma_{inc} \sim 1/Q^4$ , which testifies sharp borders of small scattering objects in the polymer matrices.

The parameter A proportional to the total area of the inner borders  $S_i$  was normalized to the incoherent cross section (B). The latter is a measure of proton concentration in the sample. Thus, such a normalization allows calculating the specific area of borders  $\sim A/B$  per unit mass of the sample. This is really significant, since of very different densities of the samples and probable their inhomogeneity. As a result, in the expanded samples as compared to the compact ones, the averaged  $A/B \sim S_i$  magnitude indicates an inner borders' area higher by 15 % (Table 3). Further analysis of scattering has been devoted to the evaluation of characteristic dimensions of

structural elements forming the polymer matrix. The scales of these entities are clear visible if the dominating  $Q$ -dependence of the cross sections  $\sigma(Q) - \sigma_{inc} \sim 1/Q^4$  is compensated in the Porod's presentation shown in Figure 9, in which the coherent part  $\sigma_C = \sigma(Q) - \sigma_{inc}$  is plotted for the sample 1 (left).

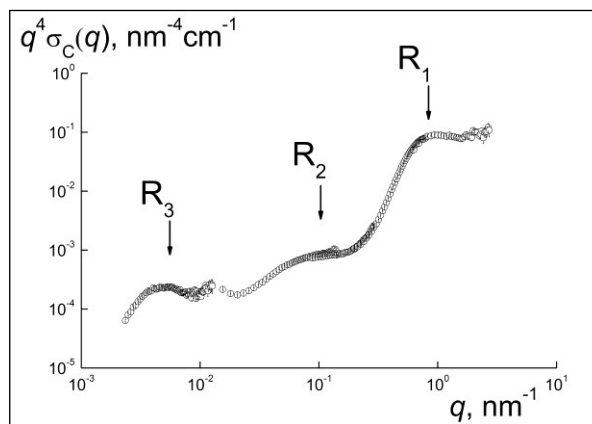


**Figure 9.** Coherent part of cross section  $\sigma_C(Q)$  vs. momentum transfer for the sample 1 (left).

In Figure 9 the characteristic radii of structural elements are shown. As above discussed, the first radius  $R_1 \sim \pi/Q^* \sim 5$  nm is a measure of small ordered regions with dense parallel package of chain segments. The second radius  $R_2 \sim \pi/Q^{**} \sim 50$  nm characterizes the aggregates composed of entangled (linked) chains. The third size  $R_3 \sim \pi/Q^{***} \sim 500$  nm is defined by the position of the kink-point  $Q^{***} \sim 0.005$  nm<sup>-1</sup> corresponding to large domains formed by the aggregates.

Practically, the same picture can be drawn for other samples. The large-sized structures are observed at the lower edge of  $Q$ -diapason, and their gyration radii ( $R_G$ ) are determined directly from the data Guinier approximation (Figure 10),

$$\sigma_C(Q) = \sigma_o \exp[-(QR_G)^2/3] \quad (2)$$

where  $\sigma_o$  is the forward cross section. The parameters of the function (2) are listed in Table 4.

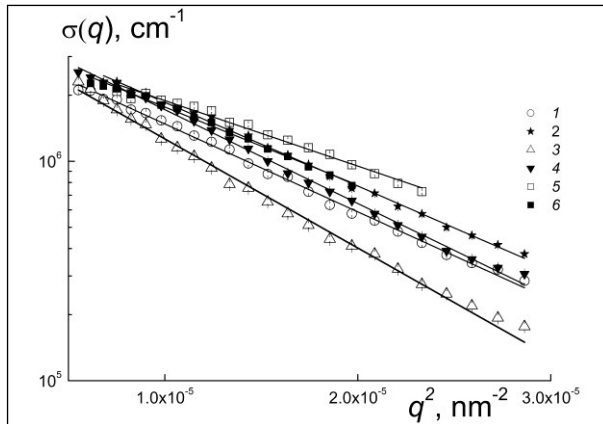


**Figure 10.** Guinier-approximation of the scattering data for the samples 1, 2 and 4. Measurements in the points left (1,3,5) and right (2,4,6).

The domains in the dense sample 2 have larger dimensions  $R_G \sim 540$ -590 nm, while in the expanded samples 1 and 4 smaller domains with the radii  $R_G \sim 450$ -530 nm are observed.

The difference in the package of the polymers of high or low density is revealed by the analysis of the forward cross sections as defined by the polymer scattering length density  $K = 2.5 \cdot 10^{10} \text{ cm}^{-2}$ , the relative value of the mass density fluctuations ( $\Delta\rho/\rho$ ), the correlation volume  $V_C = (4\pi/3)^{3/2} R_G^3$ .

The treatment of the scattering data has been performed taking into account the possible presence of meso (macro) scopic cavities in the samples. The small angle scattering is induced by smaller imperfections in the nano (micro) sized range of dimensions. Therefore, we estimated the concentrations of protons in the samples from the incoherent cross sections,  $\sigma_{inc} = B$  (Table 3), using known magnitudes of  $\sigma_{inc}$  for light water [12].

It enables us to calculate the shares of bulk polymer in the samples and to make the necessary corrections to get the real values of the forward cross sections  $\sigma_{oN} = K^2 (\Delta\rho/\rho)^2 V_C$ .

Finally, we have found the characteristic mass density fluctuations  $\Delta\rho/\rho \sim 7$ -16 % in the samples (Table 4). As it is showed, the dense compact sample 2 is composed of larger domains with lower deviations in mass density,  $\Delta\rho/\rho \sim 7$ -8 %, comparatively to the expanded samples 1 and 4 being more inhomogeneous,  $\Delta\rho/\rho \sim 8$ -16 %. These magnitudes of density fluctuations should be compared to the share of the samples' volume  $\Phi_P$  occupied by the bulk polymer (the residual part is related to the free volume, i.e. the macroscopic cavities) (Table 4).

**Table 4.** Parameters of the Guinier function (2): measured forward cross section ( $\sigma_o$ ) and gyration radius ( $R_G$ ), normalized cross section ( $\sigma_{oN}$ ) and relative estimated density fluctuations ( $\Delta\rho/\rho$ ).

Sample No	$\sigma_o \cdot 10^{-6}, \text{ cm}^{-1}$	$R_G, \text{ nm}$	$\sigma_{oN} \cdot 10^{-6}, \text{ cm}^{-1}$	$\Delta\rho/\rho, \%$	$\Phi_P, \%$
1, left	$3.72 \pm 0.04$	$526 \pm 2$	$5.29 \pm 0.06$	$8.3 \pm 0.1$	$70 \pm 10$
1, right	$4.47 \pm 0.04$	$513 \pm 2$	$4.83 \pm 0.04$	$8.2 \pm 0.1$	$93 \pm 10$
2, left	$3.97 \pm 0.05$	$586 \pm 2$	$7.18 \pm 0.09$	$8.2 \pm 0.1$	$55 \pm 10$
2, right	$4.60 \pm 0.05$	$543 \pm 2$	$4.68 \pm 0.05$	$7.4 \pm 0.1$	$98 \pm 10$
4, left	$3.77 \pm 0.05$	$454 \pm 3$	$11.53 \pm 0.15$	$15.2 \pm 0.2$	$33 \pm 10$
4, right	$4.01 \pm 0.05$	$496 \pm 3$	$16.50 \pm 0.21$	$15.9 \pm 0.2$	$24 \pm 10$

Indeed, in the sample 4 a large amount of free volume ( $1 - \Phi_P$ )  $\sim 70$ -80% correlates with high density fluctuations,  $\Delta\rho/\rho \sim 15$ -16 %, while in the samples 1, 2 a lower free volume part ( $1 - \Phi_P$ )  $\sim 20\%$  in average corresponds to moderate magnitudes of density fluctuation in the bulk polymer,  $\Delta\rho/\rho \sim 7$ -8 %.

The specific structural features of high- and low-density polymers are better revealed at nanoscale as a result of analysis in terms of correlation functions. For the samples 1-4, the distribution of distances between the scattering centres (segments, regions of short range order, aggregates of macromolecules) have been

restored,  $G(R) = R^2 \gamma(R)$ , where  $\gamma(R)$  is a pair correlation function (see Figure 11).

The correlation spectra demonstrate the presence of tiny particles (diameter  $\sim 10$  nm) visible at low radii as a weak peak (sample 3) or masked by intense peak in the interval  $R \sim 10$ -150 nm. In Fig.1,3 these small particles are revealed as hump in the position  $Q^* \sim 0.5 \text{ nm}^{-1}$  and a kink corresponding to the radius  $R_l \sim 5$  nm. They compose much larger structures having characteristic radii  $R_m \sim 50$ -80 nm (maximum position) (Figure 11). Quite symmetric profiles of the correlation spectra for the samples 1, 2 and 4 are satisfactory described by the sum of two Gaussians,

$$G(R) = g_1 R^2 \exp[-(R/R_1)^2] + g_2 R^2 \exp[-(R/R_2)^2] \quad (3)$$

where the short-range correlations with characteristic radius  $R_1$  are presented by the first term, and more extended correlation at distance  $\leq R_2$  should be attributed to the second term.

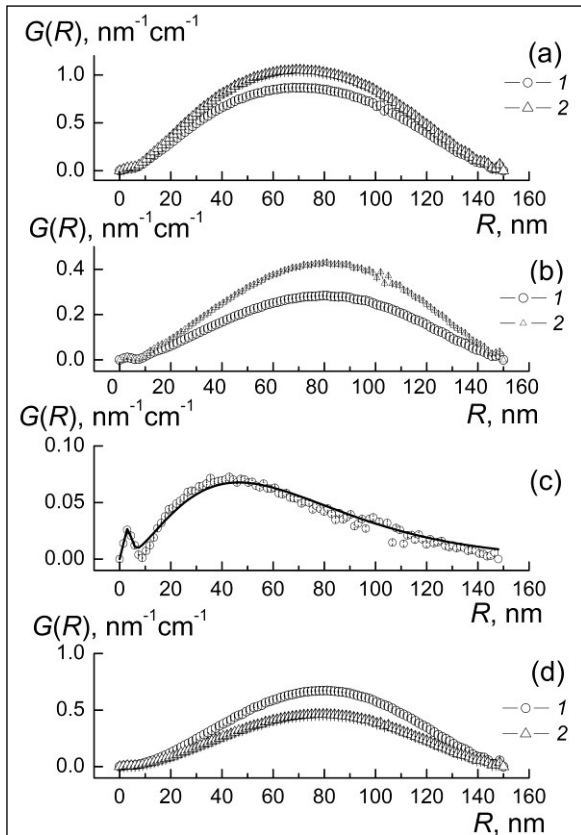


**Figure 11.** Spatial correlations in the polymers 1-4 (a-d), functions  $G(R)$  vs. radii. Data for left and right points are indicated (1, 2). The curve (d) represent the model function (3).

These terms have the weight factors  $g_1$ ,  $g_2$ . The parameters  $R_1$ ,  $R_2$  give the magnitudes of gyration radii of corresponding entities,  $r_{g1,2} = (3/4)^{1/2} R_{1,2}$  (Tab.3). On the other hand, the sample 3 exhibits asymmetric spectrum which obey another law,

$$G(R) = g_1 R^2 \exp[-(R/R_1)^2] + g_2 R^2 \exp[-(R/R_{2C})^2] \quad (4)$$

where the second term is exponential one with correlation radius  $R_{2C}$  which defines the gyration radius of the observed structures,  $r_{gC} = \sqrt{6} \cdot R_{2C}$  ( see Table 5).

The data in Table 5 show the rays of small and middle structural dimensions close to each other in the series of samples,  $r_{g1} \sim 2.3-2.8$  nm and  $r_{g2} \sim 52-63$  nm. In the dense polymer 2 the size of the small globules ( $r_{g1}$ ) becomes less than that in the expanded polymer 1 by 20 %, but the relationship between large radii  $r_{g2}$  is inverse. In the dense polymer, the size  $r_{g2}$  has grown by  $\sim 20$  %.

**Table 5.** Gyration radii of small and middle-sized structures in the samples 1-4.

Sample No	$r_{g1}$ , nm	$r_{g2}$ , nm
1, left	$2.56 \pm 0.01$	$52.43 \pm 0.02$
1, right	$2.71 \pm 0.01$	$52.54 \pm 0.02$
2, left	$2.27 \pm 0.01$	$61.92 \pm 0.02$
2, right	$2.25 \pm 0.01$	$62.87 \pm 0.02$
3	$2.56 \pm 0.01$	$56.98 \pm 0.10$
4, left	$2.77 \pm 0.01$	$62.53 \pm 0.01$
4, right	$2.67 \pm 0.01$	$61.72 \pm 0.02$

The expanded polymer 4 demonstrates enhanced size of small globules, while large structures in them have quite the same size as in the dense sample 2. The sample 3 exhibits well pronounced structuring when both types of structures are clear visible separately. Obviously, these subtle structural features should influence on mechanical (functional) properties of materials.

#### 4. Conclusions

A complicated structural organization of polyurethanes may have a strong influence on the materials functional properties. Under particular conditions such as mechanical and thermal loading and aging, it leads to the material degradation, even in fresh-prepared bulk polymers and especially if defects are present in the material. SANS technique has helped to characterize polyurethanes manufactured with varied known reactant mixture ratios with dissimilar branching levels and obtained from different zones of the production mould. The micro- and nano-properties of these materials could be compared to macroscopic characteristics (e.g., strength, density and bending resistance). The results could contribute to:

- better understand quality and inner defects of the considered polyurethane mixtures, which can be correlated with the macroscopic functional properties or performances and also with functional parameters of the injection device;
- obtain indications to improve the dimensional stability to control and predict such functional properties, strongly depending on size and amount of defects as well as on their total area;
- study the possible replacement of components in the mixture, with the purpose of reducing the costs without worsening characteristics and performances.

## REFERENCES

- [1] Tsang F. Y., Alger D. M., Brugger R. M., (1978), *Neutron gauging to detect voids in polyurethane*, Nuclear Technology 37/1, p. 73-78 U.S.A.
- [2] Stein R. S., (1990), *Small Angle Neutron Scattering Studies of Polymer Orientation & Phase Separation*, Molecular Crystals and Liquid Crystals 180/1, p. 119-146 United Kingdom
- [3] Hammouda B., (1993), *SANS from Homogeneous Polymer Mixtures: A Unified Overview*, Advances in Polymer Science 106, p. 87-134 Germany
- [4] Higgins J., Benoit H., (1994), *Polymers and neutron scattering*, Clarendon Press, Oxford, United Kingdom
- [5] Scheyer Y., Levelut C., Pelous J., Durand D., (1998), *Cross-link density influence on the relaxations in glass- and gel-forming polyurethanes by neutron and Brillouin scattering*, Physical Review B 57, p. 11212-11220 U.S.A.
- [6] Rogante M., Lebedev V. T., (2007), *Microstructural characterization of polymeric materials by small angle neutron scattering*, Polymer Engineering and Science 47/8, p.1213-1219 U.S.A.
- [7] Rogante M., Rosta L., Heaton M. E., (2013), *Neutron beam measurement of industrial polymer materials for composition and bulk integrity*, Measurement Science and Technology 24, 105601 (8pp) United Kingdom
- [8] Rogante M., Söllradl S., (2016), *Characterization of mono-ethylene-glycol based industrial polyurethanes samples by fast-neutron radiography and neutron tomography*, Journal of Physics: Conference Series 746/1, 012042 (7pp) United Kingdom
- [9] Williams C., May R. P., Guinier A., (1994), *Small-Angle Scattering of X- rays and Neutrons*, Characterisation of Materials, "Materials Science and Technology", VCH Verlagsgesellschaft, Weinheim, Vol. 2B p. 611-656 Germany
- [10] Rogante M., (2008), *Applicazioni Industriali delle Tecniche Neutroniche*, Proc. 1st Italian Workshop for Industry "Industrial Applications of Neutron Techniques", Civitanova Marche, Italy
- [11] Rogante M., (1999), *Caratterizzazione, mediante scattering neutronico, di materiali e componenti per l'impiantistica nucleare ed industriale*, PhD thesis, University of Bologna, Italy
- [12] Lindner P., (2000), *Water calibration at DLL verified with polymer samples*, Journal of Applied Crystallography 33, p. 807-811 United Kingdom

# Advantages of additive manufacturing in production of gears for planetary reducers

**Goran SALOPEK<sup>1)</sup>, Marko DUNĐER<sup>1)</sup>,  
Mladen PERINIĆ<sup>2)</sup>, David  
IŠTOKOVIĆ<sup>2)</sup>, Zoran JURKOVIĆ<sup>2)</sup> and  
Maja MARKOVIĆ<sup>2)</sup>**

1) University of Rijeka, Department of  
Polytechnics/ Sveučilišna avenija 4, 51000  
Rijeka/Croatia

2) University of Rijeka, Faculty of  
Engineering, Vukovarska 58, 51000 Rijeka,  
Hrvatska/Croatia

E-mail: [gsalopek@uniri.hr](mailto:gsalopek@uniri.hr)  
[marko.dundjer@uniri.hr](mailto:marko.dundjer@uniri.hr)  
[david.istokovic@riteh.hr](mailto:david.istokovic@riteh.hr)  
[mladen.perinic@riteh.hr](mailto:mladen.perinic@riteh.hr)  
[zoran.jurkovic@riteh.hr](mailto:zoran.jurkovic@riteh.hr)  
[maja.markovic@riteh.hr](mailto:maja.markovic@riteh.hr)

## Keywords

Additive manufacturing  
Planetary gear reducer  
SCARA robot  
3D model

## Professional article

**Abstract:** Increase in global competitiveness, requirements for smaller parts and space saving have led to development of advanced processes for gears manufacturing. Engineers and researchers are constantly searching for novel solutions to improve quality and productivity of gear manufacturing processes. This study investigates benefits of additive manufacturing technology in gear manufacturing. Machining processes for gear manufacturing such as form cutting, template process or generation process need a groove or extra space for tool output due to its geometry. This is especially a problem in the production of planetary gear reducers. Sun gear input shaft, because of its design, needs groove between the gear and disc on which the planet gears are mounted. This groove is the weakest part of the planetary gear unit and limiting power transfer factor. In this paper we are presenting solution for increasing power transfer in planetary gear reducer by using direct metal laser sintering additive manufacturing technique in producing sun gear input shaft and disc on which the planets are mounted as one part. In this way we have stronger gearbox, while the external dimensions of the reducers are unchanged.

## 1. Introduction

Additive Manufacturing (AM) is an appropriate name to describe the technologies that build 3D objects by adding layer-upon-layer of material, whether the material is plastic, metal or concrete. AM can also be described as a process of turning digital designs into three-dimensional objects. Today, AM is on the step to serial production, industries ranging from aerospace and medical to energy and automotive benefit from the possibility to design and manufacture products in a completely new way. The International Organization for Standardization (ISO)/American Society for Testing and Materials (ASTM) 52900:2015 standard classify standard, AM processes into seven categories:

1. Binder jetting (BJ)
2. Direct energy deposition (DED)
3. Material extrusion (ME)
4. Material jetting (MJ)
5. Powder bed fusion (PBF)
6. Sheet lamination (SL) and
7. Vat photopolymerization (VP)

According to the group of researchers [1] from 2015. visible areas of application and what part belongs to them are presented in figure 1.

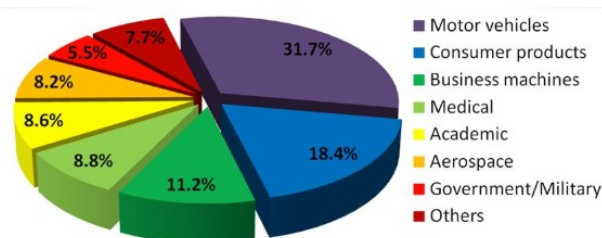


**Figure 1:** Areas of AM application

One of the technologies most used by today's 3d printers for printing metal parts is innovative DMLS (Direct Metal Laser Sintering) system. This method allows to create products with extremely complex geometries such as free-form surfaces, deep slots, gears, coolant ducts etc. DMLS is an AM process [2,3] by which digital 3D design data is used to build up a component in layers by depositing metal material. The process starts by applying a thin layer of the metal powder material to the building platform. After each layer, a laser beam fuses the powder at the points defined by the computer-generated data, using a laser scanning optic. The platform is then lowered and another layer of powder is applied. Once again, the material is fused so as to bond with the layer below at the predefined points resulting in a complex part [3] (Fig. 2). Benefits of DMLS are quick turnaround, can be heat treated, can be painted, post process machining and polishing.



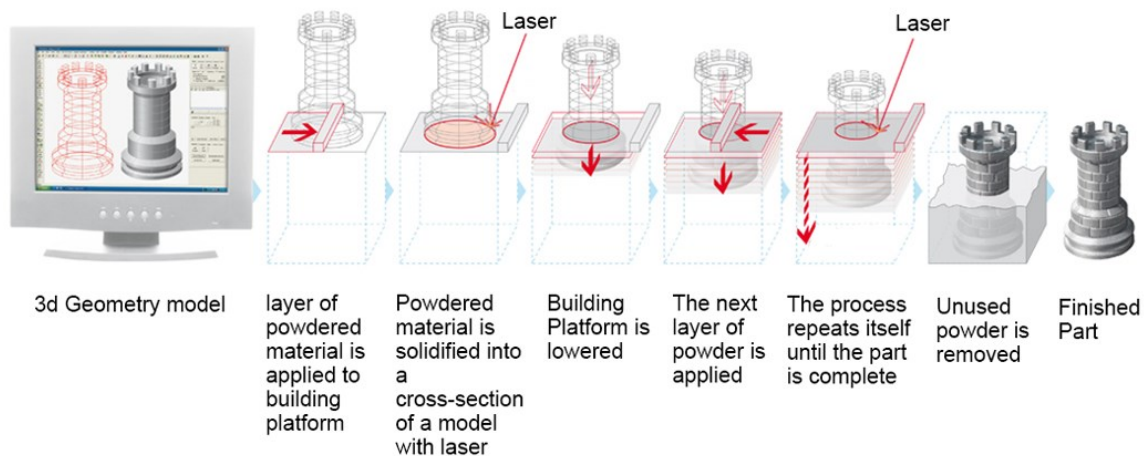


Figure 2: DMLS process [5]

### 1.1. Material for DMLS

The main classes of metal materials, and their approximate relevance, indicated by the size of the circle, for the most relevant application areas are summarized in figure 3. [4] It can be seen that DMLS already covers a board range of metal types and application.

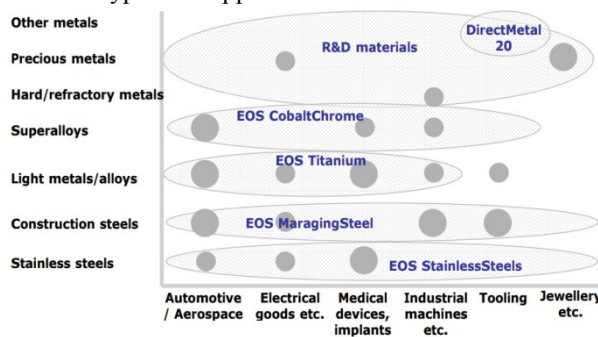


Figure 3: Classes of materials for DMLS

Direct metal 20 is a bronze-nickel-based, multi-component powder, which can be processed with layer thickness as low as 20µm. Primarily used for rapid tooling application, and therefore optimized for high build speed. Typical applications include injection molds and inserts for moulding up to a few tens of thousands of parts in all standard thermoplastics using standard injection parameters, and direct manufacture of functional metal prototypes. [4]

Stainless steel are widely used in many industrial applications and are typically characterized by mechanical properties and corrosion resistance at relatively low cost. Parts laser-sintered in this material have very acceptable ultimate tensile strength (approx. 1000 MPa) and remarkably high elongation (around 25%), but rather low yield strength and hardenability. Construction and tool steel (EOS Maraging Steel MS1) is an ultra high-strength steel with composition corresponding to European 1.2709 and German X3NiCoMoTi 18-9-5 classification. It has very high

strength combined with high toughness. It is easily machinable after the binding process and can be easily post-hardened of up to approx. 55 HRC by simple thermal age-hardening process.

Superalloys are class of metals characterized by high strength and good performance at high temperatures. They are generally either nickel or cobalt-based alloys. Superalloys are mainly used in aerospace and biomedical applications such as implants.

Light alloys types are aluminium or titanium-based. Titanium-based alloy parts are generally difficult to cast and to machine, and therefore DMLS is ideal for making titanium-based alloy parts. Typical application include parts requiring a combination of high mechanical properties and low specific weight. In contrast, aluminium alloys are typically easy and cheap to cast and to machine, enabling low-cost conventional manufacture. [4]

## 2. Problem

Planetary gear trains provide high power density in comparison to standard parallel axis gear trains. They provide a reduction volume, multiple kinematic combinations, purely torsional reactions, and coaxial shafting. Disadvantages include high bearing loads, constant lubrication requirements, inaccessibility, and design complexity. [6] [7] [8]

Sun gear input shaft, because of its design, needs groove between the gear and disc on which the planets are mounted. This groove is the weakest part of the planetary gear unit and limiting power transfer factor. In our case it was planetary reducer 57PX-36 (Figure 4) with specifications in table 1. Reducer was used in SCARA robot for rotation of 1<sup>st</sup> axis. Due to the need to put additional mass on the robot and keeping the same acceleration and speed of the robot, the planetary gearbox could not withstand the load and sun gear input shaft broke (Fig. 5).



**Figure 4:** 57PX-36 Planetary gear reducer

**Table 1:** Specifications of 57PX-36 planetary gear reducer

Model	57PX-36
Application	NEMA23 (Flange 57)
Input shaft	8mm
Output shaft	14mm
Speed ratio	36:1
Step distance precision	5%
Backlash	Less than 18 Arcmin
Efficiency	80%
Max. Output torque	90Nm

The problem was shaft diameter reduction because of groove for tool exiting in machining process (Fig. 6). We had three planetary reducers, two of which broke because of extra mass. First broke closer to the gear and second one broke closer to the disc.



**Figure 5:** Sun gear input shaft with disc



**Figure 6:** Broken sun gear input shaft

### 3. Solution

Because there was not space for bigger reducer, and also, we didn't have time to change whole construction and order new stronger reducer, we decide to make sun gear input shaft by using additive manufacturing, which allows us to produce sun gear without groove for tool output. In normal circumstances, when time is not a limiting factor, the gear manufacturing process would not be profitable because it is possible to buy planetary reducer from manufacturer, but the problem is the delivery time of almost two months. The 3D solid model of the shaft and its components was built using *SolidWorks* (Fig. 7, 8).

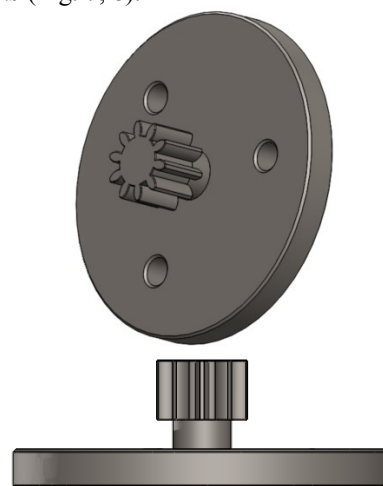


**Figure 7:** Original sun gear input shaft

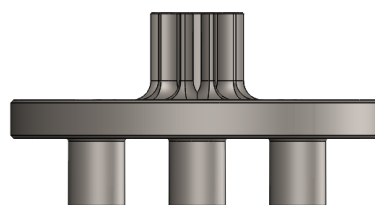
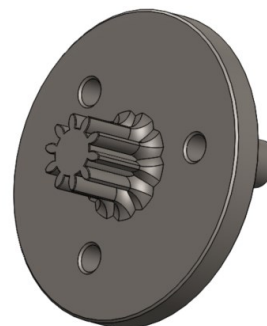


**Figure 8:** Gear input shaft for AM

For producing 3D printed part, we used *EOSINT M280* machine. Part was printed from EOS MaragingSteel MS1, martensite-hardenable steel with properties in table 2. Parts built in EOS MaragingSteel MS1 have a chemical composition (Tab. 3) corresponding to European 1.2709 and German X3NiCoMoTi 18-9-5. This kind of steel is characterized by having very good mechanical properties and being easily heat treatable using a simple thermal age-hardening process to obtain excellent hardness and strength. Parts built from EOS MaragingSteel MS1 are easily machinable after the building process and can be easily post-hardened to more than 50 HRC by age-hardening at 490 °C (914 °F) for 6 hours. In both as-built and age-hardened states the parts can be machined, spark-eroded, welded, micro shot-peened, polished and coated if required

Due to the layer wise building method, the parts have a certain anisotropy, which can be reduced or removed by appropriate heat treatment

Before printing the part, simulation was made in Solidwork Simulation®. In the simulation, fixed points are placed in the position of the planetary gears (green arrows) while force of 300N was defined on gear teeth (brown arrows). Results of simulation have shown the zone of the shaft gear crack on exact place as it actually happened (Fig. 9). The same simulation test was done with 3D solid model of the shaft and its components designed for AM. Results of simulation (Fig. 10) have shown that sun gear input shaft designed in way without groove between the gear and disc can withstand the acceleration and speed with additional mass on the robot..

**Table 2:** Properties of EOS MaragingSteel MS1

Mechanical properties of parts at 20°C		
	As built	After age hardening*
Tensile strength		
In horizontal direction	1100 ± 100 MPa	2050 ± 100 MPa
In vertical direction	1100 ± 100 MPa	
Yield strength		min. 1862 MPa
In horizontal direction	1050 ± 100 MPa	1990 ± 100 MPa
In vertical direction	1000 ± 100 MPa	
Modulus of elasticity		
In horizontal direction	160 ± 25 GPa	180 ± 20 GPa
In vertical direction	150 ± 20 GPa	
Hardness	33 – 37 HRC	50 – 56 HRC
Ductility (Notched Charpy impact test)	45 ± 10 J	11 ± 4 J

**Table 3:** EOS MaragingSteel MS1 material composition

Material composition	Ni (17 – 19 wt-%)
	Co (8.5 – 9.5 wt-%)
	Mo(4.5 – 5.2 wt-%)
	Ti(0.6 – 0.8 wt-%)
	Al(0.05 – 0.15 wt-%)
	Cr, Cu (each ≤ 0.05 wt-%)
	C (≤ 0.03 wt-%)
	Mn, Si (each ≤ 0.1 wt-%)
	P, S (each ≤ 0.01 wt-%)
Relative density	Approx.. 100%
Density	8.0 – 8.1 g/cm <sup>3</sup>

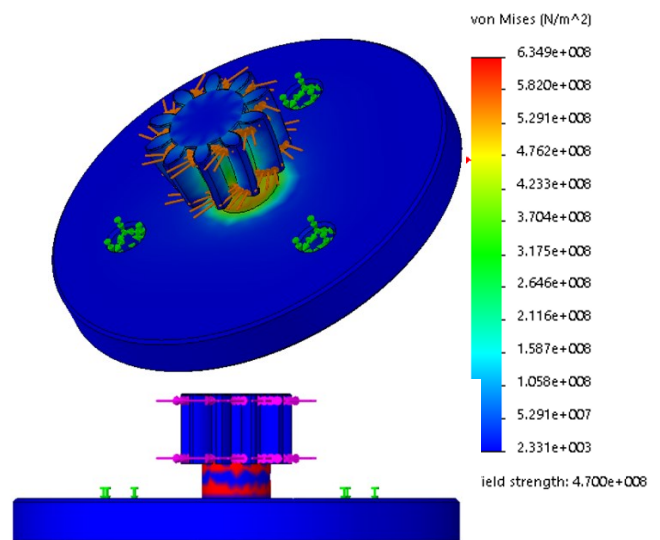


**Figure 9:** Results of simulation for original part



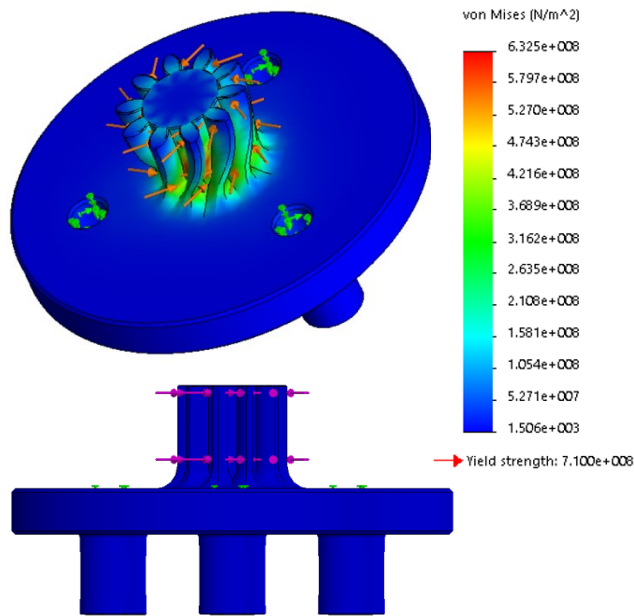


Figure 10: Results of simulation for proposed 3D printed part

#### 4. Results

Figure 11 shows a 3D printed part. The total time of making part was 20 hours and 30 minutes. From that time four hours went to preparing the machine, nine hours on actual 3D printing, four hours on cleaning machine and three and a half hour on additional part milling.

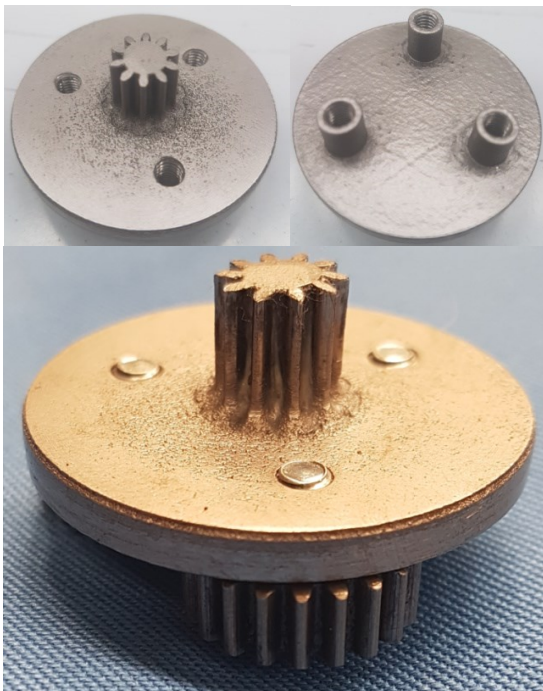


Figure 11: 3D printed part



Figure 12: Assembly with planet gears



Figure 13: Second stage assembly

#### 5. Summary and conclusion

Figure 12 and 13 shows finished gear assembly. It has been shown that with direct metal laser sintering we can produce high quality parts, in our case sun gear input shaft of 2-stage planetary gear reducer that can withstand higher loads while keeping the same external dimensions of planetary gear reducer. This is because DMLS enable us to produce part without groove for tool exiting in conventional production methods.

Sun gear input shaft made by conventional methods broke due to fatigue, due to that, we didn't age hardened printed part because with that process we will increase hardness by 80%, but in the same time we will be lowering the ductility by 400%.

DMLS is still relatively unknown and little understood in industry. In the other side DMLS offers an ideal platform for developing completely new products and applications. It is also possible to vary geometry and internal structure of the material in interminable variety of ways. This offers possibilities for designing and optimizing parts properties and behaviour.

**REFERENCES**

- [1] Additive manufacturing [carmelo.demaria@centropiaggio.unipi.it](mailto:carmelo.demaria@centropiaggio.unipi.it) <http://goo.gl/forms/lwaZwAEUir>
- [2] I. Yadroitsev: Selective laser melting (2009). *Direct manufacturing of 3D-objects by selective laser melting of metal powders*, LAP LAMBERT Academic Publishing
- [3] A. Gebhardt (2007) *Generative Fertigungsverfahren* Hanser Verlag, München.
- [4] T. Grünberger, R. Domröse (2015). „*Direct Metal Laser Sintering Identification of process phenomena by optical in-process monitoring*”; Laser Technik Journal 1/
- [5] <http://additivemanufacturing.weebly.com/artifacts/category/all>
- [6] M. Shellabear O. Nyrhilä (2017). „*Materials for Direct Metal Laser-Sintering*”, EOS, e-Manufacturing Solutions,
- [7] H. LinkeLinke, H. Börner, Jörg, H. Ralf (2016). *Cylindrical Gears Calculation – Materials – Manufacturing*, Carl Hanser Verlag GmbH & Co. KG
- [8] Damir T. Jelaska (2012). *Gears and Gear Drives*, Wiley



# Investigation of Materials Behavior in Autogenous Grinding Mill

**Nikolay STOIMENOV, Nikola SABOTINKOV and Bogomil POPOV**

Institute of Information and Communication Technologies, at the Bulgarian Academy of Sciences.

Acad. G. Bonchev str., block 2, 1113 - Sofia,

**BULGARIA**

nikistoimenow@gmail.com

## Keywords

AG Mill

Lifters

Grinding

Simulation

Modelling

*Original scientific article*

**Abstract:** In the presented paper attention is paid to semi-autogenous and autogenous grinding mills. Software, working on discrete element method is used for the simulations. A simulation using both standard and innovative lifter shape is made. Comparative analysis of an innovative lifter shape and a standard lifter shape is implemented. The angles of the shoulder and the toe of the mill are determined. Relative wear of the lifters is considered. For starting material of the simulation is used iron ore material. Analyses of the simulations are made.

## 1. Introduction

In the mining industry the most used method for minimizing the particles size is the use of ball mills. Mostly the mills are used in a various technological continuous processes in metallurgy, mining, cement and other industries. Mills, used in mining industry are few types. In this paper, attention is paid to semi-autogenous and autogenous mills. Autogenous mills (AG) works with lifters, produced of rubber or of metal. AG mills grinds the ore by rotating the drum of the mill, which causes lifting of the ore material to a specific height. In the inner surface of the mill drum are placed lifters. After the ore is lifted, it starts falling by its own weight. When falls, the ore causes brakeage of itself and other ore material in the mill. Semi-Autogenous Grinding (SAG) mills uses the same method as autogenous mills, but uses also a grinding media – mostly balls, which helps for the grinding. The SAG mills are used in the first stage of grinding [1], [2], [3], [4].

The grinding bodies are made of materials meeting the requirements of Bulgarian, EN, ISO, requirements about the cleanness of the material, etc., such as steels, alloys of steel, porcelain, ceramics, etc. [1], [2], [3], [4].

In today's operating conditions, besides technological, constructive and economic requirements, attention is paid to ecology, energy efficiency, operational reliability as well as human factor.

The aim of this paper is to investigate the material behavior in autogenous grinding mill.

## 2. Software using discrete element method

We use EDEM software, [5], working on discrete element method for investigating the behavior of the iron ore in AG mill. The software can provide results like mass of particles, volume, velocity, torque compressive force, potential energy, etc.

Generally, the selected software is divided into three modules. The first module is the creator section, where parameters such as used materials, equipment geometry, physics, etc. should be selected. Another step in this first step of the process is the particles properties, needed for setting simulations. Properties of the particles include: density, Poisson's ratio, coefficient of static friction, coefficient of rolling friction, coefficient of restitution, and interactions between materials of particles and geometry. The next parameter in creator tab is the equipment properties, which is used for setting the material and properties of the used in the simulation equipment. After setting all the particles parameters and equipment parameters, next required parameters to set are the geometries, used for the simulation.

The software gives an opportunity to import geometry from other Computer-Aided Design (CAD) software, which procedure eliminates the risk for utilizing wrong, or not accurate CAD models and particle behavior. In the CAD model, it also may be chosen some different properties of the objects and movements such as linear rotations, linear translations, acceleration, velocity, etc. The chosen software also provides different models of calculations of the simulations. Some of the models are Hertz-Mindlin (no slip), Hertz-Mindlin (no slip) with RVD Rolling friction, Hertz-Mindlin (no slip) with JKR

Cohesion, etc. An attempt for simulation the behavior of iron ore in AG mill is selected the Hertz-Mindlin (no slip) model. The Hertz-Mindlin (no slip) model is based of Hertzian contact theory (1882) [6, 7] and the Mindlin model is based on the tangential force [8, 9].

### 3. Simulating the process

Iron ore is chosen for simulation material. The required properties of the parameters setting for the simulation are obtained from the software cloud library. The cloud library contains plenty of properties, data, coefficients, etc., and it is updated periodically. The data for the simulation contains: bulk density of the material - 2768 [kg/m<sup>3</sup>]; coefficient of restitution – 1; coefficient of static friction - 0,5; coefficient of rolling friction - 0,01. Number of the particles for the both simulations are: 1000. The mill is filled with 30-35% from the volume of the mill. The software gives detailed information for each particle, or group of particles such as speed, torque, force, etc.

The chosen shape for the iron ore in the simulation is selected from the software library templates.

The next step is setting the properties for equipment material (the mill). Steel is selected, also from the software library. Density of the material is 7850 kg/m<sup>3</sup> with coefficient of restitution 0.5, coefficient of static friction 0.5 and coefficient of rolling friction 0.01. Other geometry parameters are: duration of the simulation – 10s, rotational speed of the drum – 12.4 rpm, with this rotational speed is achieved the most used working regime in mill industries.

For the diameter of the mill is chosen 5m. The length of the mill is set to 0.5 m, this optimizes the required time for the simulation process. The lifters number is 32.

For the geometry are chosen two types of AG mills, with standard lifter shape (fig.1 - trapezoidal), and with innovative lifter shape (fig. 2 – triangle Reloe). More detailed view of the innovative shape is presented on fig. 3 – Bulgarian Patent Application with authors Dimitar Karastoyanov and Nikolay Stoimenov [10].

The aim of both simulations is to be investigated the behavior of iron ore material with this specific geometry, which contains lifters with innovative shape, and with the standard used lifter shape in the production process. Both lifter shapes are modelled in CAD software, with only difference - the shape of the lifter. When setting the simulation, the modelled objects are separated in different sections, which gives opportunity for fast and accurate change of desired part from the models.

For comparative analysis of innovative lifter shape and standard lifter shape are chosen the following parameters: shoulder and toe of the mill, relative wear of the lifters, and compressive force.

The simulation has been managed by following the innovative approach of Lean Startup method which basically requires iterative approach and validation at each step as part of the innovation development [11, 12].

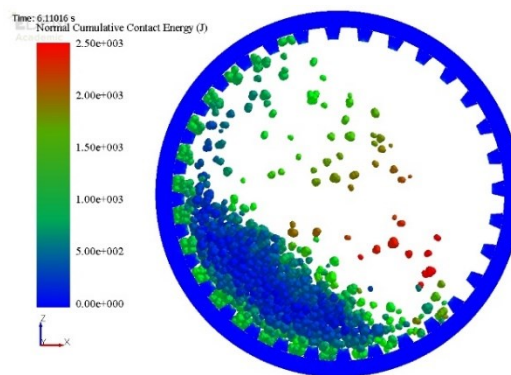


Figure 1. Ball mill with standard lifter shape.

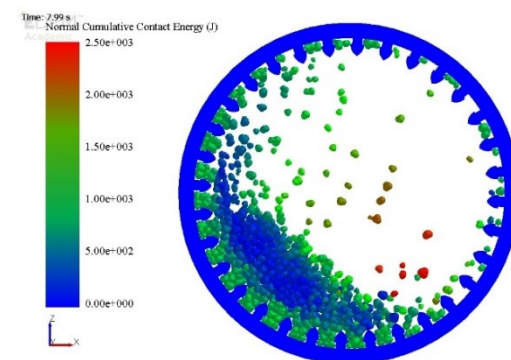


Figure 2. Ball mill with innovative lifter shape.

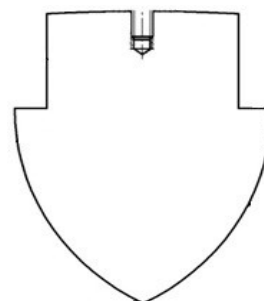
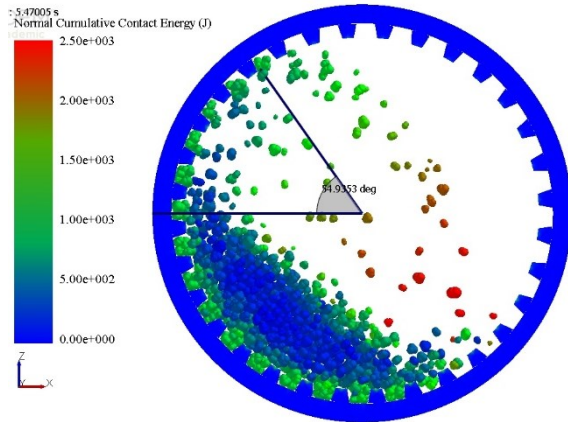


Figure 3. Innovative lifter shape.

### 4. Comparative analysis of the obtained results from the simulations

The obtained results from the simulation with standard lifter shape show that the shoulder angle (angle of separation from the top of the mill, when the material separates from the mill) is 54.93 ° at the time of simulation 5.47 s from the simulation start. The time is selected randomly. A group of particles material is investigated, and the angle is obtained when the particles separate from the mill. For 0 angle is set horizontal line from the left corner to the centre of the mill (fig.4).

The behaviour of the selected group is traced until it reaches the mill toe (when it falls at the bottom part of the mill and interacts with the equipment). The toe angle is 133.42° at the time 6.51 s from the simulation (fig. 5).



**Figure 4.** Shoulder angle with standard lifter shape.

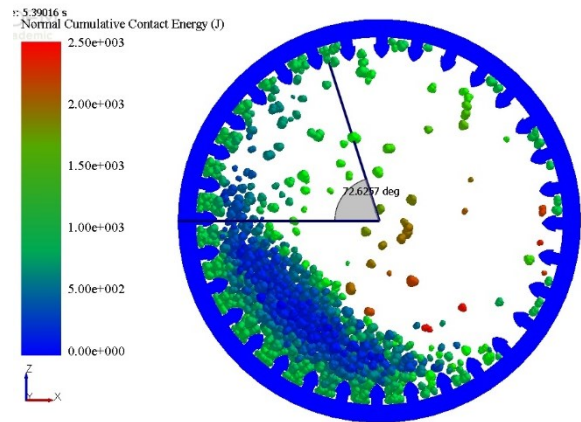


**Figure 6.** Shoulder angle with innovative lifter shape.

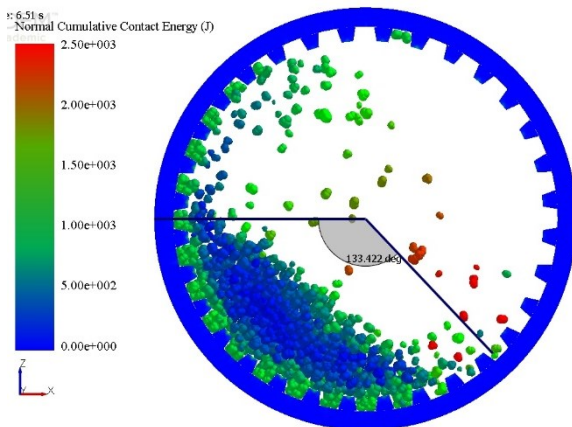


**Figure 5.** Toe angle with standard lifter shape.

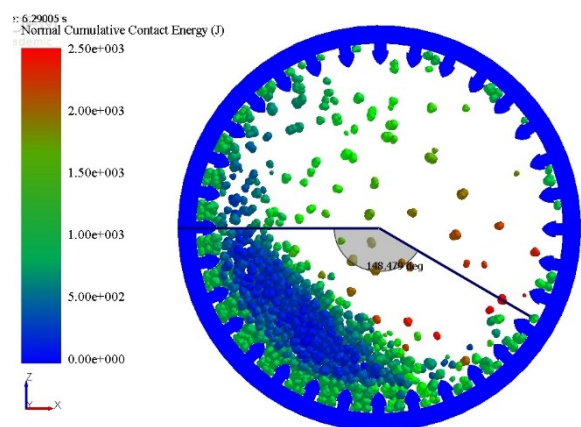


**Figure 7.** Toe angle with standard lifter shape.

The obtained data from simulating the innovative lifter shape angles: shoulder angle is  $72.62^\circ$  at time 5,39s (fig. 6). Again is traced a group of particles, and the angle is obtained when the particles separates from the mill shell. The particles trajectory is traced, until they reach the toe angle, which is  $148.48^\circ$  at time of simulation – 6.29 s, shown on fig. 7.

The software gives an option for recording the relative wear. It has been accomplished, based on the mesh of the 3D objects and the identified contact with particles. The calculation is based on relative velocity and connected between particles and equipment forces of the produced from the software particles [5].

Figure 8 shows the relative wear of standard lifter shape, and figure 9 shows the relative wear of the innovative lifter shape.

Maximum reached compressive force of standard used lifter shape is 22422N, and innovative lifter shape is 23835N.

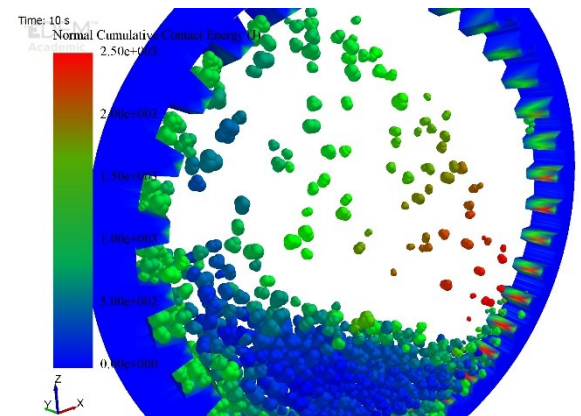


**Figure 8.** Relative wear of standard lifter shape.

The selected groups of particles for the standard and for the innovative lifter shapes are traced. The compressive force obtained when particles contacts with the mill are: 2426N – standard; 5885N – innovative lifter. And when falling on lifter are: 3725N – standard (fig. 10); 6854N – innovative lifter (fig. 11).



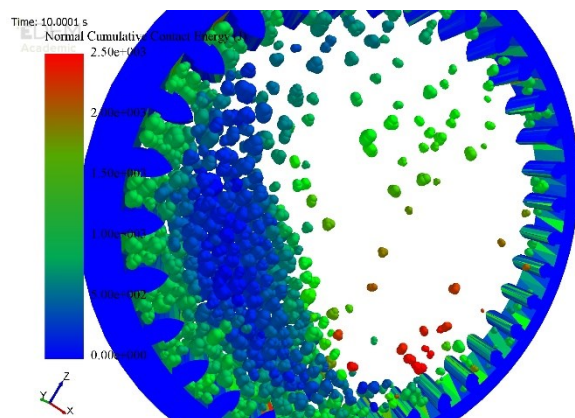


Figure 9. Relative wear of innovative lifter shape.

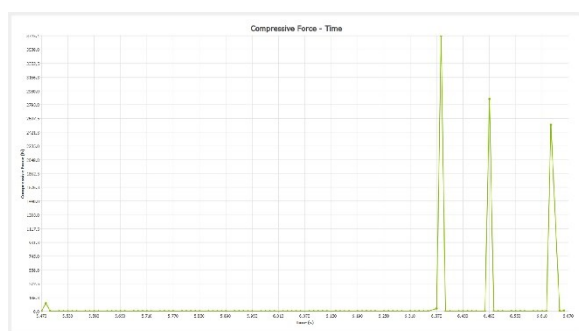


Figure 10. Compressive force of standard lifter.

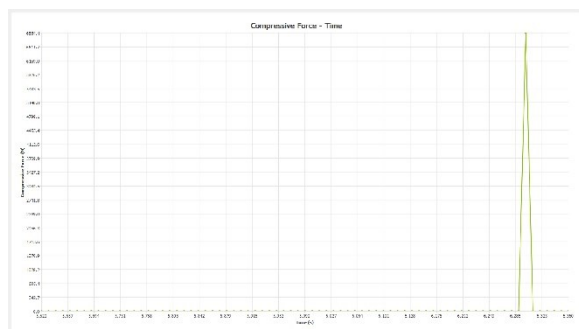


Figure 11. Compressive force of innovative lifter.

## 5. Conclusion

In conclusion, from the comparative analysis of the simulation results for two different lifter shapes in these specific simulations, it can be concluded that the innovative lifter shape produces larger angle of shoulder of the mill instead of the standard lifter with the same rotational speed of the mill.

Toe angle also is increased, due to the lifter shape. This can contribute to reducing the speed of the mill, which also will contribute to the energy efficiency of the mill. The velocity of the particles also is examined, and due to the bigger shoulder and toe angle, the velocity of the particles in the modelled mill with innovative lifter shape is bigger than the standard.

The increased velocity and angles, increases also the compressive force of the particles. This increased compressive force can reduce the milling time, required for milling the material to desired size. This will help to reduce the needed time for milling the material.

## Acknowledgements

The paper is supported by Bulgarian NFS Grant "Young Scientists – 2017" No DM 17/8 - 2017.

## REFERENCES

- [1] Jultov A., (1980) *Machines for construction materials*, Technika, Sofia, Bulgaria.
- [2] Tsvetkov H. (1988) *Mineral processing machines*, NP "Technology", Sofia, Bulgaria.
- [3] V. Monov, D. Karastoyanov and T. Penchev., (2013) *Advanced Control Methods and Technologies for Two Industrial Processes.*, Third IEEE International Conference on Information Science and Technology ICIST, March 23-25, 2013; Yangzhou, Jiangsu, China., 978-1-4673-2764-0/13/ ©2013 IEEE., pp 187-194
- [4] Stoimenov N., Sabotinkov N., (2017), *Investigation of iron ore material behavior in semi-autogenous grinding mill. Part I: Grinding with innovative lifter shape*, Problems of Engineering Cybernetics and Robotics, vol. 68, „Prof. Marin Drinov“ Publishing House of Bulgarian Academy of Sciences, Sofia, ISSN 0204-9848, pp 39-48
- [5] EDEM Software manual – dem-solutions.com
- [6] Hertz H., (1882), *On the contact of elastic solids*, J. reine und angewandte Mathematik, 92 pp 156-171
- [7] Mindlin R. D., (1949), *Compliance of elastic bodies in contact*, Journal of Applied Mechanics, 16 pp 259-268
- [8] Mindlin R. D., Deresiewicz H., (1953), *Elastic spheres in contact under varying oblique forces*, ASME, pp 327-344
- [9] Stoimenov N., Sabotinkov N., Sokolov B., (2016), *Investigation relative wear of lifters with EDEM Software.*, International Conference Robotics, Automation and Mechatronics'16 RAM, Byaga, Bulgaria, October 3-4, 2016, стр. 70-73, ISSN 1314-4634.
- [10] Karastoyanov D., Stoimenov N., Lifter, Bulgarian Patent Application, Reg.No 112174, priority from 14.12.2015
- [11] Yordanova, Z., (2017), *Knowledge transfer from lean startup method to project management for boosting innovation projects' performance*, Int. J. Technological Learning, Innovation and Development, Vol. 9, No 4, pp. 292-309
- [12] Yordanova, Z., (2018), *Lean Startup Method Hampers Breakthrough Innovations and Company's Innovativeness*, International Journal of Innovation and Technology Management, Vol. 15, No 2

# Concept of Learning Factory at FSRE

**Željko STOJKIĆ<sup>(1)</sup> and Igor BOŠNJAK<sup>(2)</sup>**

1) University of Mostar, Faculty of Mechanical Engineering, Electrical Engineering and Computing  
Sveučilište u Mostaru, Fakultet strojarstva, računarstva i elektrotehnike  
Matice hrvatske b.b. Mostar, **Bosnia and Herzegovina**

2) University of Mostar, Faculty of Mechanical Engineering, Electrical Engineering and Computing  
Sveučilište u Mostaru, Fakultet strojarstva, računarstva i elektrotehnike  
Matice hrvatske b.b. Mostar, **Bosnia and Herzegovina**

zeljko.stojkic@fsre.sum.ba

## Keywords

*Manufacturing education*

*Learning factory*

*Competence development*

## Ključne riječi

*Proizvodna edukacija*

*Tvornica za učenje*

*Razvoj kompetencija*

## Review article

**Abstract:** Employee's competencies are the key resources of an enterprise to quickly adapt to ever changing conditions. In this context competency development at all levels is needed for those adaption processes. One promising approach for effective development of competencies is the learning factory concept. In the last years, learning factories as close-to-industry environments for education and research have proven to be an effective concept addressing these challenges. In this paper, the background of term Learning factory will be presented, its different definition that are found in the literature, establishment of the term "learning factory" and its description model. The concept of Learning Factory at Faculty of Mechanical Engineering, Computing and Electrical Engineering, University of Mostar has been presented. Current state has been described regarding, space, equipment and infrastructure. At the end are presented future plans regarding fulfillment the LF concept on FSRE.

## Pregledni članak

**Sažetak:** Kompetencije zaposlenika ključni su resursi poduzeća u brznoj prilagodbi promjenjivim uvjetima. U tom kontekstu potrebno je razvijanje kompetencija na svim razinama za taj procese prilagodbe. Jedan obećavajući pristup učinkovitom razvoju kompetencija je koncept tvornice za učenje. U posljednjih nekoliko godina, tvornice za učenja kao blisko-industrijska okruženja za obrazovanje i istraživanje pokazale su se učinkovitim konceptom koji se bavi ovim izazovima. U ovom će se radu predstaviti pozadina pojma Tvornice za učenje, njene različite definicije koje se mogu naći u literaturi, nastanak pojma "tvornica učenja" i njegov opisni model. Predstavljen je koncept tvornice za učenja na Fakultetu strojarstva, računarstva i elektrotehnike Sveučilišta u Mostaru. Opisano je trenutno stanje koja se odnose na prostor, opremu i infrastrukturu. Na kraju su predstavljeni budući planovi o ispunjenju koncepta LF-a na FSRE-u.

## 1. Introduction

The production sector is one of the most important pillars of today's economies. Current challenges range from the increasing fragmentation of markets, individually customized products or inconsistent demand and sales. To cope with such challenges companies need to enable quick adaptations to changing market conditions. This strongly depends on employees whose abilities to act in a self-organized and creative way in unknown problem situations is key to a successful business.[1][2]

Employee's competencies are the key resources of an enterprise to quickly adapt to ever changing conditions.[3] In this context competency development at all levels is needed for those adaption processes.[1] One promising approach for effective development of competencies is the learning factory concept. In recent years more and more learning factories were built up in industry and academia. [4][5]

Collaboration between academia and industry is crucial. Producing knowledge through research, diffusing knowledge through education as well as using and applying knowledge through innovation (the "knowledge triangle") is the appropriate approach. [6] Universities and industrial training facilities are confronted with the challenge to identify future job profiles and correlated competence requirements, and they have to adapt and enhance their education concepts and methods. Especially, innovative learning environments must be able to react to the mentioned challenges in an interdisciplinary manner. In the last years, learning factories as close-to-industry environments for education and research have proven to be an effective concept addressing these challenges (Fig. 1).[7]



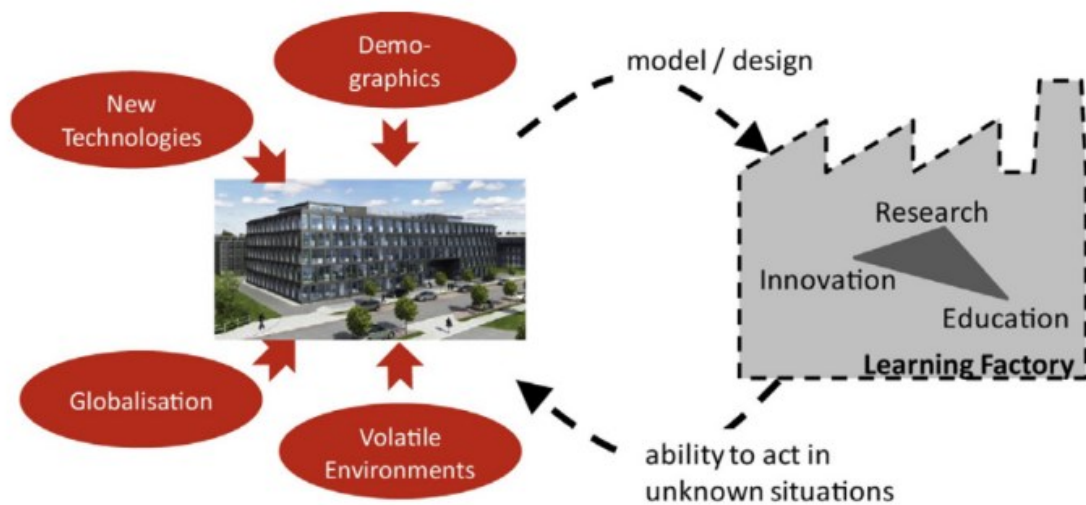


**Figure 1.** The learning factory as a model of a real factory—incorporating the three poles of the “knowledge triangle”[4]

**Slika 1.** Tvornica za učenje kao model stvarne tvornice – obuhvaća tri stuba “trokuta znanja”

## 2. Concept of learning factory

### 2.1. Definition

There are several definitions of Learning Factory that may be found in the literature. The first known definition of a learning factory by Ref. [8] describes a facility for product and process realization that can be used for academic education. Additional key factors include active participation of trainees and an agile environment. Abele et al. [9] base their definition on principally the same assumptions, but emphasize the need for closeness to reality of all aspects of such a facility in an authentic simulation. The teaching factory concept of Chrysosouris et al. [10] [11] [12] connects the real factory with the classroom using advanced information and communication technologies (ICTs) for bi-directional knowledge exchange. The result of an investigation of more than 25 learning factories, Wagner et al. [13] fortify the postulation of authenticity and changeability of the factory environment and claim the suitability of learning factories for different target groups as well as the purpose of test and transfer of theoretical knowledge to the industry. With the intent to identify a methodical approach for developing action-oriented, competency-based learning factories, the definition of Tisch et al. [14] focuses on a systematic configuration of the learning environment. The members of the Initiative on European learning factories [15] agreed on a comprehensive definition with regard to realistic processes and the didactical concept. Sihn (2014) referenced in Ref. [12] differentiates between physical and virtual settings of learning factories and includes both types in his definition. Further definitions cover partial aspects (see [16], or Tracht (2014) referenced in Ref. [12]).[7] Within the CIRP CWG (Collaborative

Working Group) numerous explicit and implicit definitions of the term “learning factories” were identified, analyzed, and compared, in order to strive for a common understanding. The definitions are summarized in the CIRP Encyclopedia:

“A Learning Factory in a narrow sense is a learning environment specified by processes that are authentic, include multiple stations, and comprise technical as well as organizational aspects, a setting that is changeable and resembles a real value chain, a physical product being manufactured, and a didactical concept that comprises formal, informal and non-formal learning, enabled by own actions of the trainees in an on-site learning. Depending on the purpose of the Learning Factory, learning takes place through teaching, training and/or research.

Consequently, learning outcomes may be competency development and/or innovation. An operating model ensuring the sustained operation of the Learning Factory is desirable. In a broader sense, learning environments meeting the definition above but with a setting that resembles a virtual instead of a physical value chain, or a service product instead of a physical product, or a didactical concept based on remote learning instead of on-site learning can also be considered as Learning Factories.”[17]

### 2.2. Background

The term “learning factory” was first time established in 1994, by the Penn State University, United States, who received a grant to develop a “learning factory. It referred to an interdisciplinary hands-on engineering design approach with strong links and interactions to industry (Penn State University, 2016). This program run by Penn State University was awarded the National Academy of

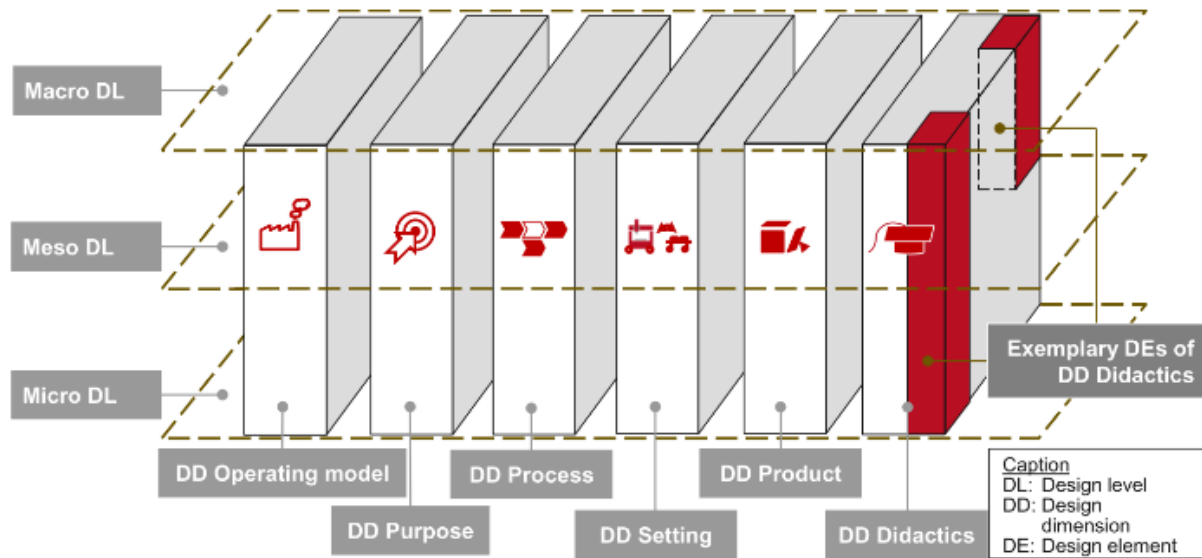


**Figure 2.** The description model of learning factories [10]

**Slika 2.** Opisni model tvornice za učenje

Engineering's Gordon prize for innovation in Engineering in 2006. Since then, the use of learning factories has increased, particularly in Europe. [18] Another less famous, more industry- focused approach was established in the late 1980s in Germany with the "Lernfabrik" (German for "learning factory") for a qualification program related to Computer Integrated Manufacturing (CIM).[19][7] Since then, the rapid increase of the learning factories happened in the Europe and worldwide. The rapid increase of funding made available and the high success of the learning factories stimulated the academic world and became a topic of general conversation, which lead to its popularity as a research topic. The numerous research efforts have produced a variety of topics, ranging from the validation of the success of learning factories, to design and implementation methodologies, and improvement and expansion processes.[18]

### 2.3. Learning factory description model

According to Enke et. al. [21], the description model for learning factories consists of three key features: Design dimensions (DD), design elements (DE) and design levels (DL). The DD of learning factories consist of "operating model", "purpose & targets", "process", "setting", "product" and "didactics" according to [4] and [22]. While the dimension "setting" examines the learning environment, the dimension "process" covers the implemented production processes. All dimensions are further detailed in individual DE. In the DD "setting" eight elements are given ranging from the changeability of the used equipment, to enable learners to experiment with the given factory environment, to the level of the work system with the characteristics varying from a single work place up to a whole network of companies. For a more detailed presentation of the DE and DD see

[19]. In addition to the dimensions and the elements three DL of learning factories are identified [20]. On the macro level the socio-technical infrastructure as well as the general learning factory concept is considered. On the meso level, the learning modules and courses are depicted, while on the micro- level single teaching-learning situations are examined. The combination of the DD, DE and DL forms the description model for learning factories. The DL are crossed by the six interdependent DD. The DD are operationalized with 52 DE, while the elements may be either part of a single, two or all levels. Figure 1 visualizes the description model with an exemplary relationship between DE and DL within one DD. Between levels, dimensions and elements following possible relationships are assumed: Not all DE are relevant for the design of all levels. Some elements have a strong correlation to certain DL, several have a weak correlation, and there may be even elements, which have no correlation to a particular DL at all. Furthermore, it is assumed that all DD affect all DL. Learning factory experts were asked to rate the correlation between the three levels and the 52 elements. For example, all experts identified a strong correlation between the macro-level and the DE "development" from the dimension "operating model". In contrary, no correlation could be found between the micro- level and the DE "operating organization".[21]

### 3. Learning factory on FSRE

On the Faculty of Mechanical Engineering, Computing and Electrical Engineering, University of Mostar, the initiative of development of Learning Factory has started in January, 2018. Based on the good experience from partner faculties/universities the decision was made in that direction.

Faculty has applied on the project co financed by European Union and implemented by GIZ and received a certain amount of funds for project Increasing Competitiveness of Small and Medium Enterprises through Creating Business Associations and Establishing a Learning Factory, within the EU ProLocal programme. In this project, Faculty is leader and partners are 9 local metal and plastic industries (SIK d.o.o. Mostar, Škutor d.o.o. Mostar, TT Kabeli d.o.o. Široki Brijeg, TEM Mandeks d.o.o. Široki Brijeg, Feal d.o.o. Široki Brijeg, Bilton d.o.o. Grude, Weltplast d.o.o. Posušje, Miviko d.o.o. Posušje and Femis d.o.o. Posušje), city of Široki Brijeg and Posušje municipality.

The role of the faculty in the project, in addition to the role of the lead applicant, is the development of the concept of a learning factory in collaboration with enterprises and development of curricula and support to enterprises in the field of education and research. The role of enterprise in the project is a contribution to the development of lifelong learning curricula and the transfer of knowledge in the field of practical training in the "Learning Factory". The role of the local community is to support the construction of infrastructure, fostering better cooperation between the academic community and SMEs, as well as raising awareness of innovation among citizens through activities and workshops on the project. Faculty is at the point of writing this article at the stage of defining the product and manufacturing process for the FSRE Learning Factory.

### 3.1. Current state

The Faculty already has a part of the infrastructure for the Learning Factory concept. Through the project "Increasing the competitiveness of the company in the metal sector through the introduction of the Lean Tool and the establishment of the Lean Competency Centre" will be partially developed the infrastructure from the Lean area. One of the additional objectives of this project is the establishment of the basic concept of the FSRE Learning Factory with the maximum use of existing equipment and infrastructure, in cooperation with the faculties from Germany and Croatia, local companies that are project partners and the local community. Realization of this project would create a platform and initial preconditions for joint action in the field of education, research and training in the real environment.

#### 3.1.1. Space and equipment

The current state of machinery on the FSRE is not at a satisfactory level - most machines are over 50 years old or not in operation. The plan is to get rid of unnecessary machines and those that are still in function to bring in the best possible condition. Workspace area is around 250 m<sup>2</sup>. Workspace also needs to be renovated (floor, walls, electric installations, etc.)

At the moment of writing this text, construction work on the workshop premises (facades, doors, windows, floors and the like) began. It is working the analysis of a new

layout. It is planned to use some of the software to create the factory's internal layout (visTable, Autodesk Factory Design Utilities, CATIA).



**Figure 3.** Current state of machines

**Slika 3.** Trenutno stanje strojeva



**Figure 4.** Current state of workspace (inside)

**Slika 4.** Trenutno stanje prostora (unutra)

Below you can see the current state of the workspace from the outside and the future look of the workshop after the works.



**Figure 5.** Current state of workspace (outside)

**Slika 5.** Trenutno stanje radnog prostora (izvana)

#### 3.1.2. Infrastructure

FSRE, in addition to equipment and space as the initial preconditions for the LF, it also has a certain infrastructure that can fit into the entire LF concept.

##### 3.1.2.1. Information system

FSRE has knowledge, experience and the required infrastructure for ERP and CRM business information systems to support the entire LF concept.

As part of the information systems lab we have various sensors, accompanying microcomputers (Arduino, Raspberry Pi etc.) and PLCs required for automation.





**Figure 6.** Future state of workspace (outside)  
**Slika 6.** Buduće stanje radnog prostora (izvana)

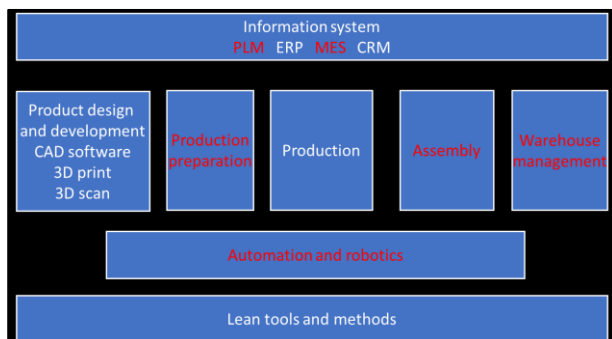


**Figure 7.** FSRE Learning Factory structure  
**Slika 7.** Struktura FSRE tvornice za učenje

### 3.1.2.2. Product design and development

Regarding product design and development, FSRE has long tradition and knowledge (CAD software, 3D printers, 3D scanner and other necessary tools/methods).

### 3.1.2.3. Production

Here production stands for material, product or semiproduct processing. Faculty has educated personal and some of the equipment for machining and welding.

### 3.1.2.4. Lean tools and methods

Through the other project (Increasing Competitiveness of Enterprises in the Metal Sector through the Lean Tool Implementation and the Establishment of the Lean Centre) at faculty is established Lean Centre consisting of people, infrastructure and curricula for further education in the lean methodology. The Faculty has many years of experience in implementing lean tools in companies from the region and very good cooperation with higher education institutions and institutes that are also involved in introducing lean to other companies / organizations.

## 3.2. Future state

As shown on the Fig.7, the entire concept lacks information systems elements (PLMs and MESs), production preparation, assembly and warehouse management. The faculty has a plan in the near future to supplement these elements. We are already in the process of purchasing assembly sites (warehouses) – Fig. 8, which will be equipped with a system that will enable the

automation of the assembly and storage process ("Pick by light" system – Fig. 9).

For automation and robotics, the faculty already owns certain equipment (mobile robots and PLC controllers), but we have a plan to purchase a robotic hand that will enable automation of the production process.



**Figure 8.** Assembly workplaces with supermarkets[22]  
**Slika 8.** Montažna mjesta sa samoposlugama



**Figure 9.** Pick by light system[23]  
**Slika 9.** Sustav "pick by light"

## 4. Conclusion

Competency development at all levels is needed for ever changing conditions adaption. LF is proven as one effective approach for development of competencies in manufacturing education. In this paper, a concept of LF at FSRE has been presented. Current state regarding space, equipment and infrastructure has been shown and also the elements that should fulfil the whole concept. One of the limitations is high investments required for equipment and infrastructure. In future work, faculty need to develop curriculum for FSRE LF, purchase more equipment and work on the selection of LF product and its manufacturing process.

## Acknowledgements

This work has been fully supported by the Unity Through Knowledge Fund (UKF), 1C My First Collaboration Grant, under the project 11/17 Development of integrative procedure for management of production and service improvement process.

## REFERENCES

- [1] S. Adolph, M. Tisch, and J. Metternich, (2014). "Challenges and Approaches to Competency Development for Future Production", *J. Int. Sci. Publ.*, vol. 12, pp. 1001–1010,
- [2] J. Enke, R. Glass, and J. Metternich, (2017). "Introducing a Maturity Model for Learning Factories," *Procedia Manuf.*, vol. 9, no. December, pp. 1–8,
- [3] E. Abele and G. Reinhart (2011). "Zukunft der Produktion," *München: Hanser*, pp. 53–58,.
- [4] E. Abele *et al.*, (2015). "Learning factories for research, education, and training" *Procedia CIRP*, vol. 32, no. Clf, pp. 1–6,.
- [5] M. Tisch, H. Laudemann, A. Kreß, and J. Metternich, (2017). "Utility-based Configuration of Learning Factories Using a Multidimensional, Multiple-choice Knapsack Problem" *Procedia Manuf.*, vol. 9, pp. 25–32.
- [6] *Mobilising the brainpower of Europe: enabling universities to make their full contribution to the Lisbon Strategy*. Communication from the Commission. COM (2005) 152 final, 20 April 2005, 2005.
- [7] E. Abele *et al.*, (2017). "Learning factories for future oriented research and education in manufacturing," *CIRP Ann. - Manuf. Technol.*, vol. 66, no. 2, pp. 803–826.
- [8] J. E. Jorgensen, J. S. Lamancusa, J. L. Zayas-Castro, and J. Ratner, (1995). "The learning factory," in *Proceedings of the Fourth World Conference on Engineering Education, St. Paul, Minneapolis, USA*.
- [9] E. Abele, R. Tenberg, J. Wennemer, and J. Cachay (2010). "Kompetenzentwicklung in Lernfabriken für die Produktion," *ZWF Zeitschrift für wirtschaftlichen Fabrikbetr.*, vol. 105, no. 10, pp. 909–913.
- [10] G. Chrysosolouris, D. Mavrikios, and D. Mourtzis, (2013). "Manufacturing Systems: Skills & Competencies for the Future," *Procedia CIRP*, vol. 7, pp. 17–24.
- [11] G. Chrysosolouris, D. Mavrikios, and L. Rentzos, (2016). "The Teaching Factory: A Manufacturing Education Paradigm," *Procedia CIRP*, vol. 57, pp. 44–48.
- [12] WP1 (2014). Definitions of Learning Factories, "No Title"
- [13] U. Wagner, T. AlGeddawy, H. ElMaraghy, and E. M"Yller, (2012). "The state-of-the-art and prospects of learning factories," *Procedia CiRP*, vol. 3, pp. 109–114.
- [14] M. Tisch, C. Hertle, J. Cachay, E. Abele, J. Metternich, and R. Tenberg, (2013). "A systematic approach on developing action-oriented, competency-based Learning Factories," *Procedia CIRP*, vol. 7, pp. 580–585,
- [15] (2013). "General Assembly of the Initiative on European Learning Factories." Munich,
- [16] D. Kreimeier, F. Morlock, C. Prinz, B. Krückhans, D. C. Bakir, and H. Meier, (2014). "Holistic Learning Factories – A Concept to Train Lean Management, Resource Efficiency as Well as Management and Organization Improvement Skills," *Procedia CIRP*, vol. 17, pp. 184–188.
- [17] E. Abele, (2016). "Learning Factory." CIRP Encyclopedia of Production Engineering.
- [18] C. du Plessis and K. von Leipzig, (2015). "THE DEVELOPMENT OF AN INDUSTRIE 4.0 IMPLEMENTATION FRAMEWORK WITHIN LEARNING FACTORIES," *Learn. Factory, An Annu. Ed. from Netw. Innov. Learn. Factories*, vol. 1, no. 1, p. 32.
- [19] M. Tisch, C. Hertle, J. Metternich, and E. Abele, (2015). "Goal-oriented improvement of learning factory trainings," *Learn. Factory, An Annu. Ed. from Netw. Innov. Learn. Factories*, vol. 1, no. 1, pp. 7–12.
- [20] M. Tisch, C. Hertle, E. Abele, J. Metternich, and R. Tenberg, (2016). "Learning factory design: a competency-oriented approach integrating three design levels," *Int. J. Comput. Integr. Manuf.*, vol. 29, no. 12, pp. 1355–1375
- [21] J. Enke, R. Glass, and J. Metternich, (2017). "Introducing a Maturity Model for Learning Factories," *Procedia Manuf.*, vol. 9, pp. 1–8.
- [22] "Ergonomic Pivoting Flow Rack - YouTube." [Online]. Available: <https://www.youtube.com/watch?v=59k7LuamSY4>. [Accessed: 16-May-2018].
- [23] "Pick To Light (PTL)." [Online]. Available: <https://www.gebhardt-foerdertechnik.de/en/software/order-picking/pick-to-light-ptl/>. [Accessed: 16-May-2018].



# Using the 3-point bending method to study fracture behaviour of cast in-situ TiAl matrix composite

**Michaela ŠTAMBORSKÁ, Juraj LAPIN, Alena KLIMOVA, Tatiana PELACHOVÁ and Oto BAJANA**

Institute of Materials & Machine  
Mechanics Slovak Academy of Sciences,  
Dúbravská cesta 9, 845 13 Bratislava,  
Slovakia

michaela.stamborska@savba.sk

## Keywords

Fracture toughness  
Intermetallics  
TiAl matrix composites  
Finite element analysis

## Original scientific paper

**Abstract:** The fracture behaviour of in-situ TiAl matrix composite reinforced with  $\text{Ti}_2\text{AlC}$  particles prepared by centrifugal casting was studied using three-point bending tests and numerical simulations. The brittle fracture behaviour of the in-situ composite includes crack deviation, microcrack formation, carbide fragmentation, delamination on the matrix-carbide interfaces and pull-out of the carbide particles from the TiAl matrix. The measured data from acoustic emission shown crack initiation and propagation during three-point bending tests. The finite element analysis (FEA) was used for numerically calculation of a critical stress leading to a crack initiation in the notch region for quasi-static loading conditions. Our measured fracture toughness values are comparable to the values from the test of some in-situ TiAl matrix composites prepared by casting and reactive processing.

## 1. Introduction

As cast TiAl-based alloys are attractive for high-temperature structural applications providing a unique set of physical and mechanical properties for stationary gas turbines, automotive engines and aircraft engines [1–4]. However, their inherent poor ductility at room temperature and insufficient strength at high temperatures (above 800 °C) limit their wide-scale applications. Intermetallic matrix composites may improve the deficiency of these lightweight alloys at high temperatures because of good combination of the properties of intermetallic TiAl matrix and reinforcement [5–11]. Latest studies have shown that in-situ TiAl matrix composites reinforced with homogeneously distributed carbide particles can be prepared by melting followed by centrifugal casting (CC) or gravity casting (GC) of TiAl-based alloys with various content of carbon [9,10]. Besides the coarse primary  $\text{H-Ti}_2\text{AlC}$  particles, the additional strengthening of TiAl matrix composites can be achieved by fine secondary  $\text{P-Ti}_3\text{AlC}$  and  $\text{H-Ti}_2\text{AlC}$  precipitates similarly to that reported for several low carbon TiAl-based alloys [12–15]. The carbide particles improve fracture toughness of the in-situ TiAl matrix composites but alloying with carbon deteriorates

their room-temperature tensile ductility [14,15]. The increase of the fracture resistance was attributed to crack trapping and crack bridging mechanisms [16]. In spite of the previous studies [7–11], only limited information is available about the effect of  $\text{Ti}_2\text{AlC}$  particles on fracture behaviour of in-situ TiAl matrix composites prepared by CC. The CC represents widely applied technology for processing near net shape industrial components from TiAl-based alloys which might facilitate potential applications of the in-situ composites [9, 17].

The aim of present work is to investigate room-temperature fracture behavior of in-situ TiAl matrix composite reinforced with carbide particles prepared by CC of Ti-44.5Al-8Nb-5.2C-0.8Mo-0.1B (at%) alloy. Quasi-static three-point bending is carried to study crack initiation and propagation using V-notch specimens. A blunt notch is used because a fatigue pre-cracking was found to be inconvenient to create an appropriate crack in the studied in-situ composite. Acoustic emission and interrupted three-point bending tests combined with microstructural observations and numerical calculations are performed to identify a critical load and stress leading to a crack initiation during quasi-static loading conditions [17].

## Symbols

$V_p$	- volume fraction, at%	$w$	- width of specimen, mm
$a_c$	- content of carbon, at%	$a$	- length of the notch, mm
$F$	- fracture load, N	CC	- centrifugal casting
$L$	- span of the loading, mm	HIP	- hot-pressing sintering
$K_s$	- static fracture toughness, $\text{MPa m}^{0.5}$	RHP	- reactive hot pressing
$b$	- thickness of specimen, mm	RP	- reactive processing

## 2. Experimental material and procedures

Samples of the in-situ composite reinforced with carbide particles were prepared by a high frequency induction melting of Ti-44.5Al-8Nb-5.2C-0.8Mo-0.1B (at%) alloy followed by a CC into a graphite mould. In order to remove casting porosity, the as-cast samples with a diameter of 15 mm and length of 150 mm were subjected to hot isostatic pressing (HIP) at a temperature of 1250 °C and applied pressure of 200 MPa for 4 h in argon. The HIP-ed samples were consequently annealed at a temperature of 900 °C for 25 h and furnace cooled to room temperature in air. After the casting and heat treatments (HT) Vickers hardness measurements were carried out at an applied load of 300 N. The loading time was 10 s. Room-temperature tensile tests were carried out on threaded-head cylindrical specimens with a gauge diameter of 6 mm and gauge length of 30 mm prepared by lathe machining. The surface of the gauge section was polished to a roughness better than 0.3 µm. The tests were carried out at an initial strain rate of  $1 \times 10^{-4} \text{ s}^{-1}$  using universal testing machine. Elongation was measured by a laser extensometer.

Three-point bending tests at a cross head speed of 0.5 mm/min were carried out on V-notch specimens with a thickness of 10 mm, width of 10 mm, length of 55 mm and notch length of 2 mm prepared from the in-situ composite with 5.2 at.% C after HT. Due to the brittle nature of the in-situ composite no fatigue pre-crack was made. The quasi-static three-point bending tests were carried out at a cross head speed of  $8.33 \times 10^{-6} \text{ m/s}$  at room temperature. The acquisition of load-deflection data was done electronically during the tests.

Microstructural evaluation was performed by scanning electron microscopy (SEM) and SEM in back scattered electron (BSE) mode. Metallographic preparation of the samples consisted of standard grinding on abrasive papers and polishing on diamond pastes with various grain sizes up to 0.25 µm. SEM samples were etched in a reagent of 150 ml H<sub>2</sub>O, 25 ml HNO<sub>3</sub> and 10 ml HF.

Numerical simulation was realized using software Ansys Workbench. A geometry model of the supporting and loading pins was modelled as 3D cylinders and the three-point bending specimen was built as a 3D cuboid with a notch and tip radius. Material model was built-up using the achieved experimental data from the three-point bending tests. Deformable hexahedral elements with a size of 0.1 and 0.5 mm were used to mesh the cylinders and notch specimen, respectively. In total, the mesh created by finite element analysis (FEA) was composed of 485 117 hexahedral elements, adding up to 2 007 867 nodes in total.

## 3. Results and discussion

### 3.1. Microstructural characterization

The CC leads to a relatively uniform distribution of coarse carbide particles (1, 2) within the matrix (3), as seen in Fig. 1. The coarse carbide particles belong to Ti<sub>2</sub>AlC phase and are formed during solidification according to phase transformation pathway  $L + \text{TiC}_{1-x} \rightarrow L + \text{Ti}_2\text{AlC}$  [9]. This solidification pathway affects the morphology of the carbide particles. The Ti<sub>2</sub>AlC particles which were formed directly by transformation of TiC<sub>1-x</sub> particles present in the melt, are frequently nearly spherical and occasionally irregular shaped ones (2). The particles which are formed directly from the melt in the  $L + \text{Ti}_2\text{AlC}$  phase region are plate-like (1), as shown in Figs. 1a and 1b.

Fig. 2 shows the typical microstructures of the studied in-situ TiAl matrix composite prepared by the CC of Ti-44.5Al-8Nb-5.2C-0.8Mo-0.1B (at%) alloy after HIP followed by annealing. The volume fraction of the carbide particles is measured to be  $(21.5 \pm 0.7) \text{ vol.}\%$ . The mean length and diameter of plate-like and regular shaped Ti<sub>2</sub>AlC particles are measured to be  $(17.3 \pm 0.7) \mu\text{m}$  and  $(9.8 \pm 0.4) \mu\text{m}$ , respectively [17]. Figs. 2a and 2b clearly indicate that the intermetallic  $\gamma(\text{TiAl})$  matrix is reinforced by bimodal sized carbide particles. Besides the coarse primary carbides, the in-situ composite contains fine secondary Ti<sub>2</sub>AlC particles (4) which are formed during the heat treatments.

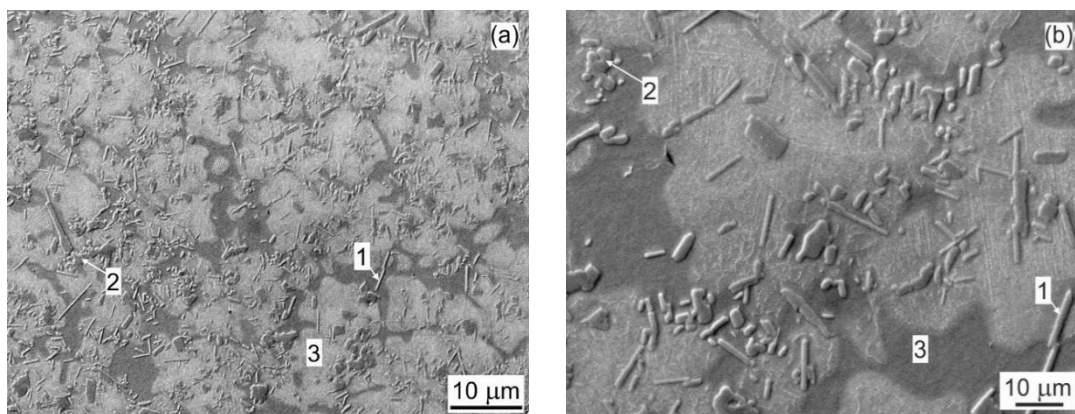


**Figure 1.** SEM micrographs showing the microstructure of the in-situ composites after CC: (a) Distribution of carbide particles in TiAl matrix; (b) Morphology of carbide particles. 1, 2 –Ti<sub>2</sub>AlC particles; 3 -  $\gamma$  (TiAl) matrix.

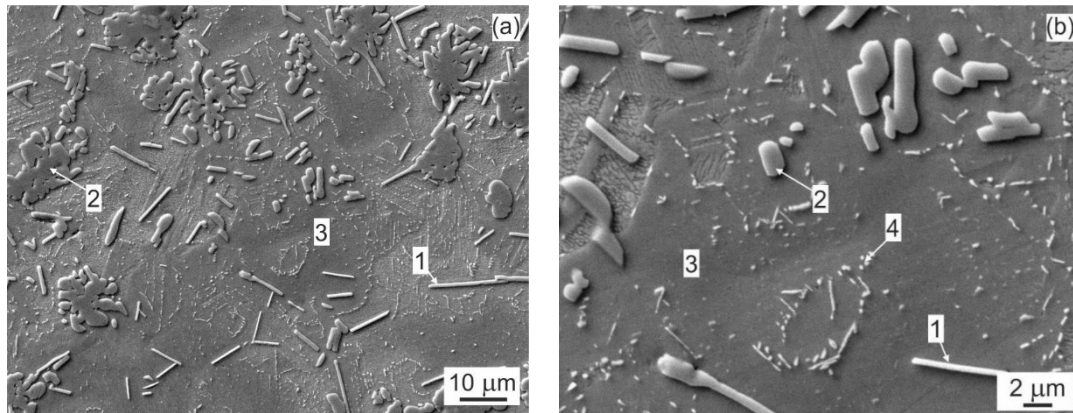


**Figure 2.** SEM micrographs showing the microstructure of in-situ composites after HIP and HT: (a) Distribution of carbide particles in TiAl matrix; (b) Morphology of carbide particles. The analysed regions marked in the figures are 1, 2 – primary Ti<sub>2</sub>AlC particles; 3 – γ (TiAl) matrix; 4 – fine secondary Ti<sub>2</sub>AlC particles.

These fine carbides with an average width of  $(29.5 \pm 0.7)$  nm and length of  $(84.7 \pm 4.3)$  nm precipitate preferentially within the coarse γ grains (grain size of 28 μm) and along the γ grain boundaries.

### 3.2. Hardness and tensile properties

The studied in-situ TiAl matrix composite shows brittle behaviour without yielding during the room-temperature tensile tests. Average values (5 tested specimens) of hardness and tensile properties are shown in Table 1.

**Table 1:** Hardness and tensile properties

Ultimate tensile strength [MPa]	Vickers hardness	Elastic modulus [GPa]
330± 15	310	185± 5

The stress increases nearly linearly with the strain up-to a fracture. Leguillon et al. [18,19] have reported that the tensile strength of brittle materials is higher than flexural one because fewer randomly distributed defects in the material are involved in bending than in tension in case of specimens of the same size. However, such effect is minimized in the present work by selecting the size of tensile specimens which is close to the size of the tested three-point bending specimens stressed in tension [17].

### 3.3. Three-point bending tests

Lapin et al. [17] have reported three point bending load-deflection curve of the standard V-notch specimen prepared from the studied in-situ composite after HT.

**Table 2:** Fracture toughness

Composition	Fracture toughness [MPam <sup>0.5</sup> ]	Produced	Ref.
Ti-44.5Al-8Nb-5.2C-0.8Mo-0.1B	11.6 ± 0.6	CC	[17]
Ti-44.5Al-8Nb-4.8C-0.8Mo-0.1B	13.7	CC	[9]
TiAl/Ti <sub>2</sub> AlC	7.8	RHP	[21]
TiAl/Ti <sub>3</sub> AlC <sub>2</sub> -Ti <sub>2</sub> AlC	7.3	HPS	[22]
TiAl-Ti <sub>2</sub> AlC	12–17.8	RP	[23]

A large number of acoustic emission (AE) events were produced by the applied AE sensors during the quasi-static loading. The frequency of these events increased with increasing load and deflection. Most of the AE events of amplitudes ranging from 70 to 90 dB occurred at a deflection higher than 0.031 mm. The crack propagation was connected with the events of amplitudes up to 100 dB. The fracture of the specimen was observed at a maximum load of 1580 N and deflection of 0.036 mm.

The fracture toughness of the V-notch specimen can be calculated according to relationship [17, 20]

$$K_S = 1.5 \frac{FLa^{0.5}}{bw^2} \left[ \frac{1.99 - a/w(1-a/w)(2.15 - 3.93a/w + 2.7(a/w)^2)}{(1+2a/w)(1-2a/w)^{1.5}} \right] \quad (1)$$

where  $F$  is the fracture load,  $L$  is the span of the loading,  $b$  is the thickness of specimen,  $w$  is the width of specimen and  $a$  is the length of the notch. Since the ASTM specifications for fracture toughness testing concerning notch geometry and pre-cracking were not rigorously followed in the present study, the toughness values are denoted as  $K_S$ . The calculated value of fracture toughness of 11.6 MPam<sup>0.5</sup> for the studied in-situ composite can be compared with those of some in-situ TiAl matrix composites prepared by casting and reactive processing, as seen in Table 2. The effectiveness of these extrinsic toughening mechanisms depends strongly on the applied processing techniques, volume fraction and size of the carbide particles [9, 21–23].



### 3.4. Fractography

The initiation of short cracks in the vicinity of the notch tip was observed at a load of 1418 N which corresponded to a deflection of 0.031 mm and AE events with an amplitude of about 90 dB. These cracks initiated preferentially in the  $\gamma$ (TiAl) matrix were arrested by the carbide particles. Further increase of the load to 1580 N resulted in a fast propagation of the main crack through the specimen. The main crack was accompanied with several short cracks which were usually initiated along the grain boundaries, how we saw during the experiment. The primary  $\text{Ti}_2\text{AlC}$  particles served as the effective obstacles to the crack propagation, deviate the main crack and arrested the short secondary cracks. Fig. 3 shows brittle fracture mode of the in-situ composite after three-point bending test. The fracture surface is macroscopically smooth, as seen in Fig. 3a. The pull-out of the coarse carbide particles, decohesion along the matrix-carbide particle interfaces and delamination of the carbides can be well identified on the fracture surface, as shown in Fig. 3b. The extraction of the primary carbide particles from the matrix increases the fracture energy of the TiAl matrix composites [9]. Fig. 3b shows the

fracture propagation through lamellar  $\gamma/\gamma$  interfaces with numerous fine secondary carbide particles, which were formed during the heat treatments. Fig. 3c clearly indicates the cleavage fracture surface of the regular shaped and delamination along the crystallographic planes leading to a step-like fracture of the plate-like particles. The laminated tearing of the primary carbides and the kink boundaries indicate that these particles contribute to the damage tolerance of the in-situ composite when compared with a single TiAl matrix. The embedded carbides in the matrix retard the crack propagation and increase the fracture energy [17].

As shown by Rao et al. [16] for ductile TiNb particles in TiAl matrix and Ramaseshan et al. [23] for  $\text{Ti}_2\text{AlC}$  particles in lamellar  $\text{Ti}_3\text{Al}+\text{TiAl}$  matrix, the increase of the fracture toughness of the composites results from crack trapping and its re-nucleation. The fracture toughness can be increased by increasing strength of the reinforcement. In the case of the studied in-situ composite, the phase composition of the primary carbide particles can be influenced by the applied processing routes [9].

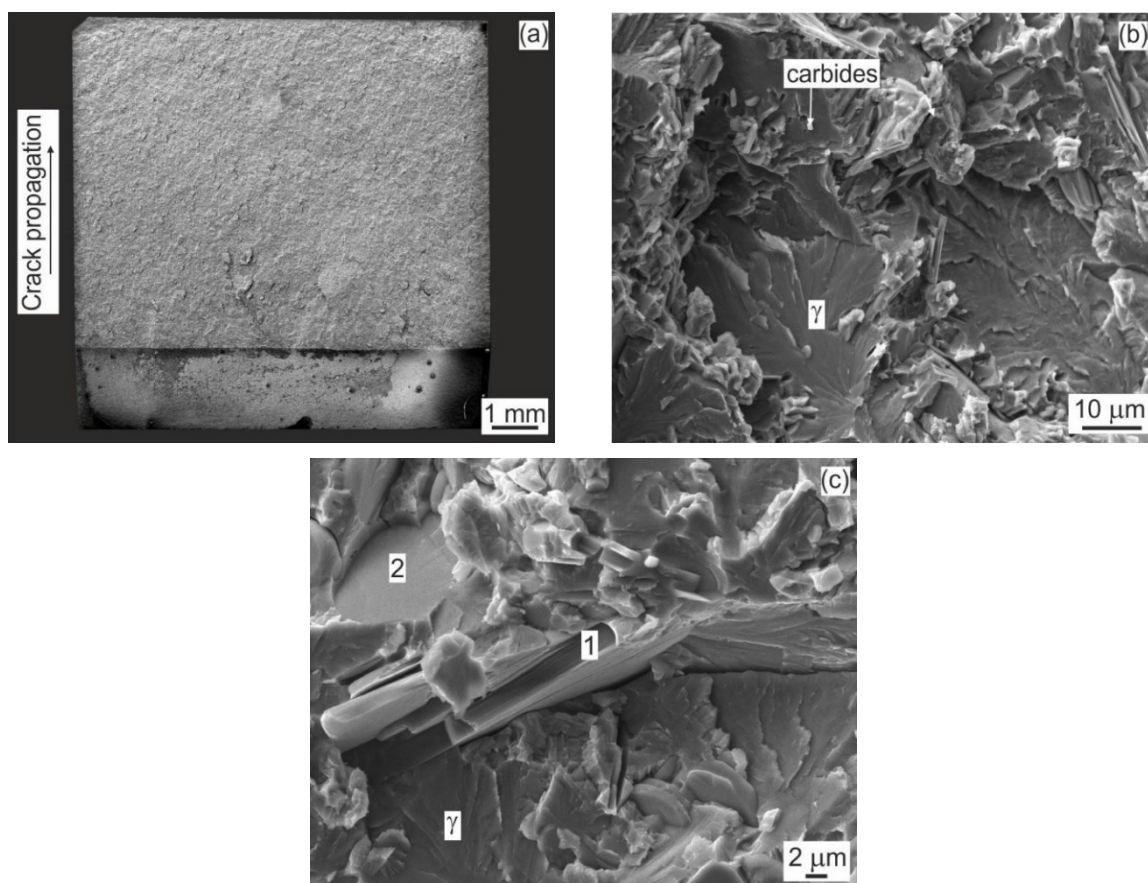


**Figure 3.** The typical brittle fracture of the in-situ composite after three-point bending test: (a) Smooth fracture surface, SEM; (b) Fracture mode of  $\text{Ti}_2\text{AlC}$  particles and fine secondary carbide particles embedded in the  $\gamma$  matrix, BSE; (c) Brittle fracture of primary plate-like (1) and regular shaped (2)  $\text{Ti}_2\text{AlC}$  particles, BSE.

### 3.5. Numerical simulations

During the quasi-static three-point bending tests the notch creates a stress concentrator and increases local stresses in the specimen. The condition for the crack initiation are fulfilled when a local stress in the vicinity of the notch tip achieve a critical value corresponding to a flexural strength of the material [19]. The analysis of fracture behaviour shows that an average critical load of  $F = (1418 \pm 37)$  N is required to initiate a crack in the notch tip region of the studied in-situ composite during the interrupted three-point bending tests. This experimentally measured critical load is used to calculate stress distribution within the notched specimen and to determine a critical stress required for the crack initiation. Fig. 4 shows the distribution of numerically calculated equivalent (von-Mises) stresses within the notched specimens corresponding to a load of 1418 N. A maximum local stress of 347 MPa is calculated by FEA in the tip notch region shown in detail (Fig. 4). This calculated maximum local stress is close to the measured average ultimate tensile strength of  $(330 \pm 15)$  MPa of the studied in-situ composite [17].

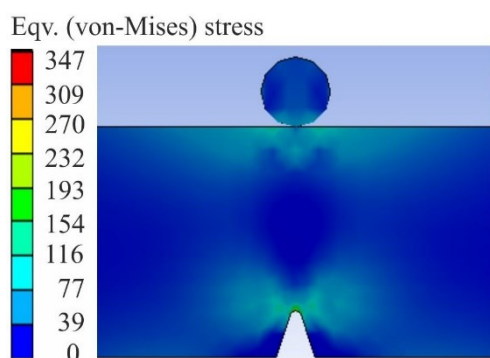


**Figure 4.** Equivalent (von-Mises) stress distribution calculated at a critical load corresponding to a crack initiation during three-point bending test.

## 4. Conclusions

The static fracture behaviour of the in-situ TiAl matrix composite reinforced with carbide particles was studied. The following conclusions are reached:

1. The microstructure of the in-situ TiAl matrix composite prepared by CC followed by HIP and annealing consists of the TiAl matrix reinforced by bimodal sized  $\text{Ti}_2\text{AlC}$  particles.
2. A critical load and deflection for a crack initiation in the notch tip region of test specimens is determined by the acoustic emission measurements combined with the metallographic analysis during interrupted quasi-static three-point bending tests at room temperature.
3. The stress distribution in the notched specimen and critical stress leading to a crack initiation in the notch tip region are numerically calculated using finite element analysis software ANSYS. The calculated critical stress

is close to the measured ultimate tensile strength of the studied in-situ TiAl matrix composite.

4. The fracture toughness values measured on V-notch specimens using quasi-static three-point bending at room temperature are comparable to those of some in-situ matrix composites prepared by casting and reactive processing.

5. The brittle fracture behaviour of the in-situ composite includes crack deviation, zone shielding by microcrack toughening, carbide fragmentation, delamination on the matrix-carbide interfaces and pull-out of the carbide particles from the TiAl matrix.

## Acknowledgements

This work was financially supported by the Slovak Research and Development Agency under the contract APVV-15-0660 and the Slovak Grant Agency for Science under the contract VEGA 2/0125/16. The experimental work was carried out thanks to the infrastructure supported by the Competence Centre for New Materials, Advanced Technologies and Energy under the contract ITMS 26240220073.

## REFERENCES

- [1] Bewlay B.P., Nag S., Suzuki A., Weimer M.J., (2016) *TiAl alloys in commercial aircraft engines*, Mater. High Temp. 33, p. 549–559.
- [2] Shouren W., Peiquan G., Liying Y., (2008) *Centrifugal precision cast TiAl turbocharger wheel using ceramic mold*, J. Mater. Process. Technol. 204, p. 492–497.
- [3] Lapin J., Nazmy M., (2004) *Microstructure and creep properties of a cast intermetallic Ti-46Al-2W-0.5Si alloy for gas turbine applications*, Mater. Sci. Eng. A 380, p. 298–307.
- [4] Lapin J., Pelachová T., Dománková M., (2018) *Long-term creep behaviour of cast TiAl-Ta alloy*, Intermetallics 95, p. 24–32.
- [5] Lapin J., Ondruš L., Bajana O., (2003) *Effect of  $\text{Al}_2\text{O}_3$  particles on mechanical properties of directionally solidified intermetallic Ti-46Al-2W-0.5Si alloy*, Mater. Sci. Eng. A 360, Iss. 1-2, p. 85–95.
- [6] Niu H.Z., Xiao S.L., Kong F.T., Zhang C.J., Chen Y.Y., (2011) *Microstructure characterization and mechanical properties of  $\text{TiB}_2/\text{TiAl}$  in situ composite by induction skull melting process*, Mater. Sci. Eng. A 532, p. 522–527.
- [7] Song X.J., Cui H.Z., Hou N., Wei N., Han Y., Tian J., Song Q., (2016) *Lamellar structure and defect of  $\text{Ti}_2\text{AlC}$  on properties of prepared in-situ TiAl matrix composites*, Ceram. Int. 42, p. 13586–13592.
- [8] Song X., Cui H., Han Y., Hou N., Wei N., Ding L., Song Q., (2017) *Effect of carbon reactant on*



- microstructures and mechanical properties of TiAl/Ti<sub>2</sub>AlC composites*, Mater. Sci. Eng. A 684, p. 406–412.
- [9] Lapin J., Klimová A., Gabalcová Z., Pelachová T., Bajana O., Štamborská M., (2017) *Microstructure and mechanical properties of cast in-situ TiAl matrix composites reinforced with (Ti,Nb)<sub>2</sub>AlC particles*, Mater. Des. 133, p. 404–415.
- [10] Klimová A., Lapin J., Pelachová T., (2017) *Characterization of TiAl based alloys with various content of carbon*, IOP Conf. Ser. Mater. Sci. Eng. 179, Iss. 1.
- [11] Ramkumar J., Malhotra S.K., Krishnamurthy R., Mabuchi H., Demizu K., Kakitsuji A., Tsuda H., Matsui T., Morii K., (2003) *Microstructure and dry sliding wear of Ti–50Al alloy and Ti–47Al–3W/Ti<sub>2</sub>AlC composite produced by reactive arc-melting*, Mater. Trans. 44, p. 1861–1865.
- [12] Schwaighofer E., Staron P., Rashkova B., Stark A., Schell N., Clemens H., Mayer S., (2014) *In situ small-angle X-ray scattering study of the perovskite-type carbide precipitation behavior in a carbon-containing intermetallic TiAl alloy using synchrotron radiation*, Acta Mater. 77, p. 360–369.
- [13] Cegan T., Szurman I., (2017) *Thermal stability and precipitation strengthening of fully lamellar Ti–45Al–5Nb–0.2B–0.75C alloy*, Kov. Mater. 55, p. 421–430.
- [14] Wu Z., Hu R., Zhang T., Zhang F., Kou H., Li J., (2017) *Understanding the role of carbon atoms on microstructure and phase transformation of high Nb containing TiAl alloys*, Mater. Charact. 124, p. 1–7.
- [15] Li M., Xiao S., Xiao L., Xu L., Tian J., Chen Y., (2017) *Effects of carbon and boron addition on microstructure and mechanical properties of TiAl alloys*, J. Alloy. Compd. 728, p. 206–221.
- [16] Venkateswara Rao K.T., Odette G.R., Ritchie R.O., (1994) *Ductile-reinforcement toughening in  $\gamma$ -TiAl intermetallic-matrix composites: effects on fracture toughness and fatigue-crack propagation resistance*, Acta Metall. Mater. 42, p. 893–911.
- [17] Lapin J., Štamborská M., Pelachová T., Bajana O., (2018) *Fracture behaviour of cast in-situ TiAl matrix composite reinforced with carbide particles*. Mat Sci Eng A-Struct 721, p. 1-7.
- [18] Leguillon D., Martin É., Lafarie-Frenot M.C., (2015) *Flexural vs. tensile strength in brittle materials*, Comptes Rendus – Mec. 343, p. 275–281.
- [19] Leguillon D., (2002) *Strength or toughness? A criterion for crack onset at a notch*, Eur. J. Mech. A/Solids 21, p. 61–72.
- [20] Cao R., Lei M.X., Chen J.H., Zhang J., (2007) *Effects of loading rate on damage and fracture behavior of TiAl alloys*, Mater. Sci. Eng. A 465, p. 183–193.
- [21] Yang C., Wang F., Ai T., Zhu J., (2014) *Microstructure and mechanical properties of in situ TiAl/Ti<sub>2</sub>AlC composites prepared by reactive hot pressing*, J. Eur. Ceram. Soc. 40, p. 8165–8171.
- [22] Ai T.T., Wang F., Feng X.M., Ruan M.M., (2014) *Microstructural and mechanical properties of dual Ti<sub>3</sub>AlC<sub>2</sub>-Ti<sub>2</sub>AlC reinforced TiAl composites fabricated by reaction hot pressing*, Ceram. Int. 40, p. 9947–9953.
- [23] Ramaseshan R., Kakitsuji A., Seshadri S.K., Nair N.G., Mabuchi H., Tsuda H., Matsui T., Morii K., (1999) *Microstructure and some properties of TiAl-Ti<sub>2</sub>AlC composites produced by reactive processing*, Intermetallics 7, p. 571–577.

# Offline numerička simulacija kinematskog mehanizma CAD modela robota 2AJ-RV koristeći Labview i SolidWorks

**Amra TALIC-ČIKMIŠ<sup>1)</sup> Fuad  
HADŽIKADUNIĆ<sup>1)</sup>, Malik  
ČABARAVDIĆ<sup>1)</sup> and Kenan VARDA<sup>1)</sup>**

1) Faculty of Mechanical Engineering of  
University of Zenica  
Department of constructions and CAD  
technologies  
Fakultetska br 1, Zenica, Bosna i  
Hercegovina

[acikmis@mf.unze.ba](mailto:acikmis@mf.unze.ba)  
[hfuad@mf.unze.ba](mailto:hfuad@mf.unze.ba)  
[mcabaravdic@mf.unze.ba](mailto:mcabaravdic@mf.unze.ba)  
[kenan.varda@gmail.com](mailto:kenan.varda@gmail.com);

## Keywords

Mitsubishi 2AJ-RV  
robot  
simulation  
SW motion  
mechanism,  
SolidWorks motion  
LabView  
SoftMotion

## Ključne riječi

Mitsubishi 2AJ-RV  
robot  
simulacija  
SolidWorks motion  
mehanizam  
SolidWorks  
LabView  
SoftMotion

## Offline numerical simulation of 2AJ-RV robot kinematic mechanism CAD model using Labview and SolidWorks

*Original scientific paper*

**Abstract:** More recently, numerical motion simulations are increasingly used in Robotics and Mechatronics, especially in determining more complex paths and tasks that a robotic arm should perform in a particular system. Based on the Mitsubishi 2AJ-RV robot, which has its own characteristics related to movement restrictions, precisely defined geometry and degrees of movement freedom of joints, a credible CAD model is created in the SolidWorks software. The robot consists of six parts, which has five joints. Within the SolidWorks Motion package, motors that run each of these five joints are defined and will serve as a base for connecting to the control unit. Within this package, the limitations of the robot CAD model as well as the actual model, are set.

NI LabView software has the ability to create a virtual control unit, and for each of these joints a special control unit that manages the joints and moves them in the allowed axes of movement is created. With the Labview SoftMotion package, a virtual control unit is connected with each of the motors on the CAD model's joints and a direct connection is established. After that, few numerical motion simulations were performed in different environment and with different boundary conditions.

This approach is very useful and can contribute greatly to saving time when creating tasks for a robotic arm, where we can define the entire environment for operations that this robotic arm should perform.

*Izvorni znanstveni rad*

**Sažetak:** U novije vrijeme, numeričke simulacije kretanja se sve više koriste u robotici i mehatronici, posebno za određivanje kompleksnih putanja i zadataka koje robotska ruka treba izvesti u određenom sustavu. Na osnovi Mitsubishi 2AJ-RV robota, koji ima svoje karakteristike vezane za ograničenje kretanja i jasno definiranu geometriju i stupnjeve slobode gibanja zglobova, kreiran je vjerodostojan CAD model robota u softveru SolidWorks. Robot se sastoji od šest dijelova i posjeduje pet zglobova. Unutar paketa Motion u SolidWorks-u, motori koji pokreću ovih pet zglobova su definirani i služe kao baza za povezivanje modela i upravljačke jedinice. Unutar ovog paketa, ograničenja kretanja CAD modela su definirana pojednako kao na realnom modelu.

Softver NI LabView ima mogućnost kreiranja virtualne upravljačke jedinice i za svaki od pet zglobova je kreiran upravljački dio koji upravlja zglobovima i pomiče ih u dozvoljenim osima gibanja. Pomoću paketa SoftMotion, virtualna upravljačka jedinica je povezana sa svakim od motora na zglobovima CAD modela i uspostavljena je njihova direktna veza. Nakon toga, nekoliko numeričkih simulacija je provedeno u različitim okruženjima i sa različitim graničnim uvjetima.

Ovaj pristup je veoma koristan i može uveliko doprinijeti smanjenju vremena kod kreiranja zadataka jedne robotske ruke, gdje se može definirati cijelo okruženje za operacije koje ova robotska ruka treba izvršiti.



(Mates) prave veze susjednih dijelova modela<sup>[7]</sup>. Pomoću standardnih geometrijskih odnosa i veza (podudarnost, okomitost, tangentnost, koncentričnost itd.) kreira se nedjeljivi sklopni model robota koji će se kasnije koristiti za simulacije gibanja.

Bitno je prilikom definiranja veza dopustiti gibanje zglobova, odnosno susjednih dijelova jednog u odnosu na drugi u dozvoljenim osima gibanja kako je to definirano na realnom robotu<sup>[4]</sup>.

## 2.2 Priprema CAD modela za simulaciju

U softveru SolidWorks je bitno aktivirati pakete SolidWorks Motion i SolidWorks Simulation, koji su neophodni za provođenje studije pokreta. Prilikom startanja softvera, u padajućem meniju Add-Ins se aktiviraju navedeni paketi.

Kada se pokrene studija pokreta za simulaciju, definira se prethodno kreirani sklopni model robota kao model za simuliranje.

U paketu SolidWorks motion se kreiraju motori na svakom od zglobova i definira se os i smjer rotacije svake od komponenti sklopa (slika 3)<sup>[6]</sup>.

Na grafičkom okruženju, zelenom bojom je označena lokacija motora na kojoj je isti smješten, plavom bojom je označen smjer rotacije, gdje je moguće odabrati i suprotan smjer rotiranja, zavisno kako je postavljen početni smjer. Žutom bojom je označena komponenta u odnosu na koju će se relativno kretati komponenta pogonjena motorom. Crvenom bojom je označen motor koji se podešava u okviru i definira se funkcija motora koja se podešava na opciju "Distance" (udaljenost) jer je neophodna veza sa softverom NI LabView koji će biti upravljačka jedinica modela robota<sup>[10]</sup>.

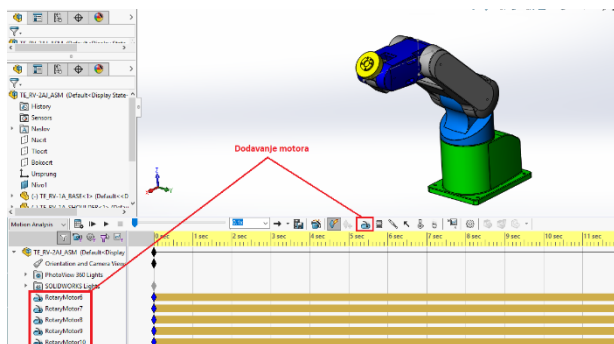


Figure 3: Motor creation for every component of the robot assembly model

Slika 3: Kreiranje motora za svaku od komponenti modela sklopa robota

## 3. Upravljačka jedinica

Virtualna upravljačka jedinica se sastoji od industrijski standardiziranog računala ili radne stanice koji su opremljeni s jakim softverima, isplativim hardverima kao što su uključne ploče i "driver" softvera, koji zajedno izvršavaju funkciju tradicionalnih upravljačkih jedinica i instrumenata<sup>[2]</sup>.

Softver Labview je korišten za kreiranje virtualne instrumentizacije i pruža razvojno okruženje aplikacije koja je jednostavna za korištenje i dizajnirana za potrebe inženjera i znanstvenika. Labview posjeduje grafičko radno okruženje i jednostavno je rukovati odabranim hardverom, odnosno komunicirati sa drugim softverom kao što je to ovdje slučaj.

Kreiranje projekta u LabView softveru se počinje pravljenjem blok dijagrama koji sadrži izvorni grafički kod LabView softvera i glavna uloga mu je da razdvoji grafički izvorni kod od korisničkog sučelja (slika 4). Objekti s upravljačke ploče se pojavljuju kao terminali na blok dijagramu<sup>[8]</sup>.

Pokretanjem "Timed Loop" opcije kreira se virtualni instrument sa višestrukom stopom vremenskih kapaciteta. Pored osnovnih opcija i alatki softvera LabView, potrebno je posjedovati dodatni paket NI SoftMotion, koji je potreban za povezivanje SolidWorks Motion paketa i LabView upravljačke jedinice.

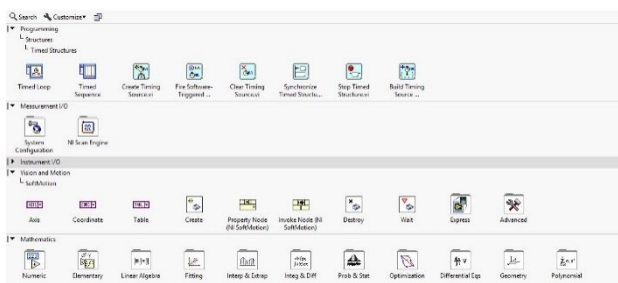


Figure 4: Function blocks choosing  
Slika 4: Odabir funkcijskih blokova

Naredni alat koji se dodaje je funkcijski blok za pravocrtno kretanje (Straight-Line Move Function Block), slika 5. Funkcijski blok ima nekoliko ulaza i izlaza koji se vezuju žicama sa drugim objektima na blok dijagramu. Funkcijski blok je automatski podešen na relativno kretanje i predstavlja izvršavanje pravolinijskog pokreta poštujući trenutnu poziciju u momentu kada je simulacija pokrenuta.

U narednim koracima se kreiraju numeričke kontrole i spajanje funkcijskih blokova sa drugim objektima. Definišu se pozicije (positions), brzina (velocity) i izlazni indikator (done).

Svaka virtualna upravljačka jedinica sadrži i prednju ploču na kojoj se može dizajnirati korisničko sučelje. Može se također koristiti prednja ploča kao način propuštanja ulaza i primanja izlaza kada se pozove virtualni instrument iz drugog blok dijagrama<sup>[3]</sup>.

Na konkretnom primjeru prednje ploče kreirana su gumbići, brojčanici, klizači i stringovi. Ove funkcije imitiraju ulazne uređaje instrumenta i snabdijevaju podacima blok dijagram u pozadini upravljačke jedinice (slika 6).

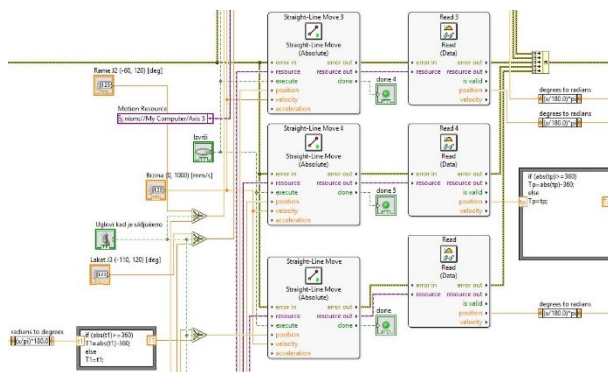


Figure 5: Block diagram of virtual instrument  
Slika 5: Izgled blok dijagrama upravljačke jedinice

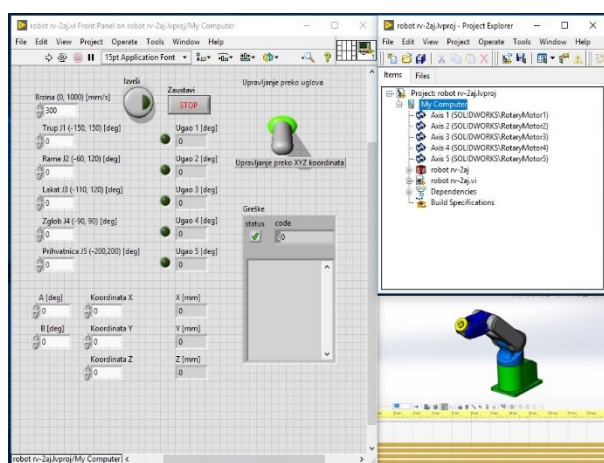


Figure 6: Virtual instrument board  
Slika 6: Izgled upravljačke ploče

Na upravljačkoj jedinici se vide numeričke kontrole upravljanja motorima. Motorima se može upravljati na dva načina, preko kutova zakretanja i koordinata x, y i z. Prikazani su nazivi zglobova i vrijednosti kutova koji se mogu unijeti u polja definirana za unos. Također, definirano polje u koje se može unositi brzina kretanja zglobova u mm/s. Definirani su numerički i led

indikatori. Numerički indikatori prikazuju vrijednost otklona svakog dijela robota te poziciju hvataljke u Kartezijском koordinatnom sustavu, dok led indikatori signaliziraju koji dio robota je u pokretu, a koji u mirovanju.

Na kraju, na upravljačkoj jedinici su definirani gumbi za pokretanje robota i za zaustavljanje cijelog programa izvršenja.

#### 4. Zaključak

Kreiranje virtualne upravljačke jedinice za upravljanje CAD modelom robota i simuliranjem putanja je veoma kvalitetan način pravljenja ušteda vremena kod kreiranja zadataka jednog robotskog manipulatora. Jednostavan je način unosa koordinata i ostalih parametara kretanja u odnosu na realni instrument i postoji mogućnost podešavanja svih parametara i jednostavnog izvršenja komandi u nizu. Također, jedna od mogućnosti je kreiranje online veze upravljačke jedinice i realnog instrumenta za upravljanje robotom za kreiranje online simulacija.

#### REFERENCE

- [1] Bruno Siciliano, Lorenzo Sciavicco, Luigi Villani, Giuseppe Oriolo, Robotics: (2009). *Modelling, Planning and Control* (Advanced Textbooks in Control and Signal Processing) 1st edition
- [2] Mark W. Spong, Seth Hutchinson, M. Vidyasagar, (2005). *Robot Modeling and Control* - First edition
- [3] Vlatko Doleček, Isak Karabegović, (2002). *ROBOTIKA*, Tehnički fakultet, Bihać
- [4] Rickard Nillson, (2009) Inverse Kinematics,
- [5] Jasmin Velagić, (2008). *Uvod u robotiku*,
- [6] Borut Zupančič, Računalniška simulacija, Univerza v Ljubljana
- [7] [www.3ds.com](http://www.3ds.com) - Dassaulta systemes
- [8] [www.ni.com](http://www.ni.com) - National Instruments
- [9] [www.mitsubishirobots.com](http://www.mitsubishirobots.com) - Mitsubishi robotics
- [10] Dassaulta Systemes, SolidWorks Motion, 2013



# The influence of pH and electrolyte temperature on corrosion behaviour of CuAlMnTi alloy ribbons in NaCl solution

Ladislav VRŠALOVIĆ<sup>1)</sup>, Radosna JERČIĆ<sup>1)</sup>, Senka GUDIĆ<sup>1)</sup>, Ivana IVANIĆ<sup>2)</sup>, Stjepan KOŽUH<sup>2)</sup>, Borut KOSEC<sup>3)</sup>, Milan BIZJAK<sup>3)</sup> and Mirko GOJIĆ<sup>2)</sup>

1) University of Split, Faculty of Chemistry and Technology, Ruđera Boškovića 35, 21000 Split, Croatia

2) University of Zagreb, Faculty of Metallurgy, Aleja narodnih heroja 3, 44103 Sisak, Croatia

3) University of Ljubljana, Faculty of Natural Science and Engineering, Aškerčeva cesta 12, 1000 Ljubljana, Slovenia

ladislav@ktf-split.hr

senka@ktf-split.hr

iivanic@simet.hr

kozuh@simet.hr

borut.kosec@ntf.uni-lj.si

milan.bizjak@ntf.uni-lj.si

gojic@simet.hr

## Keywords

CuAlMnTi alloy

NaCl solution

corrosion

polarization

SEM/EDS

## Original scientific paper

**Abstract:** The influence of pH and temperature of 0.9% NaCl solution on corrosion behaviour of CuAlMnTi alloy ribbons, produced by rapid solidification using melt spinning method, were investigated by electrochemical methods. Open circuit potential measurement, linear and potentiodynamic polarization were employed during the investigation, and the measurements were conducted in the electrolyte temperature of 10, 24, 37 and 50 °C and in solution pH of 7.4, 5.4 and 3.4. It has been found that corrosion rate generally increases with increasing the temperature of the electrolyte while the influence of pH change on CuAlNiTi ribbon corrosion is little less pronounced. After polarization measurements CuAlNiTi ribbon surfaces were investigated with light microscope and with SEM/EDS analysis.

## Izvorni znanstveni rad

**Sažetak:** U radu je elektrokemijskim metodama ispitan utjecaj pH i temperature 0.9% NaCl otopine na korozijsko ponašanje legure CuAlMnTi koja je proizvedena u obliku trake naglim hlađenjem melt spinning metodom. Tijekom ispitivanja primijenjene su metode mjerenja potencijala otvorenog strujnog kruga, linearne i potenciodinamičke polarizacije a ispitivanja su provedena na temperaturama 10, 24, 37 i 50 °C i pri pH vrijednostima otopine od 7.4, 5.4 i 3.4. Nađeno je da se brzina korozije povećava s povećanjem temperature elektrolita dok je utjecaj promjene pH na koroziju CuAlMnTi traka nešto manje izražen. Nakon polarizacijskih mjerenja površine CuAlMnTi traka su ispitane pomoću svjetlosnog mikroskopa a također je napravljena i SEM/EDS analiza.

## 1. Introduction

Cu-based shape memory alloys (SMA) are considered to be commercially attractive alloys for technological applications due to their shape memory effect (SME) and pseudoelasticity (PE). Their important advantage over Ni-Ti alloys lies in their lower production cost and the possibility of using at higher temperatures (around 200 °C) [1-4]. Cu-based SMA-s are currently derived from three binary alloy systems i.e. Cu-Zn, Cu-Al and Cu-Sn [5]. Cu-Zn based alloy containing alloying elements such as Al, Si, Sn, Ga or Mn as ternary alloy and Cu-Al based ternary alloys containing Ni, Be, Zn and Mn as alloying elements have been explored for their potential use [6-10]. One of the major drawback of CuAlNi and CuZnAl shape memory alloy are their brittleness and susceptibility to intergranular fracture due to its coarse grain structures and high elastic anisotropy [11, 12]. To overcome these particular problems, several ways have been identified by the researcher so far such as thermomechanical procession, use of micro-alloy elements for grain refinement and use rapid solidification

process in alloys production [12-15]. Generally there are four advantages of rapid solidification over the slow conventional solidification techniques. These are an ability to form metastable phases, increasing the solubility above the equilibrium solubility, decreasing the segregation of additions and refining the microstructure [13-15]. Introduction of a less soluble forth alloying element in CuAlNi or CuAlMn alloy can improve ductility of the alloy. For example Ti has proved to be an effective  $\beta$ -grain growth inhibitor that inhibits the grain coarsening of the alloy during annealing [4]. Adachi et al. [16] revealed that the Ti-doped in Cu-Al-Ni SMA can reduce grain size and leads to enhancing the mechanical properties, while Morris and Gunter [17] refer in their study to the fact that the addition of boron and zirconium can lead to an improvement in the mechanical properties. This paper aims to investigate corrosion behaviour of CuAlMnTi alloy ribbons, produced by rapid solidification using melt spinning method in NaCl solution of different temperatures and different pH values of electrolyte.

**Symbols/Oznake**

$E_{oc}$	- open circuit potential, V - potencijal otvorenog strujnog kruga	$SCE$	- saturated calomel electrode - zasićena kalomel elektroda
$i_{corr}$	- corrosion current density, $\mu Acm^{-2}$ - gustoća korozijske struje	$wt. \%$	- maseni postotak, - weigh percentage
$E_{corr}$	- corrosion potential, V - korozijski potencijal	$at. \%$	- atomski postotak - atomic percentage
$R_p$	- polarization resistance, $\Omega cm^2$ - polarizacijski otpor		

**2. Experimental setup**

Rapidly solidified ribbons of CuAlMnTi with the composition of 82.3 wt.% Cu, 8.3 wt.% Al 9.4 wt.% Mn and 1 wt.% Ti were manufactured with the single roll melt spinning apparatus. The cast precursors were inserted into the graphite crucible and inductively melted in Ar atmosphere and sprayed through the nozzle into the cooled rotating copper wheel. The CuAlMnTi alloy ribbon samples for the electrochemical measurements were prepared by cutting to the appropriate dimensions and then soldered on an insulated copper wire to gain proper electrical contact. Soldered joint points are insulated with Polirepar S protective mass to prevent the evaluation of galvanic corrosion in contact with the electrolyte. Due to its small thickness, mechanical treatment by grinding and polishing of the CuAlNiTi ribbons could not be performed, so the surface of the electrode was processed by ultrasonic degassing in ethanol, washed with deionized water and immersed in the electrolyte.

Experiments were performed with a PAR 273A potentiostat/galvanostat in a double walled three-electrode glass cell thermostated at 37°C, with Pt-plate auxiliary electrode and saturated calomel electrode (SCE) as a reference electrode, which was located in the Luggin capillary. The evaluation of corrosion behaviour of CuAlMnTi alloy in 0.9% NaCl solution was performed by open circuit potential measurements (EOC) in 60 minutes time period, linear polarization method in the potential region of  $\pm 20$  mV around corrosion potential, with the scanning rate of  $0.2 \text{ mV s}^{-1}$  and potentiodynamic polarization method in the potential region of  $-0.250 \text{ V}$  from open circuit potential to  $0.7 \text{ V}$ , with the scanning rate of  $0.5 \text{ mV s}^{-1}$ .

After corrosion testing the surface of investigated samples was photographed by a Canon Ixus 1000 HS digital camera and with light microscope MXFMS-BD, Ningbo Sunny Instruments co.. Detailed surface morphology of the samples after the potentiodynamic measurements was examined by scanning electron microscope (SEM) Tescan Vega TS5136LS. The quantitative analysis of the elements on the electrode surface was determined by energy dispersive spectroscopy (EDS).

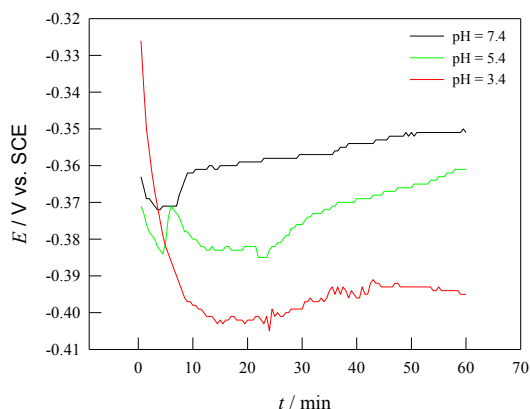
**3. Results**

Figure 1 shows the open circuit potential  $E_{oc}$  measurements for the CuAlMnTi alloy in 0.9% NaCl solution ( $T = 37^\circ \text{C}$ ) at different pH of the solution. Immediately after immersion in the solution  $E_{oc}$  was shift towards negative potential due to the adsorption of the chloride ions on the electrode surface. The highest negative drop of potential was recorded in the NaCl solution with the lowest pH value ( $\text{pH} = 3.4$ ). The initial decline in potential is followed by its stabilization and change in the positive direction indicating formation of protective surface layer. From the Figure 1 it can be seen that  $E_{oc}$  for the CuAlMnTi alloy in NaCl solution at  $\text{pH} = 7.4$  and  $5.4$  have similar values, and the value of  $E_{oc}$  for the measurement in NaCl solution  $\text{pH} = 3.4$  have the most negative values. Increasing the electrolyte temperature also leads to the displacement of the open circuit potential value towards negative values.

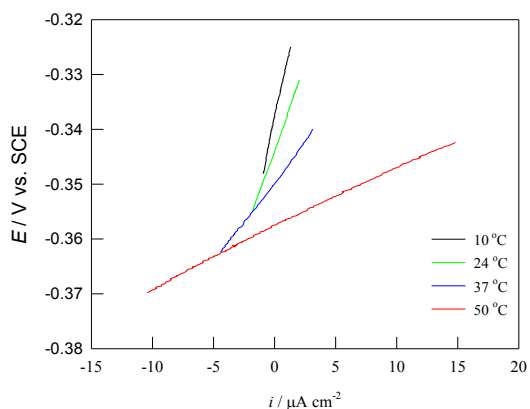
Linear polarization measurements were conducted in order to determine the influence of temperature and pH of the NaCl solution on polarization resistance values. In a linear polarization measurement, the potential vs. current density is measured in a narrow area around the  $E_{oc}$  and the slope of the potential-current density curve is then calculated and equal to  $R_p$  value. As  $R_p$  value is reverse proportional to the corrosion current density ( $i_{corr}$ ), higher value of  $R_p$  means lower value of  $i_{corr}$  i.e. lower corrosion.

Figure 1 shows the results of linear polarization measurements for CuAlMnTi alloy in 0.9% NaCl solution ( $\text{pH} = 37^\circ \text{C}$ ) at different electrolyte temperature. The slopes of the linear parts of the curves decreased with increasing electrolyte temperature indicating higher corrosion of CuAlMnTi in NaCl solution. Lowering the pH of the solution has a similar effect on the values of polarization resistance.

The potentiodynamic polarization behaviour of the alloy in 0.9 % NaCl solution ( $T = 37^\circ \text{C}$ ) with different pH values are presented in Figure 3. Lowering the pH values of NaCl solution lead to the increase in anodic and cathodic current density resulting in the higher value of the corrosion current density. Corrosion parameters for CuAlMnTi alloy obtained by polarization measurements, are given in Table 1



**Figure 1.** Variation of the open circuit potentials with time for the CuAlMnTi alloy in 0.9% NaCl solution at different pH values of solution



**Figure 2.** Results of linear polarization measurements for CuAlMnTi alloy in 0.9% NaCl solution (pH = 7.4) at different electrolyte temperatures

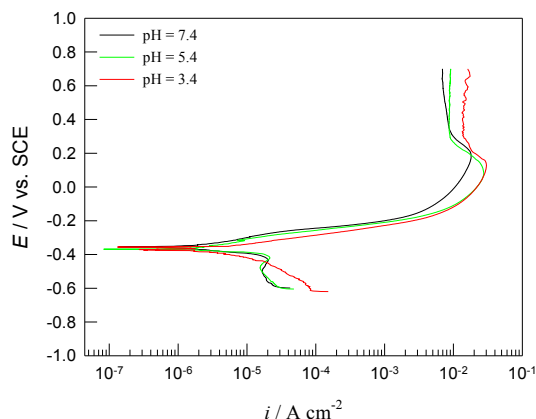


**Figure 3.** Potentiodynamic polarization curves for CuAlMnTi alloy in 0.9% NaCl solution (T = 37 °C) at different pH values

**Table 1.** Corrosion parameters for CuAlMnTi alloy in 0.9% NaCl solution

Measurement conditions	$E_{corr}$ / V	$i_{corr}$ / $\mu\text{A cm}^{-2}$	$R_p$ / $\text{k}\Omega \text{ cm}^2$
10 °C; pH = 7.4	-0.314	1.17	9.440
24 °C; pH = 7.4	-0.339	1.62	4.214
37 °C; pH = 7.4	-0.357	1.94	2.909
37 °C; pH = 5.4	-0.365	2.16	2.456
37 °C; pH = 3.4	-0.362	4.03	1.194
50 °C; pH = 7.4	-0.352	2.80	1.395

After polarization measurements, electrode surfaces were cleaned ultrasonically in deionized water, dried in desiccator and then photographed in macro mode with digital camera Canon Ixus 1000 and examined with light microscope. Results of these investigations are presented in Figure 4.

From the Figure 4 it can be seen that at higher electrolyte temperatures on the surface of the electrode there are more corrosion damages as well as more corrosion products. Pitting corrosion is observed at the highest investigated temperature (50 °C) while on lower temperatures uniform corrosion take place.

More detailed information on the electrodes surface condition after electrochemical measurement was obtained by scanning electron microscope, while the elemental composition was determined by XRD method, and the results are shown in Figures 5 and 6.

After potentiodynamic polarization measurements at 10 °C corrosion products can be found on the electrode surface which contains all of the alloying elements along with chloride and oxide (Figure 5 a) and b). Reduction in the percentage of alloying elements indicates its dissolution from the surface and the formation of chloride and oxide compounds. Potentiodynamic polarization measurements at 50 °C leads to significant corrosion damages on the electrode surface (Figure 6 a)). EDS analysis revealed significant reduction in % of all alloying elements (Figure 6 b)). The slightest reduction was noted for Ti, which is also the most stable element of this alloy.

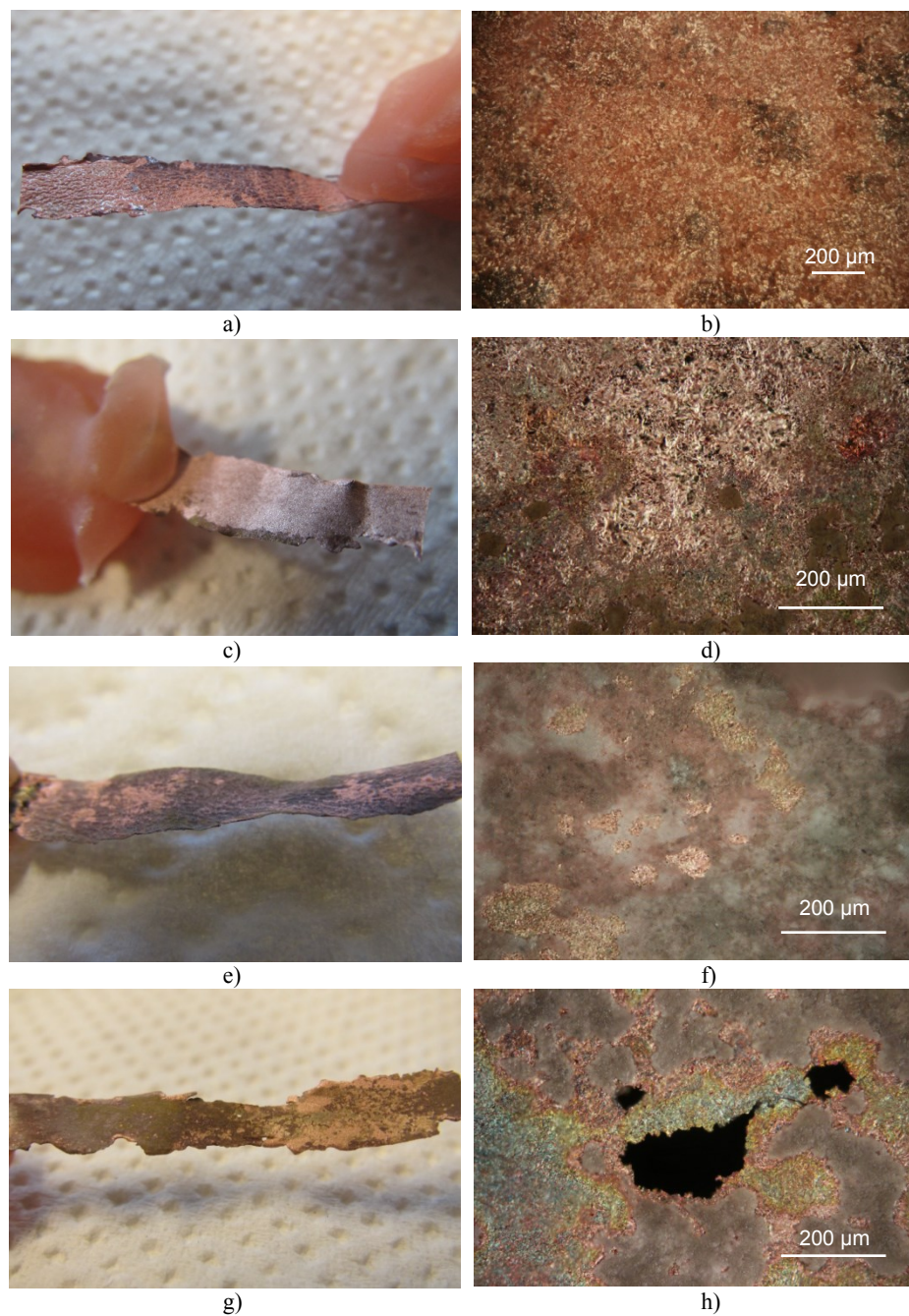


**Figure 4.** Macro images and optical micrographs of the corroded CuAlMnTi alloy surface in 0.9% NaCl solution at 10 °C a) and b); 24 °C c) and d); 37 °C e) and f) and 50 °C g) and h)



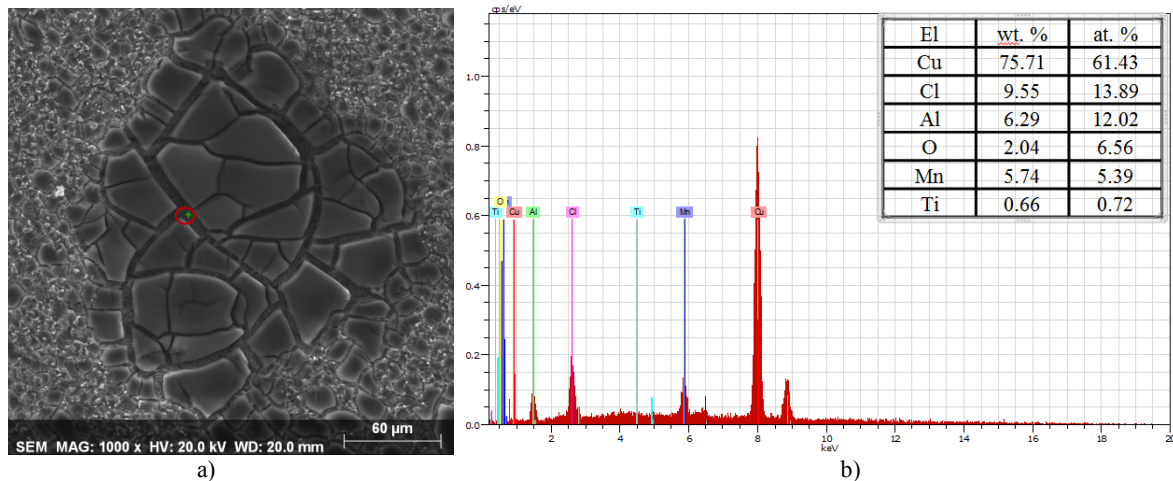


**Figure 5.** a) SEM images of the CuAlMnTi alloy surface after potentiodynamic polarization measurement in 0.9% NaCl solution (pH = 7.4, T = 10 °C); b) EDS analysis

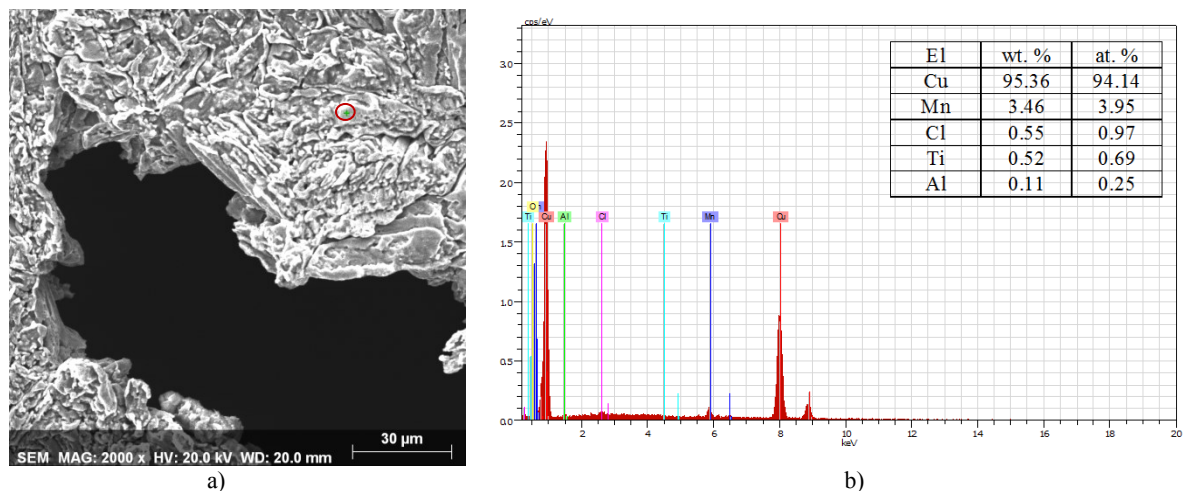


**Figure 6.** a) SEM images of the CuAlMnTi alloy surface after potentiodynamic polarization measurement in 0.9% NaCl solution (pH = 7.4, T = 50 °C); b) EDS analysis

#### 4. Conclusions

- Open circuit potential for the CuAlMnTi alloy shifts in the negative direction by decreasing the pH value of the 0.9% NaCl solution. Increasing the electrolyte temperature also leads to the displacement of the open circuit potential value towards negative values.
- Increase in electrolyte temperature as well as decrease pH value of NaCl solution leads to decrease the polarization resistance values and increase the values of corrosion currents density, which indicates a more intense corrosion process.
- Macro images of the electrode surfaces after polarization measurements with a digital camera

and an light microscope have shown that increasing the electrolyte temperature increases the surface damages of the electrode due to more intense corrosion. Pitting corrosion is observed at the highest investigated temperature while on lower temperatures uniform corrosion take place.

- SEM surface images of CuAlMnTi electrodes after polarization measurements have confirmed that with elevation electrolyte temperature a more intense corrosion attack occurs. EDS surface analysis indicated all alloying elements on the electrode surface along with oxygen and chlorine for the measurements at 10 °C. For the measurements at 50 °C dominant element on the surface is copper, while other elements are present in significantly less% than in initial composition of the alloy.



## Acknowledgements

This work has been fully supported by the Croatian Science Foundation under the project HRZZ-IP-2014-09-3405.

## REFERENCES

- [1] Ivanić I., Gojić M., Kožuh S., (2014), *Slitine s prisjetljivosti oblika (I. dio): najznačajnija svojstva*, Kem. Ind. 63, p 323-330.
- [2] Ivanić I., Gojić M., Kožuh S., (2014), *Slitine s prisjetljivosti oblika (II. dio): podjela, proizvodnja i primjena*, Kem. Ind. 63, p. 331-344.
- [3] Saud S. N., Hamzah, E., Abubakar T., Bakhsheshi-Rad H. R., (2015), *Microstructure and corrosion behavior of Cu-Al-Ni shape memory alloys with Ag nanoparticles*, Materials and Corrosion 66, p. 527-534.
- [4] Sobrero C. E., Roca P. La., Roatta A., Bolmaro R. E., Malarria J. (2012), *Shape memory properties of high textured Cu-Al-Ni-(Ti) alloys*, Mater. Sci. Eng. A, 536, p 207-215.
- [5] Sathish S., Mallik U. S., Raju T. N., (2014), *Microstructure and shape memory effect of Cu-Zn-Ni shape memory alloys*, JMMCE, 2, p 71-77.
- [6] Kainuma, R., Takahashi, S., Ishida, K. (1996), *Thermoelastic Martensite and Shape Memory Effect in Ductile Cu-Al-Mn Alloys*, Metallurgical and Materials Transactions A, 27A, p 2187-2195.
- [7] Kainuma, R., Satoh, N., Liu, X. J., Ohnuma, I. and Ishida, K. (1998) *Phase Equilibria and Heusler Phase Stability in Cu-Rich Portion of the Cu-Al-Mn System*, Journal of Alloys and Compounds, 266, 191-200.
- [8] Gojić M., Vrsalović L., Kožuh S., Kneissl A., Anžel I., Gudić S., Kosec B., Kliškić M., (2011), *Electrochemical and microstructural study of Cu-Al-Ni shape memory alloy*, J. Alloy. Compd. 509 p 9782-9790.
- [9] Rittapai A., Urapepon S., Kajornchaivakul J., Harniratisai C., (2014), *Properties of experimental copper-aluminium-nickel alloys for dental post and core applications*, J. Adv. Prosthodont, 6, p 215-223.
- [10] Yang S., Zhang F., Wu J., Lu, Y., Shi Z. Wang C. Liu X. (2017), *Superelasticity and shape memory effect in Cu-Al-Mn-V shape memory alloys*, Materials and Design 115, p 17-25.
- [11] Kožuh, S., Gojić, M., Ivanić, I., Holjevac Grgurić, T., Kosec, B., Anžel, I., (2018), *The Effect of heat treatment on the microstructure and mechanical properties of Cu-Al-Mn shape memory alloy*, Kem. Ind., 67, p 11-17.
- [12] Alaneme, K. K., Okotete, E. A. Bodunrin M. O., (2017), *Microstructural analysis and corrosion behavior of Fe, B and Fe-B-modified Cu-Zn-Al shape memory alloys*, Corros. Rev., 35, p 1-9.
- [13] Matsuoka, S., Hasebe, M., Oshima R., Fujita F. E., (1983) *Improvement of ductility of melt spun Cu-Al-Ni shape memory alloy ribbons by addition of Ti or Zn*, Japanese Journal of Applied Physics, 22, p L528-L530.
- [14] Bizjak, M., Karpe, B., Jakša, G., Kovač, J., (2013), *Surface precipitation of chromium in rapidly solidified Cu-Cr alloys*, Apply. Surf. Sci. 277, p 83-87.
- [15] Kim, Y-W., Yun, Y-M., Nam, T-H., (2006), *The effect of the melt spinning processing parameters on the solidification structures in Ti-30 at.% Ni-20 at.% Cu shape memory alloys*, Mat. Sci. Eng. A, 438-440, p 545-548.
- [16] Adachi K., Shoji K., Hamada Y., (1989), *Formation of (X) phases and origin of grain refinement effect in Cu-Al-Ni shape memory alloys added with titanium*, ISIJ Int., 29, p 378-87.
- [17] Morris MA, Gunter S., (1992), *Effect of heat treatment and thermal cycling on transformation temperatures of ductile Cu-Al-Ni-Mn-B alloys.*, Scripta Metallurgica et Materiala. 26, p 1663-1668.

# The influence of copper content on corrosion behavior of ductile iron and austempered ductile iron

Ladislav VRSALOVIĆ<sup>1)</sup>, Nikša ČATIPOVIĆ<sup>2)</sup>, Dražen ŽIVKOVIĆ<sup>2)</sup>, Zvonimir DADIĆ<sup>2)</sup>, Stjepan KOŽUH<sup>3)</sup>, Mirko GOJIC<sup>3)</sup> and Josip BATINOVIĆ<sup>2)</sup>

<sup>1)</sup> University of Split, Faculty of Chemistry and Technology, Ruđera Boškovića 35, 21000 Split, Croatia

<sup>2)</sup> University of Split, Faculty of Electrical Engineering, Mechanical Engineering and Naval Architecture, Ruđera Boškovića 32, 21000 Split, Croatia

<sup>3)</sup> University of Zagreb, Faculty of Metallurgy, Aleja narodnih heroja 3, 44103 Sisak, Croatia

ladislav@ktf-split.hr  
niksa.catipovic@fesb.hr  
drazen.zivkovic@fesb.hr  
zvonimir.dadic@fesb.hr  
gojic@simet.hr  
kozuh@simet.hr  
jbatin00@fesb.hr

## Keywords

Ductile Iron  
Austempered ductile iron  
SEM  
EDS

**Abstract:** The effect of copper content on corrosion behavior of ductile iron and austempered ductile iron was investigated in 0.5 mol dm<sup>-3</sup> NaCl solution at T = 20°C by open circuit potential measurements, linear and potentiodynamic polarisation methods. Ductile iron specimens used in this paper had: 0.031 wt.% Cu and 0.91 wt.% Cu. Specimens were austenitised at 850°C for 60 min and then austempered at 420°C for 60 min in 50% NaNO<sub>3</sub> and 50% KNO<sub>3</sub> salt bath. The mechanism of the corrosion attack developed on the material surface was analysed by light microscopy, scanning electron microscopy (SEM) and energy dispersive X-ray analysis (EDX). The results of the electrochemical investigations indicated that corrosion rate generally decrease with the increase in copper content in alloy. Also, higher corrosion resistance showed austempered ductile iron samples compared to ductile iron samples with the same chemical composition.

## Utjecaj sadržaja bakra na korozijsko ponašanje žilavog lijeva i izotermički poboljšanog žilavog lijeva

*Izvorni znanstveni rad*

**Sažetak:** Utjecaj sadržaja bakra na korozijsko ponašanje žilavog lijeva i izotermički poboljšanog žilavog lijeva ispitano je u 0.5 mol dm<sup>-3</sup> NaCl otopini pri T = 20 °C mjerenjem potencijala otvorenog strujnog kruga, metodom linearne i potenciodinamičke polarizacije. Uzorci žilavog lijeva korišteni u ovom radu su imali: 0,031 wt.% Cu and 0,91 wt.% Cu. Uzorci su austenitizirani na 850°C i držani 60 min te potom izotermički poboljšani na 420°C i držani 60 min u solnoj kupki sastava 50% NaNO<sub>3</sub> i 50% KNO<sub>3</sub>. Mehanizam korozijskog napada analiziran pomoću svjetlosnog mikroskopa, pretražnog elektronskog mikroskopa i energetske disperzivne analize X-zrakama (EDS). Rezultati elektrokemijskih mjerenja pokazali su da dolazi do smanjenja brzine korozije s povećanjem sadržaja bakra u leguri. Također, veću korozijsku otpornost pokazali su uzorci izotermički poboljšanog lijeva u odnosu na uzorke žilavog lijeva istog kemijskog sastava.

## 1. Introduction

Ductile (nodular) irons are high carbon cast ferrous materials with the composition similar to grey iron [1, 2]. Ductile irons are widely used in various industrial applications such as production of machine parts, tubes, automotive parts etc. [3-5]. The reason for its great use is its advantages over steel castings and grey iron castings. The strength, hardness and wear resistance of ductile iron can be increased by appropriate heat treatment and alloying. Through austempering treatment, ductile iron can be unique material in which acicular ferrite and retained austenite are both in its microstructure [6]. Austempered ductile iron (ADI) was introduced in the 1970s, and since then its application has been growing steadily because of its high tensile strength, good fatigue resistance under dynamic loading conditions and high wear resistance [5-9]. Most studies have focused on the

investigations of mechanical properties of ductile and austempered irons but the related information on the corrosion behavior of these materials appears to be limited. This paper deals with the investigations of the influence of Cu content on corrosion behaviour of the ductile iron and austempered ductile iron in 0.5 mol dm<sup>-3</sup> NaCl solution. The as-cast specimens of ductile iron were first austenitised at 850°C for 60 min and then austempered in 50% NaNO<sub>3</sub> - 50% KNO<sub>3</sub> salt bath at 420°C for 60 min to produce ADI.

## 2. Experimental procedure

### 2.1. Sample preparation

The working electrodes were made from ductile iron cylindrical samples Φ10 x 8 mm which were soldered on insulated copper wire and then protected by two-component epoxy resin leaving a surface area of 0.5 cm<sup>2</sup>

to contact the solution. The chemical composition of the used ductile iron samples is shown in Table 1.

The electrochemical cell was a three-electrode glass cell, with a platinum counter electrode and saturated calomel reference electrode. Before each experiment, the working electrode was polished mechanically using successive grades of emery papers up to 1200 grit, degreased ultrasonically in ethanol, washed with deionised water and transferred quickly to the electrolytic cell. Electrochemical measurements were carried out in a stagnant, naturally aerated chloride solution ( $0.5 \text{ mol dm}^{-3} \text{ NaCl}$ ,  $T = 20^\circ \text{C}$ ). The electrochemical polarization measurements were performed using the Princeton Applied Research PAR M 273A potentiostat/galvanostat. The potentials were referred to the saturated calomel electrode (SCE).

The evaluation of corrosion behaviour of ductile iron and austempered ductile iron in  $0.5 \text{ mol dm}^{-3} \text{ NaCl}$  solution

were performed by open circuit potential measurements ( $E_{oc}$ ) in 60 min time period, linear polarization method in the potential region of  $\pm 20 \text{ mV}$  around corrosion potential, with the scanning rate of  $0.2 \text{ mV s}^{-1}$  and potentiodynamic polarization method in the potential region of  $-0.250 \text{ V}$  to  $0.600 \text{ V}$  towards open circuit potential, with the scanning rate of  $0.5 \text{ mV s}^{-1}$ .

After the polarization measurements the surface of the electrode were washed in deionized water, dried in the desiccator and then visualized by Canon IXUS1000 camera in macro mode and the light microscope MXFMS-BD, Ningbo Sunny Instruments co.. A more detailed surface analysis was performed with Scanning Electron Microscope Tescan Vega 5136 MM paired with Energy Dispersive Spectroscopy Microscopy (SEM/EDS).

**Table 1.** Chemical composition of ductile iron samples

wt.%	C	Si	Mn	Cu	S	P	Cr	V	Ni	Mo	Al	Ti	Sn	W	Mg
	3.63	2.61	0.135	0.031	0.0035	0.022	0.005	0.004	0.085	0.003	0.017	0.013	0.033	0.017	0.041
	3.63	2.61	0.135	0.91	0.0035	0.022	0.005	0.004	0.085	0.003	0.017	0.013	0.033	0.017	0.041

## 2.2. Electrochemical measurements

Open-circuit potentials of ductile iron and austempered ductile iron were followed over 60 min in  $0.5 \text{ mol dm}^{-3}$  chloride solution at  $20^\circ \text{C}$  and the results were shown in Fig. 1 for samples that contain 0.031% and 0.91% Cu.

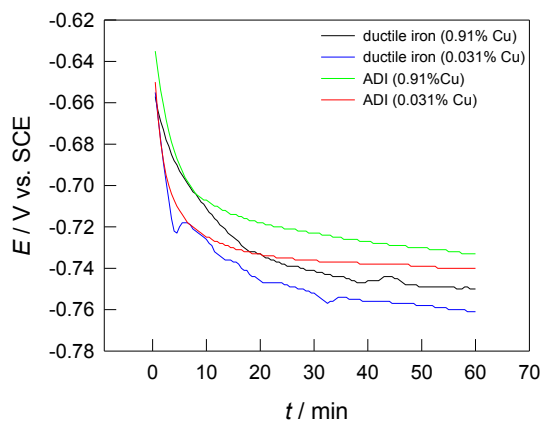


**Figure 1.** Variation of the open-circuit potentials of ductile iron and austempered ductile iron (ADI) with time in  $0.5 \text{ mol dm}^{-3} \text{ NaCl}$  solution, at  $20^\circ \text{C}$

The electrode potentials for all investigated samples shifts to the negative values after immersion into the electrolyte solution due to the adsorption of chloride ions on the electrode surface. This change is most noticeable in the first 20 minutes of electrode immersion, after which potential changes with time become less pronounced and the stabilization of the open circuit potential values occurred. It can be seen that higher content of Cu in samples leads to the evolution of the

positive values of  $E_{oc}$  of ductile iron and austempered ductile iron. Also, austempered ductile iron samples showed more positive  $E_{oc}$  values which indicate higher corrosion resistance compared with ductile iron samples. Linear polarization measurements were performed in order to determine the values of polarization resistance, which represent the resistance of materials to corrosion. Polarization resistance is defined as the resistance of the specimen to oxidation during the application of an external potential. Registered  $R_p$  values are contrariwise proportional to the corrosion current (higher polarization resistance means lower corrosion current). Results of the examination were presented in Fig. 2 for the samples of ductile iron and austempered ductile iron which contains 0.031% Cu.

Linear polarization resistance is defined by the slope of the polarization curve near the corrosion potential, by the equation (1):

$$R_p = \frac{\Delta E}{\Delta i} \quad (\Omega \text{ cm}^2) \quad (1)$$

Values of polarization resistance for ductile iron samples and austempered ductile iron samples were presented in Table 2. The austempered ductile iron sample has higher values of polarization resistance which means that have higher corrosion resistivity.

Final electrochemical method which was used in this investigation was potentiodynamic polarization method which was performed in wide potential area from  $-250$  to  $600 \text{ mV}$  versus  $E_{oc}$ . Results of the examination were presented in Fig. 2 for the samples of ductile iron and austempered ductile iron which contains 0.031% Cu.

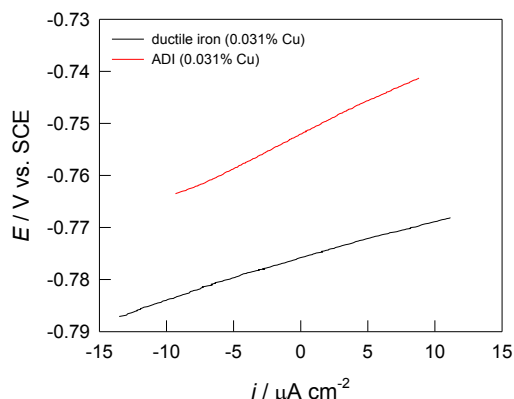


**Figure 2.** Linear polarization curves for ductile iron and austempered ductile iron in 0.5 mol dm<sup>-3</sup> NaCl solution, at 20 °C

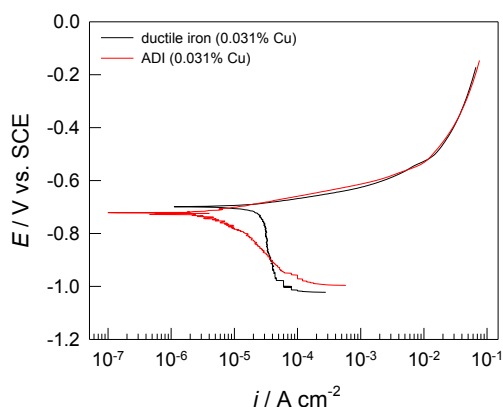


**Figure 3.** Potentiodynamic polarization curves for ductile iron and austempered ductile iron in 0.5 mol dm<sup>-3</sup> NaCl solution, at 20 °C

The differences in corrosion behaviour between ductile iron and austempered iron are visible in the cathodic part of the polarization curve in which austempered iron samples show lower cathodic current density values, which result with the less value of the corrosion current density. Corrosion parameters for ductile iron and austempered ductile iron as obtained by polarization measurements, are given in Table 2.

**Table 2.** Corrosion parameters for ductile iron and austempered iron in 0.5 mol dm<sup>-3</sup> NaCl solution

Sample	$E_{corr}$ / V	$i_{corr}$ / $\mu\text{A cm}^{-2}$	$R_p$ / $\text{k}\Omega \text{ cm}^2$
ductile iron (0.91% Cu)	-0.670	9.27	1.3505
ductile iron (0.031% Cu)	-0.693	21.78	0.771
ADI (0.91% Cu)	-0.672	6.34	1.7095
ADI (0.031% Cu)	-0.715	6.96	1.275

From the Table 2 it can be seen that higher Cu content in ductile and austempered ductile iron lead to the lower values of corrosion current density and to higher values of polarization resistance values, which means the higher corrosion resistance of the alloy.

After polarization measurements, electrode surfaces were cleaned ultrasonically in deionized water, dried in desiccator and whereupon electrodes were photographed in macro mode with digital camera Canon Ixus 1000 and also examination of their surfaces were done with light microscope.

Figure 4 shows the results of this surface examination for ductile iron and austempered ductile iron with Cu content of 0.031%.

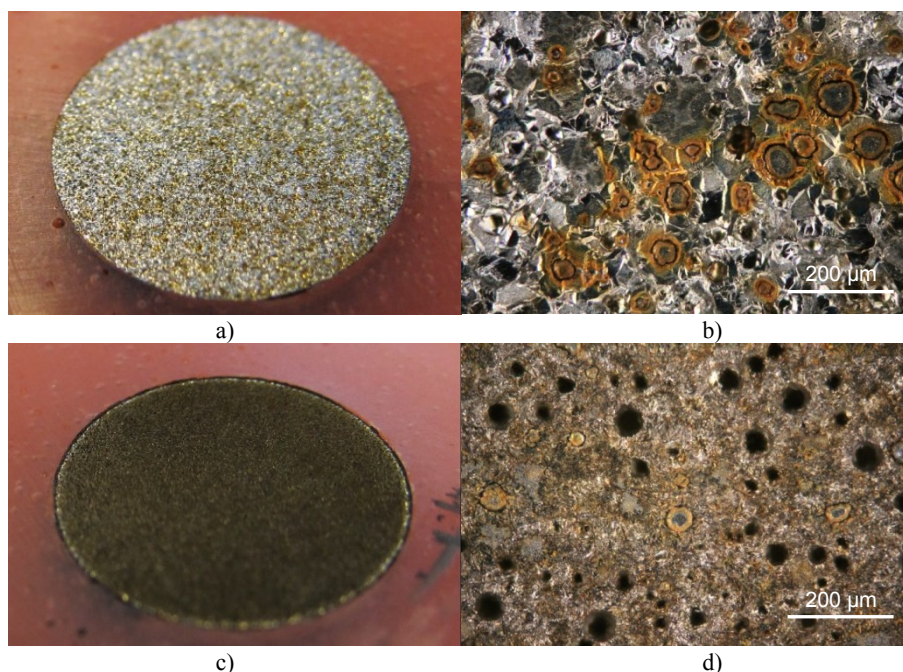


**Figure 4.** Macro images and optical micrographs of corroded surfaces of ductile iron a) and b) and austempered ductile iron c) and d)

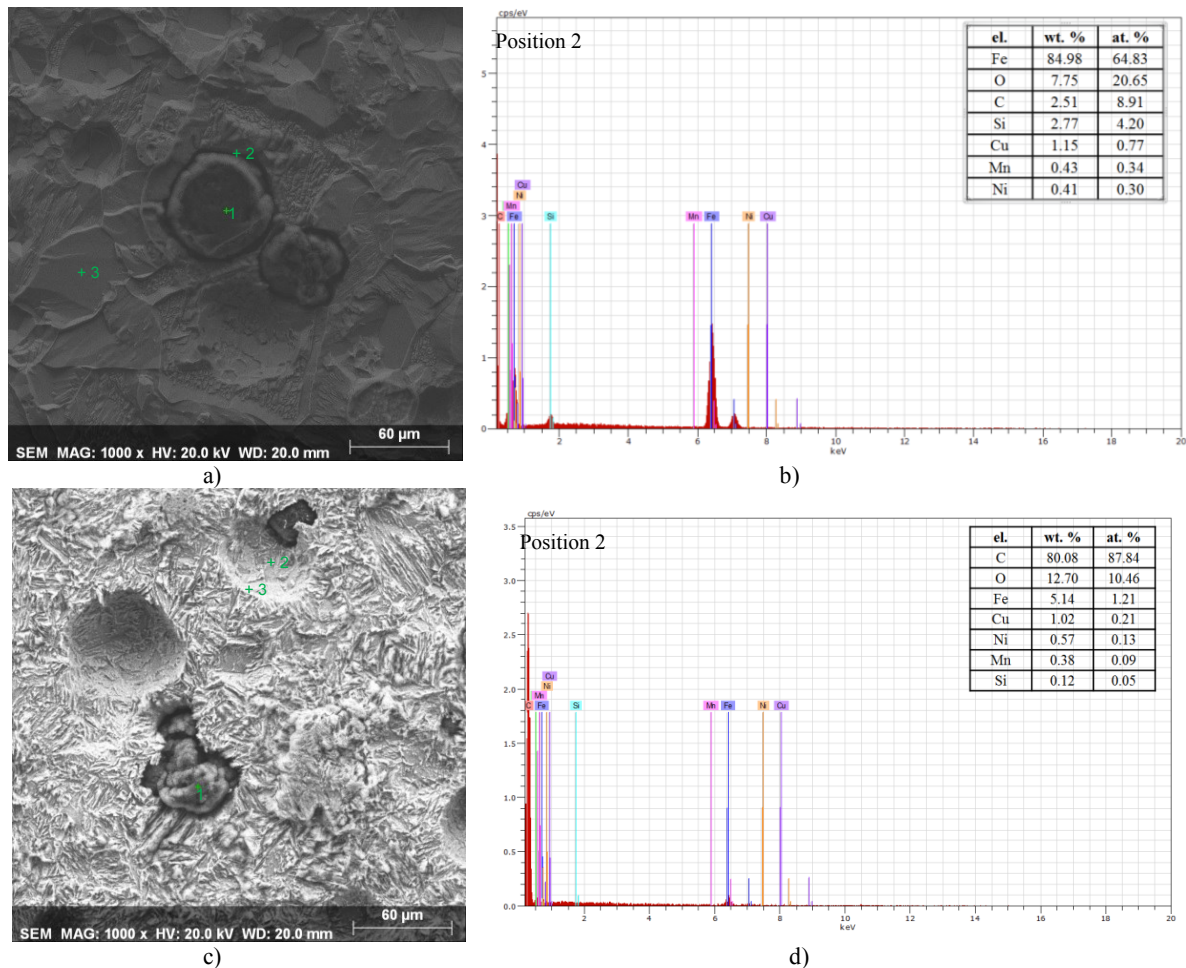


**Figure 5.** SEM images and EDS analysis of ductile iron (a) and b)) and austempered ductile iron (c) and d)) with Cu content of 0.031 %, after potentiodynamic polarization measurements

**Table 3.** EDS elemental analysis in different position on the electrode surface

Sample	Ductile iron			Austempered ductile iron		
	Position 1	Position 2	Position 3	Position 1	Position 2	Position 3
Element	wt. %	wt. %	wt. %	wt. %	wt. %	wt. %
C	87.49	2.51	0.93	74.69	80.08	7.18
O	8.69	7.75	1.77	18.40	12.70	7.51
Fe	2.02	84.98	92.85	5.02	5.14	82.64
Cu	0.91	1.15	1.21	0.79	1.02	0.82
Ni	0.38	0.41	0.59	0.58	0.57	0.27
Mn	0.35	0.43	0.70	0.38	0.38	0.55
Si	0.15	2.77	1.95	0.15	0.12	1.03

From the Figure 4 it can be seen significant differences in the appearance of the surface between corroded ductile iron and austempered ductile iron. On the Figure 4 b) it is clearly visible corroded matrix (anode) around the graphite (cathode) which results in corrosive cracks. This corrosive appearance was indicative of graphite corrosion and uniform attack. Corroded surface of ADI have significant less corrosive cracks on surface which can be explained due to occurrence of the retained austenite in the microstructure [7].

Detail surface morphology examinations of the corroded samples were examined by scanning electron microscope (SEM). The quantitative analysis of the elements on the electrode surface was determined by energy dispersive spectroscopy (EDS). Results of SEM/EDS analysis of ductile and austempered iron surface after were shown in Figure 5. EDS elemental analysis of electrode surfaces were presented in Table 3:

Figure 5 shows SEM micrographs of the ductile iron and austempered ductile iron after polarization test. As shown in Figures 5 a) and c), the matrix (anode) around the



graphite (cathode) was corroded to form the corrosive cracks, and peel-off of the graphite was observed on the surfaces of the both specimens. This corrosive appearance was indicative of graphite corrosion and uniform attack. In the cases of ADI and the phenomenon of peel-off of the graphite still took place, but uniform attack was reduced due to the occurrence of the retained austenite in the microstructure [10]. The published research about corrosion of ductile and austempered ductile iron in literature indicated that the corrosion behaviour of ductile iron depends on the nodular graphite quantity as well as the retained austenite content in the microstructure, and that the corrosion resistance is related to the interface of the graphite/matrix [7,11]. A lower nodular graphite quantity and more retained austenite content which were achieved by thermal processing and conversion of ductile iron in austempered ductile iron could provide better corrosion resistance which were confirmed in this investigations. The EDS analysis was performed on 3 different sites on the sample surface and the results of the analysis are shown in Figure 5 b) and d) and Table 3. Surface analysis have confirmed that round particle represent graphite nodules with highest content of carbon along with significantly less quantity of oxygen and iron. Matrix have the highest quantity of iron but the percentage of alloying elements, which have noble potential compare to iron, are higher than in the produced alloy before polarization measurements. This can be explained by dominant dissolution of iron from the matrix, which leads to increase the content of alloying elements on the surface.

### 3. Conclusion

- Higher content of Cu in samples leads to the evolution of the positive values of open circuit potential of ductile iron and austempered ductile iron. Also, austempered ductile iron samples showed more positive  $E_{oc}$  values which indicate higher corrosion resistance compared with ductile iron samples.
- Higher Cu content in ductile and austempered ductile iron lead to the lower values of corrosion current density and to higher values of polarization resistance values, which means the higher corrosion resistance of the alloy. Austempered ductile iron shows higher values of polarization resistance and lower values of corrosion current density which means higher corrosion resistance compared to ductile iron.
- Macro images and microscopic images of electrode surfaces after polarization measurements showed significant differences between ductile iron and austempered ductile iron samples which manifests in intensive graphite corrosion for ductile iron samples and

significant less corrosive cracks on surface of ADI, due to retained austenite in ductile iron structure which mitigate corrosion rate.

- Results of SEM/EDS analysis have shown that the surface of the samples was significantly damaged by corrosion. The corrosive appearance was indicative of graphite corrosion and uniform attack. In the cases of ADI and the phenomenon of peel-off of the graphite still took place, but uniform attack was reduced due to the occurrence of the retained austenite in the microstructure. EDS analysis have confirmed that round particle represent graphite nodules with highest content of carbon while around matrix have the highest quantity of iron, and the higher percentage of alloying elements than in the produced alloy before polarization measurements. This can be explained by dominant dissolution of iron from the matrix, which leads to increase the content of alloying elements on the surface.

### Acknowledgements

This work has been fully supported by Croatian Science Foundation under the project 5371.

### REFERENCES

- [1] Paris M., Bruniere B., (1957), *The corrosion resistance of ductile iron in sea water and petroleum tanker services*, Corrosion p 292-296.
- [2] Laque F. L., (1958), *The corrosion resistance of ductile iron*, Corrosion p 485-492.
- [3] Hemanth J. (2000) *The solidification and corrosion behaviour of austempered chilled ductile iron*, Journal of Materials Processing Technology, 101 p 159-166.
- [4] Hsu C.-H., Lin K.-T., (2011), *A study on microstructure and toughness of copper alloyed and austempered ductile irons*, Mater. Sci. Eng. A 528 p 5706-5712.
- [5] Harding, R. A.: *The production, properties and automotive applications of austempered ductile iron*, Kovove Mater., 45, 2007, p. 1-16.
- [6] Han Ch. F., Wang Q. Q., Sun Y. F., Li J. (2015), *Effects of molybdenum on the wear resistance and corrosion resistance of carbide austempered ductile iron*, Metallogr. Microstruct. Anal., 4 p 298-304.
- [7] Hsu C.-H., Chen M.-Li, (2010), *Corrosion behaviour of nickel alloyed and austempered ductile irons in 3.5% sodium chloride*, Corros. Sci. 52, p 2945-2949.

- [8] Labrecque C, Gagne M, (1998), *Review ductile iron: fifty years of continuous development*, Can. Metall. Q. 37, p 343-378.
- [9] Gaston F., Jorge S., Ricardo D., (2008), *Abrasion resistance of ductile iron austempered by two step process*, Mater. Sci. Eng. A, 485, p 46-54.
- [10] Hsu C.-H., Lin K.-T., (2014), *Effects of copper and austempering on corrosion behavior of ductile iron in 3.5 pct sodium chloride*, Metallurgical and Materials Transactions A, 45, p. 1517-1523.
- [11] Krawiec H., Lelito J., Tyrała E., Banas' J., (2009), *Relationships between microstructure and pitting corrosion of ADI in sodium chloride solution*, J. Solid State Electrochem. 13 p. 935–942.

# Zagrijte se za uštedu.

Odabir EVN zemnog plina  
nećete ni osjetiti...  
Osim topline.

Zemni plin jedan je od najpovoljnijih izvora energije na tržištu.  
Potrošnja se može precizno regulirati i kontrolirati kako biste plaćali ono što zaista trebate.  
Odaberite EVN i cijele godine budite ugodno i sigurno opskrbljeni zemnim plinom.

**Priključite se na EVN zemni plin.**  
**0800 820 820**

[www.evn.hr](http://www.evn.hr)

Za ugodniji život. **EVN**



Split

*Tourist Board of Split*

TURISTIČKA ZAJEDNICA